

Solid Mechanics in Brazil 2011

EDITED BY

*Eduardo Alberto Fancello
Paulo de Tarso R. Mendonça
Marcílio Alves*

This book contains articles presented in the Second International Symposium on Solid Mechanics, held in Florianópolis, Brazil, 25-27 May 2011.

The book features articles on many topics, ranging from meshless methods, fatigue, failure, composite materials, structural impact, corrosion and optimisation.

It is believed that the forty chapters herein are a good sample of what is being investigated in this field by engineers and scientists working in Brazilian universities and research institutes.

The book is a valuable source of technical information and it is hoped that it can assist and inspire the investigator working in Solid Mechanics.

Published by ABCM

**Brazilian Society of
Mechanical Sciences and Engineering
ABCM - Symposium Series**

ISBN xxxxxxxx



EDITORS

*Eduardo Alberto Fancello
Paulo de Tarso R. Mendonça
Marcílio Alves*

Solid Mechanics in Brazil 2011



Solid Mechanics in Brazil

1102

*Edited by
Eduardo Alberto Fancello
Paulo de Tarso R. Mendonça
Marcílio Alves*

ABCM

Associação Brasileira de Engenharia
e Ciências Mecânicas



Solid Mechanics in Brazil 2011

Brazilian Society of Mechanical Sciences and Engineering

Ficha Catalográfica

ABCM – Associação Brasileira de Engenharia e Ciências Mecânicas
Fancello, Eduardo
Mecânica dos Sólidos / Eduardo Fancello, Paulo de Tarço R. Mendonça, Marcílio
Alves Associação Brasileira de Engenharia e Ciências Mecânicas, 2011

578p.
Inclui bibliografia

ISBN 978-85-85769-46-8

Preface

This book contains articles presented at the Third International Symposium on Solid Mechanics, held in Florianópolis, Brazil, 25-27 May 2011. The International Symposium on Solid Mechanics – MecSol – is the first Brazilian series of conference fully dedicated to this branch of the engineering science. It had its first edition in 2007 in São Paulo, then in Rio de Janeiro in 2009.

The MecSol Symposium is organized under the aegis of the Solid Mechanics Committee of the Brazilian Society of Mechanical Sciences and Engineering. The present book reflects the effort of the committee and authors to spread in the technical society knowledge in the field of Solid Mechanics.

As in the previous books, this edition features articles with focus on fundamental and applied issues, including computational, theoretical and experimental contributions, drawing upon the various branches of engineering science and the allied areas within applied mathematics, materials science, structural engineering and applied physics.

The editors would like to thank all the contributors to this volume for their effort in producing such fine articles. We also would like to thank Renato Yamassaki for formatting the whole book. Finally, we would like to acknowledge the support of the Brazilian Society of Mechanical Sciences and Engineering and the Department of Mechanical Engineering from the Federal University of Santa Catarina to this event.

Eduardo Fancello
Paulo de Tarço R. Mendonça
Marcílio Alves

Contents

A study of macroscopic failure of laminates with phases exhibiting softening hyperelasticity using a two-scale asymptotic homogenization method A.R. AGUIAR AND L.D. PÉREZ-FERNÁNDEZ	1
A load survey for a lifting operation of an emergency tower for electrical energy lines transmission A.R. ALBERTI, J.C. DE C. PEREIRA AND L.C. NICOLAZZI	13
Graphene based nanoparticles as ultrahigh frequency nanomechanical resonators: modal vibration response A.F. ÁVILA, A. SILVA NETO AND A.C. EDUARDO	25
A comparison of deterministic, reliability-based and risk-based structural optimization under uncertainty A.T. BECK AND W.J.S. GOMES	41
An elementwise least square approach for explicit integration methods applied to elasticity M.L. BITTENCOURT AND F.A.C. FURLAN	63
Numerical solution of boundary inverse problems for anisotropic solids I. BRILLA	77
Postbuckling analysis of aeronautical panels manufactured using friction stir welding technology I. CAVALLANTE, M.V. DONADON, A.R. DE FARIA, P. RIZZI, S.F.M. DE ALMEIDA	89
Mechanical behavior of GFRP laminates at varying strain rates and temperatures J.L.V. COELHO, J.M.L. REIS AND H.S. DA COSTA-MATTOS	103
Analysis of special hydrostatic tests performed in produced water pipelines H.S. DA COSTA MATTOS, L.M. PAIM AND J.M.L. REIS	113

A finite displacement visco-hypoelasticity model H.P.A. DE DEUS AND M.K. ALVES	131
A variational boundary element method based on generalized Westergaard stress functions N.A. DUMONT AND E.Y.M. VARGAS	143
On buckling enhancement of laminated plates with piezoelectric actuators via stress stiffening A.R. DE FARIA AND M.V. DONADON	159
Topology optimization with stress constraints using superconvergent patch recovery J.M.C. FARIAS, E.L. CARDOSO AND P.A. MUÑOZ-ROJAS	175
Multicriteria optimization of an aircraft reinforced composite panel subjected to non uniform loading A.P.C.S. FERREIRA AND S.F.M. DE ALMEIDA	197
Finite element analysis of reinforced concrete slabs regarded as elastoplastic multiphase media: the role of reinforced zone extent M.P. FIGUEIREDO, S. MAGHOUS AND A. CAMPOS FILHO	215
Dynamics and energy absorption of structural elements under blast and impact D. KARAGIOZOVA	231
Consideration of size effect multifractal theory in fracture analysis by means of the truss-like Discrete Element Method (DEM) L.E. KOSTESKI, I. ITURRIOZ AND J.D. RIERA	249
Vertical response of a rigid circular foundation embedded on a transversely isotropic bi-material interface J. LABAKI, E. MESQUITA AND N. RAJAPAKSE	267
Analysis and optimization of stepped conical shells with cracks J. LELLEP AND E. PUMAN	277
Simulating occupants injury in rollover crashes A. DE LIMA AND R.J. MARCZAK	291
Reliability-based design optimization strategies based on form: a review R.H. LOPEZ AND A.T. BECK	311
Improvements on the numerical structural assessment of a half scale model of a nuclear spent fuel elements transportation package under 9m drop tests M. MATTAR NETO, C.A. DE JESUS MIRANDA, G. FAINER AND R.P. MOURÃO	327

Limit moment of local wall thinning in rigid pipeline repaired with composite material under bending R. MATTEDI AND L.C.S. NUNES	341
Evaluating velocity and mass correction when scaling structures subjected to impact loading L.M. MAZZARIOL, R.E. OSHIRO, M.A.G. CALLE, R.T. MOURA AND M. ALVES	353
On the use of spherical, ellipsoidal and prismatic hulls to predict equivalent stress ranges in multiaxial fatigue M.A. MEGGIOLARO AND J.T.P. DE CASTRO	367
Modeling nonlinear viscoelastic behavior of high density polyethylene (HDPE): application of stress-time equivalence versus interpolation of rheological properties P.A. MUÑOZ-ROJAS, A. KÜHL, P.T.R. DE MENDONÇA, I.J. BENVENUTTI AND G.J. CREUS	381
Topology design of Kirchhoff plates based on topological derivative and a level-set domain representation A.A. NOVOTNY AND D.E. CAMPEÃO	401
Analysis of non-linear hyperelastic constitutive models under simple shear deformation L.C.S. NUNES	421
Peridynamic analysis for predicting damage initiation and growth in metallic and composite structures E. OTERKUS AND E. MADENCI	431
Hybrid and mixed variational principles for the fully nonlinear analysis of shells of Reissner-Mindlin type P.M. PIMENTA	445
Dynamical analysis of a van der Pol oscillators system used for human gait simulation A.C. DE PINA FILHO AND M.S. DUTRA	455
Teaching and assessing threshold concepts in solid mechanics using adaptive tutorials B.G. PRUSTY	467
An experimental investigation on the static structural behavior of helical bars M.A. RABELO, C.P. PESCE AND A.L.C. FUJARRA	477
Time domain analysis of concrete gravity dams using a generalized single degree of freedom approach P.M.V. RIBEIRO AND L.J. PEDROSO	489

Reliability assessment of composite plates against normally struck conical-nosed projectiles N.A. SIDDIQUI	505
Elastic collapse of corroded pipe repaired with composite material under uniform external pressure T.C. SILVA AND L.C.S. NUNES	517
Simultaneous structural and control design for piezoelectric actuated structures using topology optimization O.A.A. DA SILVEIRA AND J.S.O. FONSECA	527
Mechanical behavior of fiber-reinforcement beams with fiber orientation L. VANALLI, N.T. MASCIA, M.R. SCOARIS AND R.R. PACCOLA	541
Identification of material parameters for elastoplastic model using a Digital Image Correlation method J.M. VASSOLER, A.C.B. GUIMARÃES NETO, L.F.C. BOTEGA AND E.A. FANCELLO	555
Author Index	571

A study of macroscopic failure of laminates with phases exhibiting softening hyperelasticity using a two-scale asymptotic homogenization method

A. R. Aguiar, L. D. Pérez-Fernández

*Department of Structural Engineering, São Carlos School of Engineering,
University of São Paulo, Brazil. Av. Trabalhador São carlense 400, Centro,
13566-590
São Carlos – SP, Brazil*

Abstract

In classical hyperelastic models, the strain energy density becomes unbounded as the strain becomes large. In reality, defects, such as voids and microcracks, are created and accumulate inside a body as the strain becomes large, reducing its strength to further deformation. Also, no real material can sustain large enough strains. Based on these considerations, we investigate a class of softening hyperelastic materials that, while preserving classical hyperelastic behavior for moderate deformations, captures softening behavior of materials at large strains. It is based on the introduction of a limiter for the strain energy, which quantifies the amount of deformation the material can undergo hyperelastically before failing. Softening hyperelasticity has been successfully applied to various problems of interest in engineering and biomedicine that involve cavitation and fracture. To the best of our knowledge, the macroscopic failure induced by the microscopic softening of softening hyperelastic constituents of composite materials has not been studied yet. We adopt a homogenization-based approach by applying the two-scale asymptotic homogenization method to predict the macro-failure of laminate composites with softening hyperelastic phases; in particular, we investigate bilaminates under uniaxial deformation parallel to the lamination direction.

Keywords: hyperelasticity, softening, composites, asymptotic homogenization, material failure.

1 Introduction

Material failure is usually addressed via the phenomenological approach of damage mechanics. From the theoretical point of view, such an approach is known to be very flexible, as it allows considering physical processes that cause macroscopic damage at small length scales. In practice, however, the calibration of damage model via experimental procedures is anything but simple, as measuring relevant damage parameters and other technicalities are typically complex. Thus, alternative theories describing material failure in ways simpler than traditional damage mechanics are desirable [1–4].

An alternative theory is based on an atomistic analysis of fracture, linking material debonding to atomic separation. In [5, 6], the atomistic and continuum material descriptions are combined to simulate the failure process. The ensuing method applies the Cauchy–Born rule linking microscopic and macroscopic length scales to certain empirical potentials, which include the possibility of full atomic separation. Such continuum-atomistic linkage leads to the formulation of a macroscopic strain energy function, which allows for softening and strain localization. The method is very effective at small length scales, where purely atomistic analysis becomes computationally intensive. However, addressing macroscopic damage becomes unpractical as it involves the numerical averaging of the inter-atomic potentials over a representative volume.

An alternative to the continuum-atomistic method addressing macroscopic failure is the so-called softening hyperelastic model presented in [7]. This is a phenomenological model in which softening is controlled by a limiter for the strain energy that quantifies the amount of deformation the material can undergo hyperelastically before failing. Therefore, any classical hyperelastic model can be enhanced by including softening in it, so that moderate strains will produce hyperelastic deformations while large ones will cause failure via hyperelastic softening.

In the present contribution, we use the softening hyperelastic model to investigate a composite material formed by microscopically-arranged hyperelastic constituents that can undergo softening. Can macroscopic failure of such material be described via a homogenization-based approach? This work is an attempt to address such a question, which has the potential of theoretically control the macro-failure in terms of the parameters describing phase failure. Here, the two-scale asymptotic homogenization method described in [8, 9] is applied to such endeavor.

2 Finite elastostatics

Let $B \subset \mathbb{R}^3$ be the region occupied by a heterogeneous body with volume $|B|$ and smooth boundary ∂B . Here, a material point of the body coincides with a point $\mathbf{X} \in B$ in the reference configuration. Let $\mathbf{x} : B \rightarrow \mathbb{R}^3$ be a deformation field acting on the body. The corresponding displacement field and deformation gradient are given by, respectively, $\mathbf{u}(\mathbf{X}) = \mathbf{x}(\mathbf{X}) - \mathbf{X}$ and

$$\mathbf{F} = \text{grad}\mathbf{x} = \mathbf{1} + \text{grad}\mathbf{u}, \quad \mathbf{X} \in B, \quad (1)$$

where $\text{grad} : \mathbb{R}^3 \rightarrow \mathbb{R}^3 \otimes \mathbb{R}^3$ is the gradient operator for vector fields, and $\mathbf{1}$ is the identity tensor. Then, $\mathbf{F}, \text{grad}\mathbf{u} : B \rightarrow \text{Lin}$, where Lin is the set of second-order tensors.

The body is in equilibrium under the action of a body force $\mathbf{b} : B \rightarrow \mathbb{R}^3$, that is,

$$\text{div}\mathbf{P} + \mathbf{b} = \mathbf{0}, \quad \mathbf{X} \in B, \quad (2)$$

where $\text{div} : \text{Lin} \rightarrow \mathbb{R}^3$ is the divergence operator for tensor fields, and $\mathbf{P} : B \rightarrow \text{Lin}$ is the first Piola-Kirchhoff stress tensor. In a rectangular Cartesian coordinate system fixed at the origin, definition (1) and equilibrium equation (2) are written as

$$F_{ij} = \frac{\partial x_i}{\partial X_j} = \delta_{ij} + \frac{\partial u_i}{\partial X_j}, \quad \mathbf{X} \in B \quad (3)$$

and

$$\frac{\partial P_{ij}}{\partial X_j} + b_i = 0, \quad \mathbf{X} \in B, \quad (4)$$

where $i, j \in \{1, 2, 3\}$, and F_{ij} , x_i , X_j , δ_{ij} , u_i , P_{ij} , and b_i are the components of \mathbf{F} , \mathbf{x} , \mathbf{X} , $\mathbf{1}$, \mathbf{u} , \mathbf{P} and \mathbf{b} , respectively. In (4) and, unless stated otherwise, in what follows, the usual summation convention over repeated lower case Latin subscripts is adopted.

The constitutive behavior of the body is formally stated by an endomorphism over Lin such that $\mathbf{F} \mapsto \mathbf{P}(\mathbf{F})$. The realization of such constitutive law will depend on the particularities of the material to be studied. In this work, the body is assumed to behave hyperelastically, that is, there exists a stored energy function $W : Lin \rightarrow \mathbb{R}$, $\mathbf{F} \mapsto W(\mathbf{F})$, such that

$$P_{ij} = \frac{\partial W}{\partial F_{ij}}, \quad \mathbf{X} \in B. \quad (5)$$

Substitution of (5) into the equilibrium equations (4) yields

$$\frac{\partial}{\partial X_j} \left[\frac{\partial W}{\partial F_{ij}} \right] + b_i = 0, \quad \mathbf{X} \in B, \quad (6)$$

which, together with (1) and an appropriate boundary condition, say,

$$\mathbf{u} = \bar{\mathbf{u}}, \quad \mathbf{X} \in \partial B, \quad (7)$$

where $\bar{\mathbf{u}} : \partial B \rightarrow \mathbb{R}^3$ is a known displacement field over the boundary, defines a boundary value problem for the determination of the displacement $\mathbf{u} : B \rightarrow \mathbb{R}^3$.

A well-known particular case of (7) corresponds to the uniform displacement $\bar{\mathbf{u}} = (\bar{\mathbf{F}} - \mathbf{1}) \mathbf{X}$, where $\bar{\mathbf{F}} = \langle \mathbf{F} \rangle$ and $\langle \cdot \rangle = \frac{1}{|B|} \int_B (\cdot) d\mathbf{X}$ is the average operator over the body. In this case, a usual practice is to take $\mathbf{u} = \bar{\mathbf{u}} + \mathbf{u}'$ where $\mathbf{u}' = \mathbf{0}$ on the boundary. Then, it follows from (1) that $\mathbf{F} = \bar{\mathbf{F}} + \mathbf{F}'$, where $\mathbf{F}' = \text{grad} \mathbf{u}'$ and $\langle \mathbf{F}' \rangle = \mathbf{0}$.

3 Softening hyperelasticity

In classical hyperelastic models, the stored energy function W grows unbounded as the deformation gradient tends to infinity:

$$\|\mathbf{F}\| \rightarrow \infty \Rightarrow W \rightarrow \infty, \quad (8)$$

where $\|\cdot\|$ is an appropriate norm. This is an ideal elastic behavior since no real material is able to undergo increasingly large deformations without exhibiting irreversible changes due to the formation

and accumulation of micro-defects. To account for more realistic behavior, we introduce $\psi : Lin \rightarrow \mathbb{R}$ which keeps the classical hyperelastic behavior predicted by W under moderate deformations and tends to a limiting constant value $\Phi \in \mathbb{R}$ accounting for material failure as the deformation becomes large, that is,

$$\|F\| \rightarrow \infty \Rightarrow \psi \rightarrow \Phi. \quad (9)$$

An expression for ψ that satisfies (9) is proposed in [7] and is given by

$$\psi = \Phi - \Phi \exp \left\{ -\frac{W}{\Phi} \right\}. \quad (10)$$

Observe from (10) that the following properties hold:

$$W = 0 \Rightarrow \psi = 0, \quad (11)$$

$$W \rightarrow \infty \Rightarrow \psi \rightarrow \Phi, \quad (12)$$

$$W \ll \Phi \Rightarrow \psi \approx W. \quad (13)$$

Observe from the exposition above that (12) satisfies (9). Property (13) follows by taking the power series expansion of (10) and clearly states that classical hyperelastic behavior is kept. By replacing W with ψ in (5), we obtain

$$P_{ij} = \frac{\partial \psi}{\partial F_{ij}} = \frac{\partial W}{\partial F_{ij}} \exp \left\{ -\frac{W}{\Phi} \right\}. \quad (14)$$

4 Composites

In this work, we consider a heterogeneous body composed by N distinct phases that are periodically distributed inside the body. This is the case, for instance, of a bilaminate composed of two types of lamina with an alternating stacking sequence. Each phase occupies a region B_r with volume $|B_r|$ and boundary ∂B_r , such that $\bigcup_{r=1}^N B_r = B$ and $B_r \cap B_s = \emptyset$, $\forall r, s = 1, 2, \dots, N, r \neq s$. We use the characteristic function $\chi_r : B \rightarrow \{0, 1\}$ to identify each phase in the composite material. Assuming local softening hyperelastic behavior, phase r is modeled by an energy function $\psi_r : Lin \rightarrow \mathbb{R}$ defined as in (10), that is, related to a classically-hyperelastic energy function $W_r : Lin \rightarrow \mathbb{R}$ and with the corresponding failure energy Φ_r . Then, the stored energy density $\psi : Lin \times B \rightarrow \mathbb{R}$ is a piecewise function over B defined by

$$\psi = \psi_r \chi_r, \quad X \in B. \quad (15)$$

Substituting (15) in (14) and then substituting the resulting expression in (4), we obtain the equilibrium equations

$$\chi_r \frac{\partial}{\partial X_j} \left[\frac{\partial \psi_r}{\partial F_{ij}} \right] + b_i = 0, \quad \mathbf{X} \in B. \quad (16)$$

For the formulation of the problem to be complete, boundary conditions of the form (7) and continuity conditions for tractions and displacements on the interfacial surfaces $\Gamma_{rs} = \partial B_r \cap \partial B_s$, $\forall r, s = 1, 2, \dots, N, r \neq s$, must be imposed. The ideal case of perfectly bonded phases implies continuity of tractions and displacements across the interfaces, that is,

$$\llbracket P_{ij} \nu_j \rrbracket_{\Gamma_{rs}} = 0, \quad \llbracket \mathbf{u} \rrbracket_{\Gamma_{rs}} = \mathbf{0}, \quad (17)$$

where $\llbracket \cdot \rrbracket_{\Gamma_{rs}}$ denotes the jump operator across interface Γ_{rs} , and $\boldsymbol{\nu}$ is the unit normal vector to Γ_{rs} .

The solution of the boundary value problem given by (16), (17) and (7) is sought in a way similar to the one employed for linear composites, that is, we take $\mathbf{u} = \chi_r \mathbf{u}_r$ to be a piecewise linear vector field with $\mathbf{u}_r = \bar{\mathbf{u}} + \mathbf{u}'_r$ and $\chi_r \mathbf{u}'_r = \mathbf{u}'$. The corresponding deformation gradient is $\mathbf{F} = \chi_r \mathbf{F}_r$ with $\mathbf{F}_r \in Lin$ constant, $\mathbf{F}_r = \bar{\mathbf{F}} + \mathbf{F}'_r$ with $\mathbf{F}' = \chi_r \mathbf{F}'_r$ and $\mathbf{F}'_r = \text{grad} \mathbf{u}'_r$. With such considerations, we ensure compatibility of deformation. Also, note that $\langle \mathbf{F}' \rangle = \mathbf{0}$ and $\langle \mathbf{F} \rangle = \bar{\mathbf{F}}$ as above.

5 Two-scale asymptotic homogenization

Now, assume that the characteristic sizes of the phases in the heterogeneous body are small when compared to a characteristic size of the composite. For instance, the thicknesses of laminae in a laminate are much smaller than the thickness of the laminate. This means that the constitutive behavior of the composite exhibits rapid oscillations. Moreover, if the phases are periodically distributed inside the composite, that is, the composite can be reproduced by replicating some periodicity cell Ω inside the region B , so are such oscillations. In the case of a bilaminate, Ω is formed by any two consecutive laminae. The ratio of the characteristic size of Ω to the characteristic size of the composite is a small geometric parameter $\varepsilon > 0$. In order to account for these periodic oscillations, we define the local “fast” variable $\mathbf{Y} = \varepsilon^{-1} \mathbf{X}$. Using this definition, the average operator becomes $\langle \cdot \rangle = \frac{1}{|\varepsilon \Omega|} \int_{\varepsilon \Omega} (\cdot) d\mathbf{X} = \frac{1}{|\Omega|} \int_{\Omega} (\cdot) d\mathbf{Y}$.

The solution \mathbf{u} of the boundary value problem defined by (1), (7), and (14)-(17) is sought as a two-scale asymptotic expansion in powers of ε :

$$\mathbf{u} = \mathbf{u}^{(0)} + \varepsilon \mathbf{u}^{(1)} + \varepsilon^2 \mathbf{u}^{(2)} + O(\varepsilon^3), \quad (\mathbf{X}, \mathbf{Y}) \in B \times \Omega, \quad (18)$$

where the (macroscopic) displacement field $\mathbf{u}^{(0)} : B \rightarrow \mathbb{R}^3$ depends only on \mathbf{X} , while the other coefficients $\mathbf{u}^{(i)} : B \times \Omega \rightarrow \mathbb{R}^3$, $i \geq 1$, depend on both variables \mathbf{X} and \mathbf{Y} and are Ω -periodic in \mathbf{Y} . Notice that such Ω -periodicity of $\mathbf{u}^{(i)}$ implies that $\langle \text{grad} \mathbf{u}^{(i)} \rangle = \mathbf{0}$.

Substitution of (18) into (1) and substitution of the resulting expression into (5) together with the chain rule $\frac{\partial}{\partial X_j} (\cdot) \equiv \frac{\partial (\cdot)}{\partial X_j} + \frac{1}{\varepsilon} \frac{\partial (\cdot)}{\partial Y_j}$ yields

$$\mathbf{F} = \mathbf{F}^{(0)} + \varepsilon \mathbf{F}^{(1)} + O(\varepsilon^2), \quad (\mathbf{X}, \mathbf{Y}) \in B \times \Omega \quad (19)$$

and

$$\mathbf{P} = \mathbf{P}^{(0)} + \varepsilon \mathbf{P}^{(1)} + O(\varepsilon^2), \quad (\mathbf{X}, \mathbf{Y}) \in B \times \Omega, \quad (20)$$

where $\mathbf{F}^{(i)}, \mathbf{P}^{(i)} : B \times \Omega \rightarrow Lin$, $i = 0, 1$. Using rectangular Cartesian coordinates, the components of $\mathbf{F}^{(0)}$, $\mathbf{F}^{(1)}$, and $\mathbf{P}^{(0)}$ are given by, respectively,

$$F_{ij}^{(0)} = \delta_{ij} + \frac{\partial u_i^{(0)}}{\partial X_j} + \frac{\partial u_i^{(1)}}{\partial Y_j}, \quad (\mathbf{X}, \mathbf{Y}) \in B \times \Omega, \quad (21)$$

$$F_{ij}^{(1)} = \frac{\partial u_i^{(1)}}{\partial X_j} + \frac{\partial u_i^{(2)}}{\partial Y_j}, \quad (\mathbf{X}, \mathbf{Y}) \in B \times \Omega \quad (22)$$

and

$$P_{ij}^{(0)} = \left. \frac{\partial \psi}{\partial F_{ij}^{(0)}} \right|_{F^{(0)}}, \quad (\mathbf{X}, \mathbf{Y}) \in B \times \Omega. \quad (23)$$

As the coefficients $\mathbf{u}^{(i)}$ are Ω -periodic in \mathbf{Y} , so are $\mathbf{F}^{(i)}$ and $\mathbf{P}^{(i)}$. Moreover, averaging of (19) with (21) yields

$$\bar{\mathbf{F}} = \langle \mathbf{F} \rangle_{\varepsilon \rightarrow 0^+} = \langle \mathbf{F}^{(0)} \rangle = \mathbf{1} + \text{grad} \mathbf{u}^{(0)}. \quad (24)$$

Substitution of both (20) and (18) into the perfect bonding conditions for tractions (17)₁ and displacements (17)₂ yield, respectively,

$$\left[\left[P_{ij}^{(0)} \nu_j \right] \right]_{\Gamma_{rs}} = 0, \quad \left[\left[P_{ij}^{(1)} \nu_j \right] \right]_{\Gamma_{rs}} = 0, \quad (25)$$

and

$$\left[\left[\mathbf{u}^{(0)} \right] \right]_{\Gamma_{rs}} = \mathbf{0}, \quad \left[\left[\mathbf{u}^{(1)} \right] \right]_{\Gamma_{rs}} = \mathbf{0}, \quad \left[\left[\mathbf{u}^{(2)} \right] \right]_{\Gamma_{rs}} = \mathbf{0}. \quad (26)$$

Also, by substituting (18) into the boundary condition (7), we find that

$$\mathbf{u}^{(0)} = \bar{\mathbf{u}}, \quad \mathbf{u}^{(1)} = \mathbf{0}, \quad \mathbf{u}^{(2)} = \mathbf{0}, \quad (\mathbf{X}, \mathbf{Y}) \in \partial B \times \partial \Omega. \quad (27)$$

Next, substitution of (20) into the equilibrium equation (16) together with the application of the chain rule yields

$$\varepsilon^{-1} \frac{\partial P_{ij}^{(0)}}{\partial Y_j} + \varepsilon^0 \left[\frac{\partial P_{ij}^{(0)}}{\partial X_j} + \frac{\partial P_{ij}^{(1)}}{\partial Y_j} + b_i \right] + O(\varepsilon) = 0, \quad (\mathbf{X}, \mathbf{Y}) \in B \times \Omega. \quad (28)$$

Now, substitute both (23) and (21) into (28), group the terms together by the powers of ε , and equate to zero the resulting coefficients to obtain a sequence of Partial Differential Equations (PDEs) for the determination of the unknowns $\mathbf{u}^{(i)}$ in (18). In particular, the PDE corresponding to the first member of the sequence is

$$\frac{\partial P_{ij}^{(0)}}{\partial Y_j} = 0, \quad (\mathbf{X}, \mathbf{Y}) \in B \times \Omega. \quad (29)$$

Since $\mathbf{P}^{(0)}$ and $\mathbf{F}^{(0)}$ are given by, respectively, (23) and (21), we can use the PDE (29), the perfect bonding conditions (25)₁ and (26)₂, and the boundary condition (27)₂, to define a local problem for the determination of $\mathbf{u}^{(1)}$. Observe from (21) that this local problem for $\mathbf{u}^{(1)}$ involves knowledge of $\text{grad} \mathbf{u}^{(0)}$, which is obtained below. Thus, in fact, we have a family of local problems defined in terms of $\text{grad} \mathbf{u}^{(0)}$.

In order to obtain the macroscopic displacement $\mathbf{u}^{(0)}$, we apply the average operator onto the coefficient of ε^0 in (28) and recall from above that $\mathbf{P}^{(i)}$ are Ω -periodic in \mathbf{Y} . We then obtain that

$$\frac{\partial \langle P_{ij}^{(0)} \rangle}{\partial X_j} + b_i = 0, \quad (\mathbf{X}, \mathbf{Y}) \in B \times \Omega, \quad (30)$$

where,

$$\langle P_{ij}^{(0)} \rangle = \left. \frac{\partial \langle \psi \rangle}{\partial \langle F_{ij}^{(0)} \rangle} \right|_{\mathbf{F}^{(0)}}, \quad (\mathbf{X}, \mathbf{Y}) \in B \times \Omega. \quad (31)$$

To obtain (31), we have used (21) together with the macroscopic homogeneity condition $\langle F_{ij} \rangle \langle P_{ij} \rangle = \langle F_{ij} P_{ij} \rangle$ presented by Hill in [10]. Relation (31) is the effective law of the composite and represents the macroscopic realization of the local constitutive relation (5). Expression (31) can also be written as

$$\bar{P}_{ij} = c_r \left. \frac{\partial \psi_r}{\partial F_{ij}} \right|_{\mathbf{F} = \bar{\mathbf{F}} + \mathbf{F}'_r}, \quad (32)$$

where $\bar{\mathbf{P}} = \langle \mathbf{P}^{(0)} \rangle$, $c_r = \langle \chi_r \rangle = \frac{|B_r|}{|B|}$, $\sum_{r=1}^N c_r = 1$, \mathbf{F}'_r is the restriction of $\text{grad} \mathbf{u}^{(1)}$ to phase r , and $\mathbf{u}^{(1)}$ is the solution of the local problem.

The system of PDEs (30), the effective law (31), or, (32), together with $\bar{\mathbf{F}} = \langle \mathbf{F}^{(0)} \rangle = \mathbf{1} + \text{grad} \mathbf{u}^{(0)}$, and the boundary condition (27)₁ define the macroscopic, or, *homogenized* problem for the determination of $\mathbf{u}^{(0)}$.

In the following example, we obtain the effective laws of periodic bilaminates by prescribing $\bar{\mathbf{F}} = \mathbf{1} + \text{grad}\mathbf{u}^{(0)}$, solving the corresponding local problems to obtain $\mathbf{F}' = \text{grad}\mathbf{u}^{(1)}$, and then substituting $\bar{\mathbf{F}} + \mathbf{F}' = \mathbf{1} + \text{grad}\mathbf{u}^{(0)} + \text{grad}\mathbf{u}^{(1)}$ into the effective law (32).

6 Example: homogenization of periodic bilaminates

Consider a two-phase ($N = 2$) laminate composite formed of periodically alternating homogeneous laminae along the Y_2 -direction. The periodicity cell of such a bilaminate is $\Omega = \Omega_1 \cup \Omega_2$, where, for a given $c_1 \in (0, 1)$, $\Omega_1 = (0, 1) \times (0, c_1) \times (0, 1)$ e $\Omega_2 = (0, 1) \times (c_1, 1) \times (0, 1)$. Considering a fixed orthonormal basis $(\mathbf{e}_1, \mathbf{e}_2, \mathbf{e}_3)$ for the rectangular Cartesian coordinate system, continuity of both displacement $\mathbf{u}^{(1)}$ and traction $P_{i2}^{(0)} = \mathbf{e}_i \cdot \mathbf{P}^{(0)}\mathbf{e}_2$ across the contact surface $\Gamma_{12} = \partial\Omega_1 \cap \partial\Omega_2 = \{\mathbf{Y} : Y_1, Y_3 \in [0, 1], Y_2 = c_1\}$ are guaranteed by assuming that the laminae are perfectly bonded to each other.

Based on the exposition above, it is reasonable to assume that $F_{i2}^{(0)}$ depend on the lamination direction only, which is parallel to the coordinate $Y \equiv Y_2$. Thus, $\mathbf{F}^{(0)} = \chi_1 \mathbf{F}_1^{(0)} + \chi_2 \mathbf{F}_2^{(0)}$ with $\mathbf{F}_r^{(0)} = \bar{\mathbf{F}} + \mathbf{F}'_r$, $r = 1, 2$, where $\bar{\mathbf{F}} = \mathbf{1} + \text{grad}\mathbf{u}^{(0)}$, $F'_{ij} = 0$, $j \neq 2$, and $F'_{i2} = \frac{\partial u_i^{(1)}}{\partial Y}$, which is to be obtained from the local problem. Then, recalling that $\mathbf{u}^{(1)}$ is Ω -periodic, it follows from the application of the average operator to \mathbf{F}' that $\langle \mathbf{F}' \rangle = c_1 \mathbf{F}'_1 + c_2 \mathbf{F}'_2 = \mathbf{0}$. Since $c_2 = 1 - c_1$, we have that $\mathbf{F}'_2 = -\frac{c_1}{c_2} \mathbf{F}'_1$. Denoting $\mathbf{G} \equiv \mathbf{F}'_1$, we have that $\mathbf{F}' = \mathbf{G} \left(\chi_1 - \frac{c_1}{c_2} \chi_2 \right)$. It then follows from the exposition above that the components G_{ij} of \mathbf{G} are such that $G_{ij} = 0$, $j \neq 2$, and G_{i2} is the restriction of $\frac{\partial u_i^{(1)}}{\partial Y}$ to Ω_1 . Then,

$$F_{ij}^{(0)} = \bar{F}_{ij} + \delta_{j2} G_{ij} \left(\chi_1 - \frac{c_1}{c_2} \chi_2 \right), \quad (\mathbf{X}, \mathbf{Y}) \in B \times \Omega. \quad (33)$$

Moreover, PDEs (29) of the local problem become $\frac{\partial P_{i2}^{(0)}}{\partial Y} = 0$, which implies that the components $P_{i2}^{(0)}$ do not depend on Y . The other components $P_{ij}^{(0)}$, $j \neq 2$, can still depend on the heterogeneity direction, which we recall from above is parallel to Y .

On the other hand, the perfect bonding condition (25)₁ of the local problem is now $\left[P_{i2}^{(0)} \right]_{Y=c_1} = 0$. Since $P_{i2}^{(0)}$ is independent of Y , its continuity is guaranteed for every $Y \in \Omega$ and not only for $Y = c_1$. Thus, the components of $\mathbf{P}^{(0)}$ that are independent of Y satisfy

$$\left. \frac{\partial \psi_1}{\partial F_{i2}} \right|_{\mathbf{F}=\mathbf{F}_1^{(0)}} = \left. \frac{\partial \psi_2}{\partial F_{i2}} \right|_{\mathbf{F}=\mathbf{F}_2^{(0)}}, \quad (\mathbf{X}, \mathbf{Y}) \in B \times \Omega, \quad (34)$$

where the components of $\mathbf{F}_r^{(0)}$ are obtained from (33) for $Y \in \Omega_r$. Notice that the conditions (34) yield a system of nonlinear algebraic equations that are employed to obtain the \mathbf{G} corresponding to each fixed $\bar{\mathbf{F}}$. With these considerations, the effective law (32) becomes

$$\bar{P}_{ij} = \begin{cases} c_r \frac{\partial \psi_r}{\partial \bar{F}_{ij}} \Big|_{\mathbf{F}=\bar{\mathbf{F}}}, & j \neq 2 \\ \frac{\partial \psi_R}{\partial \bar{F}_{i2}} \Big|_{\mathbf{F}=\bar{\mathbf{F}}+\mathbf{F}'_R}, & R = 1 \text{ or } 2, \quad j = 2 \end{cases}, \quad (35)$$

where

$$\mathbf{F}'_R = \begin{cases} \mathbf{G}, & R = 1 \\ -\frac{c_1}{c_2} \mathbf{G}, & R = 2 \end{cases} \quad (36)$$

and \mathbf{G} is the solution of (34). In (35), the equality for $j = 2$ is a consequence of taking \mathbf{F}'_r constant in phase r in (32), and (34) being identically satisfied for \mathbf{G} .

Let us now consider that the stored energy function of each lamina is given by

$$W_r = \mu_r I(\mathbf{F}_r^{(0)} - \mathbf{1}), \quad r = 1, 2, \quad (37)$$

where μ_r is a material property, $I(\mathbf{F}) \equiv \mathbf{F}^T \cdot \mathbf{F}$ for $\mathbf{F} \in Lin$, with the superscript T denoting the transpose of a tensor, and $\mathbf{F}_r^{(0)}$ is of the form given by (33) with $Y \in \Omega_r$ and \mathbf{G} being the solution of (34). An expression similar to (37) is employed in [9] to analyze reinforced hyperelastic elastomers at finite strain.

In the case of a hyperelastic material without softening, we replace ψ_r by W_r given by (37) in (35) to obtain

$$\bar{P}_{ij} = 2\hat{\mu}(\bar{F}_{ij} - \delta_{ij}), \quad \hat{\mu} = \begin{cases} \langle \mu \rangle = c_1 \mu_1 + c_2 \mu_2, & j \neq 2 \\ \langle \mu^{-1} \rangle^{-1} = \left(\frac{c_1}{\mu_1} + \frac{c_2}{\mu_2} \right)^{-1}, & j = 2 \end{cases}. \quad (38)$$

In the case of a hyperelastic material with softening, we use the expressions (10) and (37) to obtain the stored energy function for each lamina, which is given by

$$\psi_r = \Phi_r - \Phi_r \exp \left\{ -\frac{\mu_r}{\Phi_r} I(\mathbf{F}_r^{(0)} - \mathbf{1}) \right\}, \quad r = 1, 2. \quad (39)$$

Then, substitution of (39) into (34) yields the following system of nonlinear algebraic equations for G_{i2} :

$$\frac{\mu_1}{\Phi_1} (\bar{F}_{i2} + G_{i2} - \delta_{i2}) \exp \left\{ E(\mathbf{F}^{(0)}) \right\} - \frac{\mu_2}{\Phi_2} \left(\bar{F}_{i2} - \frac{c_1}{c_2} G_{i2} - \delta_{i2} \right) = 0, \quad i = 1, 2, 3, \quad (40)$$

where

$$\begin{aligned} \mathbb{E} \left(\mathbf{F}^{(0)} \right) = & \left(\frac{\mu_2}{\Phi_2} - \frac{\mu_1}{\Phi_1} \right) (\bar{F}_{ij} \bar{F}_{ij} - 2\bar{F}_{ii} + 3) \\ & - 2 \left(\frac{c_1 \mu_2}{c_2 \Phi_2} + \frac{\mu_1}{\Phi_1} \right) (\bar{F}_{i2} G_{i2} - 2G_{22}) + \left[\left(\frac{c_1}{c_2} \right)^2 \frac{\mu_2}{\Phi_2} - \frac{\mu_1}{\Phi_1} \right] G_{i2} G_{i2} \end{aligned} \quad (41)$$

Now, in order to illustrate the influence of softening hyperelasticity of phases on the effective behavior of the bilaminate, consider the simple case of uniaxial extension in the lamination direction. Denoting by $\bar{\lambda}_i$ the principal macro-stretches and by $\bar{J} = \det \bar{\mathbf{F}}$ the determinant of the macroscopic deformation gradient, (33) becomes

$$F_{22}^{(0)} = \bar{\lambda}_2 + G_{22} \left(\chi_1 - \frac{c_1}{c_2} \chi_2 \right), F_{11}^{(0)} = F_{33}^{(0)} = \bar{\lambda}_1 = \sqrt{\frac{\bar{J}}{\bar{\lambda}_2}}, F_{ij}^{(0)} = 0, i \neq j. \quad (42)$$

In this case, it follows from (42) and (39) that $\langle P_{11}^{(0)} \rangle = \langle P_{33}^{(0)} \rangle$ and $P_{ij}^{(0)} = \langle P_{ij}^{(0)} \rangle = 0, i \neq j$, and system (40)-(41) reduces to a single equation for the determination of G_{22} , which is given by

$$\frac{\mu_1}{\Phi_1} \left(\frac{\bar{J}}{\bar{\lambda}_1^2} + G_{22} - 1 \right) \exp \left\{ \mathbb{E}_\lambda \left(\mathbf{F}^{(0)} \right) \right\} - \frac{\mu_2}{\Phi_2} \left(\frac{\bar{J}}{\bar{\lambda}_1^2} - \frac{c_1}{c_2} G_{22} - 1 \right) = 0, \quad (43)$$

where

$$\begin{aligned} \mathbb{E}_\lambda \left(\mathbf{F}^{(0)} \right) = & \left(\frac{\mu_2}{\Phi_2} - \frac{\mu_1}{\Phi_1} \right) \left[2\bar{\lambda}_1^2 + \left(\frac{\bar{J}}{\bar{\lambda}_1^2} \right)^2 - 4\bar{\lambda}_1 - 2\frac{\bar{J}}{\bar{\lambda}_1^2} + 3 \right] \\ & - 2 \left(\frac{c_1 \mu_2}{c_2 \Phi_2} + \frac{\mu_1}{\Phi_1} \right) \left(\frac{\bar{J}}{\bar{\lambda}_1^2} - 1 \right) G_{22} + \left[\left(\frac{c_1}{c_2} \right)^2 \frac{\mu_2}{\Phi_2} - \frac{\mu_1}{\Phi_1} \right] G_{22}^2 \end{aligned} \quad (44)$$

Finally, by substituting the solution G_{22} of (43)-(44) into (35) with (39), the non-null components of the effective law are obtained.

We now present numerical results concerning the uniaxial extension of homogenized composites, which are obtained from the application of the two-scale asymptotic homogenization on two periodic bilaminates. The phases of the two bilaminates behave according to, respectively, the classical hyperelastic model given by (37) and the softening hyperelastic model given by (39). In both cases, we have that $\mu_1 = 2, \mu_2 = 4, \Phi_1 = \Phi_2 = 1, c_1 = c_2 = 0.5$, and $\bar{J} = 1.1$. In Fig. 1, we show the components $\bar{P}_{11} = \langle P_{11}^{(0)} \rangle$ and $\bar{P}_{22} = \langle P_{22}^{(0)} \rangle$ of the effective first Piola-Kirchhoff stress tensor plotted against the principal macro-stretch $\bar{\lambda}_1$.

Observe from Fig. 1 that the homogenization method is capable of predicting the macroscopic failure of the composite induced by local failure of the laminae. Also, the shape of the curve of \bar{P}_{11} in the softening hyperelastic case resembles the one presented in Fig. 8 of [7] for the failure behavior and

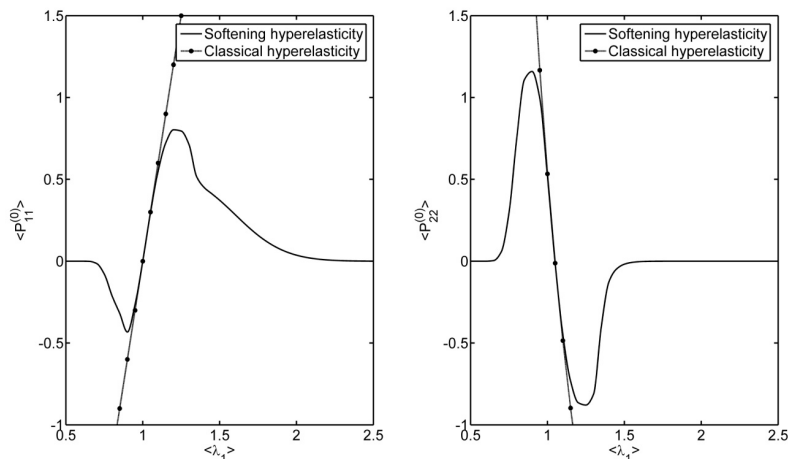


Figure 1: Effective behavior obtained via a two-scale asymptotic homogenization for two periodic bilaminates composed of, respectively, classical and softening hyperelastic phases.

rupture of a softening Fung-type balloon under inflation. Observe also from Fig. 1 that both curves are on the top of each other for small to moderate stretches, which indicates that the softening hyperelastic model is capable of obtaining the same behavior of a classical model for moderate deformations, as predicted by property (13).

7 Conclusions

In this work, we addressed the problem of macroscopic failure of hyperelastic composite materials. We employed softening hyperelasticity to model the local failure of the phases, and then applied a two-scale asymptotic homogenization to predict the corresponding effective behavior. We solved an example problem involving the uniaxial extension in the lamination direction of two periodic bilaminates, which are composed by, respectively, classical and softening hyperelastic laminae. The results indicate that, even when softening is local, the homogenization procedure is capable of predicting classical macroscopic hyperelastic behavior for moderate deformation and macroscopic failure for large enough deformations.

Acknowledgement Financial support for this research was provided by the National Council for Scientific and Technological Development of Brazil, CNPq, through grants numbers 150004/2010-9, 504778/2009-9 and 314410/2009-0.

References

- [1] Kachanov, L.M., *Introduction to Continuum Damage Mechanics*. Martinus Nijhoff Dordrecht: The Netherlands, 1986.
- [2] Krajcinovic, D., *Damage Mechanics*. North Holland Series in Applied Mathematics and Mechanics, Elsevier, 1996.
- [3] Lemaitre, J. & Desmorat, R., *Engineering Damage Mechanics: Ductile, Creep, Fatigue and Brittle failures*. Springer: Berlin, 2005.
- [4] Skrzypek, J. & Ganczarski, A., *Modeling of Material Damage and Failure of Structures*. Springer: Berlin, 1999.
- [5] Volokh, K.Y. & Gao, H., On the modified virtual internal bond method. *J Appl Mech*, **72**, pp. 969–971, 2005.
- [6] Volokh, K.Y. & Ramesh, K.T., An approach to multi-body interactions in a continuum-atomistic context: application to analysis of tension instability in carbon nanotubes. *Int J Solids Struct*, **43**, pp. 7609–7627, 2006.
- [7] Volokh, K.Y., Hyperelasticity with softening for modeling materials failure. *J Mech Phys Solids*, **55**, pp. 2237–2264, 2007.
- [8] Bakhvalov, N.S. & Panasenko, G.P., *Homogenization: Averaging processes in periodic media*. Kluwer: Dordrecht, 1989.
- [9] Pruchnicki, E., Hyperelastic law for reinforced elastomer at finite strain with edge effects. *Acta Mech*, **129**, pp. 139–162, 1998.
- [10] Hill, R., On constitutive macro-variables for heterogeneous solids at finite strain. *Proc R Soc Lond*, **A326**, pp. 131–147, 1972.

A load survey for a lifting operation of an emergency tower for electrical energy lines transmission

A.R. Alberti, J.C. de C. Pereira, L.C. Nicolazzi

Federal University of Santa Catarina – UFSC, Mechanical Engineering Depto. –

EMC 88040-900, Florianópolis – Brazil

Abstract

The emergency towers for electrical energy lines transmission are structures that should be light weight and easily assembled for a quickly replacement of damaged towers. In this context, some devices must be used in the lifting operation in order to reduce the total time of assembling. These devices named ginpole can be used in a lifting operation of horizontal assembled towers. So, this work concerns a numerical analysis for a load survey for lifting operation of a guyed truss emergency tower using fixed ginpole. These loads will be used to design the ginpole and to optimize the position of the cables fixed on the emergency tower in the lifting operation. This load survey is analyzed from geometrical position and dimensions of all devices used in the lifting operation as: emergency tower, ginpole, engine power and cables. The free software SciLab is used to solve the non linear equilibrium equations due to the relationship between all parameters involved.

Keywords: tower, restoration, electrical energy, transmission, computational methods.

1 Introduction

Electrical energy is usually produced in hydroelectric and thermoelectric plants far from the consumer centers, and is transmitted by means of transmission lines that cross large areas with the most varied topography. The electricity supply interruption because of the fall of the towers due to hurricanes, rock and earth landslides, foundation erosion, tower corrosion, vandalism, may result in serious economic losses for the society. Therefore, the power restoration transmission system as soon as possible is the primary goal to be achieved by company's teams of maintenance services. The restoration tower or emergency tower used for the immediate line restoration after these events is the first step to be taken. However, sometimes the field topography presents major difficulties for the team to maintain, as a place of difficult access, land on steep slopes, marshy ground, which makes the assembly of the emergency towers to be in a slow way. To meet these peculiarities, the restoration towers shall have the main features, easy transport, easy assembly and low cost or cheaper than the ordinary towers.

This present work concerns one of all steps of the emergency tower design. It concerns a numerical analysis for a load survey for lifting operation of the tower using fixed ginpole and these ones can be used to design the ginpole and to optimize the position of the cables fixed on the emergency tower in the lifting operation. The loads are analyzed from geometrical position and dimensions of all devices used in the lifting operation as: emergency tower, ginpole, engine power and cables. At each instant of the lifting operation, the loads acting on the ginpole and the internal forces and moments in the tower can be obtained by solving the equilibrium equations. These equilibrium equations represent a non linear problem due to the relationship between all parameters involved.

2 The mathematical model of the problem

In the lifting operation of an emergency tower assembled on a horizontal position it should be used a ginpole device in order to create an upward force. As any other device of the emergency tower to be designed, it should be obtained the loads acting over the ginpole in this operation. Moreover, the position of the cables should be calculated in order to avoid failure at any structural element of the tower and at the whole tower itself due to the force imposed by an engine power used to lift it. So, for determination of these forces it is necessary the resolution of equilibrium equations obtained from geometrical evaluations of the parameters involved. Figure 1 presents a model that describes the emergency tower and all elements used in the lifting operation.

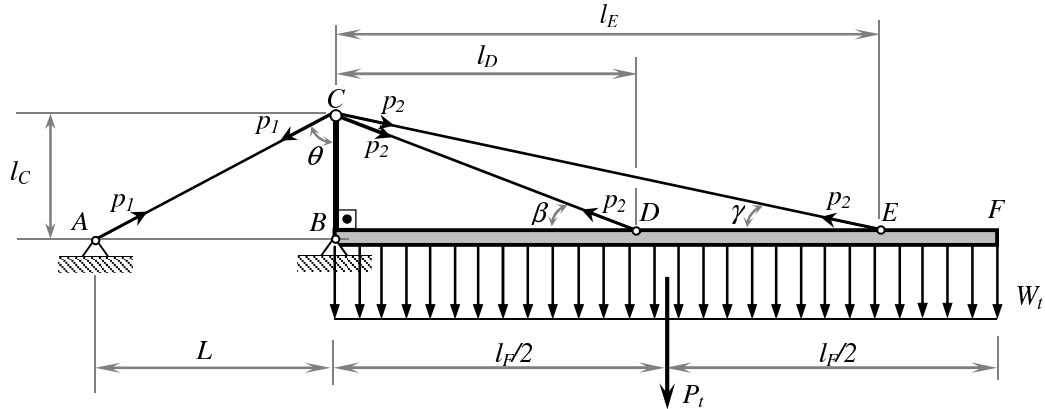


Figure 1: The lifting operation model of the emergency tower on a horizontal position.

In this model, BF represents the emergency tower with its own weight W_t , BC represents the ginpole, and the segments AC , DCE represent cables. At A is placed the engine power, B represents an articulation and C a roller that permits the slipping of the cables. The loads acting on the cables are named p_1 and p_2 . The tower is 34m high, the ginpole is l_C high and the distance between the

engine power and the tower is L . These lengths are fixed by line transmission specifications. D and E are points where cables are anchorage on the tower. The position of these points, l_D and l_E , and the position of the tower in each instant of the lifting operation regulate the loads over the ginpole and internal forces and moments in the tower.

Figure 2 presents the emergency tower at any other position on the lifting operation. Due to the fixation of the ginpole at the tower, it will be always normal to the tower throughout the lifting operation. So, BCD and BCE triangles sides are fixed in the first stage of this operation, as shown later. Nevertheless, the triangle ABC changes its internal angles by the reduction of the segment AC .

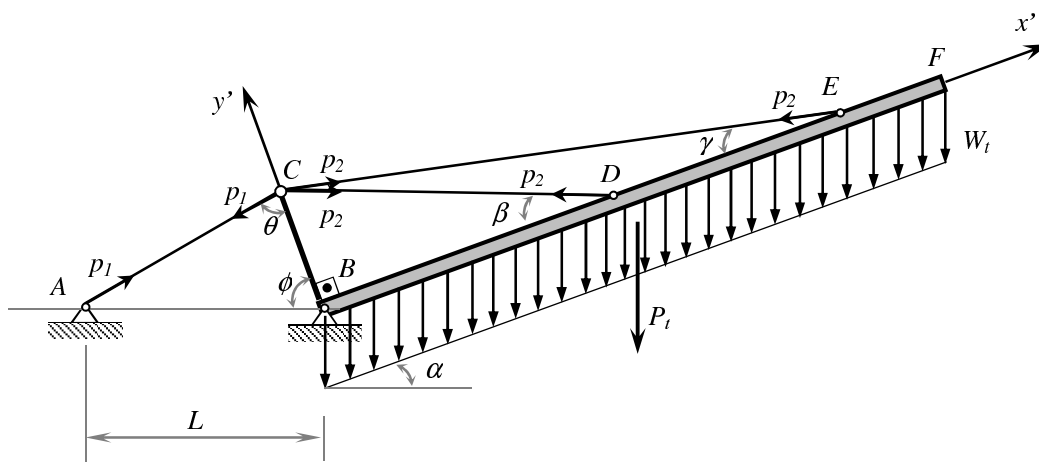


Figure 2: The lifting operation model of the emergency tower on any other position.

The survey of the loads in this operation should be divided in two stages: a) in the first stage in which the ginpole is loaded at its top, and, b) in the second stage in which the ginpole is no more loaded. The transition between these two stages is defined by the angle α_t , Figure 3 presents this situation.

At this instance, it could be stated from triangle CDE :

$$\omega + (\pi - \beta) + \gamma = \pi \Rightarrow \omega = \beta - \gamma \quad (1)$$

From the extension of segment AC , it could be found at C the relation:

$$\theta + \left(\frac{\pi}{2} - \beta\right) + \frac{\omega}{2} = \pi \Rightarrow \theta = \frac{(\pi + \beta + \gamma)}{2} \quad (2)$$

where $\beta = \arctan\left(\frac{l_C}{l_D}\right)$ and $\gamma = \arctan\left(\frac{l_C}{l_E}\right)$.

On the ABC triangle, the cosine rule on θ can be shown as:

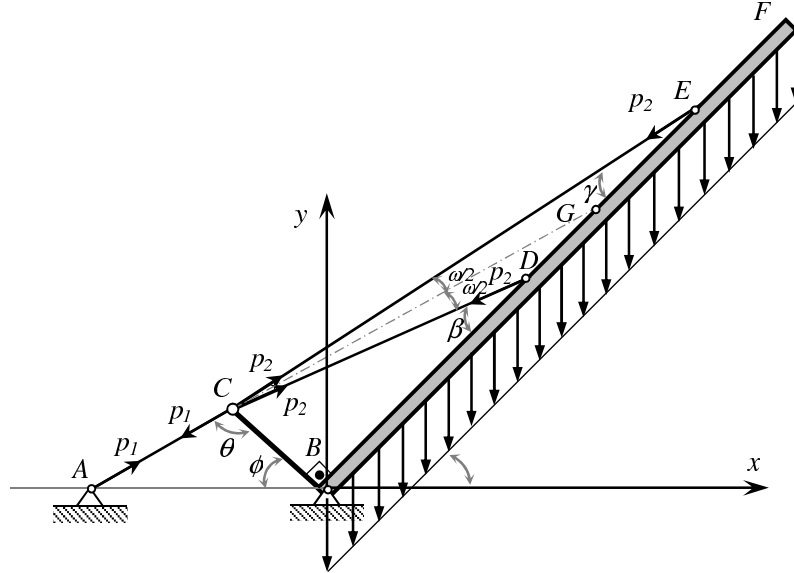


Figure 3: The transition between the two stages on the lifting operation.

$$L^2 = \overline{AC}^2 + l_C^2 - 2 \cdot \overline{AC} \cdot l_C \cdot \cos \theta \quad (3)$$

So, the segment AC at this instant can be found by rearranging equation (3):

$$\overline{AC}^2 - (2 \cdot l_C \cdot \cos \theta) \cdot \overline{AC} + (l_C^2 - L^2) = 0 \quad (4)$$

$$\overline{AC} = \frac{2 \cdot l_C \cdot \cos \theta + \sqrt{\Delta}}{2} \quad (5)$$

where $\Delta = (2 \cdot l_C \cdot \cos \theta)^2 - 4 \cdot (l_C^2 - L^2)$.

The angles ϕ and α can also be related as:

$$\phi + \frac{\pi}{2} + \alpha_t = \pi \quad (6)$$

So:

$$\phi = \frac{\pi}{2} - \alpha_t \quad (7)$$

It could be find that:

$$\sin(\alpha_t) = \cos(\phi) \quad (8)$$

On the same ABC triangle, the cosine rule on ϕ can be shown as:

$$\overline{AC} = l_C^2 + L^2 - 2.l_C.L.\cos(\phi) \quad (9)$$

So, the angle α_t from which the ginpole has no load over it is:

$$\alpha_t = \arcsin\left(\frac{l_C^2 + L^2 - \overline{AC}^2}{2.l_C.L}\right) \quad (10)$$

It can be observed from equations (2), (5) and (10) that α_t is function of γ and β , thus function of the positions of the anchorages D (l_D) and E (l_E).

So, if the goal is to determine the internal forces and moments in the tower, the equilibrium equations should be imposed in each stage individually. As it will be seen later, on the first stage the equilibrium equations can be solved analytically, and on the second stage equilibrium equations should be solved numerically due to the its non linearity.

2.1 Equilibrium equations on the first stage

From Figure 2, the equilibrium of momentum imposed at B is as:

$$\frac{l_F}{2}.P_t.\cos\alpha = p_2.(D.\sin\beta + E.\sin\gamma) \quad (11)$$

where $\beta = \arctan\left(\frac{l_C}{l_D}\right)$ and $\gamma = \arctan\left(\frac{l_C}{l_E}\right)$.

So, the load imposed by the cables over the tower is:

$$p_2 = \frac{l_F.P_t.\cos\alpha}{2.(D.\sin\beta + E.\sin\gamma)} \quad (12)$$

And also:

$$\frac{l_F}{2}.P_t.\cos\alpha_t = l_C.p_1.\sin\theta \quad (13)$$

So, the load imposed by the engine power is:

$$p_1 = \frac{l_F.P_t.\cos\alpha_t}{2.l_C.\sin\theta} \quad (14)$$

In the intention to determine the internal forces and moments, the tower is divided in 3 patches named BD , DE , EF . After that, analytical functions of the internal forces and moments can be obtained from equilibrium.

By the equilibrium conditions, the internal forces and moments can be obtained in each patch as: axial force P , shear force Q and bending moment M .

a. *Patch CB* ($0 < x' < D$):

Axial force P –

$$P(x') = -(l_F - x') \cdot W_p \cdot \sin \alpha - p_2 \cdot (\cos \beta + \cos \gamma) \quad (15)$$

Shear force Q –

$$Q(x') = p_2 \cdot (\sin \beta + \sin \gamma) - W_t \cdot \cos \alpha \cdot (l_F - x') \quad (16)$$

Bending Moment M –

$$M(x') = p_2 \cdot ((l_D - x') \cdot \sin \beta + (l_E - x') \cdot \sin \gamma) - \frac{W_t \cdot \cos \alpha \cdot (l_F - x')^2}{2} \quad (17)$$

b. *Patch DE* ($D < x' < E$):

Axial force P –

$$P(x') = -W_t \cdot \sin \alpha \cdot (l_F - x') - p_2 \cdot \cos \gamma \quad (18)$$

Shear force Q –

$$Q(x') = p_2 \cdot \sin \gamma - W_t \cdot \cos \alpha \cdot (l_F - x') \quad (19)$$

Bending Moment M –

$$M(x') = p_2 \cdot \sin \gamma \cdot (l_E - x') - \frac{W_t \cdot \cos \alpha \cdot (l_F - x')^2}{2} \quad (20)$$

c. *Patch DE* ($E < x' < F$):

Axial force P –

$$P(x') = -W_t \cdot \sin \alpha \cdot (l_F - x') \quad (21)$$

Shear force Q –

$$Q(x') = -W_t \cdot \cos \alpha \cdot (l_F - x') \quad (22)$$

Bending Moment M –

$$M(x') = \frac{-W_t \cdot \cos \alpha \cdot (l_F - x')^2}{2} \quad (23)$$

2.2 Equilibrium equations on the second stage

On this stage, the geometrical parameters considered earlier change, so the angles β and γ are no more constants, as on the first stage. Thus, β' and γ' represent these angles in each instant. Figure 4 presents the geometrical configuration on this stage.

The determination of the internal forces and moments in the tower depends on the inclinations β' and γ' of the cables, in order to find the components of all forces action on it. In this way, these components are function of the coordinates of point $C(x,y)$ and position of the anchorage D and E on the tower. The line passing through point G is the prolongation of the line that defines the segment AC . Thus, the segment CG is the bisectrix of the angle formed by segments CD and CE .

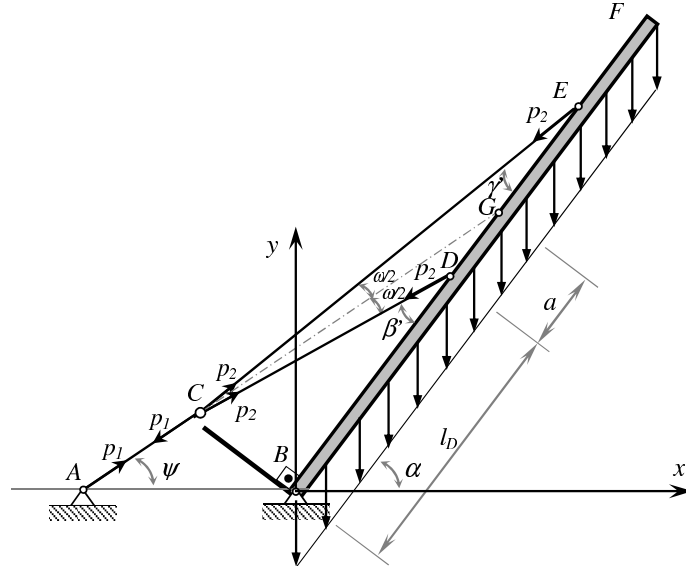


Figure 4: Geometrical configuration on the second stage.

The coordinates of the points involved in this analysis are:

$$A = (-L, 0), \quad B = (x, y), \quad C = (0, 0)$$

$$D = (l_D \cdot \cos \alpha, l_D \cdot \sin \alpha), \quad E = (l_E \cdot \cos \alpha, l_E \cdot \sin \alpha), \quad G = ((l_D + a) \cdot \cos \alpha, (l_D + a) \cdot \sin \alpha)$$

As it can be observed, the unknown of the coordinates of these points are x , y and a . For the resolution of this problem three equations should be stated:

1. The length of the cable DBE is constant throughout the lifting operation:

$$DCE = \sqrt{(l_D^2 + l_C^2)} + \sqrt{(l_E^2 + l_C^2)} \quad (24)$$

So, the equation (25) should be satisfied:

$$\sqrt{(l_D \cdot \sin \alpha - y)^2 + (l_D \cdot \cos \alpha - x)^2} + \sqrt{(l_E \cdot \sin \alpha - y)^2 + (l_E \cdot \cos \alpha - x)^2} - DCE = 0 \quad (25)$$

2. Point C should be on the straight line passing to points A and G . This stating is shown by the equation:

$$y - \frac{((l_D + a) \cdot \sin \alpha)}{((l_D + a) \cdot \cos \alpha + L)} \cdot x - \frac{((l_D + a) \cdot \sin \alpha)}{((l_D + a) \cdot \cos \alpha + L)} \cdot L = 0 \quad (26)$$

3. The segment AB and the bisectrix of the angle DCE should be collinear. To satisfy this condition the inclination of segments \overline{CD} , \overline{CE} , and \overline{CG} about the x axis should be found. So, to warrant the third statement, at point C it can be set the expression:

$$\arctan\left(\frac{l_E \cdot \sin \alpha - y}{l_E \cdot \cos \alpha - x}\right) - \psi = \psi - \arctan\left(\frac{l_D \cdot \sin \alpha - y}{l_D \cdot \cos \alpha - x}\right) \quad (27)$$

Rearranging equation (27) as a function of x , y and a , it suits:

$$2 \cdot \arctan\left(\frac{(l_D + a) \cdot \sin \alpha}{(l_D + a) \cdot \cos \alpha - L}\right) - \arctan\left(\frac{l_E \cdot \sin \alpha - y}{l_E \cdot \cos \alpha - x}\right) - \arctan\left(\frac{l_D \cdot \sin \alpha - y}{l_D \cdot \cos \alpha - x}\right) = 0 \quad (28)$$

The latest equation (27) and (28) are non linear for the unknowns x , y and a .

In this work, the Newton Method was used to solve the non linear equation systems. Tests were performed in order to verify the convergence of the resolution and to validate the results. The free software SciLab was used to program the numerical method for the resolution of these equations.

The Newton Method searches the roots of non linear equation systems in a linearization procedure such as:

$$J(X^k) \cdot X^k = -F(X^k) \quad (29)$$

where vector $F(X^k)$ is composed by the three equations that form the system:

$$\begin{aligned} F(1) &= y - \frac{(D+a) \cdot \sin \alpha}{(D+a) \cdot \cos \alpha + L} \cdot x - \frac{(D+a) \cdot \sin \alpha}{(D+a) \cdot \cos \alpha + L} \cdot L \\ F(2) &= \sqrt{(l_D \cdot \sin \alpha - y)^2 + (l_D \cdot \cos \alpha - x)^2} + \sqrt{(l_E \cdot \sin \alpha - y)^2 + (l_E \cdot \cos \alpha - x)^2} \\ &\quad - \left(\sqrt{l_C^2 + l_D^2} + \sqrt{l_C^2 + l_E^2} \right) \\ F(3) &= 2 \cdot \arctan\left(\frac{(l_D + a) \cdot \sin \alpha - y}{(l_D + a) \cdot \cos \alpha - x}\right) - \arctan\left(\frac{l_E \cdot \sin \alpha - y}{l_E \cdot \sin \alpha - x}\right) - \arctan\left(\frac{l_D \cdot \sin \alpha - y}{l_D \cdot \sin \alpha - x}\right) \end{aligned} \quad (30)$$

Vector X^k is the solution of equation (30), at the k iteration is:

$$X^K = \begin{Bmatrix} x^K \\ y^K \\ a^K \end{Bmatrix} \quad (31)$$

In the equation (29), $J(X^k)$ represents the Jacobian matrix composed by the partial derivatives of vector $F(X^k)$ in respect to the variables x , y and a , as:

$$J(X^K) = \begin{bmatrix} \frac{\partial F(1)}{\partial x} & \frac{\partial F(1)}{\partial y} & \frac{\partial F(1)}{\partial a} \\ \frac{\partial F(2)}{\partial x} & \frac{\partial F(2)}{\partial y} & \frac{\partial F(2)}{\partial a} \\ \frac{\partial F(3)}{\partial x} & \frac{\partial F(3)}{\partial y} & \frac{\partial F(3)}{\partial a} \end{bmatrix} \quad (32)$$

The actualization of the solution of the non linear system is done by:

$$X^{K+1} = X^K + \delta \quad (33)$$

where δ is the step of the iteration process. The convergence is reached when δ is lower than 10^{-8} .

After the resolution of the non linear system, where the variables x , y and a are found, the internal forces and moments on the second stage of the lifting operation can be found using the same equations presented earlier, from (15) to (23).

As an example of the determination of the internal forces and moments in the tower on the first and second stage, it is proposed the data: $l_C = 6\text{m}$, $l_D = 16\text{m}$, $l_E = 30\text{m}$, $l_F = 34\text{m}$, $L = 12\text{m}$ and the equivalent force due to self weight of the tower $P_t = 10.000\text{N}$. Figures 5 and 6 present the internal forces and moments diagrams for $\alpha = 0^\circ$, on the first stage, and for $\alpha = 60^\circ$, on the second stage, respectively. It can be observed in these figures the effect of the distributed load W_t , especially on the axial internal effort P .

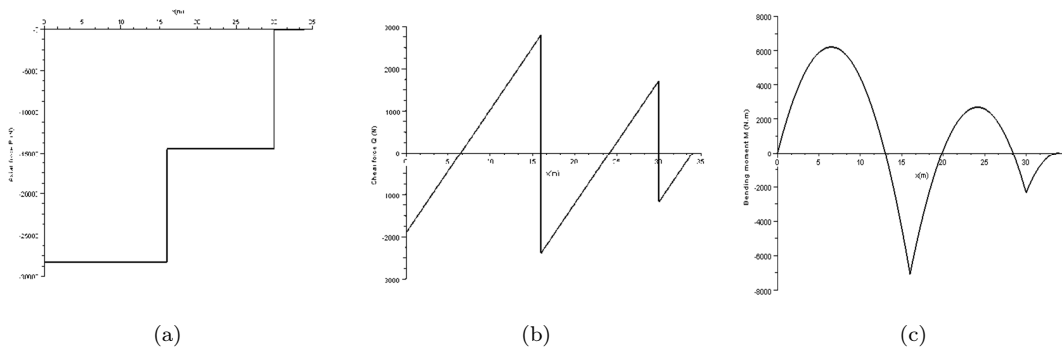


Figure 5: Internal forces and moments diagrams in the tower for $\alpha = 0^\circ$: (a) axial force P , (b) shear force Q and (c) bending moment M .

Figure 7 presents the axial and transversal loads acting at the top of the ginpole. It can be observed that for the design of this device, concerning its stability and strength, the critical position is for $\alpha = 0^\circ$.

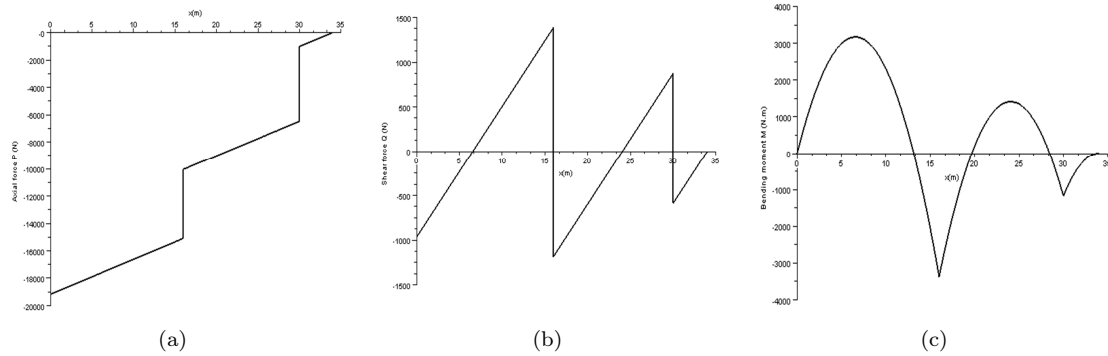


Figure 6: Internal forces and moments diagrams in the tower for $\alpha = 60^\circ$: (a) axial force P , (b) shear force Q and (c) bending moment M .

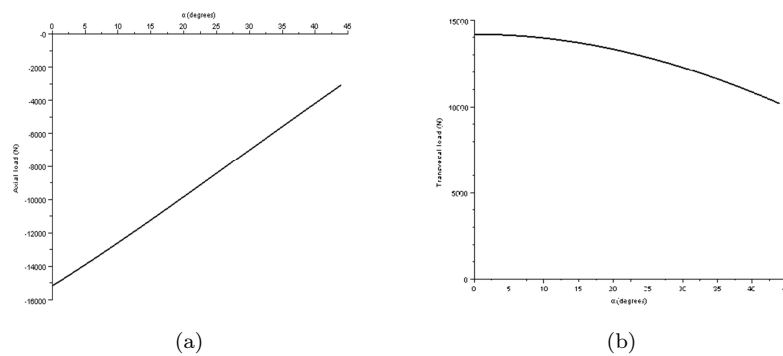


Figure 7: Load acting at the top of the ginpole: (a) axial load and (b) transversal load.

3 Conclusions

This work deals with the survey load in the lifting operation of an emergency tower used to restore damaged transmission lines. These loads are used to design the devices used in this operation, especially the ginpole. Moreover, in order to find the better position of the cables anchored on the tower to avoid failure at the whole tower itself in this operation. In this context, the loads acting over the ginpole and the internal forces and moments should be found. The determination of these loads induces to a resolution of a non linear equation system that involves geometrical parameters. The Newton Method was used to solve numerically this non linear equation system. The results have shown the robustness of the Newton Method for this kind of problem.

Acknowledgment The authors thanks to the National Electrical Energy Agency-ANEEL and the Centrais Elétricas do Sul do Brasil-ELETROSUL for financing this research.

References

Graphene based nanoparticles as ultrahigh frequency nanomechanical resonators: modal vibration response

Antonio F. Ávila, Almir Silva Neto, Alexandre C. Eduardo
*Universidade Federal de Minas Gerais, Department of Mechanical Engineering,
6627 Antonio Carlos Avenue, Belo Horizonte, 31270-901, MG – Brazil*

Abstract

This paper deals with the molecular mechanics simulations of graphene nanostructures and their vibration behavior for potential applications on nano-electronics and nanocomposites. These nanostructures are good candidates to nano resonators due to high specific stiffness and strength and elevated aspect ratio. The fundamental frequencies for CNTs range from 10-250 GHz and 100-1000 GHz for the cantilevered and bridged conditions, respectively. As the ratio length/diameter increases the fundamental frequency decreases, as expected. A decrease on fundamental frequencies with the bending waviness was noticed for all conditions. The mode shape for bent carbon nanotubes seems to be a superposition of the vibration mode and the bending mode for the zigzag configuration. Multi-layered graphene were also investigated. The fundamental frequencies ranged from 50-150 GHz, with an odd/even shape mode switch.

Keywords: graphene nanostructures, carbon nanotubes, vibration analysis, molecular mechanics, nano resonators.

1 Introduction

As commented by Campanella [1], one of the key components into micro electromechanical systems (MEMS) is the resonator. Nanotechnology allowed the development of the so called nano electromechanical systems, NEMS for short. Reduction in the size of a resonator enhances its resonant frequency and reduces its energy consumption. According to Jah [2], sensors sensitivity are directed related to the resonant frequency, i.e. higher resonant frequency means higher sensitivity. Nowadays, more and more wireless communication devices are required, the usage of higher frequency resonators enable the production of higher frequency filters, oscillators, and mixers. The improvement of high-frequency NEMS brings about new applications ranging from signal processing [3] to biosensors [4]. Potential candidates to nano resonators are carbon nanotubes and graphene nanosheets.

According to Saito and his co-workers [5], carbon nanotube is a honeycomb lattice rolled into a cylinder. Carbon nanotubes (CNTs) have been the center of many researches due to their dimensions

and remarkable electro-mechanical properties. In general, a CNT diameter has a nanometer size and its length can be more than $1\mu\text{m}$. Its large aspect ratio (length/diameter) is appointed as one of the reasons for the CNTs notable properties. As mentioned by Kalamkarov et al [6], CNTs have predicted specific strength around 600 times larger than steel.

CNT capabilities have been observed experimentally and verified by numerical simulations. Among the different numerical simulations, two different approaches are the most common, i.e. molecular dynamics [7], atomistic simulations [8] also known as molecular mechanics [9]. The traditional molecular dynamics (MD) simulations are limited because is computational intensive, while the molecular mechanics is more flexible and more computational efficient.

As discussed by Gibson and co-workers [10], the knowledge of vibration behavior of CNTs is critical in a large number of nanomechanical devices such as oscillators, clocks, field emission devices and sensors. Furthermore, during the sonication process for nanocomposites synthesis of carbon based nanoparticles, e.g. CNTs and graphene, vibration takes place. Therefore, the development of an accurate model for the natural frequencies and mode shapes of carbon based nanoparticles is an important issue.

Here the concept of molecular mechanics described by Li and Chou [9] and Tserpes and Papanikos [11], and extended by Ávila and Lacerda [12] is associated to the three-dimensional finite element model and later on employed to predict the vibrational behavior of carbon based nanoparticles, i.e., carbon nanotubes and graphene nanosheets.

2 Structure of a single wall carbon nanotube

The molecular mechanics approach can be described by numerical methods where the equilibrium configuration of the model system is required by minimizing the energy, which consists of the sum of the inter-atomic potential minus any work by external forces. SWNT may be thought of as a sheet of graphene rolled along a chiral vector, C , as described by Fig. 1.

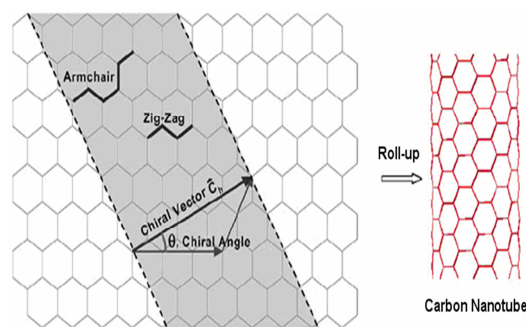


Figure 1: Chiral angle and vector representation adapted from Ávila and Lacerda [12].

Dresselhaus and co-workers [13] described SWNT in terms of nanotube diameter (d) and its chiral angle (θ). The chiral vector (C_h) was defined in terms of the graphene sheet lattice translation integer indices (n, m) and the unit vectors (a_1, a_2) and it is defined as:

$$\vec{C}_k = n\vec{a}_1 + m\vec{a}_2 \quad (1)$$

where the unit vectors in (x,y) coordinates are defined as:

$$\vec{a}_1 = \left(\frac{\sqrt{3}}{2}, \frac{1}{2} \right) a \quad \vec{a}_2 = \left(\frac{\sqrt{3}}{2}, -\frac{1}{2} \right) a \quad (2)$$

the length of the unit vector a is defined as 2.46 angstroms, or 1.73 times the carbon-carbon distance, i. e. 1.421 angstroms. The nanotube circumference (p) was defined by:

$$p = |C_k| = a\sqrt{n^2 + m^2 + nm} \quad (3)$$

from simple geometry, it is possible to obtain the nanotube diameter (d) as:

$$d = \frac{p}{\pi} = \frac{\sqrt{n^2 + m^2 + nm}}{\pi} a \quad (4)$$

and the chiral angle (θ), between 0 and $\pi/6$ rad, was described by Dresselhaus et al [13] by

$$\sin \theta = \frac{\sqrt{3}m}{2\sqrt{n^2 + nm + m^2}} \quad \cos \theta = \frac{2n + m}{2\sqrt{n^2 + nm + m^2}} \quad (5)$$

The three main SWNT configurations were described by Kalamkarov et al [6] in Fig. 2. Notice that each configuration has its own cap distinct formation. As the aspect ratio (length/diameter) is in general large, it is possible to discard the cap effect without loss of generality.

3 Molecular mechanics basics

As stated by Li and Chou [9], the carbon atoms in the nanotube are held together by covalent bonds of characteristic bond length and bond angles, and the corresponding molecular forces constrain any displacement of individual atoms. In the molecular structural mechanics approach, a single-walled carbon nanotube is simulated as a space frame structure, with the covalent bonds and carbon atoms as connecting beams and joint nodes, respectively. If the beam elements simulating the covalent bonds are assumed to be of round section, then only three stiffness parameters, i. e., the tensile resistance EA , the flexural rigidity EI and the torsional stiffness GJ , need to be defined for deformation analysis. Figure 3 describes the correlation between the atomic interactions and their molecular mechanics equivalent.

Ávila and Lacerda [12], based on the energy equivalence between local potential energies in computational chemistry and elemental strain energies in structural mechanics, established a direct relationship

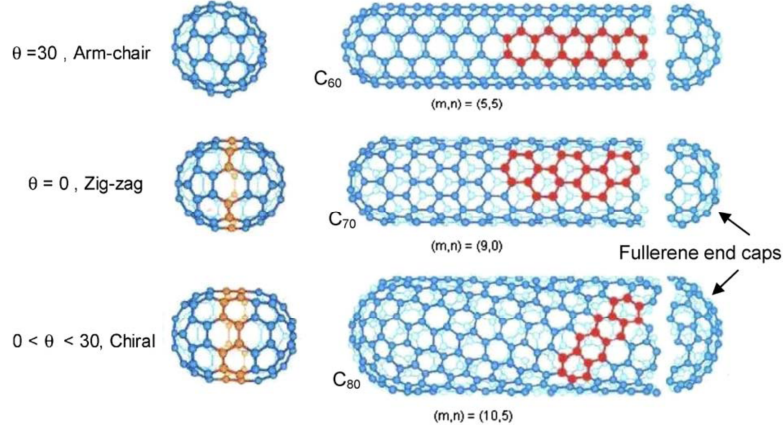


Figure 2: SWNT configurations and their caps adapted from Kalamkarov and collaborators [6].

between the structural mechanics parameters and the molecular mechanics force field constants. Such parameters are mathematically represented by:

$$\frac{EA}{L} = k_r, \quad \frac{EI}{L} = k_\theta, \quad \frac{GJ}{L} = k_\tau \quad (6)$$

where L denotes the bond length, and k_r , k_θ and k_τ are the force field constants in molecular mechanics. By assuming a circular beam cross section (bond) with diameter d_b , and setting the area, moment of inertia and polar moment of inertia as $A_b = \pi d_b^2/4$, $I_b = \pi d_b^4/64$ and $J_b = \pi d_b^4/32$, Tserpes and co-workers [11] presented the covalent bond equivalent E_b and G_b as

$$d_b = 4 \sqrt{\frac{k_\theta}{k_r}}, \quad E_b = \frac{k_r^2 L}{4\pi k_\theta}, \quad G_b = \frac{k_r k_\tau L}{8\pi k_\theta^2} \quad (7)$$

In order to compute the fundamental frequencies and vibrational modes of a carbon nanotube, Li and Chou [14] simulated the nested tube layers by equivalent space frame structures and the Van der Waals interactions between tubes by spring elements. The van de Waals forces were approximated by the Lennard-Jones forces. The equation of motion for the free vibration of an undamped structure is described as,

$$[\mathbf{M}] \{\ddot{\mathbf{y}}\} + [\mathbf{K}] \{\mathbf{y}\} = \{\mathbf{0}\} \quad (8)$$

where $[\mathbf{M}]$ and $[\mathbf{K}]$ are, respectively, the global mass and stiffness matrices. The nodal acceleration and the displacement vectors are represented by $\{\ddot{\mathbf{y}}\}$ and $\{\mathbf{y}\}$, respectively.

The C-C bonds were replaced by beam elements with properties based on chemical potentials. Therefore, once the chemical-mechanical equivalence was established, the global stiffness matrix $[\mathbf{K}]$

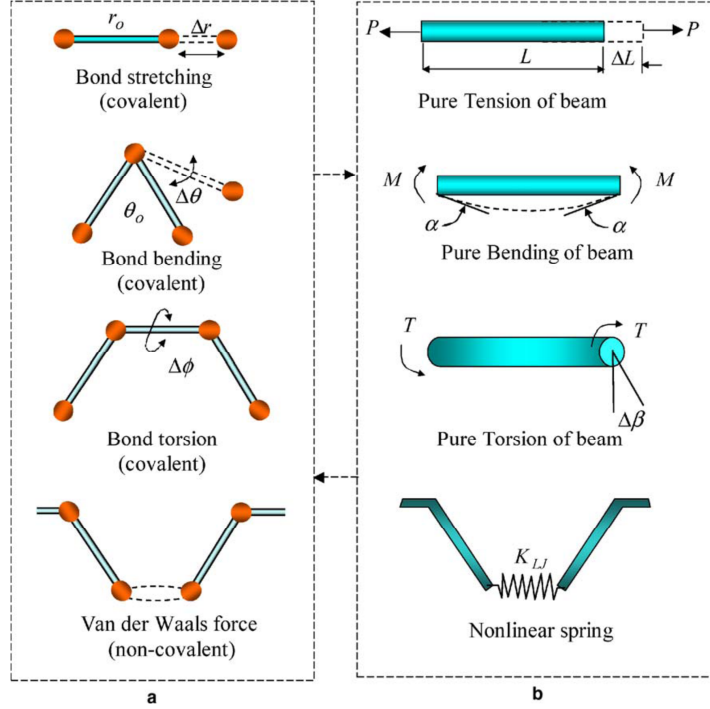


Figure 3: Equivalence between molecular and structural mechanics. (a) molecular mechanics; (b) structural mechanics adapted from Tserpes and Papanikos [13].

followed the conventional finite element assemblage procedure as described in Bathe [15]. As commented by Li and Chou [14], there are two kinds of elemental stiffness matrix $[K]^e$. One is for the beam element in tube layers, i.e.

$$[K]_b^e = \begin{bmatrix} [k_{ii}] & [k_{ij}] \\ [k_{ji}] & [k_{jj}] \end{bmatrix} \quad (9)$$

where the sub matrices $[k_{ii}]$, $[k_{ij}]$, $[k_{ji}]$, and $[k_{jj}]$ are stiffness coefficients related to the cross-sectional parameters of beam element $i-j$. The second elemental matrix is based on non-linear spring element representing Van der Waals interactions, i.e.

$$[K]_{vdw}^e = \begin{bmatrix} [k_{ii}] & [k_{ij}] \\ [k_{ji}] & [k_{jj}] \end{bmatrix}, \quad [k_{ii}] = [k_{jj}] = \begin{bmatrix} [A] & [0] \\ [0] & [0] \end{bmatrix}, \quad [k_{ij}] = -[k_{ji}] \quad (10)$$

where $[0]$ is a null matrix and

$$[A] = \begin{bmatrix} \alpha & 0 & 0 \\ 0 & 0 & 0 \\ 0 & 0 & 0 \end{bmatrix}, \quad \alpha = 24 \frac{\epsilon}{\sigma^2} \left[26 \left(\frac{\sigma}{r} \right)^{14} - 7 \left(\frac{\sigma}{r} \right)^7 \right] \quad (11)$$

The global mass matrix $[M]$ is based on the atomistic feature of a carbon nanotube, like in Li and Chou [14]. The masses of electrons are neglected and the masses of carbon nuclei ($m_c = 1.9943 \times 10^{-26}$ kilogram) are assumed to be located at the centers of atoms, i. e., the joints of beam members. The flexural rotation and torsional rotation are assumed to be identical to zero as the carbon nuclei radius are extremely small ($r_c = 2.75 \times 10^{-6}$ nm). Based on these considerations, and the fact that in a CNT each carbon atom is bonded to three others, the elemental mass matrix was described by Li and Chou [14] as,

$$[M]^e = \text{diag} \left[m_c/3 \quad m_c/3 \quad m_c/3 \quad 0 \quad 0 \quad 0 \right] \quad (12)$$

Following Mackerle [16], the natural frequencies and mode shapes of a finite element formulation are obtained solving an eigenvalue problem as,

$$([K] - \omega^2 [M]) \{y\} = 0 \quad (13)$$

where the angular frequency is defined as $\omega = 2\pi f$.

4 Vibrational behavior studies

According to Gibson et al [10], the knowledge of vibrational behavior of carbon based nanoparticles is critical for various industrial applications, e.g. oscillators, nanocomposites. To be able to investigate the vibrational behavior of such nanoparticles, two groups were considered, i. e. carbon nanotubes and graphene nanosheets. For CNTs, two major boundary conditions were applied. The first one was the cantilever beam and the second one the bridged carbon nanotubes. To be able to validate the proposed model a numerical simulation of resonant frequencies of bridged zigzag and armchair carbon nanotubes were performed. These cases were studied by Li and Chou [14] and the results are available for comparison. Another set of data available for to be used as benchmark is the one provided by Sakhaee-Pour and co-workers [17]. Table 1 shows a comparison between the present model and data from Sakhaee-Pour et al. [17], for an armchair configuration. As it can be noticed, a small difference (less than 2%) is noticed between the two models. This difference can be attributed to the geometric differences between the two models. Sakhaee-Pour et al [17] provided the nanotube diameter (0.814 nm) and the nanotube length (5.660 nm). For a (6,6) armchair configuration, the calculated diameter was equal to 0.808 nm, while the length employed was 5.600 nm. Table 2 summaries the zigzag configuration results. In this case, the difference between Sakhaee-Pour et al [17] results and the present model was higher. The largest difference was around 8%. This difference can be attributed to two factors. The differences into the geometry, for Sakhaee-Pour et al [17] considered a diameter of 0.626 nm and length of 5.826 nm, while the present model for a (8,0) configuration the diameter is

0.622 nm and the length of 5.80 nm. The second factor is the zigzag configuration itself. As commented by Gibson et al [10], for zigzag nanotubes small geometric variations can lead to variations on natural frequencies due to atoms distribution.

Table 1: Natural frequencies (GHz) for the armchair SWNT configuration.

Mode ID	Sakhaee-Pour		Present model		Absolute error [%]	
	Cantilevered	Bridged	Cantilevered	Bridged	Cantilevered	Bridged
1	104	557	104	551	0.0	1.1
2	104	557	104	558	0.0	0.1
3	562	1280	566	1270	0.7	0.7
4	562	1280	566	1278	0.7	0.1
5	650	1320	640	1296	1.5	1.8
6	947	1910	954	1873	0.7	1.9

Table 2: Natural frequencies (GHz) for the zigzag SWNT configuration.

Mode ID	Sakhaee-Pour		Present model		Absolute error [%]	
	Cantilevered	Bridged	Cantilevered	Bridged	Cantilevered	Bridged
1	72	427	76	462	5.6	8.2
2	72	427	76	462	5.6	8.2
3	421	1050	443	1128	5.2	7.6
4	421	1050	443	1128	5.2	7.6
5	628	1270	646	1332	2.9	4.9
6	882	1780	923	1895	4.6	6.5

Another benchmark problem is the one published by Harrar and Gibson [18]. They developed a finite element model based on shell elements that can be applied to carbon based nanostructures, in special carbon nanotubes. Table 3 shows, for the bridged configuration, the three zigzag nanotubes studied by Harrar and Gibson [18], by Li and Chou [19] and the present model.

The large maximum absolute error for small L/D ratio (3.55) can be attributed to differences on boundary conditions applied by Li and Chou [19], i.e. nanotube diameter and mass distribution due to the number of atoms (each carbon atom has a correspondent node). Notice that both models, the

Table 3: Natural frequency (GHz) for the zigzag SWNT with different aspect ratios.

Diameter [nm]	Length [nm]	Li and Chou	Harrar and Gibson		Present model	Max. Absolute Error [%]
			Space frame model	Shell model		
1.1	3.9	1041	1167	1092	1197	14.9
1.1	5.6	662	692	656	705	7.4
1.1	8.0	380	377	374	382	2.1

one described by Harrar and Gibson [18] and the present model, used the same software for nanotube generation, i.e. Nanotube Modeler [20]. The diameter for the (14,0) nanotube for both cases are identical (1.08 nm) and the number of carbon atoms is also the same (518 carbon atoms). The mass distribution is the same, and consequently the natural frequencies are approximately the same. This hypothesis is confirmed by the close results obtained by the present model and the data presented by Harrar and Gibson [18].

As discussed by Li and Chou [14] and Gibson et al. [10], the fundamental frequency of carbon nanotubes can be influenced by various factors, e.g. boundary conditions and geometric configurations. To investigate how these parameters affect natural frequencies and vibration modes, a series of numerical simulations were performed. The nanotube diameters ranged from 0.38 nm to 0.89 nm, while length/diameter ratios varied from 6 to 19. As it can be observed in Fig. 4, the fundamental frequencies were in the range of 10-250 GHz and 100-1000 GHz, for cantilevered and bridged nanotubes, respectively. These results are in good agreement with those presented by Li and Chou [14]. However, for the bridged, the peak value obtained using the proposed model was lower (998 GHz) than the one reported by Li and Chou [14], i. e. 1042 GHz. This difference can be due to the boundary conditions applied and the number of atoms considered in each model. In the present model, one layer of node (atoms) was constrained, while in Li and Chou [14] a different number of layers were probably used. Note that in another paper, Li et al. [21] constrained 5 layers of atoms as a clamped condition. Small differences on length lead to different numbers of atoms and consequently different total mass. Yet, the results obtained by the present model are in good agreement with the one presented by Li and Chou [14, 19].

Another issue that must be investigated is the carbon nanotube waviness. As described by Gibson and colleagues [10], carbon nanotubes are naturally curved due to the synthesis process. To be able to investigate the waviness effect on carbon nanotubes fundamental frequencies, a fixed aspect ratio L/d of 18, the largest aspect ratio employed by Li and Chou [19], was assumed. Two different configurations, one armchair and another zigzag, were selected. Furthermore, the waviness was simulated by bending the nanotube with respect to z axis from 0 to 90 deg at 30 deg interval. As commented by Gibson and co-workers [10], a macro mechanical correlation between models for vibrating curved beams and arches show that the curvature of the beam or arch has strong effect on modal frequencies.

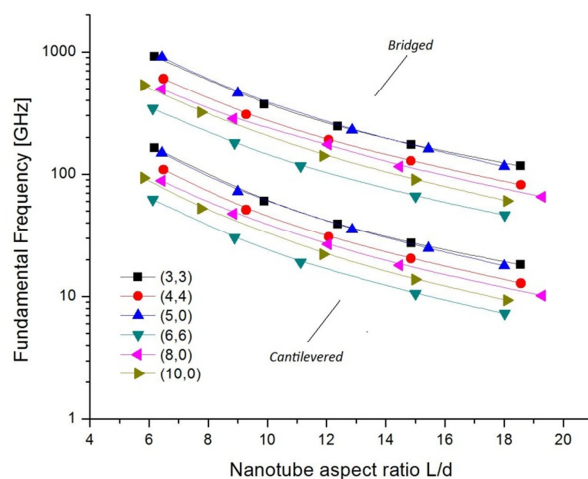


Figure 4: Fundamental frequencies of single-wall carbon nanotubes.

The work done by Lee and Wilson [22] showed that for fixed-fixed arches the natural frequencies decrease with the increase of curvature. This behavior was also noticed for the set of bridged nanotubes configurations studied. As it can be shown in Figure 5, the nanotubes with smaller diameters (3,3) and (5,0) seem to be the ones with the smallest variations. Notice that according to Harrar and Gibson [18], variations on natural frequencies of wavy nanotubes are related to the projected length of the nanotube. Another issue must be added to this analysis, the diameter variation due to bending. Small diameters will lead to smaller differences on cross section diameter, thus smaller variations on natural frequencies, as equation (1) in Harrar and Gibson [18] demonstrates. This hypothesis is also corroborated by Stokey [23]. In his investigation, Stokey [23] recalled the *Timoshenko Beam Theory* for considering the effects of shear deflection and cross section rotation. By analyzing the governing equations described by Stokey [23], it is possible to conclude that natural frequencies are directly proportional to the radius of gyration of the curved beam. By applying this analogy to curved carbon nanotubes, it is possible to conclude that curved nanotubes, under bridged configuration, with larger diameters will have larger gyration radius and greater variations on natural frequencies when curvature changes. The two configurations with the smallest diameters, i.e. (5,0) with 0.38 nm and (3,3) with 0.40 nm, are the ones less affected by the curvature effect. As the carbon nanotube radius increase, the largest radius is 0.81 nm for the (6,6) configuration, the decrease on natural frequency is more evident ($\approx 23\%$). Nevertheless, the (10,0) configuration with 0.78 nm diameter seems to be virtually insensible to curvature effect (variation of approximately 6%). As discussed by Li and Chou [19], this phenomenon can be explained by the perfect symmetry on mass distribution for the (10,0) SWNT configuration.

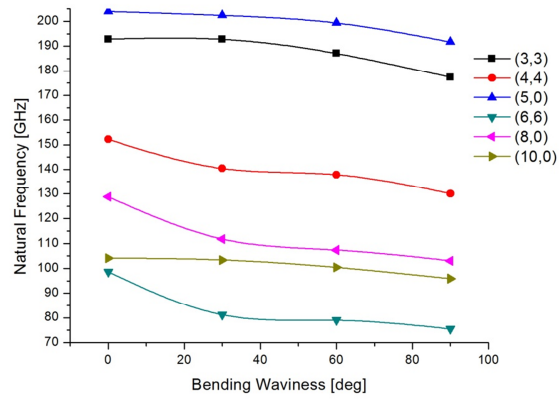


Figure 5: Waviness effect on SWNT fundamental frequencies – bridged.

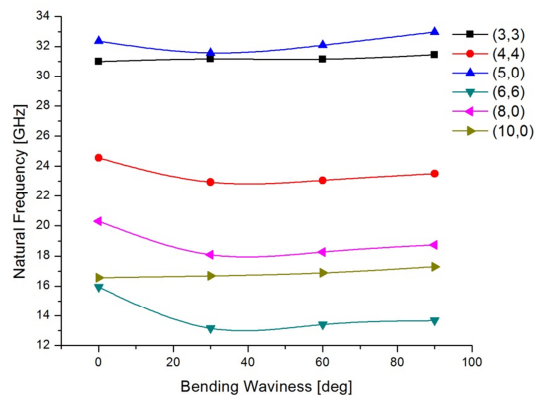


Figure 6: Waviness effect on SWNT fundamental frequencies – cantilevered.

When the boundary condition is changed from bridged to cantilevered, the natural frequencies variation is smaller as it can be noticed in Fig. 6. This behavior was expected as the same trend was observed for straight SWNT. Furthermore, as commented by Stokey [23], variations curvature has no practical influence on fundamental frequency (first vibration mode) for the cantilevered configuration. This behavior is true for the nanotubes with small diameters, i.e. (3,3), (5,0) and (4,4). For these configurations variations on natural frequencies due to bending ranged from 1.6% to 6.5%, while for the large diameter nanotubes the peak variation on natural frequency was around 17.6%. Once more the (10,0) configuration presented a small variation on natural frequency ($\approx 4.2\%$) despite of its large diameter 0.78 nm.

To investigate the vibration modes changes as function of the bending waviness, a well-known CNT, i.e. (14,0) with length of 3.9 nm and bridged boundary condition, was selected as benchmark. This SWNT was studied by Gibson and co-workers [10], Li and Chou [19] and Harrar and Gibson [18]. Figure 7 shows the first five vibration modes. These vibration modes are identical the ones showed by Gibson et al [10]. Figure 8 shows the first five vibration modes for the same SWNT configuration with a bending waviness of 30 deg. As it can be noticed, the bending waviness seems to be superimposed to the vibration modes of the straight nanotubes. The same pattern is observed for the 60 deg and 90 deg bending waviness, as shown in Figs. 9-10.

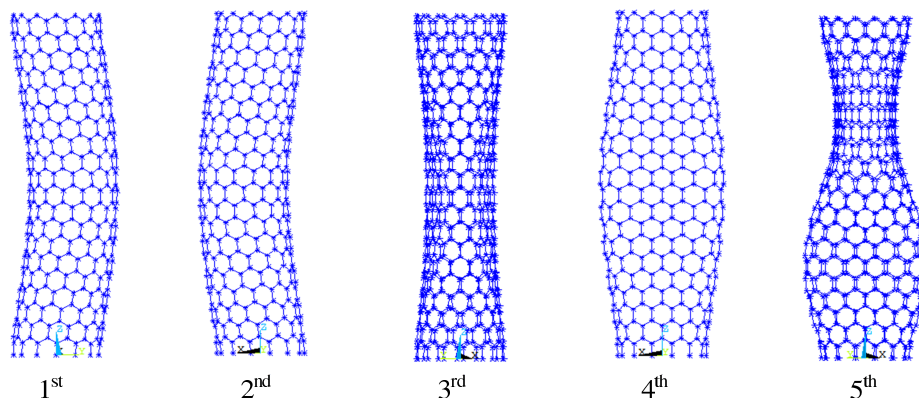


Figure 7: Vibration modes for the (14,0) SWNT straight.

Shape modes for bent SWNT seem to be essentially a superposition of each vibration mode and the bending waviness. Recalling Gibson et al [10], carbon nanotube can be described as one dimensional entity. Therefore, a different approach must be employed for analyzing graphene nanosheets as they are similar to plates. However, as discussed by Ávila et al. [24], for some nanocomposites manufacturing, the graphene nanosheets are usually exfoliated in blocks. Therefore, this research focuses on vibrational behavior of multi-layered graphene nanosheets. According to Ávila and co-workers [25] and Li and

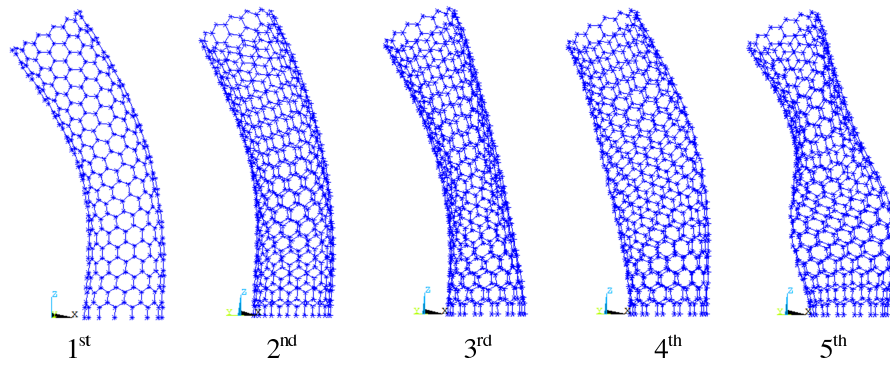


Figure 8: Vibration modes for the (14,0) SWNT with bending waviness of 30 deg.

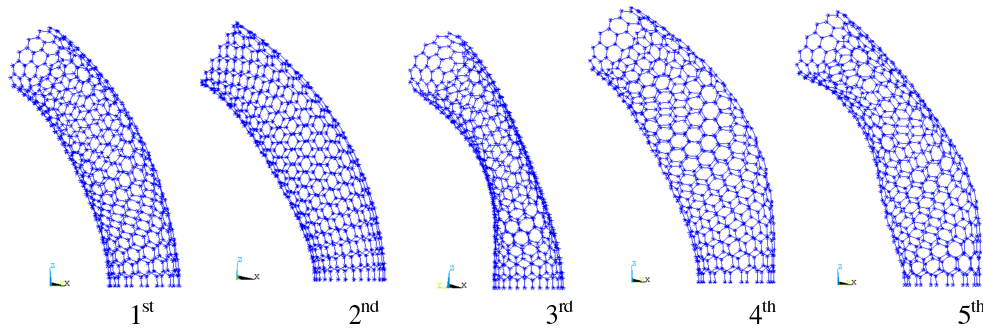


Figure 9: Vibration modes for the (14,0) SWNT with bending waviness of 60 deg.

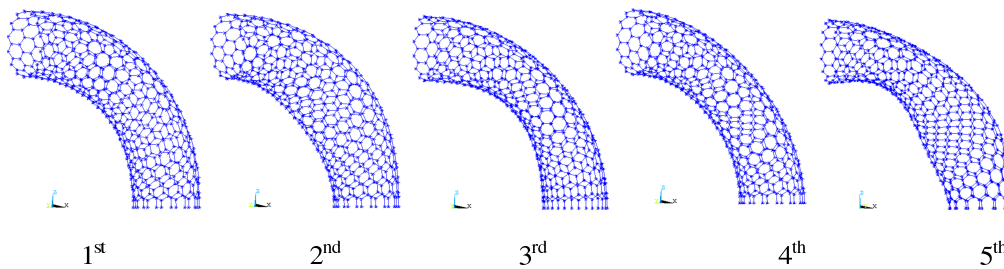


Figure 10: Vibration modes for the (14,0) SWNT with bending waviness of 90 deg.

Chou [14], the inter-graphene inter layer spacing is 0.34 nm. As the Lennard-Jones potential force approaches to zero for distances bigger than 0.85 nm, only atoms around this distance are considered. As it can be noticed from Figs. 11 and 12 (multi-layered graphene cantilevered and bridged), the Van der Waals forces act as a “*control system*”. They allow the graphene nanosheets to deform on even shape modes and let the graphene nanosheets return to equilibrium (non-deformed shape) on odd shape modes. This odd/even behavior alternates with the number of layers. The same pattern is noticed for both configurations, i. e. cantilevered and bridged. Furthermore, for one single graphene nanosheets or blocks, the fundamental frequency for a 2.5 nm by 2.5 nm square graphene nanosheets is around 52.87 GHz and 148.45 GHz, for cantilevered and bridged configurations, respectively.

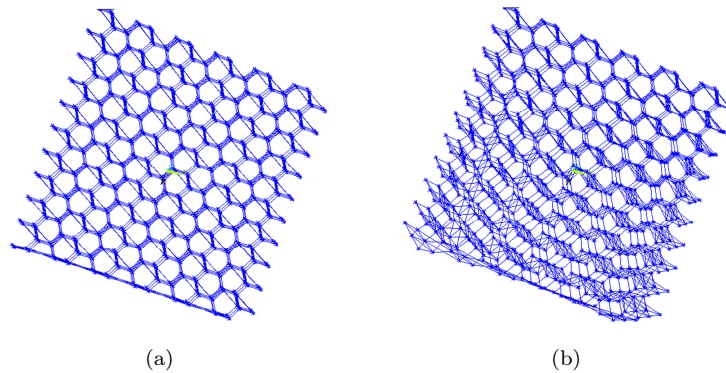


Figure 11: Multi-layer graphene shape modes for cantilevered condition. (a) even; (b) odd.

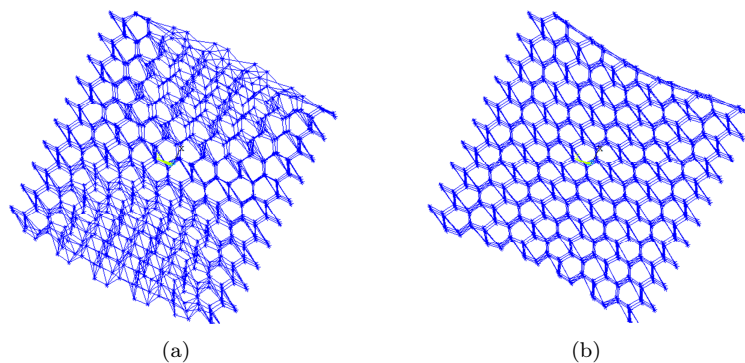


Figure 12: Multi-layer graphene shape modes for bridged condition. (a) even; (b) odd.

5 Conclusions

Carbon nanotubes were investigated considering two major boundary conditions, i. e. cantilevered and bridged. Those are the ones with larger potential applications for nano mechanical resonators. The length over diameter ratio (L/d), the nanotube configuration (armchair and zigzag) and the waviness effect were investigated. The fundamental frequencies ranged from 10-250 GHz and 100-1000 GHz for the cantilevered and bridged conditions, respectively. As the ratio L/d increased, the fundamental frequency decreased, as expected. For carbon nanotubes under the bridged configuration, the bending waviness effects lead to a decrease on natural frequencies. Large variations, up to 23%, on natural frequencies were observed on carbon nanotubes with large diameters. The only exemption was the (10,0) configuration where despite of the large diameter (0.78 nm), the natural frequencies were practically constant with the bending waviness variation. This phenomenon can be explained by the perfect symmetry on mass distribution for the (10,0) SWNT configuration. Numerical predictions on shape modes for a (14,0) configuration, the same used by Li and Chou [19] for straight nanotubes, indicate a mode superposition of the bending shape and the vibration modes.

Multi-layered graphene nanosheets were also studied. In this case, the Van der Waals forces were considered. It seems that the Van de Waals forces acts a “control system”. They allow the graphene nanosheets to deform on even shape modes and let the graphene nanosheets return to equilibrium (non-deformed shape) on odd shape modes. This odd/even behavior alternates with the number of layers.

Acknowledgments The author would like to acknowledge the financial support provided by the Brazilian Research Council (CNPq) Grants 472213/2007-5 and 300434/2008-1 and the student grant provided by the Graduate Studies Program in Mechanical Engineering via CAPES foundation.

References

- [1] Campanella, H., *Acoustic wave and electromechanical resonators : concept to key applications*. Artech House: Norwood, 2010.
- [2] Jha, A., *MEMS and nanotechnology-based sensors and devices for communications, medical and aerospace applications*. CRC Press: Boca Raton, 2008.
- [3] Leondes, T., *MEMS/NEMS: Handbook techniques and applications*. Springer: Berlin, 2006.
- [4] Doraiswami, R., *Biosensors micro and nano integration*. *BioNanoFluidics MEMS*, ed. P. Hesketh, Springer: Berlin, 2008.
- [5] Saito, R., Dresselhaus, G. & Dresselhaus, M., *Physical Properties of Carbon Nanotubes*. Imperial College Press: London, 2005.
- [6] Kalamkarov, A., Georgiades, A., Rokkam, S., Veedu, V. & Ghasemi-Nejhad, M., Analytical and numerical techniques to predict carbon nanotubes properties. *Int J Solid Struct*, **43**, pp. 6832–6854, 2006.
- [7] Frankland, S., Harik, V., Odegard, G., Brenner, D. & Gates, T., The stress–strain behavior of polymer–nanotube composites from molecular dynamics simulation. *Compos Sci Tech*, **63**, pp. 1655–1661, 2003.
- [8] Belytschko, T., Xiao, S., Schats, G. & Ruoff, R., Atomistic simulations of nanotube fracture. *Phys Rev B*, **65**, pp. 2354301–2354308, 2002.

- [9] Li, C. & Chou, T.W., A structural mechanics approach for the analysis of carbon nanotubes. *Int J Solids Struct*, **40**, pp. 2487–2499, 2003.
- [10] Gibson, R.F., Ayorinde, E.O. & Wen, Y.F., Vibrations of carbon nanotubes and their composites: A review. *Compos Sci Tech*, **67**, pp. 1–28, 2007.
- [11] Tserpes, K. & Papanikos, P., Finite element modeling of single-walled carbon nanotubes. *Compos Part B*, **36**, pp. 468–477, 2005.
- [12] Ávila, A. & Lacerda, G., Molecular mechanics applied to single-walled carbon nanotubes. *Mat Res Ibero Amer Mat J*, **11**, pp. 239–247, 2008.
- [13] Dresselhaus, M., Dresselhaus, G. & Saito, R., Physics of carbon nanotubes. *Carbon*, **33**, pp. 883–891, 1995.
- [14] Li, C. & Chou, T.W., Vibrational behaviours of multiwalled-carbon-nanotube-based nanomechanical resonators. *Appl Phys Lett*, **84**, pp. 121–123, 2004.
- [15] Bathe, K.J., *Finite Element Procedure in Engineering Analysis*. Prentice Hall: NY, 1989.
- [16] Mackerle, J., Finite element vibration of beams, plates and shell. *Shock Vib*, **6**, pp. 97–109, 1999.
- [17] Sakhaee-Pour, A., Ahmadian, M. & Vafai, A., Vibrational analysis of single-walled carbon nanotubes using beam element. *Thin-Walled Struct*, **47**, pp. 646–652, 2009.
- [18] Harrar, M. & Gibson, R., Numerical simulation of modal vibration response of wavy carbon nanotubes. *J Comp Mat*, pp. 501–515, 2009.
- [19] Li, C. & Chou, T.W., Single-walled carbon nanotubes as ultrahigh frequency nanomechanical resonators. *Phys Review B*, **68**, p. 073405, 2003.
- [20] *Nanotube Modeler JCrystalsoft, version 1.6.4*, 2010.
- [21] Li, C., Ruoff, R. & Chou, T.W., Modeling of carbon nanotube clamping in tensile tests. *Compos Sci Tech*, **65**, pp. 2407–2415, 2005.
- [22] Lee, B. & Wilson, J., Free vibrations of arches with variable curvature. *J Sound Vibr*, **136**, pp. 75–89, 1990.
- [23] Stokey, W., Vibration of systems having distributed mass and elasticity. *Harris' Shock and Vibration Handbook*, eds. C. Harris & A. Piersol, McGraw-Hill. Chapter 7.
- [24] Ávila, A., Donadon, L. & Duarte, H., Modal analysis on nanoclay epoxy-based fiber glass laminates. *Compos Struct*, **83**, pp. 324–333, 2008.
- [25] Ávila, A.F., Yoshida, M., Carvalho, M.R., Dias, E. & de Ávila Jr., J., An investigation on post-fire behavior of hybrid nanocomposites under bending loads. *Compos Part B*, **41**, pp. 380–387, 2010.

A comparison of deterministic, reliability-based and risk-based structural optimization under uncertainty

André Teófilo Beck, Wellison José de Santana Gomes
*Department of Structural Engineering, São Carlos School of Engineering,
University of São Paulo, 13566-590, São Carlos, SP – Brazil*

Abstract

In Deterministic Design Optimization (DDO), constraints are given by codified design rules involving allowable stresses, strains or deflections. Uncertainties in structural loads, material resistances and other problem parameters are taken into account in a subjective and indirect way, by means of partial safety factors specified in design codes. By definition, the optimum structure will have more failure modes designed against the limit: hence, the optimum structure obtained via DDO will be less safe than the original, non-optimal structure. This is a consequence of treating uncertainties in an implicit way. Hence, it can be said that DDO yields the shape or configuration of a structure that is optimum in terms of mechanics, but the formulation grossly neglects the effects of parameter uncertainties on structural safety. Reliability-based Design Optimization (RBDO) has emerged as an alternative to properly model the safety-under-uncertainty part of the problem. In RBDO, allowable failure probabilities are specified as design constraints, and it is possible to ensure that a minimum (and measurable) level of safety is achieved by the optimum structure. The general RBDO formulation, however, addresses the minimization of manufacturing costs, with no account for the expected costs of failure. Risk optimization (RO) increases the scope of the problem, by quantifying the monetary consequences of failure, as well as the costs associated to construction, operation and maintenance. Risk Optimization stands for the minimization of total expected costs, addressing the compromising goals of economy and safety. In this paper, results obtained with DDO, RBDO and RO are compared for some example problems. The wider-scope RO solution is found first, yielding the optimum safety coefficients and optimum failure probabilities for each problem. These values are used as constraints in DDO and RBDO, respectively. Results show that even when the optimum safety coefficients are used as constraint in DDO, the formulation leads to optimum configurations which respect these design constraints, reduce manufacturing costs but increase total expected costs (including expected cost of failure). When the optimum system failure probability is used as constraint in RBDO, the formulation also leads to a reduction of manufacturing costs, but to increases in total expected costs. This happens when the costs associated to different failure modes are distinct. Hence, it is shown in this paper that the optimum structural configuration can only be found by the wider-scope risk optimization formulation.

Keywords: structural optimization, optimum design, DDO, RBDO, reliability analysis.

1 Introduction

In a competitive environment, structural systems have to be designed taking into account not just their functionality, but their expected construction and operation costs, and their capacity to generate profits. This capacity depends on the risk that construction and operation of a given facility implies to the user, to employees, to the general public or to the environment. The capacity to generate profits can be adversely affected by the costs of failure.

The performance and safety of structural systems is affected by uncertainties, or natural randomness, in the resistance of structural materials and in loading conditions. Uncertainty implies risk, or the possibility of undesirable structural response.

In monetary terms, risk (or the expected cost of failure) is given as the product of the cost of failure by a failure probability. Failure probabilities, in their turn, are directly affected by the level of safety adopted in the design, construction and operation of a given facility. This includes the safety coefficients adopted in design, safety and quality assurance measures adopted during construction and the levels of inspection and maintenance practiced during operation.

In structural engineering design, economy and safety are competing goals. Generally, increasing safety implies greater costs, and reducing costs may require a compromise in safety. Hence, designing a structural system involves a tradeoff between safety and economy. In common engineering practice, this tradeoff is addressed subjectively. In codified design, the issue is decided by a code committee, which defines safety coefficients to be used in design, and basic safety measures to be adopted in construction and operation. In general, the tradeoff between economy and safety in structural design can be addressed by structural optimization.

In this paper, the effects of uncertainty on optimum structural design are investigated by comparing three distinct formulations of the structural optimization problem. Deterministic Design Optimization (DDO) grossly neglects the effects of parameter uncertainty and failure consequences, but it allows one to find the shape or configuration of a structure that is optimum in terms of mechanics. As a general rule, the result of DDO is a structure with more failure modes designed against the limit: hence, the optimum structure compromises safety, in comparison to the original (non-optimal) structure. Reliability-Based Design Optimization (RBDO) has emerged as an alternative to properly model the safety-under-uncertainty part of the problem [1–8]. With RBDO one can ensure that a minimum (and measurable) level of safety is achieved by the optimum structure. However, RBDO does not account for the economical consequences of failure, since the safety level is a constraint, and not an optimization variable. DDO and RBDO can both be used to achieve mechanical structural efficiency, but they do not address the safety-economy tradeoff.

Risk Optimization (RO) increases the scope of the problem, by including the (expected) cost of failure in the economic balance [9–15]. Hence, RO allows one to find the optimum tradeoff point between the competing goals of economy and safety [15]. RO aims at finding the optimum level of safety to be achieved in a given structural system, in order to minimize the total expected cost or maximize the expected profit. It is as a tool for decision making in the presence of uncertainty. RO is complementary to DDO or RBDO, in the sense that the most economic structural design also requires mechanical efficiency.

2 Failure probability and expected cost of failure

Let \mathbf{X} and \mathbf{z} be vectors of structural system parameters. Vector \mathbf{X} represents all random system parameters, and includes geometric characteristics, resistance properties of materials or structural members, and loads. Some of these parameters are random in nature; others cannot be defined deterministically due to uncertainty. Typically, resistance parameters can be represented as random variables and loads are modeled as random processes of time. Vector \mathbf{z} contains all deterministic system parameters to be optimized, like nominal member dimensions, partial safety factors, design life, parameters of the inspection and maintenance programs, etc. Vector \mathbf{z} may also include some parameters of random variables in \mathbf{X} .

The existence of uncertainty implies risk, that is, the possibility of undesirable structural responses. The boundary between desirable and undesirable structural responses is given by limit state functions $g(\mathbf{z}, \mathbf{x})=0$, such that:

$$\begin{aligned} D_f &= \{\mathbf{z}, \mathbf{x} | g(\mathbf{z}, \mathbf{x}) \leq 0\} && \text{is the failure domain} \\ D_s &= \{\mathbf{z}, \mathbf{x} | g(\mathbf{z}, \mathbf{x}) > 0\} && \text{is the safety domain} \end{aligned} \quad (1)$$

Each limit state describes one possible failure mode of the structure, either in terms of performance (serviceability) or ultimate capacity. The probability of undesirable structural response, or probability of failure, is given by:

$$P_f(z) = P[g(\mathbf{z}, \mathbf{X}) \leq 0] \quad (2)$$

where $P[\cdot]$ stands for *probability*. The probabilities of failure for individual limit states and for system failure are evaluated using traditional structural reliability methods such as FORM and SORM [16, 17].

The life-cycle cost of a structural system subject to risk can be decomposed in an initial or construction cost, cost of operation, cost of inspections and maintenance, cost of disposal and expected costs of failure ($J^{expected}$). The expected cost of failure, or failure risk, is given by the product of failure cost ($J^{failure}$) by failure probability [9–15]:

$$J^{expected}(\mathbf{z}) = J^{failure}(\mathbf{z}) P_f(\mathbf{z}) \quad (3)$$

Failure costs include the costs of repairing or replacing damaged structural members, removing a collapsed structure, rebuilding it, cost of unavailability, cost of compensation for injury or death of employees or general users, penalties for environmental damage, etc. All failure consequences have to be expressed in terms of monetary units, which can be a problem when dealing with human injury, human death or environmental damage. Evaluation of such failure consequences in terms of the amount of compensation payoffs allows the problem to be formulated, without directly addressing matters about the value of human life [18, 19].

For each structural component or system failure mode, there is a corresponding failure cost term. The total (life-cycle) expected cost of a structural system becomes:

$$\begin{aligned}
J^{total}(\mathbf{z}) = & J^{initial\ or\ construction}(\mathbf{z}) \\
& + J^{operation}(\mathbf{z}) \\
& + J^{inspection\ and\ maintenance}(\mathbf{z}) \\
& + J^{disposal}(\mathbf{z}) \\
& + \sum_{failure\ modes} J^{failure}(\mathbf{z})P_f(\mathbf{z})
\end{aligned} \tag{4}$$

The initial or construction cost increases with the safety coefficients used in design and with the practiced level of quality assurance. More safety in operation involves more safety equipment, more redundancy and more conservatism in structural operation. Inspection cost depends on intervals, quality of equipment and choice of inspection method. Maintenance costs depend on maintenance plan, frequency of preventive maintenance, etc. When the overall level of safety is increased, most cost terms increase, but the expected costs of failure are reduced.

Any change in \mathbf{z} that affects cost terms is likely to affect the expected cost of failure. Changes in \mathbf{z} which reduce costs may result in increased failure probabilities, hence increased expected costs of failure. Reduction in expected failure costs can be achieved by targeted changes in \mathbf{z} , which generally increase costs. This compromise between safety and costs is typical of structural systems.

3 Structural optimization formulations

3.1 Deterministic Design Optimization (DDO)

In deterministic design optimization, uncertainties and consequences (cost) of failure are not explicitly taken into account. A typical formulation of DDO reads:

$$\begin{aligned}
& \text{find : } \mathbf{z}^* \\
& \text{which minimizes: } \text{cost}(\mathbf{z}) \text{ or } \text{volume}(\mathbf{z}) \\
& \text{subject to: } \text{deterministic failure criteria}(\sigma(\mathbf{z}) < \sigma_{yield}/\lambda)
\end{aligned} \tag{5}$$

In Eq. (5), λ is a safety coefficient, given by some design code and not an optimization variable. The cost function only includes cost (or volume) of structural materials, and sometimes life-cycle and/or manufacturing costs. The formulation allows finding a structure which is optimal in terms of mechanics but, due to lack of a quantitative measure of safety, expected costs of failure cannot be considered. Since safety is not quantified, the resulting optimal structure may compromise safety, in comparison to the original (non-optimal) structure.

3.2 Reliability-Based Design Optimization (RBDO)

One formulation which allows uncertainty to be taken explicitly into account is known as reliability-based design optimization. A typical formulation of RBDO reads [1–8]:

$$\begin{aligned} & \text{find : } \mathbf{z}^* \\ & \text{which minimizes: } \text{manufacturing cost}(\mathbf{z}) \text{ or volume}(\mathbf{z}) \\ & \text{subject to: } P_f(\mathbf{z}) < P_{f_{admissible}} \end{aligned} \quad (6)$$

Generally, the cost term in this formulation is the same as for DDO, that is, it does not include expected costs of failure. RBDO allows finding a structure which is optimal in mechanical sense, and which does not compromise safety. However, results depend on the admissible failure probability used as constraint. The balance between safety and economy cannot be addressed, because failure probability is not an optimization variable.

3.3 Risk Optimization (RO)

When expected costs of failure are included in the analysis, it is possible to find the best point of compromise between safety and economy. Risk optimization (reliability-based) will also look for the optimum failure probabilities [9–15]:

$$\begin{aligned} & \text{find : } \mathbf{z}^*, \lambda^* \text{ and } P_f^*(\mathbf{z}^*, \lambda^*) \\ & \text{which minimizes: } J^{total}(\mathbf{z}) \end{aligned} \quad (7)$$

where $J^{total}(\mathbf{z})$ is the total expected cost given by Eq. (4). Partial safety factors λ are included as design variables in the risk optimization formulation (Eq. 7). Hence, the formulation yields optimum partial safety factors λ^* , which are associated to optimum failure probabilities, P_f^* . In comparison to RBDO, risk optimization is an unconstrained optimization problem, since all failure probability “constraints” now appear in the cost function (Eq. 4). Multiple reliability constraints [20] are also “automatically” included in the RO formulation, as Eq. 4 admits one cost term for each failure mode. Considering the solution of a constrained optimization problem like Eq. (6) via penalty methods, one observes that, in the RO formulation, the cost of failure terms (Eq. 4) are equivalent to the “penalties” for exceeding failure probability constraints in RBDO. However, these are no artificial penalties; they are the actual costs of designing away from the optimum. Hence, the RO formulation yields a smoother problem which is, nevertheless, not easier to solve.

Risk optimization can be achieved by controlling failure probabilities and/or the cost of failure. Risk mitigation through preparation, education, training, and so on, is out of scope of this investigation. Although failure costs are constants in the present formulation, it is important to note that it does allow for a trade-off between different costs for different failure modes. Hence, service and ultimate limit states, with their intrinsically different costs of failure, are readily accounted for in the present formulation.

If social or non-monetary consequences of failure are involved (like death or environmental damage), failure probabilities constraints can be included in the RO formulation:

$$\begin{aligned} & \text{find : } \mathbf{z}^*, \lambda^* \text{ and } P_f^*(\mathbf{z}^*, \lambda^*, \mathbf{X}) \\ & \text{which minimizes: } J(\mathbf{z}) \\ & \text{subject to: } P_f(\mathbf{z}, \mathbf{X}) < P_{f_{admissible}} \end{aligned} \quad (8)$$

The revenue to be obtained with a structural system is generally independent of \mathbf{z} or \mathbf{X} , that is, it only depends on the facility been available. Hence, an alternative risk optimization problem can be formulated as:

$$\begin{aligned} & \text{find : } \mathbf{z}^*, \lambda^* \text{ and } P_f^*(\mathbf{z}^*, \lambda^*, \mathbf{X}) \\ & \text{which maximizes: } \text{profit} = \text{revenue} - J(\mathbf{z}) \end{aligned} \quad (9)$$

Figure 1 illustrates the scope of the three formulations just presented. It is clear that the formulations are not equivalent, but complementary, each addressing a different part of the problem. The RO formulation is complementary to DDO or RBDO, since the most economic structure also needs to be mechanically efficient. In fact, the RO formulation increases the scope of the problem, by considering the costs of failure. It is noted that DDO, in comparison to RO, does not account for the effects of uncertainty. RBDO considers uncertainty, but it neglects one of the main consequences of uncertainty: the expected costs of failure.

It should be noted that the nomenclature used in this paper is not necessarily in accordance with the literature: in many cases, the name RBDO is used for problems where expected costs of failure are also considered [9–15]. In the present paper, it is convenient to refer to RBDO and RO as two different formulations due to the objective of exposing the difference in the results obtained using each formulation. Another common approach to structural optimization in presence of uncertainties, robust optimization [21, 22], is not considered in the present paper because results are not directly comparable to DDO, RBDO or RO.

In the literature, there are a number of approaches which simplify the RBDO problem by replacing it by an equivalent DDO problem [23–25]. The conditions under which this simplification is possible are not comprehensively investigated in these papers. For example, Qu and Hafta [23] use a single safety factor to make the conversion from reliability to deterministic constraints. In the present paper, it will be shown that this is not always possible. It is also not known whether the RO problem can be replaced by equivalent DDO or RBDO formulations. These issues are addressed in the present paper, by means of comparative optimization analyses.

4 Comparative optimization analyses

In sections 2 and 3, optimization formulations were presented in very general terms. In order to study the effects of uncertainty in optimum structural design, these formulations are used in this paper in

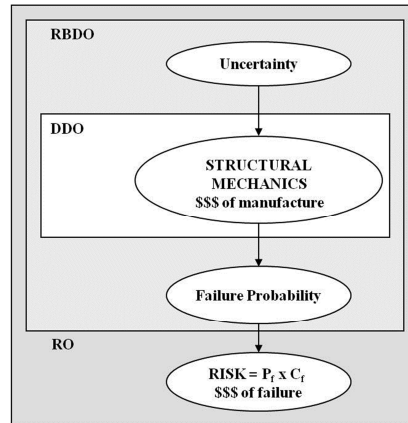


Figure 1: Scope of structural optimization formulations.

a number of different ways [26]. This section explains how these formulations are applied to some example problems in the sequence.

It is clear that the three formulations are not directly comparable, because their scope is different. Results of DDO clearly depend on the safety coefficient(s) used as constraint(s). Similarly, results of RBDO of course depend on failure probabilities used as constraints. Now suppose that *optimum safety coefficients* and *optimum failure probabilities* are first obtained from a (greater scope) risk optimization analysis and then used as constraints in DDO and RBDO, respectively. One could expect that, by using *optimum* constraints in DDO and RBDO, one would obtain the same optimum structure obtained in risk optimization (RO). This is not always so, as will be shown in the sequence.

In the numerical examples that follow, the RO solution is found first. Since the scope of RO is larger, and includes the scopes of DDO and RBDO, this general RO solution is used as reference. In order to compare results, total expected costs (Eq. 4) are evaluated for the optimum structures resulting from each formulation. Hence, following DDO or RBDO analyses, failure probabilities and costs of failure are computed. In order to understand the differences between the results, (manufacturing) cost functions used in DDO and RBDO analyses are also computed for RO for comparison.

In real world problems, one does not know optimal failure probabilities or optimal safety coefficients before designing a structure. Hence, a “natural” order of solution for real problems would be a DDO (or RBDO) analysis, followed (or not) by a risk optimization (RO) analysis. In this paper, the implications of performing a DDO analysis first, followed by a RO analysis, are studied. In this case, the optimum structural configuration is found in the DDO analysis. The risk optimization that follows maintains aspect ratios, but scales the structure in order to find its optimum failure probability (or optimal safety coefficients). Table 1 summarizes the different optimizations considered in this paper, and presents the keywords that identify each solution.

Table 1: Summary of comparative optimization analysis.

Keyword	Description	Result
RO	Complete RO, used as reference for other analyses.	optimum configuration (\mathbf{z}^*) and safety factors (λ^*); hence also optimum P_f^*
RBDO	RBDO, with P_f^* used as constraint	optimum configuration (\mathbf{z}^*)
DDO1	DDO, with single optimum safety coefficient λ^* used as constraint	optimum configuration (\mathbf{z}^*)
DDOn	DDO, with n optimum safety coefficients λ_i^* , $i=1, \dots, n$ used as constraints, for n design (limit state) equations	optimum configuration (\mathbf{z}^*)
RO_esc	DDO, followed by a scaled RO which maintains aspect ratios but looks for the optimum P_f^*	optimum config. (\mathbf{z}^*) by DDO, optimum P_f^* by RO

5 Numerical examples

5.1 Three-bar parallel system

This problem involves a parallel system composed of three bars, each made of a different material. The mean resistance is the same for all materials, but the coefficient of variation (c.o.v.) is different for each material, reflecting differences in manufacturing quality control. The cost of each material is also different, as presented in Table 2.

Table 2: Summary of random variable data for three-bar parallel system.

Random Variable	variant	distribution	mean	c.o.v.	cost
Load (P)	-	normal	75 kN	15%	-
Elastic modulus (E)	-	normal	200 GPa	3%	-
Material strength (f_y)	material 1	lognormal	250 MPa	15%	1 (reference)
	material 2	lognormal	250 MPa	10%	1.05
	material 3	lognormal	250 MPa	5%	1.10

The optimization variables for this problem are the cross-section areas of each bar, and the number of bars (maximum 3). If the optimization algorithm reduces the area of any bar to 0.1 cm² or below,

the bar is considered not necessary and eliminated. Hence, $\mathbf{z} = \{A_1, A_2, A_3\}$. The only deterministic design restriction for this problem is given by:

$$g = \sum_i (f_{yi} \cdot A_i) - P \cdot \lambda \geq 0 \quad (10)$$

where λ is the safety coefficient, f_{yi} is the strength of the i th material, and A_i is the area of the i th bar.

The stiffness of the i th bar is given by $K_i = EA_i/L$. The load factor for bar 1 is given as $RSF_1 = K_1/K_S$, where K_S is the total stiffness, given by: $K_S = K_1 + K_2 + K_3$. Hence, the limit state equation used to evaluate the probability that bar 1 fails, given that no other bar has failed before, is given by:

$$g_1(z) = f_{y1} \cdot A_1 - RSF_1 \cdot P \quad (11)$$

Failure of the first bar (be it bar 1, 2 or 3) is considered a service failure, since the remaining bars will carry the load. Given that bar 1 has failed, the load factor for bar 2 becomes $RSF_2 = K_2/K_S$, where K_S is now: $K_S = K_2 + K_3$. The limit state equation for failure of bar 2, given that bar 1 has failed, is given by:

$$g_2(z) = f_{y2} \cdot A_2 - RSF_2 \cdot (P - \eta \cdot f_{y1} \cdot A_1) \quad (12)$$

This is again considered a service failure, because the third bar will carry the load. In Eq. (12), variable η is used to model brittle and ductile material failures, following Hendawi and Frangopol [27]. A perfectly elastic material with brittle (fragile) failure is modeled with $\eta=0$. An elastic-perfectly plastic material with ductile failure is modeled using with $\eta=1$. The term $\eta \cdot f_{y1} \cdot A_1$ in Eq. (12) gives the residual strength of bar 1, which is zero when material failure is brittle.

The collapse failure probability, for failure sequence 1-2-3, is given by the probability that bar 3 fails, given that bars 1 and 2 have failed. The limit state equation is:

$$g_3(z) = f_{y3} \cdot A_3 - (P - \eta \cdot (f_{y1} \cdot A_1 + f_{y2} \cdot A_2)) \quad (13)$$

In a similar way, all possible failure sequences are considered. Equations (11) to (13) are used to evaluate the corresponding probabilities, with a proper change in the indexes. If the j th failure sequence is denoted by S_j , the system collapse probability is given by the union:

$$P_f|_{system}(z) = P \left[\bigcup_j S_j(z) \right] \quad (14)$$

The objective function for DDO and RBDO is a “manufacturing” cost function, which includes cost of materials and workmanship. Cost of materials is given by:

$$C_{mat} = \$_{mat} \cdot \rho \cdot L \cdot (A_1 + 1.05 \cdot A_2 + 1.10 \cdot A_3) \quad (15)$$

where $\$_{mat}$ is the unit cost of material 1 (per weight), ρ is material density, L is length of the bars, 1.05 and 1.10 are the relative cost factors for materials 2 and 3. A fixed reference cost, C_{ref} , is evaluated

from an initial, deterministic design, for a central safety factor $\lambda = 2.0$. This cost is obtained as $C_{ref} = 5.5 \cdot \$_{mat}$. Cost of workmanship is given by:

$$C_{work} = C_{ref} + 0.2 \cdot C_{mat} + C_{ref} \cdot 0.05 \cdot (N_{bars} - 1) \quad (16)$$

The first term in Eq. (16) is a fixed cost of labor, the second term is a fraction of cost of materials, and the last term is a penalty for complexity, i.e., considering that a system with three parallel bars is more elaborate to manufacture than a system with a single bar. The manufacturing cost function becomes:

$$CM = 1.2 \cdot C_{mat} + C_{ref} \cdot [1 + 0.05 \cdot (N_{bars} - 1)] \quad (17)$$

The objective function for RO is the total expected cost, which is the sum of manufacturing costs and expected costs of failure. The cost of service failures is assumed equal to C_{ref} , and the cost of ultimate failure is $10 \cdot C_{ref}$. If E_i denotes the event that the i^{th} bar failed, then the total expected cost is:

$$J^{total}(z) = CET = CM + C_{ref} \cdot \sum_{i=1}^{N_{bars}} P[E_i] + C_{ref} \cdot \sum_{j=1, j \neq i}^{N_{bars}} \cdot P[E_j | E_i] + 10 \cdot C_{ref} \cdot P_f|_{system}(z) \quad (18)$$

where CET is the total expected cost, referred to in the tables and figures to follow. Solutions are obtained for three variants of the problem, as shown in Table 3. Optimum structural configurations are presented in Table 4. Table 5 compares manufacturing and total expected costs obtained with alternative formulations, with respect to the reference RO solution.

Table 3: Variants of three-bar parallel system problem.

Variant	brittle-ductile material (η)	Cost of service failure
(1A)	0	C_{ref}
(1B)	1	C_{ref}
(1C)	1	0

For problem variant (1A), with brittle material and including service failure costs, the RO and DDO solutions converge to a system of a single bar, made of the best-quality material (material 3). Hence, manufacturing costs and total expected costs are identical for these formulations, including the “scaled” RO_esc (DDO followed by RO) solution. Clearly, for brittle materials there is no safety (or economical) advantage in having two or more bars, instead of a single bar of greater cross-sectional area. Nevertheless, the RBDO formulation does converge to a different solution: two bars, made of materials 2 and 3, and such that $A_3 > A_2$. In Table 5 it can be observed that, with this solution, the

Table 4: Optimum results for variants of three-bar parallel system problem.

Variant	Solution	A_1	A_2	A_3	λ	P_f
(1A)	RO	0	0	4.3575	1.4525	$3.270 \cdot 10^{-3}$
	RBDO	0	0.1	3.8035	1.3010	$3.270 \cdot 10^{-3}$
	DDO1	0	0	4.3575	1.4525	$3.270 \cdot 10^{-3}$
	RO_esc	0	0	4.3570	1.4524	$3.277 \cdot 10^{-3}$
(1B)	RO	0	4.0740	0.1075	1.3938	$6.246 \cdot 10^{-4}$
	RBDO	0	2.5220	1.5728	1.3649	$6.246 \cdot 10^{-4}$
	DDO1	0	0	3.8472	1.2824	$4.216 \cdot 10^{-2}$
	RO_esc	0	0	4.3575	1.4525	$3.270 \cdot 10^{-3}$
(1C)	RO	0	3.0394	0.8887	1.3093	$2.660 \cdot 10^{-3}$
	RBDO	0	3.0395	0.8885	1.3093	$2.660 \cdot 10^{-3}$
	DDO1	0	0	3.6787	1.2262	$8.230 \cdot 10^{-2}$
	RO_esc	0	0	4.3575	1.4525	$3.270 \cdot 10^{-3}$

Table 5: Optimum cost results for variants of three-bar parallel system problem.

Problem variant	CM/CMref				CET/CETref			
	RO	RBDO	DDO1	RO_esc	RO	RBDO	DDO1	RO_esc
(1A)	1.000	0.980	1.000	1.000	1.000	1.033	1.000	1.000
(1B)	1.000	0.998	0.957	1.010	1.000	1.006	1.164	1.006
(1C)	1.000	1.000	0.960	1.032	1.000	1.000	1.405	1.035

RBDO formulation is able to reduce manufacturing costs, but by compromising total expected costs. The reasons for this behavior will be made clear in the sequence (problems 1B and 1C).

For ductile materials (problem variant 1B), the reference RO solution is a system of two bars, made of materials 2 and 3, with $A_2 \gg A_3$. The second bar is a “wire” of minimal area and made of the best material, which provides an alternative load path in case of failure of the first bar. For the ductile material, this two-bar solution is cheaper than the single bar solution obtained for problem (1A). None of the alternative formulations reaches the optimum obtained by the reference risk-based solution. DDO (and also RO_esc) yield a single-bar, made of the best material, just as for problem (1A). Hence, it is observed that (such simple) deterministic formulation does not account for the materials post-failure behavior, and its effect on system safety. The RBDO solution for this problem

yields a system of two bars, but with $A_2 > A_3$. The solution is not the same as RO because the areas of the bars are similar (no “wire bar”). In Table 5 it is observed that this RBDO solution minimally affects manufacturing costs, but increases total expected costs. This difference in optimum solution, and also the differences observed for problem (1A) can be explained by the cost of service failure, as follows.

Problem variant (1C) considers ductile materials but no service failure costs. In Table 5 it is observed that the RBDO solution now agrees with the reference RO solution, which is identical to the reference solution obtained for problem (1B) – one bar of material 2 and a thin “wire” of material 3. Hence, it is observed that the RBDO formulation does respect the system failure probability constraint, but it does not account for the costs associated to service failure. For the formulations to become equivalent, it would be necessary to specify “optimum” failure probability constraints for all service and ultimate failure modes. It is also observed in Table 5 that DDO and RO_esc optimum solutions (single bar of best material) yield much higher total expected costs. The DDO formulation is able to find an optimum which reduces manufacturing costs, but which results in larger total expected costs. The RO_esc formulation, which tries to improve on the DDO solution by finding the optimum safety coefficient, following a DDO analysis, does reduce the total expected costs, but cannot match the results obtained in the more general risk-based formulation.

5.2 Three-bar series system

This problem is based on the three-bar parallel system (same bars made of the same materials), but the bars are connected as a series system. For this problem, the four formulations yielded the same results, when 3 different (optimal) safety coefficients were used in DDO. Using a single safety coefficient (the largest between the 3 optimal values) resulted in slight increases in optimal DDO manufacturing and total expected costs.

5.3 Built-up column

The column illustrated in Figure 2 is made of U-section struts ($U200 \times 75 \times 2.65$ mm), with L-section braces and battens ($L30 \times 2.25$ mm) [26]. The total length is L and the column is subject to a load P . Optimization variables are the width b and the number of braces and battens ($N = L/d$), hence $\mathbf{z} = \{b, N\}$. Random variables are the load P , the elasticity modulus and the materials yield stress, as summarized in Table 6.

Table 6: Summary of random variable data for column problem.

Random Variable	distribution	mean	c.o.v.
Load (P)	normal	300 kN	15%
Elastic modulus (E)	normal	210 GPa	3%
Material strength (f_y)	lognormal	250 MPa	10%

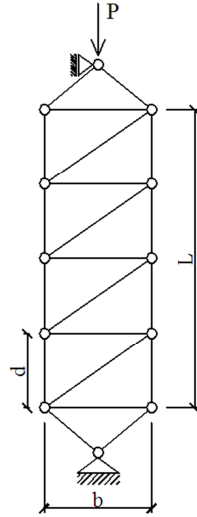


Figure 2: Built-up column.

The design equations for this problem relate to local and global buckling. Ideal truss behavior and elastic (Euler) buckling are assumed. Local buckling of the U-shaped struts is given by:

$$g_L(z) = \frac{\pi^2 \cdot E \cdot I_U}{d^2} - \lambda_1 \cdot \frac{P}{2} \quad (19)$$

where I_U is the moment of inertia of the U-section. Global column buckling is given by:

$$g_G(z) = \frac{\pi^2 \cdot E \cdot I_G}{L^2} - \lambda_2 \cdot P \quad (20)$$

where I_G is the moment of inertia of the column cross-section, given by:

$$I_G = 2 \cdot (I_U + A_U \cdot (b/2)^2) \quad (21)$$

The limit state equations are equivalent to Eqs. (19) and (20), but with unitary safety factors.

One unit of braces and battens is considered as one horizontal and one diagonal L-shape. The total length of one brace-batten unit is:

$$L_{bb} = \sqrt{b^2 + (L/N)^2} + b \quad (22)$$

The basic cost of materials is given by:

$$C_{mat} = \$_{mat} \cdot \rho \cdot (N \cdot L_{bb} \cdot A_L + 2 \cdot L \cdot A_U) \quad (23)$$

The fixed, reference cost is $C_{ref} = 150 \cdot \$_{mat}$. Cost of workmanship includes a fixed term, a term proportional to cost of materials, and a term for each additional brace-batten unit, after the first:

$$C_{work} = C_{ref} + 0.2 \cdot C_{mat} + (N - 1) \cdot 0.025 \cdot C_{ref} \quad (24)$$

Total manufacturing cost becomes:

$$CM = 1.2 \cdot C_{mat} + C_{ref} \cdot [1 + 0.025 \cdot (N - 1)] \quad (25)$$

Cost of failure is equal to $10 \cdot C_{ref}$, for any of the possible failure modes, hence the total expected cost is:

$$J^{total}(\mathbf{z}) = CET = CM + 10 \cdot C_{ref} \cdot P_f|_{system}(\mathbf{z}) \quad (26)$$

where the series-system failure probability is

$$P_f|_{system}(\mathbf{z}) = P \left[\bigcap_i \{g_i(\mathbf{z}) \leq 0\} \right] \quad (27)$$

The problem is first solved for $L=7.5\text{m}$. The optimum structural configuration found in the reference RO analysis has $b=16.77\text{ cm}$ and 4 brace-battens units ($N=4$). Optimum central safety coefficients are $\lambda_1 = 1.875$ and $\lambda_2 = 1.676$; optimum failure probabilities are $P_{f1} = 2.374 \cdot 10^{-8}$ and $P_{f2} = 9.624 \cdot 10^{-6}$, for local and global buckling, respectively, and $P_{fSYS} = 9.624 \cdot 10^{-6}$ for the series system. Interestingly, although both safety coefficients refer to the same failure mode (elastic buckling), the optimal safety coefficient with respect to local buckling is larger than the optimal safety coefficient due to global buckling. Correspondingly, failure probability is smaller for local in comparison to global buckling. This can be explained by the restriction of an integer number of brace-batten units. When the number of brace-batten units jumps from 3 to 4, column length for local buckling is reduced, hence λ_1 is increased. According to the analysis, increasing distance b in order to also increase λ_2 is not worthwhile.

The optimum configuration found in RO is also found by the RBDO and DDO2 analyses. For this problem, the RBDO formulation yields the same result as RO because there are neither service failures nor costs associated to it. If a single safety coefficient is used (DDO1), the optimum number of brace-battens becomes $N = 5$. If this number is fixed and a scaled (RO_esc) analysis is made, manufacturing and total expected costs cannot be reduced. Manufacturing and total expected costs are compared in Figure 3.

The problem is solved again, varying column length L from 7.5m up to 40m. For all column configurations, the RBDO result agrees with RO. For some column lengths, the DDO1 and RO_esc solutions agree with RO: this happens when the optimum number of braces and battens is (coincidentally) the same for all solutions. Manufacturing and total expected cost ratios are evaluated by dividing *optimum* costs found by the DDO1 and RO_esc formulations by the reference optimal costs found through RO. Total expected cost ratios are shown in Figure 4, and manufacturing cost ratios are shown in

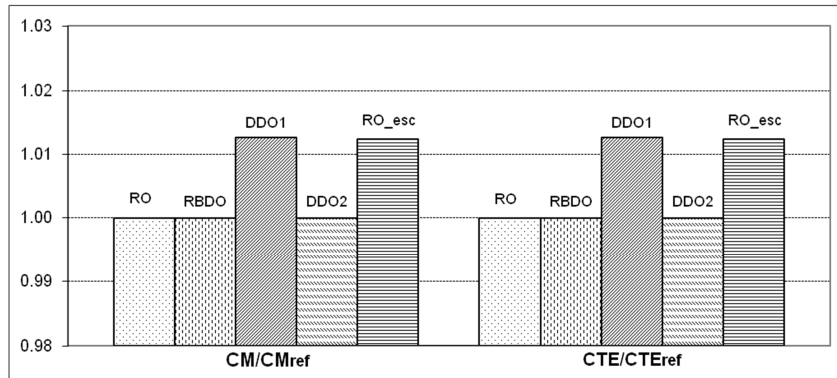


Figure 3: Comparison of optimum costs for the column problem.

Figure 5. It is verified that, for some values of column length L , the same optimal number of brace and battens is found, hence total expected and manufacturing costs are the same for the DDO1, RO_esc and reference RO solutions. For other values of L , however, the DDO1 and RO_esc formulations yield different numbers of braces and battens, making both manufacturing and total expected costs larger than those obtained in the reference RO formulation.

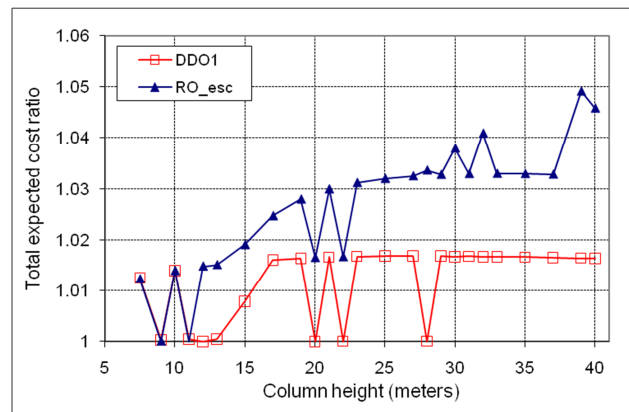


Figure 4: Ratio of total expected costs obtained in DDO1 and RO_esc solutions, with respect to reference RO solution.

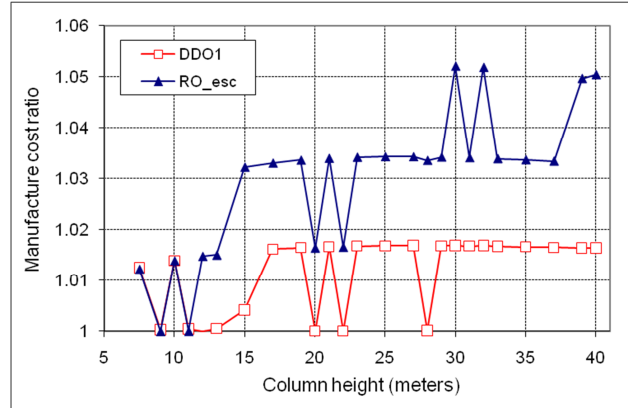


Figure 5: Ratio of manufacturing costs obtained in DDO1 and RO_esc solutions, with respect to reference RO solution.

5.4 Cable-stayed tower

The cable-stayed tower considered in this example is illustrated in Figure 6 [26]. Considering tower, cable and loading symmetry, only one set of three cables needs to be considered, as shown in the figure. For simplicity, design of the vertical part of the tower is not included in the problem. The optimization problem refers to the number of, location and depth of the foundations supporting the cables. A horizontal wind load is assumed on the tower, with linear variation from zero to W_0 in the lower segment, and constant value W_0 in the higher segments, following Figure 6. Random variable data for this problem is presented in Table 7. Wind load and resistance of the foundations are considered as random variables. Without loss of generality, non-dimensional units are considered throughout the problem. Total tower height is $H = 30$ meters.

Table 7: Summary of random variable data for cable-stayed tower problem.

Random Variable	distribution	mean	c.o.v.
Wind load (W)	Gumbel	w_0	30%
Foundation resistances (R_f)	lognormal	1.0	20%

Foundation depth is assumed proportional to the vertical component of cable force (f_v) and to the safety factor for foundation design (λ_i). Hence, the design equations are:

$$d_{f_i}(\lambda_i, x_i) = \lambda_i \cdot f_{v_i}(x_i, w_0) \quad (28)$$

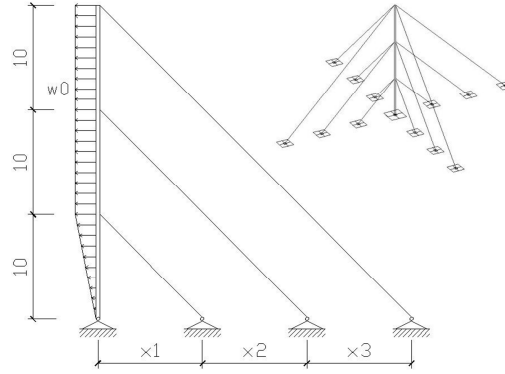


Figure 6: Cable-stayed tower.

where d_{f_i} is the depth of i^{th} foundation. Foundation resistance is assumed directly proportional to foundation depth, hence the random resistance of the i^{th} foundation is obtained as:

$$R_{f_i}(\lambda_i, x_i) = d_{f_i}(\lambda_i, x_i) \cdot R_f \quad (29)$$

where R_f is a non-dimensional random (variable) foundation resistance (Table 8). Limit state functions for this problem relate to foundation failure, hence:

$$g_i(R_f, W) = \lambda_i \cdot f_{vi}(x_i, w_0) \cdot R_f - f_{vi}(x_i, W) \quad (30)$$

Failure of any foundation is assumed to cause collapse of the tower; hence the system limit state is:

$$P_f|_{system} = P \left[\bigcap_i \{g_i \leq 0\} \right] \quad (31)$$

Optimization of the cable support for the tower involves 6 optimization variables, hence $\mathbf{z} = \{x_1, x_2, x_3, \lambda_1, \lambda_2, \lambda_3\}$. Moreover, if during the optimization process two foundations come closer than one meter, they are merged into a single foundation, with depth equal to the sum of depths. Hence, the number of foundations is also a design variable.

Objective functions for this problem involve manufacturing costs (material plus workmanship) and expected failure costs. The cost of one square meter of land, in the location where the tower is to be built, is assumed as reference cost (C_{ref}). All other cost terms are related to this value, which is assumed unitary. Cost of land, required to install the tower and its supporting cables, is given by:

$$C_{land} = \pi \cdot \max_i (x_i)^2 \cdot C_{ref} \quad (32)$$

Cost of the foundations is proportional to foundation depth:

$$C_{foundation} = 125 \cdot C_{ref} \cdot \sum_{i=1}^{\#foundations} (d_{fi})^{1.1} \quad (33)$$

where $125C_{ref}$ is the cost per meter of foundation. The unitary cost of cables (per meter) is assumed as $50C_{ref}$ and total length of cables (L_{cables}) is a function of foundation positions (x_1, x_2, x_3). The cost of workmanship is fixed at $105C_{ref}$. Putting all these terms together, manufacturing cost becomes:

$$CM = C_{land} + C_{foundation} + 50 \cdot C_{ref} \cdot L_{cables} + 105 \cdot C_{ref} \quad (34)$$

Failure costs, for tower collapse, are the cost for reconstructing the tower ($CM - C_{land}$), plus the cost of damage, if the tower hits third party facilities when falling. Damage to third parties will only occur if the land bought for tower erection is less than tower height, $H = 30\text{m}$. In the risk optimization problem, it will be decided whether buying this amount of land is worthwhile. The potential area for damage is:

$$A_{potential} = \max \left[0, \frac{\pi}{8} \cdot (H^2 - \max_i(x_i)^2) \right] \quad (35)$$

where it is assumed that a tower collapse hits $(1/8)^{th}$ of the encircling area. Compensation payouts to third parties is assumed proportional to the potential area:

$$C_{damage} = 2 \cdot 10^4 \cdot C_{ref} \cdot A_{potential} \quad (36)$$

Hence, the total expected cost function becomes:

$$J^{total}(z) = CET = CM + (CM - C_{land} + C_{damage} \cdot P[damage|failure]) \cdot P_f|_{system} \quad (37)$$

where $P[damage|failure] = 0.75$ (assuming that not all area around the tower has been built up by third parties).

For many configurations of this problem (different ratios between cost terms), the reliability-based risk optimization (RO) yields an optimum solution where the farthest foundation is located within the potential damage area. For these configurations, both DDO3 and RBDO yield the same optimum solutions. In case of RBDO, this happens because no service failures are considered in this problem. Expected failure costs are controlled by failure probabilities, which are controlled by the foundation safety factors. Hence, DDO with three optimum safety factors as constraints also yields the same optimum solution.

However, for the problem configuration presented here, results are quite different, as shown in Figure 7 and Table 8. For this configuration, which can be said to be of “cheap land”, the RO formulation yields an optimum solution where the farthest foundation is located at $x_3 = 30\text{m}$. Hence, expected failure costs are controlled by reducing to zero the potential damage area. This configuration is not achieved in any of the alternative formulations (DDO1, DDO3, RDBO), because expected costs of failure are not account for. Even when optimum safety coefficients and failure probabilities are used as constraints, the three formulations yield optimum solutions where manufacturing costs are reduced,

but by compromising total expected costs. It is observed that the RBDO formulation leads to an increase of nearly 4% in total expected costs. For the RO_esc solution, both manufacturing and total expected costs are higher. This solution is obtained by performing a DDO optimization first, with $\lambda = 2$, and then performing a risk optimization, with fixed values of $\{x_1, x_2, x_3\}$.

It is also observed that, for many optimum configurations (Table 8), the distance between foundations was reduced to one meter, but they were not merged together by the algorithm. This may have happened because of the non-linear exponent (1.1) in the foundation cost function (Eq. 33).

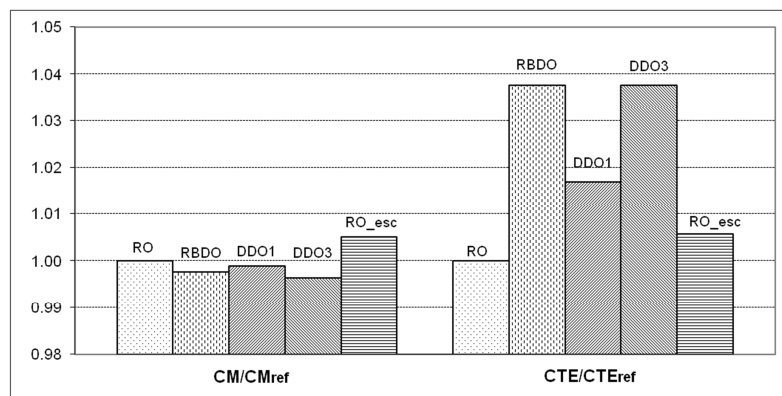


Figure 7: Comparison of optimum costs for the cable-stayed tower problem.

Table 8: Optimum cable and foundation configurations for cable-stayed tower problem.

Solution	Optimization variables						$P_f _{system}$
	x_1	x_2	x_3	λ_1	λ_2	λ_3	
RO	25.00	29.00	30.00	1.9767	1.8877	1.8521	$2.6428 \cdot 10^{-3}$
DDO1	22.56	23.56	24.56	1.9767	1.9767	1.9767	$1.2473 \cdot 10^{-3}$
DDO3	22.52	23.52	24.52	1.9767	1.8877	1.8521	$2.6428 \cdot 10^{-3}$
RBDO	23.00	25.77	26.77	2.0245	1.8174	1.9341	$2.6428 \cdot 10^{-3}$
RO_esc	20.91	23.01	24.01	2.2505	2.1735	2.1548	

6 Concluding remarks

This paper presented a study of the effects of uncertainty on optimum structural design, by means of comparisons of the optimum solutions obtained by different formulations of the optimization problem. Results were presented for four example problems.

Deterministic Design Optimization (DDO) yields a structure which is optimum in terms of mechanics but, since parameter uncertainty and its effects on system safety are not taken into account, safety of the optimum structure will be compromised. Results obtained for the three bar parallel system and for the cable-stayed column examples have shown that, even if a set of *optimum* safety coefficients is provided as constraints in the DDO analysis, the formulation leads to an optimum configuration which respects these design constraints, reduces manufacturing costs but increases total expected costs. If a single *optimum* safety coefficient is used as constraint (the largest in the optimum set), results are even worse: the extra safety margin increases manufacturing costs much more than it reduces expected costs of failure. When a risk optimization is performed, in order to find the optimum safety coefficient *after* a DDO, but respecting the structural configuration found in this DDO, total expected costs can be reduced, but not to a level of agreement with a more general formulation, where both structural configuration *and* risk are optimized simultaneously.

Reliability-based Design Optimization (RBDO) does improve on the DDO formulation, by considering parameter uncertainty and one of its main consequences: the probability of failure. Failure probabilities are used as design constraints in order to guarantee that the optimum structure will not sacrifice safety. Results, of course, do depend on the values of failure probabilities used as constraints. Using the *optimum* system failure probability as constraint in an RBDO analysis may not be sufficient, when failure modes with different costs are present. Results presented in this paper have shown that, when service failure is considered, the RBDO formulation may (also) find an optimum which reduces manufacturing costs but increases total expected costs. Equivalence to risk optimization is only obtained if multiple, optimum reliability constraints are used, one for each failure mode.

Most RBDO formulations encountered in the literature pretend to be minimizing costs but, in fact, minimize volume of structural materials or manufacturing costs. It is not possible to get more than what one bargains for: if one optimizes for volume, one gets a slim, slender structure. In order to minimize costs, the monetary consequences of failure, or expected costs of failure, have to be taken into account.

Results obtained for the three bar parallel system and for the cable-stayed column examples have shown that it is not always possible to establish an equivalence between the risk optimization and DDO or RBDO formulations. In both examples, it was observed that the risk-based optimum structural design is not controlled by failure probabilities nor safety coefficients, but by the actual structural configuration. In this situation, safety coefficients or failure probabilities used as constraints cannot reproduce the risk-based optimum structural design. In consideration of uncertainty and the monetary consequences of failure, the optimum structure can only be found by a risk optimization formulation, where structural configuration and safety margins are optimized simultaneously, and which yields a structure optimum in terms of mechanics and in terms of the compromise between costs and safety.

The risk optimization formulation presented herein leads to a challenging optimization problem,

which cannot be solved by simple, first or second order mathematical optimization methods. Due to the presence of multiple local minima, heuristic evolutionary algorithms are required. A hybrid, auto-regulated Particle Swarm - Simplex - Powell algorithm [26] was employed in the solution of the 4 risk optimization problems presented herein, and good performance and high reliability were observed. Improvements of this hybrid algorithm are still under investigation.

Acknowledgements Sponsorship of this research project by the São Paulo State Foundation for Research – FAPESP (grant number 2008/02214-0) and by the National Council for Research and Development - CNPq (grant number 301679/2009-6) is greatly acknowledged.

References

- [1] Frangopol, D., Structural optimization using reliability concepts. *Journal of Structural Engineering (ASCE)*, **111(A2011)**, pp. 2288–2301, 1985.
- [2] Frangopol, D., Multicriteria reliability-based structural optimization. *Structural Safety*, **3(1)**, pp. 23–28, 1985.
- [3] Frangopol, D. & Corotis, R., Reliability-based structural system optimization: state-of-the-art versus state-of-the-practice. *Proceedings of the Conference on Analysis and Computation*, pp. 67–78, 1996.
- [4] Tu, J., Choi, K. & Park, Y., A new study on reliability-based design optimization. *J Mech Des*, **121(4)**, pp. 557–565, 1999.
- [5] Youn, B. & Choi, K., A new response surface methodology for reliability-based design optimization. *Computers and Structures*, **82**, pp. 241–256, 2004.
- [6] Chiralaksanakul, A. & Mahadevan, S., First-order approximation methods in reliability-based design optimization. *Journal of Mechanical Design (ASME)*, **127**, pp. 851–857, 2005.
- [7] Jensen, H., Structural optimization of non-linear systems under stochastic excitation. *Probabilistic Engineering Mechanics*, **21(4)**, pp. 397–409, 2006.
- [8] Taflanidis, A. & Beck, J., Stochastic subset optimization for optimal reliability problems. *Probabilistic Engineering Mechanics*, **23(2-3)**, pp. 324–338, 2008.
- [9] Soltani, M. & Corotis, R., Failure cost design of structural systems. *Structural Safety*, **5(4)**, pp. 239–252, 1988.
- [10] Aktas, E., Moses, F. & Ghosn, M., Cost and safety optimization of structural design specifications. *Rel Eng and Sys Safety*, **73**, pp. 205–212, 2001.
- [11] Frangopol, D. & Maute, K., Life-cycle reliability-based optimization of civil and aerospace structures. *Computers & Structures*, **81(7)**, pp. 397–410, 2003.
- [12] Streicher, H. & Rackwitz, R., Time-variant reliability-oriented structural optimization and a renewal model for life-cycle costing. *Probabilistic Engineering Mechanics*, **19(1-2)**, pp. 171–183, 2004.
- [13] Bucher, C., Dan, M. & Frangopol, D., Optimization of lifetime maintenance strategies for deteriorating structures considering probabilities of violating safety, condition, and cost thresholds. *Probabilistic Engineering Mechanics*, **21(1)**, pp. 1–8, 2006.
- [14] Haukaas, T., Unified reliability and design optimization for earthquake engineering. *Probabilistic Engineering Mechanics*, **23(4)**, pp. 471–481, 2008.
- [15] Beck, A. & Verzenhassi, C., Risk optimization of a steel frame communications tower subject to tornado winds. *Latin American Journal of Solids and Structures*, **5**, pp. 187–203, 2008.

- [16] Ang, A. & Tang, W., *Probability Concepts in Engineering: Emphasis on Applications to Civil and Environmental Engineering*. John Wiley and Sons, 2nd edition, 2007.
- [17] Melchers, R., *Structural Reliability Analysis and Prediction*. John Wiley and Sons: NY, 2nd edition, 1999.
- [18] Rackwitz, R., Optimization and risk acceptability based on the life quality index. *Structural Safety*, **24**, pp. 297–331, 2002.
- [19] Rackwitz, R., Life quality index revisited. *Structural Safety*, **26**, pp. 443–451, 2004.
- [20] Papadopoulos, V. & Lagaros, N., Vulnerability-based robust design optimization of imperfect shell structures. *Structural Safety*, **31**, pp. 475–482, 2009.
- [21] Beyer, H. & Sendhoff, B., Robust optimization – a comprehensive survey. *Computer Methods in Applied Mechanics and Engineering*, **196**, pp. 3190–3218, 2007.
- [22] Schuëller, G. & Jensen, H., Computational methods in optimization considering uncertainties – an overview. *Computer Methods in Applied Mechanics and Engineering*, **198(1)**, pp. 2–13, 2008.
- [23] Qu, X. & Hafta, R., Design under uncertainty using monte carlo simulation and probabilistic factor. *Proceedings of ASME DETC'03 Conference*, Chicago, IL, 2003.
- [24] Ching, J. & Wei-Chih, H., Transforming reliability limit-state constraints into deterministic limit-state constraints. *Structural Safety*, **30**, pp. 11–33, 2008.
- [25] Mínguez, R. & Castillo, E., Reliability-based optimization in engineering using decomposition techniques and FORMS. *Structural Safety*, **31**, pp. 214–223, 2009.
- [26] Gomes, W., *On the Effects of Uncertainty on Optimum Structural Design*. Master's thesis, São Carlos School of Engineering, University of São Paulo, 2010. (in Portuguese).
- [27] Hendawi, S. & Frangopol, D., System reliability and redundancy in structural design evaluation. *Structural Safety*, **16**, pp. 47–71, 1994.

An elementwise least square approach for explicit integration methods applied to elasticity

Marco L. Bittencourt, Felipe A. C. Furlan

Department of Mechanical Design, Faculty of Mechanical Engineering, University of Campinas, Brazil.

P.O. Box 6122, Zip Code 13083-970, Campinas, SP, Brazil

Abstract

This paper presents a least square algorithm based on the eigenvalue decomposition of the elemental mass and stiffness matrices, which may be used for nodal and modal high-order finite element methods. For meshes of line elements, straight squares and hexahedra and straight triangles and tetrahedra, the jacobian is constant and works as a scaling factor to the eigenvalues of the local mass matrix. For meshes of quadrilaterals and hexahedra, the eigenvalues of the mass matrix are calculated after the Schur complement. The solution procedure is performed for each element of the mesh and the results are smoothed on the boundary of the elements using a least square approach. This approach is used to implement an elementwise version of the explicit central difference method. Results are presented for three-dimensional projection and linear elastic problems.

Keywords: Finite Element Method, high-order methods, projection problem, Explicit Central Difference Method.

1 Introduction

The high-order FEM has been applied to many transient problems including Fluid Mechanics, Electromagnetism, Structural Analysis and Powder Metallurgy [1–4]. The time discretization is solved by implicit and explicit methods, which require the solution of systems of equations which involve the mass matrix. For the Lagrange nodal bases and meshes of quadrilaterals, the lumped or spectral diagonal mass matrix is generally used with explicit methods, which corresponds to applying the Gauss-Legendre-Lobatto (GLL) coordinates as integration and collocation points [5]. Due to the missed points, the numerical integration is not exact for polynomial functions, which may affect the convergence rate of the approximated solutions. For the generalized Jacobi polynomial basis, the mass matrix is not diagonal and multilevel substructuring procedures have been used [1].

In [6, 7], nodal and modal tensor-based bases were analyzed for many element shapes in terms of conditioning and sparsity. The high-order mass and stiffness matrices are denser and require more

multiplications for the solution of systems of equations by iterative methods. This paper presents an elementwise least square procedure for the solution of interpolation and time dependent problems by the explicit central difference method, which is based on the eigenvalue decomposition of the elemental mass matrix. In this case, due to the eigenvalue decomposition, the element mass matrices are diagonal and the cost for the solution of the systems of equations is trivial. The procedure may be applied for meshes of any element shape and nodal or modal bases.

The solutions obtained for each element must be combined to achieve a global continuous solution. Due to the eigenvalue decomposition, the connectivity information may not be used to assemble a global mass matrix, as the i -th eigenpar is not necessarily related to the i -th element degree of freedom (DOF). In addition, the eigenvector bases for the element mass matrices are not the same as the eigenvector basis for the global mass matrix. To overcome this problem, a smoothing procedure applied to the element boundary DOFs, based on the least square method, is presented to obtain a global continuous solution in Section 2. This procedure is also extended to the explicit central difference time integration method in Section 3.

While for quadrilaterals meshes, the GLL points make possible to obtain a diagonal mass matrix, for unstructured meshes the nodal points may be taken from [8, 9]. But they do not work well as general integration points for any polynomial order [10–12]. In [13], it was shown that it is not possible to construct a similar set of GLL quadrilateral points for triangles. Another possibility is the use of simultaneous diagonalization of the Laplace mass and stiffness matrices as presented in [14]. As the procedure presented here may be used for any element shape, it is also possible to obtain diagonal mass matrices for triangles and tetrahedra.

This paper is organized as follows. First, the least square smoothing procedure and the elementwise explicit method are considered. Results for interpolation and time dependent problems are presented. Finally, the main conclusions are addressed.

2 Least square approach to the global continuity

Given a function u and a finite element basis $[N]$, an approximated function \bar{u} to u is given by [1]

$$\bar{u} = [N]\{a\},$$

where $\{a\}$ is the vector of the global approximation coefficients which are obtained using the Galerkin method in the domain Ω as [1]

$$\left(\int_{\Omega} [N]^T [N] d\Omega \right) \{a\} = \int_{\Omega} [N]^T u d\Omega.$$

In matrix notation, the projection or interpolation problem is

$$[M]\{a\} = \{f\}$$

and $[M]$ is the global mass matrix and $\{f\}$ is the body load vector. They can be obtained by the assembling procedure of the elemental mass matrices $[M_e]$ and load vectors $\{f_e\}$ as [1]

$$[M] = \bigcup_{e=1}^{Nel} [M_e] \quad \text{and} \quad \{f\} = \bigcup_{e=1}^{Nel} \{f_e\},$$

where Nel is the number of elements. It should be observed that, in the case of an interpolation problem, $\{f\}$ does not represent a physical load vector.

In this paper, the global mass matrix and load vector are not assembled. Instead, the eigenvalue decomposition of the mass matrix for each element e is calculated and the load vectors are transformed to the eigenvector bases. The system of equations for element e is expressed as

$$[M_e]\{a_e\} = \{f_e\}.$$

In the eigenvector basis,

$$[\hat{U}_e]^T [M_e] [\hat{U}_e] \{\hat{a}_e\} = [\hat{U}_e]^T \{f_e\} = \{\hat{f}_e\},$$

where $[\hat{U}_e]$ is the matrix of eigenvectors of the elemental mass matrix. This results in the following decoupled diagonal system for each element

$$[\Lambda_e] \{\hat{a}_e\} = \{\hat{f}_e\}.$$

The modal coefficients $\{\hat{a}_e\}$ are transformed back to the physical space coefficients $\{a_e\}$ using

$$\{a_e\} = [\hat{U}_e] \{\hat{a}_e\}.$$

The approximated elemental solutions

$$u_e = [N_e] \{a_e\} \quad e = 1, \dots, Nel \quad (1)$$

are not continuous on the element boundaries. A smooth procedure based on the least square method is presented below to achieve a continuous global solution.

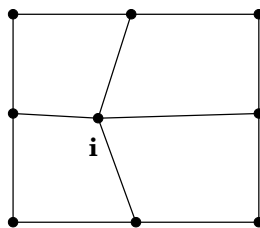


Figure 1: Patch of elements for node i .

Consider the following least square functional which gives the square of the error between the global (\bar{u}) and element (u_e) solutions for the patch of elements associated to node i as illustrated in Figure 1

$$\mathfrak{F}(\{a\}) = \bigcup_{e=1}^{Nel_p} \int_{\Omega_e} (\bar{u} - u_e)^2 |J_e| d\Omega_e = 0, \quad (2)$$

where Nel_p is the number of elements of the patch.

On each element e , the global solution is approximated as

$$\bar{u} = [N_e]\{a\}. \quad (3)$$

Replacing the previous equation in (2), the minimum condition of functional \mathfrak{F} results in

$$\left(\bigcup_{e=1}^{Nel_p} \int_{\Omega_e} [N_e]^T [N_e] |J_e| d\Omega_e \right) \{a\} = \bigcup_{e=1}^{Nel_p} \int_{\Omega_e} [N_e]^T u_e |J_e| d\Omega_e.$$

Assuming a nodal spectral Lagrange basis and using (1), the previous equation reduces to

$$\left(\bigcup_{e=1}^{Nel_p} \int_{\Omega_e} |J_e| d\Omega_e \right) \{a\} = \bigcup_{e=1}^{Nel_p} \left(\int_{\Omega_e} |J_e| d\Omega_e \{a_e\} \right).$$

For the global coefficient a_i , the previous expression gives

$$\left(\bigcup_{e=1}^{Nel_p} \int_{\Omega_e} |J_e| d\Omega_e \right) a_i = \bigcup_{e=1}^{Nel_p} \left(\int_{\Omega_e} |J_e| d\Omega_e a_e^i \right)$$

where a_e^i is the solution obtained for node i using the local solution of the element e . The term in parenthesis in the left hand side is the patch measure (length, area or volume), while the right hand side term in parenthesis is the measure of each element multiplied by the element solution for node i . Therefore,

$$a_i = \frac{\sum_{e=1}^{Nel_p} meas(\Omega_e) a_e^i}{\sum_{e=1}^{Nel_p} meas(\Omega_e)} = \frac{\sum_{e=1}^{Nel_p} S_e a_e^i}{S_p}. \quad (4)$$

Although the previous presentation considered a nodal basis, it may be also applied to modal bases using Jacobi polynomials, as both bases span the same approximation space. Once the local coefficients $\{a_e\}$ for a modal expansion are calculated, equation (1) is used to obtain the solution on the collocation points, which corresponds to the coefficients of the nodal expansion due to the collocation property of the Lagrange polynomials. A simpler approach is to use the smooth procedure (4) directly to the modal coefficients.

3 Elementwise explicit method

Consider the time-dependent discrete linear equation of motion for an undamped structure given by

$$[M]\{\ddot{U}^t\} + [K]\{U^t\} = \{R^t\}, \quad (5)$$

where $[M]$ and $[K]$ are the global mass and stiffness matrices; $\{\ddot{U}^t\}$ and $\{U^t\}$ are the acceleration and displacement vectors for the degrees of freedom (DOFs) in time t ; $\{R^t\}$ is the vector of the equivalent loads applied to the DOFs at time t . The purpose here is to integrate (5) in the time interval $[t_0, t_f]$ with n time steps of size Δt .

Given the displacement vectors for times $t - \Delta t$, t and $t + \Delta t$, the central difference explicit method uses, respectively, the following approximations for the acceleration and velocity vectors in time t [15]

$$\{\ddot{U}^t\} = \frac{1}{(\Delta t)^2} (\{U^{t-\Delta t}\} - 2\{U^t\} + \{U^{t+\Delta t}\}), \quad (6)$$

$$\{\dot{U}^t\} = \frac{1}{2\Delta t} (-\{U^{t-\Delta t}\} + \{U^{t+\Delta t}\}). \quad (7)$$

Substituting (6) in equation (5), the approximation for the displacement vector at $t + \Delta t$ is obtained by the solution of a system of equations in terms of the mass matrix as

$$[\hat{M}]\{U^{t+\Delta t}\} = \{\hat{R}^t\}, \quad (8)$$

where

$$[\hat{M}] = a_0[M] \quad (9)$$

and

$$\{\hat{R}^t\} = \{R^t\} - [K]\{U^t\} + [M](a_2\{U^t\} - a_0\{U^{t-\Delta t}\}). \quad (10)$$

The constants are given, respectively, by $a_0 = \frac{1}{\Delta t^2}$, $a_1 = \frac{1}{2\Delta t}$, $a_2 = 2a_0$ and $a_3 = \frac{1}{a_2}$. For a lumped mass matrix, the computational cost for the solution of (8) is trivial. However, as the explicit method is conditionally stable, a small time step should be used to achieve convergence in time.

Given the initial displacement vector $\{U^0\}$, the initial acceleration is obtained using equation (5) as

$$\{\ddot{U}^0\} = [M]^{-1}(\{R^0\} - [K]\{U^0\}). \quad (11)$$

Expression (10) requires the displacement vector $\{U^{-\Delta t}\}$ for $t = t_0$, which it is obtained using equations (6) and (7). Therefore,

$$\{U^{-\Delta t}\} = \{U^0\} - \Delta t\{\dot{U}^0\} + \frac{(\Delta t)^2}{2}\{\ddot{U}^0\}. \quad (12)$$

One of the main difficulties to develop an elementwise explicit procedure is related to the way the Dirichlet boundary conditions are handled, as they influence the problem solution globally. For that purpose, the external loads are considered in the respective elements where they are applied, as in the

global assembling procedure. The homogeneous boundary conditions are replaced by the respective reaction loads and assembled in the load vectors of the elements that share the DOFs where the boundary conditions are applied. The values of the reactions loads are determined along the iterations as explained below.

Given the initial displacement and acceleration vectors, equation (5) may be partitioned in terms of the free (f) DOFs and those ones with homogeneous Dirichlet boundary conditions (d) as

$$\begin{Bmatrix} \{R_f^0\} \\ \{R_d^0\} \end{Bmatrix} = \begin{bmatrix} [M_{ff}] & [M_{fd}] \\ [M_{df}] & [M_{dd}] \end{bmatrix} \begin{Bmatrix} \{\ddot{U}_f^0\} \\ \{0\} \end{Bmatrix} + \begin{bmatrix} [K_{ff}] & [K_{fd}] \\ [K_{df}] & [K_{dd}] \end{bmatrix} \begin{Bmatrix} \{U_f^0\} \\ \{0\} \end{Bmatrix}.$$

The reaction forces are calculated as

$$\{R_d^0\} = [M_{df}] \{\ddot{U}_f^0\} + [K_{df}] \{U_f^0\}. \quad (13)$$

Observe that the vector $\{R_f^0\}$ represents the external load vector $\{R^0\}$ for the initial time t_0 .

For any time step t , the external load vector $\{R_e^t\}$ for the element e is obtained from the external global load vector $\{R^t\}$ using the element DOF numbers and the smoothing procedure (4) as

$$\{R_e^t\} \leftarrow \{R^t\} \frac{S_e}{S_p}. \quad (14)$$

The previous equation means that the coefficients of the global load vector $\{R^t\}$, which correspond to the element DOFs, are multiplied by $\frac{S_e}{S_p}$ and assigned to the element load vector $\{R_e^t\}$.

The global initial condition vectors may be assigned to the element vectors using again the DOF numbering by

$$\{U_e^0\} \leftarrow \{U^0\}, \quad \{\dot{U}_e^0\} \leftarrow \{\dot{U}^0\} \quad \text{and} \quad \{\ddot{U}_e^0\} \leftarrow \{\ddot{U}^0\}. \quad (15)$$

Based on that, the displacement vector $\{U_e^{-\Delta t}\}$ may be calculated for each element e as

$$\{U_e^{-\Delta t}\} = \{U_e^0\} - \Delta t \{\dot{U}_e^0\} + a_3 \{\ddot{U}_e^0\}. \quad (16)$$

Using the smooth procedure, the global vector is calculated by

$$\{U^{-\Delta t}\} = \bigcup_{e=1}^{Nel} \{U_e^{-\Delta t}\} \frac{S_e}{S_p} \quad (17)$$

and Nel is the number of elements.

For each time step, the following system of equations, similar to (8), is solved for each element e

$$[\hat{M}_e]\{U_e^{t+\Delta t}\} = \{\hat{R}_e^t\}. \quad (18)$$

The effective load vector for element e is

$$\{\hat{R}_e^t\} = \{R_e^t\} - [K_e]\{U_e^t\} + [M_e](a_2\{U_e^t\} - a_0\{U_e^{t-\Delta t}\}). \quad (19)$$

The mass matrix written in its eigenvector basis $[X_e]$ reduces to the eigenvalue matrix $[\Lambda_e]$ and the solution of (18) in the physical space is given by

$$\{U_e^{t+\Delta t}\} = [X_e] \left(\frac{1}{a_0} [\Lambda_e]^{-1} [X_e]^T \{\hat{R}_e^t\} \right). \quad (20)$$

The velocity and acceleration vectors on each element are calculated, respectively, as

$$\{\ddot{U}_e^t\} = a_0(\{U_e^{t-\Delta t}\} - 2\{U_e^t\} + \{U_e^{t+\Delta t}\}), \quad (21)$$

$$\{\dot{U}_e^t\} = a_1(-\{U_e^{t-\Delta t}\} + \{U_e^{t+\Delta t}\}). \quad (22)$$

From the element solution vectors, the global displacement, velocity and acceleration vectors are obtained by the assembling procedure smoothed using the element and patch measures. Therefore,

$$\{U^{t+\Delta t}\} = \bigcup_{e=1}^{Nel} \{U_e^{t+\Delta t}\} \frac{S_e}{S_p}, \quad (23)$$

$$\{\dot{U}^t\} = \bigcup_{e=1}^{Nel} \{\dot{U}_e^t\} \frac{S_e}{S_p}, \quad (24)$$

$$\{\ddot{U}^t\} = \bigcup_{e=1}^{Nel} \{\ddot{U}_e^t\} \frac{S_e}{S_p}. \quad (25)$$

The coefficients of the previous global vectors which correspond to the homogeneous boundary conditions are assigned zero values. Once the global vectors are obtained, the displacement, velocity and acceleration load vectors $\{U_e^{t+\Delta t}\}$, $\{\dot{U}_e^t\}$ and $\{\ddot{U}_e^t\}$ for each element e are obtained analogously to equation (15).

The equivalent nodal force vector for element e is calculated as

$$\{R_e\} = [M_e]\{\ddot{U}_e^t\} + [K_e]\{U_e^{t+\Delta t}\}. \quad (26)$$

It can be observed that acceleration vector $\{\ddot{U}_e^t\}$ is available for time step t , while the displacement vector $\{U_e^{t+\Delta t}\}$ is calculated for time $t + \Delta t$. This delay in time for the acceleration vector does not affect the reaction forces for time $t + \Delta t$. However, the forces for the free DOFs are not equal to the

values for the external loads for the same time step. To solve this problem, a global load vector is assembled from the element load vectors $\{R_e\}$ as

$$\{R_g\} = \bigcup_{e=1}^{Nel} \{R_e\}. \quad (27)$$

The global external load vector $\{R^{t+\Delta t}\}$ is calculated for time $t + \Delta t$ and the following difference is calculated

$$\{\Delta R\} = \{R^{t+\Delta t}\} - \{R_g\}. \quad (28)$$

This global difference vector is assigned back to the free DOFs of each element and used in the next time step $t + \Delta t$. Therefore,

$$\{R_e^{t+\Delta t}\} \leftarrow \{\Delta R\} \frac{S_e}{S_p}. \quad (29)$$

Observe that beginning from the second time step, only the residual force represented $\{\Delta R\}$ is considered. This procedure is repeated until the final time t_f is reached.

4 Results

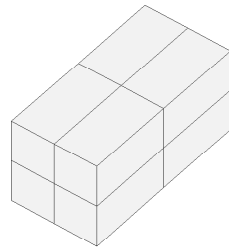
4.1 Interpolation problem

Consider the two meshes of hexahedra given in Figures 2(a) and 2(b). The function to be interpolated is $u(x, y, z) = x^3(x-2)^3y^4(y-4)$ in the domain $[x, y, z] \in [0, 2] \times [0, 4] \times [0, 2]$. Figure 3 plots the error behavior for the given meshes and the eigenvalue based Lagrange and Jacobi mass matrices and the spectral Lagrange mass matrix. It may be observed that the convergence rate for the approximations using the spectral mass matrix depends on the mesh refinement.

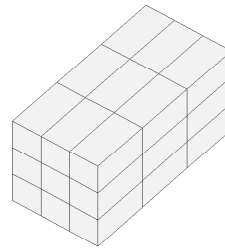
The CPU times to solve the considered projection problem on the coarsest mesh with $P = 6$ were 3.0 seconds using the eigenvalue decomposition with Jacobi and Lagrange polynomials, 1.7 seconds for the nodal spectral Lagrange mass matrix and 267.4 seconds for the global consistent mass matrix calculated using Jacobi polynomials. In the case of the nodal spectral matrix, the relative error norm was 7.11×10^{-8} , while for the other mass matrices, the relative error norms were about 10^{-15} . To achieve a similar relative error norm for the nodal spectral mass matrix, it was necessary to consider $P = 8$ and the CPU time was 2.1 seconds. For the mesh with 27 elements and $P = 6$, the CPU times were 12.6 and 13.1 seconds for the nodal spectral and eigenvalue based Jacobi matrices, respectively. To improve the accuracy of the solution obtained with the nodal spectral mass matrix from 1.74×10^{-11} to 6.48×10^{-15} , $P = 8$ was required and the CPU time increased to 16.1 seconds. These results depend on the code implementation, the considered optimizations, mesh size and element order. The purpose here was to give a qualitative behavior of the proposed least square procedure in terms of the CPU time when compared to the spectral mass matrix.

Figure 2(c) illustrates a distorted mesh with 27 elements. In this case, the eigenvalue problem must be solved for each element. The relative error norms of the approximations obtained for the Lagrange consistent eigenvalue based and lumped mass matrices are given in Figure 3(c). It may be observed that

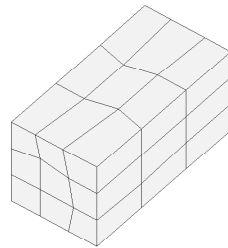
the solutions obtained with the two considered mass matrices achieve spectral convergence rates, but again the convergence rate for the approximations with the lumped mass matrix is worse. The CPU times for $P = 6$ were 15.0 and 2.0 seconds for the proposed algorithm and the lumped mass matrix, respectively. The respective relative error norms were 4.89×10^{-10} and 2.64×10^{-14} . However, 11.0 seconds were consumed for the calculation of the consistent mass matrices and only 2.5 seconds for the eigenvalue decomposition for all elements. For $P = 8$, the relative error norm for the approximated solution obtained with the lumped mass matrix was 1.32×10^{-15} and the CPU time 11.0s. Therefore, for similar convergence rates, both procedures have also similar computational performance.



(a) 8 elements; 27 nodes.



(b) 27 elements; 64 nodes.

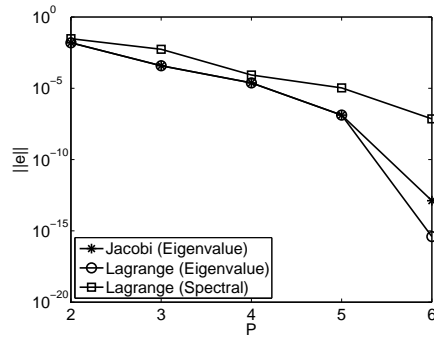


(c) 27 elements; 64 nodes.

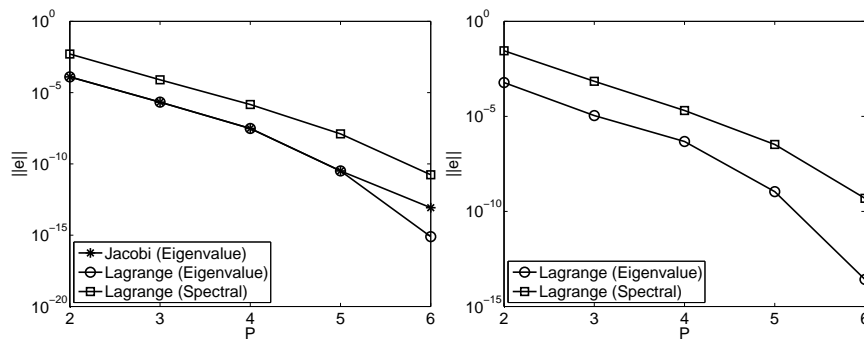
Figure 2: Hexahedron meshes.

4.2 Time dependent cases

In this section, the explicit elementwise procedure is applied to a time dependent linear elastic solid problem. The time interval $[t_o; t_f] = [0; 0.25]$ with $\Delta t = 0.0025s$ (100 time steps) and the mesh of four hexahedra illustrated in Figure 4 are considered. Unity values are taken for the Young modulus (E) and density (ρ) and the Poisson ratio is $\nu = 0.25$. The consistent mass matrices are calculated using



(a) 8 elements.



(b) 27 elements.

(c) 27 distorted elements.

Figure 3: Error behavior for the projection problem in the hexahedron meshes.

Lagrange polynomials. The purpose here is to compare the convergence error for the explicit method using the lumped and eigenvalue-based mass matrices.

The analytical solution for the displacement components is given by

$$\begin{aligned}
 u_x(x, y, z) &= \frac{1}{1000} x^4 y^4 z^4 \sin(2\pi t), \\
 u_y(x, y, z) &= \frac{1}{1000} x^4 y^4 z^4 \sin(2\pi t), \\
 u_z(x, y, z) &= \frac{1}{1000} x^4 y^4 z^4 \sin(2\pi t).
 \end{aligned} \tag{30}$$

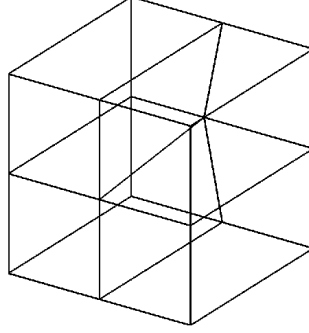


Figure 4: Mesh of four hexahedra used in the explicit method.

After the substitution of the analytical solution (30) in the Navier equations, the components of the body force are

$$\begin{aligned}
 f_x &= \frac{\sin(2\pi t)}{5000} [-20\pi^2 x^4 y^4 z^4 - 24x^2 y^2 z^2 (x^2 y^2 + x^2 z^2) - 64x^3 y^3 z^3 (y + z) - 72x^2 y^4 z^4], \\
 f_y &= \frac{\sin(2\pi t)}{5000} [-20\pi^2 x^4 y^4 z^4 - 24x^2 y^2 z^2 (x^2 y^2 + y^2 z^2) - 64x^3 y^3 z^3 (x + z) - 72x^4 y^2 z^4], \\
 f_z &= \frac{\sin(2\pi t)}{5000} [-20\pi^2 x^4 y^4 z^4 - 24x^2 y^2 z^2 (x^2 z^2 + y^2 z^2) - 64x^3 y^3 z^3 (x + y) - 72x^4 y^4 z^2].
 \end{aligned} \tag{31}$$

The faces with coordinates $x = y = z = 0$ are clamped. For the other element faces on the domain boundary, the traction field $\mathbf{t} = (t_x, t_y, t_z)$ with the following components are applied:

$$\begin{aligned}
 t_x &= \frac{\sin(2\pi t)}{1000} [4x^3 y^3 z^3 ((xy + xz)\lambda + yz(\lambda + 2\mu))n_x + 4\mu x^3 y^3 z^4 (x + y)n_y + 4\mu x^3 y^4 z^3 (x + z)n_z], \\
 t_y &= \frac{\sin(2\pi t)}{1000} [4\mu x^3 y^3 z^4 (x + y)n_x + 4x^3 y^3 z^3 (\lambda(yz + xy) + (\lambda + 2\mu)xz)n_y + 4\mu x^4 y^3 z^3 (y + z)n_z], \\
 t_z &= \frac{\sin(2\pi t)}{1000} [4\mu x^3 y^4 z^3 (x + z)n_x + 4\mu x^4 y^3 z^3 (y + z)n_y + 4x^3 y^3 z^3 (\lambda(xz + yz) + (\lambda + 2\mu)xy)n_z].
 \end{aligned} \tag{32}$$

where $\mathbf{n} = (n_x, n_y, n_z)$ is the normal vector on the element faces. The previous expressions are obtained using the Neumann boundary conditions given by $\mathbf{T}\mathbf{n} = \mathbf{t}$, where \mathbf{T} is the Cauchy stress tensor. For an isotropic linear elastic material, \mathbf{T} is written in terms of the infinitesimal strain tensor $\mathbf{E} = \frac{1}{2}(\nabla\mathbf{u} + \nabla\mathbf{u}^T)$ using the Hooke's law as

$$\mathbf{T} = \mathcal{C}\mathbf{E}$$

and \mathcal{C} is the fourth-order linear elasticity tensor. Its components are written in terms of the Lamé coefficients λ and μ related to the Young modulus and Poisson ratio as

$$\begin{aligned}\lambda &= \frac{\nu E}{(1 + \nu)(1 - 2\nu)}, \\ \mu &= \frac{E}{2(1 + \nu)}.\end{aligned}\tag{33}$$

The components of the initial displacement and velocity are:

$$\begin{aligned}u_x &= 0, & u_y &= 0, & u_z &= 0, \\ \dot{u}_x &= \frac{2\pi}{1000}x^4y^4z^4, & \dot{u}_y &= \frac{2\pi}{1000}x^4y^4z^4, & \dot{u}_z &= \frac{2\pi}{1000}x^4y^4z^4.\end{aligned}\tag{34}$$

Figure 5 illustrates the relative error norms for the u_x component at the final time t_f of the explicit method using the eigenvalue and spectral mass matrices and polynomial orders $P = 2$ to $P = 5$. It may be observed that both results show spectral convergence, but the lumped mass matrix has a lower convergence rate. Similar results were obtained for the u_y and u_z components. The under-integration of the spectral mass matrix may be also observed for this fourth-order analytical solution for $P = 2$ to $P = 4$. For $P = 5$, this fact can not be observed and both schemes have close error norms.

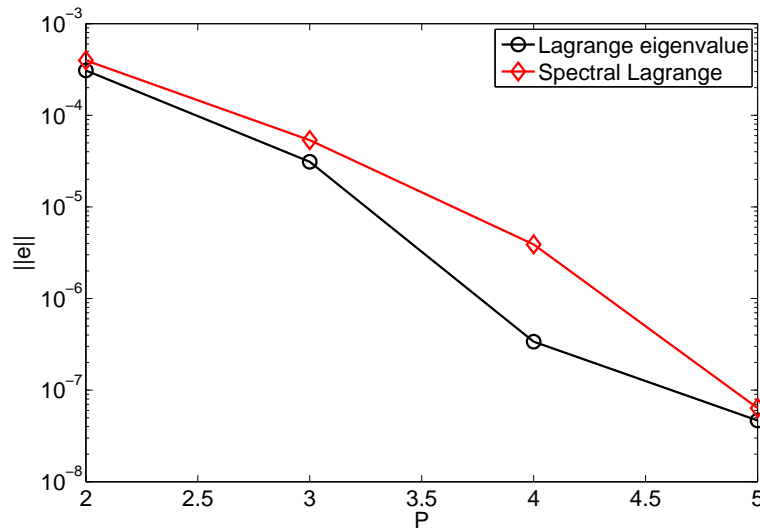


Figure 5: Relative error for explicit method using the spectral and eigenvalue based mass matrices.

5 Conclusions

This work presented elementwise interpolation and explicit methods based on the eigenvalue decomposition of the element mass matrices and a least square smoothing procedure. The convergence rates of these methods are still exponential and better when compared to the results for the lumped Lagrange mass matrices.

In addition, the methods may be applied for any element shape and finite element bases. Due to the local feature of the presented procedures, they seem to be very suitable in parallel and GPU based architectures.

References

- [1] Karniadakis, G.E. & Sherwin, S.J., *Spectral/hp Element Methods for CFD*. Oxford University Press: Oxford, 1999.
- [2] Yosibash, Z., Hartmann, S., Heisser, U., Düster, A., Rank, E. & Szanto, M., Axisymmetric prepressure boundary loading for finite deformation analysis using p-fem. *Comput Methods Appl Mech Engng*, **196**, pp. 1261–1277, 2007.
- [3] Heisserer, U., Hartmann, S., Düster, A., W. Bier, Z.Y. & Rank, E., p-fem for finite deformation powder compaction. *Comput Methods Appl Mech Engng*, (**197**), pp. 727–740, 2008.
- [4] Dong, S. & Yosibash, Z., A parallel spectral element method for dynamic three-dimensional nonlinear elasticity problems. *Computer & Structures*, (**4**), pp. 61–85, 2008.
- [5] Patera, A., A spectral method for fluid dynamics: Laminar flow in a channel expansion. *Journal of Computational Physics*, **54**, pp. 468–488, 1984.
- [6] Bittencourt, M., Fully tensorial nodal and modal shape functions for triangles and tetrahedra. *Int Journal for Numerical Methods in Engineering*, **63(2)**, pp. 1530–1558, 2005.
- [7] Bittencourt, M., Vazquez, M.G. & Vazquez, T.G., Construction of shape functions for the h - and p -versions of the fem using tensorial product. *Int Journal for Numerical Methods in Engineering*, **71(5)**, pp. 529–563, 2007.
- [8] Taylor, M., Wingate, B. & Vincent, R., An algorithm for computing Fekete points in the triangle. *SIAM Journal on Numerical Analysis*, **38**, pp. 1707–1720, 2000.
- [9] Hesthaven, J., From electrostatics to almost optimal nodal sets for polynomial interpolation in a simplex. *SIAM Journal on Numerical Analysis*, **35**, pp. 655–676, 1998.
- [10] Cohen, G., Joly, P., Roberts, J. & Tordjman, N., Higher order triangular finite elements with mass lumping for the wave equation. *SIAM Journal on Numerical Analysis*, **38**, pp. 2047–2078, 2001.
- [11] Taylor, M. & Wingate, B., A generalized diagonal mass matrix spectral element method for non-quadrilateral elements. *Applied Numerical Mathematics*, **33**, pp. 259–265, 2000.
- [12] Giraldo, F.X. & Taylor, M., A diagonal-mass-matrix triangular-spectral-element method based on cubature points. *Journal of Engineering Mathematics*, **56**, pp. 307–322, 2006.
- [13] Helenbrook, B., On the existence of explicit hp-finite element methods using Gauss-Lobatto integration on the triangle. *SIAM Journal on Numerical Analysis*, **47**, pp. 1304–1318, 2009.
- [14] Shen, J. & Wang, L.L., Fourierization of the legendre-galerkin method and a new space-time spectral method. *Applied Numerical Mathematics*, **57**, pp. 710–720, 2007.
- [15] Bathe, K., *Finite Element Procedures*. Prentice Hall: New-Jersey, 1996.

Numerical solution of boundary inverse problems for anisotropic solids

Igor Brilla

*Department of Mathematics,
Faculty of Electrical Engineering and Information Technology,
Slovak Technical University, Ilkovičova 3, 812 19 Bratislava – Slovakia*

Abstract

We deal with numerical analysis of inverse problems for plane anisotropic solids when measured data are given only on the boundary of the domain. In this paper we have elaborated an iterative procedure to the solution of inverse problems for plane anisotropic solids when input data measured from suitable states are sufficient for determination of unknown material parameters. We derive the number of measured input states and conditions for these measured input states which secure determinability of the numerical solution. We deal with numerical experiments. We study influence of measured input data on stability of the numerical solutions.

Keywords: inverse problems, anisotropic solids, PDE, FDM.

1 Introduction

Inverse problems are very important from a practical point of view and interesting from a theoretical point of view as they are improperly posed problems. An important class of inverse problems is a class of identification problems. These problems are important, for example, in the non-destructive testing of materials, the identification of material parameters, the study of aquifer problems as well as for electrical impedance tomography, etc.

We deal with analysis of inverse problems for anisotropic solids when measured data is given only on the boundary of the domain. The inverse problems for anisotropic solids have special features in comparison with those for isotropic solids. In order to solve anisotropic problems, more unknown material parameters of governing differential equations than the total number of equations must be determined and therefore, in order to determine them, we need input data measured from more than one field state. These input states as we show cannot be chosen arbitrarily. This fact leads to new theoretical problems in the analysis of inverse problems for anisotropic solids and also complicates numerical analysis.

For numerical analysis of such problems we apply discrete methods. These are very convenient because in the case of practical problems we have to measure input states in discrete points. In this paper, we have elaborated an iterative procedure to the numerical solution of plane anisotropic boundary inverse problem when the input data measured from suitable states are sufficient to determine the unknown material parameters. We derive the number of measured input states and conditions for these measured input states which secure determinability of the numerical solution. We also deal with numerical experiments. Since input data is measured in the case of practical problems, we also study its influence on the stability of the numerical solutions. This approach is generalization of the methods derived in Brilla [1]. Another approaches are derived in Grebennikov [2] and Grebennikov [3].

2 Problem formulation

Governing equations of plane anisotropic solids have the following form

$$(c_{ijkl}u_{k,l})_{,j} + f_i = 0 \text{ in } \Omega, \quad i, j, k, l = 1, 2, \quad (1)$$

where c_{ijkl} are elastic coefficients, u_i are displacements and f_i are volume forces. We assume that Ω is a two dimensional Lipschitz domain. We apply the summation and differentiation rule with respect to indices. The elastic coefficients are symmetric. It holds $c_{ijkl} = c_{klij} = c_{jikl} = c_{ijlk}$.

The equation (1) can be written in the following forms in Ω

$$\begin{aligned} & (E1u_{x,x} + E4u_{x,y} + E4u_{y,x} + E3u_{y,y})_{,x} + \\ & (E4u_{x,x} + E2u_{x,y} + E2u_{y,x} + E5u_{y,y})_{,y} + f_x = 0, \\ & (E4u_{x,x} + E2u_{x,y} + E2u_{y,x} + E5u_{y,y})_{,x} + \\ & (E3u_{x,x} + E5u_{x,y} + E5u_{y,x} + E6u_{y,y})_{,y} + f_y = 0, \end{aligned} \quad (2)$$

where we use following notations $c_{1111} = E1$, $c_{1212} = E2$, $c_{1122} = E3$, $c_{1112} = E4$, $c_{1222} = E5$, $c_{2222} = E6$.

In the case of the inverse problems we have to determine the elastic coefficients we need for their determination boundary conditions

$$\begin{aligned} E1(s) &= a_1(s), E2(s) = a_2(s), E3(s) = a_3(s), \\ E4(s) &= a_4(s), E5(s) = a_5(s), E6(s) = a_6(s), \\ & s \in \partial\Omega. \end{aligned} \quad (3)$$

In the case of the boundary inverse problems we have also to determine the displacements u_x and u_y using measured values of the displacements u_x and u_y on the boundary $\partial\Omega$. We consider for the displacements u_x and u_y Dirichlet boundary conditions

$$u_x(s) = g_1(s), u_y(s) = g_2(s), \quad s \in \partial\Omega \quad (4)$$

and over specified Neumann boundary conditions

$$u_{x,n}(s) = g_3(s), u_{y,n}(s) = g_4(s), \quad s \in \partial\Omega, \quad (5)$$

where $(\cdot)_{,n}$ denotes the differentiation in direction of the outer normal.

In our approach we consider Neumann's boundary problem (2), (5) in the following way. We consider Hooke's law

$$\tau_{ij} = c_{ijkl}\varepsilon_{k,l},$$

where τ is stress tensor and ε is strain tensor. Hooke's law can be written for our 2D anisotropic problem in the following forms

$$\begin{aligned} {}^u\tau_{xx} &= E1u_{x,x} + E4(u_{x,y} + u_{y,x}) + E3u_{y,y}, \\ {}^u\tau_{xy} &= E4u_{x,x} + E2(u_{x,y} + u_{y,x}) + E5u_{y,y}, \\ {}^u\tau_{yy} &= E3u_{x,x} + E5(u_{x,y} + u_{y,x}) + E6u_{y,y}. \end{aligned} \quad (6)$$

Using (6) relations (2) and (5) can be written in the forms

$$\begin{aligned} {}^u\tau_{xx,x} + {}^u\tau_{xy,y} + f_x &= 0, \quad {}^u\tau_{xy,x} + {}^u\tau_{yy,y} + f_y = 0 \quad \text{in } \Omega, \\ {}^u\tau_{xx}(s) &= {}^u j_1(s), {}^u\tau_{yy}(s) = {}^u j_2(s), {}^u\tau_{xy}(s) = {}^u j_3(s), \quad s \in \partial\Omega. \end{aligned} \quad (7)$$

However, in the case of 2D anisotropic problem, the system of equations (2) - (4), (6), (7) does not form a complete system of equations and is not sufficient for determination of the unknown elastic coefficients. We show that for determination of the unknown elastic coefficients, it is necessary to add input data measured from next two state of the displacements v_x , v_y and w_x , w_y . For these next states of input data we consider the equations and boundary conditions analogical to (2) and (4)

$$\begin{aligned} &(E1v_{x,x} + E4v_{x,y} + E4v_{y,x} + E3v_{y,y})_{,x} + \\ &(E4v_{x,x} + E2v_{x,y} + E2v_{y,x} + E5v_{y,y})_{,y} + p_x = 0, \\ &(E4v_{x,x} + E2v_{x,y} + E2v_{y,x} + E5v_{y,y})_{,x} + \\ &(E3v_{x,x} + E5v_{x,y} + E5v_{y,x} + E6v_{y,y})_{,y} + p_y = 0; \end{aligned} \quad (8)$$

$$v_x(s) = g_5(s), \quad v_y(s) = g_6(s), \quad s \in \partial\Omega; \quad (9)$$

$$\begin{aligned}
& (E1w_{x,x} + E4w_{x,y} + E4w_{y,x} + E3w_{y,y})_{,x} + \\
& (E4w_{x,x} + E2w_{x,y} + E2w_{y,x} + E5w_{y,y})_{,y} + q_x = 0, \\
& (E4w_{x,x} + E2w_{x,y} + E2w_{y,x} + E5w_{y,y})_{,x} + \\
& (E3w_{x,x} + E5w_{x,y} + E5w_{y,x} + E6w_{y,y})_{,y} + q_y = 0;
\end{aligned} \tag{10}$$

$$w_x(s) = g_7(s), \quad w_y(s) = g_8(s), \quad s \in \partial\Omega \tag{11}$$

corresponding equations of Hooke's law

$$\begin{aligned}
{}^v\tau_{xx} &= E1v_{x,x} + E4(v_{x,y} + v_{y,x}) + E3v_{y,y}, \\
{}^v\tau_{xy} &= E4v_{x,x} + E2(v_{x,y} + v_{y,x}) + E5v_{y,y}, \\
{}^v\tau_{yy} &= E3v_{x,x} + E5(v_{x,y} + v_{y,x}) + E6v_{y,y};
\end{aligned} \tag{12}$$

$$\begin{aligned}
{}^w\tau_{xx} &= E1w_{x,x} + E4(w_{x,y} + w_{y,x}) + E3w_{y,y}, \\
{}^w\tau_{xy} &= E4w_{x,x} + E2(w_{x,y} + w_{y,x}) + E5w_{y,y}, \\
{}^w\tau_{yy} &= E3w_{x,x} + E5(w_{x,y} + w_{y,x}) + E6w_{y,y}
\end{aligned} \tag{13}$$

and corresponding equations and boundary conditions for stresses

$$\begin{aligned}
{}^v\tau_{xx,x} + {}^v\tau_{xy,y} + p_x &= 0, \quad {}^v\tau_{xy,x} + {}^v\tau_{yy,y} + p_y = 0 \quad \text{in } \Omega, \\
{}^v\tau_{xx}(s) &= {}^v j_1(s), \quad {}^v\tau_{yy}(s) = {}^v j_2(s), \quad {}^v\tau_{xy}(s) = {}^v j_3(s), \quad s \in \partial\Omega;
\end{aligned} \tag{14}$$

$$\begin{aligned}
{}^w\tau_{xx,x} + {}^w\tau_{xy,y} + q_x &= 0, \quad {}^w\tau_{xy,x} + {}^w\tau_{yy,y} + q_y = 0 \quad \text{in } \Omega, \\
{}^w\tau_{xx}(s) &= {}^w j_1(s), \quad {}^w\tau_{yy}(s) = {}^w j_2(s), \quad {}^w\tau_{xy}(s) = {}^w j_3(s), \quad s \in \partial\Omega.
\end{aligned} \tag{15}$$

Now the question of whether the states u_x , u_y and v_x , v_y and w_x , w_y can be chosen arbitrarily arises. We show that these states cannot be chosen arbitrarily.

3 Problem solution

For solving boundary inverse problem (2) – (4), (6) – (15) we can use the following iterative procedure which is generalization of the method for the solution of 2D orthotropic boundary inverse problems derived in Brilla [1]:

- determination of an initial approximation of the elastic coefficients $E1^0, E2^0, E3^0, E4^0, E5^0, E6^0$ as the linear interpolation of the boundary conditions (3);
- determination of the displacements $u_x^0, u_y^0; v_x^0, v_y^0$ and w_x^0, w_y^0 from (2), (8), (10);
- determination of the stresses ${}^u\tau_{xx}^0, {}^u\tau_{xy}^0, {}^u\tau_{yy}^0$ from (7) rewritten in the following forms

$$\begin{aligned} {}^u\tau_{xx,x}^0 &= -f_x - [E4^0 u_{x,x}^0 + E2^0 (u_{x,y}^0 + u_{y,x}^0) + E5^0 u_{y,y}^0], \\ {}^u\tau_{xy,y}^0 &= -f_x - [E1^0 u_{x,x}^0 + E4^0 (u_{x,y}^0 + u_{y,x}^0) + E3^0 u_{y,y}^0], \\ {}^u\tau_{yy,y}^0 &= -f_y - {}^u\tau_{xy,x}^0 \quad \text{in } \Omega \end{aligned}$$

and ${}^v\tau_{xx}^0, {}^v\tau_{xy}^0, {}^v\tau_{yy}^0, {}^w\tau_{xx}^0, {}^w\tau_{xy}^0, {}^w\tau_{yy}^0$ using similar equations which we obtain from (14) and (15). All these equations we can consider as ordinary differential equations of the first order;

- determination of new state of the elastic coefficients $E1^1, E2^1, E3^1, E4^1, E5^1, E6^1$ from (6), (12) and (13) using following formulas

$$\begin{aligned} E1^1 &= \frac{b_1^0 d_4^0 - b_2^0 d_2^0}{d_1^0 d_4^0 - d_2^0 d_3^0}, & E2^1 &= \frac{b_3^0 d_8^0 - b_4^0 d_6^0}{d_5^0 d_8^0 - d_6^0 d_7^0}, \\ E3^1 &= \frac{b_5^0 d_{12}^0 - d_6^0 d_{10}^0}{d_9^0 d_{12}^0 - d_{10}^0 d_{11}^0}, & E4^1 &= \frac{b_2^0 d_1^0 - b_1^0 d_3^0}{d_1^0 d_4^0 - d_2^0 d_3^0}, \\ E5^1 &= \frac{b_4^0 d_5^0 - b_3^0 d_7^0}{d_5^0 d_8^0 - d_6^0 d_7^0}, & E6^1 &= \frac{b_6^0 d_9^0 - b_5^0 d_{11}^0}{d_9^0 d_{12}^0 - d_{10}^0 d_{11}^0}, \end{aligned} \quad (16)$$

where

$$\begin{aligned} d_1^0 &= u_{x,x}^0 w_{y,y}^0 - u_{y,y}^0 w_{x,x}^0, & d_2^0 &= (u_{y,x}^0 + u_{x,y}^0) w_{y,y}^0 - u_{y,y}^0 (w_{y,x}^0 + w_{x,y}^0), \\ d_3^0 &= v_{x,x}^0 w_{y,y}^0 - v_{y,y}^0 w_{x,x}^0, & d_4^0 &= (v_{y,x}^0 + v_{x,y}^0) w_{y,y}^0 - v_{y,y}^0 (w_{y,x}^0 + w_{x,y}^0), \\ d_5^0 &= (u_{y,x}^0 + u_{x,y}^0) w_{x,x}^0 - u_{x,x}^0 (v_{y,x}^0 + v_{x,y}^0), & d_6^0 &= u_{y,y}^0 w_{x,x}^0 - u_{x,x}^0 w_{y,y}^0, \\ d_7^0 &= (v_{y,x}^0 + v_{x,y}^0) w_{x,x}^0 - v_{x,x}^0 (w_{y,x}^0 + w_{x,y}^0), & d_8^0 &= v_{y,y}^0 w_{x,x}^0 - v_{x,x}^0 w_{y,y}^0, \\ d_9^0 &= u_{x,x}^0 (w_{y,x}^0 + w_{x,y}^0) - (u_{y,x}^0 + u_{x,y}^0) w_{x,x}^0, \\ d_{10}^0 &= u_{y,y}^0 (w_{y,x}^0 + w_{x,y}^0) - (u_{y,x}^0 + u_{x,y}^0) w_{y,y}^0, \\ d_{11}^0 &= v_{x,x}^0 (w_{y,x}^0 + w_{x,y}^0) - (v_{y,x}^0 + v_{x,y}^0) w_{x,x}^0, \\ d_{12}^0 &= v_{y,y}^0 (w_{y,x}^0 + w_{x,y}^0) - (v_{y,x}^0 + v_{x,y}^0) w_{y,y}^0, \\ b_1^0 &= {}^u\tau_{xx}^0 w_{y,y}^0 - {}^w\tau_{xx}^0 u_{y,y}^0, & b_2^0 &= {}^v\tau_{xx}^0 w_{y,y}^0 - {}^w\tau_{xx}^0 v_{y,y}^0, \\ b_3^0 &= {}^u\tau_{xy}^0 w_{x,x}^0 - {}^w\tau_{xy}^0 u_{x,x}^0, & b_4^0 &= {}^v\tau_{xy}^0 w_{x,x}^0 - {}^w\tau_{xy}^0 v_{x,x}^0, \\ b_5^0 &= {}^u\tau_{yy}^0 (w_{y,x}^0 + w_{x,y}^0) - {}^w\tau_{yy}^0 (u_{y,x}^0 + u_{x,y}^0), \\ b_6^0 &= {}^v\tau_{yy}^0 (w_{y,x}^0 + w_{x,y}^0) - {}^w\tau_{yy}^0 (v_{y,x}^0 + v_{x,y}^0); \end{aligned}$$

- we can continue with determination of $u_x^1, u_y^1, v_x^1, v_y^1, w_x^1, w_y^1, \tau_{xx}^1, \tau_{xy}^1, \tau_{yy}^1, v_{xx}^1, v_{xy}^1, v_{yy}^1, w_{xx}^1, w_{xy}^1, w_{yy}^1, E1^2, E2^2, E3^2, E4^2, E5^2, E6^2$, and etc.

From (16) we can see that the iterative procedure can be used only if

$$\begin{aligned} d_1^i d_4^i - d_2^i d_3^i &\neq 0, d_5^i d_8^i - d_6^i d_7^i \neq 0, \\ d_9^i d_{12}^i - d_{10}^i d_{11}^i &\neq 0, \\ i &= 0, 1, \dots, \quad \text{in } \Omega, \end{aligned}$$

it means that the displacements $u_x, u_y; v_x, v_y$ and w_x, w_y cannot be chosen arbitrarily.

For determination of new states of the elastic coefficients we use the system of equations (6), (12) and (13). If we consider only the system of equations (6) and (12) we have six equations with six unknown elastic coefficients. However the determinant of the system (6) and (12) is equal zero, it means that this system is not sufficient for determination of six unknown elastic coefficients. It is the reason why we add input data measured from the third state of the displacements w_x, w_y .

4 Numerical analysis

For numerical analysis we can apply discrete methods. They are very convenient because in the case of practical problems we have to measure input states in discrete points. We assume that the domain Ω is rectangle. Using central differences we can rewrite the iterative procedure from previous part to discrete form.

We deal with numerical experiments from mathematical point of view. This means that we construct the problem with the exact solution, afterwards we compute the numerical solution of this problem using discrete form of the iterative procedure and in the end we compare the computed solution with the exact one.

We use discrete form of the iterative procedure with stopping condition such that the difference of two computed consecutive states of the elastic coefficients is less than 10^{-7} . We consider the following domain $\Omega = \langle 0, 2 \rangle \times \langle 0, 1 \rangle$. For example for the following constant elastic coefficients

$$\begin{aligned} E1 &= 10, & E2 &= 5, & E3 &= 2, \\ E4 &= 1, & E5 &= 3, & E6 &= 8 \end{aligned} \tag{17}$$

the displacements

$$\begin{aligned} u_x &= (x+1)^2 + (y+1), & u_y &= (y+1), \\ v_x &= (x+1), & v_y &= (x+1) + (y+1)^2, \\ w_x &= (x+1) + 2(y+1), & w_y &= 3(x+1) + (y+1) \end{aligned} \tag{18}$$

and corresponding stresses and volume forces

$$\begin{aligned}
{}^u\tau_{xx} &= 20(x+1) + 3, & {}^u\tau_{xy} &= 2(x+1) + 8, & {}^u\tau_{yy} &= 4(x+1) + 11, \\
{}^v\tau_{xx} &= 4(y+1) + 11, & {}^v\tau_{xy} &= 6(y+1) + 6, & {}^v\tau_{yy} &= 16(y+1) + 5, \\
{}^w\tau_{xx} &= 17, & {}^w\tau_{xy} &= 29, & {}^w\tau_{yy} &= 25;
\end{aligned} \tag{19}$$

$$\begin{aligned}
f_x &= -20, & f_y &= -2, \\
p_x &= -6, & p_y &= -16, \\
q_x &= 0, & q_y &= 0
\end{aligned} \tag{20}$$

using (20) and the boundary conditions constructed from (17) - (19), using discrete form of the iterative procedure we obtain on all meshes results at once with the error about $10^{-7}\%$. Similar situation is also for the linear material parameters.

Different situation is for the nonlinear material parameters. For example for

$$\begin{aligned}
E1 &= (x+1)(y+1)^2, & E2 &= (x+1)(y+1), & E3 &= (x+1) + (y+1), \\
E4 &= (y+1), & E5 &= (x+1), & E6 &= (x+1)^2(y+1)
\end{aligned} \tag{21}$$

the displacements given by (18) and corresponding stresses and volume forces

$$\begin{aligned}
{}^u\tau_{xx} &= 2(x+1)^2(y+1)^2 + (x+1) + 2(y+1), & {}^u\tau_{xy} &= 3(x+1)(y+1) + (x+1), \\
{}^u\tau_{yy} &= (x+1) + (x+1)^2(y+1) + 2(x+1)^2 + 2(x+1)(y+1), \\
{}^v\tau_{xx} &= (x+1)(y+1)^2 + 2(y+1)^2 + 2(x+1)(y+1) + (y+1), \\
{}^v\tau_{xy} &= 3(x+1)(y+1) + (y+1), & {}^v\tau_{yy} &= 2(x+1)^2(y+1)^2 + 2(x+1) + (y+1), \\
{}^w\tau_{xx} &= (x+1)(y+1)^2 + (x+1) + 6(y+1), \\
{}^w\tau_{xy} &= 5(x+1)(y+1) + (x+1) + (y+1), \\
{}^w\tau_{yy} &= (x+1)^2(y+1) + 6(x+1) + (y+1);
\end{aligned} \tag{22}$$

$$\begin{aligned}
f_x &= -4(x+1)(y+1)^2 - 3(x+1) - 1, & f_y &= -(x+1)^2 - 2(x+1) - 3(y+1) - 1, \\
p_x &= -(y+1)^2 - 3(x+1) - 2(y+1) - 1, & p_y &= -4(x+1)^2(y+1) - 3(y+1) - 1, \\
q_x &= -(y+1)^2 - 5(x+1) - 2, & q_y &= -(x+1)^2 - 5(y+1) - 2
\end{aligned} \tag{23}$$

in the Table 1 we are able to see the percentage of errors in the computed solutions in the second column with respect to the exact solutions of the meshes given in the first column. In the third column

we report the numbers of iterations after which we obtain the numerical solution with the specific stopping condition on the given mesh. We can see from the results that we obtain very small errors for a course mesh and when the number of grid points increases, errors also increase slightly but are still small.

Table 1: Results for the problem (18), (21)-(23).

Mesh	Errors (%)	Number of iterations
8 x 4	$2.7 \cdot 10^{-5}$	111
12 x 6	$8.2 \cdot 10^{-5}$	258
16 x 8	$1.6 \cdot 10^{-4}$	465

If we change the displacements

$$\begin{aligned}
 u_x &= (x + 1) + 2(y + 1), & u_y &= (y + 1), \\
 v_x &= (x + 1), & v_y &= 3(x + 1) + (y + 1), \\
 w_x &= (x + 1) + (y + 1), & w_y &= 2(x + 1) + 3(y + 1)
 \end{aligned} \tag{24}$$

for corresponding stresses and volume forces

$$\begin{aligned}
 {}^u\tau_{xx} &= (x + 1)(y + 1)^2 + (x + 1) + 3(y + 1), \\
 {}^u\tau_{xy} &= 2(x + 1)(y + 1) + (x + 1) + (y + 1), \\
 {}^u\tau_{yy} &= (x + 1)^2(y + 1) + 3(x + 1) + (y + 1), \\
 {}^v\tau_{xx} &= (x + 1)(y + 1)^2 + (x + 1) + 3(y + 1), \\
 {}^v\tau_{xy} &= 3(x + 1)(y + 1) + (x + 1) + (y + 1), \\
 {}^v\tau_{yy} &= (x + 1)^2(y + 1) + 4(x + 1) + (y + 1), \\
 {}^w\tau_{xx} &= (x + 1)(y + 1)^2 + 3(x + 1) + 6(y + 1), \\
 {}^w\tau_{xy} &= 3(x + 1)(y + 1) + 3(x + 1) + (y + 1), \\
 {}^w\tau_{yy} &= 3(x + 1)^2(y + 1) + 4(x + 1) + (y + 1);
 \end{aligned} \tag{25}$$

$$\begin{aligned}
f_x &= -(y+1)^2 - 2(x+1) - 2, & f_y &= -(x+1)^2 - 2(y+1) - 2, \\
p_x &= -(y+1)^2 - 3(x+1) - 2, & p_y &= -(x+1)^2 - 3(y+1) - 2, \\
q_x &= -(y+1)^2 - 3(x+1) - 4, & q_y &= -(x+1)^2 - 3(y+1) - 4
\end{aligned} \tag{26}$$

we obtain similar results for the same elastic coefficients as it is shown in the Table 2.

Table 2: Results for the problem (21), (24)-(26).

Mesh	Errors (%)	Number of iterations
8 x 4	1.9 10 ⁻⁵	88
12 x 6	6.5 10 ⁻⁵	198
16 x 8	1.3 10 ⁻⁴	356

For another elastic coefficients

$$\begin{aligned}
E1 &= (x+1)^2(y+1), & E2 &= (x+1)(y+1), & E3 &= (x+1) + (y+1), \\
E4 &= (y+1), & E5 &= (x+1), & E6 &= (x+1)(y+1)^2
\end{aligned} \tag{27}$$

the displacements given by (18) and for their corresponding stresses and volume forces

$$\begin{aligned}
{}^u\tau_{xx} &= 2(x+1)^3(y+1) + (x+1) + 2(y+1), & {}^u\tau_{xy} &= 3(x+1)(y+1) + (x+1), \\
{}^u\tau_{yy} &= (x+1) + (x+1)(y+1)^2 + 2(x+1)^2 + 2(x+1)(y+1), \\
{}^v\tau_{xx} &= (x+1)(y+1)^2 + 2(y+1)^2 + 2(x+1)(y+1) + (y+1), \\
{}^v\tau_{xy} &= 3(x+1)(y+1) + (y+1), & {}^v\tau_{yy} &= 2(x+1)(y+1)^3 + 2(x+1) + (y+1), \\
{}^w\tau_{xx} &= (x+1)^2(y+1) + (x+1) + 6(y+1), \\
{}^w\tau_{xy} &= 5(x+1)(y+1) + (x+1) + (y+1), \\
{}^w\tau_{yy} &= (x+1)(y+1)^2 + 6(x+1) + (y+1);
\end{aligned} \tag{28}$$

$$\begin{aligned}
f_x &= -6(x+1)^2(y+1) - 3(x+1) - 1, & f_y &= -2(x+1)(y+1) - 2(x+1) - 3(y+1) - 1, \\
p_x &= -2(x+1)(y+1) - 3(x+1) - 2(y+1) - 1, \\
p_y &= -6(x+1)(y+1)^2 - 3(y+1) - 1, \\
q_x &= -2(x+1)(y+1) - 5(x+1) - 2, & q_y &= -2(x+1)(y+1) - 5(y+1) - 2
\end{aligned} \tag{29}$$

as it is obvious from the Table 3 the accuracy of computation is not so good. This fact is caused by the discretization error, which is in this case rather greater than in previous cases.

Table 3: Results for the problem (18), (27)-(29).

Mesh	Errors (%)	Number of iterations
8 x 4	3.6	123
12 x 6	4.7	277
16 x 8	6.1	575

However using the displacements given by (24) we obtain for the same elastic coefficients and corresponding stresses and volume forces very good results as we can see from the Table 4 because now the finite approximation of our problem has improved.

$$\begin{aligned}
{}^u\tau_{xx} &= (x+1)^2(y+1) + (x+1) + 3(y+1), \\
{}^u\tau_{xx} &= (x+1)^2(y+1) + (x+1) + 3(y+1), \\
{}^u\tau_{yy} &= (x+1)(y+1)^2 + 3(x+1) + (y+1), \\
{}^v\tau_{xx} &= (x+1)^2(y+1) + (x+1) + 4(y+1), \\
{}^v\tau_{xy} &= 3(x+1)(y+1) + (x+1) + (y+1), \\
{}^v\tau_{yy} &= (x+1)(y+1)^2 + 4(x+1) + (y+1), \\
{}^w\tau_{xx} &= (x+1)^2(y+1) + 3(x+1) + 6(y+1), \\
{}^w\tau_{xy} &= 3(x+1)(y+1) + 3(x+1) + (y+1), \\
{}^w\tau_{yy} &= 3(x+1)(y+1)^2 + 4(x+1) + (y+1);
\end{aligned} \tag{30}$$

$$\begin{aligned}
f_x &= -2(x+1)(y+1) - 2(x+1) - 2, & f_y &= -2(x+1)(y+1) - 2(y+1) - 2, \\
p_x &= -2(x+1)(y+1) - 3(x+1) - 2, & p_y &= -2(x+1)(y+1) - 3(y+1) - 2, \\
q_x &= -2(x+1)(y+1) - 3(x+1) - 4, & q_y &= -6(x+1)(y+1) - 3(y+1) - 4
\end{aligned} \tag{31}$$

Table 4: Results for the problem (24), (27), (30), (31).

Mesh	Errors (%)	Number of iterations
8×4	$8.7 \cdot 10^{-6}$	108
12×6	$2.3 \cdot 10^{-5}$	225
16×8	$1.4 \cdot 10^{-5}$	594

Until now we considered that all input data are exact numbers but when measured they turn out to have numerous errors in measurement. We determine condition number only by numerical experiments. The dependence of the condition number on the number of grid points is shown in Table 5. This means that the iterative procedure is stable.

Table 5: Range of the condition number.

Mesh	Condition number
8×4	2.2 – 9.9
12×6	3.9 – 17.7
16×8	6.4 – 29.1

5 Conclusion

In this paper we have elaborated iterative procedure to the numerical solution of plane anisotropic boundary inverse problems when the input data measured from three suitable states are sufficient for determination of six unknown elastic coefficients.

From computed examples we can see that the errors of computed solutions depend on the discretization errors. If we want to obtain better results we have to use better discretization scheme. We also study influence of measured input data on stability of the numerical solutions and we obtain that the iterative procedure is stable.

This work was supported by the grant VEGA 1/0687/09 of the Grant Agency of Slovakia.

References

- [1] Brilla, I., Numerical solution of boundary inverse problems for orthotropic solids. *Numerical Modeling of Coupled Phenomena in Science and Engineering*, eds. M. Suárez Arriaga, J. Bundschuh & F. Dominguez-Mota, CRC Press, Taylor & Francis Group: Boca Raton, London, New York, Leiden, pp. 11–19, 2009.
- [2] Grebennikov, A.I., *Spline Approximation Method and its Applications*. MAX Press: Moscow, 2004.
- [3] Grebennikov, A., Solution of direct and inverse problems for laplace type equations by gr-method. *Proceedings of the WSEAS International Conferences MATH'05*, Cancun, pp. 1–6, 2005. (CD).

Postbuckling analysis of aeronautical panels manufactured using friction stir welding technology

Isabella Cavallante, Maurício V. Donadon, Alfredo R. de Faria, Paulo Rizzi, Sérgio F. M. de Almeida
Instituto Tecnológico de Aeronáutica – ITA, São José dos Campos, SP – Brazil

Abstract

Flat and curved panel elements constitute a major portion of the aircraft structure. They are found in the aircraft components as primary load carrying structures (such as wing surfaces), horizontal and vertical stabilizers, and fuselage sections. With the advent of the new joining techniques such as Friction Stir Welding (FSW) and their incorporation in the aircraft structures there is an imperative need for a better understanding of their behavior. To this end, more adequate methods of analysis, taking into account their specific features, have to be developed and implemented in order to exploit the considerable load bearing capacity of these panels in the postbuckling regime.

Within this context, this paper presents a numerical model for postbuckling analysis of aeronautical panels manufactured using friction stir welding joining technology (FSW). The proposed model takes into account material and geometric nonlinearities, geometric imperfections, failure as well as the mechanical interaction between skin and stiffener in the welding zone. The predicted postbuckling performance of the FSW panels was compared with numerical results obtained for similar riveted panels. The simulations indicated that the FSW panel has a better postbuckling performance with respect to the riveted panel. It was also found that theoretical predictions significantly underestimate the buckling load of aeronautical stiffened panels.

Keywords: FSW, stiffened panels, postbuckling, finite elements.

1 Introduction

Stiffened panels are widely used in fuselages and wings to build structurally optimized and lightweight airplanes. Buckling and post-buckling are major concerns for those parts. In most applications it is required that those panels resist buckling and support loads in the range of post-buckling in order to save some structural weight. Thus, the understanding of buckling and post-buckling is essential in aircraft design.

Panels are composed by a board member (skin) and stiffeners. They are very simple to manufacture and can endure a high load-to-weight rate. Therefore they are very attractive for aerospace and

shipbuilding industries. Although they represent only a small fraction of the total structural weight, they contribute substantially to the stability and load bearing. Stiffeners are used for both to increase the buckling tension of the plate, so as to bear some of the compression loads. The stiffeners are sized to buckle at approximately the same tension that the skin. In that way, structures are more efficient and keep the aerodynamic softness until higher levels of loading.

Four forms of instability may occur if the stiffened panels are subjected to compression loading: plate induced overall buckling (PI), stiffener induced overall buckling (SI), stiffener tripping (ST) and plate buckling (PB). According to Wang et al. [1], it is common for the panel to start buckling with a local buckling of the skin. When tensions reach very high values the local buckling evolves into global buckling. The most critical condition for the panel takes place precisely in this passage from local to global buckling. At this time, the panel completely loses strength and that's when final failure occurs. The presence of rivets or the material characteristics of the joint may reduce the panels resistance and change the failure modes [2].

There is no theoretical solution for the local failure tension. The constraints in the boundary between flange and plate elements are unknown and it is not precisely understood how the tension increases in the regions of the corners [3]. Therefore, solving the problem using the finite element code is more than welcome. The correct modeling of the problem and the numerical solution allow us to solve problems which would only be possible experimentally.

Since the mechanical properties of FSW joints were superior to those of the rivets, the FSW joint is able to replace without change the rivets in a wide range of applications. However, for the aerospace industry, it is not only important that the FSW joints are mechanically superior to the rivets. It is as important that the joints are equally or more efficient than rivets in buckling and post-buckling loading in order to guarantee lighter structures. This work aims to study the replacement of rivets by FSW in aeronautical stiffened panels. It intends to benchmark the performance of two similar boards - a riveted and welded by FSW - in buckling and post-buckling because these are the most critical situations for these structures. In this work the finite element method has been used for this purpose. The finite element method is available in several commercial software. Here we opted for the use of ABAQUS which has shown satisfactory results in similar studies [4].

To simplify the simulations, plate and stiffeners were modeled as Reissner-Mindlin plate elements. The FSW joint was modeled as solid element with the properties proposed by Marques [5] and Fioravanti [6] and the rivets were modeled as beam elements. We proved that these simplifications can consistently represent the actual panels and provide good estimates on the behavior of both panels under buckling and post-buckling.

2 Finite element modeling

2.1 Skin/stiffener interface model

The proposed skin/stiffener interface model was developed based on pull-out tests for the two representative samples of the panels to be studied - one using FSW joint and the other rivets for comparison purposes. The first step in the finite element modeling was to recreate such pull-out tests in Abaqus

and verify if the simulation results provided by the software were consistent with the experimental data available in the literature. The dimensions of the specimens used for the pull-out tests and simulations are represented in Figure 1.

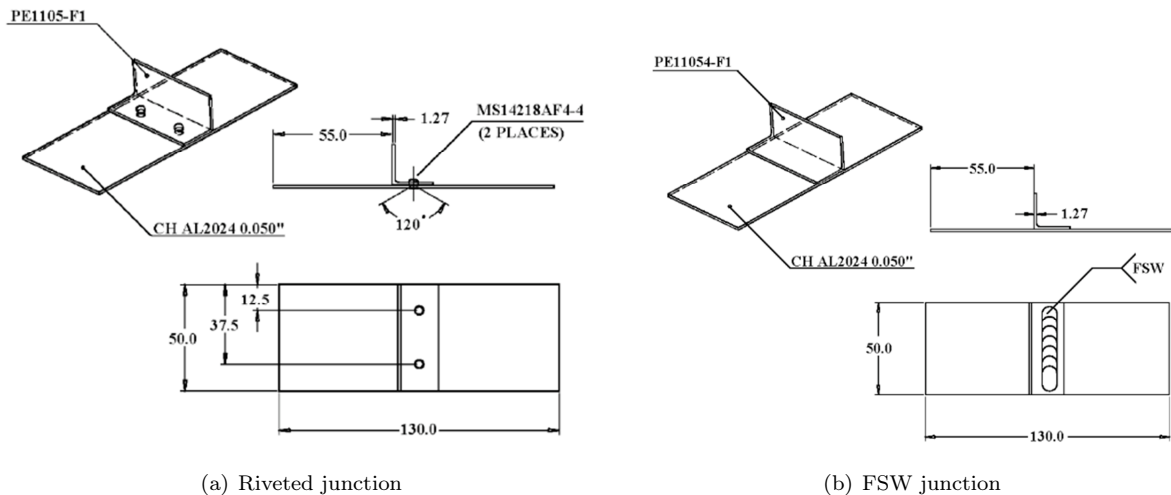


Figure 1: Specimen dimensions for pull-out tests.

The skin and the stiffeners are the major tangential load carriers. Therefore they could be modeled as plate elements in Abaqus. Rivets were modeled as beam elements and the FSW joint as a solid element. It was firstly intended to model the rivets as fasteners – a property that is available on Abaqus. The fasteners determine a kinematic connection between two nodes and allow the definition of boundary conditions for the six degrees of freedom for each node. However, it is not possible to add models of plasticity and failure which made the use of this feature impossible. Instead we used beam element with constraints in its outer nodes. This works exactly as the fasteners, with the advantage that it is possible to impose models of plasticity and failure. The setting of the rivets to the skin and the stiffeners is represented by Abaqus constraint *TIE*, as we can see in Figure 2. The TIE constraint restricts movement of the nodes in the six degrees of freedom, working similarly to the rivet's head. The skin of the panels is constructed in AA-2024 and the stiffeners are in AA-7075. The properties of both alloys can be found in [7, 8]. The rivets used in the studied panels are MS14218AD4-4 rivets. This means that they are AA-2117 rivets with 4 mm diameter and 4 mm length. The properties of AA-2117 alloy were also extracted of [7, 8]. Marques [5] modeled the mechanical properties of FSW joints in aluminum alloys. In the present paper, the mechanical properties of the joint's ZAT region studied in the aforementioned work are used to model the solid element that represents the FSW joint in the panels. Fioravanti [6] obtained the mechanical properties of FSW joints welded in aluminum alloys with different tools and provided important information about the failure of the joint. To represent the

failure behavior of the FSW joint of this work, we found appropriate to assume use of tools with 12 mm shoulder, 1250 rpm, 10 mm/min feed rate, according to Fioravanti's work [6]. It was also important to model the contact between the stiffener and the skin to avoid penetration of the stiffeners in the skin during the simulation. The modeling of contact in Abaqus is done by applying the iteration of contact between surfaces (surface-to-surface contact) one desires to establish contact. In this work, it was sufficient to define property contact as tangential and frictionless, but Abaqus has several options for more complex needs.

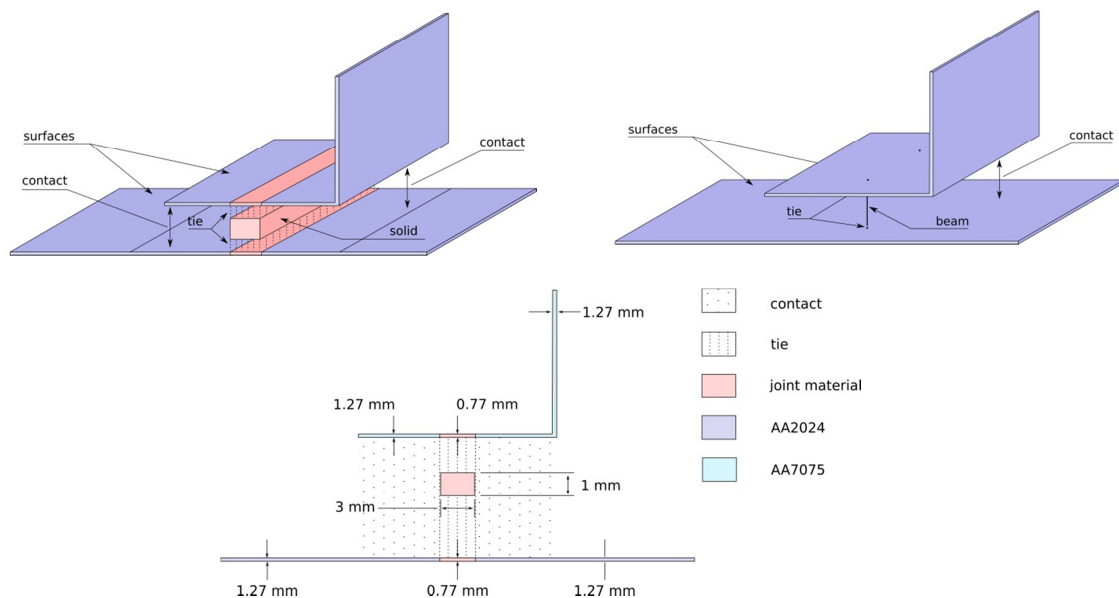


Figure 2: Skin/stiffener mechanical interaction.

The modeling of the specimens includes plastic behavior of materials, failure models and iterations of contact. However, not all methods of analysis for Abaqus are able to deal with these peculiarities. To represent nonlinear problems like these, we chose to use the method of analysis * DYNAMIC EXPLICIT. The * DYNAMIC option was chosen precisely because it is capable of dealing with nonlinear problems. EXPLICIT refers to the method of solution. In this case, ABAQUS uses small increments of time that allow the solution to proceed without iterations and therefore without the need to recalculate the tangent stiffness matrix at each iteration. The DYNAMIC EXPLICIT * procedure was designed for the analysis of dynamic events, but also applies to quasi-static processes, as happened here.

The analyses were carried out under displacement control by using the dynamic relaxation method. This method consists in loading the structure quasi-statically in a way that the dynamic effects are minimized. To minimize the dynamic oscillations, a Rayleigh proportional damping is defined as a linear combination between the tangential stiffness matrix and mass matrix [9].

The pull-out problem boundary condition is the restriction of all six degree of freedom of the skin. At the upper end of the stiffener, a displacement of 2.5 mm was prescribed, so to have as output of the simulation the load of that same end.

2.2 Stiffened panel model

The panels studied in this work are represented in Figure 3 and their dimensions are shown in Figure 4 and Table 1.

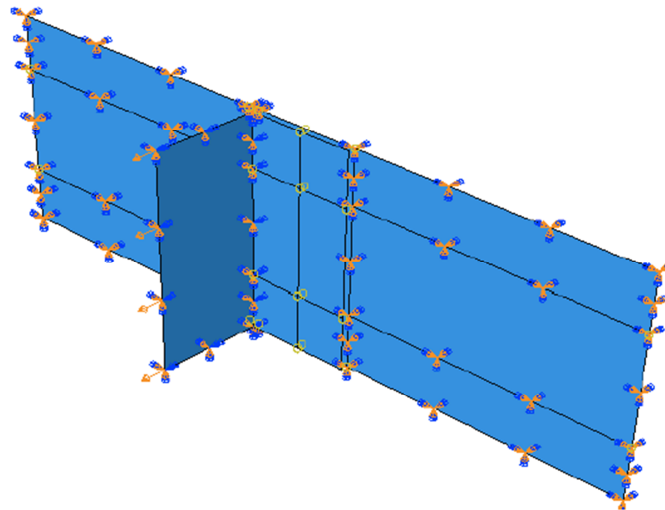


Figure 3: FE model of the pull-out specimens.

In the second round of simulations, the whole panels were compressed by imposing longitudinal (y direction) uniform displacement in one of its transverse edges ($y = L$). In $y = 0$, the condition of support is assumed to be simply supported. The longitudinal edges are free. In the central panel, rotation in Z is restricted in order to force symmetric displacements with respect to the free edges. Figure 5 illustrates those boundary conditions.

One of the panels has its stiffeners attached by rivets using the same spacing between the rivets as in the pull-out model. The second panel has the stiffeners attached to the skin by the FSW joint with the same characteristics as the FSW joint of its respective pull-out model. ABAQUS assumes that the geometry of the panels is perfect. Therefore, the direction of buckling which develops in

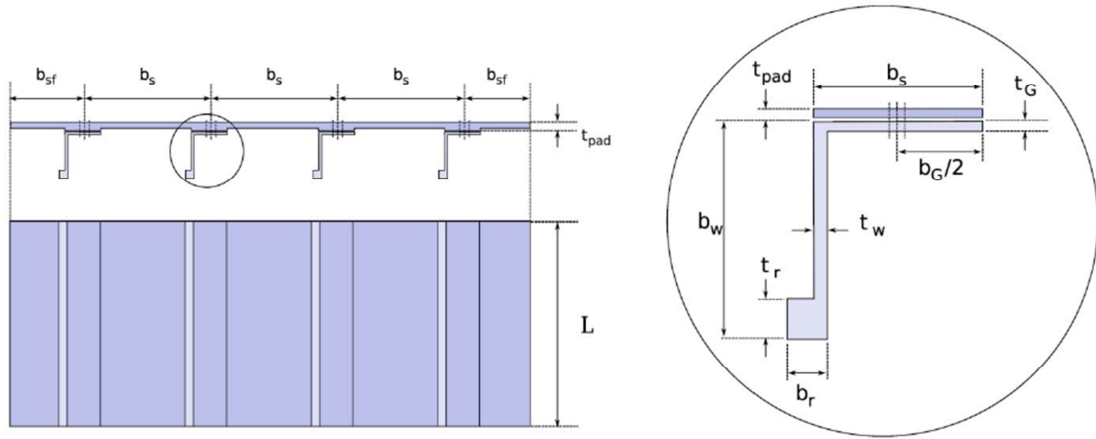


Figure 4: Typical fuselage panel and stiffeners.

Table 1: Panel dimensions.

Skin		Stiffener	
AA2024		AA7057	
L (mm)	224	L (mm)	224
b_s (mm)	163	t_g (mm)	18
b_{sf} (mm)	70	b_g (mm)	1.2
t_s (mm)	1.00	b_w (mm)	17
t_{pad} (mm)	0,27	t_w (mm)	1,2
b_{pad} (mm)	23	b_f (mm)	5
		t_f (mm)	3

the nonlinear analysis is arbitrary, and small changes in the numerical formulation of the problem can cause the buckling direction to change. The only way to prescribe the direction of buckling is to insert imperfections into the models. For each of the panels, this was done using the result of a previous analysis of linear buckling. The linear buckling analysis is performed using the method of analysis * LINEAR BUCKLE available in Abaqus. The loads and their buckling modes were obtained by solving the eigenvalue buckling problem [9]. The determination of eigenvalues and eigenvectors was numerically solved using algorithms of subspace iterations available in the software. The post-buckling simulations were performed similarly to the pull-out simulations. Materials, constraints and contact

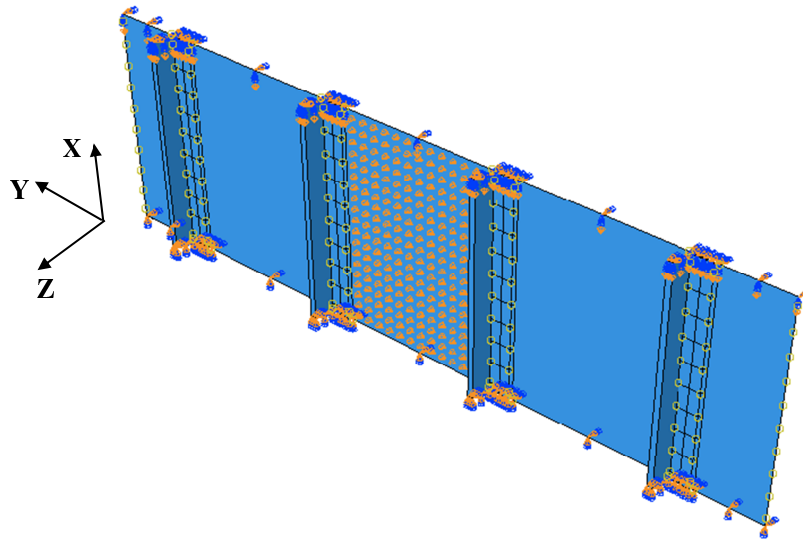


Figure 5: FE model of a typical fuselage panel and stiffeners.

surfaces were modeled as previously. The method chosen was also * DYNAMIC EXPLICIT applied quasi-statically. The meshes allocated to the various elements were the same. In the input file we added the command line * Imperfection, FILE = linear_buckling, 1e-6. This adds to the panel an imperfection with the shape of the first linear buckling mode (available on our linear_buckling output file) and maximum amplitude 1e-6 mm.

Abaqus uses the Updated Lagrangian formulation to create the mesh. It divides the domain into nodes and elements which deform and move with the deformation of the material. For the skin, rivets and stiffeners, a square structured mesh was chosen. For the solid representing the FSW joint, it was chosen a solid hexahedral structured mesh.

3 Numerical simulations

3.1 Pull-out tests

The results of the pull-out simulations are shown in Figure 6 and Figure 7. We can see that the adopted models provide a good match with the experimental test, confirming that they are sufficiently representative of the real scenario.

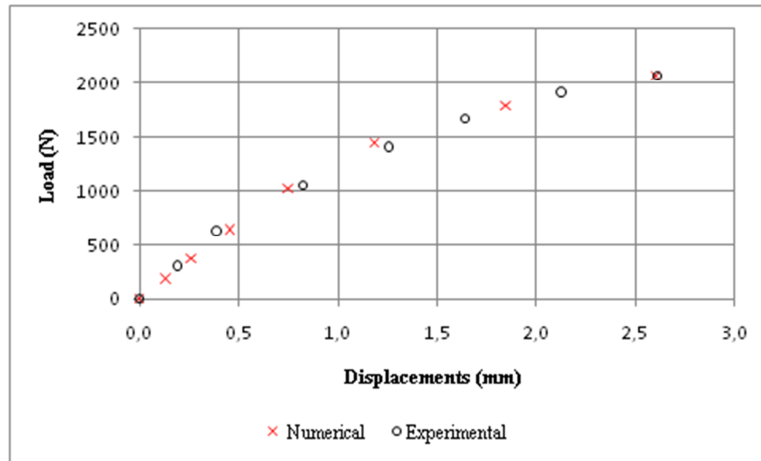


Figure 6: Comparison between numerical predictions and experimental results for the riveted junction.

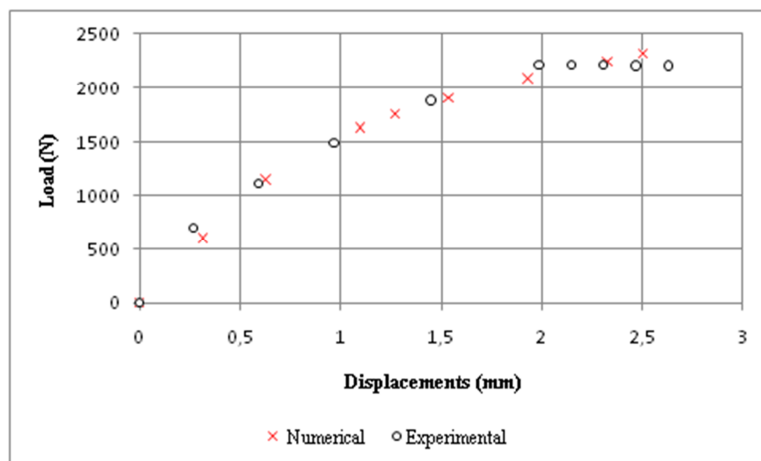


Figure 7: Comparison between numerical predictions and experimental results for the FSW junction.

3.2 Postbuckling and collapse analyses

The postbuckling analyses were performed using a two-step procedure. Firstly, we obtained the results for the linear buckling analysis. As said before, the important issue here was not to determine the buckling load, but get the buckling mode to serve as imperfection for nonlinear analysis. Table 2 and Figure 8 show the results of linear buckling analysis of the two panels.

Table 2: Eigenvalues comparison.

Eigenvalues	
Riveted panel	12.79
FSW panel	14.17

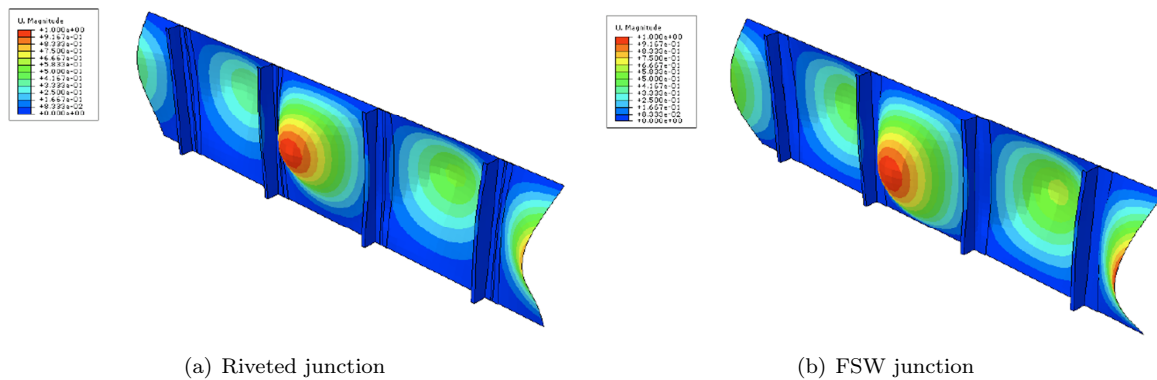


Figure 8: Buckling modes.

The riveted panel’s eigenvalue is slightly smaller than the one for the FSW panel, indicating that in the linear analysis the second one resists a little more loading before losing its stiffness. The panels have approximately the same stiffness module until the failure. The stiffness module decreases drastically when buckling starts – at a load of approximately 40 kN for both panels. The initial buckling mode is local, so buckling occurs only in skin members between rivets. The collapse of the panels occurs when the buckling mode changes from local to global – then, the stiffeners also buckle. The FSW panel requires a load slightly higher than the riveted panel for the inversion and the consequent collapse to occur. Figure 9 and Figure 10 show the evolution of buckling until failure of riveted panel and FSW panel, respectively.

In both panels, the failure starts with the skin’s local buckling and evolves onto global buckling along the post-buckling range, finally crashing when the weld or rivet yield. We can see that less stable members (skin) suffer elastic buckling and the most stable portions of the panel section (stiffeners) suffer an axial inelastic compression.

The most critical condition for the panel buckling occurs in the transition from local buckling to global buckling. At this point, the panels lose all resistance, failing. This happens immediately after the inversion, approximately 153 kN to FSW panel and 149 kN to the riveted panel. This values are summarized in Table 3.

The riveted panel is the first to lose stiffness, enter plastic deformation mode, global buckling, and

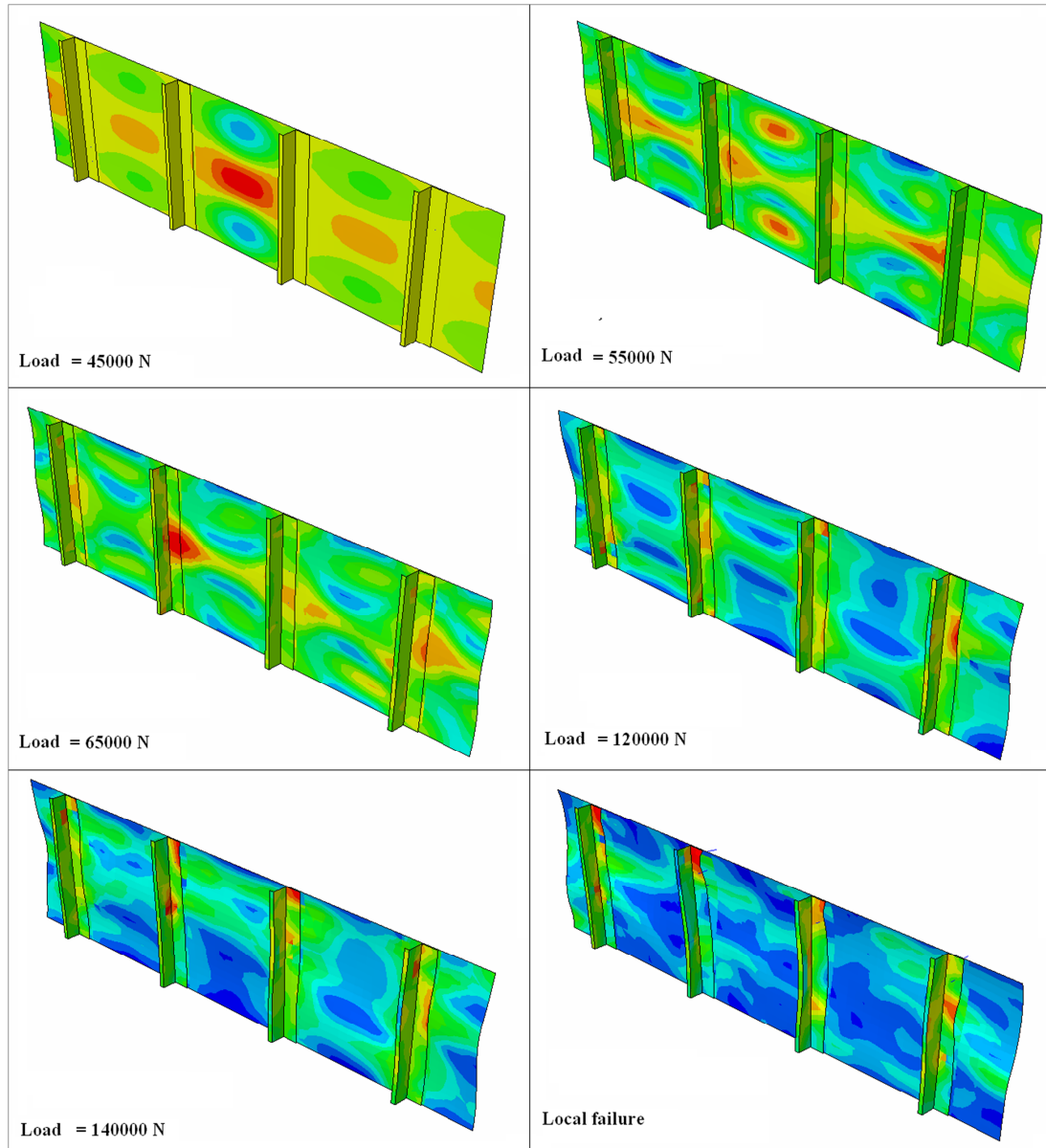


Figure 9: Predicted buckling evolution for riveted panels.

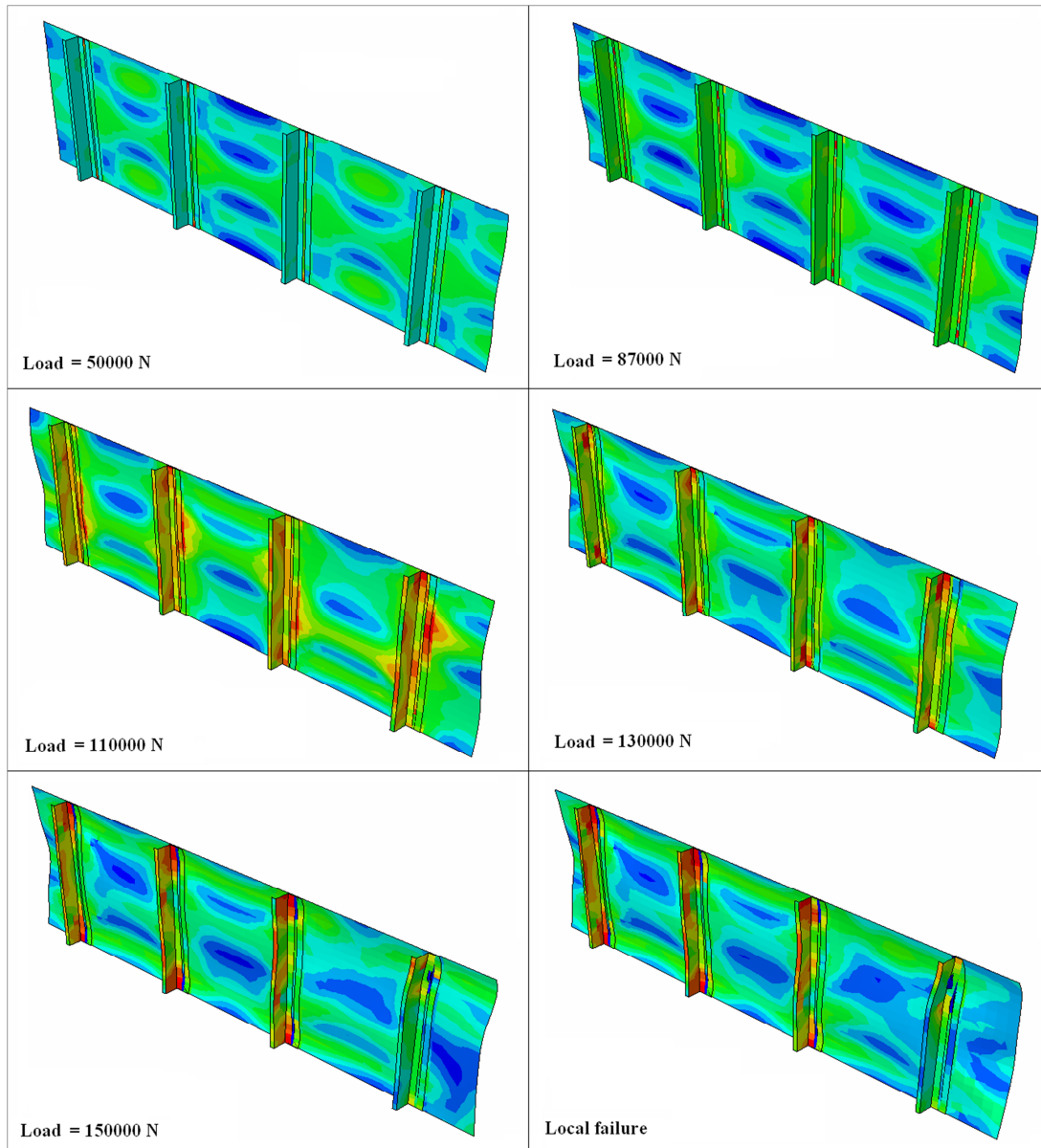


Figure 10: Predicted buckling evolution for panels manufactured using FSW.

therefore failing. Its failure loading is very close to the theoretical failure load of 150kN, predicted according the methods of reference [2]. The FSW panel failure loading is 3% higher than the failure loading of the riveted panel. When buckling occurs, the stiffness moduli decrease, and tensions grow slowly with respect to the increase in the displacements. This indicates that the panels have lost stiffness, but still are capable of sustaining the loading. The structural performance of both panels in the post-buckling regime was evaluated based on the *Global Stiffness Degradation Parameter* (DG) [10], which is defined as $D_G = 1 - K_S/K_0$ where K_0 is the initial stiffness defined by the linear portion of the load-displacement curve and K_S is the secant stiffness extracted from the load-displacement curve in the post-buckling regime. Figure 11 shows a comparison in terms of load-displacement and global stiffness degradation parameter between riveted and FSW panels.

Table 3: Failure load comparison.

	Theoretical [2]	Abaqus riveted	Abaqus FSW
Failure load (kN)	133	149	153

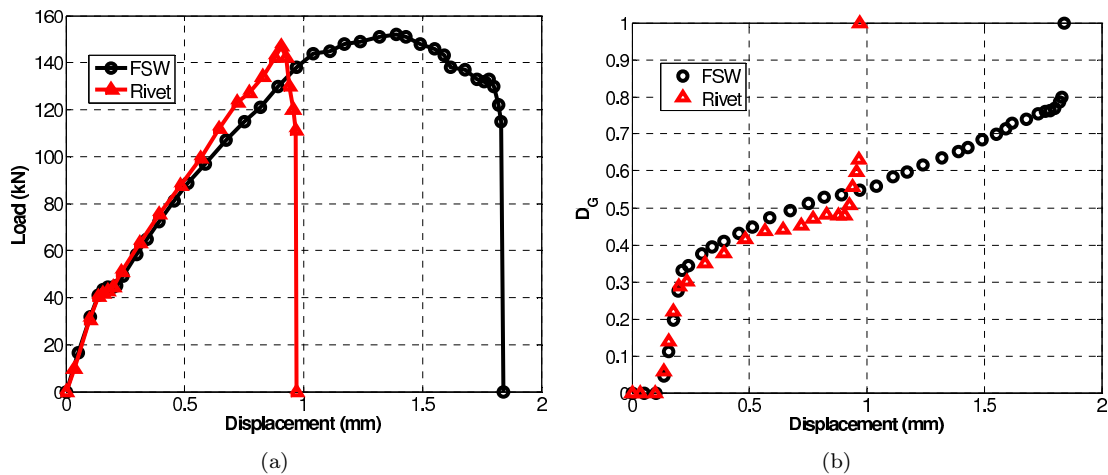


Figure 11: Structural performance comparison between riveted and FSW panels: (a) Load-displacement curve, (b) Global stiffness degradation parameter.

The failure of the riveted panel is abrupt. When the first rivet fails, the panel loses completely its stiffness, and it is not able to bear any more loading. FSW panel fails more smoothly. Only a small portion of the joint breaks, and the panel does not fail immediately. It is only when a larger share of

the joint breaks that the panel fails completely. Thus, a larger load is required to trigger the failure of the FSW panel. Besides, the FSW panel behaves much better after failure than the riveted panel does, because it supports some load after the initial rivet failure.

4 Conclusions

The development of FSW joint promises a technology that can replace the rivets in aircraft applications. This study aimed to evaluate the buckling behavior of an aircraft stiffened panel with FSW joints compared to the equivalent riveted panel to prove the benefits of using FSW instead of rivets. Two flat stiffened panels, typical of the fuselage structure were modeled and simulated in the finite element software Abaqus. The skin and the stiffeners were modeled as plate elements. The rivets were modeled as beam elements, and the FSW joint as a solid. The mechanical properties of FSW joint were modeled as suggested in [2] and [3]. The first step of the study was to validate the junction model. This was done by comparing pullout tests simulated in ABAQUS with experimental values available for both panels. The simulation results were close to the available experimental data, proving to be possible to adopt the proposed simplifications in the buckling analysis. Once validated, the full panel models were simulated for nonlinear buckling. This was done using the *EXPLICIT DYNAMIC mode of Abaqus. The panels were simply supported at $y = 0$. A 2.5 mm displacement was prescribed at $y = L$, which was responsible for the buckling and failure of the panel. The edges $x = 0$ and $x = L$ were free. The plasticity and failure modes of materials were included in this modeling strategy. The simulation results showed that the FSW panel has a higher buckling load with respect to the riveted panel. The FSW panel failure load was 27% greater than the theoretical value provided by the Boeing method of [2], and 3% higher than the simulated riveted panel. In addition to collapsing at a higher load, the FSW panel did not immediately lose all of its ability to bear loading after initial failure.

References

- [1] Wang, C.L.E., Grondin, G. & Elwi, A., Interaction buckling failure of stiffened steel plates. Technical report, Department of Civil and Environmental Engineering, University of Alberta, 2006.
- [2] Rizzi, P., Estabilidade de estruturas aeronáuticas. Technical report, Instituto Tecnológico de Aeronáutica – ITA, São José dos Campos, 2009. Apostila do Curso de estruturas Aeronáuticas.
- [3] Cruz, M. & Neto, C., Friction stir welding – review: Potencial de alpicção na indústria aeroespacial. *SIGE: Simpósio de Aplicações Operacionais em áreas de Defesa*, São José dos Campos, 2009.
- [4] Donadon, M.V., Rizzi, P. & Almeida, A., A numerical study on the postbuckling behavior of shallow singly-curved panels. *VI Congresso Nacional de Engenharia Mecânica*, Campina Grande, 2010.
- [5] Marques, H., Modelação das propriedades mecânicas de juntas soldadas por fricção linear. Technical report, FCT-UNL, Lisboa, 2009.
- [6] Fioravanti, A.S., *Soldagem por FSW de ligas de alumínio ALCAD AA2024-T3 e AA7075-T6*. Master's thesis, Universidade Federal do Rio Grande do Sul, Porto Alegre, 2008.
- [7] *Aerospace Structural Metals Handbook*, volume II - Non-ferrous alloys. CINDAS/Purdue University, 1994.
- [8] Department of Transportation, Washington, DC, USA, *MIL-HDBK-5: Metallic Materials Properties Development and Standardization*, 2003.

- [9] *ABAQUS 6.5 Theoretical Manual*, 2005.
- [10] Arbelo, M., Almeida, S. & Donadon, M., A numerical model for post-buckling analysis of composite shear webs. *Mechanics of Advanced Materials and Structures*, **17**, pp. 1–7, 2010.

Mechanical behavior of GFRP laminates at varying strain rates and temperatures

J.L.V. Coelho, J.M.L. Reis, H.S. da Costa-Mattos

*Theoretical and Applied Mechanics Laboratory – LMTA, Mechanical Engineering
Post Graduate Program – PGMEC,*

*Universidade Federal Fluminense – UFF, Rua Passo da Pátria, 156, Niterói, RJ
– Brazil*

Abstract

In this work, the mechanical response of a composite material based on glass fiber reinforced polymer (GFRP) was analytically predicted as a function of strain rate and temperature and subsequently compared with experimental data. It was shown that for the temperature range from 20 to 80 °C at varying strain rates, the predicted elastic properties of the composite agreed closer. The agreements between the analytically predicted and experimentally determined stress–strain curves of the composite were found to be dependent on temperature and strain rate. The experimental and analytical research data and the approaches presented in this work should significantly extend our knowledge of the effect of elevated temperatures on the mechanical behavior of high temperature polymer matrix composites.

Keywords: mechanical response, GFRP, strain rate effect, temperature effect, experiments, modeling.

1 Introduction

Over the last decade, composite materials have been used to repair damaged gas and liquid transmission pipelines. Mechanical damage involving dents with gouges is one of the leading causes of transmission pipeline failures in terms of both static and cyclic pressure loading. Because of the severity of this defect type, pipeline companies are required to respond to these anomalies by either removing damaged sections or repair using welded sleeves. Since in some fields repair work cannot be performed using heat, composite materials gain a significant importance. Composite materials have been used to repair corroded pipelines and their use has gained wide acceptance across the pipeline industry. However, the mechanical responses of fiber-reinforced polymeric composites are sensitive to the rate at which they are loading and temperature operation. In many technological applications, under dynamic loading conditions, the response of a structure designed with static properties might be too conservative. The main reason is that mechanical properties of composites vary significantly

with changing the strain rate and temperature. Unlike metals, which have been studied extensively over a wide range of strain rates and temperatures, only limited amount of information is available on the effects of strain rate and temperature on the response of fibrous composites.

Many researchers studied composite materials at different strain rate and others have studied their behavior at different temperature but few combined both.

The work performed by Rotem and Lifshitz [1] investigated the tensile behavior of unidirectional glass fiber/epoxy composites over a wide range of strain rates from 10^{-6} to 30s^{-1} and found that the dynamic strength is three times higher than the static strength and the dynamic modulus is 50% higher than the static modulus. However, while investigating angle ply glass/epoxy laminates, Lifshitz [2] found that the elastic modulus and failure strain were independent on the strain rate and the dynamic failure stress was only 20–30% higher than the static failure stress.

Tensile tests were performed on a glass epoxy laminate at different rates ($1.7 \cdot 10^{-2}$ -2000 mm/s) by Okoli and Smith [3, 4] to determine the effects of strain rate on Poisson's ratio (ratio of transverse strain to the corresponding axial strain below the proportional limit) of the material. Poisson's ratio was found to be rate insensitive. It was suggested that the rate insensitivity in Poisson's ratio of the laminates tested is due to the presence of fibers in the composites. The effect of strain rate on the tensile properties of a glass/epoxy composite was investigated by Okoli and Smith [5] strain rate was attributed to the increased strength of the glass fibers with strain rate. In other studies the effects of strain rate on the tensile, shear, and flexural properties of glass/epoxy laminate was investigated by Okoli and Smith [3–6].

Tensile modulus increased by 1.82%, tensile strength increased by 9.3%, shear strength increased by 7.06%, and shear modulus increased by 11.06% per decade increase in log of strain rate. The above observation was in agreement with the results of the investigation conducted by Armenakas and Sciamarella [7] that suggested a linear variation of the tensile modulus of elasticity of unidirectional glass/epoxy composites with the log of strain rate.

A systematic study of the strain rate effects on the mechanical behavior of glass/epoxy angle ply laminates was done by Staaband and Gilat [8, 9] using a direction tension split Hopkinson bar apparatus for the high strain rate tests and a servo hydraulic testing machine for the quasi-static tests. The tensile tests at higher strain rates (in the order of 1000 s^{-1}) showed a marked increase in the maximum normal stress and strain when compared to the values obtained in the quasi-static tests. Although both fibers and matrix are strain rate sensitive, the fibers were thought to influence laminate rate sensitivity more than the matrix.

To achieve the high performance required in the material's projected applications, a good understanding of the dynamic deformation of GFRP under different temperatures is essential.

The aim of this paper is first to present experimental results illustrating the effect of strain rate and temperature on the mechanical response for GFRP under a wide range of strain rates and temperatures and then compare to analytical models.

2 Experimental work

The apparatus and procedure used to obtain the tensile properties in the GFRP laminates are described below.

The tensile tests were performed according to the method prescribed in ASTM D3039 [10]. The test specimens were cut from hand lay-up sheets. The glass was a cross-ply plain weave e-glass [0/90] fabric with 326 g/cm² weight. The composite had a fiber weight fraction of 70% with 8 layers of glass. The epoxy resin system used was RR515 from SILAEX based on a diglycidyl ether bisphenol A and an aliphatic amine hardener, being processed with a maximum mix ratio of 4:1 (with low viscosity). The resin systems properties provided by the manufacturers are presented in Table 1.

Table 1: Properties of the epoxy resin.

Property	Epoxy
Viscosity at 25°C μ (cP)	12000-13000
Density ρ (g/cm ³)	1.16
Heat Distortion Temperature HDT (°C)	50
Modulus of Elasticity E (GPa)	5.0
Flexural Strength (MPa)	60
Tensile Strength (MPa)	73
Maximum Elongation (%)	4

The specimens were cut 250 mm by 25 mm, leaving a gauge section of 200 mm. The tensile tests were performed on a Shimadzu AG-X tensile testing machine at 3 different strain rates, $1.6 \cdot 10^{-5}$, $1.6 \cdot 10^{-4}$, $1.6 \cdot 10^{-3} \text{s}^{-1}$. Attached to the testing machine a thermostatic chamber was used to set the temperature test environment. The test temperature used was, 20°C, 40°C, 60°C and 80°C. These temperatures were chosen since heat distortion temperature is 50°C, so tests were performed at $\text{HDT} \pm 30^\circ\text{C}$. For each temperature the GFRP specimens were tested at all strain rates.

3 Results and discussion

3.1 Experimental results

Experimental data determining the dynamic response of a composite structure loaded at different strain rates is limited by the range of strain rates, which can practically be applied for a particular test method. It is desirable to obtain information about strain rates outside the range that can be achieved experimentally, in order to predict the behavior of materials over very long loading times.

Figure 1 presents the typical stress vs. strain results of GFRP at 20°C, 40°C, 60°C and 80°C and at all strain rates used ($1.6 \cdot 10^{-5}$, $1.6 \cdot 10^{-4}$, $1.6 \cdot 10^{-3} \text{s}^{-1}$).

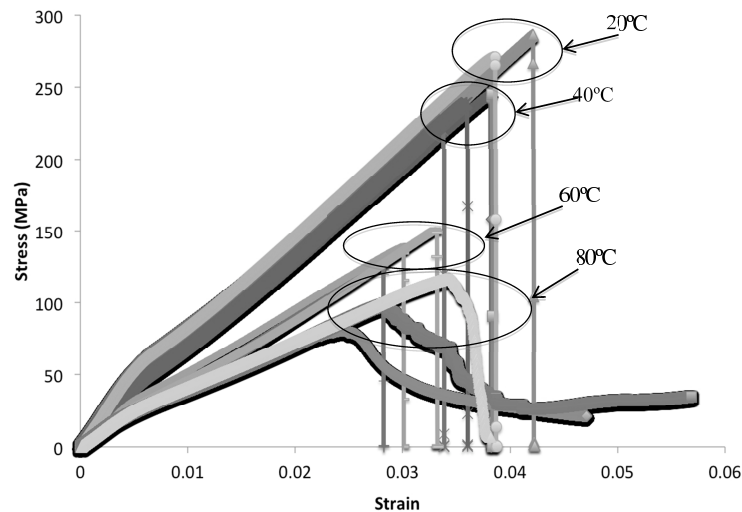


Figure 1: Stress vs. strain curves for GFRP at 20°C, 40°C, 60°C and 80°C at $1.6 \cdot 10^{-5}$, $1.6 \cdot 10^{-4}$, $1.6 \cdot 10^{-3} \text{s}^{-1}$ strain rates.

Analyzing the stress-strain curves presented in figure 1 it is clear that only the temperature affects the modulus of elasticity. Increasing temperature, modulus of elasticity decreases making GFRP less stiff. The modulus of elasticity, E , measured at 20°C, 40°C, 60°C and 80°C were 70.3 GPa, 66.5 GPa, 45.2 GPa and 32.11 GPa, respectively.

Figure 2 displays the stress vs. strain curves for GFRP at 20°C, 40°C, 60°C and 80°C at all strain rates used in the research where 1, 2 and 3 means $1.6 \cdot 10^{-5}$, $1.6 \cdot 10^{-4}$, $1.6 \cdot 10^{-3} \text{s}^{-1}$ strain rates, respectively.

Analyzing the stress vs. strain curves presented in figure 2 at all temperatures tested the ultimate tensile strength are significantly affected by the strain rates, i.e. high strain rates, elevated ultimate tensile strength and lower strain rate contributes to lowering the ultimate strength. Also, at 80°C, softer failure occurs, GFRP becomes less brittle as temperature increases. Table 2 presents the ultimate strength in MPa of GFRP at different temperatures at $1.6 \cdot 10^{-5}$, $1.6 \cdot 10^{-4}$, $1.6 \cdot 10^{-3} \text{s}^{-1}$ strain rates.

From table 2 it can be seen that at higher loading rate leads to high ultimate strength. At 20°C, laboratory temperature, a decrease of 15.5% is observed when loading rate decreases 10 times compared to standard strain rate. Also an increase of 5.8% is computed for 10 times higher strain rate. This behavior follows all tested temperatures, i.e., increasing loading rate, higher ultimate strength and the opposite occurs for strain rate decrement.

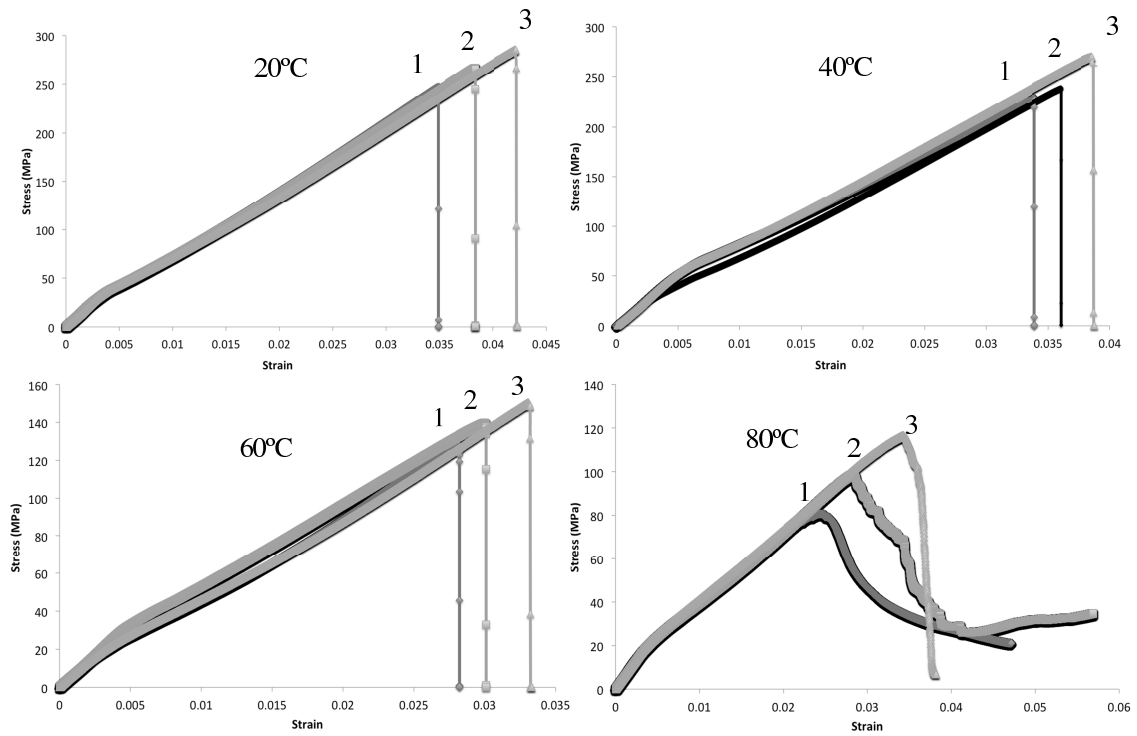


Figure 2: Stress vs. strain curves at 20°C, 40°C, 60°C and 80°C at all strain rates.

Table 2: Ultimate Tensile Strength (MPa) at different temperatures at 1.6×10^{-5} , 1.6×10^{-4} , $1.6 \times 10^{-3} \text{ s}^{-1}$ strain rates.

Strain rate (s^{-1})	Test Temperature ($^{\circ}\text{C}$)			
	20	40	60	80
1.6×10^{-5}	227.46 ± 12.46	214.92 ± 12.73	113.44 ± 11.87	72.61 ± 7.06
1.6×10^{-4}	269.23 ± 15.98	240.44 ± 14.32	141.85 ± 4.96	86.21 ± 11.23
1.6×10^{-3}	284.95 ± 5.1	273.24 ± 5.83	153.61 ± 3.36	101.61 ± 10.39

3.2 Temperature dependency

According to the test results, see figure 2, the modulus of elasticity decrease substantially with temperature, lowering GFRP stiffness. Figure 3 displays the modulus of elasticity as function of test temperature. This behavior can be predicted following a polynomial function of the third degree displayed in equation 1.

$$E = 0.004\theta^3 - 0.00607\theta^2 + 2.4218\theta + 42.677 \quad (1)$$

where E is the modulus of elasticity in GPa and θ represents the test temperature in °C.

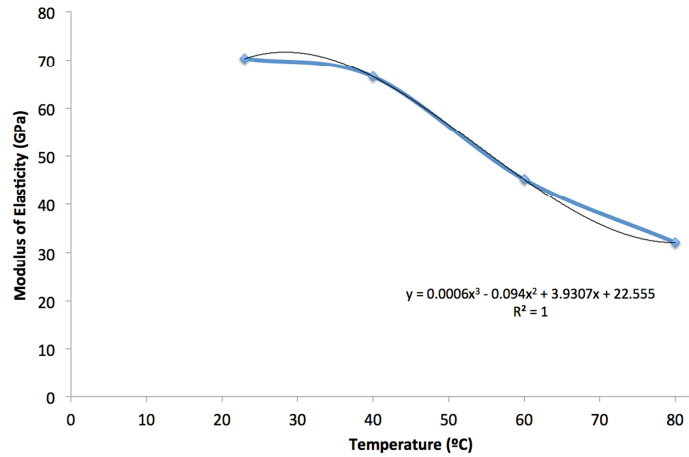


Figure 3: GFRP modulus of elasticity at different temperatures.

3.3 Ultimate Tensile Strength dependency of strain rate at different temperature.

The experimental results showed that the modulus of elasticity are not affected by strain rate, $\dot{\epsilon}$, in a tensile test. However, the ultimate tensile strength are highly sensible to strain rate variations. The main objective of this section is to propose a simple analytical model which describe the strain rate influence in the ultimate tensile strength, σ_u , at different temperatures, θ .

For the ultimate tensile strength σ_u , is proposed

$$\sigma_U(\dot{\epsilon}) = K(\theta)\dot{\epsilon}^N \quad (2)$$

where $K(\theta)$ is a function of the test temperature and N is a constant in which both can be experimentally determined using the least square method from the $\sigma \times \dot{\epsilon}$ or, in a simple form, from the $\log(\sigma_U)$ vs. $\log(\dot{\epsilon})$ supposing σ_U is equal to σ_U obtained in a test at $\dot{\epsilon} = 1.6 \times 10^{-4}$. Under

this approach the experimental curve is approximated to a straight line in a log vs. log where N is the slope of this straight line and $\log(K(\theta))$ the vertical axis cross point, since $\log(\sigma_U)$ vs. $\log(\dot{\epsilon}) = \log(K(\theta)\dot{\epsilon}^N) = \log K(\theta) + N \log(\dot{\epsilon})$.

Figure 3 presents the experimental results $(\sigma_U, \dot{\epsilon})$ at different test temperature.

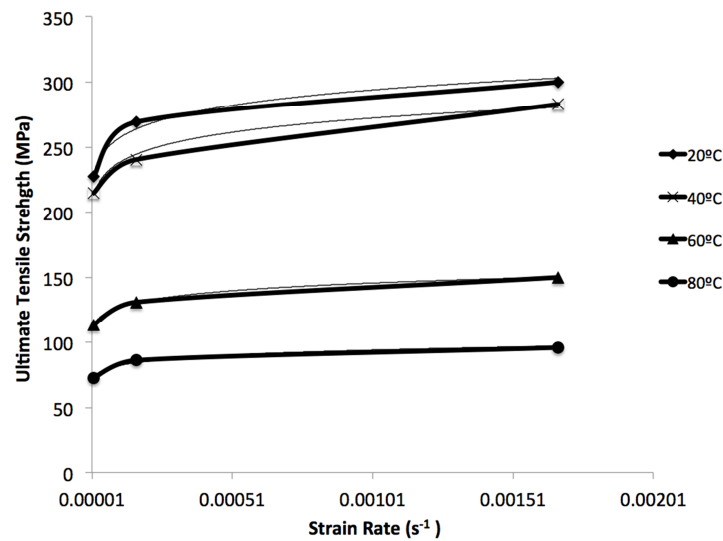


Figure 4: Ultimate strength vs. strain rate. Experimental and model.

The values used for $K(\theta)$ followed equation 3 and N was 0.06.

$$K(\theta) = 0.006\theta^3 - 0.9405\theta^2 + 38.97\theta - 26.696 \quad (3)$$

The comparison between the proposed model with experimental results are presented in table 3.

According to table 3 we can evaluate that the experimental results are within or close to the analytically predicted ranges for the entire temperature and strain rate range considered. The maximum variation observed was 7.9% at 60°C at $1.6 \times 10^{-4} \text{ s}^{-1}$.

4 Conclusions

The mechanical response of a cross-ply glass fiber reinforced plastic (GFRP) composite was experimentally measured for temperatures ranging from 20 to 80 °C at three different strain rates ($1.6 \cdot 10^{-5}$, $1.6 \cdot 10^{-4}$, $1.6 \cdot 10^{-3} \text{ s}^{-1}$) and predicted based on the fundamental properties of its constituents using an analytical and approach. These results showed that GFRP is strongly affected by strain rate and temperature. In particular the ultimate tensile strength is only dependent from strain rate and

Table 3: Comparison between proposed model and experimental test results.

Temperature (°C)	Strain Rate (s ⁻¹)	σ_u EXP (MPa)	σ_u MOD (MPa)	% variation
20	1.6×10^{-5}	227.46	230.02	+1.1
	1.6×10^{-4}	269.23	264.09	-1.9
	1.6×10^{-3}	284.95	303.22	+6.4
40	1.6×10^{-5}	214.92	212.53	-1.1
	1.6×10^{-4}	240.44	244.02	+1.5
	1.6×10^{-3}	273.24	280.17	+2.5
60	1.6×10^{-5}	113.44	114.43	+0.9
	1.6×10^{-4}	131.38	141.85	+7.9
	1.6×10^{-3}	150.85	153.61	+1.8
80	1.6×10^{-5}	72.61	73.90	+1.8
	1.6×10^{-4}	86.21	84.85	-1.6
	1.6×10^{-3}	97.42	101.61	+4.3

temperature affects the GFRP stiffness. Good agreements were observed between the predictions of the elastic properties and the experiment. The predict model represented an excellent possibility to estimate the stress vs. strain curves of any constant strain rate ranging from 0 to $1.6 \cdot 10^{-3} \text{ s}^{-1}$.

Acknowledgements The financial support of FAPERJ (Rio de Janeiro State Funding), CNPq (Research and Teaching National Council) and CAPES (Coordination of Improvement of Higher Level Personnel) are gratefully acknowledged.

References

- [1] Rotem, A. & Lifshitz, J., Longitudinal strength of unidirectional fibrous composite under high rate of loading. *Proceedings of the 26th annual technical conference*, Society for Plastics Industry, Reinforced Plastics/Composites Division: Washington, DC, pp. 1–10, 1971. Section 10-G.
- [2] Lifshitz, J., Impact strength of angle ply fiber reinforced materials. *Journal of Composite Materials*, **10**, pp. 92–101, 1976.
- [3] Okoli, O. & Smith, G., Overcoming inertial problems in the high strain rate testing of a glass/epoxy composite. *Proceedings of Society of Plastics Engineers Annual Technical Conference (ANTEC)*, Advanced Polymer Composites Division, volume 2, pp. 2998–3002, 1995.
- [4] Okoli, O. & Smith, G., The effect of strain rate and fibre content on the poisson's ratio of glass/epoxy composites. *Composite Structures*, **48**, pp. 157–161, 2000.
- [5] Okoli, O.I. & Smith, G., Aspects of the tensile response of random continuous glass epoxy composites. *Journal of Reinforced Plastics and Composites*, **18**, pp. 606–661, 1999.
- [6] Okoli, O.I., The effects of strain rate and failure modes on the failure energy of fibre reinforced composites. *Composite Structures*, **54**, pp. 299–303, 2001.
- [7] Armenakas, A. & Sciammarella, C., Response of glass-fiber-reinforced epoxy specimens to high rates of tensile loading. *Experimental Mechanics*, **13**, pp. 433–440, 1973.
- [8] Staab, G. & Gilat, A., High strain rate response of angle-ply glass/epoxy laminates. *Journal of Composite Materials*, **29**, pp. 1308–1320, 1995.
- [9] Staab, G.H. & Gilat, A. *Proceedings of the 9th International Conference on Composite Materials, ICCM IX*, Madrid, Spain, pp. 278–28, 1993.
- [10] Standard test method for tensile properties of polymer matrix composite materials. Technical Report ASTM D3039 - 08, ASTM, 2008.

Analysis of special hydrostatic tests performed in produced water pipelines

H.S. da Costa Mattos, L.M. Paim, J.M.L. Reis

*Laboratório de Mecânica Teórica e Aplicada, Programa de Engenharia Mecânica,
Universidade Federal Fluminense, Rua Passo da Pátria 156, 24210-240,
Niterói, RJ – Brazil*

Abstract

The present work is concerned with the analysis of special hydrostatic tests performed in metallic pipelines used to convey produced water in offshore oil and gas platforms. Burst and long-term hydrostatic tests are generally recommended for assessing the structural integrity of these pipelines. Nevertheless, since a real pipeline is not a closed-ended cylinder, misleading conclusions can be made if the perturbations caused by the closed ends of the specimen are neglected in the analysis. Elastoplasticity theory and thermodynamics are used in the modelling of these tests. Model predictions are compared with experimental results showing a good agreement.

Keywords: produced water pipelines, burst tests, long-term hydrostatic tests, elasto-plasticity, epoxy repair systems, failure analysis.

1 Introduction

In a recent paper [1] it was presented a new methodology to repair localized corrosion damage in metallic pipelines with epoxy resins. The main motivation for the use of such kind of repair system is corrosion defects in produced water pipelines used in offshore oil exploitation [2]. Since offshore platforms are hydrocarbon atmospheres, any repair method using equipment that may produce heat and/or sparking is forbidden. Although the operation pressure of these pipelines is not very high, the water temperature is between 60°C to 90°C, which can be a major shortcoming for the use of polymeric material as repair systems.

The petroleum as found in the nature is actually a mixture, basically composed of oil, gas and water. Oil reservoirs frequently contain large volumes of water, while gas reservoirs tend to produce only small quantities. At the surface, produced water is separated from the hydrocarbons, treated to remove as much oil as possible, and then either discharged into the sea or injected back into the wells. In addition, some installations are able to inject produced water into other suitable geological formations.

After treatment, produced water still contains traces of oil and, thus, discharge into the sea is strictly controlled by legislation. Produced water contains various chemicals such as heavy metals, polynuclear aromatic hydrocarbon, and radionuclides, is one of the most significant wastewater discharges in the offshore oil industry.

The present paper is concerned with the analysis of some special tests developed for analysing the structural integrity of metallic pipelines used convey produced water in offshore oil and gas platforms: (i) yield and burst test performed to check the strength of undamaged specimens, and (ii) long-term tests performed at constant pressure (generally above 3 MPa) with water temperature between 60°C to 90°C in damaged specimens to check the durability some kind of epoxy repair system.

Hydrostatic tests are normally conducted under industry and/or customer requirements or specifications. They are usually performed taking as specimen cylindrical vessels closed at the ends and are often used to assess information about the mechanical strength of a given pipeline (or about the effectiveness of a given repair or reinforcement system in a damaged pipeline). The material, diameter and wall thickness of the specimen are normally the same than the pipeline. The cylinder is closed at the extremities using a welded cap or a bolted pressure flange. Nevertheless, since the real pipeline is not a closed vessel, mistaken conclusions can be made if the perturbation caused by the closed ends of the specimen is not taken into account.

In order to identify and eventually “correct” or even eliminate the perturbation caused by the closed ends of the specimen on experimental results, a theoretical analysis is performed making use of a particular set of elasto-plastic constitutive equations and also a special state law for liquid water at high pressures.

In the case of yield and burst tests, the axial stress induced by the pressure applied at the extremities of the specimen can be important. In the present work the problem is modelled in the context of elasto-plasticity as a thin-walled cylinder closed at the extremities under pressure. An analytical solution is obtained and it is shown that both yield and burst pressures obtained experimentally for the specimen is approximately $2/\sqrt{3}$ (1.155) higher than the one obtained in a long pipeline. The particular nature of the specimens may lead to mistaken conclusions. Real pipelines are long and the effect of axial stresses in straight lines is almost negligible, what is not the case of the specimens for hydrostatic testing. Hence, such a difference must be taken into account or the strength of the pipeline is overestimated. The predictions of burst pressures of different specimens using the elasto-plastic model are in good agreement with experimental results. The predicted results are closer to the experimental results that the obtained using the ASME Boiler and Pressure Vessel Code [3].

In the case of long-term tests (over 1000 hours) under higher fluid temperatures, wrong predictions may occur depending on how the testing system is prepared. In these tests, specimens with through-wall corrosion defects repaired with some epoxy system are submitted to a constant pressure (generally above 3 MPa) under temperatures between 60 °C and 90 °C. The idea is to check the durability of the repair. Experimentally it is verified that, in a closed pressure vessel with water under similar if a pressure relief valve is not used (hence, the specimen is completely closed and the mass of fluid is constant inside it), a very small temperature variation (even 1 K) may induce a huge pressure variation, eventually leading the repair to failure. In the present study, a simple constitutive equation is proposed for water at very high pressures. It is a very simple state law that extends the Tait equation of state

for barotropic fluids (or called the Murnaghan equation of state in the context of an elastic solid [4–6]) to account for small temperature variations. The predictions of pressure variations caused by small temperature variations using the proposed state law are in agreement with experimental results. With this state law, it is also possible to verify the pressure peak induced by a small temperature variation. Therefore, long-term hydrostatic tests must be performed with the use of a pressure relief system. Without a relief valve, the durability and effectiveness of the repair system may be underestimated due to failure caused by undesirable and unexpected pressure peaks induced by very small temperature variations admitted by the temperature control system.

2 Modelling the burst pressure of elasto-plastic cylinders

The axial stress induced by the pressure applied at the extremities of the specimen can be important in the case of burst tests of pressurized cylinders. Although a variety of papers concerned with this subject have been developed within the framework of modern continuum plasticity [7–10], the goal of this section is to propose a theoretical analysis restricted to thin-walled pipes and considering a particular set of elasto-plastic constitutive equations in order to obtain a simple expression useful for failure pressure estimates. Curiously, one of the main motivations for carrying experimental investigations on the burst tests of pressurized cylinders is the evaluation of the failure behaviour of steel rocket motor cases under internal pressure [11, 12].

2.1 Summary of the elasto-plastic constitutive equations

The following set of elasto-plastic constitutive equations is a particular case of the constitutive equations discussed in [13] but restricted to isotropic hardening. These equations are adequate to model the monotonic inelastic behaviour of metallic material at room temperature.

In the framework of small deformations and isothermal processes, besides de stress tensor $\underline{\underline{\sigma}}$ and the strain tensor $\underline{\underline{\varepsilon}} = \frac{1}{2}[\nabla\underline{\underline{u}} + (\nabla\underline{\underline{u}})^T]$ ($\underline{\underline{u}}$ is the displacement at a given material point), in this theory it is considered the following auxiliary variables: the plastic strain tensor $\underline{\underline{\varepsilon}}^p$, the cumulated plastic strain p and another variable Y , related to the isotropic hardening. A complete set of elasto-plastic constitutive equations is given by:

$$\underline{\underline{\sigma}} = \frac{\nu E}{(1 + \nu)(1 - 2\nu)} \text{tr}(\underline{\underline{\varepsilon}} - \underline{\underline{\varepsilon}}^p) \underline{\underline{1}} + \frac{E}{(1 + \nu)} (\underline{\underline{\varepsilon}} - \underline{\underline{\varepsilon}}^p) \Rightarrow (\underline{\underline{\varepsilon}} - \underline{\underline{\varepsilon}}^p) = \frac{(1 + \nu)}{E} \underline{\underline{\sigma}} - \frac{\nu}{E} \text{tr}(\underline{\underline{\sigma}}) \underline{\underline{1}} \quad (1)$$

$$\underline{\underline{\varepsilon}}^p = \frac{3}{2J} \underline{\underline{S}} \dot{p} \quad (2)$$

$$Y = \sigma_y + v_1 [1 - \exp(-v_2 p)] \quad (3)$$

$$\dot{p} \geq 0; F = (J - Y) \geq 0; \dot{p}F = 0 \quad (4)$$

with

$$J = \sqrt{\frac{3}{2}(\underline{\underline{S}} : \underline{\underline{S}})} = \sqrt{\frac{3}{2} \sum_{i=1}^3 \sum_{j=1}^3 (S_{ij})^2} \quad (5)$$

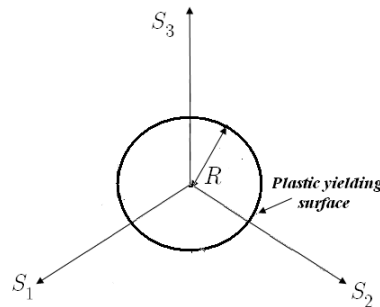


Figure 1: Elasticity domain in the space of the principal directions of the deviatoric stress tensor.

Where E is the Young modulus, ν the Poisson's ratio and σ_y , v_1 , v_2 are positive constants that characterize the plastic behaviour of the material. $\underline{\underline{1}}$ is the identity tensor, and $tr(\underline{\underline{\bullet}})$ is the trace of a tensor $(\underline{\underline{\bullet}})$. $\underline{\underline{\sigma}}$ is the stress tensor and $\underline{\underline{S}}$ is the deviatoric stress tensor given by

$$\underline{\underline{S}} = \left[\underline{\underline{\sigma}} - \left(\frac{1}{3} \right) tr(\underline{\underline{\sigma}}) \underline{\underline{1}} \right] \quad (6)$$

J is the von Mises equivalent stress. Y is an auxiliary variable related with the isotropic hardening. Noting the eigenvalues of $\underline{\underline{S}}$ by $\{S_1, S_2, S_3\}$, the elastic domain can be represented in the space of the principal directions of the deviatoric stress as a sphere centred at the origin with radius $R = \sqrt{2/3}Y$ (see Fig. 1).

p is usually called the accumulated plastic strain and \dot{p} can be interpreted as Lagrange multiplier associated to the constraint $F \leq 0$. Function F characterizes the elasticity domain and the plastic yielding surface. From eq. (2) it is possible to verify that

$$\dot{p} = \sqrt{\frac{2}{3} \underline{\underline{\dot{\epsilon}}^p : \underline{\underline{\dot{\epsilon}}^p}} \Rightarrow p(t) = p(t=0) + \int_{t=0}^t \left(\sqrt{\frac{2}{3} \underline{\underline{\dot{\epsilon}}^p(\zeta) : \underline{\underline{\dot{\epsilon}}^p(\zeta)}} \right) d\zeta \quad (7)$$

If $F < 0$, from the second relation in (4) it follows that $J < Y$. Hence, from relation $\dot{p}F = 0$, it is possible to conclude that $\dot{p} = 0$. If $\dot{p} \neq 0$, from condition $\dot{p}F = 0$ it comes that necessarily $F = 0$. Besides, from eqs. (2) and (3) it is possible to verify that, in this case $\underline{\underline{\dot{\epsilon}}^p} \neq \underline{\underline{0}}$ and $\dot{Y} \neq 0$. Therefore, the elasto-plastic material is characterized by an elastic domain in the stress space where yielding doesn't occur ($\dot{p} = \dot{Y} = 0$ if $F < 0$). Generally the following initial conditions are used for a "virgin" material

$$p(t = 0) = 0, \underline{\underline{\varepsilon}}^P(t = 0) = \underline{\underline{0}} \quad (8)$$

From now on, initial conditions (8) are assumed to hold in the analysis. It is also important to remark that the evolution law (2) with boundary condition (9) and definition (6) imply that the principal directions the stress tensor, of the deviatoric stress tensor and of the plastic strain tensor are the same. From evolution law (2) and considering initial conditions (8), it is possible to verify that the following relation always holds

$$\frac{S_i}{S_j} = \frac{\varepsilon_i^P}{\varepsilon_j^P} \quad \forall (i, j = 1, 2, \text{ or } 3) \quad (9)$$

With $S_i (i = 1, 2 \text{ or } 3)$ and $\varepsilon_i^P (i = 1, 2 \text{ or } 3)$ being the principal components (eigenvalues) respectively of $\underline{\underline{S}}$ and $\underline{\underline{\varepsilon}}^P$.

2.2 Thin-walled elasto-plastic cylinder under internal pressure

This section it is considered an elasto-plastic cylinder with internal radius r_i , thickness e submitted to an internal pressure P . The internal radius r_i and the thickness e are such that

$$\frac{r_i}{e} > 10 \quad (10)$$

The components of the stress tensor $\underline{\underline{\sigma}}$ in cylindrical coordinates for a thin-walled cylinder are classically approximated in the framework of membranes theory by the following expressions:

$$\underline{\underline{\sigma}} = \begin{bmatrix} \sigma_r & 0 & 0 \\ 0 & \sigma_\theta & 0 \\ 0 & 0 & \sigma_z \end{bmatrix} \quad \text{with } \sigma_r = 0; \quad \sigma_\theta = \frac{Pr_i}{e}; \quad \sigma_z = \begin{cases} 0, & \text{for open - ended cylinders} \\ \frac{Pr_i}{2e} = \frac{\sigma_\theta}{2}, & \text{for closed - ended cylinders} \end{cases} \quad (11)$$

σ_r is the radial stress component, σ_θ the circumferential stress component and σ_z the axial stress component. All other components are considered to be equal to zero. Since the circumferential and axial components are not independent in the case of closed-ended pipes ($\sigma_z = \sigma_\theta/2$), additional simplifications can be obtained. The trace of the stress tensor is then given by

$$\frac{1}{3}tr(\underline{\underline{\sigma}}) = \frac{1}{3}(\sigma_r + \sigma_\theta + \sigma_z) = \begin{cases} \frac{\sigma_\theta}{3}, & \text{for open - ended cylinders} \\ \frac{\sigma_\theta}{2}, & \text{for closed - ended cylinders} \end{cases} \quad (12)$$

Introducing eqs. (11), (12) in eq. (6), it is possible to conclude that the radial, circumferential and axial components S_r, S_θ, S_z of the deviatoric stress tensor $\underline{\underline{S}}$ are its only non-zero components: $S_r = (\sigma_r - \frac{\sigma_\theta}{3}) = -\frac{\sigma_\theta}{3}$; $S_\theta = (\sigma_\theta - \frac{\sigma_\theta}{3}) = \frac{2\sigma_\theta}{3}$, $S_z = (\sigma_z - \frac{\sigma_\theta}{3}) = -\frac{\sigma_\theta}{3}$ for open-ended cylinders and $S_r = 0 - \frac{\sigma_\theta}{2} = -\frac{\sigma_\theta}{2}$; $S_\theta = \sigma_\theta - \frac{\sigma_\theta}{2} = \frac{\sigma_\theta}{2}$; $S_z = \frac{\sigma_\theta}{2} - \frac{\sigma_\theta}{2} = 0$, for closed-ended cylinders. Hence

$$\underline{\underline{S}} = \underbrace{\begin{bmatrix} S_r = -\frac{1}{3}\sigma_\theta & 0 & 0 \\ 0 & S_\theta = \frac{2}{3}\sigma_\theta & 0 \\ 0 & 0 & S_z = -\frac{1}{3}\sigma_\theta \end{bmatrix}}_{\text{open-ended cylinders}}; \quad \underline{\underline{S}} = \underbrace{\begin{bmatrix} S_r = -\frac{\sigma_\theta}{2} & 0 & 0 \\ 0 & S_\theta = \frac{\sigma_\theta}{2} & 0 \\ 0 & 0 & S_z = 0 \end{bmatrix}}_{\text{closed-ended cylinders}} \quad (13)$$

It is important to observe that the principal components of the deviatoric stress and of the plastic deformation are not independent, what allows introducing additional simplifications in the equations. From eq. (9), it comes that

$$\frac{S_r}{S_\theta} = \frac{\varepsilon_r^p}{\varepsilon_\theta^p} \quad (14)$$

In particular, from eqs. (13) and (14), it is possible to verify that the following relations always hold

$$\varepsilon_r^p = \varepsilon_z^p = -\frac{1}{2}\varepsilon_\theta^p, \quad \text{for open-ended cylinders} \quad (15a)$$

$$\varepsilon_r^p = -\varepsilon_\theta^p, \quad \varepsilon_z^p = 0, \quad \text{for closed-ended cylinders} \quad (15b)$$

Therefore, using eq. (2) and the initial conditions (8), it is possible to conclude that the plastic strain tensor is given by

$$\underline{\underline{\varepsilon}}^p = \underbrace{\begin{bmatrix} \varepsilon_r^p = -\frac{1}{2}\varepsilon_\theta^p & 0 & 0 \\ 0 & \varepsilon_\theta^p & 0 \\ 0 & 0 & \varepsilon_z^p = -\frac{1}{2}\varepsilon_\theta^p \end{bmatrix}}_{\text{open-ended cylinders}}; \quad \underline{\underline{\varepsilon}}^p = \underbrace{\begin{bmatrix} \varepsilon_r^p = -\varepsilon_\theta^p & 0 & 0 \\ 0 & \varepsilon_\theta^p & 0 \\ 0 & 0 & \varepsilon_z^p = 0 \end{bmatrix}}_{\text{closed-ended cylinders}} \quad (16)$$

Using the definition (5) and eq. (13) it is possible to obtain the von Mises equivalent stress

$$J = |\sigma_\theta| = \frac{Pr_i}{e}; \quad \text{for open-ended cylinders} \quad (17a)$$

$$J = \frac{\sqrt{3}}{2} |\sigma_\theta| = \frac{\sqrt{3}}{2} \frac{Pr_i}{e}; \quad \text{for closed-ended cylinders} \quad (17b)$$

Introducing eqs (11), (16), (17) in (1) – (4), it is possible to obtain the following set of constitutive equations for thin-walled cylinders

$$(\varepsilon_\theta - \varepsilon_\theta^p) = \frac{1}{Ee} Pr_i, \quad \text{for open-ended cylinders} \quad (18a)$$

$$(\varepsilon_\theta - \varepsilon_\theta^p) = \frac{(2 - \nu)}{2Ee} Pr_i, \quad \text{for closed-ended cylinders} \quad (18b)$$

$$\dot{\varepsilon}_\theta^p = \dot{p}, \quad \text{for open-ended cylinders} \quad (19a)$$

$$\dot{\varepsilon}_\theta^p = \frac{\sqrt{3}}{2} \dot{p}, \quad \text{for closed-ended cylinders} \quad (19b)$$

$$\dot{p} \geq 0; \quad F \leq 0; \quad \dot{p}F = 0 \quad \text{with} \quad (20)$$

$$F = \frac{Pr_i}{e} - Y \leq 0, \quad \text{for open-ended cylinders} \quad (21a)$$

$$F = \frac{\sqrt{3} Pr_i}{2e} - Y \leq 0, \quad \text{for closed-ended cylinders} \quad (21b)$$

$$Y = \sigma_y + v_1[1 - \exp(-v_2 p)] \quad (22)$$

The set of equations (18), (19), (20), (21), (22) models the behaviour of an elasto-plastic cylinder (close-ended or open-ended). The radial and axial strains are not independent and can be obtained from the circumferential strains as follows

$$(\varepsilon_r + \frac{\varepsilon_\theta^p}{2}) = (\varepsilon_z + \frac{\varepsilon_\theta^p}{2}) = -\nu(\varepsilon_\theta - \varepsilon_\theta^p), \quad \text{for open-ended cylinders} \quad (23a)$$

$$(\varepsilon_r + \varepsilon_\theta^p) = -\frac{3\nu}{(2 - \nu)}(\varepsilon_\theta - \varepsilon_\theta^p); \quad \varepsilon_z = \frac{(1 - 2\nu)}{(2 - \nu)}(\varepsilon_\theta - \varepsilon_\theta^p), \quad \text{for closed-ended cylinders} \quad (23b)$$

For a monotonic loading (i.e. $P = \alpha t$, $\alpha > 0$), the behaviour of the cylinder is elastic ($\varepsilon_\theta^p = 0$) while $F \leq 0$. From condition $\dot{p}F = 0$ in (20), it is possible to conclude that $F = 0$ when $\dot{p} > 0$ (and hence when yielding occurs: $\dot{\varepsilon}_\theta^p > 0$). Using the definition of F in eqs. (21a) and (21b), it comes that

$$F = 0 \Rightarrow \frac{Pr_i}{e} - Y = 0 \Rightarrow P = \frac{e}{r_i} [\sigma_y + v_1[1 - \exp(-v_2 \varepsilon_\theta^p)]], \quad \text{for open-ended cylinders}$$

$$F = 0 \Rightarrow \frac{\sqrt{3} Pr_i}{2e} - Y = 0 \Rightarrow P = \frac{2e}{\sqrt{3} r_i} [\sigma_y + v_1[1 - \exp(-v_2 \varepsilon_\theta^p)]], \quad \text{for closed-ended cylinders}$$

As a consequence, since the load is monotonic, pressure P is related with the circumferential plastic strain component ε_θ^p by the following relation

$$P = \frac{e}{r_i} [\sigma_y + v_1[1 - \exp(-v_2 \varepsilon_\theta^p)]], \quad \text{if } \frac{Pr_i}{e} \geq \sigma_y \quad \text{for open-ended cylinders} \quad (24a)$$

$$P = \frac{2e}{\sqrt{3} r_i} [\sigma_y + v_1[1 - \exp(-v_2 \varepsilon_\theta^p)]], \quad \text{if } \frac{\sqrt{3} Pr_i}{2e} \geq \sigma_y \quad \text{for closed-ended cylinders} \quad (24b)$$

The yield pressure P_y is obtained taking $\varepsilon_\theta^p = 0$

$$P_y = \sigma_y \frac{e}{r_i}, \quad \text{for open-ended cylinders} \quad (25a)$$

$$P_y = \frac{2}{\sqrt{3}} \sigma_y \frac{e}{r_i}, \quad \text{for closed-ended cylinders} \quad (25b)$$

The rupture pressure is the maximum pressure P_{\max} is obtained taking the limit of P as $\varepsilon_\theta^p \rightarrow \infty$. Hence

$$\begin{aligned} P_{\max} &= \lim_{\varepsilon_\theta^p \rightarrow \infty} \left[\frac{e}{r_i} [\sigma_y + v_1 [1 - \exp(-v_2 \varepsilon_\theta^p)]] \right] =, \quad (\text{for open-ended cylinders}) \quad (26a) \\ &= \frac{e}{r_i} (\sigma_y + v_1) = \frac{e}{r_i} (\sigma_{\max}) \end{aligned}$$

$$\begin{aligned} P_{\max} &= \lim_{\varepsilon_\theta^p \rightarrow \infty} \left[\frac{2e}{\sqrt{3} r_i} [\sigma_y + v_1 [1 - \exp(-v_2 \varepsilon_\theta^p)]] \right] =, \quad (\text{for closed-ended cylinders}) \quad (26b) \\ &= \frac{2}{\sqrt{3}} \frac{e}{r_i} (\sigma_y + v_1) = \frac{2}{\sqrt{3}} \frac{e}{r_i} (\sigma_{\max}) \end{aligned}$$

It is possible to show [13] that $\sigma_{\max} = (\sigma_y + v_1)$ is the rupture stress obtained in a tensile test. Since $\sigma = [\sigma_y + v_1 [1 - \exp(-v_2 \varepsilon_\theta^p)]]$, if $\sigma \geq \sigma_y$ then

$$\sigma_{\max} = \lim_{\varepsilon_\theta^p \rightarrow \infty} [\sigma_y + v_1 [1 - \exp(-v_2 \varepsilon_\theta^p)]] = (\sigma_y + v_1) \quad (27)$$

Eqs. (25a), (25b) and (26a), (26b) show that, in order to determine both yield pressure and burst pressure for a given cylinder with internal radius r_i and wall thickness e (with $r_i \geq 10e$), it is only necessary to know the yield stress σ_y and the rupture stress σ_{\max} (also named the ultimate stress) obtained experimentally in a tensile test of the pipe material. Besides, eqs. (25a), (25b) and (26a), (26b) show that both the yield pressure and burst pressure in a close-ended cylinder are $\frac{2}{\sqrt{3}}$ times higher (1.155 times – 15.5 %) than in an open-ended cylinder.

Long straight thin-walled pipelines are reasonably modelled by the open-ended cylinder model. Hydrostatic specimens are better modelled by the closed-ended cylinder model. Hence, both yield pressure and burst pressure of a metallic specimen measured in a laboratory test tend to be higher than the ones of a long straight thin-walled pipeline with same material, diameter and wall thickness. This means that the results of burst tests may be used with care since they may lead to an overestimation of the strength of a real line.

3 Modelling the effect of small temperature variations of the water in long-term hydrostatic tests

The rehabilitation of corroded pipelines with epoxy repair systems is becoming a well accepted engineering practice and an interesting alternative to the classical repair methods for metallic pipes, mainly in the oil industry, saving time and allowing safer operations.

In these repair systems, a piping or vessel segment is reinforced by wrapping it with concentric coils of composite material after the application of epoxy filler in the corrosion defect. Corroded pipelines with through-walls defects can also be repaired with different epoxy systems (see [1], for instance). In this case, the challenge is to assure a satisfactory level of structural integrity and to assure that the pipe won't leak after repair.

In the case of through-walls corrosion defects in produced water pipelines used in offshore oil exploitation, the water temperature is a major shortcoming for the use of polymeric material as repair systems. In this case, it is usual to perform long-term hydrostatic tests (between 1000 to 2000 hours) with constant internal pressure and temperature (between 60 °C to 90 °C) to check the repair effectiveness to avoid leaking.

Long-term hydrostatic tests at this temperature range (between 60 °C to 90 °C) may be performed whether using a pool with hot water in which the specimen is immersed or a system especially designed for this procedure (see [1]) in which the whole system (including the electrical resistance) is threaded at one extremity of the specimen.

No matter the long-term hydrostatic test apparatus adopted, to accurately control temperature without extensive operator involvement, a temperature control system relies upon a controller, which accepts a temperature sensor such as a thermocouple or RTD as input. It compares the actual temperature to the desired control temperature, or set point, and provides an output to a control element. The controller is one part of the entire control system, and the whole system should be analyzed in selecting the proper controller. There are a few different types of controllers but the simplest and most usual in this kind of testing is the "on-off" controller. Generally the temperature oscillations are small compared to the control temperature (set point). Nevertheless, in a closed vessel with liquid water at high pressure, a small variation of the temperature above the desired control temperature may cause a huge pressure variation. In the case of a long-term test in a damaged pipe repaired with an epoxy system, very small variations of temperature due to the control systems may cause a pressure peak leading to failure. Generally this kind of the pressure peak is very fast and eventually is not recorded, what may cause mistaken conclusions about the durability of the epoxy repair system. The failure of the repair may be caused by pressure variation and not because of the temperature effect on the polymer behaviour.

3.1 Summary of the equation of state for liquid water at high pressures

The goal of this section is to present an equation of state for liquid water at high pressures. The proposed equation is a generalization of Tait equation of state to include very small temperature variations. Tait equation of state for compressible liquids (or called the Murnaghan equation of state in the context of an elastic solid [4, 6]) models a liquid such as water as a compressible, barotropic liquid whose bulk modulus is an affine function of pressure. Hence, this equation of state involves only the density and pressure variables. However, it is a highly non-linear equation of the form

$$P = (P_o + B) \left(\frac{\rho}{\rho_o} \right)^\gamma - B \Rightarrow \rho = \rho_o \left[\frac{P + B}{P_o + B} \right]^{(1/\gamma)} \quad (28)$$

where P and ρ denote the pressure and the density, respectively. P_o and ρ_o are the pressure and density at a reference state. B and γ are positive parameters.

Two alternative constitutive equations are suggested to extend the state law (28) in order to account very small temperature variations from a reference temperature θ_o

$$\frac{\rho}{\rho_o} = \left[\frac{P+B}{P_o+B} \right]^{(1/\gamma)} [1 - \eta(\theta - \theta_o)] \Rightarrow P = (P_o + B) \left(\frac{\rho}{\rho_o} [1 - \eta(\theta - \theta_o)]^{-1} \right)^\gamma - B \quad (29a)$$

or

$$\frac{\rho}{\rho_o} = \left[\frac{P+B}{P_o+B} \right]^{(1/\gamma)} - \eta(\theta - \theta_o) \Rightarrow P = (P_o + B) \left(\frac{\rho}{\rho_o} + \eta(\theta - \theta_o) \right)^\gamma - B \quad (29b)$$

With η being a positive pressure dependent parameter.

4 Results and discussion

4.1 Burst tests

This section aims at comparing the model prediction of the burst pressure of close-ended cylindrical pressure vessels with some experimental results. The following expression to compute the burst pressure is found at the ASME Boiler and Pressure Vessel Code [3]

$$P_{\max} = \frac{\omega e}{r_i + 0.6e} (\sigma_{\max}) \quad (30)$$

Where σ_{\max} is the rupture stress obtained in a tensile test; ω ($0 < \omega \leq 1$) is the efficiency of the welded joint = 1 (for seamless pipe); r_i is the internal radius (in) and e the wall thickness (in). From now on, the burst pressure of a specimen will be approximated by using two different approaches: (i) multiply the rupture stress obtained in tensile test by a factor $\frac{\omega e}{r_i + 0.6e}$ (ASME standard) or (ii) multiply the rupture stress obtained in tensile test by a factor $\frac{2\omega e}{r_i \sqrt{3}}$ (elasto-plasticity model).

Hydrostatic tests performed by Loureiro in [14] in seamless pipes were chosen as a preliminary step to evaluate the adequacy of the model prediction of the burst pressure. The internal radius and wall thickness of the pipe were, respectively, $r_i = 2.52''$ (64.01 mm) and $e = 0.258''$ (6.55 mm) and pipe material was an aluminium alloy SB – 241 6063 –T5 whose composition is shown in table 1

Table 1: Aluminium alloy chemical composition [14].

Al	Si	Fe	Cu	Mn	Mg	Zn	Ti
98.83	0.41	0.07	0.003	0.004	0.19	0.006	0.003

The average value for σ_{\max} was 25762 psi (177.62 MPa), obtained after 5 tensile tests performed according to ASTM B557 standard [15]. In these burst tests, pressure was gradually raised until rupture. Table 2 presents the experimental and predicted burst pressures. The burst pressure for this seamless pipe predicted using ASME standard eq (26) is $\approx 82.5\%$ of the pressure measured experimentally (respectively 17.13 MPa and 20.76 MPa). The burst pressure predicted using the elasto-plasticity model was 20.99 MPa ($\approx 1.0\%$ above than experimental). The ASME code prediction is more conservative, while the elasto-plastic theory result is closer to reality. Predictions using expression provided by the ASME code are more adequate for long lines which can be modelled as open-ended pipes. In the case of closed-ended pipes, the estimate burst pressure from ASME code and from elasto-plasticity can be used respectively as lower and upper limits for designers.

Table 2: Predicted burst pressures.

Experimental burst pressure [13]	3011 psi (20.76 MPa)
ASME burst pressure prediction	2485 psi (17.13 MPa)
Model burst pressure prediction	3044 psi (20.99 MPa)

Burst tests of rocket motor cases made performed by Beena et al [11] were also used to check the adequacy of the model prediction. The internal radius wall thickness of the pipe were $r_i = 103.3$ mm and $e = 2.6$ mm and pipe material was a 15CDV6 steel with $\sigma_{\max} = 1010.0$ MPa. The name 15CDV6 is a French designation in which the first number is equal to 100 times the concentration of carbon. The letters which follow indicate the other elements present, in the decreasing order of concentration. The last digit is equal to four times the concentration of chromium. In this French notation, C stands for chromium, D for molybdenum, and V for vanadium. It therefore follows that, in 15CDV6 steel, the concentration of carbon is 0.15%, while that of chromium is 1.5%, and the concentrations of molybdenum and vanadium are less than 1.5% each. Hence, it is a low-alloy steel, in which the proportion by weight of all the alloying elements combined is less than 5%.

The experimental burst pressures obtained in two tests were 28.86 MPa and 29.23 MPa (average 29.05 MPa). The burst pressure predicted using eq. (28) is 25.48 MPa. The predicted burst pressure using the elasto-plasticity model is 29.39 MPa (1.15 times the ASME standard) which is in good agreement with the two burst test results of the rocket motor cases. The experimental 0.2% yield stress measured in a tensile test was 915.27 MPa. The experimental yield pressure was 26.49 MPa. The predicted yield pressure using the elasto-plasticity theory is 26.63 MPa.

As it can be verified, once again ASME predictions of the burst pressures are closer to the ones obtained using the elasto-plasticity theory for open-ended pipes (the burst pressure for a close-ended pipe is 15.5% times higher than in an open-ended pipe). Therefore ASME predictions are more adequate for long lines that can better be modelled as open-ended cylinders.

In the results presented in table 3 it was adopted and efficiency $\omega = 1$, but the cases are not seamless pipes and the authors in [11] affirm that the weld efficiency is 93.5-98% ($0.935 \leq \omega \leq 0.98$). With this

correction, the burst pressure predicted using the elasto-plastic model is even closer than the obtained experimentally.

Table 3: Predicted burst pressures.

Experimental burst pressure [11]	29.05 MPa
ASME burst pressure prediction	25.48 MPa
Model burst pressure prediction	29.39 MPa

Finally, results of burst tests in maraging steel rocket motor cases performed in [16] and presented in [12] were considered. The internal radius of the pipe was $r_i = 45$ mm and the maximum strength $\sigma_{\max} = 2155$ MPa. The tests results for 5 different values of the wall thickness are presented in table 4 (each column corresponds to a different test)

Table 4: Predicted burst pressures for different values of the wall thickness.

Wall thickness (mm)	1.630	1.735	1.756	1.763	1.793
Experimental burst pressure (MPa) [12]	86.62	92.30	94.50	94.00	94.00
ASME burst pressure prediction (MPa)	76.72	81.28	82.23	82.56	83.93
Model burst pressure prediction (MPa)	90.13	95.94	97.10	97.49	99.14

The difference between the predicted results from elasto-plasticity theory and experimental is higher. However it is important to explain that the steel pipes used to perform those tests were not seamless and the efficiency ω of the welded joint is lower than 1. In this specific case it is recommended, in analogy with the ASME code, a correction factor due to the welded joint

$$P_{\max} = \frac{2\omega e}{r_i \sqrt{3}} (\sigma_{\max}) \quad (31)$$

In the previous case this factor would be approximately $\omega = 0.96$ (efficiency of 96%).

4.2 Long-term hydrostatic tests

Long-term hydrostatic tests were performed with a constant internal pressure $P_o = 1500$ psi (≈ 10.34 MPa) at 80°C. An experimental set up was conceived to check the effectiveness of the methodology, trying to approximate a real repair operation. 2" (50.8 mm) diameter schedule 80 API 5L grade B steel pipes, normally used in offshore platform for produced water, with a circular hole of 10 mm were used to build the specimens for hydrostatic tests. The epoxy repair system is described in details in

[1]. A commercial fast curing polymer-based system (called System II in [1]) consisting of a mixture of epoxy resin and aluminium powder was used to perform the repair of the through-thickness damage in each specimen. The whole system to control water temperature (including the electrical resistance) is threaded at one extremity of the specimen. Fig. 2 and 3 shows the basic set-up apparatus and temperature control system. The control system allows a ± 1 °C temperature variation.

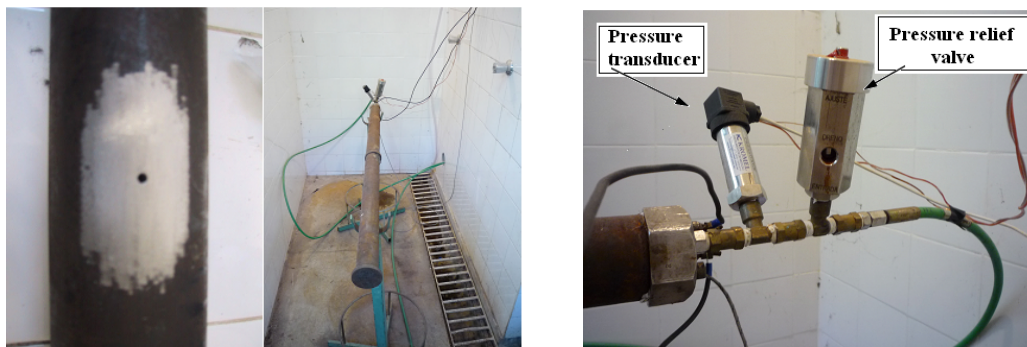


Figure 2: Basic test set-up apparatus.

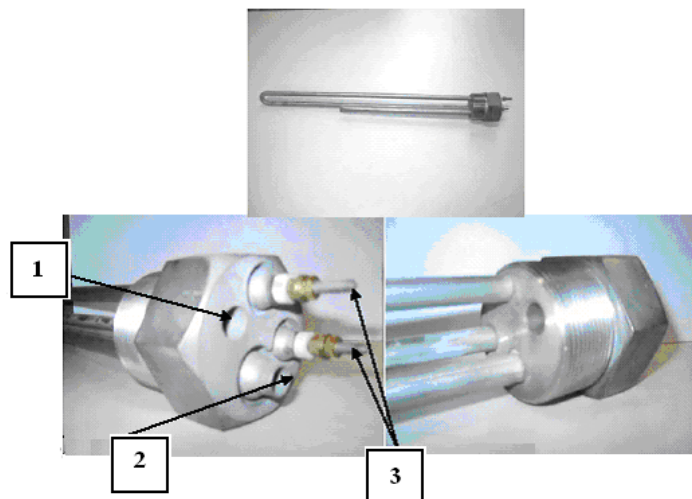


Figure 3: Temperature control system. 1 is the pressure water machine connection, 2 is the temperature control thermostat and 3 is the electrical resistance.

Fig 4 shows a curve pressure versus time in a typical test without an automatic system that relieves liquid pressure above a pre-set limit (a pressure relief valve). It can be verified peaks of pressure even with such a limited temperature variation. Rupture has occurred after 6 days, when a pressure peak much above the static strength of the repair occurred. The pressure peaks can be explained using constitutive eqs (29a) or (29b) that are proposed for small variations of temperature of liquid water at high pressures. Considering the initial state: $P_o = 1054604 \text{ Kg.m}^{-2}$ ($\approx 1500 \text{ psi} \approx 10.34 \text{ MPa}$); $\rho_o = 958 \text{ Kg.m}^{-3}$; $\theta_o = 353.15 \text{ K}$, a reasonable approximation for the parameters B and γ that appear in Tait equation [15] is $B = 2.9 \times 10^8 \text{ Kg.m}^{-1}.\text{s}^{-2}$ and $\gamma = 7.15$. In order to identify the additional parameter η that appears in eqs (29a) and (29b) it is interesting to observe Fig. 5, that shows how density varies with pressure for a constant pressure of 1 atm ($\approx 0.1 \text{ MPa}$).

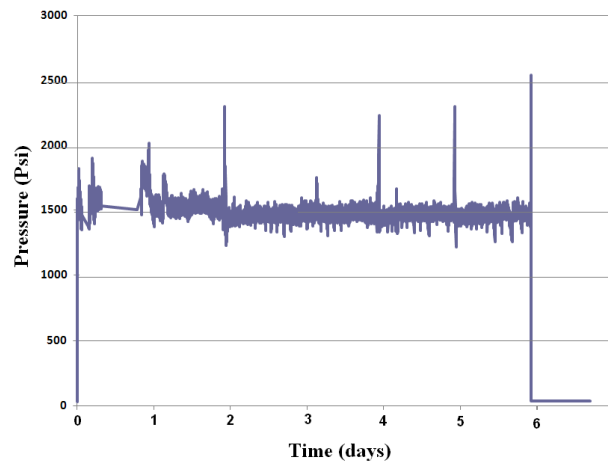


Figure 4: Typical pressure versus time curve at average pressure of 1500 psi ($\approx 10.34 \text{ MPa}$) and temperature of $80 \text{ }^\circ\text{C}$. The temperature control system allows a $\pm 1 \text{ }^\circ\text{C}$ variation. Test performed without a pressure relief valve.

Although curve $\rho \times \theta$ shown in Fig. 5 presents a non-linear behaviour, it can be approximated by a linear function in the neighbourhood of the reference temperature θ_o (see Fig. 6). η is a pressure dependent parameter. Nevertheless, from Fig. 6, assuming small temperature variations from the reference temperature θ_o it is reasonable to assume a constant value $\eta = 6.5 \times 10^{-4} \text{ K}^{-1}$.

In the case of a vessel without a pressure relief valve, the density ρ tends to increase when a higher pressure is applied: $\left(\frac{\rho}{\rho_o}\right) > 1$. Table 5 presents the pressure variation obtained using eqs. (29a) and (29b), the material parameters presented in Table 6 and assuming $\left(\frac{\rho}{\rho_o}\right) \approx 1$. The pressure predicted using eqs. (29a) and (29b) are very close, what means that, for a very small temperature variation from the reference temperature, it is almost indifferent to consider any of them. For very small temperature variation, the pressure variation $(P - P_o)$ increases almost linearly with $(\theta - \theta_o)$ as shown in Fig. 7.

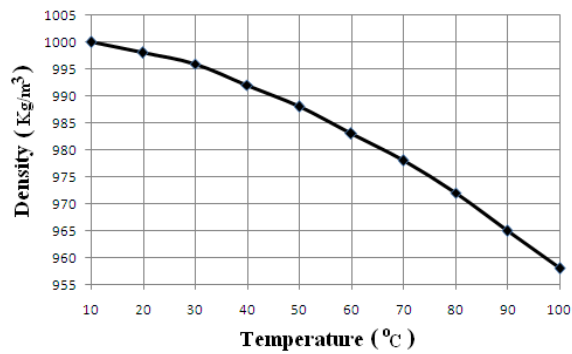


Figure 5: Curve $\rho \times \theta$. Water at a constant pressure of 1 atm.

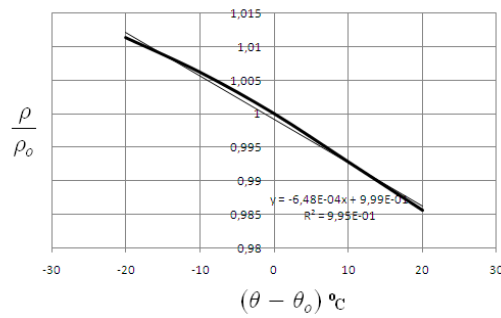


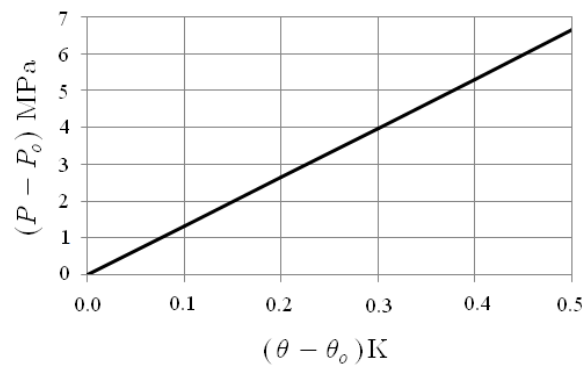
Figure 6: Detail of the curve $\rho \times \theta$ presented in Fig. 5. $\theta_0 = 80 \text{ }^\circ\text{C}$.

Table 5: Pressure variation with temperature from the reference state, using eqs (29).

Temperature °C	Pressure Eq. (29a)	Pressure Eq.(29b)
80.0	1500.00 psi (10.34 MPa)	1500.00 psi (10.34 MPa)
80.5	2463.25 psi (16.98 MPa)	2462.94 psi (16.98 MPa)
81.0	3429.06 psi (23.64 MPa)	3427.81 psi (23.63 MPa)

Table 6: Water. Material parameters.

B (Kg.m ⁻¹ .s ⁻²)	γ	η (K ⁻¹)
2.9×10^8	7.15	6.5×10^{-4}

Figure 7: Curve $(P - P_o) \times (\theta - \theta_o)$ obtained using eq. (28.1).

The mean failure pressure measured in hydrostatic tests in which a monotonically increasing load is applied until the failure of the repair is $P_f = 1465$ psi (≈ 17 MPa). As it can be verified in the test shown in Fig. 4, the internal pressure in the specimen reached the limit pressure P_r due to the temperature oscillation admitted by the control system (always smaller than 1 °C). Therefore, the prediction of a strong pressure variation made in table 5 is confirmed experimentally what indicates that a very small temperature variation (around 0.5 °C) can eventually lead the repair to failure and that the use of a pressure relief valve is essential in order to avoid big pressure oscillations during the testing. All specimens repaired with the same epoxy system and tested under the same pressure and temperature conditions (5 specimens) but using the relief valve did not fail after 2000 hours.

5 Concluding remarks

Hydrostatic tests are normally conducted under industry and/or customer requirements or specifications. They are usually performed taking as specimen cylindrical vessels closed at the ends and are often used to assess information about the mechanical strength of a given pipeline (or about the effectiveness of a given repair or reinforcement system in a damaged pipeline). The material, diameter and wall thickness of the specimen are normally the same than the pipeline. The cylinder is closed at the extremities using a welded cap or a bolted pressure flange. Nevertheless, since the real pipeline is not a closed cylinder, mistaken conclusions can be made if the perturbation caused by the closed ends

of the specimen is not taken into account.

The present paper uses elasto-plastic constitutive equations and also a thermodynamic framework to correct special hydrostatic tests developed for analysing the structural integrity of produced water pipelines used in offshore oil exploitation and to propose adequate test procedures to eventually “correct” the perturbation caused by the closed ends of the specimen on experimental results. The proposed theory allows a better understanding the differences between the strength of specimens used in hydrostatic tests (better modelled as closed-ended cylinders) and of long pipelines (better modelled as open-ended cylinders).

An interesting result is that burst and yield pressure in a pipe can be predicted through the knowledge of the one-dimensional stress-strain curve and both burst pressure and yield pressures measured in a typical hydrostatic test specimen are about $\frac{2}{\sqrt{3}}$ times higher (15.5%) than the burst and yield pressure of a long line.

It is also important to remark that wrong conclusions can be made if a pressure relief valve is not used in long-term hydrostatic tests performed at temperatures between 60 °C and 90 °C. In these cases, no matter the long-term hydrostatic test apparatus adopted, the temperature control system relies upon a controller, which accepts a temperature sensor that compares the actual temperature to the desired control temperature, or set point, and provides an output to a control element. It is shown both experimentally and theoretically that, without a pressure relief valve, a small variation of temperature above the desired control temperature may cause a huge pressure variation in a closed vessel with liquid water at high pressure. In the case of a long-term test in a damaged pipe repaired with an epoxy system, very small variations of temperature due to the control systems cause a pressure variation that may lead the repair to failure. Generally this kind of the pressure peak is very fast and eventually is not recorded, what may cause mistaken conclusions about the durability of the epoxy repair system.

References

- [1] da Costa Mattos, H., Reis, J., Perrut, V. & Sampaio, R., An alternative methodology to repair localized corrosion damage in metallic pipelines with epoxy resins. *Materials and Design*, **30**, pp. 3581–3591, 2009.
- [2] Veil, J., Puder, M., Elcock, D. & Redweik Jr., R., White paper describing produced water from production of crude oil, natural gas, and coal bed methane. Technical report, Argonne National Laboratory, Argonne, Illinois, 2004. U.S. Department of Energy, National Energy Technology Laboratory, http://www.evs.anl.gov/pub/dsp_detail.cfm?PubID=1715.
- [3] *ASME Boiler and Pressure Vessel Code – Section VII – Division 1*, 1992. Ed. 1995 addenda.
- [4] Murnaghan, F., *Finite Deformation of an Elastic Solid*. Wiley: New York, 1951.
- [5] Shyue, K., A fluid-mixture type algorithm for barotropic two-fluid flow problems. *Journal of Computational Physics*, **200**, pp. 718–748, 2004.
- [6] Farhat, C., Rallu, A. & Shankaran, S., A higher-order generalized ghost fluid method for the poor for the three-dimensional two-phase flow computation of underwater explosions and implosions. *Journal of Computational Physics*, **227**, pp. 7674–7700, 2008.
- [7] Durban, D., Large strain solution for pressurized elasto-plastic tubes. *Trans ASME J Appl Mech*, **46**, pp. 228–30, 1979.

- [8] Durban, D., A finite strain axially symmetric solution for elastic tubes. *Int J Solids Struct*, **24**, pp. 675–82, 1988.
- [9] Durban, D. & Kubi, M., A general solution for the pressurized elasto-plastic tube. *Trans ASME J Appl Mech*, **59**, pp. 20–6, 1992.
- [10] Law, M. & Bowie, G., Prediction of failure strain and burst pressure in high yield-to-tensile strength ratio linepipe. *Int J Pres Ves & Piping*, **84**, pp. 487–492, 2007.
- [11] Beena, A., Sundaresan, M. & Nageswara Rao, B., Destructive stress of 15cdv6 steel rocket motor cases and their application to lightweight design. *Int J Pres Ves & Piping*, **62(3)**, pp. 313–320, 1995.
- [12] Subhananda Rao, A., Venkata Rao, G. & Nageswara Rao, B., Effect of long-seam mismatch on the burst pressure of maraging steel rocket motor cases. *Engineering Failure Analysis*, **12(2)**, pp. 325–336, 2005.
- [13] da Costa Mattos, H. & Soares Filho, P., Approximate local elasto-plastic solution for notched plates undergoing cyclic tensile loading. *Materials and Design*, **31**, pp. 4336–4347, 2010.
- [14] Loureiro, S., *Reinforcement of cylindrical pressure vessels using polymeric composites*. Master's thesis, COPPE - Universidade Federal do Rio de Janeiro, 1999. (in Portuguese).
- [15] *ASTM Standart B557. Standard test methods for tension testing wrought and cast aluminum- and magnesium-alloy products*.
- [16] Margetson, J., Burst pressure predictions of rocket motors. *AIAA/SAE 14th Joint Propulsion Conference Las Vegas, NV USA*, 1978. AIAA Paper No.78-1567.

A finite displacement visco-hypoelasticity model

Hilbeth Parente Azikri de Deus

Department of Mechanical Engineering, Federal University of Technology –

UTFPR,

Nucleus of Applied and Theoretical Mechanics – NuMAT, Campus Curitiba,

Avenida Sete de Setembro, 3165, 80230-901, Curitiba, PR – Brazil

Marcelo Krajnc Alves

Department of Mechanical Engineering, Federal University of Santa Catarina –

UFSC,

Trindade Campus, CP 476, 88010-970, Florianopolis, SC – Brazil

Abstract

The objective of the work is to propose a dual visco-hypoelasticity model and a numerical procedure for the analysis of Polymeric materials subjected to large displacements and rotations. In the proposed dual approach, the Hencky's logarithm strain measure is a function of the rotated Kirchhoff stress history in terms of a convolution equation. The material is assumed to be isotropic and the kernel functions, associated with the shear and bulk compliance moduli, are represented in Prony series. The problem is formulated within a Total Lagrangian framework and employs the Galerkin finite element method in the discretization process. Finally some numerical examples are presented in order to attest the proposed model and to verify the robustness and performance of the proposed numerical scheme.

Keywords: dual visco-hypoelasticity model, total lagragian, finite element.

1 Introduction

Viscoelastic behavior is typical of a number of materials such as polymers and plastics. These materials have memory, i.e., the stress depends on the entire history of the deformation and typically this memory fades with time. In a dual formulation the strain can be represented as a functional of the stress history. This hereditary constitutive equation, in order to be consistent, must satisfy the principle of material frame indifference. This requirement leads to reasonably complex relations, even in the “*simplest*” of constitutive relations.

The objective of this paper is to propose a dual finite visco-hypoelastic model based on the logarithm Hencky strain and the rotated Kirchhoff stress measures, which may be employed in the viscoelastic analysis of components undergoing large displacement and rotations. This paper is a continuation

of the work presented in [1] where we present the fully implicit algorithm in detail and derive the consistent tangent operator associated with the proposed implicit scheme.

1.1 Linear visco-hypoelastic constitutive model

Let's consider, initially, linear viscoelastic materials. These materials have memory, i.e., the stress depends on the entire history of the motion, and typically this memory fades with time. There are a number of approaches for constructing constitutive models describing the viscoelastic behavior of materials. Mathematical relations which describes how stress can depend on the history of the deformation are either given in integral form or in differential form. In integral form the stress at time t is given in terms of an expression which involves an integral over previous times. The integral in such an expression is known as a history integral. In contrast, in the differential form of constitutive model, the history of the deformation is taken into account by certain ordinary differential equations which describe how certain quantities known as internal variables evolve in time. For a more detailed presentation of both ways of representing viscoelastic constitutive responses see, [2-5].

To describe the linear viscoelastic response of components, one applies the Boltzmann superposition principle, which follows by that in each strain step the stress evolution is given by Hooke's law. In this sense, the evolution in each strain step component is approximated with a piecewise continuous step function. For sufficiently smooth fields, the general linear constitutive equation for the linear viscoelastic (small deformation) solid is given by

$$\sigma(\mathbf{x}, t) = D(t) \varepsilon(\mathbf{x}, 0) + \int_0^t \mathbf{D}(t-s) \varepsilon(\dot{\mathbf{u}}(\mathbf{x}, s)) ds. \quad (1)$$

Considering now a viscoelastic isotropic material

$$\mathbf{D} = 2 G \mathbf{II}_{dev} + K (\mathbf{I} \otimes \mathbf{I}) \quad (2)$$

in which $\mathbf{II}_{dev} = \{\mathbf{II}_S - \frac{1}{3}(\mathbf{I} \otimes \mathbf{I})\}$, $(\mathbf{II}_S)_{ijkl} = \frac{1}{2}(\delta_{ik}\delta_{jl} + \delta_{il}\delta_{jk})$ and \mathbf{I} is the identity tensor.

The kernel functions are represented in terms of Prony series and given by:

$$G(t) = G_\infty + \sum_{i=1}^{n_G} G_i \exp\left(-\frac{t}{\tau_i^G}\right) \quad \text{and} \quad K(t) = K_\infty + \sum_{i=1}^{n_K} K_i \exp\left(-\frac{t}{\tau_i^K}\right) \quad (3)$$

in which G_∞ and G_i are shear elastic moduli, K_∞ and K_i are bulk elastic moduli and τ_i^G and τ_i^K are the relaxation times for each Prony component.

An alternative formulation for the quasi-static rate model is the constitutive equation given, see [6], as

$$\varepsilon(t) = \mathbf{C}(t-t_0)\sigma(t_0) + \int_{t_0}^t \mathbf{C}(t-\xi)\dot{\sigma}(\xi)d\xi \quad (4)$$

where

$$\mathbf{C} = \frac{B}{9}(\mathbf{I} \otimes \mathbf{I}) + \frac{J}{2}\mathbf{II}_{dev}. \quad (5)$$

The kernel functions are also represented in terms of Prony series [7], as follows:

$$J(\xi) = J_0 + \sum_{i=1}^{n_j} J_i \left(1 - \exp\left(-\frac{\xi}{\tau_i^J}\right)\right) \quad \text{and} \quad B(\xi) = B_0 + \sum_{i=1}^{n_B} B_i \left(1 - \exp\left(-\frac{\xi}{\tau_i^B}\right)\right) \quad (6)$$

in which J_0 and J_i are shear compliance moduli, B_0 and B_i are bulk compliance moduli and τ_i^J and τ_i^B are the relaxation times for each Prony component.

The objective of this paper is to extend the alternative formulation to large displacement and rotation problems, defined in a Total Lagrangian framework. The motivation of using the total Lagrangian description is due to its adequacy for the consideration of reinforced plastics resulting in anisotropic viscoelastic responses.

In order to preserve objectivity of the integration process, in the hereditary constitutive equation, one employs adequate stress and strain measures, defined here at the unrotated configuration of the body, as will be properly defined. Here, one proposes a consistent extended hereditary constitutive equation and develop an implicit algorithm, using the Galerkin Finite Element method, for the solution of viscoelastic problems subjected to large displacements and rotations. The determination of the consistent tangent operator, associated with the proposed implicit method, is also presented together with the validation of the numerical scheme and proposed model.

2 Finite visco-hypoelasticity model

2.1 Motion and deformation of a body B

Let P_a be a particle of B that occupies a position \mathbf{x}_o in the reference configuration Ω_o . The motion of a body B is described by the position vector $\mathbf{x} = \varphi(\mathbf{x}_o, t)$ of the point \mathbf{x}_o , occupied by each particle P_a of B, at each time instant t .

$$\mathbf{x} = \varphi(\mathbf{x}_o, t) = \varphi_t(\mathbf{x}_o) \quad \text{and} \quad \mathbf{x}_o = \varphi_t^{-1}(\mathbf{x}). \quad (7)$$

The gradient of the deformation function is given as $\mathbf{F}(\mathbf{x}_o, t) = \nabla \varphi_t(\mathbf{x}_o)$, whose polar decomposition is given by $\mathbf{F} = \mathbf{R}\mathbf{U}$. The displacement field is defined as

$$\mathbf{u}(\mathbf{x}_o, t) = \mathbf{x} - \mathbf{x}_o = \varphi_t(\mathbf{x}_o) - \mathbf{x}_o. \quad (8)$$

The gradient of the displacement field, $\nabla \mathbf{u} = \nabla \mathbf{x} - \nabla \mathbf{x}_o$, leads to $\mathbf{F} = \nabla \mathbf{u} + \mathbf{I}$.

2.2 Weak formulation of the problem: Reference configuration

Let Ω_o , defined at t_o , be a bounded domain with a Lipschitz boundary $\partial\Omega_o$ subjected to a prescribed body force \mathbf{b} , a prescribed surface traction \mathbf{t}_o defined on Γ_o^t and a prescribed displacement defined on Γ_o^u , where $\partial\Omega_o = \Gamma_o^u \cup \Gamma_o^t$ with $\Gamma_o^u \cap \Gamma_o^t = \emptyset$. The weak formulation of the problem, may be stated as: Determine $\mathbf{u}(x_o, t) \in \text{Kin}_o^u$, for each $t \in [0, t_f]$, such that

$$\mathfrak{S}(\mathbf{u}; \hat{\mathbf{v}}) = \int_{\Omega_o} \mathbf{P} \cdot \nabla \hat{\mathbf{v}} d\Omega_o - \int_{\Omega_o} \rho_o \mathbf{b} \cdot \hat{\mathbf{v}} d\Omega_o - \int_{\Gamma_o^t} \mathbf{t}_o \cdot \hat{\mathbf{v}} d\Omega_o = 0 \quad \forall \hat{\mathbf{v}} \in Var_o^u. \quad (9)$$

Here, ρ_o is the density at the reference configuration, \mathbf{P} is the first Piola-Kirchhoff stress tensor, $\mathbf{P} = J\sigma\mathbf{F}^{-T} = \tau\mathbf{F}^{-T}$, with $J = \det[\mathbf{F}]$, σ is the Cauchy stress and τ the Kirchhoff stress tensor.

2.3 Work conjugation and stress measures

According to Hill, a stress-strain pair, $(\boldsymbol{\Sigma}, \gamma)$, defined at the reference configuration, is conjugate if the rate of stress work per unit of mass is invariant, i.e.,

$$\dot{W} = \frac{1}{\rho} (\sigma \cdot \mathbf{D}) = \frac{1}{\rho_o} (\boldsymbol{\Sigma} \cdot \dot{\gamma}). \quad (10)$$

where ρ is the current mass density, with $J\rho = \rho_o$. Moreover, see [1, 8], one has

$$\dot{W} = \frac{1}{\rho_o} (\boldsymbol{\Sigma} \cdot \dot{\gamma}) = \frac{1}{\rho_o} (\tau \cdot \mathbf{D}) = \frac{1}{\rho_o} (\mathbf{P} \cdot \dot{\mathbf{F}}) = \frac{1}{\rho_o} (\bar{\boldsymbol{\tau}} \cdot \dot{\mathbf{E}}), \quad (11)$$

in which \mathbf{D} is the symmetric part of \mathbf{L} , $\mathbf{L} = \dot{\mathbf{F}}\mathbf{F}^{-1}$, $\bar{\boldsymbol{\tau}}$ is the rotated Kirchhoff stress tensor, given by $\bar{\boldsymbol{\tau}} = \mathbf{R}^T \boldsymbol{\tau} \mathbf{R}$ and \mathbf{E} is the Hencky's logarithm strain measure, $\mathbf{E} = \ln(\mathbf{U})$.

2.4 Rotational-neutralized form of the constitutive model

Let us define the rotation tensor $\boldsymbol{\Lambda}(t)$, as the solution to the following initial value problem: Given $\boldsymbol{\Omega}(t)$, Find $\boldsymbol{\Lambda}(t)$ that solves

$$\dot{\boldsymbol{\Lambda}}(t) = \boldsymbol{\Omega}(t) \boldsymbol{\Lambda}(t). \quad (12)$$

with $\boldsymbol{\Lambda}(0) = \mathbf{I}$. Considering here, $\boldsymbol{\Omega} = \dot{\mathbf{R}}\mathbf{R}^T$, where \mathbf{R} is determined from the polar decomposition of \mathbf{F} , $\mathbf{F} = \mathbf{R}\mathbf{U}$, one derives by inspection that $\boldsymbol{\Lambda}(t) = \mathbf{R}(t)$.

Definition Here, one defines the pull back transformation of \mathbf{v} , \mathbf{A} , and \mathbf{B} as

$$\begin{aligned} \bar{\mathbf{v}}(t) &= \boldsymbol{\Lambda}(t)^T \mathbf{v}(t), \\ \bar{\mathbf{A}}(t) &= \boldsymbol{\Lambda}(t)^T \mathbf{A}(t) \boldsymbol{\Lambda}(t), \\ \bar{\mathbf{B}}(t) &= \boldsymbol{\Lambda}(t)^T \boldsymbol{\Lambda}(t)^T \mathbf{B}(t) \boldsymbol{\Lambda}(t) \boldsymbol{\Lambda}(t). \end{aligned} \quad (13)$$

From continuum mechanics, one has $\bar{\mathbf{F}}(t) = \boldsymbol{\Lambda}(t)^T \mathbf{F}(t)$ and $\bar{\mathbf{D}}(t) = \boldsymbol{\Lambda}(t)^T \mathbf{D}(t) \boldsymbol{\Lambda}(t)$. These pull back (rotation neutralized) quantities with $\boldsymbol{\Lambda}(t)$ are used to define a convenient framework in which the integration of the constitutive model is performed.

By applying the pull back operator to the conjugate stress-strain pair, $(\boldsymbol{\Sigma}, \gamma)$, one may extend the hereditary constitutive equation as

$$\bar{\gamma}(t) = \bar{\mathbf{C}}(t)\bar{\boldsymbol{\Sigma}}(0) + \int_0^t \bar{\mathbf{C}}(t-\xi) \dot{\bar{\boldsymbol{\Sigma}}}(\xi) d\xi, \quad (14)$$

in which $\bar{\boldsymbol{\Sigma}}(t) = \boldsymbol{\Lambda}(t)^T \boldsymbol{\Sigma}(t) \boldsymbol{\Lambda}(t)$ and $\bar{\gamma}(t) = \boldsymbol{\Lambda}(t)^T \gamma(t) \boldsymbol{\Lambda}(t)$.

In the particular case where $\boldsymbol{\Lambda}(t) = \mathbf{R}(t)$ the pull back of the Kirchhoff stress leads to the rotated Kirchhoff stress, defined as $\bar{\tau}(t) = \mathbf{R}(t)^T \tau(t) \mathbf{R}(t)$. Also, one can show that $\dot{\bar{\tau}}(t) = \boldsymbol{\Lambda}(t)^T \overset{\circ}{\tau}(t) \boldsymbol{\Lambda}(t)$, where $\overset{\circ}{\tau}(t)$ is the Green-Naghdi rate of the Kirchhoff stress. Moreover, $\bar{\mathbf{D}} = \dot{\bar{\mathbf{E}}}$, see [8], where $\bar{\mathbf{D}}(t) = \mathbf{R}(t)^T \mathbf{D}(t) \mathbf{R}(t)$. As a result, the extended hereditary constitutive equation, may be written as

$$\mathbf{E}(t) = \bar{\mathbf{C}}(t)\bar{\tau}(0) + \int_0^t \bar{\mathbf{C}}(t-\xi) \dot{\bar{\tau}}(\xi) d\xi. \quad (15)$$

Considering the material to be isotropic, one has $\bar{\mathbf{C}} = \mathbf{C}$, which yields

$$\mathbf{E}(t) = -\frac{B(t)}{3} \bar{p}(0) \mathbf{I} + \frac{J(t)}{2} \bar{\tau}^D(0) + \int_0^t \left\{ \frac{B(t-\xi)}{3} \dot{\bar{p}}(\xi) \mathbf{I} + \frac{J(t-\xi)}{2} \dot{\bar{\tau}}^D(\xi) \right\} d\xi. \quad (16)$$

in which $\dot{\bar{\tau}}^D(t) \equiv \mathbf{II}_{dev} \dot{\bar{\tau}}(t)$ and $\dot{\bar{p}}(t) \equiv \frac{1}{3} tr \left[\dot{\bar{\tau}}(t) \right]$ are the deviator and hydrostatic part of $\dot{\bar{\tau}}(t)$. Now, decomposing the strain tensor as $\mathbf{E}(t) = e(t) \mathbf{I} + \mathbf{E}^D(t)$ gives

$$e(t) = \frac{B(t)}{3} \bar{p}(0) + \int_0^t \frac{B(t-\xi)}{3} \dot{\bar{p}}(\xi) d\xi \quad (17)$$

and

$$\mathbf{E}^D(t) = \frac{J(t)}{2} \bar{\tau}^D(0) + \int_0^t \frac{J(t-\xi)}{2} \dot{\bar{\tau}}^D(\xi) d\xi. \quad (18)$$

Now, introducing the Prony series for $J(t)$ and $B(t)$ finally gives

$$\mathbf{E}^D(t) = -\frac{J_0}{2} \bar{\tau}^D(t) + \sum_{i=1}^{n_j} \frac{J_i}{2} \left(1 - \exp\left(-\frac{t}{\tau_i^J}\right) \right) \bar{\tau}^D(0) + \sum_{i=1}^{n_j} \int_0^t \left\{ \frac{J_i}{2} \left(1 - \exp\left(-\frac{t-\xi}{\tau_i^J}\right) \right) \right\} \dot{\bar{\tau}}^D(\xi) d\xi \quad (19)$$

and

$$e(t) = -\frac{B_0}{3} \bar{p}(t) + \sum_{i=1}^{n_B} \frac{B_i}{3} \left(1 - \exp\left(-\frac{t}{\tau_i^B}\right) \right) \bar{p}(0) + \sum_{i=1}^{n_B} \int_0^t \left\{ \frac{B_i}{3} \left(1 - \exp\left(-\frac{t-\xi}{\tau_i^B}\right) \right) \right\} \dot{\bar{p}}(\xi) d\xi. \quad (20)$$

3 Discretization of the visco-hypoelasticity model

3.1 Incremental weak formulation of the problem

Let $\mathbf{u}_{n+1} = \mathbf{u}(\mathbf{x}_o, t_{n+1})$, $\mathbf{u}_n = \mathbf{u}(\mathbf{x}_o, t_n)$, $\mathbf{F}_{n+1} = \mathbf{I} + \nabla \mathbf{u}_{n+1}$ and $\mathbf{F}_n = \mathbf{I} + \nabla \mathbf{u}_n$. Assume now that the configuration Ω_n and the state variables are known at t_n and enforce the equilibrium equations at Ω_{n+1} . As a result, one can determine the incremental weak formulation of the problem, between t_n and t_{n+1} , stated by: Determine $\mathbf{u}_{n+1} \in Kin_o^u$ so that

$$\mathfrak{S}(\mathbf{u}_{n+1}; \hat{\mathbf{v}}) = \int_{\Omega_o} \mathbf{P}(u_{n+1}) \cdot \nabla \hat{\mathbf{v}} d\Omega_o - \int_{\Omega_o} \rho_o \mathbf{b} \cdot \hat{\mathbf{v}} d\Omega_o - \int_{\Gamma_o^t} \mathbf{t}_o \cdot \hat{\mathbf{v}} dA_o = 0 \quad \forall \hat{\mathbf{v}} \in Var_o^u \quad (21)$$

with $\mathbf{u}_{n+1} = \mathbf{u}_n + \Delta \mathbf{u}_n$.

Since the problem is non-linear, one applies Newton's method leading to the solution of a sequence of linearized problems, described as follows: Let \mathbf{u}_{n+1}^k be the estimator at the k -th iteration and consider that $\mathbf{u}_{n+1}^k = \mathbf{u}_n$ at $k = 0$. For the k -th iteration of the solution procedure, one has

$$\mathbf{u}_{n+1}^{k+1} = \mathbf{u}_{n+1}^k + \Delta \mathbf{u}_{n+1}^k \quad (22)$$

The determination of $\Delta \mathbf{u}_{n+1}^k$ is obtained by assuming $\mathfrak{S}(\circ)$ to be Gâteaux differentiable and by enforcing $\mathfrak{S}(\mathbf{u}_{n+1}^k + \Delta \mathbf{u}_{n+1}^k; \mathbf{w}) = 0 \quad \forall \mathbf{w} \in \mathbf{V}_u$. As a result, one derives

$$D\mathfrak{S}(\mathbf{u}_{n+1}^k; \mathbf{w}) [\Delta \mathbf{u}_{n+1}^k] = -\mathfrak{S}(\mathbf{u}_{n+1}^k; \mathbf{w}) \quad (23)$$

where

$$D\mathfrak{S}(\mathbf{u}_{n+1}^k; \mathbf{w}) [\Delta \mathbf{u}_{n+1}^k] = \frac{d}{d\epsilon} [\mathfrak{S}(\mathbf{u}_{n+1}^k + \epsilon \Delta \mathbf{u}_{n+1}^k; \mathbf{w})]_{\epsilon=0} \quad (24)$$

Now, since Ω_o is fixed and the prescribed loading are assumed to be independent of the displacement field, one derives

$$\frac{d}{d\epsilon} [\mathfrak{S}(\mathbf{u}_{n+1}^k + \epsilon \Delta \mathbf{u}_{n+1}^k; \hat{\mathbf{v}})]_{\epsilon=0} = \int_{\Omega_o} \frac{d}{d\epsilon} [\mathbf{P}(\mathbf{u}_{n+1}^k + \epsilon \Delta \mathbf{u}_{n+1}^k)]_{\epsilon=0} \cdot \nabla \hat{\mathbf{v}} d\Omega_o \quad (25)$$

However, $\mathbf{P} = \mathbf{P}(\mathbf{F}(\mathbf{u}_{n+1}^k + \epsilon \Delta \mathbf{u}_{n+1}^k))$ which leads to

$$D\mathfrak{S}(\mathbf{u}_{n+1}^k; \hat{\mathbf{v}}) [\Delta \mathbf{u}_{n+1}^k] = \int_{\Omega_o} \mathbf{A}(u_{n+1}^k) \nabla (\Delta u_{n+1}^k) : \nabla \hat{\mathbf{v}} d\Omega_o \quad (26)$$

with $[\mathbf{A}(\mathbf{u}_{n+1}^k)]_{ijkl} = \frac{\partial P_{ij}}{\partial F_{kl}} \Big|_{\mathbf{u}_{n+1}^k}$.

3.2 Determination of the consistent tangent modulus

Now, since $\mathbf{P}_{n+1}^T = \tau_{n+1}^T \mathbf{F}_{n+1}^{-T}$ one derives

$$[\mathbf{A}(\mathbf{u}_{n+1}^k)]_{ijkl} = \frac{\partial \tau_{ip}}{\partial F_{kl}} F_{jp}^{-1} - \tau_{ip} F_{jk}^{-1} F_{lp}^{-1} \quad (27)$$

However, $\tau_{n+1} = \mathbf{R}_{n+1} \bar{\tau}_{n+1} \mathbf{R}_{n+1}^T$, which leads to

$$\frac{\partial \tau_{n+1}}{\partial \mathbf{F}_{n+1}} = \frac{\partial \mathbf{R}_{n+1}}{\partial \mathbf{F}_{n+1}} \bar{\tau}_{n+1} \mathbf{R}_{n+1}^T + \mathbf{R}_{n+1} \hat{\mathbf{D}}_{n+1} \mathbf{R}_{n+1}^T + \mathbf{R}_{n+1} \bar{\tau}_{n+1} \frac{\partial \mathbf{R}_{n+1}^T}{\partial \mathbf{F}_{n+1}} \quad (28)$$

where $\hat{\mathbf{D}}_{n+1} = \frac{\partial \bar{\tau}_{n+1}}{\partial \mathbf{F}_{n+1}}$, $\frac{\partial \mathbf{R}_{n+1}}{\partial \mathbf{F}_{n+1}} = \frac{\partial \mathbf{F}_{n+1}}{\partial \mathbf{F}_{n+1}} (\mathbf{U}_{n+1})^{-1} - \mathbf{R}_{n+1} \frac{\partial \mathbf{U}_{n+1}}{\partial \mathbf{F}_{n+1}} (\mathbf{U}_{n+1})^{-1}$ and $\frac{\partial \mathbf{U}_{n+1}}{\partial \mathbf{F}_{n+1}}$ is determined from the relation $\mathbf{C}_{n+1} = \mathbf{F}_{n+1}^T \mathbf{F}_{n+1} = \mathbf{U}_{n+1}^2$.

The determination of $\hat{\mathbf{D}}_{n+1}$ requires the computation of \mathbf{E}_{n+1} , in which $\mathbf{E}_{n+1} = e_{n+1} \mathbf{I} + \mathbf{E}_{n+1}^D$ with e_{n+1} and \mathbf{E}_{n+1}^D denoting respectively the volumetric and deviator part of \mathbf{E}_{n+1} . In fact,

$$\mathbf{E}_{n+1}^D = \mathbf{E}_{n+1}^{D(0)} + \sum_{i=1}^{n_j} \mathbf{E}_{n+1}^{D(i)} \quad \text{with} \quad \mathbf{E}_{n+1}^{D(0)} = -\frac{J_0}{2} \bar{\tau}_{n+1}^D \quad (29)$$

and

$$\begin{aligned} \mathbf{E}_{n+1}^{D(i)} = & \frac{J_i}{2} \left(1 - \exp\left(-\frac{t_{n+1}}{\tau_i^J}\right) \right) \bar{\tau}^D(0) + \int_0^{t_n} \left\{ \frac{J_i}{2} \left(1 - \exp\left(-\frac{t_{n+1}-\xi}{\tau_i^J}\right) \right) \right\} \frac{\partial \bar{\tau}^D}{\partial \xi}(\xi) d\xi \\ & - \int_{t_n}^{t_{n+1}} \left\{ \frac{J_i}{2} \left(1 - \exp\left(-\frac{t_{n+1}-\xi}{\tau_i^J}\right) \right) \right\} \frac{\partial \bar{\tau}^D}{\partial \xi}(\xi) d\xi \end{aligned} \quad (30)$$

Defining $t_{n+1} = t_n + \Delta t$, $t_{n+\frac{1}{2}} = t_n + \frac{\Delta t}{2}$ and $\bar{\tau}_{n+1}^D = \bar{\tau}_n^D + \Delta \bar{\tau}_n^D$ one derives

$$\begin{aligned} \mathbf{E}_{n+1}^{D(i)} = & \frac{J_i}{2} \bar{\tau}_0^D - \frac{J_i}{2} \exp\left(-\frac{t_n}{\tau_i^J}\right) \exp\left(-\frac{\Delta t}{\tau_i^J}\right) \bar{\tau}_0^D \\ & + \int_0^{t_n} \frac{J_i}{2} \frac{\partial \bar{\tau}^D}{\partial \xi}(\xi) d\xi - \left\{ \int_0^{t_n} \frac{J_i}{2} \exp\left(-\frac{t_n-\xi}{\tau_i^J}\right) \frac{\partial \bar{\tau}^D}{\partial \xi}(\xi) d\xi \right\} \exp\left(-\frac{\Delta t}{\tau_i^J}\right) \\ & + \int_{t_n}^{t_{n+1}} \frac{J_i}{2} \frac{\partial \bar{\tau}^D}{\partial \xi}(\xi) d\xi - \left\{ \int_{t_n}^{t_{n+1}} \frac{J_i}{2} \exp\left(-\frac{t_n-\xi}{\tau_i^J}\right) \frac{\partial \bar{\tau}^D}{\partial \xi}(\xi) d\xi \right\} \exp\left(-\frac{\Delta t}{\tau_i^J}\right). \end{aligned} \quad (31)$$

Now, applying Euler's method leads to the following approximation

$$\mathbf{E}_{n+1}^{D(i)} \simeq \frac{J_i}{2} \bar{\tau}_{n+1}^D - \check{\mathbf{E}}_n^{D(i)} \exp\left(-\frac{\Delta t}{\tau_i^J}\right) - \frac{J_i}{2} \Delta \bar{\tau}_n^D \exp\left(-\frac{\Delta t}{2\tau_i^J}\right) \quad (32)$$

in which $\check{\mathbf{E}}_n^{D(i)}$ may be approximated by applying Euler's method as

$$\check{\mathbf{E}}_n^{D(i)} = \mathbf{E}_{n-1}^{D(i)} \exp\left(-\frac{\Delta t}{\tau_i^J}\right) + \frac{J_i}{2} \Delta \bar{\tau}_{n-1}^D \exp\left(-\frac{\Delta t}{2\tau_i^J}\right) \quad (33)$$

Moreover,

$$e_{n+1} = e_{n+1}^{(0)} + \sum_{i=1}^{n_B} e_{n+1}^{(i)} \quad \text{with} \quad e_{n+1}^{(0)} = \frac{B_0}{3} \bar{p}_{n+1} \quad (34)$$

and

$$e_{n+1}^{(i)} = \frac{B_i}{3} \left(1 - \exp \left(-\frac{t_{n+1}}{\tau_i^B} \right) \right) \bar{p}_0 + \int_0^{t_{n+1}} \left\{ \frac{B_i}{3} \left(1 - \exp \left(-\frac{t_{n+1} - \xi}{\tau_i^B} \right) \right) \right\} \frac{\partial \bar{p}}{\partial \xi}(\xi) d\xi. \quad (35)$$

Now, defining $\bar{p}_{n+1} = _p_n + \Delta \bar{p}_n$ yields

$$\begin{aligned} e_{n+1}^{(i)} &= \frac{B_i}{3} \bar{p}_0 - \frac{B_i}{3} \exp \left(-\frac{t_n}{\tau_i^B} \right) \exp \left(-\frac{\Delta t}{\tau_i^B} \right) \bar{p}_0 \\ &+ \int_0^{t_n} \frac{B_i}{3} \frac{\partial \bar{p}}{\partial \xi}(\xi) d\xi - \left[\int_0^{t_n} \frac{B_i}{3} \exp \left(-\frac{t_n - \xi}{\tau_i^B} \right) \frac{\partial \bar{p}}{\partial \xi}(\xi) d\xi \right] \exp \left(-\frac{\Delta t}{\tau_i^B} \right) \\ &+ \int_{t_n}^{t_{n+1}} \frac{B_i}{3} \frac{\partial \bar{p}}{\partial \xi}(\xi) d\xi - \left[\int_{t_n}^{t_{n+1}} \frac{B_i}{3} \exp \left(-\frac{t_n - \xi}{\tau_i^B} \right) \frac{\partial \bar{p}}{\partial \xi}(\xi) d\xi \right] \exp \left(-\frac{\Delta t}{\tau_i^B} \right) \end{aligned} \quad (36)$$

Applying Euler's method one derives the following approximation

$$e_{n+1}^{(i)} \simeq _e_{n+1} - \frac{B_i}{3} \bar{p}_{n+1} - \check{e}_n^{(i)} \exp \left(-\frac{\Delta t}{\tau_i^B} \right) - \frac{B_i}{3} (\Delta \bar{p}_n) \exp \left(-\frac{\Delta t}{2\tau_i^B} \right) \frac{1}{2}. \quad (37)$$

in which $\check{e}_n^{(i)}$ is approximated as

$$\check{e}_n^{(i)} = _e_{n-1} \exp \left(-\frac{\Delta t}{\tau_i^B} \right) + \frac{B_i}{3} \Delta \bar{p}_{n-1} \exp \left(-\frac{\Delta t}{2\tau_i^B} \right). \quad (38)$$

Now, since $\bar{\tau}_{n+1} = \bar{p}_{n+1} \mathbf{I} + \bar{\tau}_{n+1}^D$ one has $\hat{\mathbf{D}}_{n+1} = -\frac{\partial \bar{\tau}_{n+1}}{\partial \mathbf{F}_{n+1}} = \frac{\partial \bar{p}_{n+1}}{\partial \mathbf{F}_{n+1}} \mathbf{I} + \frac{\partial \bar{\tau}_{n+1}^D}{\partial \mathbf{F}_{n+1}}$. However, since $e_{n+1} = e_{n+1}(\bar{p}_{n+1}, \bar{\tau}_{n+1}^D)$ and $\mathbf{E}_{n+1}^D = \mathbf{E}_{n+1}^D(\bar{p}_{n+1}, \bar{\tau}_{n+1}^D)$ one may differentiate both equations with respect to \mathbf{F}_{n+1} , apply the chain rule of differentiations and derive a set of equations that is solved for $\frac{\partial \bar{p}_{n+1}}{\partial \mathbf{F}_{n+1}}$ and $\frac{\partial \bar{\tau}_{n+1}^D}{\partial \mathbf{F}_{n+1}}$.

4 Problem cases and conclusion

4.1 Example 1

Consider here a rectangular domain, as depicted in Fig. 1.

The body is submitted to a prescribed displacement condition, under a plane strain state, given by $_u(1, y, t) = \bar{u} * t$, with $_u = 0.1in$. The numerical solution is compared with an analytical solution derived as follows: Let $_x(t) = \lambda_1(t)x_o$ and $_y(t) = \lambda_2(t)y_o$. By a simple computation from the boundary condition and considering $_J(t) = 3.2386 * 10^{-8}(1 - \exp(-\frac{1}{20.2599}t)) + 5.8578 * 10^{-7}$

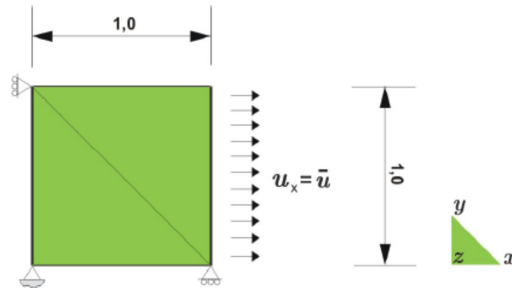


Figure 1: Description of the problem.

psi^{-1} and supposing the block is composed by a polymer with $B(t) = 4.7279 \cdot 10^{-8} (1 - \exp(-\frac{1}{19.8283}t)) + 8.7867 \cdot 10^{-7} psi^{-1}$ one may compute the exact solution for this homogeneous deformation problem and compare it with the numerical solution derived by the proposed numerical scheme.

Figure 2 shows a comparison of the exact and numerical values regarding the evolution of the σ_{xx} Cauchy stress component.

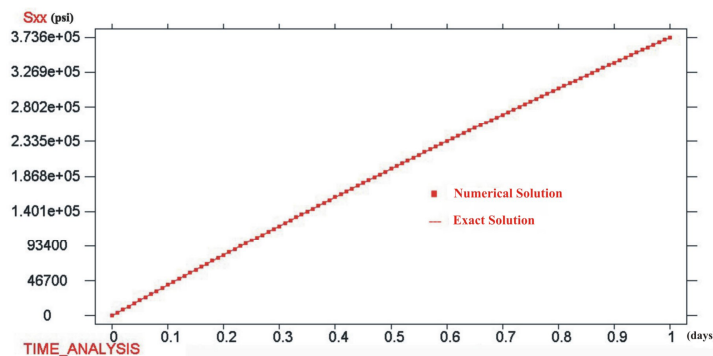


Figure 2: Evolution of the σ_{xx} Cauchy stress component (psi) versus time (days).

4.2 Example 2

Consider the problem depicted in Fig. 3, subjected to a plane strain condition. The dimensions in Fig. 3 are given all in inches.

The body is submitted to a prescribed displacement condition on the right side, as shown. The remaining boundary conditions are stress free conditions. The prescribed displacement is applied by a linear ramp and given by $u_x(t) = \bar{u} * t$, with $\bar{u} = -0.3 in$. The polymer is the same as in example 1

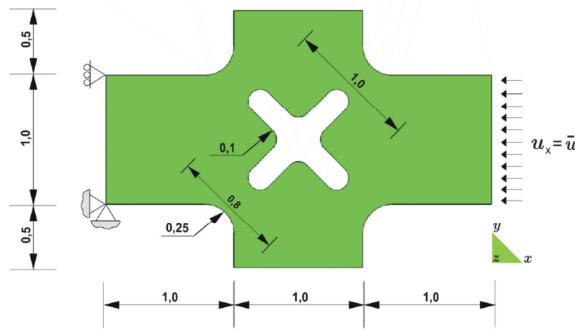
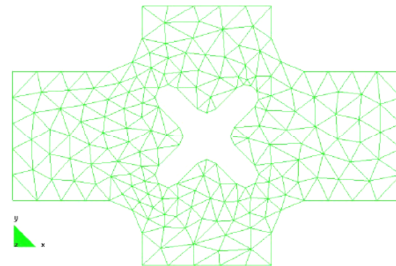


Figure 3: Description of the problem.

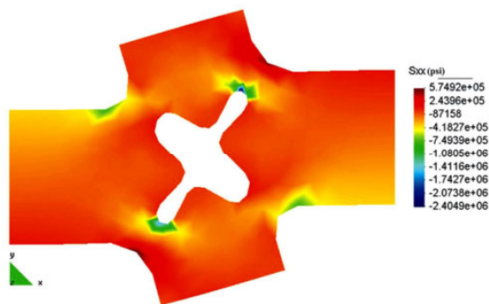
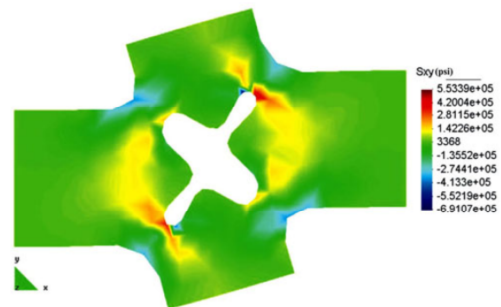
Figure 4: Description of the finite element mesh
Tri 6 element.

and the time scale is taken in days. The mesh employed 337 elements and has 755 nodes as shown in Fig. 4.

Figure 5 shows the distribution of the σ_{xx} Cauchy stress component.

Figure 6 shows the distribution of the σ_{xy} Cauchy stress component.

Figure 7 shows the distribution of the σ_{yy} Cauchy stress component.

Figure 5: Distribution of the σ_{xx} Cauchy stress component at $t=1$ day.Figure 6: Distribution of the σ_{xy} Cauchy stress component at $t=1$ day.

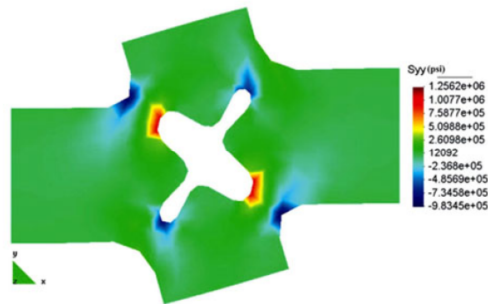


Figure 7: Distribution of the σ_{yy} Cauchy stress component at $t=1$ day.

5 Conclusion

A viscoelastic model for large displacement and rotations has been proposed. The hereditary constitutive equation is defined in terms of a stress and a strain measure defined both at the unrotated configuration of the body. An implicit algorithm was also proposed and the consistent tangent operator associated with the implicit algorithm was determined. The proposed algorithm was tested and compared with an exact analytical solution. The integration of the hereditary relation preserves objectivity so may be used to properly simulate the viscoelastic behavior of components subjected to large displacements and rotations.

References

- [1] Azikri de Deus, H.P. & Alves, M.K., A dual finite visco-hypoelastic approach. *Solid Mechanics in Brazil 2009*, ABCM Publishing: Rio de Janeiro, 2009.
- [2] Drozdov, A., *Finite Elasticity and Viscoelasticity: A Course in non-linear Mechanics of Solids*. World Scientific Publishing: New York, 1996.
- [3] Haupt, P., *Continuum Mechanics and Theory of Materials*. Springer-Verlag: Heidelberg, 2002.
- [4] Johnson, A., Quigley, C. & Mead, J., Large strain viscoelastic constitutive models for rubber, Part I: Formulations. *Rubber Chemistry and Technology*, **67**, pp. 904–917, 1994.
- [5] Reismann, H. & Pawlik, P., *Elasticity: Theory and Applications*. John Wiley and Sons, 1980.
- [6] Findley, W.N., Lai, J.S. & Onaran, K., Creep and relaxation of nonlinear viscoelastic materials (with an introduction to linear viscoelasticity). *Applied Mathematics and Mechanics*, eds. H.A. Lauwerier & W.T. Koiter, North-Holland, North-Holland Series, 1976.
- [7] Riande, E., Diaz-Calleja, R., Prolongo, M.G., Masegosa, R.M. & Salom, C., *Polymer Viscoelasticity : Stress and Strain in Practice*. Marcel Dekker, 2000.
- [8] Azikri de Deus, H.P., *Computational Propositions and Applications in Polymers*. Ph.D. thesis, Federal University of Santa Catarina, Florianopolis, 2008.

A variational boundary element method based on generalized Westergaard stress functions

Ney Augusto Dumont, Elvis Yuri Mamani Vargas

*Department of Civil Engineering,
Pontifical Catholic University of Rio de Janeiro, 22453-900, RJ – Brazil*

Abstract

A particular implementation of the hybrid boundary element method is presented for the two-dimensional analysis of potential and elasticity problems, which, although general in concept, is suited for fracture mechanics applications. Generalized Westergaard stress functions, as proposed by Tada et al in 1993, are used as the problem's fundamental solution. Problems of general topology, such as in case of unbounded and multiply-connected domains, may be modeled. The formulation, which is directly applicable to notches and generally curved, internal or external cracks, is specially suited for the description of the stress field in the vicinity of crack tips and is an easy means of evaluating stress intensity factors and of checking some basic concepts laid down by Rice in 1968. The paper focuses on the mathematical fundamentals of the formulation. One validating numerical example is presented.

Keywords: Westergaard stress functions, Hellinger-Reissner potential, variational methods, hybrid boundary element.

1 Introduction

Tada et al [1] proposed a simple and efficient method of developing Westergaard stress functions for the analysis of displacement-prescribed and stress-prescribed crack problems. Their intervention was restricted to the mathematical means of arriving at the stress functions and the illustration of several forms of crack openings – always in terms of analytical developments.

The present paper makes use of Tada et al's method and shows that such stress functions may be implemented as fundamental solutions of a generalized, two-dimensional boundary element method, and applied to problems that can be completely unrelated to fracture mechanics. On the other hand, the formulation can be directly and advantageously applied to fracture mechanics [2, 3].

Tada et al's basic idea is extremely simple [1], as shown in Section 3. Although there is no claim of originality in the developments of the next Sections [4], they highlight some relevant mathematical aspects that Westergaard-like potential functions must satisfy to be applicable in the framework of an

integral statement. Next, a fundamental solution for potential problems is constructed and singularity issues are discussed.

In the present outline, Tada et al's method is used to define a non-dimensional potential function Φ that may have an in principle arbitrary configuration, depending on the local geometrical assumptions that are made, with all developments obtained in terms of Φ and its derivatives. Several configuration possibilities of Φ have been previously studied for the modeling of potential problems in a variational framework [4]. In an extended manuscript [5], the potential function corresponds to the superposition of two elliptical half cracks, for a homogeneous slab of constant thickness under plane strain. The locally generated stresses and displacements (the latter ones evaluated except for rigid body displacements) tend to zero at a point that goes increasingly farther from the crack ($\sigma_\infty = 0$). In this paper, the developments of interest are particularized to potential problems, which present exactly the same mathematical issues as in elasticity.

This paper starts with a very brief outline of the hybrid boundary element method, as a representative formulation that can make use of the generalized Westergaard stress functions. Then, Tada et al's proposition is briefly presented and developed for a general, rotated (semi-)crack configuration, which includes the assessment of all possible singularities. The formulation is applied to the solution of the Laplace equation, which is per se relevant, but turns out to be the simplest framework for the outline of all mathematical aspects and issues related to a code implementation of the more general problem of elasticity. One numerical example is shown in order to validate the proposed developments.

2 Problem solution with the hybrid boundary element method

The hybrid boundary element method (HBEM) was introduced in 1987 on the basis of the Hellinger-Reissner potential and as a generalization of Pian's hybrid finite element method [6, 7]. The formulation requires evaluation of integrals only along the boundary and makes use of fundamental solutions (Green's functions) to interpolate fields in the domain. Accordingly, an elastic body of arbitrary shape may be treated as a single finite macro-element with as many boundary degrees of freedom as desired. In the meantime, the formulation has evolved to several application possibilities, including time-dependent problems, fracture mechanics, non-homogeneous materials and strain gradient elasticity [2, 8–10].

2.1 Problem formulation

Let an elastic body be submitted to tractions \bar{t}_i on part Γ_σ of the boundary Γ and to displacements \bar{u}_i on the complementary part Γ_u . For the sake of brevity, body forces are not included [11]. One is attempting to find the best approximation for stresses and displacements, σ_{ij} and u_i , such that

$$\sigma_{j,i,j} = 0 \quad \text{in the domain } \Omega, \quad (1)$$

$$u_i = \bar{u}_i \quad \text{along } \Gamma_u \quad \text{and} \quad t_i = \sigma_{ij} n_j = \bar{t}_i \quad \text{along } \Gamma_\sigma \quad (2)$$

in which n_j is the outward unit normal to the boundary. Indicical notation is used.

2.2 Stress and displacement assumptions

Two independent trial fields are assumed [6, 7]. The displacement field is explicitly approximated along the boundary by u_i^d , where $(\)^d$ means *displacement assumption*, in terms of polynomial functions u_{im} with compact support and nodal displacement parameters $\mathbf{d} = [d_m] \in \mathbb{R}^{n^d}$, for n^d displacement degrees of freedom of the discretized model. An independent stress field σ_{ij}^s , where $(\)^s$ stands for *stress assumption*, is given in the domain in terms of a series of fundamental solutions σ_{ijm}^* with global support, multiplied by force parameters $\mathbf{p}^* = [p_m^*] \in \mathbb{R}^{n^*}$ applied at the same boundary nodal points m to which the nodal displacements d_m are attached ($n^* = n^d$).¹ Displacements u_i^s are obtained from σ_{ij}^s . Then,

$$u_i^d = u_{im} d_m \quad \text{on } \Gamma \quad \text{such that} \quad u_i^d = \bar{u}_i \quad \text{on } \Gamma_u; \quad (3)$$

$$\sigma_{ij}^s = \sigma_{ijm}^* p_m^* \quad \text{such that} \quad \sigma_{jim,j}^* = 0 \quad \text{in } \Omega \quad (4)$$

$$\Rightarrow u_i^s = u_{im}^* p_m^* + u_{is}^r C_{sm} p_m^* \quad \text{in } \Omega \quad (5)$$

where u_{im}^* are displacement fundamental solutions corresponding to σ_{ijm}^* . Rigid body motion is included in terms of functions u_{is}^r multiplied by in principle arbitrary constants C_{sm} [11, 12].

2.3 Governing matrix equations

The Hellinger-Reissner potential, based on the two-field assumptions of the latter section, as implemented by Pian [6] and generalized by Dumont [7], leads to two matrix equations that express nodal equilibrium and compatibility requirements. Dumont [11] shows that the simplest, and still mathematically consistent, means of laying out these equations is in terms of two separately virtual work principles.

One obtains from a displacement virtual-work statement the matrix equilibrium equation

$$H_{mn} p_m^* = p_n \quad \text{or} \quad \mathbf{H}^T \mathbf{p}^* = \mathbf{p} \quad (6)$$

in which $\mathbf{H} = [H_{nm}] \in \mathbb{R}^{n^d \times n^*}$ is the same double layer potential matrix of the collocation boundary element method [13], and $\mathbf{p} = [p_n] \in \mathbb{R}^{n^d}$ are equivalent nodal forces obtained as in the displacement finite element method.

Moreover, a stress virtual-work statement leads to

$$F_{mn}^* p_n^* = H_{mn} d_n \quad \text{or} \quad \mathbf{F}^* \mathbf{p}^* = \mathbf{H} \mathbf{d} \quad (7)$$

where \mathbf{H} , which already appeared in Eq. (6), is recognized as performing a kinematic transformation, and $\mathbf{F}^* = [F_{nm}^*] \in \mathbb{R}^{n^* \times n^*}$ is a symmetric, flexibility matrix. The matrices \mathbf{H} and \mathbf{F}^* may be compactly

¹For Kelvin fundamental solutions, as in the conventional boundary element method and in the basic version of the HBEM, p_m^* are point forces. In the present outline, p_m^* are the resultants of forces applied at crack faces. The problem has the same mathematical format, although with different singularity issues. In a more generalized formulation, p_m^* may be just parameters with no special mechanical meaning [11].

defined as

$$[H_{mn} \quad F_{mn}^*] = \int_{\Gamma} \sigma_{ijm}^* n_j \langle u_{in} \quad u_{in}^* \rangle d\Gamma \quad (8)$$

Solving for \mathbf{p}^* in Eqs. (6) and (7), one arrives at the matrix system

$$\mathbf{H}^T \mathbf{F}^{*(-1)} \mathbf{H} \mathbf{d} = \mathbf{p} \quad (9)$$

where $\mathbf{H}^T \mathbf{F}^{*(-1)} \mathbf{H} \equiv \mathbf{K}$ is a stiffness matrix. The inverse $\mathbf{F}^{*(-1)}$ must be evaluated in terms of generalized inverses, as \mathbf{F}^* is singular for a finite domain Ω [11]. Results at internal points are expressed in terms of Eqs. (4) and (5) after evaluation of \mathbf{p}^* in either Eq. (6) or (7).

3 Dislocation-based formulation by Tada et al

Tada et al [1] show that, for a prescribed crack opening of the shape $f(x)$ in the interval $[x_1, x_2]$ along the x axis and symmetric with respect to this axis in the Cartesian coordinate system (x, y) , one can define a potential function $\Phi(z)$ of the complex argument $z = x + iy$,

$$\Phi(z) = -\frac{1}{2\pi} \int_{x_1}^{x_2} \frac{f(x)}{z-x} dx \quad (10)$$

and then obtain the corresponding stress and displacement functions, as a generalization of Westergaard's initial proposition in the frame of the fracture mechanics. Several crack and stress configurations are investigated by Tada et al [1], as translation and superposition of effects can always be applied to compose intricated crack patterns. Westergaard's developments for an elliptic crack opening of length $2a$ are obtained if one chooses the function

$$f(x) = \frac{\sqrt{a^2 - x^2}}{a} \quad (11)$$

and then carries out the integration of Eq. (10) in the interval $[-a, a]$.

4 Basics on a rotated semicrack

A very simple, although apparently original generalization of the above developments is obtained for a semicrack of length a_1 along a straight line that is rotated in the counter clock direction by an angle θ_1 , Fig. 1, with which it is possible to compose kinked cracks of any length [4], as developed in the rest of this paper. To make calculations as simple as possible, the crack shape function of Eq. (11), or any other shape, is initially defined for a semicrack length $a = 1$ and the integration of Eq. (10) is carried out in the interval $[0, 1]$. Although the crack shape may be rather general, as given by Tada et al [1] and as already explored in the present framework [4], the ensuing developments are given

for the elliptic semicrack corresponding to Eq. (11). The corresponding expression of Eq. (10) for the semicrack 1 is

$$\Phi_1 \equiv \Phi(Z_1) = -\frac{Z_1}{4} - \frac{1}{2\pi} \left(1 - \sqrt{1 - Z_1^2} \ln \left(-\frac{1 + \sqrt{1 - Z_1^2}}{Z_1} \right) \right) \quad (12)$$

already given as argument of $Z_1 = zT_1 \equiv \frac{z}{a_1} e^{-i\theta_1} \equiv \frac{x + iy}{a_1} e^{-i\theta_1} \equiv \frac{r}{a_1} e^{i(\theta - \theta_1)}$, from which the definition of the rotation and normalization term T_1 is inferred. The leading terms of Φ_1 at $Z_1 = 0$

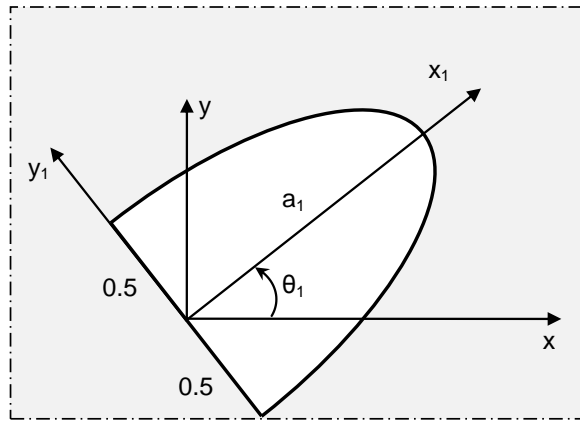


Figure 1: Semicrack of length a_1 rotated by an angle θ_1 .

are

$$\lim_{r \rightarrow 0} \operatorname{Re} \Phi_1 = \frac{-\ln(r) - 1 + \ln(2a_1)}{2\pi}; \quad \lim_{r \rightarrow 0} \operatorname{Im} \Phi_1 = \begin{cases} \frac{\pi - \theta + \theta_1}{2\pi} & \text{for } \theta_1 \leq \theta \leq \theta_1 + \pi \\ \frac{-\pi - \theta + \theta_1}{2\pi} & \text{for } \theta_1 + \pi < \theta < \theta_1 + 2\pi \end{cases} \quad (13)$$

The first derivative of $\Phi(Z_1)$ with respect to Z_1 is

$$\Phi'_1 \equiv \frac{\partial \Phi(Z_1)}{\partial Z_1} = -\frac{1}{2\pi} \left(Z_1 \ln \left(-\frac{1 + \sqrt{1 - Z_1^2}}{Z_1} \right) \frac{1}{\sqrt{1 - Z_1^2}} + \frac{1}{Z_1} + \frac{\pi}{2} \right) \quad (14)$$

with corresponding real and imaginary parts of the leading terms at $Z_1 = 0$:

$$\lim_{r \rightarrow 0} \operatorname{Re} \Phi'_1 = -\frac{\cos(\theta - \theta_1) a_1}{2\pi r} - \frac{1}{4}; \quad \lim_{r \rightarrow 0} \operatorname{Im} \Phi'_1 = \frac{\sin(\theta - \theta_1) a_1}{2\pi r} \quad (15)$$

The second derivative of $\Phi(Z_1)$ with respect to Z_1 is only required for elasticity problems and is not developed [3, 5].

5 Developments for a potential problem

The above developments are now applied to the derivation of a fundamental solution that can be used in the context of a hybrid boundary element method for potential problems. The developments in this Section are per se relevant and self contained. However, they also serve as motivation to the more involved – and less intuitive – problem of elasticity [3, 5].

5.1 Construction of a fundamental solution

A solution of the Laplace equation $\frac{\partial^2 u}{\partial x^2} + \frac{\partial^2 u}{\partial y^2} = 0$, say, for the steady-state heat transfer in a homogeneous plate of uniform thickness t with coefficient of conductivity k , can be obtained from Φ_1 , as introduced in Eq. (12), in terms of the potential

$$u_1 = \frac{1}{k} \text{Im } \Phi_1 \tag{16}$$

with fluxes referred to the global Cartesian system (x, y)

$$q_{x_1} = -k \frac{\partial u_1}{\partial x} = -\text{Im } (T_1 \Phi_1'); \quad q_{y_1} = -k \frac{\partial u_1}{\partial y} = -\text{Re } (T_1 \Phi_1') \tag{17}$$

and normal flux

$$q_{n_1} = -q_{x_1} n_x - q_{y_1} n_y \quad \text{along } \Gamma \tag{18}$$

Let two segments of lengths a_1 and a_2 rotated by angles θ_1 and θ_2 , respectively, compose lines of potential jumps (which correspond to lines of displacement discontinuities – cracks – in the elasticity case) along the boundary Γ of a body of domain Ω , with segment 1 coming before segment 2, in such a way that all phenomena along Γ are described in terms of a local variable ξ that runs in the counter clock direction, as illustrated in Fig. 2. The combined effect of the potential field is proposed as

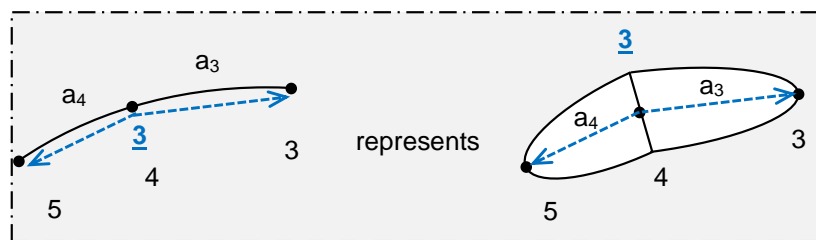


Figure 2: Representation of two semicracks that compose the crack element # 3 related to node # 4.

$$u = u_1 - u_2 \tag{19}$$

with mathematical justification that follows immediately. According to Eq. (13), the latter equation leads to

$$\lim_{r \rightarrow 0} u \equiv \frac{1}{k} \lim_{r \rightarrow 0} \text{Im}(\Phi_1 - \Phi_2) = \begin{cases} \frac{\theta_1 - \theta_2}{2\pi k} & \text{for a point outside } \Omega \\ 1 + \frac{\theta_1 - \theta_2}{2\pi k} & \text{for a point inside } \Omega \end{cases} \tag{20}$$

The practical way to evaluate $\lim_{r \rightarrow 0} u = \frac{1}{k} + \frac{\theta_1 - \theta_2}{2\pi k}$ for a point inside Ω , and for θ_1 and θ_2 in any quadrant, whenever required, is by writing $\lim_{r \rightarrow 0} u = \text{frac} \left(1 + \frac{\theta_1 - \theta_2}{2\pi} \right) \frac{1}{k}$, observing that $0 < \lim_{r \rightarrow 0} u < \frac{1}{k}$.

One checks that, for the superposition of effects given in Eq. (19),

$$\lim_{r \rightarrow 0} (T_1 \Phi'_1 - T_2 \Phi'_2) = -\frac{e^{-i\theta_1}}{4a_1} + \frac{e^{-i\theta_2}}{4a_2} \tag{21}$$

which is not only finite, but also single valued.

The projections of the outward unit normal \vec{n} , for Γ rotated by θ_1 , are $n_x = \sin \theta_1$ and $n_y = -\cos \theta_1$. Then, for the combined effect of the potential field, as in Eq. (19), the normal flux q_n on Γ is

$$\lim_{r \rightarrow 0} q_n = \lim_{r \rightarrow 0} (-q_x n_x - q_y n_y) = \frac{1}{4a_1} - \frac{\cos(\theta_2 - \theta_1)}{4a_2} \quad \text{along segment 1} \tag{22}$$

$$\lim_{r \rightarrow 0} q_n = \lim_{r \rightarrow 0} (-q_x n_x - q_y n_y) = \frac{1}{4a_2} - \frac{\cos(\theta_2 - \theta_1)}{4a_1} \quad \text{along segment 2} \tag{23}$$

Observe that there is a jump in the value of q_n as one goes from one segment to the other. If $\theta_2 = \theta_1 + \pi$, that is, segments 1 and 2 constitute a straight boundary, both limits above result in $\lim_{r \rightarrow 0} q_n = \frac{1}{4a_1} + \frac{1}{4a_2}$, which means that there is no longer a jump, although q_n varies along the segments. Additionally, if $a_1 = a_2$, q_n is constant along the entire boundary segment and the integration of q_n along the segment results in a source of unit intensity, $Q/t = 1$.

Although there are no singularities at $r = 0$, the expressions of the potential u and of the flux q_n must be carefully assessed around the origin and at the opposite extremities of the segments 1 and 2, as numerical integrations are to be ultimately carried out for the evaluation of the matrices that result from a boundary element formulation [5].

5.2 Numerical integration of the double-layer potential matrix \mathbf{H} for potential problems

The general expression of the double-layer potential matrix \mathbf{H} is

$$\mathbf{H} \equiv H_{ki} = - \int_{\Gamma} (q_{x_k} n_x + q_{y_k} n_y) N_i |J| d\xi \tag{24}$$

where k is the node of application of the potential source, i. e., the common node of two adjacent boundary segments, $\overline{k^-k}$ on the left (segment 1, rotated by an angle θ_1) and $\overline{kk^+}$ on the right (segment 2, rotated by an angle θ_2), as described in Section 5.1. The applied boundary potential varies linearly, according to the interpolation function N_i , from node i to the adjacent nodes on the left and on the right. Then, the integration interval indicated in the above equation comprehends, for the matrix coefficient H_{ki} , the two boundary segments that have i as common node (see Fig. 3). In this particular case, $|J|$ is the corresponding element length, for the natural boundary variable $\xi \in [0, 1]$.

The following Section consists in an algorithm for the numerical evaluation of Eq. (24) step by step along a segment \overline{ij} , for i varying from 1 to nn , the total number of boundary nodes, and j characterizing the node that succeeds i when one moves counterclockwise around the domain.

When $k = i$ or $k = j$, the segment \overline{ij} coincides with either $\overline{kk^+}$ or $\overline{k^-k}$ and there are in principle singularities on both extremities of the segment \overline{ij} . However, a simplification occurs for potential problems (as well as for elasticity [5]). For segment 1, for instance, the projections of the outward unit vector \vec{n} are $n_x = \sin \theta_1$ and $n_y = -\cos \theta_1$. Then, one checks that, in Eq. (24), $-q_{x_1}n_x - q_{y_1}n_y = q_{y_1(0)} = -\frac{1}{a_1} \text{Re}(\Phi'_1)$, which presents an implicit logarithmic singularity at $x_1 = 0$, but can be approximated by a low-order polynomial as $x_1 = a_1$ is approached. The fact that no singularity exists either at $x_1 = a_1$ along the segment 1 or at $x_2 = a_2$ along the segment 2 leads to the simple algorithm to be outlined in the following for the cases that $k = j$ or $k = i$.

In general, all functions $\Phi(Z)$, $\Phi'(Z)$ and $\Phi''(Z)$ present $\ln \xi$ singularity about $Z = 0$ and $1/\sqrt{\xi}$ singularity about $Z = 1$. For the purpose of numerical integration, as detailed in [5], these functions, whether in terms of Z_1 or Z_2 , are expanded about the singularity points as, illustratively for $\Phi(Z)$,

$$\Phi(Z) \approx \Phi_{ln}(Z) \ln \xi + \Phi_{reg}(Z) \quad \text{about } Z = 0 \quad (25)$$

$$\Phi(Z) \approx \Phi_{sqrt}(Z)/\sqrt{\xi} + \Phi_{reg}(Z) \quad \text{about } Z = 1 \quad (26)$$

In these equations, $\Phi_{reg}(Z)$ are *regular* parts of the general functions that are not affected by singularities, although they cannot be represented by low-order polynomials and be integrated in the frame of a Gauss-Legendre quadrature. Two simple routines, *lnproc()* and *sqrtproc()*, have been developed to carry out integration along an interval $[0, 1]$ by using subintervals that increase geometrically from $\xi = 0$ to $\xi = 1$, as referred to in the next Section [5].

5.2.1 Algorithm for the numerical integration of H

Let nn be the total number of nodes of a discretized model, which coincides with the total number of discretized boundary segments, as illustrated in Fig. 3. A body of any topology, with reentrant corners, holes and, after a slight modification of the basic code, also one-dimensional internal obstacles (which correspond to cracks in an elastic medium), can be simulated. The simulation of an internal crack is obtained as the modeling of a hole in the domain (similarly to the general numerical example of Fig. 6), then with node numbering running clockwise. However, as illustrated in Fig. 4 for a crack with n nodes, an arbitrarily placed, fictitious node $n + 3$ is introduced. After the numerical evaluation of all matrices, the rows and columns corresponding to nodes 1, $n + 2$ (which are only needed in the

definition of the crack configuration) and $n + 3$ are removed and the effect of the internal crack is consistently taken into account.

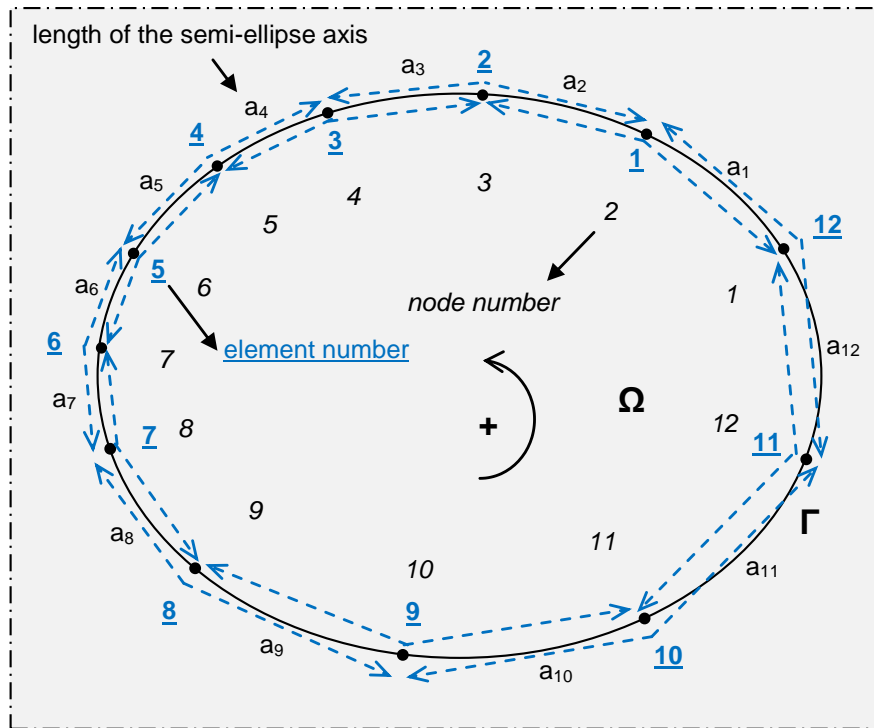


Figure 3: Illustration of a body discretized with 12 linear boundary elements and the corresponding definition of the crack segments.

Define the matrices of potential functions and the matrix \mathbf{N} of shape functions

$$\Phi' = [\Phi'_1 \quad \Phi'_2], \quad \Phi'_{ln} = [\Phi'_1 \quad \Phi'_2]_{ln}, \quad \Phi'_{sqr} = [\Phi'_1 \quad \Phi'_2]_{sqr} \quad (27)$$

$$\mathbf{N} = [N_i \quad N_j] \equiv [1 - \xi \quad \xi] \quad (28)$$

The subscripts $(\cdot)_{ln}$ and $(\cdot)_{sqr}$ indicate that the functions in the matrix coefficients are the ones defined as in Eqs. (25) and (26). Moreover, define the $nn \times nn$ matrix \mathbf{H} with all coefficients initially set as zero.

For the purpose of having the following algorithm as ready as possible for code writing, the coefficients of all matrices are referred to in brackets, whereas the primary variable is given in parentheses, such as $\Phi'(\xi)[c]$, where $c = 1, 2$ for the first matrix in Eq. (27).

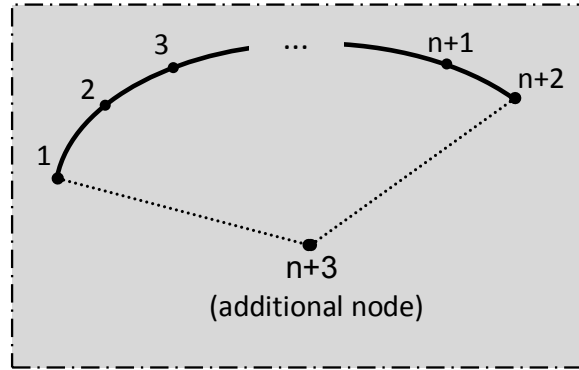


Figure 4: Fictitious node $n + 3$ for the simulation of a curved crack with n nodes and $n + 1$ segments.

5.2.1.1 External loop for the potential jumps – corresponding to the source cracks in elasticity – with k varying from 1 to nn . Determine the adjacent nodes k^- and k^+ , for the nodes numbered counterclockwise. Next, obtain $\cos \theta_1$, $\sin \theta_1$, $\cos \theta_2$, $\sin \theta_2$, according to Section 4.

Define the array of constants

$$\mathbf{C} = \begin{bmatrix} T_1 & -T_2 \end{bmatrix} \quad (29)$$

5.2.1.2 Internal loop for the integration segments with i varying from 1 to nn . Determine the subsequent node j , as integration will be carried out along the segment $\bar{i}j$.

Evaluate $x(\xi)$ and $y(\xi)$ along the segment $\bar{i}j$ as well as the projections dx and dy and the Jacobian $|J|$. Observe that, in Eq. (24), $n_x d\Gamma = dy$ and $n_y d\Gamma = -dx$. Next, evaluate $Z_1(\xi)$ and $Z_2(\xi)$, according to the text after Eq. (12).

Carry out the numerical evaluation of the 2×2 complex array \mathbf{h} in the following *logical if* structure using the procedures *lnproc()* and *sqrtproc()* given in Reference [5]. In the loops to be presented, $c = 1, 2$ refers to either semicrack 1 or 2, and $n = 1, 2$ refers to either extremity i or j of a segment.

5.2.1.3 If $i = k$, then there is an embedded logarithmic singularity at the extremity $\xi = 0$ of the segment $\bar{i}j$ caused by the *potential jumps* along both segments $\bar{k}k^+$ and \bar{k}^-k : case (a) of Fig. 5.

For c and n varying from 1 to 2 in two nested loops,

Define $f = \Phi'(\xi)[c]\mathbf{N}(\xi)[n]$, $f_{ln} = \Phi'_{ln}(\xi)[c]\mathbf{N}(\xi)[n]$, $f_{reg} = f - f_{ln}(\xi) \ln \xi$ and obtain $\mathbf{h}[n, c]$ using the procedure *lnproc(h[n, c])*.

End of the nested loops with control variables c, n .

5.2.1.4 Else if $j = k$, then there is an embedded logarithmic singularity at the extremity $\xi = 1$ of the segment $\bar{i}j$ caused by the *potential jumps* along both segments $\bar{k}k^+$ and \bar{k}^-k : case (b) of Fig. 5.

For c and n varying from 1 to 2 in two nested loops,

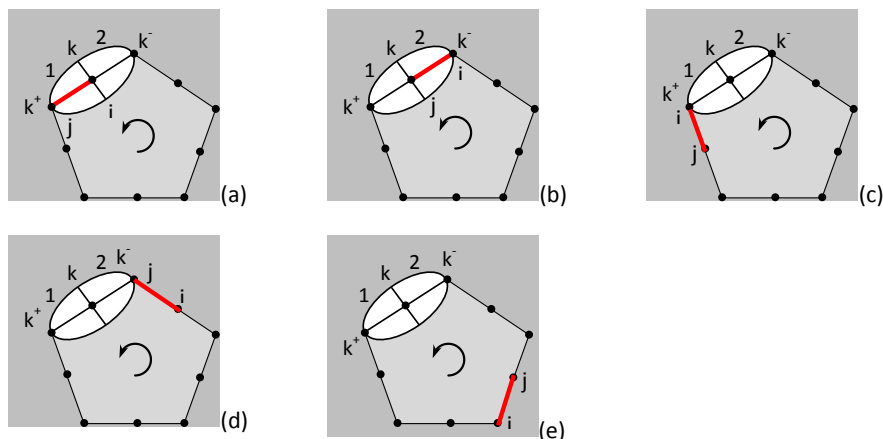


Figure 5: Illustration of the five cases to be taken into account in the numerical evaluation of the integral of Eq. (24).

Define $f = \Phi'(1 - \xi)[c]\mathbf{N}(1 - \xi)[n]$, $f_{ln} = \Phi'_{ln}(1 - \xi)[c]\mathbf{N}(1 - \xi)[n]$, $f_{reg} = f - f_{ln}(\xi) \ln \xi$ and obtain $\mathbf{h}[n, c]$ using the procedure $lnproc(\mathbf{h}[n, c])$.

End of the nested loops with control variables c, n .

5.2.1.5 Else if $i = k^+$, then there is a square-root singularity at the extremity $\xi = 0$ of the segment $\bar{i}j$ caused by the *potential jump* 1 along the segment $\bar{k}k^+$: case (c) of Fig. 5. There is no singularity associated with the *potential jump* 2.

For n varying from 1 to 2,

Define $f = \Phi'(\xi)[1]\mathbf{N}(\xi)[n]$, $f_{sqr} = \Phi'_{sqr}(\xi)[1]\mathbf{N}(\xi)[n]/\sqrt{Z_1(1) - 1}$, $f_{reg} = f - f_{sqr}(\xi)/\sqrt{\xi}$ and obtain $\mathbf{h}[n, 1]$ using the procedure $sqrtproc(\mathbf{h}[n, 1])$.

Define $f = \Phi'(\xi)[2]\mathbf{N}(\xi)[n]$ and carry out the Gauss-Legendre quadrature $\mathbf{h}[n, 2] = \sum_{i_g=1}^{n_g} f(\xi_g[i_g])w_g[i_g]$.

End of the loop with control variable n .

5.2.1.6 Else if $j = k^-$, then there is a square-root singularity at the extremity $\xi = 1$ of the segment $\bar{i}j$ caused by the *potential jump* 2 along the segment \bar{k}^-k : case (d) of Fig. 5. There is no singularity associated with the *potential jump* 1.

For n varying from 1 to 2,

Define $f = \Phi'(1 - \xi)[2]\mathbf{N}(1 - \xi)[n]$, $f_{sqr} = \Phi'_{sqr}(1 - \xi)[2]\mathbf{N}(1 - \xi)[n]/\sqrt{Z_2(0) - 1}$, $f_{reg} = f - f_{sqr}(\xi)/\sqrt{\xi}$ and obtain $\mathbf{h}[n, 2]$ using the procedure $sqrtproc(\mathbf{h}[n, 2])$.

Define $f = \Phi'(\xi)[1]\mathbf{N}(\xi)[n]$ and carry out the Gauss-Legendre quadrature $\mathbf{h}[n, 1] = \sum_{i_g=1}^{n_g} f(\xi_g[i_g])w_g[i_g]$.

End of the nested loops with control variable n .

5.2.1.7 Else there is no singularity: case (e) of Fig. 5.

For c and n varying from 1 to 2 in two nested loops,
 Define $f = \Phi'(\xi)[c]\mathbf{N}(\xi)[n]$ and carry out the Gauss-Legendre quadrature $\mathbf{h}[n, c] = \sum_{i_g=1}^{n_g} f(\xi_g[i_g])w_g[i_g]$.
 End of the nested loops with control variables c, n .

5.2.1.8 End if End of the *structured logical if*.

Define the matrix of boundary unit projections referred to the segment \overline{ij} , as introduced in Eq. (22),

$$\mathbf{n} = \begin{bmatrix} n_x & n_y \end{bmatrix} \quad (30)$$

The coefficient H_{coef} of the matrix \mathbf{H} in Eq. (24) is obtained in the following loop, according to Eq. (18), for nodes i and j given in the array $\mathbf{i} \equiv [i, j]$.

5.2.1.9 Loop for extremities i and j , with n varying from 1 to 2. Evaluate the matrix expression (an inner product, for potential problems)

$$H_{coef} = \left[\sum_{c=1}^2 \mathbf{C}[c, 1] \text{Im}(\mathbf{h}[n, c]) + \mathbf{C}[c, 2] \text{Re}(\mathbf{h}[n, c]) \right] \mathbf{n}^T \quad (31)$$

The matrix \mathbf{H} , whose coefficients may already have contribution from a preceding integration over an adjacent segment, is obtained as

$$\mathbf{H}[k, \mathbf{i}[n]] = \mathbf{H}[k, \mathbf{i}[n]] + H_{coef} \quad (32)$$

5.2.1.10 End of loops with control variables n, i, k .

6 A numerical example

A logarithmic potential source $\Phi = \ln \sqrt{(x+10)^2 + (y-25)^2} / (2\pi)$ is applied at node \mathbf{F} of an unbounded two-dimensional continuum, as illustrated in Figure 6. One cuts out the depicted irregular figure and applies the generated potential and gradients to the drawn boundaries, thus creating a problem (for the Laplace equation) of simple, known analytical solution. However, the reentrant corner and the internal hole of the figure pose some topological difficulties to the numerical simulation of the potential problem. The figure is composed of a total of 104 nodes and linear segments, which are equally spaced between the indicated corner nodes, whose coordinates are given in Table 1. A series of 51 point along the line segment \overline{AB} are also generated for the representation of numerical results at internal points.

The simplest problem that can be solved in this example is for Neumann boundary conditions, when only the matrix \mathbf{H} of Eq. (6), as developed in Eq. (24) for potential problems, needs be evaluated. Although \mathbf{H} is a singular matrix for a bounded domain, the equivalent nodal gradients \mathbf{p} of Eq. (6) are in balance and the posed linear algebra problem admits of just one solution \mathbf{p}^* , to be obtained in the frame of generalized inverse matrices [2, 3, 5, 7]. Once \mathbf{p}^* is evaluated, gradients and potentials can

Node	1	17	27	50	69	87	93	99	A	B	F
x	0	10	20	15	0	10	11	12	5	15	-10
y	0	15	10	35	20	20	21	20	20	18	25

Table 1: Cartesian Coordinates of the nodes that constitute Fig. 6.

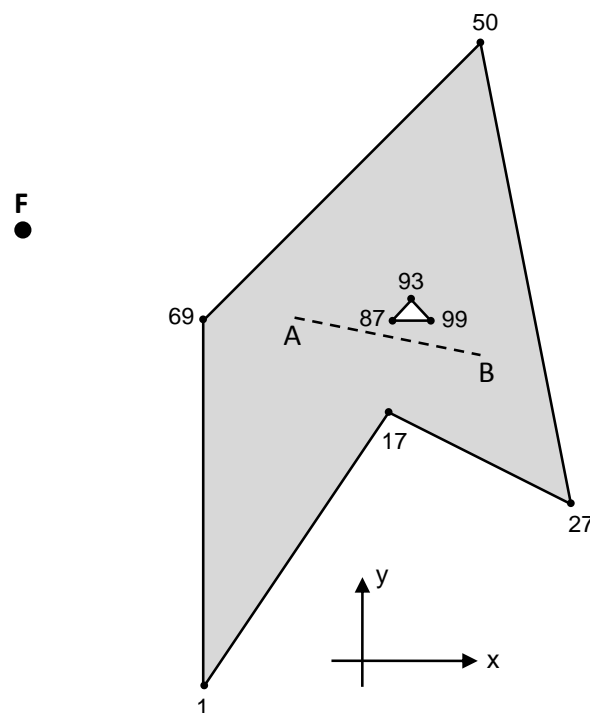


Figure 6: Cut-out model for the numerical modeling of a multiply connected body.

be obtained according to Eqs. (4) and (5). Figure 7 shows on the left both analytical and numerical values of the potential, as obtained along the line segment \overline{AB} . Since this is a Neumann problem, a constant potential was added to the numerical results in order that both analytical and numerical values best coincide. Analytical and numerical values of gradients are also shown in Fig. 7.

Comparisons with a code developed using Kelvin fundamental solution ($\Phi = \ln r$, for potential problems) have been already carried out. The accuracy is matched for internal points that are far from the boundary. However, the boundary layer effect is larger in the case of fundamental solutions defined in terms of generalized Westergaard functions. This is expected, as the gradient singularity

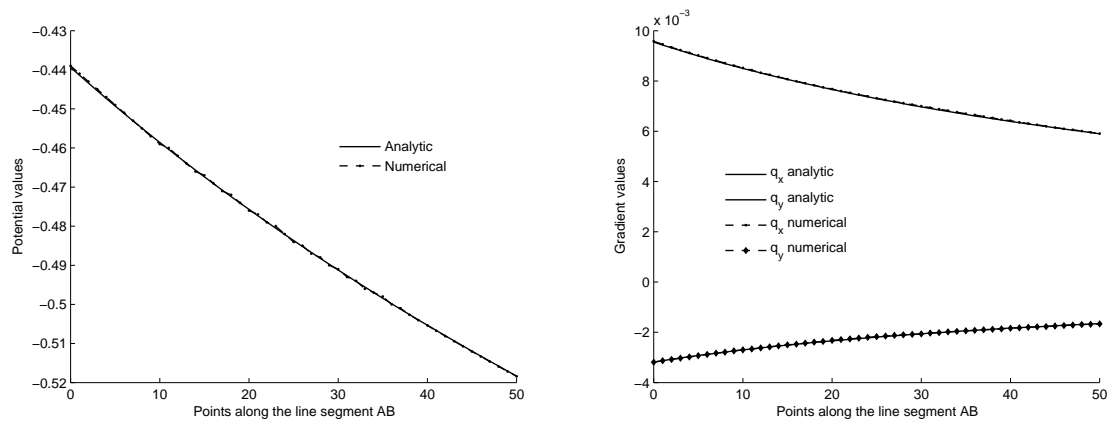


Figure 7: Comparison of some analytical and numerical results for the example of Fig. 6.

$1/r$ for Kelvin's solution is more pronounced and localized than the singularity $\sqrt{1/r}$ of the Westergaard function dealt with in this paper. In spite of this more pronounced boundary layer effect, good accuracy can be still achieved with some post-processing of the results, as done for the case of Kelvin fundamental solutions [11].

7 Conclusions

The paper presents a novel development of fundamental solutions that are based on generalized Westergaard stress functions and are suited for boundary element applications. Although this outline has used a variational framework – the hybrid boundary element method – as reference for the numerical implementations, it is possible to use these fundamental solutions in the conventional, collocation boundary element method, provided only that some concepts be borrowed from the hybrid boundary element method to allow for the evaluation of results at internal points (in order to circumvent resorting to the time-consuming Somigliana's identity). The evaluation of stress intensity factors in fracture mechanics problems – a paramount issue and the primary motivation to the present work – can be carried out easier and more accurately in the present context than using existing finite element and boundary element codes. The analytical nature of the singularity of the stress gradients around a crack tip, as dealt with in terms of Westergaard functions, offers some conceptual possibilities of better assessing the fracture mechanics problem, too.

Acknowledgments This project was supported by the Brazilian agencies CAPES, CNPq and FAPERJ.

References

- [1] Tada, H., Ernst, H. & Paris, P., Westergaard stress functions for displacement-prescribed crack problems - I. *International Journal of Fracture*, **61**, pp. 39–53, 1993.
- [2] Dumont, N.A. & Lopes, A.A.O., On the explicit evaluation of stress intensity factors in the hybrid boundary element method. *Fatigue & Fracture of Engineering Materials & Structures*, **26**, pp. 151–165, 2003.
- [3] Mamani, E.Y., *The hybrid boundary element method based on generalized Westergaard stress functions (in Portuguese)*. Master's thesis, Pontifical Catholic University of Rio de Janeiro, 2011.
- [4] Dumont, N.A., Dislocation-based hybrid boundary element method, 2008. Draft paper.
- [5] Dumont, N.A. & Mamani, E.Y., Use of generalized Westergaard stress functions in the hybrid boundary element method, 2011. (to be submitted).
- [6] Pian, T.H.H., Derivation of element stiffness matrices by assumed stress distribution. *AIAA Journal*, **2**, pp. 1333–1336, 1964.
- [7] Dumont, N.A., The hybrid boundary element method: an alliance between mechanical consistency and simplicity. *Applied Mechanics Reviews*, **42(11)**, pp. S54–S63, 1989.
- [8] Dumont, N.A. & de Oliveira, R., From frequency-dependent mass and stiffness matrices to the dynamic response of elastic systems. *International Journal of Solids and Structures*, **38(10-13)**, pp. 1813–1830, 2001.
- [9] Dumont, N.A., Chaves, R.A.P. & Paulino, G.H., The hybrid boundary element method applied to problems of potential of functionally graded materials. *International Journal of Computational Engineering Science (IJCES)*, **5**, pp. 863–891, 2004.
- [10] Dumont, N.A. & Huamán, D., Hybrid finite/boundary element formulation for strain gradient elasticity problems. *BETeq 2009 - International Conference on Boundary Element Techniques*, eds. E.J. Sapountzakis & M.H. Aliabadi, Athens, Greece, pp. 295–300, 2009.
- [11] Dumont, N.A., The hybrid boundary element method – fundamentals (to be submitted). *Engineering Analysis with Boundary Elements*, 2011.
- [12] Dumont, N.A., Variationally-based, hybrid boundary element methods. *Computer Assisted Mechanics and Engineering Sciences (CAMES)*, **10**, pp. 407–430, 2003.
- [13] Brebbia, C.A., Telles, J.F.C. & Wrobel, L.C., *Boundary Element Techniques*. Springer-Verlag, Berlin, 1984.

On buckling enhancement of laminated plates with piezoelectric actuators via stress stiffening

Alfredo R. de Faria

*Instituto Tecnológico de Aeronáutica, CTA - ITA - IEM,
São José dos Campos, 12228-900, SP - Brazil*

Maurício V. Donadon

*Instituto Tecnológico de Aeronáutica, CTA - ITA - IEA,
São José dos Campos, 12228-900, SP - Brazil*

Abstract

The prebuckling enhancement of composite plates equipped with piezoelectric actuators is the subject of this paper. Piezoelectric actuators are used to induce in-plane traction stiffening stresses in a composite plate, thereby counteracting external compressive stresses that render the structure unstable. The objective is to create in-plane piezoelectric stiffening stresses to enhance buckling loads of laminated plates. The idea is to completely restrain in-plane displacements on its boundary and to apply voltage to piezoelectric actuators symmetrically bonded to the top and bottom surfaces. This voltage is applied such that the piezoelectric actuators shrink generating traction stresses in the plate plane. Therefore, if external compressive stresses destabilize the structure the stiffening piezoelectric traction stresses will act, re-stabilizing the structure. Analytical approximations and the finite element method are used to compute the piezoelectric stiffening stresses whereas the finite element method is used to solve the buckling problem. The results presented consider bifurcation buckling, although the formulation proposed is general enough to be applicable for nonlinear analysis and critical point type of buckling.

Keywords: buckling, piezoelectric, stress stiffening, composites.

1 Introduction

Composite structures are usually thin in order to save weight, what makes them prone to buckling caused by several types of loadings (mechanical, thermal, etc.). The incorporation of sensors and actuators to composite structures is a way of increasing buckling loads. These systems, composed of host structure and active elements, are then controlled to achieve greater buckling capacity. The active control may be implemented using a variety of materials. Piezoelectric materials, extensively investigated in the last three decades [1–3], are again becoming popular. These material are applicable

in areas such as shape control, noise suppression, mitigation of residual vibrations and maximization of buckling loads.

One of the first studies addressing stability of laminated plates with piezoelectric sensors and actuators attached was carried out by Chandrashenkara and Bathia [4]. They developed finite element models, based on the theory of Reissner-Mindlin, to conduct the study. In the same year Meressi and Paden [2] obtained linearized governing equations of motion of flexible beams with piezoelectric actuators. Their conclusion was that the beam could have its buckling load increased through the use of electromechanical effects.

Piezoelectric stiffening effects, also used to advantage in the present work, were shown to significantly affect the natural frequencies of composite plates as reported by Donadon *et al.* [5]. Electromechanical finite elements were developed to numerically analyze composite plates with piezoelectric actuators and sensors bonded. Several plate configurations were investigated, numerically and experimentally.

Piezoelectric stiffening was used to increase buckling loads of axially restrained composite beams [6]. Nonzero traction forces generated by piezoelectric actuators along the beam are shown to increase stiffness elevating the loading capacity of the structure against buckling.

Kundun *et al.* [7] used the theory of nonlinear large deformations to study post-buckling of piezoelectric laminated shells with double curvature through the finite element method. Batra and Geng [8] and Shariyat [9] present proposals to enhance dynamic buckling of flexible plates.

Recently more sophisticated plate theories that consider piezoelectric effects have been developed [10–12]. Basically these theories adopt improved kinematic relations for the displacement and electric fields. In the present work a thin composite plate is investigated due to its applicability in the aerospace industry. Thus, the traditional Mindlin plate theory [13] is simple and precise enough for the purpose of this investigation and therefore has been chosen as the basis of the finite element formulations developed.

This work addresses buckling load improvement of composite plates equipped with piezoelectric actuators. These actuators generate nonzero traction forces in the plate plane which, through stress stiffening, increase the plate bending stiffness. The plate has its edges constrained in the plane and negative voltages are applied to the piezo actuators. The actuators tend to shrink inducing traction forces over the plate plane. Hence, if external compressive forces destabilize the plate, the stiffening piezoelectric traction stresses will restabilize it. Piezoelectric stiffening stresses are evaluated analytically for a simple configuration and numerically through the finite element method in more complex scenarios. The major concern is with the bifurcation type of buckling encountered in plates. However, the present formulation is general enough to be extended to nonlinear analyses and critical point type of buckling.

2 Problem formulation

The electromechanical behavior of a plate containing layers of the piezoelectric actuators bonded on its top and bottom surfaces is described by differential governing equations. In these equations the electric potential is assumed constant over the surface of the piezoelectric layers and varying linearly along the thickness of these layers whereas the buckling analysis of the laminated plate is based on

the Mindlin plate theory.

A rectangular plate equipped with an arbitrary number of patches of piezoelectric actuators symmetrically bonded to its top and bottom surfaces is taken as the basic configuration. Three possible configurations are shown in Fig. 1.

In the prebuckling regime only in-plane displacements u and v arise due to two mechanisms: (i) application of in-plane forces N_{xx0} , N_{yy0} , N_{xy0} or (ii) application of equal and nonzero voltages to the top and bottom piezoelectric patches. In this phase the plate has its four edges restrained such that $u = v = 0$. This is a typical situation of a plate mounted on a primary structure. Moreover, if the plate was free-free (completely unrestrained), there would be no piezoelectric stiffening stresses.

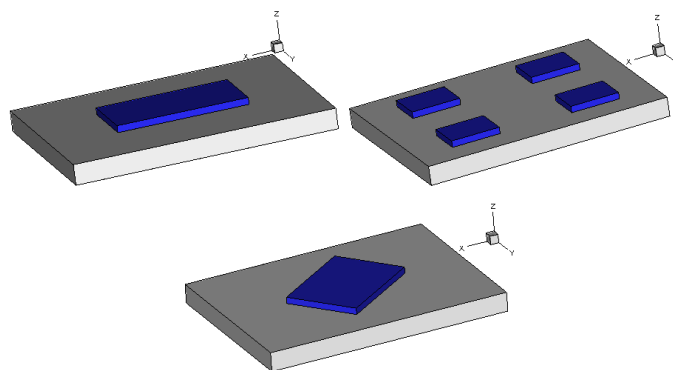


Figure 1: Basic configurations.

Assuming that the piezoelectric layers are polarized along the z direction (perpendicular to the plate) the constitutive equations are given in Eq. (1).

$$\boldsymbol{\sigma} = \bar{\mathbf{Q}}\boldsymbol{\epsilon} - \mathbf{e}^T \mathbf{E}, \quad \boldsymbol{\tau} = \bar{\mathbf{Q}}_S \boldsymbol{\gamma}, \quad \mathbf{d} = \mathbf{e}\boldsymbol{\epsilon} + \boldsymbol{\xi} \mathbf{E}, \quad (1)$$

where $\boldsymbol{\sigma}$ are in-plane stresses, $\boldsymbol{\tau}$ are out-of-plane shear stresses, $\boldsymbol{\epsilon}$ are the in-plane strains including nonlinear components, $\boldsymbol{\gamma}$ are the out-of-plane shear strains, $\bar{\mathbf{Q}}$ is the ply in-plane stiffness matrix in the structural coordinate system, $\bar{\mathbf{Q}}_S$ is the ply out-of-plane shear stiffness matrix in the structural coordinate system, \mathbf{d} is the electric displacement, \mathbf{E} is the electric field, \mathbf{e} is the electro-mechanical coupling matrix and $\boldsymbol{\xi}$ is the permittivity matrix. It can be seen that $\boldsymbol{\tau}$ is unaffected by piezoelectric effects [10]. Both composite and piezoelectric materials obey Eq. (1) but the pure composite layer has $\mathbf{e} = \mathbf{0}$.

The total potential energy of the conservative system is

$$\Pi = \frac{1}{2} \int_V \boldsymbol{\sigma}^T \boldsymbol{\epsilon} dV + \frac{1}{2} \int_V \boldsymbol{\tau}^T \boldsymbol{\gamma} dV - \frac{1}{2} \int_V \mathbf{d}^T \mathbf{E} dV - W, \quad (2)$$

where the work of external forces N_{xx0} , N_{yy0} , N_{xy0} is represented by W .

The kinematic assumption for the Mindlin plate displacement reads:

$$\tilde{u}(x, y, z) = u(x, y) + z\psi_x(x, y), \quad \tilde{v}(x, y, z) = v(x, y) + z\psi_y(x, y), \quad \tilde{w}(x, y, z) = w(x, y), \quad (3)$$

where u, v, w are the mid plane displacements ($z = 0$), ψ_x, ψ_y are the mid plane rotations and $\tilde{u}, \tilde{v}, \tilde{w}$ are the displacements of an arbitrary point in the plate. The strains ϵ are composed of three components: membrane strains ϵ_0 , curvature κ and nonlinear von Karman strains ϵ_N such that

$$\epsilon = \epsilon_0 + z\kappa + \epsilon_N = \begin{Bmatrix} u_{,x} \\ v_{,y} \\ u_{,y} + v_{,x} \end{Bmatrix} + z \begin{Bmatrix} \psi_{x,x} \\ \psi_{y,y} \\ \psi_{x,y} + \psi_{y,x} \end{Bmatrix} + \frac{1}{2} \begin{Bmatrix} w_{,x}^2 \\ w_{,y}^2 \\ 2w_{,x}w_{,y} \end{Bmatrix},$$

$$\gamma = \begin{Bmatrix} w_{,x} + \psi_x \\ w_{,y} + \psi_y \end{Bmatrix}. \quad (4)$$

Vectors $\mathbf{N} = \{ N_{xx} \ N_{yy} \ N_{xy} \}^T$, $\mathbf{M} = \{ M_{xx} \ M_{yy} \ M_{xy} \}^T$, $\mathbf{Q} = \{ Q_{xx} \ Q_{yy} \}^T$ and $\mathbf{F} = \{ F_{xx} \ F_{yy} \ F_{xy} \}^T$, and matrices $\mathbf{A}, \mathbf{B}, \mathbf{D}$ and \mathbf{A}_S are defined in Eq. (5) in order to facilitate manipulation of Eq. (2).

$$(\mathbf{A}, \mathbf{B}, \mathbf{D}) = \int_{-h/2}^{h/2} (1, z, z^2) \overline{\mathbf{Q}} dz, \quad \mathbf{A}_S = \int_{-h/2}^{h/2} \overline{\mathbf{Q}}_S dz, \quad \mathbf{Q} = \mathbf{A}_S \gamma,$$

$$\mathbf{F} = \int_{-h/2}^{h/2} \mathbf{e}^T \mathbf{E} dz, \quad \begin{Bmatrix} \mathbf{N} \\ \mathbf{M} \end{Bmatrix} = \begin{bmatrix} \mathbf{A} & \mathbf{B} \\ \mathbf{B} & \mathbf{D} \end{bmatrix} \begin{Bmatrix} \epsilon_0 + \epsilon_N \\ \kappa \end{Bmatrix}, \quad (5)$$

where the integrals are computed over the plate total thickness h . Notice that \mathbf{N}, \mathbf{F} are in-plane forces per unit length, \mathbf{Q} are shear forces per unit length, and \mathbf{M} are bending moments per unit length but, consistently with usual terminology, these will be simply referred to as forces or moments, respectively. It is important to remark that the thickness h is total, including possibly piezoelectric layers. Therefore, piezoelectric layers make a contribution to the laminate stiffness matrices $\mathbf{A}, \mathbf{B}, \mathbf{D}$ and \mathbf{A}_S . However, vector \mathbf{F} of piezoelectric force is nonzero only if there are piezoelectric layers present in the laminate and an electric potential is applied. Instead of using the electric field E_z it is common to introduce the voltage ϕ and piezoelectric layer thickness t to write $E_z = \phi/t$ such that Eq. (5d) becomes [14]

$$\begin{Bmatrix} F_{xx} \\ F_{yy} \\ F_{xy} \end{Bmatrix} = \begin{Bmatrix} e_{31}(\phi_T + \phi_B) \\ e_{32}(\phi_T + \phi_B) \\ 0 \end{Bmatrix}, \quad (6)$$

where the voltages applied to the top and bottom surfaces of the plate are denoted respectively by ϕ_T and ϕ_B . In practice $e_{32} = e_{31}$, what leads to $F_{xx} = F_{yy}$.

Considering prescribed voltages (pure actuation) Eqs. (4) and (5) can be used in Eq. (2) to yield the first variation of Π :

$$\delta\Pi = \int_{\Omega} (\mathbf{N}^T \delta\epsilon_0 + \mathbf{N}^T \delta\epsilon_N + \mathbf{M}^T \delta\kappa + \mathbf{Q}^T \delta\gamma - \mathbf{F}^T \delta\epsilon_0 - \mathbf{F}^T \delta\epsilon_N) d\Omega - \int_{\Gamma} (N_{xx0}, N_{xy0}) \cdot \vec{n} \delta u d\Gamma - \int_{\Gamma} (N_{xy0}, N_{yy0}) \cdot \vec{n} \delta v d\Gamma = 0, \quad (7)$$

where Ω is the in-plane plate domain, N_{xx0} , N_{yy0} , N_{xy0} are membrane forces applied along the plate edge Γ (the boundary of Ω), \vec{n} is the unit vector normal to Γ and the term containing $z\mathbf{F}^T \delta\kappa$ was abandoned since full symmetry ($\phi_T = \phi_B$) has been admitted. Notice that if $\phi_T \neq \phi_B$ then the prebuckling problem would result in nonzero out-of-plane displacements ($w \neq 0$) and no bifurcation type buckling would occur.

Equations (4) can be substituted into Eq. (7) and, after application of Green's theorem, allows one to derive five governing equations

$$\begin{aligned} (N_{xx} - F_{xx})_{,x} + (N_{xy} - F_{xy})_{,y} &= 0 \quad , \quad (N_{xy} - F_{xy})_{,x} + (N_{yy} - F_{yy})_{,y} = 0, \\ M_{xx,x} + M_{xy,y} &= Q_{xx} \quad , \quad M_{yy,y} + M_{xy,x} = Q_{yy}, \\ Q_{xx,x} + Q_{yy,y} + (N_{xx} - F_{xx})w_{,xx} + (N_{yy} - F_{yy})w_{,yy} + 2(N_{xy} - F_{xy})w_{,xy} &= 0 \end{aligned} \quad (8)$$

and in-plane boundary conditions valid on the plate's edges:

$$\begin{aligned} (N_{xx} - F_{xx}, N_{xy} - F_{xy}) \cdot \vec{n} \delta u &= (N_{xx0}, N_{xy0}) \cdot \vec{n} \delta u \\ (N_{xy} - F_{xy}, N_{yy} - F_{yy}) \cdot \vec{n} \delta v &= (N_{xy0}, N_{yy0}) \cdot \vec{n} \delta v. \end{aligned} \quad (9)$$

It must be clear that there are three additional boundary conditions associated with δw , $\delta\psi_x$, $\delta\psi_y$ that, although necessary to solve the buckling problem, are not present in Eq. (9).

The piezoelectric stiffening stress resultants $(N_{xx} - F_{xx})$, $(N_{xy} - F_{xy})$ and $(N_{yy} - F_{yy})$ are evident in Eqs. (8) and (9). According to Eq. (8c-e), buckling never occurs if there are no piezoelectric stiffening stresses. Actually, there are two possibilities for buckling to occur: (i) nonzero piezoelectric stiffening stresses must exist or (ii) external in-plane mechanical forces N_{xx0} , N_{yy0} or N_{xy0} must be present, what corresponds to the traditional buckling problem. Situation (i) is addressed in detail in the next section.

3 Piezoelectric stiffening stresses

The distribution of piezoelectric stiffening stresses can be obtained through solution of the differential equations (8a) and (8b) imposing the boundary conditions given in Eq. (9). A closed-form solution does not exist specially due to the stiffness and piezoelectric force discontinuities on the plate caused by piezoelectric patches. The addition of piezoelectric layers to the laminated plate obviously increases

the in-plane laminate matrix \mathbf{A} . Also, if nonzero voltages are applied to the patches, then nonzero forces F_{xx} , F_{yy} , F_{xy} arise.

The purpose of this paper is to improve buckling behavior or to increase buckling loads of structures whose buckling is of bifurcation type. This can be achieved by proper tailoring of piezoelectric stiffening stresses. Since composite plates exhibit bifurcation type of buckling they are investigated. In the bifurcation type buckling of composite plates there is no out-of-plane displacements w in the prebuckling regime when there is full symmetry on the actuators part ($\phi_T = \phi_B$ and $t_T = t_B$) and the laminate is symmetric ($\mathbf{B} = \mathbf{0}$). Under these assumptions the linear differential equations in the prebuckling regime can be obtained through specialization of Eq. (7):

$$\delta\Pi = \int_{\Omega} \begin{Bmatrix} \delta u_{,x} \\ \delta v_{,y} \\ \delta u_{,y} + \delta v_{,x} \end{Bmatrix}^T \left(\begin{bmatrix} A_{11} & A_{12} & A_{16} \\ A_{12} & A_{22} & A_{26} \\ A_{16} & A_{26} & A_{66} \end{bmatrix} \begin{Bmatrix} u_{,x} \\ v_{,y} \\ u_{,y} + v_{,x} \end{Bmatrix} - \begin{Bmatrix} F_{xx} \\ F_{yy} \\ F_{xy} \end{Bmatrix} \right) d\Omega = 0. \quad (10)$$

Even after simplification a closed-form solution to Eq. (10) is not possible. However, an approximate closed-form solution can be obtained if a symmetric configuration is investigated. If only one piezoelectric patch aligned with the plate's edges is bonded at the center of the rectangular plate (see Fig. 2) then symmetry and boundary conditions read:

- Edge $y = 0$: $v(x, 0) = v_{,x}(x, 0) = v_{,xx}(x, 0) = \dots = 0$, $u_{,y}(x, 0) = 0$;
- Edge $x = 0$: $u(0, y) = u_{,y}(0, y) = u_{,yy}(0, y) = \dots = 0$, $v_{,x}(0, y) = 0$;
- Edge $y = L_y$: $v(x, L_y) = v_{,x}(x, L_y) = v_{,xx}(x, L_y) = \dots = 0$, $u_{,y}(x, L_y) = 0$;
- Edge $x = L_x$: $u(L_x, y) = u_{,y}(L_x, y) = u_{,yy}(L_x, y) = \dots = 0$, $v_{,x}(L_x, y) = 0$.

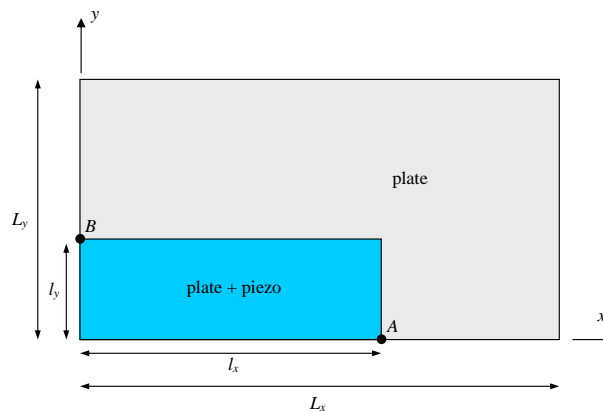


Figure 2: Basic dimensions

Symmetry of the problem allows one to conclude that $v(x, 0) = 0$, $u(0, y) = 0$, $u_{,y}(x, 0) = 0$ and $v_{,x}(0, y) = 0$. $v(x, L_y) = 0$ and $u(L_x, y) = 0$ are enforced geometric boundary conditions. For a balanced laminate ($A_{16} = A_{26} = 0$ in Eq. (10)) the conditions $u_{,y}(x, L_y) = 0$ and $v_{,x}(L_x, y) = 0$ result from the requirements that $N_{xy}(x, L_y) = N_{xy}(L_x, y) = 0$. The boundary condition in Eq. (9) also imposes that continuity on $N_{xx} - F_{xx}$ and $N_{xy} - F_{xy}$ along any line of constant y must be satisfied as well as continuity on $N_{xy} - F_{xy}$ and $N_{yy} - F_{yy}$ along any line of constant x . Moreover, since no fracture is assumed, continuity of displacements u and v throughout must be enforced.

The continuity conditions on $N_{xx} - F_{xx}$ for point A and $N_{yy} - F_{yy}$ for point B can be written, along lines $y = 0$, $x = 0$, as in Eq. (11):

$$\begin{aligned} A_{11}^* u_{,x}^*(l_x, 0) + A_{12}^* v_{,y}^*(l_x, 0) - F_{xx} &= A_{11} u_{,x}(l_x, 0) + A_{12} v_{,y}(l_x, 0), \\ A_{12}^* u_{,x}^*(0, l_y) + A_{22}^* v_{,y}^*(0, l_y) - F_{yy} &= A_{12} u_{,x}(0, l_y) + A_{22} v_{,y}(0, l_y). \end{aligned} \quad (11)$$

where a superscript (*) means that point on the xy plane has both plate and piezoelectric materials. Discontinuity on $u_{,x}(x, 0)$ and $v_{,y}(0, y)$ can be inferred from Eqs. (11). Since discontinuity in the first derivatives naturally arise in this particular problem a finite element formulation based on the classical plate theory is not applicable since it would enforce continuity on $u_{,x}$ and $v_{,y}$. Hence, Mindlin type of elements constitute a better option for they are able to capture discontinuities on the first derivatives of u and v . This element will be detailed in the next section.

Approximate solutions to Eq. (10) under boundary conditions of Eqs. (11) might be obtained using the Navier method. However, the complexity introduced by the material and geometry discontinuities would have to be properly treated. Since derivation of analytical solutions is not the main objective, the approach adopted to find approximate closed-form solutions to Eq. (10) consists in assuming that the plate depicted in Fig. 2 has a beam-like type of behavior along lines $y = 0$, $x = 0$. Obviously this means that Poisson effects, that may be significant in plate problems, are completely neglected. Thus, the in-plane differential equations simplify to $u_{,xx}(x, 0) = 0$ and $v_{,yy}(0, y) = 0$. Furthermore, Eqs. (11) become

$$\begin{aligned} A_{11}^* u_{,x}^*(l_x, 0) - F_{xx} &= A_{11} u_{,x}(l_x, 0), \\ A_{22}^* v_{,y}^*(0, l_y) - F_{yy} &= A_{22} v_{,y}(0, l_y). \end{aligned} \quad (12)$$

When the boundary conditions $u(0, 0) = u(L_x, 0) = 0$ and $v(0, 0) = v(0, L_y) = 0$ and the jump conditions of Eq. (12) are considered, $u_{,xx}(x, 0) = 0$ and $v_{,yy}(0, y) = 0$ may be solved leading to:

$$\begin{aligned} u^*(x, 0) &= \frac{\left(\frac{1}{L_x} - \frac{1}{l_x}\right) x F_{xx}}{\left[A_{11}^* \left(\frac{1}{L_x} - \frac{1}{l_x}\right) - A_{11} \frac{1}{L_x}\right]}, \quad u(x, 0) = \frac{\left(\frac{x}{L_x} - 1\right) F_{xx}}{\left[A_{11}^* \left(\frac{1}{L_x} - \frac{1}{l_x}\right) - A_{11} \frac{1}{L_x}\right]}, \\ v^*(0, y) &= \frac{\left(\frac{1}{L_y} - \frac{1}{l_y}\right) y F_{yy}}{\left[A_{22}^* \left(\frac{1}{L_y} - \frac{1}{l_y}\right) - A_{22} \frac{1}{L_y}\right]}, \quad v(0, y) = \frac{\left(\frac{y}{B} - 1\right) F_{yy}}{\left[A_{22}^* \left(\frac{1}{L_y} - \frac{1}{l_y}\right) - A_{22} \frac{1}{L_y}\right]}. \end{aligned} \quad (13)$$

The piezoelectric stiffening stress resultants given in Eqs. (11) simplify to:

$$T_{xx} = A_{11}^* u_{,x}^*(x, 0) - F_{xx} = A_{11} u_{,x}(x, 0) = \frac{F_{xx}}{\frac{A_{11}^*}{A_{11}} \left(1 - \frac{L_x}{l_x}\right) - 1},$$

$$T_{yy} = A_{22}^* v_{,y}^*(0, y) - F_{yy} = A_{22} v_{,y}(0, y) = \frac{F_{yy}}{\frac{A_{22}^*}{A_{22}} \left(1 - \frac{L_y}{l_y}\right) - 1}. \quad (14)$$

A numerical example can be solved if one adopts a few properties. Typical physical properties are given in Tab. 1. Geometric parameters are plate semi-length $L_x = 0.2$ m, plate semi-width $L_y = 0.15$ m, piezoelectric actuator semi-length $l_x = 0.15$ m and semi-width $l_y = 0.05$ m. The cross-ply laminate $[0/90]_S$ (which is symmetric and balanced) has four layers of 0.15 mm thickness. Piezoelectric layers (top and bottom) are 0.05 mm thick. A voltage of $\phi_T = \phi_B = 50$ V is applied. This voltage corresponds to the depoling field given in Tab. 1 since $50 \text{ V} / 0.05 \text{ mm} = 1000 \text{ V/mm}$.

Table 1: Physical properties

Property	G1195N	T300/5208
Young modulus E_{11} (GPa)	63.0	154.5
Young modulus E_{22} (GPa)	63.0	11.13
Poisson ratio ν_{12}	0.3	0.304
Shear modulus $G_{12} = G_{13}$ (GPa)	24.2	6.98
Shear modulus G_{23} (GPa)	24.2	3.36
Piezoelectric constant e_{31} (N/V m)	17.6	-
Piezoelectric constant e_{32} (N/V m)	17.6	-
Depoling field E_{MAX} (V/mm)	1000	-

Figures 3 and 4 present a comparison between the analytical solutions given in Eq. (13) and the FE numerical solution, where $\xi = x/L_x$ and $\eta = y/L_y$. It is clear that the analytical solution along $y = 0$ is a very good approximation to the actual displacements. Both u and $u_{,x}$ agree well. However, the same is not true for analytical solution along $x = 0$. It can be observed that, although the patterns for v and $v_{,y}$ are similar in shape, their magnitudes are completely dispair. The conclusion is that, in this particular configuration, the plate behaves much like a beam in the x direction but not in the y direction.

Closer observation of Eq. (14) reveals that the piezoelectric stiffening stress resultants depend basically on two parameters: the relative stiffness $a = A_{11}^*/A_{11}$ and the nondimensional actuator length l_x/L_x . In the particular example selected $a = 1.14$ and $l_x/L_x = 0.75$. Figure 5 shows that, the smaller a , the greater is the efficiency to generate piezoelectric stiffening stresses. Fortunately,

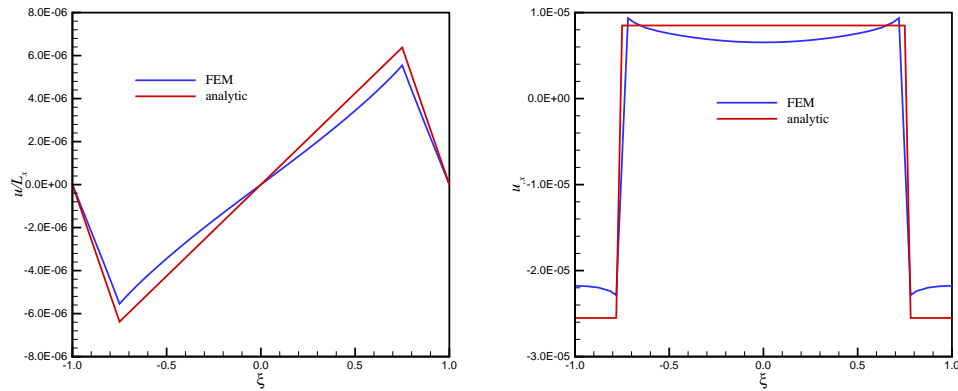


Figure 3: Comparison FEM vs. analytical solutions along $y = 0$

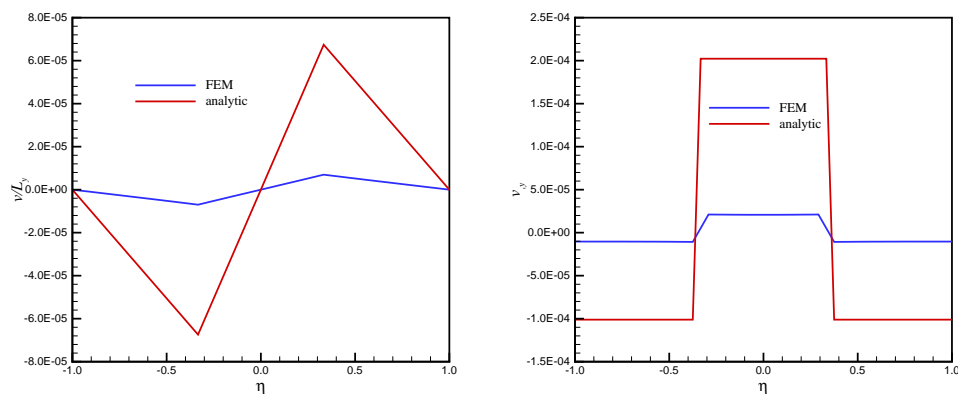


Figure 4: Comparison FEM vs. analytical solutions along $x = 0$

in aerospace applications, thin piezoelectric actuators are used leading to practical situations where $1.0 < a \leq 1.2$.

The stiffening stress resultants N_{xx} and N_{yy} are shown in Fig. 6 where the boundary of the piezoelectric actuator is highlighted in black. Notice that N_{xx} is highly discontinuous along $x = 0$ and so is N_{yy} along $y = 0$. The discontinuities observed numerically are consistent with Eq. (12). Additionally, the region where there is compression in the x direction ($N_{xx} < 0$) is mostly limited to the region underneath the actuators. However, the same cannot be said about N_{yy} . This suggests that long piezoelectric film strips with large aspect ratios are able to orient stiffening stresses more efficiently than those with aspect ratios close to unity.

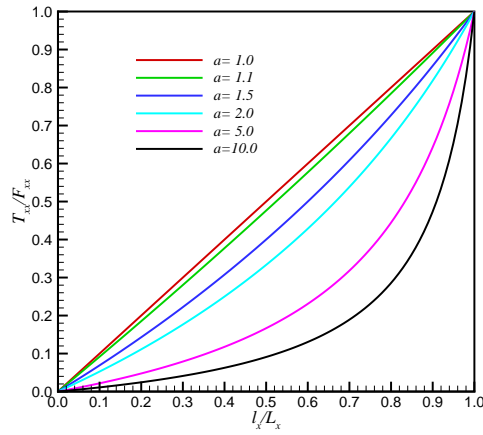


Figure 5: Stress stiffening efficiency varying with relative stiffness

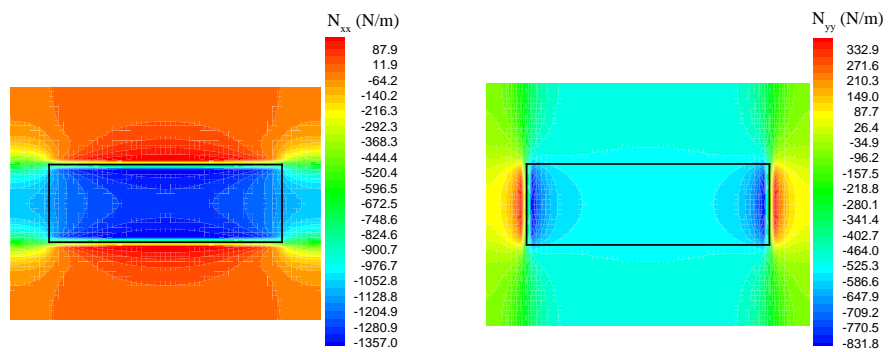


Figure 6: Stiffening stress distribution in terms of resultant forces

4 Piezoelectric stress stiffening and buckling

Considering that the membrane prebuckling problem given in Eq. (10) is satisfied, the FEM buckling equations can be derived from Eq. (7) to yield

$$\delta\Pi = \int_{\Omega} (\mathbf{M}^T \delta\boldsymbol{\kappa} + \mathbf{Q}^T \delta\boldsymbol{\gamma}) d\Omega + \int_{\Omega} (\mathbf{N} - \mathbf{F})^T \delta\boldsymbol{\epsilon}_N d\Omega. \quad (15)$$

The finite element method is used to solve the governing buckling problem Eq. (15). The element used is biquadratic depicted in Fig. 7 whose interpolation functions are:

$$\begin{aligned}
 N_1(\xi, \eta) &= \frac{1}{4}\xi(\xi - 1)\eta(\eta - 1) & N_2(\xi, \eta) &= \frac{1}{2}(1 - \xi^2)\eta(\eta - 1) & N_3(\xi, \eta) &= \frac{1}{4}\xi(\xi + 1)\eta(\eta - 1) \\
 N_4(\xi, \eta) &= \frac{1}{2}\xi(\xi - 1)(1 - \eta^2) & N_5(\xi, \eta) &= (1 - \xi^2)(1 - \eta^2) & N_6(\xi, \eta) &= \frac{1}{2}\xi(\xi + 1)(1 - \eta^2) \\
 N_7(\xi, \eta) &= \frac{1}{4}\xi(\xi - 1)\eta(\eta + 1) & N_8(\xi, \eta) &= \frac{1}{2}(1 - \xi^2)\eta(\eta + 1) & N_9(\xi, \eta) &= \frac{1}{4}\xi(\xi + 1)\eta(\eta + 1)
 \end{aligned} \tag{16}$$

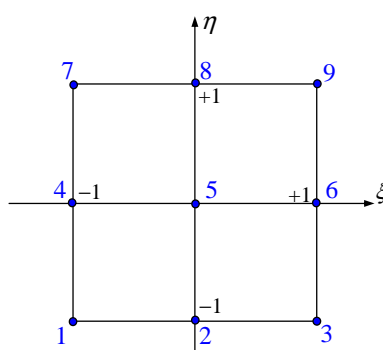


Figure 7: Biquadratic element

The interpolation functions given in Eq. (16) are used to interpolate five degrees of freedom per node: u, v, w, ψ_x and ψ_y . Hence the element contains a total of 45 degrees of freedom per element. When Eqs. (4), (5) and (16) are introduced into the first integral of Eq. (15) the finite element stiffness matrix \mathbf{K} arises. The biquadratic element is less prone to shear locking than the traditional bilinear element. However, the reduced selective integration scheme is used to compute matrix \mathbf{K} . The second integral in Eq. (15) contains the membrane forces \mathbf{N} and corresponds to a stiffening term (observe that it involves the nonlinear strains $\delta\epsilon_N$). There are two types of contributions to \mathbf{N} : (i) the traditional mechanical stresses \mathbf{N}_0 due to $N_{xx0}, N_{yy0}, N_{xy0}$, and (ii) piezoelectric stiffening stresses \mathbf{N}_p computed through solution of Eq. (10), such that $\mathbf{N} = \mathbf{N}_0 + \mathbf{N}_p$. Therefore, two geometric stiffness matrices arise: \mathbf{K}_G^P from $\int (\mathbf{N}_p - \mathbf{F})^T \delta\epsilon_N d\Omega$ and \mathbf{K}_G from $\int \mathbf{N}_0^T \delta\epsilon_N d\Omega$. Therefore, the complete FE buckling equation becomes

$$\left(\mathbf{K} + \sum_{i=1}^p \phi_i \mathbf{K}_{G_i}^P - \lambda \mathbf{K}_G \right) \mathbf{q} = \mathbf{0}, \tag{17}$$

where \mathbf{K} is the stiffness matrix, $\mathbf{K}_{G_i}^P$ is the piezoelectric geometric stiffness matrix that incorporates the piezoelectric stiffening stresses and is associated with piezoelectric pair i , \mathbf{K}_G is the geometric stiffness matrix, λ is the buckling load and \mathbf{q} is the buckling mode. Notice that the formulation presented in Eq. (17) assumes that voltages of $\phi_i = 1$ V are applied in order to form matrix $\mathbf{K}_{G_i}^P$.

In order to obtain numerical results for buckling in the presence of piezoelectric stiffening stresses consider the plate used in the previous section ($L_x = 0.2$ m and $L_y = 0.15$ m) and one rectangular actuator with $l_x = 4$ cm and $l_y = 3$ cm placed in the center of the plate whose sides are parallel to the sides of the plate. Two types of traditional loadings are applied: (i) uniform compressive loading along the x direction (λ_{xx}) and uniform shear (λ_{xy}). The actuator voltage is varied within the limits of the depoling field, i.e., -50 V $\leq \phi \leq +50$ V. Figure 8 presents the curves obtained for the $[0/90]_S$ and $[\pm 45]_S$ laminates. Points on those curves are obtained through solution of Eq. (17) for different values of ϕ . Theoretically, buckling occurs under no mechanical loading (either $N_{xx0} = 0$ or $N_{xy0} = 0$) for some value of $\phi > +50$ V for both types of loading. This conclusion agrees with the expectation that, when positive voltages are applied, compressive stiffening stresses, as those illustrated in Fig. 6, arise, impairing buckling behavior. Certainly this would not be the case in practice since $\phi > +50$ V destroys polarization of the piezoelectric material. The first buckling modes for the $[0/90]_S$ laminate subject to λ_{xx} are presented in Fig. 9 for different values of voltage. The differences between the mode shapes are not significant but the buckling load dramatically changes as seen in Fig. 8. However, the peaks of the normalized buckling modes, given in terms of transverse displacements w , become increasingly higher as the voltage is varied from -50 V to $+50$ V. The maximum $\lambda_{xx} = 660$ N/m and $\lambda_{xy} = 870$ N/m are associated with $\phi = -50$ V. It can be observed that the $[\pm 45]_S$ laminate is less sensitive to variations in ϕ . This is evidence that sensitivity to ϕ is associated with the laminate lay-up. The $[\pm 45]_S$ laminate will suffer from buckling due to stiffening stresses only for value of ϕ substantially above $+50$ V.

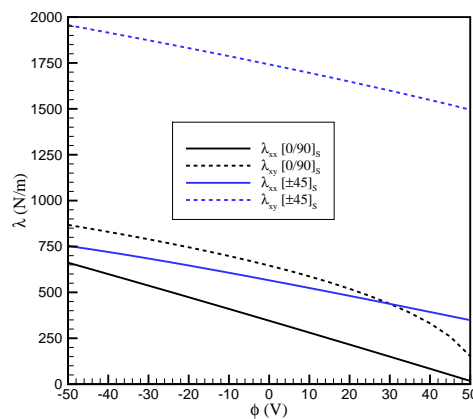


Figure 8: Buckling load vs. voltage: one patch parallel to plate's edges

A better understanding of Fig. 8 is gained if a perturbation analysis of the buckling eigenproblem is performed. Assume that the voltage of pair i is slightly perturbed by $\delta\phi_i$ such that the new eigenproblem derived from Eq. (17) becomes

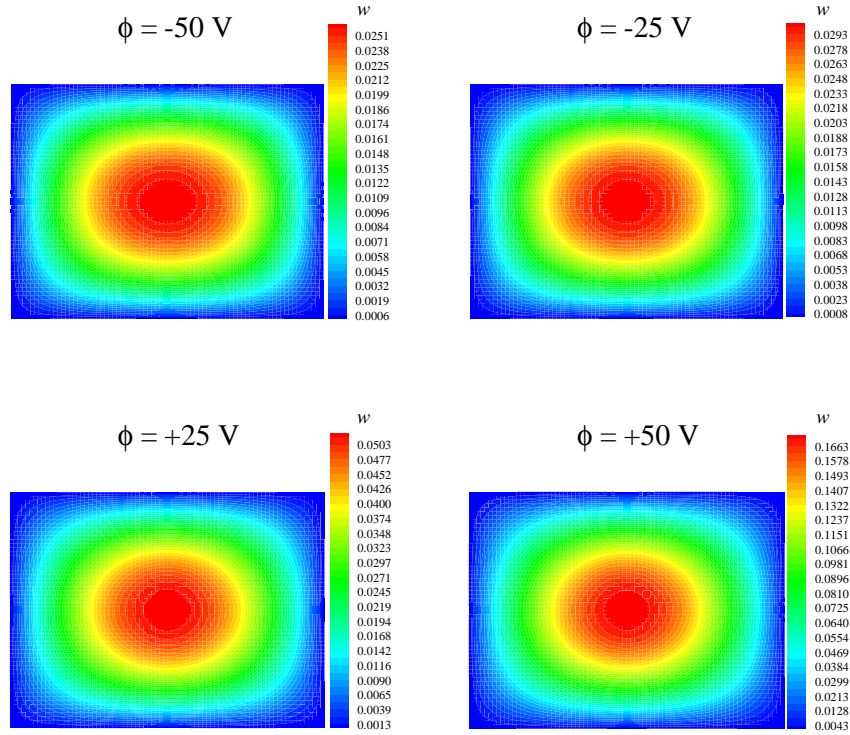


Figure 9: Buckling modes: $[0/90]_S$ laminate under λ_{xx} loading

$$\left[\mathbf{K} + \sum_{i=1}^p (\phi_i + \delta\phi_i) \mathbf{K}_{G_i}^P - (\lambda + \delta\lambda + \delta^2\lambda + \dots) \mathbf{K}_G \right] (\mathbf{q} + \delta\mathbf{q} + \delta^2\mathbf{q} + \dots) = \mathbf{0}, \quad (18)$$

The zero-, first- and second-order problems derived from Eq. (18) are respectively

$$\begin{aligned} & \left(\mathbf{K} + \sum_{i=1}^p \phi_i \mathbf{K}_{G_i}^P - \lambda \mathbf{K}_G \right) \mathbf{q} = \mathbf{0} \\ & \left(\sum_{i=1}^p \delta\phi_i \mathbf{K}_{G_i}^P - \delta\lambda \mathbf{K}_G \right) \mathbf{q} + \left(\mathbf{K} + \sum_{i=1}^p \phi_i \mathbf{K}_{G_i}^P - \lambda \mathbf{K}_G \right) \delta\mathbf{q} = \mathbf{0} \\ & \left(\sum_{i=1}^p \delta^2\phi_i \mathbf{K}_{G_i}^P - \delta^2\lambda \mathbf{K}_G \right) \mathbf{q} + \left(\sum_{i=1}^p \delta\phi_i \mathbf{K}_{G_i}^P - \delta\lambda \mathbf{K}_G \right) \delta\mathbf{q} + \left(\mathbf{K} + \sum_{i=1}^p \phi_i \mathbf{K}_{G_i}^P - \lambda \mathbf{K}_G \right) \delta^2\mathbf{q} = \mathbf{0}. \end{aligned} \quad (19)$$

Multiplication of Eq. (19b) by \mathbf{q}^T and using Eq. (19a) yields

$$\delta\lambda = \sum_{i=1}^p \frac{\mathbf{q}^T \mathbf{K}_{G_i}^P \mathbf{q}}{\mathbf{q}^T \mathbf{K}_G \mathbf{q}} \delta\phi_i. \quad (20)$$

Equation (20) shows that the sign of $\partial\lambda/\partial\phi_i$ is related to the positive-definiteness of $\mathbf{K}_{G_i}^P$, \mathbf{K}_G and the buckling mode \mathbf{q} . In the case of uniform compressive forces matrix \mathbf{K}_G is positive-definite. However, the same cannot be said about $\mathbf{K}_{G_i}^P$. In fact, Fig. 6 indicates that the term $N_{xx} - F_{xx}$ is positive in some regions over the plate and negative over others. Hence, the sign of $\mathbf{q}^T \mathbf{K}_{G_i}^P \mathbf{q}$ depends ultimately on \mathbf{q} . Figure 8 just confirms this finding.

Multiplication of Eq. (19c) by \mathbf{q}^T and using Eqs. (19a) and Eqs. (19b) yields

$$\delta^2\lambda = - \frac{\delta\mathbf{q}^T (\mathbf{K} + \sum_{i=1}^p \phi_i \mathbf{K}_{G_i}^P - \lambda \mathbf{K}_G) \delta\mathbf{q}}{\mathbf{q}^T \mathbf{K}_G \mathbf{q}}. \quad (21)$$

Matrix $(\mathbf{K} + \sum \phi_i \mathbf{K}_{G_i}^P - \lambda \mathbf{K}_G)$ is positive-definite provided buckling has not occurred. Therefore, the sign of $\delta^2\lambda$ given in Eq. (21) is certainly negative if \mathbf{K}_G is positive-definite. Notice that this may not be the case when shear loadings are applied but it is true for the case where $N_{xx0} \neq 0$ and $N_{xy0} = N_{yy0} = 0$. Figure 8 confirms that the concavity of the λ vs. ϕ curve is negative.

A network of piezoelectric actuators may be used to try to induce more favorable piezoelectric stiffening stresses. Figure 1b shows a possibility where the only patch shown in Fig. 1a is split into four smaller patches such that the total area is maintained constant. This procedure guarantees that, provided the same voltage is applied, the electric energy required is also the same. Figure 10 presents the λ vs. ϕ curves obtained assuming that equal voltages are applied to the four patches. Comparison to Fig. 8 leads one to conclude that the normal and shear buckling loads were decreased for both the $[0/90]_S$ and $[\pm 45]_S$ laminates. Therefore, this particular procedure did not bring any improvement to the buckling loads. However, this simulation suggests that the piezoelectric actuators should be placed as far from the boundaries as possible in order to boost the potential benefits of the piezoelectric stiffening stresses.

Figure 1c presents another possibility for placement of the actuators, i.e., patches with arbitrary orientation. In Fig. 1c the same rectangular patch of Figure 1a is used but it is oriented parallel to the plate diagonal. Figure 11 presents the λ vs. ϕ curves obtained. Comparison against Figs. 8 and 10 demonstrates that this configuration is the best one for both laminates whenever $\phi < 0$ V and it has good performance for $\phi > 0$ V except for extreme values of ϕ very close to +50 V. Hence, if permitted, the best strategy is to orient the patches along the diagonals, at least for the $[0/90]_S$ and $[\pm 45]_S$ laminates.

5 Conclusions

It was shown that piezoelectric actuators can be used to increase buckling loads of composite plates. A new approach is proposed where stress stiffening effects are employed. Initially, an analytical solution to the prebuckling in-plane differential equations is pursued. However, discontinuities inherent to the

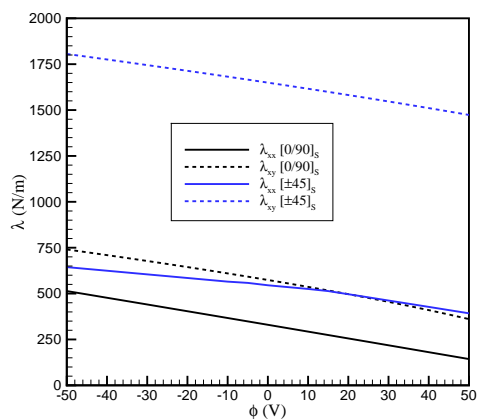


Figure 10: Buckling load \times voltage: four patches parallel to plate's edges.

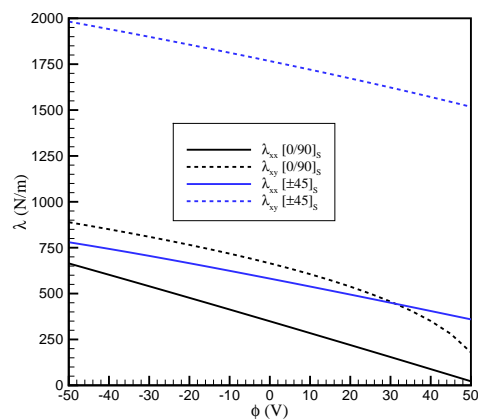


Figure 11: Buckling load \times voltage: one patch parallel to plate's diagonal.

problem preclude derivation of closed-form expressions. This initial exercise demonstrated that the treatment of discontinuities required Mindlin type of finite elements. A tapered patch design would certainly smooth out discontinuities but it is not considered because of the little practicableness.

The approximate closed-form solution obtained is applicable to patches of extreme aspect ratios (length much larger than width). Thus, a numerical solution was proposed using Mindlin type finite elements in order to compute the piezoelectric stiffening stress distributions. Even though the governing differential equations (8) cannot be analytically solved they serve to prove that buckling cannot occur if there are no stiffening stresses $N_{xx} - F_{xx}$, $N_{yy} - F_{yy}$ or $N_{xy} - F_{xy}$. In other words, for buckling to occur, external in-plane forces (N_{xx0} , N_{yy0} , N_{xy0}) must be applied or else nonzero piezoelectric stiffening stresses must be present, which are induced by nonzero voltages and geometric boundary constraints.

Numerical simulations considered two symmetric laminates: $[0/90]_S$ and $[\pm 45]_S$. These were selected because the former is a typical lay-up in aeronautical construction and the later is the optimal lay-up against buckling in the normal direction (λ_{xx}). All the results show that buckling behavior is improved for negative voltages and is impaired for positive voltages. This is obviously a result of piezoelectric stiffening stresses over the composite plate. As a practical recommendation piezoelectric actuators should have their orientations carefully chosen, but the most important finding is that they should be placed as far as possible from the edges in order to maximize the beneficial effects of the piezoelectric stiffening stresses.

Acknowledgements This work was partially financed by the Brazilian agency CNPq (grants no. 300236/2009-3 and 303287/2009-8).

References

- [1] Crawley, E.F. & de Luis, J., Use of piezoelectric actuators as elements of intelligent structures. *AIAA Journal*, **25(10)**, pp. 1373–1385, 1987.
- [2] Meressi, T. & Paden, B., Buckling control of a flexible beam using piezoelectric actuators. *Journal of Guidance, Control and Dynamics*, **16(5)**, pp. 977–980, 1993.
- [3] Thompson, S.P. & Loughlan, J., The active buckling control of some composite column strips using piezoelectric actuators. *Composite Structures*, **32(1-4)**, pp. 59–67, 1995.
- [4] Chandrashenkara, K. & Bathia, K., Active buckling control of smart composite plates – finite element analysis. *Smart Materials and Structures*, **2(1)**, pp. 31–39, 1993.
- [5] Donadon, M.V., Almeida, S.F.M. & de Faria, A.R., Stiffening effects on the natural frequencies of laminated plates with piezoelectric actuators. *Composites Part B: Engineering*, **33(5)**, pp. 335–342, 2002.
- [6] de Faria, A.R., On buckling enhancement of laminated beams with piezoelectric actuators via stress stiffening. *Composite Structures*, **65(2)**, pp. 187–192, 2004.
- [7] Kundun, C.K., Maiti, D.K. & Sinha, P.K., Post buckling analysis of smart laminated doubly curved shells. *Composite Structures*, **81(3)**, pp. 314–322, 2007.
- [8] Batra, R.C. & Geng, T.S., Enhancement of the dynamic buckling load for a plate by using piezoceramic actuators. *Smart Materials and Structures*, **10(5)**, pp. 925–933, 2001.
- [9] Shariyat, M., Dynamic buckling of imperfect laminated plates with piezoelectric sensors and actuators subjected to thermo-electro-mechanical loadings, considering the temperature-dependency of the material properties. *Composite Structures*, **88(2)**, pp. 228–239, 2009.
- [10] Kögl, M. & Bucalem, M.L., A family of piezoelectric MITC plate elements. *Computers & Structures*, **83(15-16)**, pp. 1277–1297, 2005.
- [11] Carrera, E., Boscolo, M. & Robaldo, A., Hierarchic multilayered plate elements for coupled multifield problems of piezoelectric adaptive structures: formulation and numerical assessment. *Archives of Computational Methods in Engineering*, **14(4)**, pp. 383–430, 2007.
- [12] Gopinathan, S.V., Varadan, V.V. & Varadan, V.K., A review and critique of theories for piezoelectric laminates. *Smart Materials and Structures*, **9(1)**, pp. 24–48, 2000.
- [13] Reddy, J.N., *Mechanics of Laminated Composite Plates: Theory and Analysis*. CRC Press: Boca Raton, 1997.
- [14] Nye, N.Y., *Physical Properties of Crystals: their representation by tensors and matrices*. Oxford University Press, 1972.

Topology optimization with stress constraints using superconvergent patch recovery

Jan-Michel Colombo Farias, Eduardo Lenz Cardoso,
Pablo Andrés Muñoz-Rojas

*State University of Santa Catarina, Department of Mechanical Engineering
89223-100, Joinville, SC – Brazil*

Abstract

When the stress accuracy is of extra interest, as in the case of topology optimization with stress constraints, one has to address the known limitations of the compatible finite element formulation. In this work we study the use of patch-based stress recovery techniques and their application to topology optimization. Also, to address the material variation inherent to topology optimization, we propose the use of a new displacement based superconvergent stress recovery technique. The effectiveness of the proposed formulation is shown with the use of two examples.

Keywords: topology optimization, stress constraints, superconvergent patch recovery.

1 Introduction

Nowadays the exponential growth of industry and the fast advance of technological tools allied with the need for the development of extreme structures and projects have pushed the structural optimization to a new level of importance. Economical and ecological issues can be transposed by the use of structural optimization tools, and more specifically the topology optimization has been playing an important role related to such topics.

A mass minimization problem with local failure criterions is among the most practical and requested applications but its proper setting is not straightforward due to theoretical and numerical difficulties. A constraint in some measure of the maximum stress of a mechanical component is essential to guarantee its safety, for example. Unfortunately, the imposition of such constraints has always been a challenging topic in structural optimization, because of two main difficulties. The first one is the singularity that appears after the relaxation of the original 0-1 problem, since as the density continuously decreases to zero, the discontinuity of stress shows up. This phenomena was first reported by [1] and since then several proposals have been presented in the literature to address this problem, such as the ε -relaxation [2] and the use of smooth envelope functions [3]. The singularity associated to the continuous material

parameterization is well understood and can be circumvented by changing the asymptotic behavior of the stress with respect to a change in the material density [4].

The second one is associated to the large number of local constraints. A precise control of the stress field inside the design domain is of major concern when dealing with structural optimization. However, due to its local nature, the stress field would have to be limited at each point of the design, and even with a discrete domain this procedure leads to a huge number of constraints, typically as numerous as the number of elements in the mesh. Despite of the high computational effort, some researchers have successfully adopted this procedure and were able to generate feasible solutions [5]. On the other hand, the use of just one constraint, or a reduced number of them, would be computationally attractive, but one generally has to deal with a weak control of the stress level [6], as for example, the use of a p -norm constraint of the von Mises stress field. Although it represents a stress field measure, it cannot be related to the maximum stress unless the p parameter tends to infinity, which leads obviously to numerical difficulties. In a recent work, [7] proposed the use of the following modified constraint

$$c \|\sigma_{eq}\|_p \leq \sigma_Y \quad (1)$$

where σ_Y is the yield stress,

$$\|\sigma_{eq}\|_p = \left(\sum_{e=1}^{np} \sigma_{eq_e}^p \right)^{\frac{1}{p}} \quad (2)$$

is the L_p norm of the effective von Mises stresses over np stress points and c is given by

$$c^{(k)} = \frac{\max(\sigma_{eq})^{(k-1)}}{\|\sigma_{eq}\|_p^{(k-1)}} \quad (3)$$

where $(k-1)$ stands for the previous iteration number and the $\max(\sigma_{eq})$ symbol means the maximum value of the effective stress field. This proposal fixes a fundamental problem of the traditional norm constraint (obtained for $c = 1$), as it only makes sense if $p \rightarrow \infty$, and for low p values there is no meaning in comparing the norm with the yield stress.

In addition to the previous presented approach, we propose the use of two superconvergent patch recovery schemes to better evaluate the stress field, leading to a more reliable evaluation of the global stress constraint.

2 Superconvergent patch recovery

The traditional compatible formulation for finite elements is commonly used to solve the equilibrium problem in topology optimization. In this formulation, the primal variables are the node displacements, such that strains and stresses are obtained by further differentiation of the displacement field inside each finite element. When the quality of the stress values is of interest, as in the topology optimization with stress constraints, one has to cope with two important aspects of the compatible finite element formulation: the proper evaluation of stresses inside each finite element and the lack of continuity among elements, specially on the boundary.

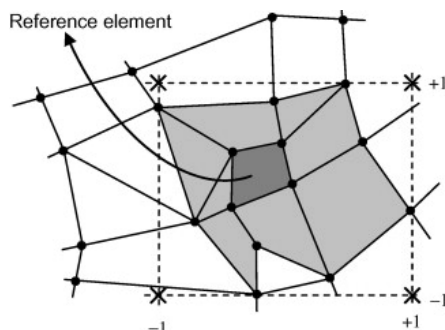


Figure 1: Patch (light gray) around a central element (dark grey)

Stress evaluation in compatible finite elements has been studied by many researchers (See [8] for an overview). Barlow [9], showed that there are specific points inside each element that give the best stress values, known as Barlow points or superconvergent points. Although those points give the best stress values inside a given element, there is no assessment on the quality of the stresses among elements or on the boundary of the domain.

To overcome those difficulties, Hinton and Campbell [10] proposed a global stress smoothing. The global smoothing has as its main drawback the increase in computational time as the number of nodes increases, and the number of back-substitutions proportional to the number of stress components. To avoid the global system of equations, one can use a patch recovery scheme proposed by Zienkiewicz and Zhu [11, 12]. In this kind of local smoothing, stresses evaluated in the neighborhood of a given element (hereafter called center element) or node are used to construct a surface that best fits the stresses in this area, known as patch. Figure 1 shows a first order patch around a center element, obtained by selecting all the elements that share at least one node with the center element. A second order patch is obtained if we include all the elements that share at least one node with the set of first order neighbors, and so on.

Using a local coordinate system inside a given patch and considering a bi dimensional problem, one can define, for each stress component $i = xx, yy, xy$,

$$\tilde{\sigma}_i(r, s) = \mathbf{p}(r, s)^T \mathbf{a}^i \quad (4)$$

where $\mathbf{a}^{iT} = [a_1^i \ a_2^i \ \dots \ a_n^i]$ is a set of coefficients used to adjust the i -th stress component and $\mathbf{p}(r, s)^T = [1 \ r \ s \ \dots]$ is a polynomial base. In order to obtain the coefficients \mathbf{a}^i , the least square method is used to fit a surface among every Barlow point residing inside the patch. The squared difference between the interpolated stresses and the superconvergent stresses inside the patch is given by

$$\Pi_i^\sigma = \frac{1}{2} \sum_{j=1}^{nsp} [\sigma_i(r_j, s_j) - \tilde{\sigma}_i(r_j, s_j)]^2 \quad (5)$$

where nsp is the number of superconvergent points inside each patch and i is the stress component. The functional Π_i^σ (5) attains its minimum value when

$$\frac{d\Pi_i^\sigma}{da_k^i} = \sum_{j=1}^{nsp} [\sigma_i(r_j, s_j) - \tilde{\sigma}_i(r_j, s_j)] \frac{d\tilde{\sigma}_i(r_j, s_j)}{da_k^i} = 0 \quad (6)$$

defining the following system of linear equations

$$\sum_{j=1}^{nsp} (\mathbf{p}_j \mathbf{p}_j^T) \mathbf{a}^i = \sum_{j=1}^{nsp} [\mathbf{p}_j \sigma_i(r_j, s_j)] \quad (7)$$

or, in a more compact notation

$$\mathbf{A}_e^\sigma \mathbf{a}^i_e = \mathbf{f}_e^\sigma \quad (8)$$

where e is the central element. This patch is known to provide quadratic convergence with respect to mesh refinement and results in a better description of stresses when compared to other approaches [8]. Also, the superconvergent patch recovery is less sensitive to mesh distortion, an important source of error when dealing with stresses. Unfortunately, when considering the spatial variation of the material parameters that arise in the topology optimization, one should not use the direct stress interpolation provided by Eq. (4).

Recently, [13] proposed a different kind of superconvergent patch recovery, based on the interpolation of the primal field obtained by the Finite Element Method. For elasticity problems, the displacement inside a patch is given by

$$\tilde{\mathbf{u}}^e(r, s) = \Psi(r, s) \Lambda^e \sum_{l=1}^n \Psi^T(r_l, s_l) \mathbf{H}_l \mathbf{U} \quad (9)$$

where

$$\Psi(r, s) = \begin{bmatrix} \mathbf{P}^T(r, s) & [\mathbf{0}]_{1 \times n} \\ [\mathbf{0}]_{1 \times n} & \mathbf{P}^T(r, s) \end{bmatrix}_{2 \times 2n},$$

is a matrix containing the polynomial evaluation of the point of interest

$$\Lambda^e = \begin{bmatrix} \mathbf{A}^{-1} & [\mathbf{0}]_{n \times n} \\ [\mathbf{0}]_{n \times n} & \mathbf{A}^{-1} \end{bmatrix}_{2n \times 2n},$$

is a matrix formed by the inverse of

$$\mathbf{A}_{n \times n} = \sum_{l=1}^{npp} \mathbf{P}(r_l, s_l) \mathbf{P}^T(r_l, s_l),$$

and \mathbf{H} is a mapping matrix, such that

$$\mathbf{H}_l \mathbf{U} = \begin{bmatrix} u_x(r_l, s_l) \\ u_y(r_l, s_l) \end{bmatrix}, \quad (10)$$

where

$$\mathbf{H}_l = \llbracket \rrbracket_{2 \times n_{nodes}}$$

has 1 in the entries corresponding to the degrees of freedom of the l -th node and zero elsewhere. The local coordinates (r, s) are related to the global (Cartesian) coordinates (x, y) by

$$\begin{aligned} r &= 2 \frac{x - x_l}{x_s - x_l} - 1 \\ s &= 2 \frac{y - y_l}{y_s - y_l} - 1 \end{aligned} \quad (11)$$

where x_l, x_s, y_l and y_s correspond to the lower and upper x, y coordinates of the patch, respectively.

The strain in a given point of a patch with central element e is given by

$$\tilde{\boldsymbol{\varepsilon}}^e(r, s) = \mathbf{L} [\tilde{\mathbf{u}}^e(r, s)] \quad (12)$$

where \mathbf{L} is the differential operator that maps the displacement into the strain. Assuming that the patch local reference system (r, s) corresponds to a scaled and translated version of the global reference system (x, y) , as shown in Eq.(11), and considering 2D elasticity, the differential operator \mathbf{L} has the form

$$\mathbf{L}(\circ) = \begin{bmatrix} \frac{d(\circ)}{dx} & 0 \\ 0 & \frac{d(\circ)}{dy} \\ \frac{d(\circ)}{dy} & \frac{d(\circ)}{dx} \end{bmatrix} = \begin{bmatrix} \frac{d(\circ)}{dr} \frac{dr}{dx} & 0 \\ 0 & \frac{d(\circ)}{ds} \frac{ds}{dy} \\ \frac{d(\circ)}{ds} \frac{ds}{dy} & \frac{d(\circ)}{dr} \frac{dr}{dx} \end{bmatrix} = \begin{bmatrix} \left(\frac{2}{x_s - x_l}\right) \frac{d(\circ)}{dr} & 0 \\ 0 & \left(\frac{2}{y_s - y_l}\right) \frac{d(\circ)}{ds} \\ \left(\frac{2}{y_s - y_l}\right) \frac{d(\circ)}{ds} & \left(\frac{2}{x_s - x_l}\right) \frac{d(\circ)}{dr} \end{bmatrix}. \quad (13)$$

As a given node in the mesh can be inside N_p patches, the final strain is obtained by a simple average

$$\tilde{\boldsymbol{\varepsilon}}(r, s) = \frac{1}{N_p} \sum_{e=1}^{N_p} \tilde{\boldsymbol{\varepsilon}}^e(r, s) \quad (14)$$

and, thus, the stress in a given point is given by

$$\tilde{\boldsymbol{\sigma}}(r, s) = \mathbf{C}(r, s) \tilde{\boldsymbol{\varepsilon}}(r, s). \quad (15)$$

The effective von Mises stress may be expressed using matricial notation [14]

$$\tilde{\sigma}_{eq} = \left(\tilde{\boldsymbol{\sigma}}^T \mathbf{M} \tilde{\boldsymbol{\sigma}} \right)^{\frac{1}{2}} \quad (16)$$

where

$$\mathbf{M} = \begin{bmatrix} 1 & -1/2 & 0 \\ -1/2 & 1 & 0 \\ 0 & 0 & 3 \end{bmatrix}$$

for plane stress problems and

$$\tilde{\boldsymbol{\sigma}} = \begin{bmatrix} \tilde{\sigma}_{xx} \\ \tilde{\sigma}_{yy} \\ \tilde{\sigma}_{xy} \end{bmatrix}$$

is a vectorial arrangement of the stress tensor, commonly used by the Finite Element Method theory.

Equation (9) has two advantages when compared to Eq. (4): the number of components to solve for is smaller in the displacement based patch, as the number of displacements components is always smaller than the number of stress components, and the constitutive relation \mathbf{C} is used only when evaluating the final stress $\tilde{\boldsymbol{\sigma}}$, allowing arbitrary spatial variation of the constitutive tensor without imposing any additional interpolation error. Also, as shown in [13], this patch retains the convergence ratio of the traditional stress based patch, with the same low sensitivity for mesh distortion. Thus, this method is preferred for topology optimization with stress constraints.

3 Formulation

As our goal is to minimize the mass of a design domain and we seek to use only one kind of material, the method may be equivalently expressed as a volume minimization problem with a von Mises stress constraint and subjected to an equilibrium variational equation

$$\min_{\mathbf{d}} V = \int \rho(\mathbf{x}) d\Omega$$

$$\text{s.t. } \sigma_{eq} \leq \sigma_y$$

$$\int \boldsymbol{\sigma}(\mathbf{u}) \cdot \boldsymbol{\varepsilon}(\boldsymbol{\eta}) d\Omega = \int \boldsymbol{\eta} \cdot \mathbf{t} d\Gamma$$

We adopted the SIMP material parametrization for the constitutive tensor $\mathbf{C} = \rho^n \mathbf{C}_0$ and a SIMP-like parametrization for the stress tensor as described by [14]

$$\boldsymbol{\sigma} = \rho^{n-q} \mathbf{C}_0 \boldsymbol{\varepsilon} \quad (17)$$

where n is the SIMP exponent, q is a relaxation factor and \mathbf{C}_0 is the fourth order constitutive tensor of the base material.

Moreover, Bruggi [15] has shown that the use of $q < n$ in Eq. (17) leads to a domain relaxation which is smoother if compared to the ε -relaxation method [2], therefore alleviating the singularity phenomena.

Recalling the known issue related to the number of stress constraints imposition, we basically followed [7] methodology of using a modified von Mises stress p-norm constraint. However in order to account for a better estimate of stresses, we propose the use of the stresses obtained by means of the

superconvergent patch recovery scheme. This can be accomplished by using $\tilde{\sigma}_{eq}$ instead of σ_{eq} in Eq. (1), such that it now reads

$$\Phi = \frac{\max(\tilde{\sigma}_{eq})^{(k-1)}}{\|\tilde{\sigma}_{eq}\|_p^{(k-1)}} \|\tilde{\sigma}_{eq}\|_p^{(k)} \leq \sigma_Y \quad (18)$$

This modification has two direct consequences: first, the stresses used to evaluate the constraint are a better estimate than the direct centroidal stresses commonly used in the topology optimization literature. Second, the stresses at different coordinates are now correlated throughout the entire patch, making the problem even more nonlinear. This second consequence can make the computations more involved, but have the benefit of making the recovered stresses less sensitive to the original stresses fluctuations. Introducing the finite element method and its discrete domain in which all the calculation is performed, the problem statement takes the following final form

$$\begin{aligned} \min_{\mathbf{d}} V &= \sum_{e=1}^{nelem} \rho_e V_e \\ \text{s.t.} \quad &\frac{\max(\tilde{\sigma}_{eq})^{(k-1)}}{\|\tilde{\sigma}_{eq}\|_p^{(k-1)}} \|\tilde{\sigma}_{eq}\|_p^{(k)} \leq \sigma_Y \\ &\mathbf{KU} = \mathbf{F} \end{aligned}$$

where \mathbf{K} is the global stiffness matrix of the finite element mesh, \mathbf{U} is the global displacement vector and \mathbf{F} is the global force vector.

In order to avoid the checkerboard phenomena and to generate a well-posed problem, we have adopted the use of filtering techniques. The use of filters in topology optimization has some advantages, such as the elimination of the checkerboard issue, as already mentioned, the solution is no longer mesh-dependent and its dependency is now transferred to a physical parameter: the filter radius. A good review about filtering techniques is given by Bruns and Tortorelli [16]. One direct consequence of setting a filtering radius is that now it is possible to control the minimum size of members [17, 18] and/or holes [19, 20] that can appear inside the design domain. We have decided to use the original linear filter proposed by Bruns and Tortorelli due to its simplicity and efficiency, albeit other projection methods or none filtering at all could be used. If the latter approach is chosen, the reader should be aware of the consequences and exploit the available solutions.

4 Sensitivity analysis

In order to impose the stress constraint it is necessary to perform the sensitivity analysis with respect to the design variables. In the following, we provide the full development of the sensitivity expressions for the superconvergent displacement based patch, while in Appendix A the derivatives of the superconvergent stress based patch are shown. Differentiating the R.H.S of Eq. (18) with respect to a design variable x_m and adopting an adjoint approach, we obtain

$$\frac{d \left(c^{(k)} \|\tilde{\sigma}_{eq}\|_p^{(k)} + \boldsymbol{\lambda}^T (\mathbf{KU} - \mathbf{F}) \right)}{dx_m} = c^{(k)} \frac{d \|\tilde{\sigma}_{eq}\|_p^{(k)}}{dx_m} + \boldsymbol{\lambda}^T \left(\frac{d\mathbf{K}}{dx_m} \mathbf{U} + \mathbf{K} \frac{d\mathbf{U}}{dx_m} - \frac{d\mathbf{F}}{dx_m} \right) \quad (19)$$

where $\boldsymbol{\lambda}$ is the adjoint vector and $c^{(k)}$ is a constant in iteration number k , since it depends of the previous iteration.

Thus, evaluating the derivative of the p-norm we obtain

$$\frac{d \|\tilde{\sigma}_{eq}\|_p^{(k)}}{dx_m} = \frac{1}{p} \left(\sum_{i=1}^N \tilde{\sigma}_{eq}^p(r_i, s_i) \right)^{\frac{1}{p}-1} \left[\sum_{i=1}^N p \tilde{\sigma}_{eq}^{p-1}(r_i, s_i) \frac{d\tilde{\sigma}_{eq}(r_i, s_i)}{dx_m} \right] \quad (20)$$

which can be written as

$$\frac{d \|\tilde{\sigma}_{eq}\|_p^{(k)}}{dx_m} = \left(\sum_{i=1}^N \tilde{\sigma}_{eq}^p(r_i, s_i) \right)^{\frac{1}{p}-1} \left[\sum_{i=1}^N \tilde{\sigma}_{eq}^{p-1}(r_i, s_i) \frac{d\tilde{\sigma}_{eq}(r_i, s_i)}{dx_m} \right] = T_1 \left[\sum_{i=1}^N \tilde{\sigma}_{eq}^{p-1}(r_i, s_i) \frac{d\tilde{\sigma}_{eq}(r_i, s_i)}{dx_m} \right] \quad (21)$$

where

$$T_1 = \left(\sum_{i=1}^N \tilde{\sigma}_{eq}^p(r_i, s_i) \right)^{\frac{1}{p}-1} \quad (22)$$

is a fixed term.

The derivative of the von Mises stress in Eq. (21) can be evaluated by means of Eq. (16), resulting in

$$\frac{d\tilde{\sigma}_{eq}(r_i, s_i)}{dx_m} = \frac{1}{\tilde{\sigma}_{eq}(r_i, s_i)} \tilde{\boldsymbol{\sigma}}^T(r_i, s_i) \mathbf{M} \frac{d\tilde{\boldsymbol{\sigma}}(r_i, s_i)}{dx_m} \quad (23)$$

and the derivative in Eq. (23) can be evaluated by means of Eq. (15), such that

$$\frac{d\tilde{\boldsymbol{\sigma}}(r_i, s_i)}{dx_m} = \frac{d\mathbf{C}}{dx_m} \tilde{\boldsymbol{\varepsilon}}(r_i, s_i) + \mathbf{C}(r_i, s_i) \frac{d\tilde{\boldsymbol{\varepsilon}}(r_i, s_i)}{dx_m}. \quad (24)$$

Evaluating the strain derivative,

$$\frac{d\tilde{\boldsymbol{\varepsilon}}(r_i, s_i)}{dx_m} = \frac{1}{N_p} \sum_{p=1}^{N_p} \frac{d\tilde{\boldsymbol{\varepsilon}}_p(r_i, s_i)}{dx_m} \quad (25)$$

where

$$\frac{d\tilde{\boldsymbol{\varepsilon}}_p(r_i, s_i)}{dx_m} = \mathbf{L} \frac{d\tilde{\mathbf{u}}_p(r_i, s_i)}{dx_m} \quad (26)$$

we obtain

$$\frac{d\tilde{\mathbf{u}}_p(r_i, s_i)}{dx_m} = \boldsymbol{\Psi}(r_i, s_i) \boldsymbol{\Lambda}^e \sum_{l=1}^n \boldsymbol{\Psi}^T(r_l, s_l) \mathbf{H}_l \frac{d\mathbf{U}}{dx_m}. \quad (27)$$

Considering Eqs. (19) thru (27),

$$\begin{aligned} \frac{dR}{dx_m} = c^{(k)} T_1 & \left[\sum_{i=1}^N \tilde{\sigma}_{eq}^{p-1}(r_i, s_i) \frac{1}{\tilde{\sigma}_{eq}(r_i, s_i)} \tilde{\boldsymbol{\sigma}}^T(r_i, s_i) \mathbf{M} \right. \\ & \left. \left(\frac{d\mathbf{C}}{dx_m} \tilde{\boldsymbol{\varepsilon}}(r_i, s_i) + \mathbf{C}(r_i, s_i) \frac{1}{N_p} \sum_{e=1}^{N_p} \mathbf{L}\boldsymbol{\Psi}(r_i, s_i) \boldsymbol{\Lambda}^e \sum_{l=1}^n \boldsymbol{\Psi}^T(r_l, s_l) \mathbf{H}_l \frac{d\mathbf{U}}{dx_m} \right) \right] + \\ & \boldsymbol{\lambda}^T \left(\frac{d\mathbf{K}}{dx_m} \mathbf{U} + \mathbf{K} \frac{d\mathbf{U}}{dx_m} - \frac{d\mathbf{F}}{dx_m} \right) \end{aligned} \quad (28)$$

or, splitting terms

$$\frac{dR}{d\rho_m} = c^{(k)} T_1 R_1 + \mathbf{R}_2 \frac{d\mathbf{U}}{dx_m} + \boldsymbol{\lambda}^T \left(\frac{d\mathbf{K}}{dx_m} \mathbf{U} - \frac{d\mathbf{F}}{dx_m} \right)$$

where

$$R_1 = \sum_{i=1}^N \tilde{\sigma}_{vm}^{p-2}(r_i, s_i) \tilde{\boldsymbol{\sigma}}^T(r_i, s_i) \mathbf{M} \frac{d\mathbf{C}}{dx_m} \tilde{\boldsymbol{\varepsilon}}(r_i, s_i)$$

and

$$\mathbf{R}_2 = c^{(k)} T_1 \sum_{i=1}^N \tilde{\sigma}_{vm}^{p-2}(r_i, s_i) \tilde{\boldsymbol{\sigma}}^T(r_i, s_i) \mathbf{M} \mathbf{C}(r_i, s_i) \frac{1}{N_p} \sum_{e=1}^{N_p} \mathbf{L}\boldsymbol{\Psi}(r_i, s_i) \boldsymbol{\Lambda}^e \sum_{l=1}^n \boldsymbol{\Psi}^T(r_l, s_l) \mathbf{H}_l + \boldsymbol{\lambda}^T \mathbf{K}.$$

The evaluation of $\frac{d\mathbf{U}}{dx_m}$ is avoided if $\mathbf{R}_2 = \mathbf{0}$, leading to the following adjoint system:

$$\mathbf{K}\boldsymbol{\lambda} = -c^{(k)} T_1 \left(\sum_{i=1}^N \tilde{\sigma}_{vm}^{p-2}(r_i, s_i) \tilde{\boldsymbol{\sigma}}^T(r_i, s_i) \mathbf{M} \mathbf{C}(r_i, s_i) \frac{1}{N_p} \sum_{e=1}^{N_p} \mathbf{L}\boldsymbol{\Psi}(r_i, s_i) \boldsymbol{\Lambda}^e \sum_{l=1}^n \boldsymbol{\Psi}^T(r_l, s_l) \mathbf{H}_l \right)^T \quad (29)$$

where the symmetry of \mathbf{K} has been used. Once the adjoint system has been solved for the adjoint vector $\boldsymbol{\lambda}$, the sensitivity takes the following form

$$\frac{dR}{dx_m} = c^{(k)} T_1 R_1 + \boldsymbol{\lambda}^T \left(\frac{d\mathbf{K}}{dx_m} \mathbf{U} - \frac{d\mathbf{F}}{dx_m} \right). \quad (30)$$

Introducing the qp approach (Eq.17), and recalling that

$$\frac{d\mathbf{C}}{dx_m}(r_i, s_i) = (n-q) \rho_i^{n-q-1} \frac{d\rho_i}{dx_m} \mathbf{C}_0 = \frac{(n-q)}{\rho_i} \frac{d\rho_i}{dx_m} \mathbf{C}(r_i, s_i),$$

R_1 can be further simplified to

$$R_1 = \sum_{i=1}^N \tilde{\sigma}_{eq}^{p-2}(r_i, s_i) \tilde{\boldsymbol{\sigma}}^T(r_i, s_i) \mathbf{M} \frac{(n-q)}{\rho_i} \frac{d\rho_i}{dx_m} \mathbf{C}(r_i, s_i) \tilde{\boldsymbol{\varepsilon}}(r_i, s_i) = \sum_{i=1}^N \frac{(n-q)}{\rho_i} \tilde{\sigma}_{eq}^p(r_i, s_i) \frac{d\rho_i}{dx_m}$$

so that Eq. (30) now reads

$$\frac{dR}{dx_m} = c^{(k)} T_1 \sum_{i=1}^N \frac{(n-q)}{\rho_i} \tilde{\sigma}_{eq}^p(r_i, s_i) \frac{d\rho_i}{dx_m} + \boldsymbol{\lambda}^T \left(\frac{d\mathbf{K}}{dx_m} \mathbf{U} - \frac{d\mathbf{F}}{dx_m} \right) \quad (31)$$

Some considerations have to be made concerning the above expression (Eq. 31). The i -th element density derivative $\frac{d\rho_i}{dx_m}$ depends on the chosen filtering technique, and must be evaluated after it has been defined. Moreover, one should not be fooled about the range of the summation in the first parcel of the equation, once the term $\frac{d\rho_i}{dx_m}$ is not null only if the m -th design variable is inside the i -th element's filtering neighborhood. So the summation drastically reduces to a few elements. If one decides not to adopt any filtering method, the derivative collapses to the Kronecker delta δ_{im} and the design variable x_m becomes the element's centroidal density ρ_m , which, after the evaluation of the stiffness matrix derivative, leads to

$$\frac{dR}{d\rho_m} = c^{(k)} T_1 \frac{(n-q)}{\rho_m} \tilde{\sigma}_{eq}^p(x_m, y_m) + n\rho_m^{n-1} \boldsymbol{\lambda}_m^T \mathbf{K}_{0m} \mathbf{U}_m, \quad (32)$$

where it was assumed that the design is load-independent. The subscript m corresponds to local properties of the m -th element, and \mathbf{K}_{0m} is the m -th element's solid stiffness matrix, *i.e.* $\rho_m = 1$. One remarkable feature of Eq. (32) is that once the adjoint problem is solved, its evaluation depends only on local properties, such as the density parameter ρ_m , the superconvergent recovered von Mises stress $\tilde{\sigma}_{vm}$, and the local entries of the adjoint and displacement vectors. Therefore the computer code implementation can be easily parallelized resulting in an efficient and fast calculation of the sensitivity.

5 Results

To assess the use of the patch recovery schemes to evaluate the stress constraint in topology optimization we address two examples. In all the examples we analyzed the following possibilities for the computation of the stress constraint:

- DIRECT: the effective stress was evaluated directly in the centroid of each element, which is commonly used in the current literature;
- SPR: the effective stress was evaluated in the centroid of each element, by means of the stress based patch recovery;
- DPR: the effective stress was evaluated in the centroid of each element, by means of the displacement based patch recovery,

also, for each one of those situations, we analyze the influence of the norm exponent, with $p = 8$ and $p = 12$. For all the examples the SIMP exponent is set to $n = 3$ and the relaxation exponent of the qp parameterization is set to $q = 2.5$, as pointed out by [15]. An implementation of the original MMA method [21] is used in all examples and in each case we assessed the convergence observing the stabilization of the objective function and of the constraint. Thus, the number of iterations in all the

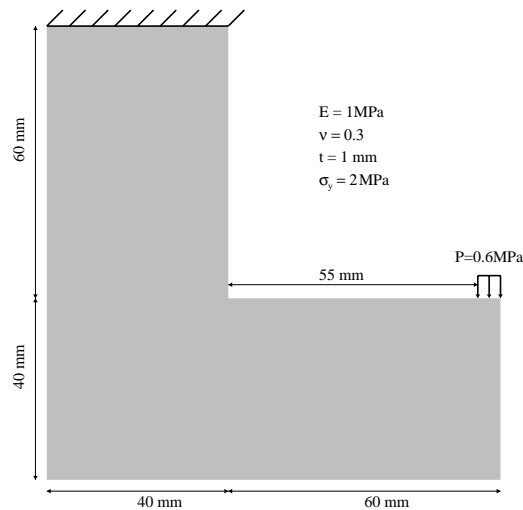


Figure 2: L-SHAPE problem definition

examples is not fixed and can be different. We used first order patches in all examples along with the four node bilinear isoparametric element and a linear density filter, as proposed by [16] and used by [7]. The plane stress hypothesis is also considered.

The first example studied is the well known L-Shape problem, defined in Fig. 2, which has an abrupt geometrical change leading to a stress concentration in its neighborhood. To overcome this problem, the topology must distribute material in order to round that corner and to redistribute the stress. In this example, we used a finite element mesh with 6400 bilinear isoparametric finite elements ($1\text{mm} \times 1\text{mm}$) and a filter radius of 2mm . The limiting stress was set to $\sigma_y = 2\text{MPa}$.

The results obtained with the different formulations for the stress recovery should be compared for the same norm exponent. For $p = 8$, the final topologies and the von Mises stress field are shown in Figs 3, 5 and 7 for the DIRECT, SPR and DPR cases. The convergence of the volume fraction for the DIRECT, SPR and DPR cases are shown on the left in Figs 4, 6 and 8. The convergence of the stress constraint is shown in the center of Figs. 4, 6 and 8, where for each example we show the three estimates for the stress, although only one is used for imposing the constraint. In the right side of Figs. 4, 6 and 8 we show the maximum von Mises stress in the last iterations of each one of the studied strategies.

Analogously, the topologies and stress distributions obtained for $p = 12$ are shown in Figs 9, 11 and 13 for the DIRECT, SPR and DPR cases. The volume and stress constraint convergence for the three cases are shown in Figs 10, 12 and 14.

As already mentioned, the use of patches highly increases the non-linearity and its use along with the p-norm parameter $p = 12$ have resulted in strong oscillations during the optimization process, as shown in Figs. 10, 12 and 14. The final volume for all cases, including $p = 8$ and $p = 12$, are quite

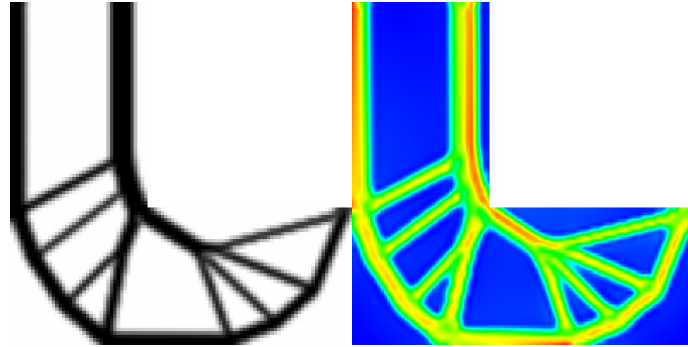


Figure 3: Topology (left) and effective stress distribution (right) obtained without patch, $p=8$

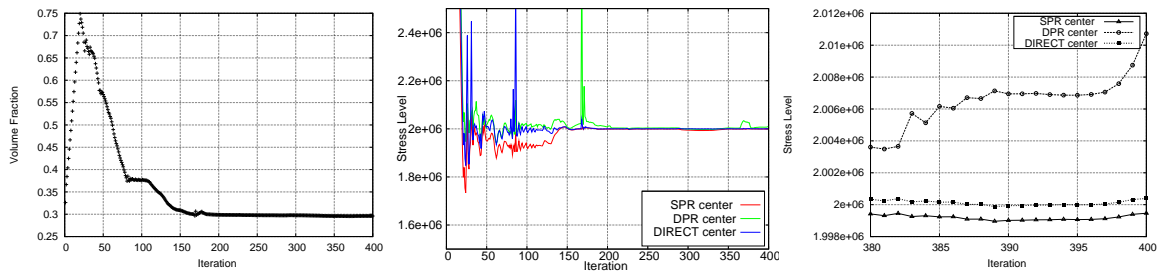


Figure 4: Volume fraction (left), Stress constraint (center) and a comparison of different stress recovery strategies in the final iterations (right) for the direct stress, $p=8$.

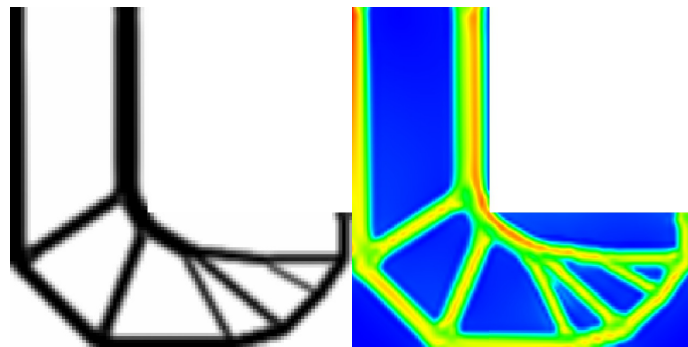


Figure 5: Topology (left) and effective stress distribution (right) obtained with stress patch, $p=8$

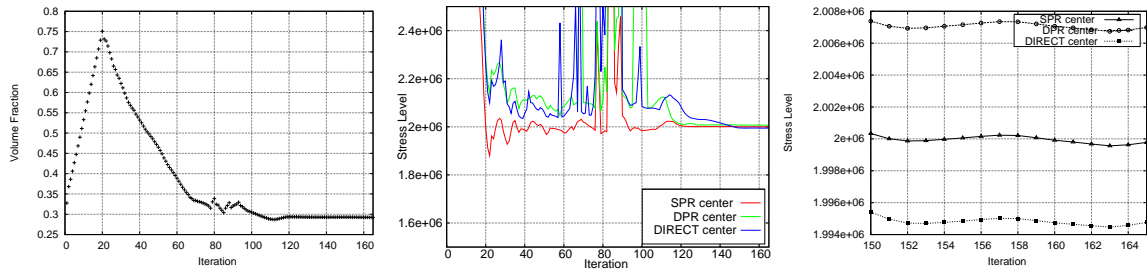


Figure 6: Volume fraction (left), Stress constraint (center) and a comparison of different stress recovery strategies in the final iterations (right) for the the stress based patch, $p=8$.

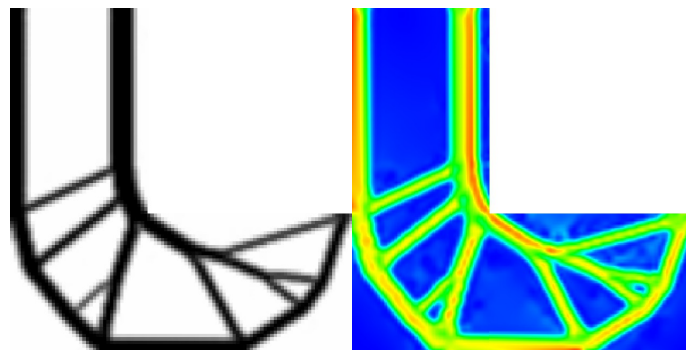


Figure 7: Topology (left) and effective stress distribution (right) obtained with displacement based patch, $p=8$

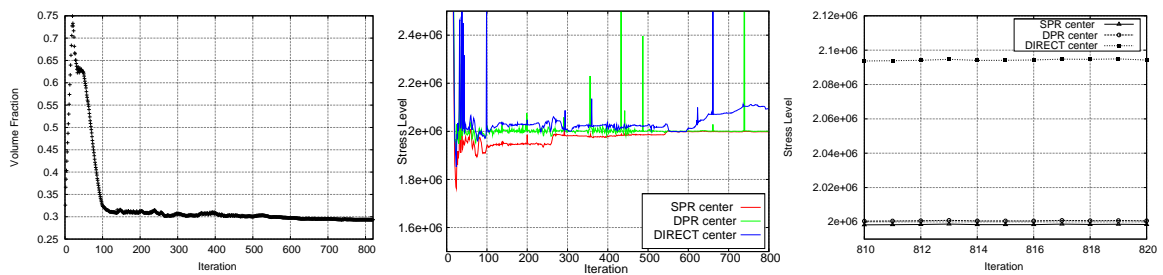


Figure 8: Volume fraction (left), Stress constraint (center) and and a comparison of different stress recovery strategies in the final iterations (right) for the the displacement based patch, $p=8$.

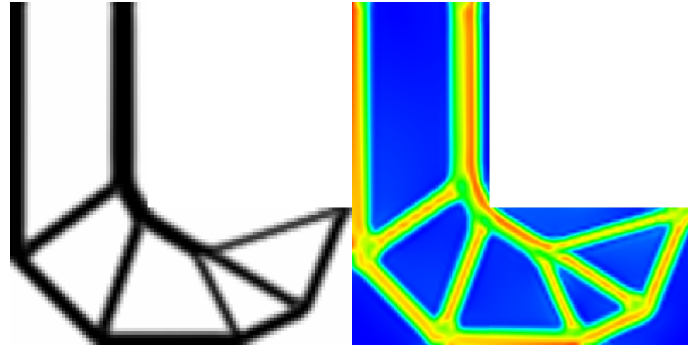


Figure 9: Topology (left) and effective stress distribution (right) obtained without patch, $p=12$

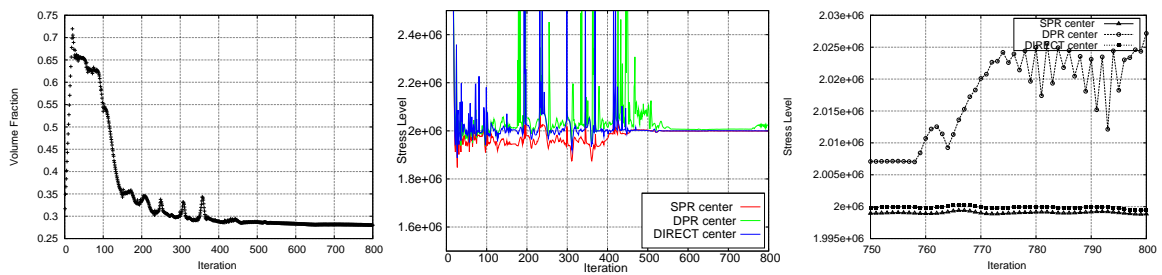


Figure 10: Volume fraction (left), Stress constraint (center) and a comparison of different stress recovery strategies in the final iterations (right) for the the direct stress , $p=12$.

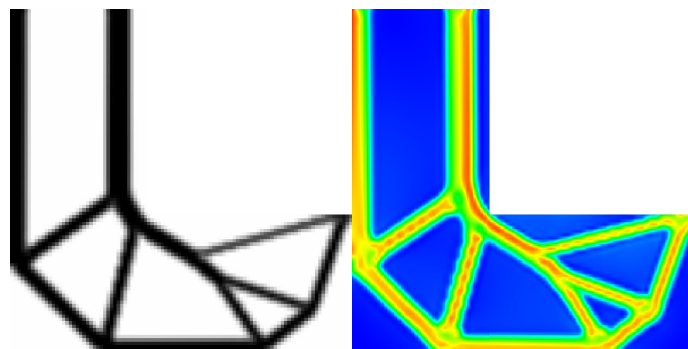


Figure 11: Topology (left) and effective stress distribution (right) obtained with stress patch, $p=12$

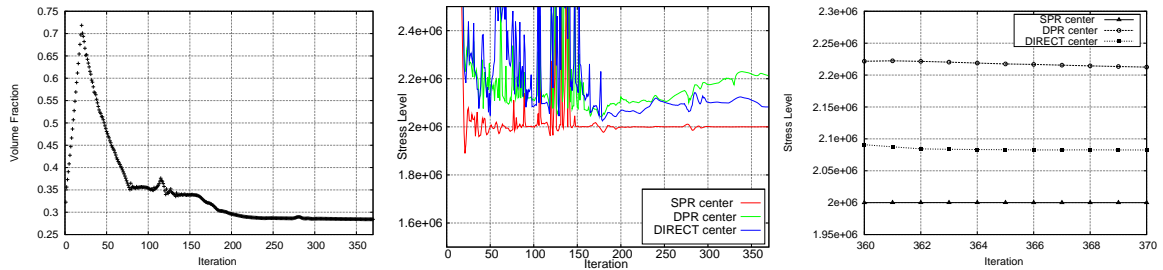


Figure 12: Volume fraction (left), Stress constraint (center) and and a comparison of different stress recovery strategies in the final iterations (right) for the the stress based patch, $p=12$.

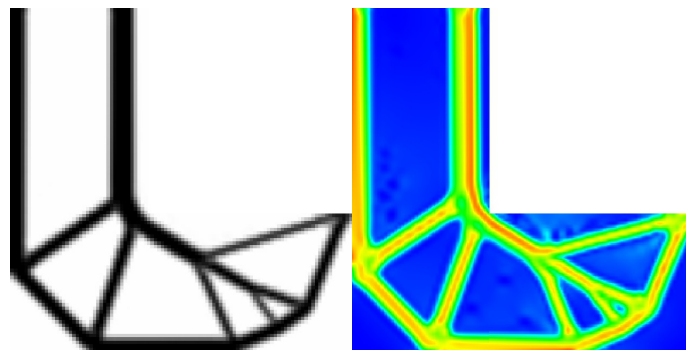


Figure 13: Topology (left) and effective stress distribution (right) obtained with displacement patch, $p=12$

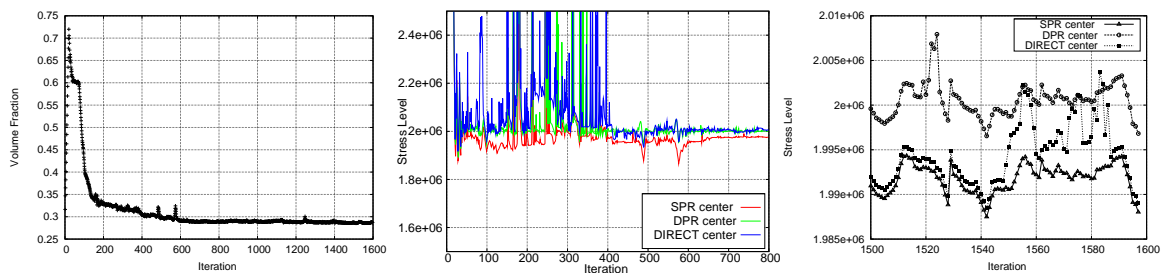


Figure 14: Volume fraction (left), Stress constraint (center) and and a comparison of different stress recovery strategies in the final iterations (right) for the the displacement based patch, $p=12$.

similar and around 30%, but the latter presented a slightly lower volume fraction. Rigorously the final topologies are different, but the overall designs are similar. Although the numerical issues, the exponent $p = 12$ gives the best topologies with respect to the rounded corner and the stress saturation.

The second example is the volume minimization with stress constraint of a 8×5 cantilever beam, defined in Fig. 15. The finite element mesh is composed by 16000 bilinear isoparametric elements ($5\text{mm} \times 5\text{mm}$) and the filter radius is set to 15 mm. The stress limit is set to 1 MPa.

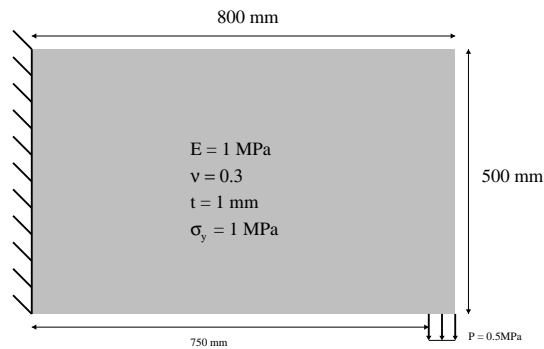


Figure 15: BEAM problem definition

In this example, only results obtained with $p = 12$ are shown, although the case $p = 8$ was also investigated. Topologies and stress distributions obtained are shown in Figs 16, 18 and 20 for the DIRECT, SPR and DPR cases respectively. The convergence history for each case is shown in Figs 17, 19 and 21,

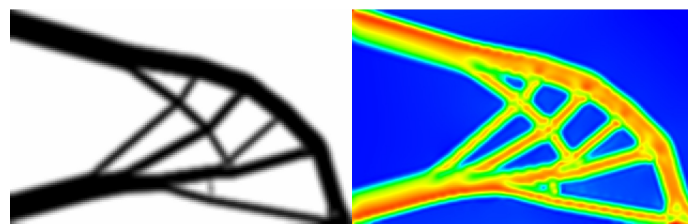


Figure 16: Topology (left) and effective stress distribution (right) obtained without patch, $p=12$

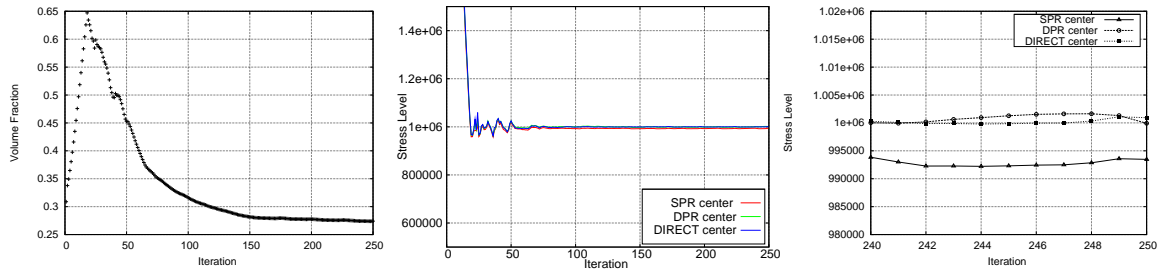


Figure 17: Volume fraction (left), Stress constraint (center) and a comparison of different stress recovery strategies in the final iterations (right) for the the direct stress, $p=12$.

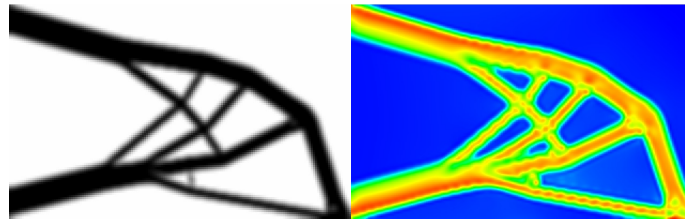


Figure 18: Topology (left) and effective stress distribution (right) obtained with the stress patch, $p=12$.

The design domain does not possess the theoretical problems related to singularity as in the previous example and the Figs.17, 19 and 21) show that the optimization process could generate feasible solutions without the strong numerical oscillations in the stress constraint. Conceptually the final topology has given special treatment to the upper and lower left corners of the design domain, where the normal stresses due to bending are higher and the clamped region leads to an artificial stress concentration. As mentioned before, the superconvergent patch recovery schemes were able to absorb the numerical variations of the original stress field, illustrated in Figs. 19 and 21, where the DPR and SPR stresses remained practically unchanged despite of the DIRECT centroidal stress oscillations. Considering the DPR case, it can be seen that the DIRECT centroidal stress converged to a value 12% higher than the permissible stress, while the stress in the patch based approaches were no greater than 1 MPa. Moreover, all topologies have converged to a approximately 28% of volume, and have well saturated the stress among its members.

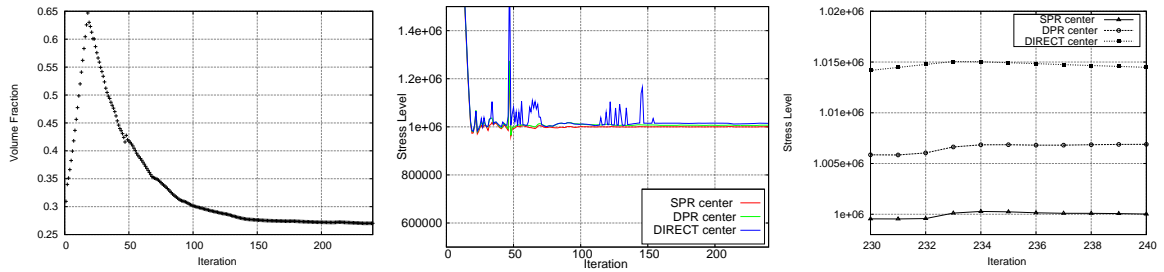


Figure 19: Volume fraction (left), Stress constraint (center) and a comparison of different stress recovery strategies in the final iterations (right) for the the stress based patch, $p=12$.

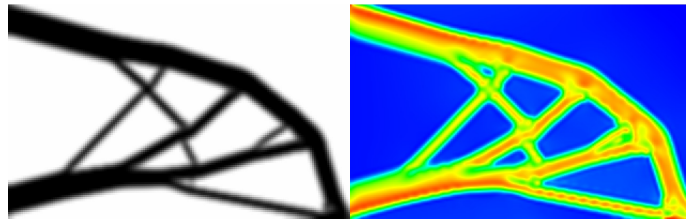


Figure 20: Topology (left) and effective stress distribution (right) obtained with the displacement based patch, $p=12$

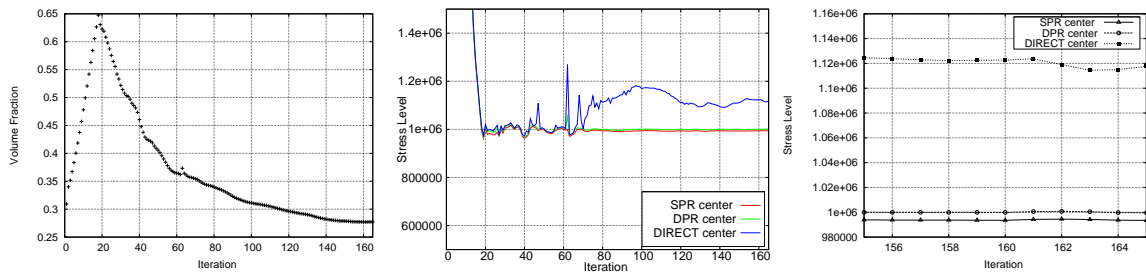


Figure 21: Volume fraction (left), Stress constraint (center) and a comparison of different stress recovery strategies in the final iterations (right) for the the displacement base patch, $p=12$.

6 Conclusions

We proposed the use of superconvergent stress recovery techniques to evaluate stress constraints in topology optimization. Also, we presented the displacement based patch that is more consistent with the spatial variation in the constitutive parameters that arise in topology optimization.

It was observed a strong variation during the iterations, due to the non-linearity of the stress constraint and the coupling provided by the use of patches. The MMA parameters used in this work must be refined to overcome this difficulty. The norm $p = 12$ showed the best compromise between numerical stability and the efficacy of stress constraint.

It can be seen that although quite similar, the maximum effective stress evaluated by means of the different schemes employed in this work are different for each topology. Also, strictly speaking, the topologies obtained are different, although leading to the same overall design. The two patch based approaches could handle the DIRECT stress oscillation and their associated stresses have remained unaffected, as shown in the cantilever beam problem. Thus, as the displacement based patch has the good convergence properties of the stress based patch recovery and is more consistent with respect to the material variation along the domain, we suggest its use to evaluate the stress constraint. Moreover, the displacement based stress recovery is prone to be used with topology optimization of FGM structures, since the spatial variation of properties in this case is more pronounced.

References

- [1] Kirsch, U., On singular topologies in structural design. *Structural Optimization*, **2**, pp. 133–142, 1990.
- [2] Cheng, G.D. & Guo, X., ϵ -relaxed approach in structural topology optimization. *Structural Optimization*, **13**, pp. 258–266, 1997.
- [3] Rozvany, G.I.N. & Sobieszczanski-Sobieski, J., New optimality criteria methods: forcing uniqueness of the adjoint strains by corner-rounding at constraint intersections. *Structural Optimization*, **4**, pp. 244–246, 1992.
- [4] Rozvany, G.I.N., On design-dependent constraints and singular topologies. *Structural and Multidisciplinary Optimization*, **21**, pp. 164–172, 2001.
- [5] Pereira, J.T., Fancello, E.A. & Barcellos, C.S., Topology optimization of continuum structures with material failure constraints. *Structural and Multidisciplinary Optimization*, **26**, pp. 50–66, 2004.
- [6] Qiu, G.Y. & Li, X.S., A note on the derivation of global stress constraints. *Structural and Multidisciplinary Optimization*, **40**, pp. 625–628, 2010.
- [7] Le, C., Norato, J., Bruns, T., Ha, C. & Tortorelli, D., Stress-based topology optimization for continua. *Structural and Multidisciplinary Optimization*, **41**, pp. 605–620, 2010.
- [8] Jr., M.V., noz Rojas, P.A.M. & Filippini, G., On the accuracy of nodal stress computation in plane elasticity using finite volumes and finite elements. *Computers & Structures*, **87**, pp. 1044–1057, 2009.
- [9] Barlow, J., Optimal stress locations in finite element models. *International Journal for Numerical Methods in Engineering*, **10**, pp. 243–251, 1976.
- [10] Hinton, E. & Campbell, J.S., Local and global smoothing of discontinuous finite element functions using a least squares method. *International Journal for Numerical Methods in Engineering*, **8**, pp. 461–480, 1974.
- [11] Zienkiewicz, O.C. & Zhu, J.Z., Superconvergent patch recovery and a posteriori error estimation in the finite element method, part i: A general superconvergent recovery technique. *International Journal for*

- Numerical Methods in Engineering*, **33**, pp. 1331–64, 1992.
- [12] Zienkiewicz, O.C. & Zhu, J.Z., The superconvergent patch recovery (spr) and a posteriori error estimates. part 2: Error estimates and adaptivity. *International Journal for Numerical Methods in Engineering*, **33**, pp. 1365–82, 1992.
- [13] noz Rojas, P.A.M., Odorczyk, M.F., Cardoso, E.L. & Jr., M.V., A superconvergent temperature patch procedure for nodal flux recovery in finite element computations. *ECOM 2010 - CILAMCE 2010, Buenos Aires. MECOM del Bicentenario*, 2010.
- [14] Duysinx, P. & Bendsøe, M.P., Topology optimization of continuum structures with local stress constraints. *International Journal for Numerical Methods in Engineering*, **43**, pp. 1453–1478, 1998.
- [15] Bruggi, M., On an alternative approach to stress constraints relaxation in topology optimization. *Structural and Multidisciplinary Optimization*, **36**, pp. 125–141, 2008.
- [16] Bruns, T.E. & Tortorelli, D.A., Topology optimization of non-linear elastic structures and compliant mechanisms. *Computer Methods in Applied Mechanics and Engineering*, **190**, pp. 3443–3459, 2001.
- [17] Cardoso, E.L. & Fonseca, J.S.O., Complexity control in the topology optimization of continuum structures. *Journal of the Brazilian Society of Mechanical Sciences and Engineering*, **25 (3)**, pp. 293–301, 2003.
- [18] Guest, J.K., Prévost, J.H. & Belytschko, T., Achieving minimum length scale in topology optimization using nodal design variables and projection functions. *International Journal for Numerical Methods in Engineering*, **61**, pp. 238–254, 2004.
- [19] Guest, J.K., Topology optimization with multiple phase projection. *Computer Methods in Applied Mechanics and Engineering*, **199**, pp. 123–135, 2009.
- [20] Sigmund, O., Morphology-based black and white filters for topology optimization. *Structural and Multidisciplinary Optimization*, **33**, pp. 401–424, 2007.
- [21] Svanberg, K., The method of moving asymptotes – a new method for structural optimization. *International Journal for Numerical Methods in Engineering*, **24**, pp. 359–373, 1987.

Appendix A – Sensitivity for the stress based patch

If the stress based patch is used to evaluate Eq. (18), then the stress in a given coordinate is obtained by an average among the contributions of all patches that share this point

$$\tilde{\sigma}(r, s) = \frac{1}{N_p} \sum_{p=1}^{N_p} \tilde{\sigma}^{(p)}(r, s) \quad (33)$$

where $\tilde{\sigma}^{(p)}$ is the stress tensor obtained with the stress based patch considering a central element p . Analogously to Eq. (9), the stress obtained by the p -th patch $\tilde{\sigma}^{(p)}(r, s)$ is given by

$$\tilde{\sigma}^{(p)}(r, s) = \Psi(r, s) \mathbf{\Lambda}_p \sum_{b=1}^{nsp} \Psi^T(r_b, s_b) \sigma_b \quad (34)$$

where

$$\Psi(r, s) = \begin{bmatrix} P^T(r, s) & [0]_{1 \times n} & [0]_{1 \times n} \\ [0]_{1 \times n} & P^T(r, s) & [0]_{1 \times n} \\ [0]_{1 \times n} & [0]_{1 \times n} & P^T(r, s) \end{bmatrix}_{3 \times 3n},$$

$$\mathbf{\Lambda}_p = \begin{bmatrix} \mathbf{A}^{-1} & [0]_{n \times n} & [0]_{n \times n} \\ [0]_{n \times n} & \mathbf{A}^{-1} & [0]_{n \times n} \\ [0]_{n \times n} & [0]_{n \times n} & \mathbf{A}^{-1} \end{bmatrix}_{3n \times 3n},$$

$$\mathbf{A}_{n \times n} = \sum_{l=1}^{npp} \mathbf{P}(r_l, s_l) \mathbf{P}^T(r_l, s_l),$$

and

$$\boldsymbol{\sigma} = \begin{bmatrix} \sigma_{xx} \\ \sigma_{yy} \\ \sigma_{xy} \end{bmatrix}$$

share the same definitions of the already presented displacement based patch.

Introducing the stress parameterization Eq. (17)

$$\tilde{\boldsymbol{\sigma}}^{(p)}(r, s) = \boldsymbol{\Psi}(r, s) \mathbf{\Lambda}_p \sum_{b=1}^{nsp} \boldsymbol{\Psi}^T(r_b, s_b) \rho_b^{n-q} \mathbf{C}_0 \mathbf{B} \mathbf{H}_b \mathbf{U} \quad (35)$$

where the summation is now performed among all the nsp superconvergent points inside the p -th patch, and \mathbf{H}_b is the mapping matrix of the correspondig element at which the barlow point is located.

Differentiating Eq. (18) with respect to a design variable x_m and employing the chain rule of differentiation,

$$\left\{ \sum_{e=1}^n p \tilde{\sigma}_{eq}^{p-1} \frac{1}{\tilde{\sigma}_{eq}} \tilde{\boldsymbol{\sigma}}^T \mathbf{M} \frac{1}{N_p} \sum_{p=1}^{N_p} \boldsymbol{\Psi}(r_e, s_e) \mathbf{\Lambda}_p \sum_{b=1}^{nsp} \boldsymbol{\Psi}^T(r_b, s_b) \left[(n-q) \rho_b^{n-q-1} \frac{d\rho_b}{dx_m} \mathbf{C}_0 \mathbf{B} \mathbf{H}_b \mathbf{U} + \rho_b^{n-q} \mathbf{C}_0 \mathbf{B} \mathbf{H}_b \frac{\partial \mathbf{U}}{\partial \mathbf{x}_m} \right] \right\} + \boldsymbol{\lambda}^T \left(\frac{d\mathbf{K}}{d\mathbf{x}_m} \mathbf{U} + \mathbf{K} \frac{d\mathbf{U}}{d\mathbf{x}_m} - \frac{d\mathbf{F}}{d\mathbf{x}_m} \right) \quad (36)$$

Aiming at the avoidance of the displacement sensitivty $\frac{d\mathbf{U}}{d\mathbf{x}_m}$, the adjoint system can be defined and solved

$$\boldsymbol{\lambda}^T \mathbf{K} = -c^{(k)} \left(\sum_{e=1}^n \tilde{\sigma}_{eq}^p \right)^{\frac{1}{p}-1} \left\{ \sum_{e=1}^n \tilde{\sigma}_{eq}^{p-2} \tilde{\boldsymbol{\sigma}}^T \mathbf{M} \frac{1}{N_p} \sum_{p=1}^{N_p} \boldsymbol{\Psi}(r_e, s_e) \mathbf{\Lambda}_p \sum_{b=1}^{nsp} \boldsymbol{\Psi}^T(r_b, s_b) \rho_b^{n-q} \mathbf{C}_0 \mathbf{B} \mathbf{H}_b \right\} \quad (37)$$

The sensitivity is then given by

$$\frac{d \left(c^{(k)} \|\tilde{\sigma}_{vm}\|_p \right)}{dx_m} = c^{(k)} \left(\sum_{e=1}^n \tilde{\sigma}_{eq}^p \right)^{\frac{1}{p}-1} \left\{ \sum_{e=1}^n \tilde{\sigma}_{eq}^{p-2} \tilde{\boldsymbol{\sigma}}^T \mathbf{M} \frac{1}{N_p} \sum_{p=1}^{N_p} \boldsymbol{\Psi}(r_e, s_e) \mathbf{\Lambda}_p \sum_{b=1}^{nsp} \boldsymbol{\Psi}^T(r_b, s_b) \frac{(n-q)}{\rho_b} \frac{d\rho_b}{dx_m} \boldsymbol{\sigma}_b \right\} + \boldsymbol{\lambda}^T \left(\frac{d\mathbf{K}}{d\mathbf{x}_m} \mathbf{U} - \frac{d\mathbf{F}}{d\mathbf{x}_m} \right) \quad (38)$$

Multicriteria optimization of an aircraft reinforced composite panel subjected to non uniform loading

A.P.C.S. Ferreira, S.F.M. de Almeida

*Department of Mechanical Engineering,
Instituto Tecnológico de Aeronáutica – ITA, CTA-ITA-IEM,
Pça. Mal. Eduardo Gomes, n° 50, 12228-900,
São José dos Campos, SP – Brazil*

Abstract

This work presents the optimization of a composite plate subjected to non uniform loadings when two design criteria are simultaneously taken into account. The design criteria considered are buckling load and fundamental frequency. These optimization criteria are important for practical applications, particularly in the aeronautical industry. The use of minimax strategy as a bilevel procedure is proposed in order to solve the optimization problem. Furthermore, the optimization process includes a mass optimization external loop that yields efficient structures. The uncertain and non uniform loads are defined using a hypothetical aircraft load envelope, with the condition that loads must be self equilibrating.

Keywords: multicriteria optimization, buckling, fundamental frequency, composite plate, uncertain loading, non uniform loading.

1 Introduction

A commonly used approach for buckling and fundamental frequency simultaneous optimization is the use of the design criteria as constraints [1] or to use as objective function a weighted sum of the design criteria [2]. In order to use these approaches it is necessary to have some previous information so that proper constraint values can be defined. Furthermore, it is required to have some idea about the relative relevance of each criterion on the optimization problem to define a weighted sum of the design criteria.

Another common approach of performing multicriteria optimization is using Pareto optimality [3]. The Pareto optimal design ensures that, at least, one criterion is optimized and the others are satisfied. A similar strategy is the minimax strategy [4] which can either be used to minimize the maximum loss or to maximize the minimal profit. The minimax strategy allows the determination of the best design for the worst load condition.

Among the new approaches for multicriteria optimization, the genetic algorithms have reached some relevance [5]. The genetic algorithms are based on the natural evolution theory and the design variables are the initial population that should evolve. These algorithms usually present good results but they have high computational cost.

The methods described above can be combined among them or with some other optimization methods to solve multicriteria optimization problems. A good reference for traditional numerical optimization methods is Vanderplaats [6].

The multicriteria optimization process used in this work combines the minimax strategy and Powell's method [6]. The minimax strategy as proposed here is a bilevel procedure where the design criteria are maximized with respect to the design variables and minimized with respect to the load cases. Initially, the criteria are minimized with respect to the loading parameters by a random search. In a second step, the maximization with respect to the design variables is performed using Powell's method. Furthermore, a mass optimization external loop is included in the optimization process. This external loop yields minimum mass structure within prescribed safety margins previously adopted. The optimization process is described in Section III.

The use of uncertain and non uniform loads makes the design closer to real situations and, consequently, more robust. The uncertain non uniform loading is defined herein from some physical load cases combined with the condition that the loads applied to the structure must be self-equilibrating. The procedure to extract self-equilibrating load cases from physical loads is described in Section II. This type of loading representation was used in previous works [7–9]. The work of Conrado, Faria and Almeida [7] yielded very conservative results as the optimal design was able to withstand an entire class of linear piecewise loads along the rib boundary even those that are unrealistic. In the works of Gama [8] and Ferreira [9] a novel procedure is proposed to compute self-equilibrating loads that represent an arbitrary load envelope to which an aircraft could be subjected within a prescribed degree of fidelity. Moreover, parameters are introduced to control the degree of robustness of the resulting load cases. The procedure proposed in Conrado, Faria and Almeida [7] is too conservative; the present procedure can be tailored by the user to exclude non realistic load cases from the optimization procedure thus providing a solution that is applicable in actual design situations.

The structure chosen for optimization is a wing composite panel with two reinforcers. These structures are fundamental parts in aircraft design and manufacturing and their optimization is important in order to design more efficient airplanes.

Buckling and fundamental frequency are numerically computed by the finite element method. The finite element computation is done using software Abaqus[®] and the optimization algorithm was developed using a Fortran code.

2 Non uniform loading representation

When dealing with preliminary design of aircraft structures, it is important to take advantage of the fact that the structure may be considered to be in static equilibrium and possibly be statically determined. For example, in the case of a wing panel, once the aerodynamic properties of the wing, that depend only on the geometry of the wing, are known one can compute the pressure distribution

on the wing for a given maneuver using a CFD code. From these data, the bending moment and torsional moment distributions and vertical resultant stress resultants may be computed considering the wing as a beam. Naturally, the stress and strain distributions depend on the material and stiffness of the structural elements of the wing. However, with the assumptions previously stated the stress resultant forces and moments do not depend on the stiffness distribution of the wing.

Figure 1 illustrates in a simplified way this procedure for the case of pure bending moment. In this case, the stress resultant N on an arbitrary section along the wing does not depend on the stiffness distribution. Therefore, for that particular physical load case the stress resultant on a particular section of a wing panel must be N . That is, the integral of the stress distribution normal to the section along the entire length of that section must be N regardless of the design variables. Similarly, the shear stress resultant at any section along the wing may be computed from the torsional moment. These information along with the fact that the panel is considered to be in a state of static equilibrium provides a way to describe the non-uniform loading in a robust way [9].

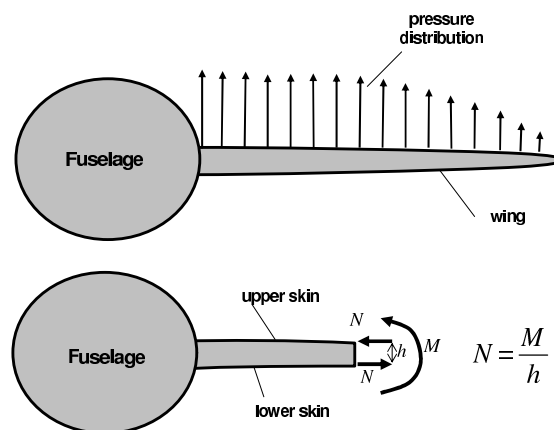


Figure 1: Forces due to physical loading.

In this loading representation the non uniform loading is discretized by piecewise linear functions, as shown in Fig. 2, defined at an arbitrary number of load control points placed on the structure boundary. The larger the number of load control points is the better is the loading representation.

Since previous works [7–9] have already described the methodology for non uniform loading representation, this work presents only the main equations. In the two dimensional case, vector $\{X\}$ contains the load magnitudes at each load control point in x and y directions:

$$\{X\}^T = \left[f_{x_1} \quad f_{y_1} \quad f_{x_2} \quad f_{y_2} \quad \dots \quad f_{x_{m/2}} \quad f_{y_{m/2}} \right] \tag{1}$$

where m is twice the number of loading control points. Vector $\{X\}$ may be computed by minimizing the following expression:

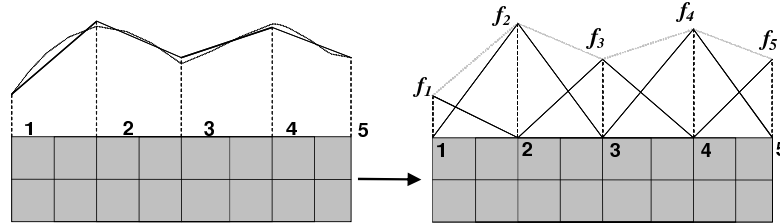


Figure 2: Load discretization [9].

$$e_j = \left(p_{ij} \bar{F}_{ij} \{n\}_j^T - \{x\}_j^T \right) \left(p_{ij} \bar{F}_{ij} \{n\}_j - \{x\}_j \right) \quad (2)$$

subjected to the condition:

$$[G]_j \{x\}_j = \{A\}_j \quad (3)$$

where $[G]$ is $(3+k) \times m$ matrix given in Ferreira [9]; $(3+k)$ are the first three lines representing the sum of forces and moments plus the k lines representing the forces acting on the edges where the physical loads are applied. The first three lines of $\{A\}_j$ are zero because they define the static equilibrium conditions. The other components (for $j > 3$) have a magnitude corresponding to the physical load integrals at the load control point, as previously illustrated. The index j refers to the load case considered and index i refers to the considered load control point. Finally, p_{ij} is a dimensionless parameter in the range $[0, 1]$ that represents the non uniform physical load in a way that is conservative, intermediate or non-conservative.

It should be remarked that in a three dimensional case the above equations still hold but with some changes. For example, the number of static equilibrium equation should be 6 rather than 3.

After some algebraic manipulations $\{X\}$ vector can be shown to be [9]:

$$\{X\}_j = \left([I] - [\bar{G}]_j^T \left([\bar{G}]_j [\bar{G}]_j^T \right)^{-1} [\bar{G}]_j \right) p_{ij} \bar{F}_{ij} \{n\}_j + [\bar{G}]_j^T \left([\bar{G}]_j [\bar{G}]_j^T \right)^{-1} \{A\}_j \quad (4)$$

where $[I]$ is the identity matrix and \bar{F}_{ij} is the magnitude of the load applied at the load control point. It is defined from the load applied on the edge where load control point is located:

$$\bar{F}_{ij} = \frac{2 A}{\int_{i-1}^i \sqrt{\left(\frac{dx(s)}{ds}\right)^2 + \left(\frac{dy(s)}{ds}\right)^2} ds + \int_i^{i+1} \sqrt{\left(\frac{dx(s)}{ds}\right)^2 + \left(\frac{dy(s)}{ds}\right)^2} ds} \quad (5)$$

where A is the load applied on the considered edge and $x(s)$ and $y(s)$ are parametric representations of the geometry of the edge.

When p_{ij} is chosen to be 1 the load magnitude at load control point i corresponding to the j -th physical load will tend to be very concentrated and the design is conservative because this type

of loading is unrealistic. When p_{ij} is chosen to be zero the load magnitude at load control point i corresponding to the j -th physical load will tend to be very uniform and the resulting design will not be robust as some physically possible loads may not be taken into account in the optimization procedure. Therefore, the robustness of the design may be controlled by parameters p_{ij} . For each load control point i and a physical load case j , a convenient p_{ij} may be chosen in the interval between 0 and 1 to realistically represent all physically possible non uniform loading thus adjusting the desired degree of robustness of the design for each load case.

3 Multicriteria optimization strategy

The buckling and fundamental frequency problems are described in matrix form in Eqs. (6) and (7), respectively. The evaluation of buckling loads and fundamental frequency is based on a prebuckling state and a linearized buckling problem that can be described in matrix form as:

$$([K] - \lambda [K]_G) \{q\} = 0 \quad (6)$$

$$([K] - \lambda [K]_G - \omega^2 [M]) \{q\} = 0, \quad (7)$$

where $[K]$ is the stiffness matrix, $[M]$ is the mass matrix and $[K]_G$ is the geometric stiffness matrix. In order to solve these problems it is first necessary to compute the prebuckling displacements, given in Eq. (8) by $\{q\}_p$, $\{p\}$ is the global vector of applied loads:

$$[K] \{q\}_p = \{p\} \quad (8)$$

The minimax strategy is used in this work with the goal of obtaining the best design for the worst load condition. It is applied as a bilevel procedure since the idea is to maximize buckling and fundamental frequency simultaneously.

$$\max_{\{t\}} \min_{\{\beta\}} \left\{ \begin{array}{l} \omega(\{t\}, \{\beta\}) \\ \lambda(\{t\}, \{\beta\}) \end{array} \right\} = \max_{\{t\}} \phi(\{t\}) \quad , \quad \phi(\{t\}) = \min_{\{\beta\}} \left\{ \begin{array}{l} \omega(\{t\}, \{\beta\}) \\ \lambda(\{t\}, \{\beta\}) \end{array} \right\} \quad (9)$$

The convexity property is especially useful in optimization processes because it significantly reduces the computational cost. Based on it, it is possible to assure that the function minimum will be associated with the loads on the convex hull of the load space. In this work it is considered a hypothetical load envelope that represents the convex hull of the load space. In the first part of the minimax strategy the objective function is minimized with respect to load cases $\{\beta\}$ that represent the load envelope. This is done by a random search.

The first part of the minimax strategy just verifies whether the structure buckles or not. If buckling occurs, the structure mass should be increased and first part repeated until a not buckled structure is obtained.

In the second part of the minimax strategy the objective function is maximized with respect to the design variables $\{t\}$. This is done by Powell's method. The buckling value computed here is non

dimensional; the fundamental frequency must be normalized by some prescribed minimum admissible value (ω_0). Therefore, the values of the design criteria may be directly compared. These frequency normalization factors are defined based on design requirements.

At the end of the second part of the minimax strategy it is checked if the structure is under or over dimensioned. If the structure satisfies the safety margins and design requirements, the optimization process is completed. If not, the mass should be updated and part two is repeated.

The optimization of an aeronautical composite panel is used as an example in this work. The constraints used for this problem were:

1. The structure must not buckle before the proof load; this condition is consistent with the definition of the proof load [10]. The proof load is defined as the limit load multiplied by a proof factor. In general, the proof factor is adopted to be 1.25; this value will be used in this work.
2. The structure must preserve a minimum fundamental frequency under the limit load to preserve its performance under dynamic loads.

These hypotheses are consistent with actual aeronautical panel design and avoid problems with objective function discontinuity and a predominance of the frequency criterion over the buckling criterion, as discussed in what follows.

The mass optimization external loop tends to bring the normalized buckling values closer to one if the frequency normalization value is low. However, occasionally during the optimization process, the buckling load can be less than one. When this occurs, the frequency value tends to zero as the structure loses its stability. This fact causes numerical problems in the eigenvalue computation and represents a discontinuity in the objective function. Moreover, when buckling values are close to one the optimization process is not multicriteria since frequency will always have the minimum value and be the dominant criterion. These problems are avoided using the problem statement described above. It must be emphasized that this assumption was not used just to avoid numerical problems. It was used because the statement of the problem as proposed is consistent with actual aircraft structural design.

4 Numerical results

The structure chosen for optimization is a rectangular composite plate with two reinforcers. The present work original contributions are the multicriteria optimization and the use of composite material; the proposed procedure provides robust preliminary optimum designs for aeronautical applications. The description of the main geometrical characteristics is repeated here because they are essential for the comprehension of the results.

For simplicity, the plate was assumed to be rectangular with dimensions 0.4 m along the y direction and 1.2 m along the x direction. It must be remarked that the procedure proposed here is quite general and is applicable to any geometrical shape of the panel. The panel skin is a crossply laminate with $[(0/90)]_s$ stacking sequence. The reinforcers are located at $x = 0.4$ m and $x = 0.8$ m. The reinforcer at $x = 0.4$ m have the design variables width (w_1) and height (h_1); the reinforcer at $x = 0.8$ m has the same design variables in order to yield a symmetric structure. These reinforcers divide the panel into three sections, as depicted in Fig 3. The thicknesses of the layers in each section are defined by another four

design variables. The thicknesses t_1 and t_2 correspond to layers 0° and 90° , respectively, of sections 1 and 3 (due to the assumed panel symmetry); t_3 and t_4 correspond to the thicknesses of the same layers in section 2. Therefore, there are a total of six design variables. Since the magnitudes of the layer thicknesses and the width and height of the reinforcers can be significantly different, the design variables must be normalized in the optimization process to avoid numerical problems.

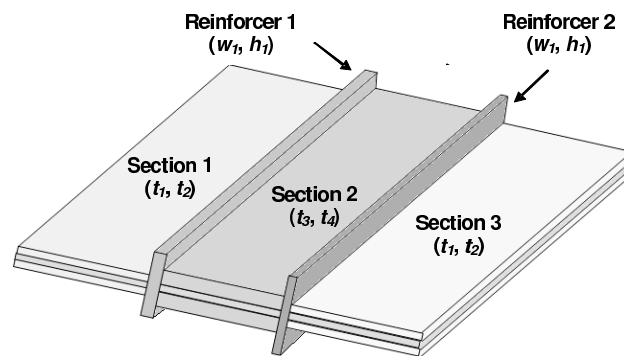


Figure 3: Reinforced panel with the design variables [9].

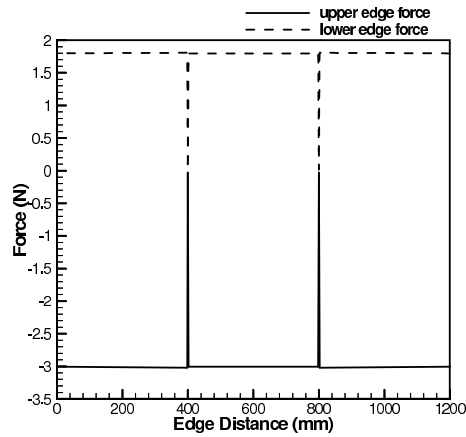
The load envelope is composed of the five load cases described in Table 1. This work presents five examples of the reinforced panel optimization where the influence of the p_{ij} variation on the loading representation and the optimization strategy performance are investigated.

Table 1: Load cases.

Case 1	Compression: 3600 N at upper edge
Case 2	Compression: 500 N at right edge
Case 3	Shear: -1200 N at upper edge and 1200 N at lower edge
Case 4	Compression: 2800 N at lower edge
Case 5	Shear: -880 N (section 3) and 720 N (section 1) at lower edge

4.1 Reinforced panel considering $p_{ij} = 0$

When p_{ij} is zero the resulting load distribution is nearly uniform as shown in the plot of Force \times Edge distance, Fig. 4. Table 2 presents the optimization results of the reinforced panel under the load cases described in Table 1.

Figure 4: Self-equilibrated loading for load case 1, $p_{ij} = 0$ [9].Table 2: Optimization results $p_{ij} = 0$.

		Initial Structure 1		Initial Structure 2		Initial Structure 3	
		Initial (mm)	Optimum (mm)	Initial (mm)	Optimum (mm)	Initial (mm)	Optimum (mm)
	t_1	0.6	0.05	0.7	0.08	0.5	0.06
	t_2	0.8	0.7	0.7	0.6	0.9	0.7
	t_3	0.6	0.4	0.7	0.2	0.9	0.09
	t_4	0.8	0.4	0.7	0.6	0.5	0.6
	w_1	4.00	4.00	3.00	1.00	2.00	1.52
	h_1	60.00	12.01	80.00	17.61	70.00	11.09
	Mass (kg)	2.396	1.208	2.396	1.101	2.271	1.117
Load	λ_1	5.82	1.02	5.23	1.00	5.01	1.01
case 1	ω_1/ω_0	3.51	1.49	3.42	1.18	3.24	1.18
Load	λ_2	20.96	3.01	20.79	2.47	20.26	2.51
case 2	ω_2/ω_0	3.53	2.37	3.44	2.08	3.27	2.08
Load	λ_3	13.39	2.51	12.42	1.99	13.17	2.08
case 3	ω_3/ω_0	3.54	2.51	3.45	2.24	3.28	2.23
Load	λ_4	7.48	1.31	6.73	1.29	6.43	1.30
case 4	ω_4/ω_0	3.51	1.89	3.42	1.58	3.25	1.57
Load	λ_5	11.91	1.78	11.39	1.78	10.43	1.47
case 5	ω_5/ω_0	3.52	2.14	3.43	1.96	3.26	1.79

The optimization process used three different groups of initial design variables in order to identify possible local maxima despite the fact that the problem is convex. It means that the optimization is done for three different initial structures. Initial structures 1, 2 and 3 are over dimensioned for the considered load cases. They support loads approximately five times larger than the ones that are applied in the example.

The buckling load is defined by the non dimensional variable λ and the normalized frequency is defined by ω/ω_0 . The frequency normalization value adopted was $\omega_0 = 20$ Hz. The used stop criterion for the optimization was 2%, that is, the optimization stops when the normalized objective function is in the range [1.00 – 1.02.]. This value was adopted for all optimization examples in this work.

The results presented in Table 2 leads to the conclusion that the load case 1 was the critical one, yielding lower buckling and fundamental frequency values before and after the optimization process. In the beginning of the optimization procedure the dominant criterion was frequency and at the end of the optimization the dominant criterion was buckling. Using the mass optimization external loop, the three initial structures converged to design variables that satisfy the design requirements and safety margins. Initial structure 2 converged to the lowest mass value and can be considered the global optimum. In this structure the 0° layer almost disappear in sections 1 and 3 and is thinner than the 90° layer in section 2.

4.2 Reinforced panel considering $p_{ij} = 1$

When $p_{ij} = 1$ the resulting load distribution for load case j is very concentrated close to load control point i . Since the critical load case in the previous subsection was case 1, this subsection represents load case 1 considering $p_{ij} = 1$ at three different load control points placed at the panel upper edge. In this way the optimization deals with seven load cases, the three already mentioned and cases 2 to 5 considering $p_{ij} = 0$.

The Force \times Edge distance plot in Fig. 5 depicts the load distribution obtained when it was considered $p_{ij} = 1$ at load control point 3 that is placed at 0.4 m from the upper edge. It can be noted that the loading is significantly concentrated close to load control point 3. This type of loading is certainly unrealistic for actual wing design and, consequently, the design will be too conservative.

From the results presented in Table 3, it is possible to conclude that for initial structures 1, 2 and 3 the critical load case was case 1 (the minimum of λ_i or ω_i/ω_0 for the initial structures are always for $i = 1, 2$, or 3 that correspond to load case1). After the optimization, the critical load continues to be case 1. Buckling is the dominant criterion for the three structures, before and after the optimization process. The optimal structures are very similar but global optimum may be assumed to be structure number 3 as it presents a mass that is slightly lower than the other optima. In this structure the 0° layers are thinner than the 90° ones in the three sections.

4.3 Reinforced panel considering $p_{ij} = 0.25$

In this subsection the optimization considers 32 self-equilibrated load cases that are obtained setting $p_{ij} = 0.25$ for load cases 1 to 5 at the respective load control points. Load case 1 is a compressive load acting on the edge with eight load control points. Setting $p_{ij} = 0.25$ at each one, yields eight self

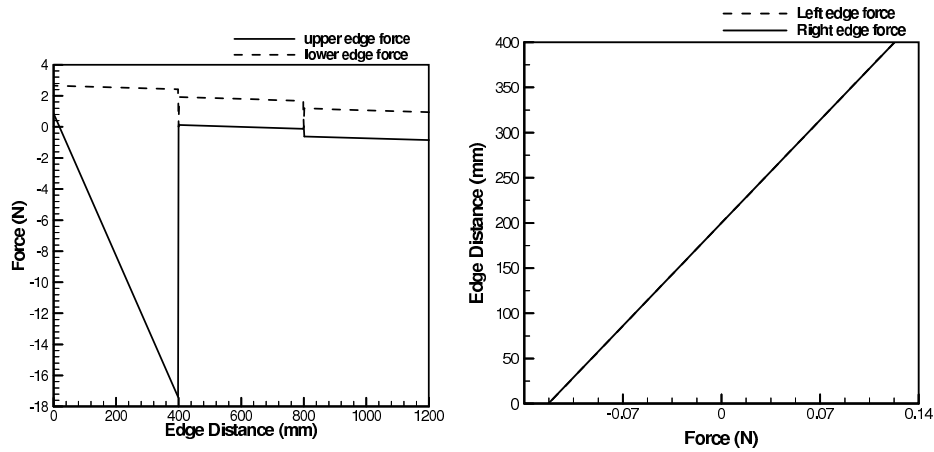


Figure 5: Self-equilibrated loading for load case 1 and load control point 3, $p_{31} = 1$ [9].

equilibrated load cases. Load case 2 acts on the edge with two load control points yielding two more self-equilibrated load cases. Load case 3 is defined on two edges that have a total of ten load control points; this yields another ten self-equilibrated load cases. Load case 4 is applied on an edge with eight load control points, yielding another eight self-equilibrated load cases. Finally, load case 5 is defined on edges segments that involve four load control points, yielding another four self-equilibrated load cases.

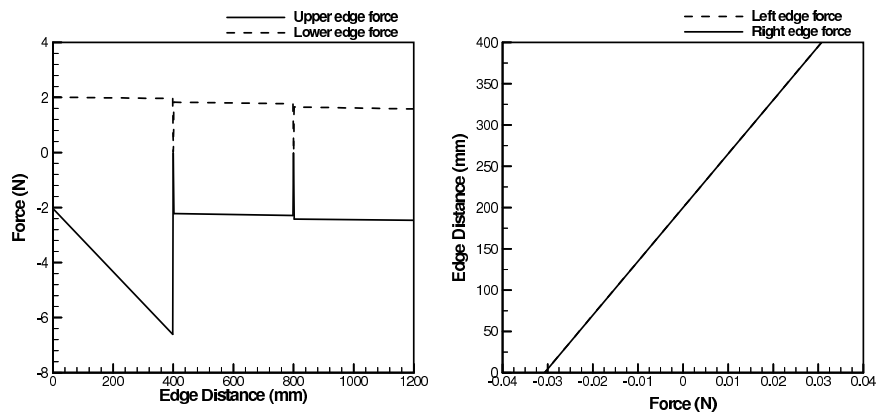


Figure 6: Self-equilibrated loading for load case 1 and load control point 3, $p_{31} = 0.25$ [9].

Table 3: Optimization results $p_{ij} = 1$.

		Initial Structure1		Initial Structure 2		Initial Structure 3	
		Initial	Optimum	Initial	Optimum	Initial	Optimum
		(mm)	(mm)	(mm)	(mm)	(mm)	(mm)
	t_1	0.6	0.3	0.7	0.1	0.5	0.3
	t_2	0.8	0.7	0.7	0.9	0.9	0.6
	t_3	0.6	0.9	0.7	0.1	0.9	0.5
	t_4	0.8	0.4	0.7	0.9	0.5	0.6
	w_1	4.00	2.53	3.00	1.59	2.00	1.97
	h_1	60.00	13.10	80.00	14.56	70.00	17.04
	Mass (kg)	2.396	1.680	2.396	1.532	2.271	1.490
Load	λ_1	3.10	1.00	2.80	1.04	3.25	1.01
case 1	ω_1/ω_0	3.51	1.52	3.42	1.64	3.24	1.75
Load	λ_2	2.72	1.10	2.47	1.02	2.07	1.02
case 1	ω_2/ω_0	3.51	1.75	3.42	1.71	3.24	1.97
Load	λ_3	3.24	1.22	2.91	1.19	3.48	1.16
case 1	ω_3/ω_0	3.51	2.00	3.42	1.92	3.24	2.07
Load	λ_4	20.96	8.02	20.79	6.34	20.26	7.25
case 2	ω_4/ω_0	3.53	2.79	3.44	3.05	3.27	3.17
Load	λ_5	13.39	5.05	12.42	5.13	13.17	4.70
case 3	ω_5/ω_0	3.54	2.80	3.45	3.15	3.28	3.26
Load	λ_6	7.48	2.95	6.73	3.08	6.43	2.85
case 4	ω_6/ω_0	3.51	2.43	3.42	2.82	3.25	2.95
Load	λ_7	11.91	6.03	11.39	3.74	10.43	4.65
case 5	ω_7/ω_0	3.52	2.76	3.43	2.97	3.26	3.14

Figure 6 shows the plot of Force \times Edge distance when p_{31} is equal to 0.25 for load case 1. Load concentration at section 1 upper edge is lower than the one that results when p_{ij} is equal to one. The loading representation is closer to a non uniform loading and could represent actual design loads.

Analyzing Table 4 it is possible conclude that for initial structures 1 and 2 the critical load cases were cases 1 and 4 (the minimum of λ_i or ω_i/ω_0 for these initial structures are always for $i = 1$ to 8 that correspond to load case1 or for $i = 21$ to 28 that correspond to load case 4). For initial structure 3 the critical load case was case 1. After the optimization, the critical load case is case 1 for the three optimal structures. At the beginning of the optimization process, frequency was the dominant criterion for the three structures and by the end of the process, buckling becomes the dominant criterion. As expected, the three optimal structures are very close as the problem is convex. The global optimum structure is structure 1 with the minimum mass. In this structure the 0° layers are thinner than the 90° layers for the three sections.

Table 4: Optimization results $p_{ij} = 0.25$.

		Initial Structure 1		Initial Structure 2		Initial Structure 3	
		Initial	Optimum	Initial	Optimum	Initial	Optimum
		(mm)	(mm)	(mm)	(mm)	(mm)	(mm)
	t_1	0.6	0.1	0.7	0.2	0.5	0.3
	t_2	0.8	0.7	0.7	0.6	0.9	0.5
	t_3	0.6	0.2	0.7	0.01	0.9	0.6
	t_4	0.8	0.6	0.7	0.8	0.5	0.3
	w_1	4.00	2.25	3.00	2.04	2.00	4.00
	h_1	60.00	10.06	80.00	12.07	70.00	12.88
	Mass (kg)	2.396	1.22	2.396	1.23	2.271	1.307
Load	l_l	5.38	1.11	4.86	1.20	5.44	1.06
case 1	ω_1/ω_0	3.51	1.44	3.42	1.63	3.24	1.65
Load	λ_2	5.16	1.02	4.66	1.09	5.05	1.01
case 1	ω_2/ω_0	3.51	1.27	3.42	1.50	3.24	1.54
Load	λ_3	6.30	1.17	5.66	1.42	5.36	1.33
case 1	ω_3/ω_0	3.51	1.46	3.42	1.90	3.24	2.06
Load	λ_4	2.82	1.01	4.35	1.00	3.79	1.02
case 1	ω_4/ω_0	3.51	1.24	3.42	1.40	3.24	1.74
Load	λ_5	4.82	1.01	4.35	1.00	3.79	1.02
case 1	ω_5/ω_0	3.51	1.24	3.42	1.40	3.24	1.74
Load	λ_6	6.30	1.17	5.66	1.42	5.36	1.33
case 1	ω_6/ω_0	3.51	1.46	3.42	1.90	3.24	2.06
Load	λ_7	5.16	1.02	4.66	1.09	5.05	1.01
case 1	ω_7/ω_0	3.51	1.27	3.42	1.50	3.24	1.54
Load	λ_8	5.38	1.11	4.86	1.20	5.44	1.06
case 1	ω_8/ω_0	3.51	1.46	3.42	1.63	3.24	1.65
	\vdots	\vdots	\vdots	\vdots	\vdots	\vdots	\vdots
Load	λ_{21}	6.91	1.43	6.25	1.54	6.99	1.36
case 4	ω_{21}/ω_0	3.51	1.78	3.42	1.94	3.25	2.04
	\vdots	\vdots	\vdots	\vdots	\vdots	\vdots	\vdots
Load	λ_{28}	6.91	1.43	6.25	1.54	6.99	1.36
case 4	ω_{28}/ω_0	3.51	1.78	3.42	1.94	3.25	2.04
	\vdots	\vdots	\vdots	\vdots	\vdots	\vdots	\vdots
Load	λ_{32}	11.80	2.35	11.28	1.37	10.33	2.74
case 5	ω_{32}/ω_0	3.52	2.27	3.43	2.15	3.26	2.54

4.4 Reinforced panel [(0/90/45/-45)]_s considering $p_{ij} = 0.25$

Since the load cases defined in Table 1 include two cases of shear loadings, the panel was also optimized including layers oriented at $\pm 45^\circ$. This optimization was done just for $p_{ij} = 0.25$ because this is the loading parameter that provides more realistic loading representation among the p_{ij} values tested in this example. The results are presented in Table 5. The design variable t_5 represents the thickness for all layers oriented at $\pm 45^\circ$.

Analyzing Table 5 it is possible to conclude that with the inclusion of the four layers oriented at $\pm 45^\circ$ the initial structure becomes significantly heavier. However, by the end of the optimization process the optimal structures have mass quite close to the mass of the [(0/90)]_s optimal structures. The inclusion of $\pm 45^\circ$ layers certainly is beneficial for the shear load cases. However, for the particular example presented, due to the existence of compressive load cases, the optimal structure with the laminate including the $\pm 45^\circ$ layers is approximately the same as the one that does not include such layers. The results indicate that the proposed optimization procedure is efficient in finding the minimal mass necessary to support the applied loading.

For initial structures 1 and 3 the critical load cases were cases 1 and 4 (the minimum of λ_i or ω_i/ω_0 for these initial structures are always for $i = 1$ to 8 that correspond to load case 1 or for $i = 21$ to 28 that correspond to load case 4). For initial structure 2 the critical load cases were cases 1, 4, and 5 (the minimum of λ_i or ω_i/ω_0 for these initial structures are always for $i = 1$ to 8 that correspond to load case 1 or for $i = 21$ to 28 that correspond to load case 4 or $i = 29$ to 32 that correspond to load case 5). After the optimization, the critical load is case 1 for the three initial structures. At the beginning of the optimization process, frequency was the dominant criterion for the three initial structures and at the end of the process buckling becomes the dominant criterion. The global optimum structure is structure 2 that presents minimum mass. Except for 0° layer in section 2, all layers have the same thicknesses in the optimal structure.

4.5 Reinforced panel [(0/90)]_s considering $p_{ij} = 0.25$, $\omega_0 = 60$ Hz

From Table 4 it is possible to conclude that the optimal result for initial structure 1 has a normalized minimum frequency value of 1.24. Therefore, it is expected that if the minimum frequency requirement and, as a consequence, the normalization value is changed to 60 Hz (instead of 20 Hz), the dominant criterion would become frequency and the mass should increase. In order to confirm these facts it was performed an optimization process using $\omega_0 = 60$ Hz, $p_{ij} = 0$ using initial structure 1. The results are presented in Table 6.

More important than confirming what was expected, these results show the importance of the multicriteria optimization. In this case, if the optimization were done without considering frequency, the structure would not satisfy the frequency design requirements.

5 Conclusions

Load representation is an important part of a structural design. The proposed methodology allows the designer to represent the loading within a prescribed degree of accuracy and obtain realistic self-

Table 5: Optimization results $[(0/90/45/-45)]_s$, $p_{ij} = 0.25$.

		Initial Structure 1		Initial Structure 2		Initial Structure 3	
		Initial	Optimum	Initial	Optimum	Initial	Optimum
		(mm)	(mm)	(mm)	(mm)	(mm)	(mm)
	t_1	0.6	0.01	0.7	0.2	0.5	0.2
	t_2	0.8	0.01	0.7	0.2	0.9	0.01
	t_3	0.6	0.01	0.7	0.1	0.9	0.01
	t_4	0.8	0.01	0.7	0.2	0.5	0.2
	t_5	0.5	0.4	0.5	0.2	0.5	0.3
	w_1	4.00	4.00	3.00	4.00	2.00	4.00
	h_1	60.00	11.22	80.00	11.80	70.00	11.36
	Mass (kg)	3.89	1.283	3.89	1.203	3.77	1.268
Load	λ_1	30.48	1.27	29.65	1.10	30.69	1.20
case 1	ω_1/ω_0	4.23	1.93	4.15	1.63	3.97	1.92
Load	λ_2	29.22	1.21	28.27	1.05	29.07	1.14
case 1	ω_2/ω_0	4.23	1.90	4.15	1.56	3.97	1.87
Load	λ_3	34.37	1.28	32.75	1.31	31.03	1.50
case 1	ω_3/ω_0	4.23	1.98	4.15	1.94	3.97	2.15
Load	λ_4	26.67	1.00	25.64	1.00	23.25	1.26
case 1	ω_4/ω_0	4.23	1.64	4.15	1.53	3.97	2.07
Load	λ_5	26.66	1.02	25.62	1.00	23.25	1.26
case 1	ω_5/ω_0	4.23	1.66	4.15	1.54	3.97	2.07
Load	λ_6	34.31	1.18	32.69	1.28	31.19	1.24
case 1	ω_6/ω_0	4.23	1.85	4.15	1.90	3.97	1.97
Load	λ_7	28.90	1.01	27.98	1.01	28.90	1.00
case 1	ω_7/ω_0	4.23	1.55	4.15	1.47	3.97	1.59
Load	λ_8	30.04	1.06	29.22	1.06	30.36	1.06
case 1	ω_8/ω_0	4.23	1.64	4.15	1.55	3.97	1.68
	\vdots	\vdots	\vdots	\vdots	\vdots	\vdots	\vdots
Load	λ_{21}	39.18	1.63	38.11	1.42	39.46	1.55
case 4	ω_{21}/ω_0	4.23	2.21	4.15	1.99	3.97	2.21
	\vdots	\vdots	\vdots	\vdots	\vdots	\vdots	\vdots
Load	λ_{28}	38.63	1.37	37.57	1.36	39.04	1.36
case 4	ω_{28}/ω_0	4.23	2.04	4.15	1.94	3.97	2.08
	\vdots	\vdots	\vdots	\vdots	\vdots	\vdots	\vdots
Load	λ_{32}	53.27	1.90	51.91	2.00	49.08	2.18
case 5	ω_{32}/ω_0	4.24	2.50	4.15	2.31	3.98	2.64

Table 6: Optimization results $[(0/90)]_s$, $p_{ij} = 0.25$, $\omega_0 = 60$ Hz.

		Initial Structure1				Initial Structure1	
		Initial	Optimum			Initial	Optimum
		(mm)	(mm)			(mm)	(mm)
	t_1	0.6	0.4		t_1	0.6	0.4
	t_2	0.8	0.6		t_2	0.8	0.6
	t_3	0.6	0.8		t_3	0.6	0.8
	t_4	0.8	0.3		t_4	0.8	0.3
	w_1	4.00	4.00		w_1	4.00	4.00
	h_1	60.00	14.92		h_1	60.00	14.92
	Mass (kg)	2.396	1.622		Mass (kg)	2.396	1.622
Load case 1	λ_1	5.38	2.28	Load case 1	λ_8	5.38	2.28
	ω_1/ω_0	1.17	1.02		ω_8/ω_0	1.17	1.02
					\vdots	\vdots	\vdots
Load case 1	λ_2	5.16	2.13	Load case 4	λ_{21}	6.91	2.94
	ω_2/ω_0	1.17	1.01		ω_{21}/ω_0	1.17	1.06
Load case 1	λ_3	6.30	2.54		\vdots	\vdots	\vdots
	ω_3/ω_0	1.17	1.06	Load case 4	λ_{28}	6.91	2.94
Load case 1	λ_4	4.82	1.79		ω_{28}/ω_0	1.17	1.06
	ω_4/ω_0	1.17	1.01		\vdots	\vdots	\vdots
Load case 1	λ_5	4.82	1.79	Load case 5	λ_{32}	11.80	5.14
	ω_5/ω_0	1.17	1.01		ω_{32}/ω_0	1.17	1.07
Load case 1	λ_6	6.30	2.54				
	ω_6/ω_0	1.17	1.06				
Load case 1	λ_7	5.16	2.13				
	ω_7/ω_0	1.17	1.01				

equilibrating load cases from a given set of physical load cases. If the designer wants a good accuracy on the load representation, it is necessary to use a larger number of load control points. The only limitation for this methodology is the available computational resources.

The p_{ij} parameters are defined in the $[0\ 1]$ range; the p_{ij} values for a certain non uniform loading representation can be selected by a comparative analyses and a judicious choice based on a clear understanding of the physical load associated with it. As a general trend, it can be said that when p_{ij} is equal to 0 the loading representation is almost uniformly distributed and the structure tends to be under dimensioned with low mass. When p_{ij} is equal to 1 the loading representation is significantly concentrated at the considered load control point and the structure tends to be super dimensioned with high mass. Therefore, the results presented in this work are consistent: the mass of the optimal

structures always increase with parameters p_{ij} .

The minimax strategy, Powell's method and the mass optimization external loop resulted in a robust optimization process. The multicriteria optimization yields the best design for the worst loading condition with adaptable structural mass. These features guarantee that the proposed design procedure is quite general and flexible. The examples presented in this work demonstrate that the present design procedure is able to minimize the structural mass while satisfying the design requirements for a typical design problem.

The main contribution of this work actually is a design procedure that provides robust preliminary optimum designs for aeronautical applications. The proposed procedure is quite flexible. The finite element code used for the examples was Abaqus[®] but any commercial or in-house finite element code could be used. This flexibility allows the application of the methodology to a wide variety of structures in the aerospace industry. Also, the Powell's method was used for the optimization procedure. The reason for this choice was primarily the simplicity of the method and the fact that it does not require computation of gradient. However, any other standard optimization procedure could be used, including those that use gradient information. Finally, the procedure may be used for multicriteria optimization of composite structures. Therefore, these features make the proposed procedure very attractive for applications in actual design of aerospace structures.

As a future work, the composite structure multicriteria optimization may be performed using the lamina angular orientation as design variable.

Acknowledgments This work is financed by the Brazilian Agency FAPESP (Grant No. 06/60929-0) and Brazilian National Council for Scientific and Technological Development (Grant 305601/2007-5).

References

- [1] Pedersen, N.L. & Nielsen, A.K., Optimization of practical trusses with constraints on eigenfrequencies, displacements, stresses, and buckling. *Struct and Multidiscip Optim*, **25**, pp. 436–445, 2003.
- [2] Topal, U., Multiobjective optimization of laminated composite cylindrical shells for maximum frequency and buckling load. *Mater and Des*, **30**, pp. 2584–2594, 2009.
- [3] Grierson, D.E., Resolving the pareto optimization conundrum. *Proceedings of the 12th AIAA/ISSMO Multidisciplinary Analysis and Optimization Conference*, AIAA 2008-5966: Victoria, British Columbia Canada, 2008.
- [4] Dem'Yanov, V.F. & Malozemov, V.N., *Introduction to minimax*. John Wiley & Sons: New York, 1974.
- [5] Kang, B., Park, J. & Kim, J., Analysis and optimal design of smart skin structures for buckling and free vibration. *Compos Struct*, **84**, pp. 177–185, 2008.
- [6] Vanderplaats, G., *Numerical optimization techniques for engineering designs: with applications*. McGraw-Hill: New York, 1984.
- [7] Conrado, A.C., Faria, A.R. & Almeida, S.F.M., Optimum design for buckling of arbitrary shaped ribs under uncertain loadings. *The Aeronaut J of the Aeronaut Soc*, pp. 609–617, 2005.
- [8] Gama, R.C., *Otimização da carga de flambagem de um painel reforçado submetido a carregamentos incertos*. Master's thesis, Instituto Tecnológico de Aeronáutica, São José dos Campos, Brasil, 2009.
- [9] Ferreira, A.P.C.S., *Projeto Aeronáutico Ótimo Simultâneo sob Carregamentos Incertos*. Ph.D. thesis, Instituto Tecnológico de Aeronáutica, São José dos Campos, Brasil, 2010.

[10] Megson, T.H.G., *Aircraft structures for engineering students*. Arnold, 1999.

Finite element analysis of reinforced concrete slabs regarded as elastoplastic multiphase media: the role of reinforced zone extent

Marcelo P. Figueiredo, Samir Maghous, Américo Campos Filho
*PPGEC-UFRGS, Av. Osvaldo Aranha, 99, 3º andar-90035-190,
Porto Alegre, RS – Brazil*

Abstract

Conceived as generalization of the homogenization method, a multiphase modeling is developed to assess the macroscopic behavior of reinforced concrete slabs within the framework of classical plasticity with account of concrete cracking. Particular emphasis is put on the effects on structure response of the thickness of the reinforced zone adopted in the modeling for the multiphase zone.

Basically, the multiphase model is quite similar to description at the macroscopic level of ordinary porous media. The macroscopic particle is regarded as the geometrical superposition of continuous media in mutual interaction, called matrix and reinforcement phases. These geometrically coincident particles are attributed different kinematics. The equations of motion are derived by means of the virtual work method. The state equations for each phase and the interaction law are formulated within the framework of generalized plasticity.

The multiphase approach is applied to analyze reinforced concrete slab structures under prescribed loading. In addition to validate the approach through confrontation of obtained results with experimental test data, the main focus of the study was the assessment of the effects of multiphase zone extent in the modeling. The analysis showed that the results converge rapidly toward the experimental ones as the multiphase zone thickness decreases, thus emphasizing the slight sensitivity of the modeling with respect to the latter.

Keywords: multiphase model, elastoplasticity, finite element method, reinforced concrete.

1 Introduction

The capacity of predicting the essential characteristics that govern the behavior of materials reinforced by stiff linear inclusions from the properties of the individual components still remains a major concern in structural engineering of composite materials, and a significant number of works has been dedicated to this subject in the last decades.

As far as the finite element modeling of reinforced concrete structures is concerned, steel bars are traditionally accounted for through three ways according to CEB [1]: 1) by means of a continuous equivalent model as often used in the case of plates and shells, substituting the dense reinforcement

by equivalent layers, 2) through a discrete modeling in which the steel bars are represented by one-dimensional elements frequently associated with appropriate adherence elements, and 3) through the so-called “embedded model” where each bar is considered as a stiffer linear inclusion embedded within the element of concrete matrix, thus resulting in an element stiffness equal to the sum of concrete matrix and steel bar contribution. However such approaches can come up against serious numerical difficulties when the number of bars involved in the structure becomes higher. Indeed, the computational cost may eventually be prohibitively large since three-dimensional analysis is generally needed to take into account interactions between concrete matrix and inclusions properly and since non-linear constitutive models, such as plasticity, have to be utilized in order to obtain relevant results.

Some features about the reinforced concrete may be pointed out now: the reinforcing inclusions take the form of linear inclusion elements (steel bars) which are incorporated into the concrete matrix, following some pattern and preferential orientations, and the stiffness of the reinforcing material are considerably higher than those of the concrete. So, taking advantage of the fact that the reinforcing inclusions are periodically distributed, the homogenization theory for heterogeneous periodic media can be legitimately applied.

An alternative approach called multiphase model, which may be conceived as a generalization of the homogenization method, was recently developed, providing a mechanically consistent framework to analyze the behavior of structures made up of materials reinforced by linear continuous inclusions. Such approach will allow to capture the macroscopic behavior of the concrete structures.

The general formulation of the model is presented in Sudret [2] together with applications in the field of geotechnical engineering. Extensions of the multiphase model have been introduced by Bennis [3] and later by Hassen [4]. The method has been applied to a large variety of problems involving reinforced soils such as reinforced earth, micropile networks and rock-bolted tunnels may be found in de Buhan and Sudret [5] or Hassen and de Buhan [6]. The main advantage of such modeling lies in a significantly reduced computational effort, compared to that required in direct numerical simulations.

2 The multiphase model for reinforced concrete

2.1 Description of the model

Consider a medium defined by a concrete matrix reinforced by steel bars, which are arranged periodically (Figure 1). The typical size of the structure being significantly greater than the diameter of the inclusions and their mutual spacing, it is suited to adopt a macroscopic scale of description in which the reinforced concrete is regarded as a homogenous medium.

Sudret [2] explains that to any point of a volume Ω of reinforced material are associated geometrically coincident particles: one particle of the matrix phase and N particles of the reinforcement phase. These $N + 1$ superposed particles form the multiphase medium.

$$d\Omega(\underline{x}) = d\Omega^m(\underline{x}) \bigcup_{r=1, \dots, N} d\Omega^r(\underline{x}) \quad (1)$$

In this way, the steel bars are grouped in a finite number of N different families, each one of

these families characterized by a direction given by a unit vector \underline{e}_r ($r = 1, \dots, N$). The number of reinforcement families will be the same to the number of directions in which the bars are disposed.

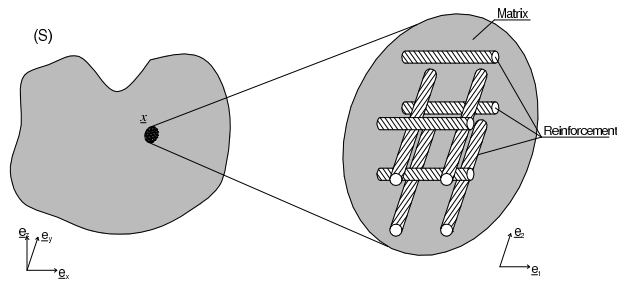


Figure 1: Description of the reinforced material [4].

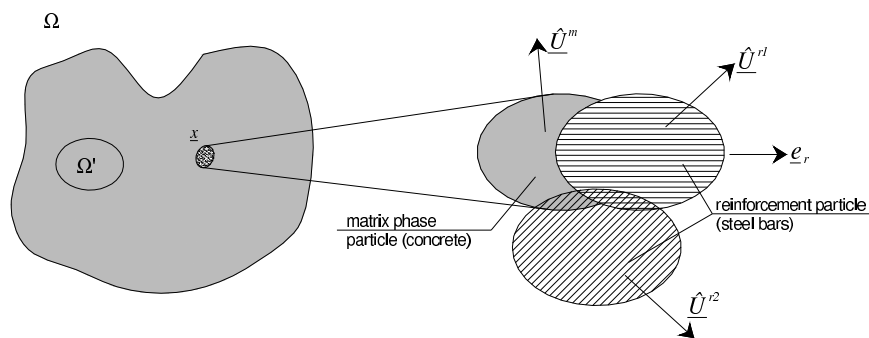


Figure 2: Description of the material with the matrix phase and two reinforcement phases.

2.2 Efforts behaviour

The matrix phase is modelled as Cauchy continuum. It can be shown that the internal forces are described by a second-order symmetrical tensor denoted by $\underline{\underline{\sigma}}^m$. This quantity will be referred to as

the matrix phase stress tensor.

It is admitted that the inclusions are assumed to take only tensile-compressive forces, that is, shear forces and bending moments are disregarded. Hassen [4] applies the multiphase model taking into account that the inclusions takes these efforts. So, the variable that describes the internal forces in the reinforcement phase turns out to be a scalar stress, noted σ^r .

Finally, due to the superposition of $N + 1$ particles in each point, body forces, I^j , are introduced to account for the interaction between phases.

The external forces applied onto a geometrical volume Ω are prescribed in each phase j separately, and consists in:

- (a) Body forces denoted by $\rho^j \underline{F}^j$ (gravity) exerted by the outside of Ω .
- (b) Tractions \underline{T}^j applied at the boundary $\partial\Omega$.

The inertial forces are computed by means of the phase acceleration fields denoted by $\underline{\gamma}^j$.

2.3 Equations of motion

The equations of motion of the multiphase model can be derived within the framework of virtual work method and related principles. They may be written as follows for each phase separately [2]:

- *Matrix phase Ω^m :*

$$\text{div} \underline{\underline{\sigma}}^m(\underline{x}) + \rho^m(\underline{x})(F^m(\underline{x}) - \gamma^m(\underline{x})) + \sum_{r=1}^N \underline{I}^r(\underline{x}) = 0 \quad (2)$$

- *Reinforcement phase Ω^r :*

$$\text{div}(\sigma^r(\underline{x}) \underline{e}_r \otimes \underline{e}_r) + \rho^r(\underline{x})(F^r(\underline{x}) - \gamma^r(\underline{x})) - \underline{I}^r(\underline{x}) = 0, \quad r = 1, \dots, N \quad (3)$$

The corresponding boundary conditions read

$$\underline{T}^m(\underline{x}) = \underline{\underline{\sigma}}^m(\underline{x}) \cdot \underline{n}(\underline{x}) \quad \text{on } \partial\Omega^m \quad (4)$$

$$\underline{T}^r(\underline{x}) = \sigma^r(\underline{x}) (\underline{n}(\underline{x}) \cdot \underline{e}_r) \underline{e}_r \quad \text{on } \partial\Omega^r, \quad r = 1, \dots, N \quad (5)$$

Equations (2) and (4) are the equations of motion of a Cauchy continuum, where the interaction forces \underline{I}^r appear as body forces. These interaction forces express, at the macroscopic scale, the interface forces between each inclusion and the surrounding matrix at the microscopic scale, and can thus be interpreted as the average of the latter on a unit volume. More precisely, \underline{I}^r represents the volume density of interaction forces exerted by the reinforcement phase r onto the matrix phase.

2.4 Perfect bonding model

All the developments presented in the sequel are restricted to the particular case of perfect bonding hypothesis: all phases have the same displacement field. This model is thus dedicated to problems

of reinforced concrete structures where slippage between the steel bars and the concrete matrix is disregarded. Accordingly,

$$\underline{\xi}^m = \underline{\xi}^r \equiv \underline{\xi} \quad (6)$$

Taking into account the perfect bonding hypothesis, is introduced, with no ambiguity, the total strain tensor:

$$\underline{\underline{\epsilon}} = \frac{1}{2} \left(\underline{\underline{grad}}\underline{\xi} + {}^t\underline{\underline{grad}}\underline{\xi} \right) \quad (7)$$

The compatibility equations between the phase strain variables are:

$$\underline{\underline{\epsilon}}^m = \underline{\underline{\epsilon}}; \quad \underline{\underline{\epsilon}}^r = \underline{\underline{\epsilon}} : (\underline{e}_r \otimes \underline{e}_r) \equiv \epsilon_{rr} \quad (8)$$

In this model, the system kinematics is described by a single displacement field $\underline{\xi}$. It is thus relevant to derive global equations of motion for the whole system. These equations are obtained by summing up Eq. (2), (3) and the Eq. (4), (5) respectively. Introducing the following notation:

$$\rho \underline{F} = \sum_j \rho^j \underline{F}^j; \quad \underline{T} = \sum_j \underline{T}^j; \quad \rho \underline{\gamma} = \sum_j \rho^j \underline{\gamma}^j \quad (9)$$

$$\underline{\underline{\Sigma}} = \underline{\underline{\sigma}}^m + \sum_{r=1}^N \sigma^r \underline{e}_r \otimes \underline{e}_r \quad (10)$$

with $j \in \{m, r = 1, \dots, N\}$, one gets:

$$\text{div } \underline{\underline{\Sigma}} + \rho (\underline{F} - \underline{\gamma}) = \underline{0} \quad (11)$$

$$\underline{T} = \underline{\underline{\Sigma}} \cdot \underline{n} \quad (12)$$

The tensor of total stress $\underline{\underline{\Sigma}}$ appears to be the sum of the partial tensor in the matrix phase and the uniaxial partial stress tensor in the reinforcement phase. With this notation, the constitutive Eq. (11) and (12) reduce to those of the classical Cauchy continuum.

To complete the description of the perfect bonding model, global constitutive equation relating $\underline{\underline{\Sigma}}$ and $\underline{\underline{\epsilon}}$ are derived. One can easily prove that the global tensor of elastic moduli $\underline{\underline{A}}$ satisfying $\underline{\underline{\Sigma}} = \underline{\underline{A}} : \underline{\underline{\epsilon}}$ in the elastic domain write:

$$\underline{\underline{A}} = \underline{\underline{a}}^m + \sum_{r=1}^N a^r \underline{e}_r \otimes \underline{e}_r \otimes \underline{e}_r \otimes \underline{e}_r \quad (13)$$

where the global tensor of elastic moduli is decomposed additively in a contribution of the matrix phase and a contribution of each reinforcement phase. It appears clearly that the directions \underline{e}_r are privileged, what is seen in the anisotropic characteristic of the behavior.

Equilibrium equations and constitutive laws have been derived, making it possible to solve boundary value problems. In order to model real reinforced structures, it is now necessary to connect the phase constitutive laws with the material characteristics of the concrete and inclusions.

Assuming that the volume fraction η^r of the inclusions is small when compared to unit (i.e., $\eta^r \ll 1$), a heuristic identification can be used:

- The matrix phase constitutive law is identified with that of the concrete.
- Since the inclusions are supposed to take purely uniaxial stresses, it is possible to evaluate the contribution a^r of the reinforcement phase stiffness in Equation (13) as:

$$a^r = \eta^r \cdot E^{inc} \quad (14)$$

where E^{inc} is the Young's modulus of the steel bars.

Remark A first attempt to extend the multiphase modeling to geotechnical structures taking into account the interaction matrix/reinforcement can be found in [3].

3 Numerical implementation of the model

The implementation formulated herein follows the steps presented by Sudret [2] and Hassen [4].

3.1 Description of the model

Considering a kinematically admissible virtual displacement field $\hat{\xi}$ and its associated linear strain field $\hat{\underline{\underline{\varepsilon}}}$, the principle of virtual work, derived from (11) and (12), writes

$$\int_{\Omega} \underline{\underline{\Sigma}} : \hat{\underline{\underline{\varepsilon}}} d\Omega - \int_{\Omega} \rho F \cdot \hat{\underline{\underline{\xi}}} d\Omega - \int_{\partial\Omega} \underline{\underline{T}}^d \cdot \hat{\underline{\underline{\xi}}} dS = 0 \quad (15)$$

Relating the elastic strain to the phase stress by $\underline{\underline{\sigma}}^m = \underline{\underline{a}}^m : (\underline{\underline{\varepsilon}}^m - \underline{\underline{\varepsilon}}_p^m)$ and $\sigma^r = a^r (\varepsilon^r - \varepsilon_p^r)$ and substituting in Eq. (11) and using the Eq. (8), the first term in Eq. (15) may be rewritten as follows:

$$\int_{\Omega} \underline{\underline{\Sigma}} : \hat{\underline{\underline{\varepsilon}}} d\Omega = \int_{\Omega} \left[\underline{\underline{A}} : \hat{\underline{\underline{\varepsilon}}} - \underline{\underline{a}}^m : \hat{\underline{\underline{\varepsilon}}}_p^m - a^r \varepsilon_p^r \underline{\underline{e}}_r \otimes \underline{\underline{e}}_r \right] : \hat{\underline{\underline{\varepsilon}}} d\Omega \quad (16)$$

The geometric volume is discretized into N_e elements. The displacement field $\underline{\xi}$ in each element ν^e is approximated as follows

$$\forall x \in \nu^e, \quad \xi(x)|_{\nu^e} = N_e(\underline{x}) \cdot \underline{u}_e \quad (17)$$

where \underline{u}_e is the vector of element nodal displacements and $N_e(\underline{x})$ are the shape functions. The strain vector is classically given by:

$$\underline{\varepsilon} = \mathbf{B}_e(\underline{x}) \cdot \underline{u}_e \quad (18)$$

where the matrix \mathbf{B}_e contains partial derivatives of the shape functions with respect to the coordinates. Consequently, the matrix phase stress vector is:

$$\underline{\sigma}^m = \mathbf{d}^m \cdot (\underline{\varepsilon} - \underline{\varepsilon}_p^m) \quad (19)$$

It is introduced now an additional notation for dealing with the reinforcement phase. Let us denote by \underline{e}_r the vector of the six components of $\underline{e}_r \otimes \underline{e}_r$. The compatibility Eq. (7) can be rewritten as:

$$\varepsilon^r = {}^t \underline{e}_r \cdot \underline{\varepsilon} = {}^t \underline{\varepsilon} \cdot \underline{e}_r \quad (20)$$

Substituting the above equations in the principle of virtual work (15) and using (16), one gets the discretized formulation, which leads to the usual linear system yielding the global vector of nodal displacement \underline{U} .

$$\mathbf{K} \cdot \underline{U} = \underline{F}^{ext} + \underline{F}_p^m + \underline{F}_p^r \quad (21)$$

The global stiffness matrix \mathbf{K} turns out to be:

$$\mathbf{K} = \sum \int_{\nu^e} {}^t \mathbf{B}_e \left(\mathbf{d}^m + \sum_{r=1}^N a^r \underline{e}_r \cdot {}^t \underline{e}_r \right) \mathbf{B}_e d\nu^e \quad (22)$$

the terms in the right-hand side of Eq. (33) are the external load vector:

$$\underline{F}^{ext} = \sum \left(\int_{\nu^e} {}^t \mathbf{N}_e \cdot \underline{\rho} \underline{F} d\nu^e + \int_{\partial\Omega \cap \nu^e} {}^t \mathbf{N}_e \cdot \underline{T}^d d\nu^e \right) \quad (23)$$

and the vector of plastic forces associated to each phase:

$$\underline{F}_p^m = \sum \int_{\nu^e} {}^t \mathbf{B}_e \cdot \mathbf{d}^m \cdot \underline{\varepsilon}_p^m d\nu^e \quad (24)$$

$$\underline{F}_p^r = \sum \int_{\nu^e} \sum_{r=1}^N a^r \varepsilon_p^r {}^t \mathbf{B}_e \cdot \underline{e}_r d\nu^e \quad (25)$$

3.2 Plastic integration algorithm

Due to the non-linearity of the phases' constitutive laws, the loading path is divided into load increments noted by $\underline{\Delta F}_j^{ext}$. For each load step, the problem is solved by an iterative algorithm.

Denoting by $\left\{ \underline{U}_n, \underline{\sigma}_n^m, \sigma_n^r, \underline{\varepsilon}_n, \underline{\varepsilon}_{p,n}^m, \varepsilon_{p,n}^r \right\}$ the set of state variables describing the system after load step n . For each variable χ in this set, let us write:

$$\Delta\chi_n = \chi_{n+1} - \chi_n \quad (26)$$

Let us apply the load increment $\underline{\Delta F}_j^{ext}$. The corresponding displacements increment $\underline{\Delta U}_n$ is obtained from the global equilibrium.

$$\mathbf{K} \cdot \underline{\Delta U}_n = \underline{\Delta F}_n^{ext} + \underline{\Delta F}_{p,n} \quad (27)$$

where $\underline{\Delta F}_{p,n} = \underline{\Delta F}_{p,n}^m + \underline{\Delta F}_{p,n}^r$ is the vector of plastic nodal forces. These forces are unknown, since the plastic strain increments $\left\{ \underline{\varepsilon}_{p,n}^m, \varepsilon_{p,n}^r \right\}$ resulting from the load increment $\underline{\Delta F}_n^{ext}$ are still unknown. The latter have to be determined in such a way that the elastoplastic constitutive laws are satisfied in each Gauss point of the mesh.

The goal is achieved by using an iterative procedure. Starting from: $\underline{\underline{\varepsilon}}_{p,n}^m(0) = \Delta\varepsilon_{p,n}^r(0) = 0$ at every Gauss point, successive evaluations $\left\{ \underline{\underline{\varepsilon}}_{p,n}^m(i), \varepsilon_{p,n}^r(i) \right\}$ of the plastic strains are calculated until convergence.

Suppose that $\left\{ \underline{\underline{\varepsilon}}_{p,n}^m(i-1), \varepsilon_{p,n}^r(i-1) \right\}$ is known at each Gauss point, the vector of plastic forces calculated by (34) and (35) being $\underline{\Delta F}_{p,n}^m(i-1)$ and $\underline{\Delta F}_{p,n}^r(i-1)$. The iteration i consists first in computing the increment of nodal displacement $\underline{\Delta U}_n(i)$ satisfying:

$$\mathbf{K} \cdot \underline{\Delta U}_n(i) = \underline{\Delta F}_n^{ext} + \underline{\Delta F}_{p,n}(i-1) \quad (28)$$

Following the global calculation yielding the displacement vector $\underline{\Delta U}_n(i)$, the constitutive laws have been checked locally in each Gauss point. The original point of the present implementation is the separate treatment of each individual phase. The power of the multiphase approach is thus totally exploited. The classical return mapping algorithm, Simo and Hughes [7], is applied in each Gauss point as follows:

At first, trial stress states are calculated for each phase by freezing the plastic strains resulting from the load increment. Then the phase yield criteria are evaluated separately. If they are negative, no additional plastic strain has developed due to $\underline{\Delta F}_n^{ext}$. If not, a closest-point projection of the trial states onto their respective yield surfaces is performed.

For the matrix phase, this leads to solving the following set of equations:

$$f^m(\underline{\underline{\sigma}}^{n+1}(i)) = 0 \quad (29)$$

$$\underline{\underline{\sigma}}^{n+1}(i) = \underline{\underline{\sigma}}_{n+1}^{trial,m}(i) - \underline{\underline{a}}^m : \underline{\underline{\Delta\varepsilon}}_{p,n}^m(i) \quad (30)$$

$$\underline{\underline{\Delta\varepsilon}}_{p,n}^m(i) = \Delta w_i \left(\frac{\partial g^m}{\partial \underline{\underline{\sigma}}^m} \right) \quad (31)$$

Considering now the reinforcement phase, the yield criterion can be written as $f^r(\sigma^r) = |\sigma^r| - \sigma_o^r$ due to the one-dimensional formulation. The solution for the projection problem and the related plastic strain increment is:

$$\sigma_{n+1}^r(i) = \begin{cases} \sigma_o^r & \text{if } \underline{\sigma}_{n+1}^{trial,r}(i) \geq \sigma_o^r \\ -\sigma_o^r & \text{if } \underline{\sigma}_{n+1}^{trial,r}(i) \leq -\sigma_o^r \end{cases} \quad (32)$$

$$\Delta \varepsilon_{p,n}^r(i) = \frac{\sigma_{n+1}^{trial,r}(i) - \sigma_{n+1}^r(i)}{a^r} \quad (33)$$

3.3 Failure criterion

The strength of concrete under multiaxial states of stress may be estimated from the so-called Ottosen failure criterion given by Eq. 34, CEB [1]. It is considered that the plasticity convex is homothetic to the failure convex.

$$\alpha \frac{J_2}{f_{cm}^2} + \lambda \frac{\sqrt{J_2}}{f_{cm}} + \beta \frac{I_1}{f_{cm}} - 1 = 0 \quad (34)$$

where

$$\begin{aligned} \lambda &= c_1 \cos [1/3 \arccos (c_2 \cos 3\theta)], \quad \cos 3\theta \geq 0; \\ \lambda &= c_1 \cos [\pi/3 - 1/3 \arccos (-c_2 \cos 3\theta)], \quad \cos 3\theta < 0; \\ \cos 3\theta &= \frac{3\sqrt{3}}{2} \frac{J_3}{J_2^{3/2}}. \end{aligned}$$

The parameters J_2 , J_3 and I_1 represent the invariants of the stress deviator and stress tensor, respectively, characterizing the state of stress considered. The coefficients are material parameters which depend on the strength ratio f_{ctm}/f_{cm} (tensile and compression concrete strength).

3.4 Stress-strain relation for concrete under compression

The hardening rule sets the yield surfaces during the plastic deformation and is determined by the effective plastic stress-strain relationship. In the present work a uniaxial stress-strain relationship for compressed concrete is assumed as hardening rule. This stress-strain diagram is calculated by the following function (CEB [1]):

$$\sigma_c = - \frac{\frac{E_{ci}}{E_{c1}} \frac{\varepsilon_c}{\varepsilon_{c1}} - \left(\frac{\varepsilon_c}{\varepsilon_{c1}}\right)^2}{1 + \left(\frac{E_{ci}}{E_{c1}} - 2\right) \frac{\varepsilon_c}{\varepsilon_{c1}}} f_{cm} \quad (35)$$

where E_{ci} is the concrete tangent modulus, $E_{ci} = -f_{cm}/0.0022$, σ_c is the strength compressive stress, ε_c is the compression strain and $\varepsilon_{c1} = -0.0022$.

3.5 Modeling of cracked concrete – Hinton [8]

The main feature of plain concrete material behavior is probably its low tensile strength, which results in tensile cracking at very low stress compared with the failure stress in compression. In the finite element context two main approaches have been used for crack representation, the *discrete crack model* that represents the individual cracks as actual discontinuities in the finite element mesh; the *smeared crack model* in which the cracked concrete is assumed to remain a continuum and the material properties are modified to account for damage. The second alternative will be adopted in this work.

3.6 The smeared crack model

The concrete is initially isotropic, but cracking induces anisotropy. After cracking, the concrete is assumed to become orthotropic, with the principal material axes oriented along the directions of cracking. The material properties depend on the state of strain and stress. The Young's modulus is reduced in the direction perpendicular to the crack plane and Poisson's effect is usually neglected. This approach is computationally attractive, since the topology of the mesh is unchanged throughout the analysis, and only the stress-strain relationship need to be updated when cracking occurs. In order to implement the smeared crack model, the following items have to be applied: a cracking criterion, a strain-softening rule and a model for shear transfer.

In the present work concrete in tension is modeled as a linear elastic-strain softening material. For a previously uncracked sampling point, the principal stresses and their directions are evaluated. If the maximum principal stress exceeds a limiting value, a crack is formed in a plane orthogonal to this stress. So, the behavior of the concrete is no longer isotropic.

Due to bond forces, cracked concrete carries between the cracks a certain amount of tensile stress normal to the cracked plane. The concrete adheres to reinforcing bars and contributes actively to the overall stiffness of the structure. This can be incorporated into the computational model assuming that the loss of tensile strength in concrete occurs gradually and such procedure has been extensively used in computational analysis of reinforced concrete structures. According to Hinton [8] it is easy to choose a tension-stiffening curve that will adequately fit experimental results, but very difficult to make a priori predictions.

For the tensile concrete it will be used the constitutive equation (Eq. 36) adopted by Prates Junior [9], Martinelli [10] and other authors.

$$\sigma_i = \alpha_t f_{ci} \left(1 - \frac{\varepsilon_{ui}}{0,01} \right) \quad (36)$$

where α_t is the reduction coefficient related to cracking strength and ε_{ui} is the strain on direction i .

3.7 Shear transfer across the crack

Experiments show that a considerable amount of shear stress can be transferred across the rough surfaces of cracked concrete. In plain concrete the main shear transfer mechanism is aggregate interlock. In reinforced concrete dowel action will play a significant role, the main variable being the reinforcement ratio.

The above-mentioned mechanisms cannot be directly included in the smeared crack model. A simplified approach is generally employed to take into account the shear transfer capacity of cracked concrete. The process consists of assigning to the shear modulus corresponding to the crack plane a reduced value, G_c , defined as $G_c = \beta G_o$, where G_o is the shear modulus of uncracked concrete and β is a reducing factor in the range of zero to one. Hinton [8] relates the value of β to the tensile strain normal to the crack plane. In this work, the following value is used.

$$\beta = 1 - (\varepsilon_t/0.005)^{k_1} \quad (37)$$

where ε_t is the tensile strain normal to the crack plane and k_1 is a parameter in the range of 0.3 to 1.0.

4 Applications

The following numerical examples were performed in order to verify the relevancy of the proposed multiphase modeling.

4.1 McNeice's and Duddeck's corner-supported reinforced concrete slab with a point load

The results of a corner-supported two-way square reinforced concrete slab, tested experimentally under a central point load by Jofriet and McNeice [11] and Duddeck et al. [12], have been used as a benchmark for verification of numerical schemes by several researchers (Zhang et al. [13], Hinton et al. [14]) and these slabs were analyzed using the multiphase model to assess the accuracy and performance of the proposed schemes for RC slabs. The geometry and reinforcement of the slabs are shown in Figure 3 and the material properties are those of Table 1.

Table 1: Material properties.

Phase	Properties	McNeice	Duddeck
Matrix (concrete)	Young's modulus	28600 MPa	16.400 MPa
	Poisson's ratio	0,15	0,15
	Compression strength	38 MPa	43 MPa
	Tensile strength	3,8 MPa	2,0 MPa
	α_t reduction coefficient	0,4	0,4
Reinforcement (steel)	Young's modulus	200.000 MPa	201.000 MPa
	Yield stress	350 MPa	670 MPa

The finite element mesh used to perform both simulations consists in two hundred twenty-noded hexahedral elements. The cross-section of the slab was divided into eight concrete layers and one or more equivalent steel layers with reinforcement in two directions, with one quarter of the slab being analyzed owing to symmetry with a 5 x 5 meshing of the quadrant (Figure 3). The slab tested by McNeice has the steel bars laid only at the bottom of the structure while Duddeck's slab has the reinforcement placed both on top and bottom, as it can be seen on Figures 4 and 5.

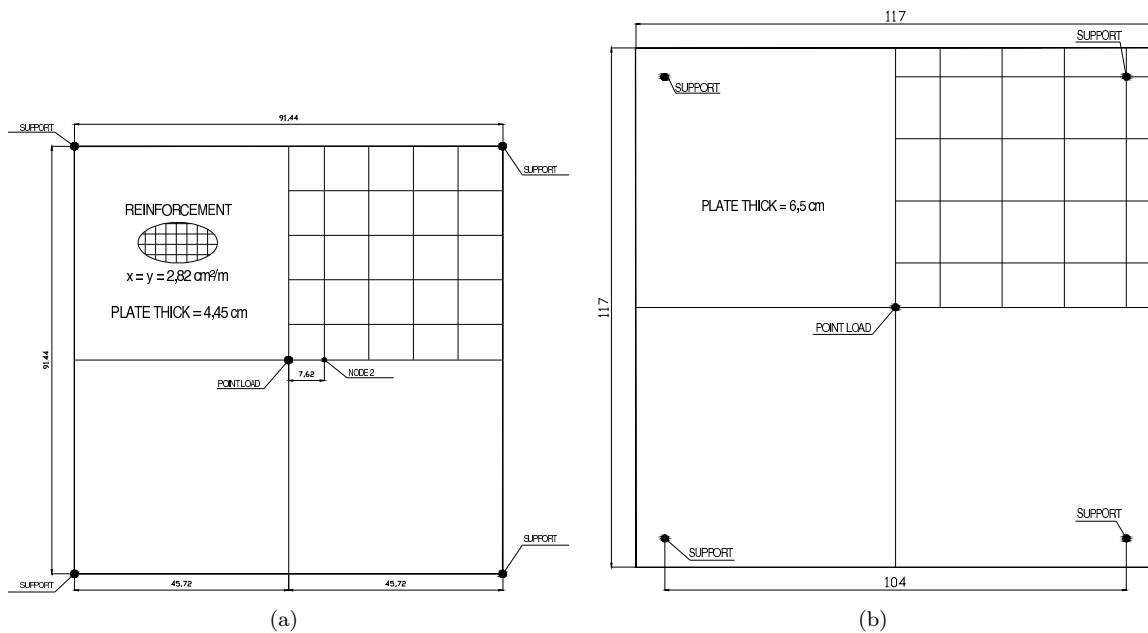


Figure 3: Geometry of the concrete slabs: (a) McNeice, (b) Duddeck

The slabs are two-way reinforced by a distribution of parallel steel bars introduced following directions e_x and e_y . The loading mode corresponds to a bending-like test with just one point loaded.

For Duddeck's plate the reinforcement ratio of steel area to the total area of the slab in both direction is $r = 0.0296$ at the top and $r = 0.061$ at the bottom. For McNeice the reinforcement, just at the bottom, is $282 \text{ mm}^2/\text{m}$.

Numerical simulations are performed corresponding to five different reinforcement distributions along the transversal section. Example 0 has no reinforcement while Example 1 has the reinforcements distributed all along the cross-section. Examples 2, 3 and 4 have the steel distributed at the inferior region of the structural element as it can be seen in Figure 6. It is very important to point out that variable called volumetric fraction η , varies in each model aiming to maintain the same amount of steel reinforcement.

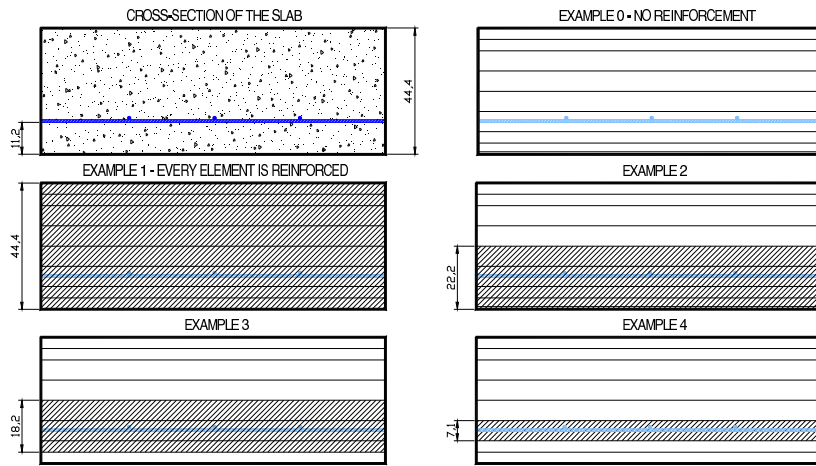


Figure 4: McNeice's reinforcement distribution: the hatched regions indicating reinforced layers.

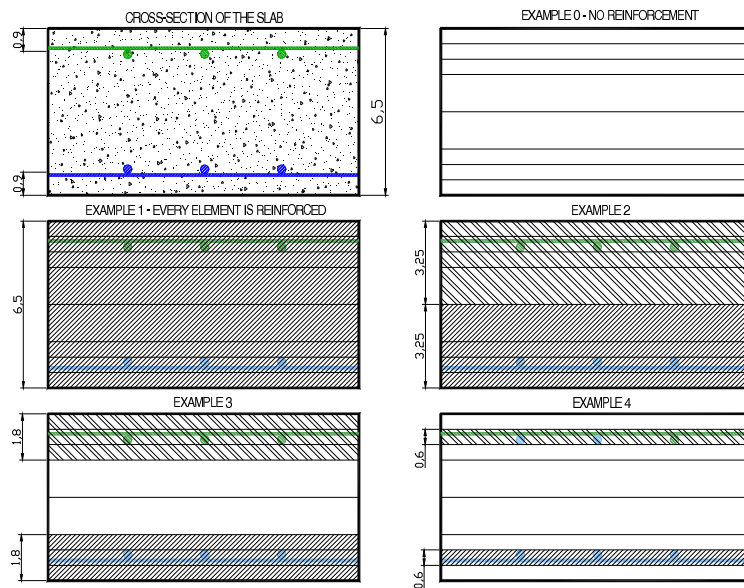


Figure 5: Duddeck's reinforcement distribution: different steel ratios on top and bottom of the plate.

For Duddeck's slab also was performed five simulations. Example 0 has no reinforcement too. In Example 1 an average reinforcement is applied along the cross-section. For Examples 2, 3 and 4, the difference of the steel rate is taken into account with the multiphase zone extent becoming smaller for

each example. The reinforcement distribution can be seen on Figure 5.

Figure 6 presents the numerical and experimental results. It has been found from the comparisons that the numerical results agree with the experimental tests. Obviously Example 1, for both comparisons, gave the worst result since the center of mass of the steel bars wasn't observed.

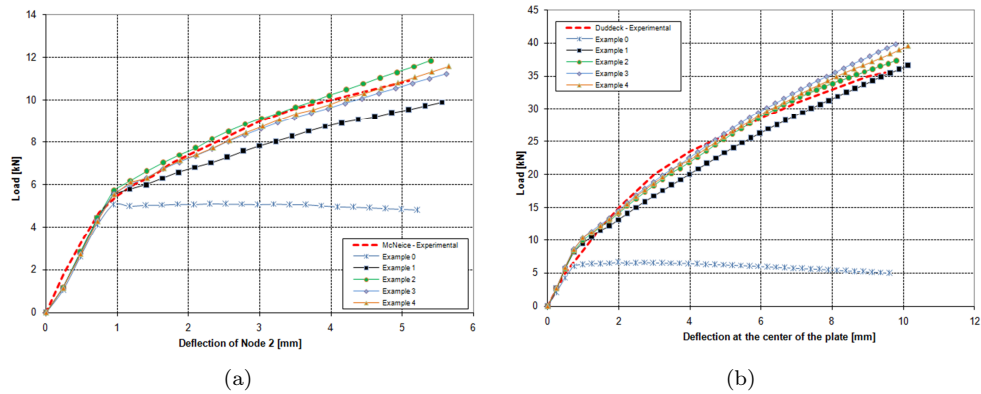


Figure 6: Load-deflection curves at node for slabs under a central point load: (a) McNeice, (b) Duddeck.

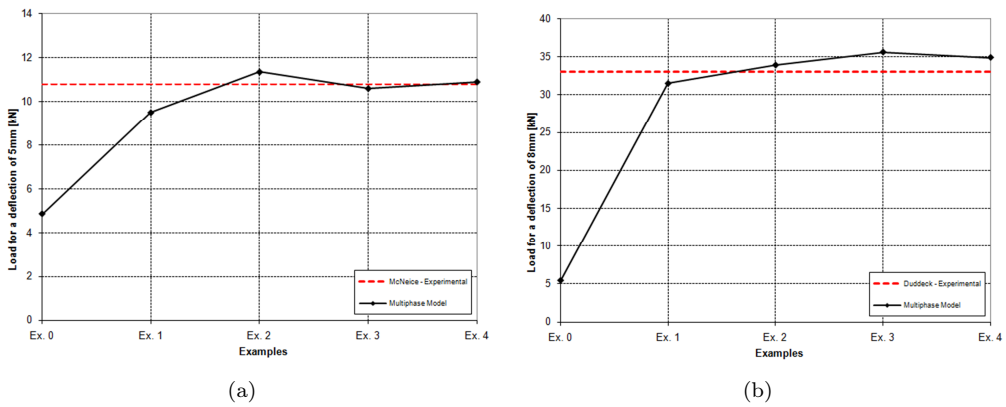


Figure 7: Load for a deflection of 5mm (McNeice (a)) and 8mm (Duddeck (b))

An important issue of the computational modeling is to determine the extent of the multiphase zone (i.e., reinforced zone). Actually, this aspect is related to the validity of the approach, since the

latter theoretically requires that the density of reinforcement is much higher for the material to be regarded at the macroscopic scale as an ‘homogeneous’ two phase material.

The analysis indicates that the configurations considered for McNeice’s slab converge rapidly toward the experimental result. This means that reinforced zones with extension of 40,9% (Example3: 1,82cm/4,44cm) or 15,9% (Example4: 0,71cm/4,44cm) prove to be enough for an appropriate representation of the reinforced zone. A similar behavior is observed for the analysis of Duddeck’s slab: the model using a multiphase zone with extension of 50% (3,25cm/6,5cm), which is rather rough, lead to satisfactory predictions.

This preliminary study constitutes an important and encouraging result. Indeed, it suggests that the modeling is slightly sensitive to the extent of the multiphase zone adopted for the calculations.

5 Concluding remarks

A multiphase model for structures of reinforced concrete with perfect bounding between the steel bars and the matrix of concrete and considering the concrete cracking was introduced. The implementation and validation of this model is the object of the doctorate thesis of the first author. The comparative studies performed produced results in good agreement with the experimental results. In terms of future development, the model will be extended to include more realistic conditions than perfect bonding, allowing some kind of sliding between the matrix phase and the reinforcement phase. These results are still to be confirmed by further investigations.

References

- [1] Application of the finite element-method to two-dimensional reinforced concrete structures. Technical Report 159, Comité Euro-International du Béton (CEB), Paris, 1983.
- [2] Sudret, B., *Modélisation multiphasique des ouvrages renforcés par inclusions*. Ph.D. thesis, École Nationale des Ponts et Chaussées, Paris, 1999.
- [3] Bennis, M., *Un modèle multiphasique pour le calcul des ouvrages renforcés par inclusions, avec prise en compte de l’interaction matrice/inclusions*. Ph.D. thesis, École Nationale des Ponts et Chaussées, Paris, 2002.
- [4] Hassen, G., *Modélisation multiphasique pour le calcul des ouvrages renforcés par inclusion rigides*. Ph.D. thesis, École Nationale des Ponts et Chaussées, Paris, 2006.
- [5] de Buhan, P. & Sudret, B., A two-phase elastoplastic model for unidirectionally-reinforced materials. *European Journal of Mechanics A/Solids*, pp. 995–1012, 1999.
- [6] Hassen, G. & de Buhan, P., Elastoplastic multiphase model for simulating the response of piled raft foundations subject to combined loadings. *International Journal for numerical and analytical methods in geomechanics*, pp. 843–864, 2006.
- [7] Simo, J.C. & Hughes, T.J.R., *Computational Inelasticity*. Springer: Berlin, 1998.
- [8] Hinton, E., *Numerical methods and software for dynamic analysis of plates and shells*. Pineridge Press: Swansea, 1988.
- [9] Prates Júnior, N.P., *Um modelo elasto-viscoplástico para análise de peças de concreto estrutural, submetidas a estados planos de tensão, através do método dos elementos finitos*. Master’s thesis, Universidade

- Federal do Rio Grande do Sul, Porto Alegre, 1992.
- [10] Martinelli, M., *Modelagem de situações de punção em lajes de concreto armado através do método dos elementos finitos*. Master's thesis, Universidade Federal do Rio Grande do Sul, Porto Alegre, 2003.
 - [11] Jofriet, J.C. & McNeice, G.M., Finite-element analysis of reinforced concrete slabs. *J Struct Div ASCE*, **97(ST3)**, pp. 785–806, 1971.
 - [12] Duddeck, H., Griebenou, G. & Schaper, G., Material and time dependent non-linear behaviour of cracked reinforced concrete slabs-finite element analysis and laboratory tests. *Non-Linear Behavior of Reinforced Concrete Spatial Structures – Prelim Report 1*, eds. G. Mehlhorn, H. Ruhle & W. Zerna, Werner: Düsseldorf, pp. 101–113, 1978.
 - [13] Zhang, Y.X., Bradford, M.A. & Gilbert, R.I., A layered shear-flexural plate/shell element using timoshenko functions for nonlinear analysis of reinforced concrete plates. *Finite Elements in Analysis and Design*, **43**, pp. 888–900, 2007.
 - [14] Hinton, E., Rahman, H. & Zienkiewicz, O., Computational strategies for reinforced concrete slab system. *Advanced Mechanics of Reinforced Concrete Structures – Final Report*, Delft, pp. 303–313, 1981.

Dynamics and energy absorption of structural elements under blast and impact

D. Karagiozova

*Institute of Mechanics, Bulgarian Academy of Sciences,
Acad. G. Bonchev Street, Block 4, Sofia 1113 – Bulgaria*

Abstract

The present article summarises the major factors, which cause an increased energy absorption capacity in materials and structural elements under intensive dynamic loading. Particular attention is paid to the inertia effects, including the propagation of stress-wave in structural elements causing an alternation of the buckling modes. The dynamic stress enhancement in cellular materials is discussed when analysing the propagation of a compaction wave in a foam material exhibiting strain hardening.

Keywords: impact, stress waves, foam, shells, buckling, energy absorption.

1 Introduction

Structural elements, which deform inelastically, are often used in energy-absorbing devices due to their simple design and the high efficiency achieved by several buckling deformation mechanisms. The progressive folding of axially loaded tubular elements, which is characterized by a constant mean load over a large stroke, is the most efficient deformation mechanism which occurs under their quasi-static compression. This is the desired behavior of an ‘ideal’ energy absorber. A literature review related to the energy absorption estimates of shell structures can be found in, e.g., [1]. In the present article, the factors which lead to the alternation of this buckling mode are highlighted when a particular attention is paid to the inertia effects. The effects of the axial inertia in ductile tubes are discussed in view of the stress-wave propagation. The effects of the lateral inertia are demonstrated on the examples of buckling of long tubes under a mass impact. A comprehensive review on the influence of the geometric and material characteristics on the dynamic elastic-plastic buckling of structural elements can be found in [2].

Similarly to the traditional structural energy absorbers, the cellular materials with different topology, honeycombs, open and closed foams, metal hollow spheres, have excellent potential characteristics as blast and impact energy absorbers due to the same reason – their ability to deform over a long

stroke at an almost constant load. While the out-of plane loaded honeycomb respond to impact loadings similarly to the response of tubular elements, other cellular materials exhibit a large strength and energy absorption enhancement under intensive dynamic loading. This phenomenon is due to the compaction waves travelling through the cellular material producing an energy dissipation which is larger than the amount that corresponds to the area under the nominal stress–strain curve [3–6]. From this view point, the understanding of the mechanism of compaction of cellular materials is important in order to obtain accurate estimates of their energy absorption capacity. A new model of compaction of foam materials exhibiting strain hardening is discussed.

2 Sandwich structures under blast loading

The deformation and velocity attenuation in a sacrificial cladding of a finite thickness comprising a Cymat foam core, steel back and cover plates with thickness H and subjected to a uniform blast loading are analysed in this section in order to reveal the phenomena which are observed during the foam deformation. The pressure pulse resulting from an air blast is applied to the cover plate as shown in Fig. 1a. Two major problems should be examined in this structural configuration – the mechanism of foam compaction and foam integrity under dynamic loading.

2.1 Foam core compaction

Different methods have been proposed in the literature to model the foam compaction. The shock wave propagation model of deformation of cellular materials was proposed by Reid and Peng [7] to explain the crush enhancement of wood specimens assuming a rigid perfectly plastic locking (RPPL) mechanism. Retaining the basic characteristics of the one dimensional shock wave models [8, 9], more detailed material models were used taking into account the elastic material properties. Elastic–plastic model with hardening was used by Harrigan et al. [10] while elastic perfectly plastic with rigid locking model was used by Lopatnikov et al. [11, 12]. Although different material models were assumed, the shock wave propagation models use either zero strain or the strain value associated with the strain of the fully locked material. Different definitions of the locking strain, ε_D , were used in [9] and [12]. More recently a phenomenological model using a power law approximation of the stress-strain curve and assuming a non-constant strain jump was proposed by Pattofatto et al. [13] which gives a more accurate prediction for the dynamic stress enhancement in some cellular materials.

Although the RPPL model gives a quick estimate of the dynamic stress enhancement, $\Delta\sigma_{dyn} = \rho_0[V]^2 / [\varepsilon_D]$ [7], the application of this model for a description of the compaction of a cellular material with strain hardening (Fig. 2a) does not always lead to accurate results as a full compaction ($\varepsilon = \varepsilon_D$) within the primary stress wave cannot be achieved in these materials. As a result, an additional compaction can occur within the reflected stress wave when a block with a finite thickness is analysed.

The compaction velocity of proximal end of the cladding is characterised by a rapid increase followed by a gradual attenuation (Fig. 1b). Shock waves can develop during the first phase for sufficiently high velocities while a plastic wave of strong discontinuity characterised by decreasing strains behind the wave front propagates in the foam during the second phase.

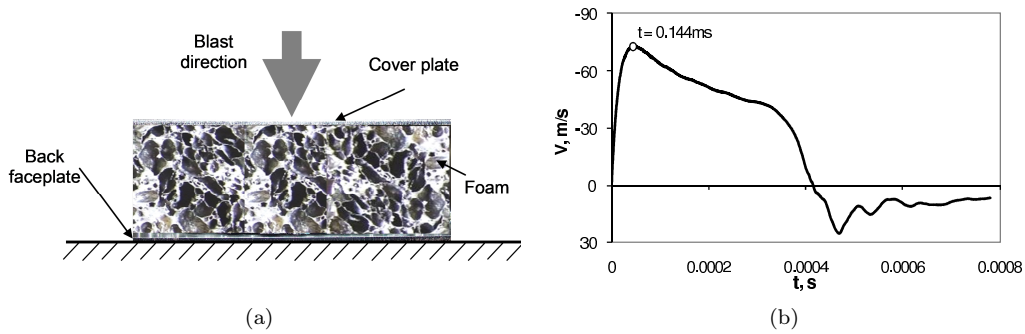


Figure 1: (a) Cladding structure cross-section; (b) Velocity of the proximal end for blast loading with $I = 13.3Ns$, $H = 2mm$, $\rho_0 = 253 \text{ kg/m}^3$ [14].

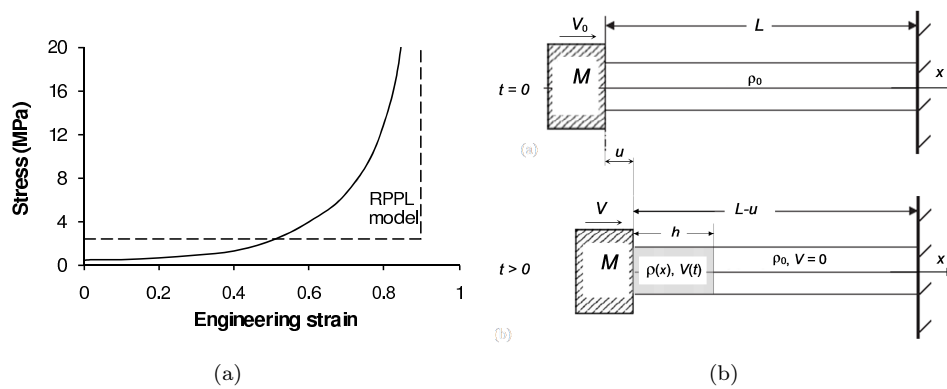


Figure 2: (a) Stress-strain relationship for Cymat foam with $\rho_0 = 253 \text{ kg/m}^3$ (taken positive in compression) and a simplifying RPPL model; (b) Model of an impact of a rigid mass against a stationary foam rod.

The following mathematical description can be employed to describe the observed behaviour. The process of loading is described by

$$\frac{\partial V}{\partial t} - c^2(\varepsilon) \frac{\partial \varepsilon}{\partial \xi} = 0, c^2(\varepsilon) = g'(\varepsilon) / \rho_0, \quad g'(\varepsilon) > 0, \quad \frac{\partial \varepsilon}{\partial t} \geq 0. \tag{1}$$

while the conditions

$$\frac{\partial u}{\partial \xi} \Big|_{t=f(\xi)} = \varepsilon_2(\xi), \tag{2a}$$

$$\frac{\partial u}{\partial t} \Big|_{t=f(\xi)} = V_2(\xi) \quad (2b)$$

should be satisfied on the wave front $t = f(\xi)$, where $\varepsilon_2(\xi)$ and $V_2(\xi)$ are calculated on the wave front and u is the longitudinal displacement (ξ is a Lagrangian coordinate).

In order to facilitate an analytical analysis, a model for the phase of the velocity attenuation was developed [14] assuming a mass impact, Fig. 2b. The conservation of the linear momentum leads to the relationship

$$[\sigma] = \rho_2 (V_2 - G) [V] \quad (3a)$$

on the wave front, where $[\]$ denotes a jump in the corresponding variable. The displacement continuity across the wave front is expressed as

$$[V] = -G [\varepsilon]. \quad (3b)$$

The relationships (3a,3b) should hold on the wave front together with the displacement continuity condition [15]

$$\rho_1 (V_1 - G) = \rho_2 (V_2 - G). \quad (3c)$$

In Eqs (3), ρ_1, V_1 and ρ_2, V_2 are the characteristic parameters ahead of and behind the wave front and $G = 1/f'(\xi)$ is the speed of the wave front.

The elastic strains in the deformed foam material behind the front of the unloading wave can be neglected and a rigid unloading can be assumed thus defining a rigid body motion of the region behind the wave front. The particle velocity, V , is independent of ξ and equal to the particle velocity of the wave front

$$V(\xi, t) = V_2(t). \quad (4)$$

In the case of a suddenly applied mass impact to the proximal end of the foam, the initial points of the positive characteristics at $t = 0$ must all coalesce at the origin, which becomes a singular point and corresponds to an initial discontinuity of all dependent variables [15].

The elastic wave front travels at speed c_0 and the particle velocity is

$$V_Y = -c_0 \varepsilon_Y = V_1, \quad (5a)$$

$$\varepsilon_Y = \sigma_Y / E. \quad (5b)$$

Using Eqs (3a-c), the velocity jump $[V]$ is obtained as

$$[V] = -([\sigma] [\varepsilon] / \rho_1)^{1/2}, \quad [V] = V_1 - V_2 \quad (6a)$$

where $\rho_1 = \rho_0 / (1 - |\varepsilon_Y|)$; $[V([\varepsilon])]$ is uniquely defined for any stress-strain relationship of the foam material.

$$[V] \approx -([\sigma] [\varepsilon] / \rho_0)^{1/2} \quad (6b)$$

when taking into account that $\rho_1 \approx \rho_0$, $|\varepsilon_Y| \ll 1$. Thus, the velocity jump can be expressed as a function of the strain jump $[\varepsilon] = \varepsilon_Y - \varepsilon$ as $[V] = F_V(\varepsilon)$ and for any given value of $V_2 = \text{const}$

there will correspond a certain maximum value of the plastic strain, ε_2 . $[V] = F_V(\varepsilon)$ is a continuous function, which increases when $[\varepsilon]$ increases.

The speed of the front of the unloading wave is expressed as

$$G(\varepsilon) = -[V] / [\varepsilon] \quad (7)$$

according to Eq. (3b). The relationship $[V] = F_V(\varepsilon)$ can be inverted to give $\varepsilon_2 = \varepsilon_2(V_2)$ [16], or $[\varepsilon] = F_e([V])$. Therefore, for a given stress-strain relationship the speed of the unloading wave front can be expressed as $G(\varepsilon) = F_G([V])$.

The velocity of the proximal end, $V(t)$, of the foam block and the development of the compacted region, $h(t)$, are defined by the following equations

$$\frac{dV}{dt} + \rho_0 G(V) \frac{V^2}{mV_0} = 0, \quad (8a)$$

$$\frac{dh}{dt} = G([\varepsilon(V)]) - V(t) \quad (8b)$$

when using the initial conditions

$$V(0) = V_0, \quad (9a)$$

$$h(0) = 0. \quad (9b)$$

The material characteristics $[\varepsilon] = F_e([V])$ and $G(\varepsilon) = F_G([V])$ are monotonic functions of V for the analysed Cymat foams when considering that $[V] = V$ at the wave front, which propagates in an undisturbed region.

According to this model, the dynamic stress enhancement is not only a function of $[V]$ but depends also on the strain jump at the wave front, $[\varepsilon] \neq const$, during the process of compaction. Examples of the strain distributions along the compacted region of the foam within the primary compaction wave are shown in Fig. 3a. The strain non-uniformity behind the compaction wave is well predicted by the model when comparing with the numerical simulations. The velocity attenuation histories as functions of the foam stroke obtained by Eqs (8,9) and predicted by the RPPL model are compared in Fig. 3b. One can see that the approximation of the actual foam stress-strain relationship by the RPPL model leads to an underestimation of the stroke, u , thus underestimating the minimum thickness of the foam block necessary to absorb the impact energy.

Another difference between the two models will become apparent when considering a foam block of a finite thickness. An increase of the reflected stress due to the new compaction within the reflected stress wave can be predicted by the current model [14] while no further compaction is possible upon stress reflection in the RPPL model. It should be noted that the approximation of a cellular material with significant strain hardening by the RPPL model can lead to a false conclusion of shock wave propagation since the critical velocities in the actual materials could be higher than those defined for the RPPL model.

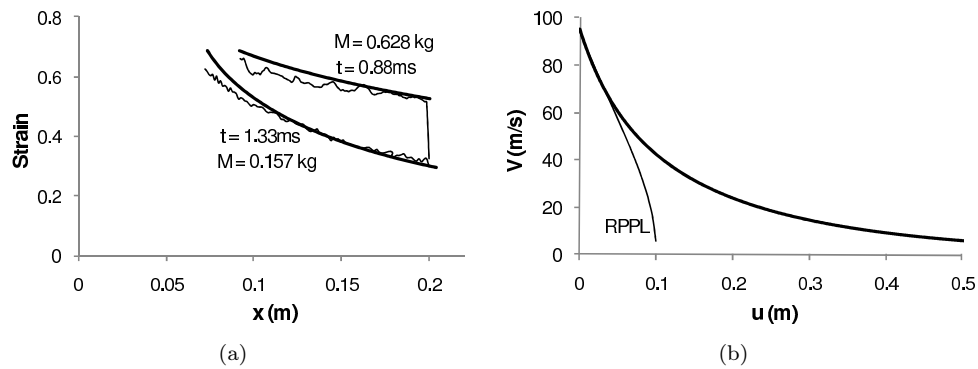


Figure 3: (a) Strain distributions through the foam thickness within the primary compaction wave, $V_0 = 145$ m/s, $L = 0.2$ m; (b) Impact velocity attenuation in an infinite foam block – the present model and RPPL model [7] $M = 0.628$ kg, $V_0 = 95$ m/s.

2.2 Foam integrity

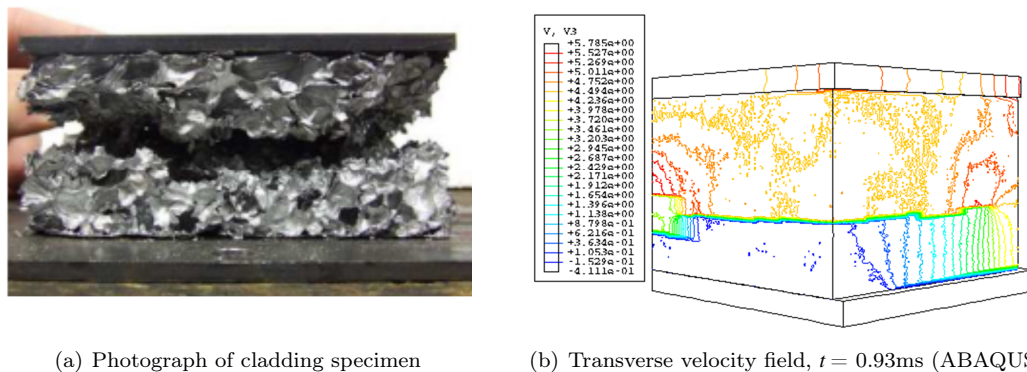
The effect of bonding the cover plate to the foam core on the integrity of the foam core was examined in [17]. Blast tests and numerical simulations using ABAQUS/Explicit were performed to give insight into the response mechanism leading to the development of cracks and subsequent disintegration of the foam. It was shown through the finite element simulations that tensile fracture of the foam occurred during the unloading phase of response and the adhesion of the cover plate to the foam caused extensive cracking which was consistent with the experimental observations, Fig. 4a.

The crushable foam model with volumetric hardening available in ABAQUS/Explicit was used for the Cymat foams. In the FE models, foam fracture is usually taken into account when the critical stress, strain or critical fracture energy is considered as a criterion for element removal [18]. However, it is straightforward to apply this procedure to a material fracture when it has not been pre-strained. In the present case, the material has been compacted to different compressive strain levels (and different resulting densities) before reverse plasticity, resulting in tensile strains, occurred. Therefore, element removal based on the virgin foam material would lead to extremely brittle fracture prediction for the compacted material. The possibility of using cohesive elements to model crack development [19] was also considered inappropriate for the particular loading configuration since the crack locations were not known in advance.

As an alternative, it was anticipated that plastic unloading with local tensile strains larger than the critical ones, $\varepsilon_{tension}^{cr} = \varepsilon_{vol, tension}^p = p_t/E$, can develop with a constant stress equal to p_t , which is an inherent feature of the foam model with volumetric hardening. Since the critical tensile stress of Cymat foam is small, the model described a rapid local weakening of the foam material once the critical strain, $\varepsilon_{vol, tension}^p$ was reached. The reverse plastic strains (in tension) start to grow rapidly in the weak zones leading to velocity discontinuity and the process was considered to be a crack development feature.

This approach of modelling the formation of ‘weak’ zones in the foam material, although simplified, appeared to be appropriate since the stress state in the analysed cladding specimens is essentially uniaxial.

The velocity field also corresponded to the crack development. Regions with constant velocities formed very rapidly and velocity discontinuities occurred at some locations Fig. 4b (a quarter of the actual specimen was modelled), confirming the presence of cracks in these locations. The velocity behaviour of the two sides of the crack can be considered as evidence for a further complete separation of the parts of the core. It should be noted that, although the foam model used in the numerical simulations overestimated the material fracture toughness, it predicted the cracking and fragmentation of the foam reasonably well [17].



(a) Photograph of cladding specimen

(b) Transverse velocity field, $t = 0.93\text{ms}$ (ABAQUS)

Figure 4: Deformation of a bonded foam cladding, $L = 50\text{ mm}$, $H = 4\text{ mm}$, $\rho_0 = 253\text{ kg/m}^3$, $I = 15.4\text{ Ns}$ [17].

3 Axial impact on ductile tubes

The buckling process of elastic-plastic shells with circular and square sections within a wide range of impact velocity and made of different ductile materials has been extensively studied for decades due to the numerous applications of these elements. This section only aims to summarize some basic results on dynamic buckling from a phenomenological viewpoint. It is well known that the various axially loaded structural members are highly inertia sensitive including the axial and lateral inertia, which can potentially lead to the increase of the critical axial load. Being a bifurcation problem by nature, buckling is sensitive to the loading path, and therefore the force-time history, which in turn is affected by the material properties. Moreover, the material properties play an essential role in the response of structures that buckle in the plastic range. Having this perception, ‘dynamic plastic’ buckling and ‘progressive’ buckling phenomena are discussed, when in the first case, coupling between the axial

compression stress wave and buckling is involved while no coupling between the axial and transverse (radial) inertia occurs in the latter case.

3.1 Moderate length tubes with circular cross-section

Two major buckling mode types are observed in circular tubes, progressive buckling (folding) and buckling within a sustained axial plastic flow. Examples are shown in Fig. 5. The results reported in the literature reveal that the stress waves within a sustained plastic flow can govern the initiation of buckling in relatively thick shells subjected to dynamic loading, while the lateral inertia properties of shells with different cross-sections play an important role in the post buckling behaviour and in the development of the final deformed shape. For example, large almost uniform stresses and strains arise from an impact of a shell on a rigid wall [20] and in this case, the lateral inertia forces in a thicker shell suppress the local growth of the radial displacements, thus allowing a further propagation of the primary wave and for buckling to develop within a sustained axial compressive plastic flow, Fig. 5e. A thinner shell subjected to the same loading conditions, however, cannot support the unbuckled shape, so the local bending deformations grow rapidly near the struck end, thus impeding the propagation of the initial plastic stress wave by partial unloading of some cross sections of a shell.

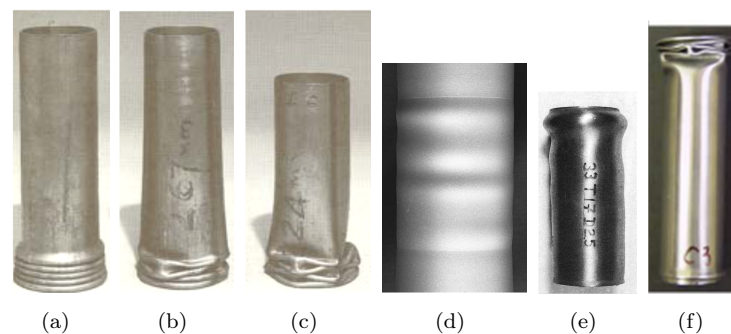


Figure 5: Types of buckling (a-d) Quasi-static loading; (a) progressive buckling with axisymmetric folds; (b) Mixed modes; (c) Asymmetric folds [21]; (d) Axisymmetric wrinkling [22]; (e) Dynamic plastic buckling, $V_0 = 108$ m/s [20]; (f) Dynamic progressive buckling, $V_0 = 78.15$ m/s [23].

The speeds of the plastic stress waves play an essential role in the development of the particular buckling mode. These wave speeds in a circular shell have been obtained [24, 26, 27] when assuming a biaxial stress state, ($\sigma_x \neq 0, \sigma_\theta \neq 0$), σ_x and σ_θ being the axial and circumferential stresses. Figures 6a and 6b show how the plastic stress wave speeds vary with the stress state for an elastic linear strain hardening material obeying the von Mises and the Tresca yield criteria. The wave speeds are presented as vectors perpendicular to the yield surface with magnitudes c/c_e . It is evident from the figures that the plastic waves can propagate at different speeds, which are bound from above by the

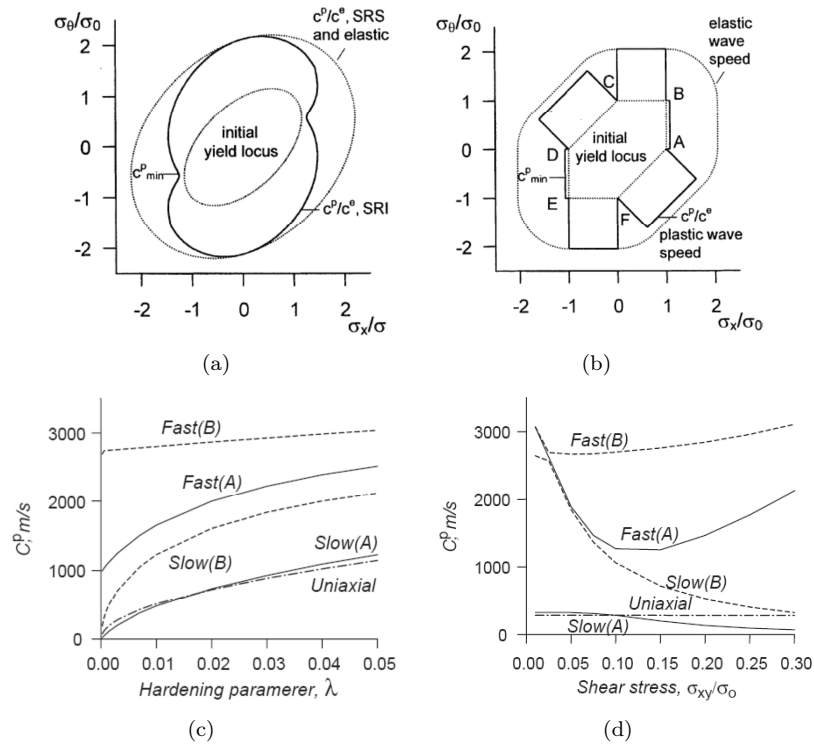


Figure 6: Speeds of the stress waves (a,b) in a circular shell – SRS: strain rate sensitive; SRI: strain rate insensitive [24]. (a) Von Mises yield criterion (b) Tresca yield criterion; (c,d) Stress wave speeds in a shell plane ($n_x = 1, n_y = 0$); A: $\sigma_{xx} < 0, \sigma_{yy} = \sigma_{xx}/2$, B: $\sigma_{xx} < 0, \sigma_{yy} = 0$ [25]; (c) Stress wave speeds as a function of $\lambda = E_h/E$ for $\sigma_{xy}/\sigma_0 = 0.15$; (d) Stress wave speeds as a function of σ_{xy} for $\lambda = 0.003$.

elastic wave speed in a shell, c_e , and from below, by a speed which is larger than the plastic wave speed propagating in a uniaxial medium. Thus, the transient process, which develops in an elastic-plastic shell as a result of an axial impact, depends not only on the yield stress and the hardening properties of a material but also on the particular yield condition that controls its plastic flow. The minimum values of the plastic wave speeds are obtained as

$$c_{\min}^p = \{4\lambda/[4\lambda(1-\nu^2) + 3(1-\lambda)]\}^{1/2} (E/\rho)^{1/2} \tag{10a}$$

for the von Mises yield criterion and

$$c_{\min}^p = \{2\lambda/[2\lambda(1-\nu^2) + (1-\lambda)\sqrt{3}]\}^{1/2} (E/\rho)^{1/2} \tag{10b}$$

for the Tresca yield criterion, where $\lambda = E_h/E$ is the ratio between the hardening modulus, E_h and the Young modulus, E .

The calculated stress wave speeds can be used for the interpretation of some numerical results related to transient deformation processes in circular shells. According to Eqs.(10a) and (10b), the plastic wave speed is determined by the hardening modulus, and its variation can lead either to dynamic plastic buckling or to dynamic progressive buckling [26, 28] for a high velocity impact. Due to this reason, the material approximation can change the predicted pattern for the initial instability and the final buckling shape of a shell. A regular buckling shape can develop in a shell made of strain-rate insensitive material with relatively large strain hardening, when buckling develops within a sustained axial plastic flow (Fig. 7b) later transforming into a progressive mode (Fig. 7c). On the other hand, the localization of strains leads to progressive buckling in shells made of materials having a low strain hardening behaviour as shown in Figs 7d and 7e.

Dynamic buckling within a sustained axial plastic flow can be observed only for particular combinations between the shell geometric characteristics and material properties. However, this type of buckling can develop for relatively low impact velocity too, provided a shell has certain inertia characteristics.

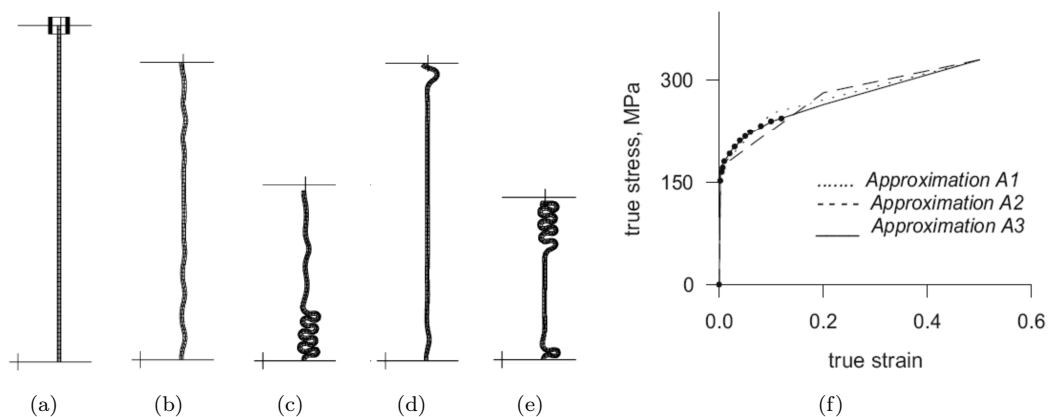


Figure 7: Influence of the material model on the buckling shape of cylindrical shells, A6063-T5, $T_0 = 2.2$ kJ, $V_0 = 75$ m/s [28]. (a) Undeformed shell wall; (b) buckling initiation, $t_0 = 0.217$ ms; (c) final shape for material approximation A2; (d) and (e) same as in (b) and (c) but for material approximation A3; (f) Material approximations

It appears that buckling within a sustained axial plastic flow is an inherent response of thicker shells. It has been registered that in shells that buckle in the plastic range under a quasi-static compression, the first instability is uniform axisymmetric wrinkling [22] that is typically treated as a plastic bifurcation. The wrinkle amplitude gradually grows and, in the process, reduces the axial

rigidity of the shell. This eventually leads to a limit load instability, beyond which the cylindrical shell fails by localized collapse. For some combinations of geometric and material characteristics, this limit load can be preceded by a second bifurcation that involves a non axisymmetric mode of deformation [29].

For certain combinations of the characteristic parameters, buckling within a sustained plastic flow could never occur regardless of the impact velocity, which explains why localized buckling is more commonly observed in experimental tests on axial impact loadings of shells. Furthermore, strain rate effects, which are characteristic of many types of steel and other ductile materials, cause more rapid strain localization [23, 26, 30].

3.2 Moderate length tubes with square cross-section

The experimental results on the response of elastic-plastic shells with square cross-sections subjected to axial impact loadings divulge features which are also characteristic for the deformation of circular shells. A numerical study of the transient deformation process reveals that similarly to the response of circular tubes, the initiation of buckling is influenced significantly by elastic and plastic stress waves [25, 31] propagating along the tube. However, large plastic strains can develop along the entire shell with a square cross section and relatively small wall thickness even for moderate impact velocities.

The propagation of in-plane stress waves in an elastic-plastic medium with $\sigma_{xx} \neq 0$, $\sigma_{yy} \neq 0$, $\sigma_{xy} \neq 0$ and having a linear strain hardening when obeying the von Mises yield criterion was discussed in Ref. [25]. Two in-plane plastic waves, named 'slow' and 'fast' plastic waves, are shown to exist, with their speeds depending on the stress state, material hardening characteristics and the direction of propagation along the shell wall (n_x, n_y). It turns out that the fast plastic wave speed can reach the elastic wave speed for certain stress states and directions of propagation Fig. 6c. For small shear stresses, the slow plastic wave that carries the largest plastic strains travels at a significantly higher speed in comparison to the uniaxial plastic wave speed (Fig. 6d, σ_0 is the yield stress).

Despite the similarities between the development of the buckling patterns in circular and square shells, attention should be called to the difference between the rates of loading, causing dynamic plastic and dynamic progressive buckling in these structural elements (Fig. 8). A circular and square shell with equal lengths, wall thicknesses, and cross-section perimeters and made of the same material could respond by different type of buckling when subjected to identical impact loadings.

An impact loading, which causes dynamic plastic buckling of a square shell, may cause progressive buckling of the corresponding circular shell [31]. Two factors contribute to this behaviour, which is related to the strain localization. It is shown in Ref. [25] that the axial plastic stress waves can travel at higher speeds in a square shell compared to the plastic stress wave speeds in a circular shell. This facilitates the compression plastic strains to propagate at a larger distance in a square shell before the significant growth of the lateral displacements due to buckling, thus supporting the development of dynamic plastic buckling. Differently, the slower axial plastic wave in a circular shell can travel a shorter distance (often comparable with a single fold length) before the development of significant radial displacement. After that, large bending deformations develop, leading to a strain localization and initiation of progressive buckling. Therefore, higher impact velocities, which increase the radial inertia, are required for the circular shell to respond by a dynamic plastic buckling mode. In addition

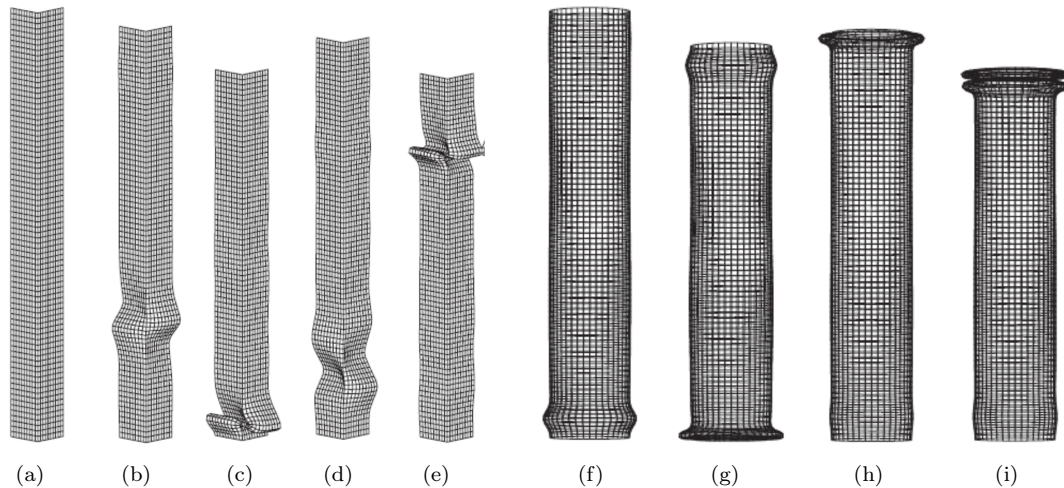


Figure 8: Final buckling shapes of geometrically equivalent square and circular tubes; (a) Initial; (b,f) $V_0 = 15.91$ m/s, $G = 0.95$ kg; (c,g) $V_0 = 35.35$ m/s, $G = 0.44$ kg; (d,h) $V_0 = 64.62$ m/s, $G = 0.103$ kg; (e,i) $V_0 = 91.53$ m/s, $G = 0.103$ kg [31].

to the different plastic stress wave speeds, the different behaviour of the post bifurcation paths that characterize the two shell geometries affects the rates of strain localization. An initial structural hardening characterizes the post-buckling of a square shell while the post-buckling path of a circular shell can be characterized as an abrupt structural softening, which leads to a rapid strain localization and progressive buckling of the circular shell.

An increase in the axial impact velocity certainly invokes lateral inertia effects on the buckling of a square tube. Some experimentally obtained final buckling shapes of aluminum alloy 6063-T5 tubes subjected to similar impact energies of about 600 J, but applied with different initial velocities, are shown in Fig. 9 together with their FE models. Thus, it could be anticipated that larger impact energy would be required to cause bottoming out of a tube when subjected to a higher impact velocity. In other words, a shell can absorb larger impact energy when this energy is applied at a higher speed, even when disregarding material strain-rate-sensitive effects.

3.3 Long circular tubes

The increase of the tube length involves a type of instability that activates an additional buckling mode. Relatively long inelastic tubes can respond by global bending, or a mixed mode, when a few folds are formed along the tube, thus presenting an inefficient buckling mode from the view-point of the energy absorption. A classification of the buckling modes, which occur in statically loaded circular tubes made from aluminum, was presented by Andrews et al [32] as a function of the radius-to-thickness ratio based on an experimental study. In particular, it was shown that the critical length

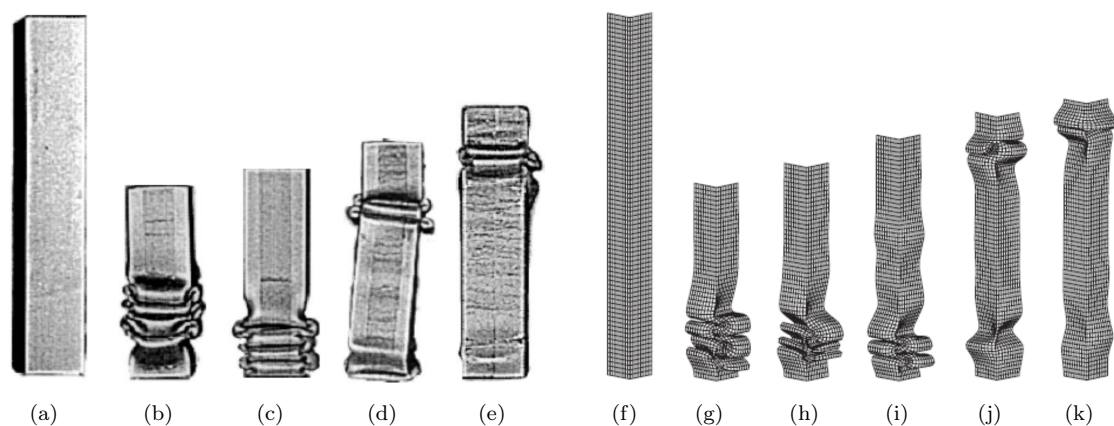


Figure 9: Lateral inertia effects in a square tube subjected to a 600 J axial impact; (a,f) Initial; (b,g) $V_0 = 14.84\text{m/s}$; (c,h) $V_0 = 25.34\text{ m/s}$; (i) $V_0 = 40.0\text{ m/s}$; (d,j) $V_0 = 64.32\text{ m/s}$; (e,k) $V_0 = 98.27\text{ m/s}$ [31].

for the buckling transition from a progressive buckling mode to an overall bending increases when increasing this characteristic parameter.

The axial dynamic loading brings into play the influence of inertia and material strain-rate sensitivity and certainly these parameters could also influence the buckling transition between the two buckling modes. The progressive buckling mode can be referred to as a ‘shell’ mode as it characterizes the post-buckling behaviour of a shell, while the overall (global) bending can be referred to as a ‘column’ mode as it characterizes the post-buckling behaviour of along column. Abramowicz and Jones [33] were the first to present experimental data on the buckling transition for circular and square mild steel tubes of various lengths when impacted by a mass with initial velocities between 4m/s and 13m/s. They found that the tube length, which marks the transition between progressive buckling and global bending, is larger for impact loadings than for the corresponding static response.

Karagiozova and Alves [34] also conducted experiments on the transition from progressive buckling to a global bending collapse mode of aluminium alloy circular tubes having a single diameter-to thickness value ($2R/h$, $2R = 50.8\text{mm}$, $h = 2\text{mm}$) and a range of lengths, with axial impact velocities up to 12 m/s. It was observed that the transition between progressive and global bending is velocity sensitive (Fig. 10a) and can occur at critical lengths, L_{cr} , as large as twice the corresponding static value when tubes were impacted with a mass of 120 kg, provided the velocity was high enough, Fig.10b. Impact experiments on long circular tubes made of AA6063-T6 were reported by Hsu and Jones [35]. A comprehensive experimental programme on square tubes was carried out by Jensen et al. [36] to study the transition between progressive and global bending of axially loaded square aluminium extrusions of alloys AA6060-T4 and AA6060-T6 under quasi-static and dynamic axial loadings.

The aforementioned test results on axial impact loadings reveal that a variation of the problem

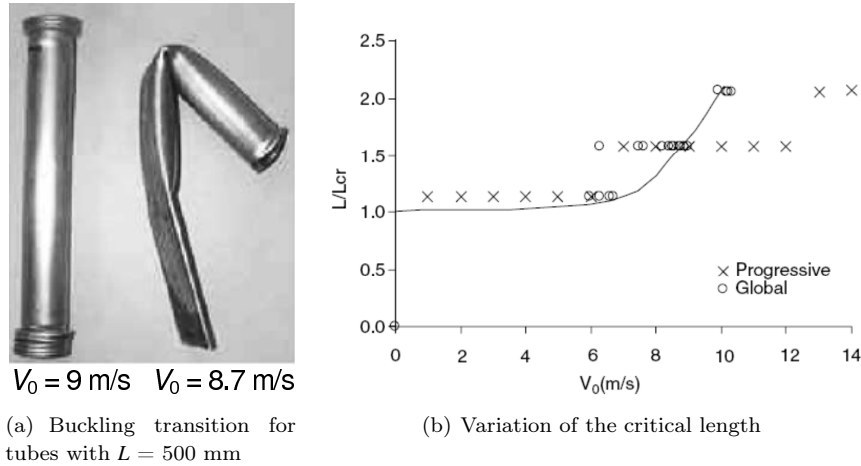


Figure 10: Influence of the impact velocity on the dynamic buckling transition of aluminum alloy circular tubes [34].

parameters over a wide range is required in order to understand the transition conditions under an axial impact. In this case, the numerical simulations can serve as a helpful tool to bring an insight into the influence of material and loading conditions on the buckling transition and on the estimation of the critical tube length.

The transition conditions between a progressive buckling mode and global bending collapse of axially impacted long circular tubes were studied by Karagiozova and Jones [37] using simplified structural models when taking into account the characteristic features of the two deformation phases: axial compression and buckling/bending. These models are used to estimate the formation time of the two principal buckling modes, which provides an insight into the buckling transition phenomenon. The dominant buckling mode is characterized by a larger vertical velocity, $V_1(t^*)$, of the proximal end of the shell at the end of the initial compression phase, $t = t^*$, leading to a rapid development of this mode during the post-buckling response. There is, however, an impact velocity associated with a particular set of geometrical and material parameters, which causes a simultaneous increase in the progressive buckling and global bending mode, i.e., $V_{1, glob}(t^*) = V_{1, progr}(t^*)$, so that no ‘leading’ mode can be selected for buckling. In this case, both buckling modes can develop rapidly during the post-buckling deformation phase, making it difficult to predict the development of a particular collapse mode, as shown in Fig. 11.

An empirical criterion for the dynamic buckling transition of circular tubes, which is based on the energy absorption by the formation of a single axisymmetric fold, $T_{p, f}$, was proposed in [37]. The lower and upper, bounds to the critical impact velocity for a buckling transition were obtained when assuming that an axisymmetric fold starts to develop near the proximal end of the tube in the case of progressive buckling. The criterion for a dynamic buckling transition can be expressed with respect

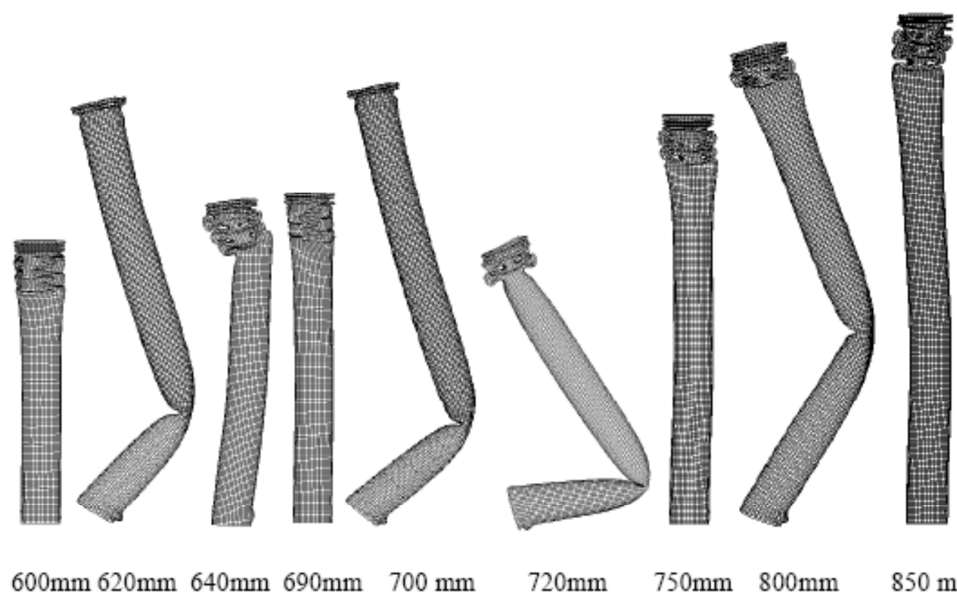


Figure 11: Counterintuitive response for circular tubes with $2R = 50.2$ mm, $h = 2.19$ mm, $\sigma_0 = 240$ MPa, $E_h = 460$ MPa, $V_0 = 10.4$ m/s, and $G = 209$ kg [37].

to the vertical velocity associated with a global bending mode as

$$V_{1,glob}(t^*) = 3\gamma\varphi_0^2 L \sinh(2\gamma t^*) \leq (2T_{p,f}/G)^{1/2} \quad (11a)$$

where the duration of the compression phase $t^* = t_{progr}^* < t_{glob}^*$ is determined by the progressive mode which is calculated using the structural models proposed in Ref. [37]. In Eq.(11a),

$$\gamma = 3L^{-1} (6\sigma_0/\rho)^{1/2} \left\{ 1 - \left(30E_h R^2 \left(\sigma_0 L^2 (1 + \sqrt{\lambda})^2 \right)^{-1} \right) \right\}^{1/2} \quad (11b)$$

and φ_0 is the magnitude of the initial imperfection associated with the global bending mode.

The analysis of the buckling process of relatively long circular tubes advises that the control on the initiation of buckling cannot guarantee a classical progressive buckling throughout the response. Thus, the introduction of an appropriate trigger – either mechanical dent or altering locally the material properties – can improve the energy absorbing characteristics of a long tube by promoting the initiation of a progressive buckling mode. However, in the case of a large impact energy, which requires a large number of folds to absorb the initial kinetic energy, the buckling initiation into the desirable buckling mode might change later from progressive buckling into a mixed buckling mode, which includes global bending. Therefore, the upper bound to the impact velocity is referred to as a

‘critical impact velocity’, which causes a classical progressive collapse of a circular tube with a given geometry when subjected to an impact with a known initial kinetic energy.

Finally, it should be mentioned that the increase of the impact velocity can bring into play the axial inertia effect in long tubes, i.e., the effect of the stress wave propagation, which is particularly important for tubes with square cross-sections. In this case, not only the length-to-thickness ratio and width-to-thickness ratio but also the actual tube length should be considered. The nonuniform distribution of the compressive plastic strains along the tube can serve as initial imperfections, which can initiate the initial fold at different locations and contribute to the ‘inconsistent’ behaviour of a tube when the impact velocity increases.

4 Conclusions

While the numerical models can capture many details of the deformation process, very often, some basic characteristic features of this process remain “concealed” due to the influence of the combined effects of the participating parameters. In view of the increased accessibility to powerful numerical packages, it is essential to develop models and methods, which would assist in understanding the influence of the various parameters on the structural behaviour. The aim of this article is to point out some dynamic effects in ductile structural elements and lightweight materials in order to aid the accurate modelling of the dynamic response of structures with more complex geometry and properties.

References

- [1] Lu, G. & Yu, T., *Energy absorption of structures and materials*. Woodhead: Cambridge, 2003.
- [2] Karagiozova, D. & Alves, M., Dynamic elastic-plastic buckling of structural elements: A review. *Applied Mechanics Reviews*, **61**(4), 2008. 040803.
- [3] Zhao, H., Elnasri, I. & Abdennadher, S., An experimental study on the behaviour under impact loading of metallic cellular materials. *Int J Mech Sci*, **47**, pp. 757–74, 2005.
- [4] Zhao, H., Elnasri, I. & Girard, Y., Perforation of aluminium foam core sandwich panels under impact loading – an experimental study. *Int J Impact Eng*, **34**, pp. 1246–57, 2007.
- [5] Elnasri, I., Pattofatto, S., Zhao, H., Tsitsiris, H., Hild, F. & Girard, Y., Shock enhancement of cellular structures under impact loading: part i experiments. *J Mech Phys Solids*, **55**, pp. 2652–71, 2007.
- [6] Montanini, R., Measurement of strain rate sensitivity of aluminium foams for energy dissipation. *Int J Mech Sci*, **47**, pp. 26–42, 2005.
- [7] Reid, S. & Peng, C., Dynamic uniaxial crushing of wood. *Int J Impact Eng*, **19**, pp. 531–70, 1997.
- [8] Tan, P., Reid, S., Harrigan, J., Zou, Z. & Li, S., Dynamic compressive strength properties of aluminium foams. Part I – experimental data and observations. *J Mech Phys Solids*, **53**, pp. 2174–205, 2005.
- [9] Tan, P., Reid, S., Harrigan, J., Zou, Z. & Li, S., Dynamic compressive strength properties of aluminium foams. Part II – ‘shock’ theory and comparison with experimental data and numerical models. *J Mech Phys Solids*, **53**, pp. 2206–30, 2005.
- [10] Harrigan, J., Reid, S., Tan, P. & Reddy, T., High rate crushing of wood along the grain. *Int J Mech Sci*, **47**, pp. 521–44, 2005.
- [11] Lopatnikov, S., Gama, B., Haque, M., Krauthauser, C., Gillespie Jr., J., Guden, M. et al., Dynamics of

- metal foam deformation during taylor cylinder– hopkinson bar impact experiment. *Compos Struct*, **61**, pp. 61–71, 2003.
- [12] Lopatnikov, S., Gama, B., Haquea, M., Krauthausera, C. & Gillespie Jr., J., High- velocity plate impact of metal foams. *Int J Impact Eng*, **30**, pp. 421–45, 2004.
- [13] Pattofatto, S., Elnasri, I., Zhao, H., Tsitsiris, H., Hild, F. & Girard, Y., Shock enhancement of cellular structures under impact loading: Part II analysis. *J Mech Phys Solids*, **55**, pp. 2672–2686, 2007.
- [14] Karagiozova, D., Langdon, G. & Nurick, G., Blast attenuation in Cymat foam core sacrificial claddings. *Int J Mech Sci*, **52**, pp. 754–776, 2010.
- [15] Nowacki, W., *Stress-Waves in Non-Elastic Solids*. Pergamon Press: UK, 1964.
- [16] Hipkins, H., The method of characteristics and its application to the theory of stress waves in solids. *Engineering Plasticity*, eds. J. Heiman & F. Leckie, Cambridge University Press, pp. 277–315, 1968.
- [17] Langdon, G., Karagiozova, D., Theobald, M., Nurick, G., Lu, G., Merrett, R. & Mayimele, N., Fracture of aluminium foam core sacrificial cladding subjected to air blast loading. *Int J Impact Eng*, **37**, pp. 638–651, 2010.
- [18] Reyes, A., Hopperstad, O., Berstad, T., Hanssen, A. & Langseth, M., Constitutive modeling of aluminum foam including fracture and statistical variation of density. *Eur J Mech A Solids*, **22**, pp. 815–835, 2003.
- [19] Lu, G., Shen, J., Hou, W., Ruan, D. & Ong, L., Dynamic indentation and penetration of aluminium foams. *Int J Mech Sci*, **50**, pp. 932–943, 2008.
- [20] Florence, A. & Goodier, J., Dynamic plastic buckling of cylindrical shells in sustained axial compressive flow. *ASME J Appl Mech*, **35**, pp. 80–86, 1968.
- [21] Jones, N., *Structural Impact*. Cambridge University Press: Cambridge, 1989.
- [22] Bardi, F. & Kyriakides, S., Plastic buckling of circular tubes under axial compression – Part I: experiments. *Int J Mech Sci*, **48**, pp. 830–841, 2006.
- [23] Karagiozova, D., Nurick, G. & Yuen, S., Energy absorption of aluminium alloy circular and square tubes under an axial explosive load. *Thin-Walled Struct*, **43**, pp. 956–982, 2005.
- [24] Karagiozova, D. & Jones, N., Influence of stress waves on the dynamic progressive and dynamic plastic buckling of cylindrical shells. *Int J Solids Struct*, **38**, pp. 6723–6749, 2001.
- [25] Karagiozova, D., Dynamic buckling of elastic-plastic square tubes under axial impact – I: Stress wave propagation phenomenon. *Int J Impact Eng*, **30**, pp. 143–166, 2004.
- [26] Karagiozova, D., Alves, M. & Jones, N., Inertia effects in axisymmetrically deformed cylindrical shells under axial impact. *Int J Impact Eng*, **24**, pp. 1083–1115, 2000.
- [27] Karagiozova, D. & Jones, N., Dynamic elastic-plastic buckling of circular cylindrical shells under axial impact. *Int J Solids Struct*, **37**, pp. 2005–2034, 2000.
- [28] Karagiozova, D. & Jones, N., On dynamic buckling phenomena in axially loaded elastic-plastic cylindrical shells. *Int J Non-Linear Mech*, **37**, pp. 1223–1238, 2002.
- [29] Bardi, F., Kyriakides, S. & Yan, H., Plastic buckling of circular tubes under axial compression – Part II: Analysis. *Int J Mech Sci*, **48**, pp. 842–854, 2006.
- [30] Wang, R., Han, M., Huang, Z. & Yang, Q., An experimental study on the dynamic axial plastic buckling of cylindrical shells. *Int J Impact Eng*, **1**, pp. 249–256, 1983.
- [31] Karagiozova, D. & Jones, N., Dynamic buckling of elastic-plastic square tubes under axial impact – II: Structural response. *Int J Impact Eng*, **30**, pp. 167–192, 2004.
- [32] Andrews, K., England, G. & Ghani, E., Classification of the axial collapse of circular tubes under quasi-static loading. *Int J Mech Sci*, **25**, pp. 687–696, 1983.
- [33] Abramowicz, W. & Jones, N., Transition from initial global bending to progressive buckling of tubes loaded statically and dynamically. *Int J Impact Eng*, **19**, pp. 415–437, 1997.

- [34] Karagiozova, D. & Alves, M., Transition from progressive buckling to global bending of circular shells under axial impact. Part I – Experimental and numerical observations. *Int J Solids Struct*, **41**, pp. 1565–1580, 2004.
- [35] Hsu, S. & Jones, N., Dynamic axial crushing of aluminium alloy 6063-T6 circular tubes. *Latin American J Solids Struct*, **1**, pp. 277–296, 2004.
- [36] Jensen, O., Langseth, M. & Hopperstad, O., Experimental investigations on the behaviour of short to long square aluminium tubes subjected to axial loading. *Int J Impact Eng*, **30**, pp. 973–1003, 2004.
- [37] Karagiozova, D. & Jones, N., On the mechanics of the global bending collapse of circular tubes under dynamic axial load – dynamic buckling transition. *Int J Impact Eng*, **35**, pp. 397–424, 2008.

Consideration of size effect multifractal theory in fracture analysis by means of the truss-like Discrete Element Method (DEM)

Luis E. Kostascki, Ignacio Iturrioz
*PROMECA, Departamento de Engenharia Mecânica, Escola de Engenharia,
Universidade Federal do Rio Grande do Sul
Porto Alegre – Brasil*

Jorge D. Riera
*Civil Engineering Department (DECIV), PPGECA, Universidade Federal do Rio
Grande do Sul (UFRGS),
Porto Alegre, RS – Brazil*

Abstract

In the truss-like Discrete Element Method (DEM) masses are considered lumped at nodal points and linked by means of uni-dimensional elements with arbitrary constitutive relations. In previous studies of the tensile fracture behavior of rock samples, it was verified that numerical predictions of fracture of non-homogeneous materials using DEM models are feasible and yield results that are consistent with the experimental evidence so far available. In the present paper a discussion of the results obtained with the DEM presented a satisfactory correlation with the theoretical model known as Carpinteri's Multifractal Law (CML). A set of rock plates of different size subjected to monotonically increasing simple tension are simulated with DEM and the results compared with CML predictions. The satisfactory correlation between the theoretical model and DEM confirms the robustness of this method as a numerical tool to model fracture processes in quasi brittle solids.

Keywords: discrete elements, fracture, size effects, multifractal law.

1 Introduction

In the truss-like Discrete Element Method (DEM) masses are considered lumped at nodal points and linked by means of uni-dimensional elements with arbitrary constitutive relations. In previous studies of the tensile fracture behavior of rock cubic samples, it was verified that numerical predictions of fracture of non-homogeneous materials using DEM models are feasible and yield results that are consistent with the experimental evidence so far available.

Results of the numerical fracture analysis of 2D systems employing the DEM are reported in this contribution and compared with predictions based on the multi-fractal theory proposed by Carpinteri *et al* [1–3]. It is shown how three fundamental coefficients related with a fractal dimension: the fracture energy, the rupture stress and the final strain, as well as their interrelation, may be calculated. A set of rock plates of different size subjected to monotonically increasing simple tension are simulated with the DEM, and the results are compared with Carpinteri's Multifractal Law (CML). The satisfactory correlation between the theoretical model and the DEM predictions confirms the robustness of this method as a numerical tool to model fracture processes in quasi brittle solids.

2 The truss-like Discrete Element Method

In the truss-like discrete element method (DEM) a continuum is represented by a set of lumped masses interconnected by a set of uni-axial elements or *bars*. In particular, Figure 1(a) and 1(b) show the discretization for a cubic system, for which the stiffness of the DEM elements corresponding to *an equivalent orthotropic linear elastic material* were obtained by Nayfeh and Hefzy [4]. The basic cubic module has 20 elements and 9 nodes. Every node has three degrees of freedom, namely the three components of the displacement vector in a global reference system. In case of an isotropic elastic material, the cross-sectional area A_i of the longitudinal elements (those defining the edges of the module and those parallel to the edges connected to the node located at the centre of the module) in the equivalent discrete model is:

$$A_i = \phi L^2 \quad (1)$$

where L is the length of the side of the cubic module under consideration. Similarly, the area A_d of the diagonal elements is:

$$A_d = \frac{2}{\sqrt{3}} \delta \phi L^2 \quad (2)$$

Note that there is a difference in length between longitudinal and diagonal elements, since:

$$L = \left(2/\sqrt{3}\right) L_d \quad (3)$$

For approximately isotropic solids:

$$\phi = (9 + 8\delta) / (18 + 24\delta) \quad (4)$$

$$\delta = 9\nu(4 - 8\nu) \quad (5)$$

in which ν is Poisson's ratio. It is important to point out that for $\nu = 0.25$, the correspondence between the equivalent discrete solid and the isotropic continuum is complete. On the other hand, for values of $\nu \neq 0.25$ small discrepancies appear in the shear terms, which may nevertheless be neglected. It is interesting to note that while no lattice or truss-like model can exactly represent a

locally isotropic continuum, it can also be argued that no perfect *locally isotropic continuum exists* in the physical world. In fact, the continuum itself does not exist. Isotropy in solids is a bulk property that reflects properties of the random distribution of the orientation of the elements. The derivation of the areas of longitudinal and diagonal elements given for a cubic array by equations (1) and (2) may be found in Nayfeh and Hefzy [4] and Dalguer et al. [5].

The equations of motion are obtained from equilibrium conditions of all forces acting on the nodal masses, resulting a system of equations of the form:

$$\mathbf{M} \ddot{\mathbf{x}} + \mathbf{C} \dot{\mathbf{x}} + \mathbf{F}(t) - \mathbf{P}(t) = 0 \quad (6)$$

in which \mathbf{x} , $\dot{\mathbf{x}}$ and $\ddot{\mathbf{x}}$ denote vectors containing the nodal displacements, velocities and accelerations, respectively, while \mathbf{M} and \mathbf{C} are the mass and damping matrices. The vectors $\mathbf{F}(t)$ and $\mathbf{P}(t)$ contain the internal and external nodal loads.

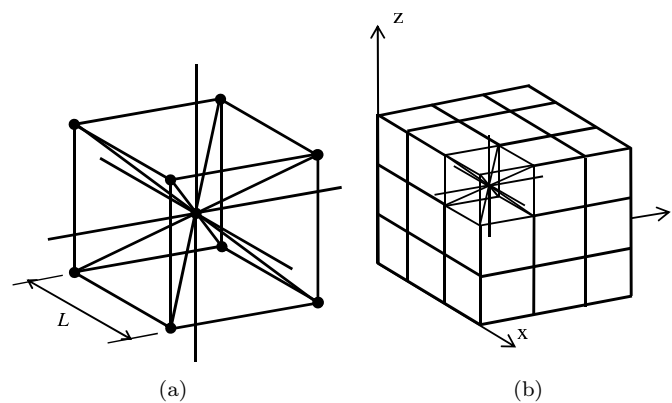


Figure 1: DEM discretization strategy: (a) basic cubic module, (b) generation of prismatic body.

Since matrices \mathbf{M} and \mathbf{C} are diagonal, equations (6) are not coupled, and they can be easily integrated in the time domain using an explicit finite difference scheme. It is worth noting that since nodal coordinates are updated at every time step, large displacements are accounted for naturally. Stability of the integration scheme is insured by adopting a time interval Δt in the integration process such that:

$$\Delta t \leq \frac{0.6L}{C_\rho} \quad (7)$$

in which C_ρ is the propagation velocity of longitudinal waves,

$$C_p = \sqrt{E/\rho} \quad (8)$$

The convergence of DEM solutions in linear elasticity and elastic instability problems was verified by Hayashi [6] and Dalguer et al. [5], among others.

2.1 Non-linear constitutive model for damaged material

Rocha *et al* [7] adopted the softening law for quasi fragile materials proposed by Hilleborg [8], extending the Discrete Element Method to handle fragile fracture by means of the bilinear constitutive relationship (ECR) shown in Figure 2, which allows accounting for the irreversible effects of crack nucleation and propagation. Therefore, the reduction in the element load carrying capacity with damage is predicted by the present formulation of the DEM. The area under the force vs. strain curve (the area of the triangle OAB in Figure 2) represents the energy density necessary to fracture the area of influence of the element. Thus, for a given point P on the force vs. strain curve, the area of the triangle OPC represents the *reversible* elastic energy density stored in the element, while the area of the triangle OAP is the energy density dissipated by damage. Once the damage energy density equals the fracture energy, the element fails and loses its load carrying capacity. On the other hand, in the case of compressive loads the material behavior is assumed linearly elastic. Thus, failure in compression is induced by indirect traction.

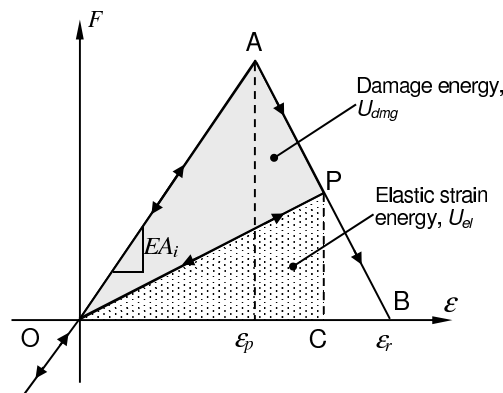


Figure 2: Bilinear constitutive law adopted for DEM uni-axial elements.

Constitutive parameters and symbols are shown in Figure 2 (see Rocha [9], and Rocha et al, [7]). The element axial force F depends on the axial strain ϵ . The area associated to each element is given by equations (1) or (2) for longitudinal and diagonal elements, respectively. An *equivalent fracture area* A_i^* of each element is defined in order to satisfy the condition that the energies dissipated by fracture of the continuum and by its discrete representation are equivalent. With this purpose, fracture of a

cubic sample of dimensions $L \times L \times L$ is considered. The energy dissipated by fracture of a continuum cube due to a crack parallel to one of its faces is:

$$\Gamma = G_f \Lambda = G_f L^2 \quad (9)$$

in which Λ is the actual fractured area, *i.e.* L^2 . On the other hand, the energy dissipated when a DEM module of dimensions $L \times L \times L$ fractures in two parts consists of the contributions of five longitudinal elements (four coincident with the module edges and an internal one) and four diagonal elements, as shown in Figure 1(a). Then, the energy dissipated by the DEM module can be written as follows:

$$\Gamma_{DEM} = G_f \left(4 \cdot 0.25 \cdot c_A + c_A + 4 \cdot c_A \cdot \left(\frac{2}{\sqrt{3}} \right)^2 \right) L^2 \quad (10)$$

The first term between brackets accounts for the four edge elements, the second term for the internal longitudinal element, while the third term represents the contribution of the four diagonal elements. The coefficient c_A is a scaling parameter used to establish the equivalence between Γ and Γ_{DEM} . Thus:

$$G_f L^2 = G_f \left(\frac{22}{3} c_A \right) L^2 \quad (11)$$

from which it follows that $c_A = 3/22$. Finally, the equivalent transverse fracture area of longitudinal elements is

$$A_l^* = (3/22)L^2 \quad (12)$$

while for diagonal elements it results:

$$A_d^* = (4/22)L^2 \quad (13)$$

The *critical failure strain* (ϵ_p) is defined as the largest strain attained by the element before the damage initiation (point A in Figure 2). The relationship between ϵ_p and the specific fracture energy G_f is given in Linear Elastic Fracture Mechanics as:

$$\epsilon_p = R_f \sqrt{\frac{G_f}{E(1-\nu^2)}} \quad (14)$$

in which R_f is the so-called failure factor, which accounts for the presence of an intrinsic defect of size a . R_f may be expressed in terms of a as:

$$R_f = \frac{1}{Y\sqrt{a}} \quad (15)$$

in which Y is a dimensionless parameter that depends on both the specimen and crack geometry. The element loses its load carrying capacity when the *limit strain* ϵ_r is reached (Point B in Figure 2). This value must satisfy the condition that, upon failure of the element, the dissipated energy density equals

the product of the element fracture area A_i^* times the specific fracture energy G_f , divided by the element length. Hence:

$$\int_0^{\varepsilon_r} F(\varepsilon) d\varepsilon = \frac{G_f \cdot A_i^*}{L_i} = \frac{K_r \cdot \varepsilon_p^2 \cdot E \cdot A_i}{2} \quad (16)$$

in which the sub index i is replaced by l or d depending on whether the element under consideration is a longitudinal or diagonal element. The coefficient K_r is a function of the material properties and the element length L_i :

$$K_r = \left(\frac{G_f}{E\varepsilon_p^2} \right) \left(\frac{A_i^*}{A_i} \right) \left(\frac{2}{L_i} \right) \quad (17)$$

In order to guarantee the stability of the algorithm, the condition $K_r = 1$ must be satisfied (Riera and Rocha, [10]). In this sense it is interesting to define the critical element length:

$$L_{cr} = 2 \left(\frac{G_f}{E\varepsilon_p^2} \right) \left(\frac{A_i^*}{A_i} \right) \quad (18)$$

Moreover:

$$(A_l^*/A_l) = (3/22)/\phi \quad (19)$$

$$(A_d^*/A_d) = (\sqrt{3}/11)/(\delta\phi) \quad (20)$$

In the special case of an isotropic continuum with $\nu = 0.25$, the value of the coefficients above are $d = 1.125$ and $f = 0.4$, which leads to $(A_l^*/A_l) \approx (A_d^*/A_d) \approx 0.34$. Thus, for practical purposes, a single value of the critical length can be used for longitudinal and diagonal elements. Therefore, the stability condition may be expressed as:

$$K_r = \frac{L_{cr}}{L_i} \geq 1 \quad \Rightarrow \quad L_i \leq L_{cr} \quad (21)$$

Finally, the expression for the limit strain is:

$$\varepsilon_r = K_r \varepsilon_p. \quad (22)$$

Besides, it is worth noting that although the DEM uses a scalar damage law to describe the uniaxial behavior of the elements, the global model accounts for anisotropic damage since it contains elements aligned in different spatial directions.

2.2 The random distribution of material parameters in the DEM environment

The first application of the DEM to fracture of concrete systems is due to Rocha [9], who assumed that the toughness G_f may be modelled by a random field with a Type III extreme value probability distribution (Weibull) with two parameters:

$$F(G_f) = 1 - \exp[-(G_f/\beta)^\gamma] \quad (23)$$

In equation (23), β and γ are the so-called scale and shape parameters, respectively. The mean value (μ) and the standard deviation (s) of G_f can be obtained in terms of β and γ by:

$$\mu = \beta [\Gamma(1 + 1/\gamma)] \quad (24)$$

$$s = \beta [\Gamma(1 + 2/\gamma) - \Gamma^2(1 + 1/\gamma)]^{1/2} \quad (25)$$

in which $\Gamma(x) = \int_0^\infty t^{x-1} e^{-t} dt$ is the *Gamma* function. In order to simulate pseudo random values of G_f the following expression was used:

$$G_f = \beta [-\ln(1 - u)]^{1/\gamma} \quad (26)$$

in which u is a random number with uniform probability distribution in the interval (0,1). Routines to generate samples of u are widely available. In earlier DEM applications, the length of the elements was set equal to the correlation length of the isotropic random field that describes the material property of interest. This is a serious limitation, because the discretization level is conditioned by a material property. In more recent studies, as well as in the present paper, the 3D random field that describes the material property is simulated using the scheme discussed by Puglia *et al* [11].

3 Scale-independent cohesive law: The Fractal criterion

Carpinteri *et al* [3], using the concept of fractal dimensions introduced by Manderblot [12], proposes a scale-independent cohesive law for quasi brittle materials. To achieve such purpose three material parameters, the tensile strength σ_u , the toughness G_f and the critical strain ε_c , must be defined in a non conventional form, known as *fractal tensile strength* σ_u^* , *fractal toughness* G_f^* and *critical fractal strain* ε_c^* .

To define these fractal parameters, a specimen with cross sectional area b^2 will be considered. The maximum tensile load F_u , *i.e.* the strength of this specimen is equal to the product of the strength σ_u times the nominal area $A_0 = b^2$. On the other hand, Carpinteri *et al* [2, 3] have shown that the area of the failure surface does not have a unique value, since it is scale dependent. In fact, the failure surface can be modelled as a lacunar fractal surface and according to the Housdorff measure of the fractal it can be written that $A_{res}^* = b^{2-d_\sigma}$. It is then possible to express the maximum tensile load F_u as the product of conventional tensile strength σ_u , and nominal area A_0 , or as the product of the fractal tensile strength σ_u^* and the fractal area A_{res}^* :

$$F_u = \sigma_u A_0 = \sigma_u^* A_{res}^* \quad (27)$$

The fractal tensile strength σ_u^* given by equation (28) is a true material constant, *i.e.* it is scale-invariant and possesses the anomalous physical dimensions $[F][L]^{-(2-d_\sigma)}$.

$$\sigma_u^* = \sigma_u b^{d_\sigma} \quad (28)$$

A similar reasoning may be applied to the fractal fracture energy. The work W necessary to split the same specimen of cross-sectional area b^2 equals the product of the fracture energy G_f and the nominal fracture area $A_0 = b^2$. The real fracture surface is not flat and its net area tends to infinity as resolution increases. Assuming that the surface can be represented as an invasive fractal surface, the work W is given by the product of the Hausdorff measure $A_{dis}^* = b^{\Delta_G} = b^{2+d_G}$ times the fractal fracture energy G_f^* . Thus:

$$W = G_f A_0 = G_f^* A_{dis}^* \quad (29)$$

Where G_f^* is the true scale invariant material parameter, that possesses the anomalous physical dimensions $[FL][L]^{-(2+d_G)}$. This material parameter can be obtained from equation (29) as:

$$G_f^* = G_f b^{d_G} \quad (30)$$

The deformation inside the damage zone must still be examined. It may be assumed that the strain field presents a fractal pattern. Carpinteri *et al* [3] proposed adopting $(1 - d_\varepsilon)$ with $(d_\varepsilon \geq 0)$ as a lacunar fractal dimension of the damage line projection. According to the fractal measure of this projection, the critical elongation w_c of the band at rupture must be given by the product of the Hausdorff measure of the damage line projection $b^* = b^{(1-d_\varepsilon)}$ times the critical fractal strain ε_c^* . In addition, the critical elongation may be computed as the product of the nominal strain ε_c and the nominal length of the damage line projection b . Thus:

$$w_c = \varepsilon_c b = \varepsilon_c^* b^{1-d_\varepsilon} \quad (31)$$

in which ε_c^* is also a true scale invariant material parameter that has an anomalous physical dimension $[L]^{(d_\varepsilon)}$. When the test specimen has exhausted all its strength then $w = w_c$. There is also a relation between fractal exponents. The integral $G_f = \int_0^{w_c} \sigma dw$ is obviously valid in a conventional scale. Substituting in this expression equations (28) and (31) it follows that:

$$G_f = \int_0^{w_c} \sigma dw = b^{1-d_\varepsilon-d_\sigma} \int_0^{\varepsilon_c^*} \sigma^* d\varepsilon^* = G_f^* b^{1-d_\varepsilon-d_\sigma} \quad (32)$$

Since the exponents of b in Eqs. (30) and (32) must be the same, d_G can be obtained as a function of d_σ and d_ε . The following fundamental relation between the scale exponents results:

$$d_\sigma + d_\varepsilon + d_G = 1 \quad (33)$$

Carpinteri [3] proves that all the exponents are positive and smaller than 1. Whereas d_ε can attain all values in the (0,1) interval, d_σ and d_G vary only between 0, corresponding to an Euclidian space, and $1/2$, when there is Brownian disorder. Equation (33) confirms that the sum of d_σ and d_G is always smaller than 1, as shown by Carpinteri [1] by means of dimensional arguments. It is important to

point out that Equation (32) cannot be applied directly to the elementary constitutive law of the DEM plotted in Figure 2, but is valid in stress-strain curves obtained by mean of DEM simulations of tensile tests.

4 Examples: rock plate with different size submitted to uniaxial tensile stress

4.1 Model description

In order to introduce Carpinteri's Multifractal Law (CML) to the DEM environment, a group of rock square plates, fixed at their lower face and subjected to monotonically increasing displacements at nodes on their upper faces were simulated. The plates were analyzed up to complete failure. The side b of the plates ranges from 0.05 to 3.50m. The smallest DEM array that leads to satisfactory results consists of $10 \times 10 \times 1$ cubic modules, with 1026 DOF, used for the smallest (0.05m) plate, while the 3.50m plate model consists of $700 \times 700 \times 1$ cubic modules, with 1472802 DOF, constituting the largest array used in this study. In all cases nodal displacements in the direction normal to the plate's middle surface were restrained, in order to simulate Plane Strain conditions. Table 1 shows the basic dimension of the samples while Table 2 indicates the relevant material properties.

Table 1: Length b of the side of the plates and number of cubic DEM cells in length.

Plate	1	2	3	4	5	6	7	8	9	10	11
b (m)	0.05	0.075	0.10	0.15	0.20	0.25	0.50	0.75	1.00	1.50	3.50
Cells	10	15	30	30	40	50	100	150	200	300	700

Table 2: Relevant material properties of rock (granite).

Material Properties	Value
E (Young's modulus)	7.5E10N/m ²
ρ (specific mass)	2700kg/m ³
ν (Poisson coefficient)	0.25
$E(G_f)$ (Expected value of specific fracture energy)	1300N/m
$CV(G_f)$ (coefficient of variation of G_f)	40%
R_f (Failure factor)	0.8

The layout of the plates showing their relative size and boundary conditions is presented in Figure 3(a). Four simulations were carried out for each size. It is important to notice that the specific fracture energy G_f is modeled as a random field with the properties indicated in Table 2, so each simulation leads to a different strength and a different stress-strain curve. The probability distribution of G_f was assumed Weibull.

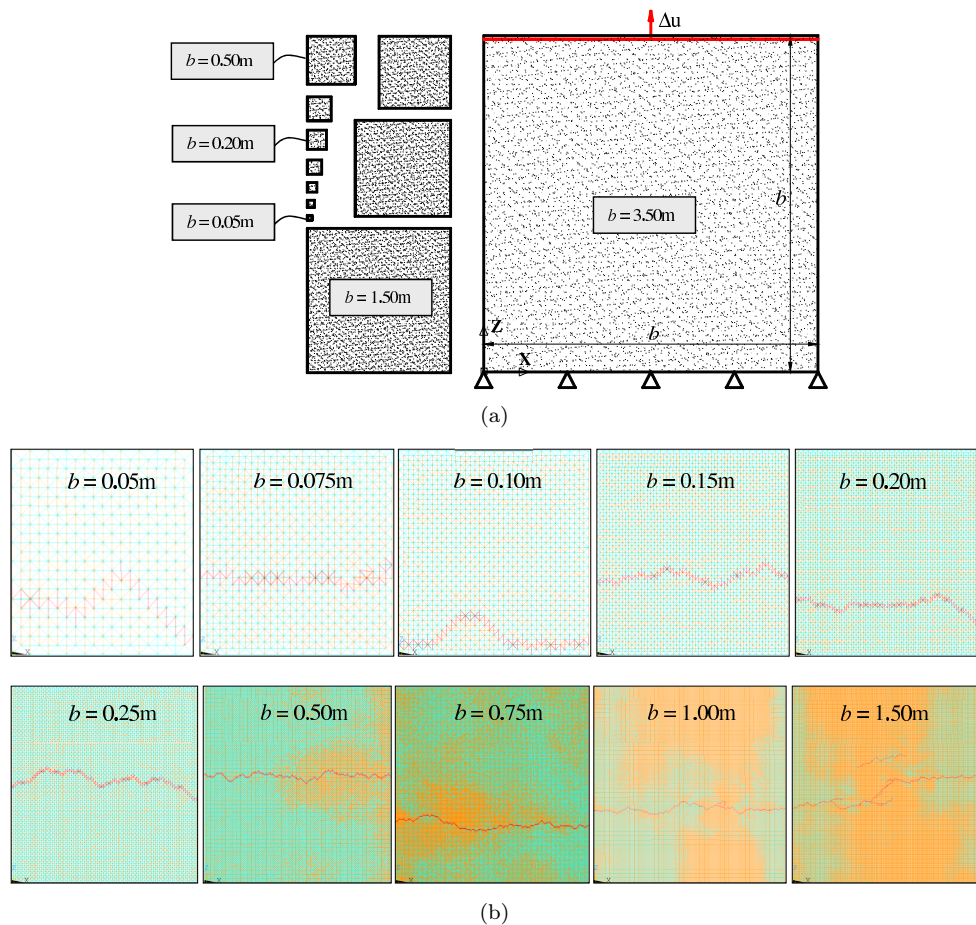


Figure 3: (a) Relative size of the plates and boundary conditions, (b) Damage distribution and rupture configuration of plates of various sizes subjected to applied displacements inducing tension.

4.2 DEM simulated response of rock plates

One sample of the final damage distribution in simulated plates of each size considered in the study is shown in Figure 3(b), in which colors cyan, orange and red represent undamaged, damaged and totally broken (failed) elements, respectively. The resulting stress-strain curves for all simulations of the 0.15 m plate, as well as the average curve, are presented in Figure 4(a). Figure 4(b) shows the mean curves for all plate sizes. It may be seen than the shape of the mean stress-strain curves varies with the specimen size. This feature has been repeatedly observed in experimental studies, such as van Vliet and van Mier [13].

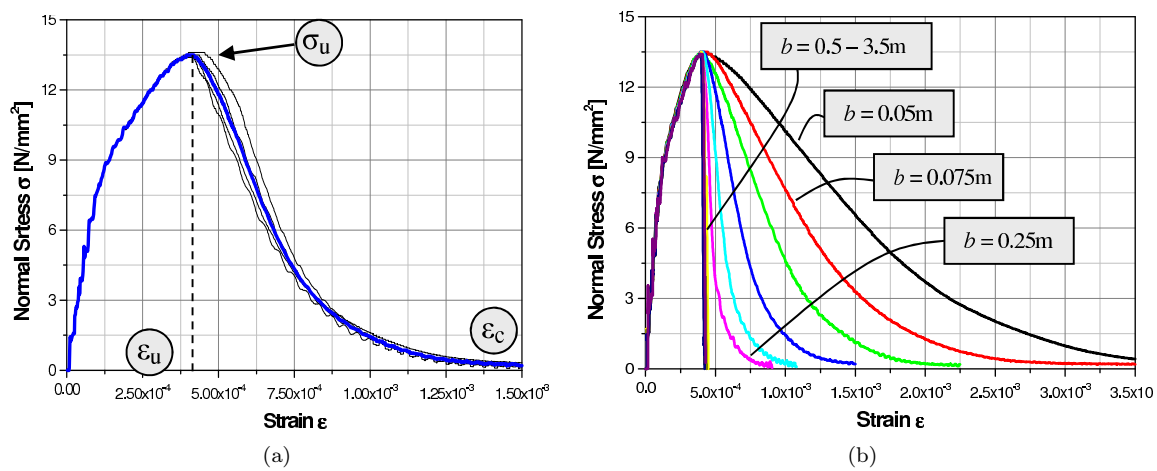


Figure 4: (a) Curves for the mean vertical stress at lower support vs mean strain for the 0.15m rock plate obtained in four simulations aand average curve (in blue) and, (b) Mean vertical stress at lower support vs mean strain for all plate sizes.

Table 3 presents the main parameters that characterize the stress-strain curves shown in Figure 4(b), in which σ_u denotes the ultimate stress, ϵ_u the the critical strain, ϵ_c the strain at the point where the strength is totally exhausted, defined for practical purposes as the strain when the stress decreases below 5% of the maximum stress (σ_u) (see figure 4a). This notation is applicable without any restriction, to plates with sides smaller than 0.5m. For plates of lengths equal to 0.5m or larger, failure occurs in a brittle manner and the ultimate strain ϵ_u cannot be distinguished from the critical strain ϵ_c .

The displacement, assuming a uniform strain distribution, is $w = \epsilon b$, in which b is the length of the plate or specimen. The unloading branch of the stress vs. displacement curve (σ_u vs. w curve) associated to damage is determined by subtracting from the total σ_u vs w curve the displacements corresponding to the loading branch. Note that the loading branch may be due to elastic strains only,

or to elastoplastic strains and that the maximum displacement of the total σ_u vs w curve equals the critical displacement w_c , defined in expression (31).

Table 3: Mean values of the peak stress and critical strain, rupture strain and displacement for different plate lengths.

b [mm]	σ_u [N/mm ²]	ε_u	ε_c	w_u [mm]	w_c [mm]
50	1.35E+07	4.29E-04	3.24E-03	0.0214	0.1619
75	1.35E+07	4.30E-04	2.30E-03	0.0323	0.1725
100	1.34E+07	3.93E-04	1.64E-03	0.0393	0.1640
150	1.35E+07	4.15E-04	1.16E-03	0.0623	0.1743
200	1.35E+07	4.06E-04	8.51E-04	0.0813	0.1703
250	1.34E+07	3.98E-04	6.94E-04	0.0996	0.1734
500	1.35E+07	4.04E-04	4.51E-04	0.2021	0.2254
750	1.35E+07	3.99E-04	4.26E-04	0.2992	0.3197
1000	1.34E+07	3.95E-04	4.18E-04	0.3954	0.4179
1500	1.34E+07	4.02E-04	4.29E-04	0.6036	0.6437
3500	1.33E+07	3.78E-04	4.12E-04	1.3243	1.4425

5 The fractal dimension calculus

5.1 Fractal tensile strength

With the aim of examining the influence of size on the simulated stress-strain curve, the evolution of σ_u with plate size is presented in Figure 5. As shown in Figure 5(a), the ultimate stress decreases marginally for the range of sizes analyzed. In the bi-logarithmic graphical representation of equation (28), shown in Figure 5(b), the fractal coefficient d_σ is negligibly small. Obviously, for a different range of sizes or material parameters this conclusion should be revised.

5.2 Fractal critical strain

Figure 6(a) shows in a bi-logarithmic scale the relations between ε_u and ε_c with the plate size b . It may be seen that ε_c presents two typical regions: for plates smaller than about 0.5m, it clearly decreases with the plate size, but for plates larger than 0.5m it remains invariant, at least within the range of sizes and material properties herein examined. This behavior is clearly illustrated by Figure 4(b), which shows that the largest plates fail in a brittle manner at the same the ε_c . For the larger

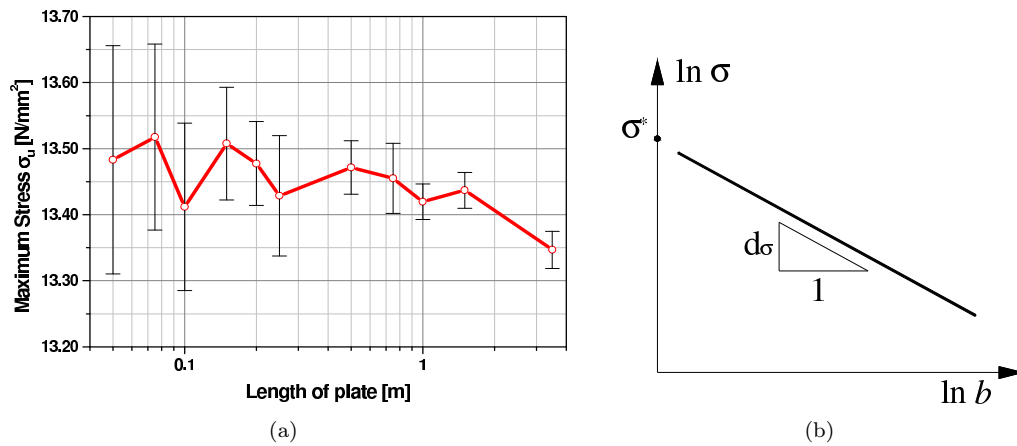


Figure 5: (a). Variation of maximum stress with plate size (logarithmic scale): Mean and one standard deviation of simulated values and (b) Graphical representation of equation (28).

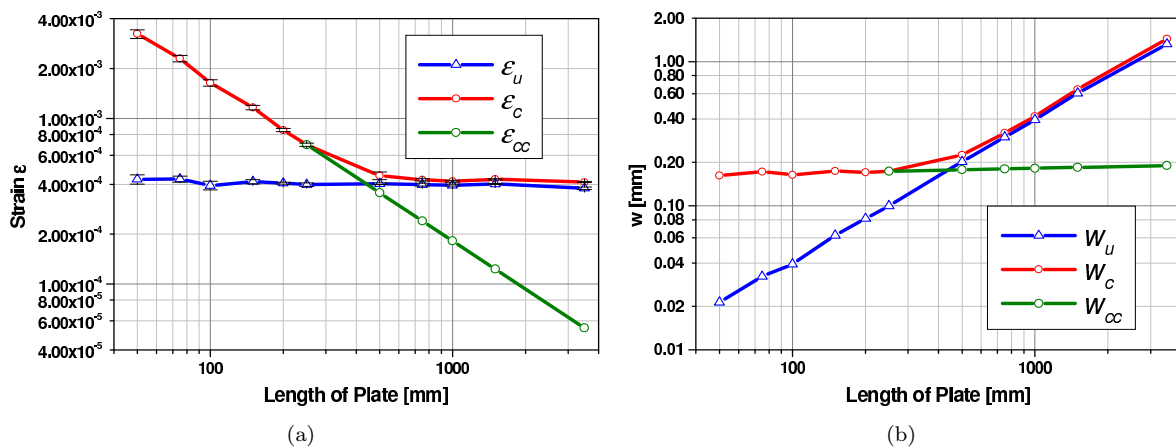


Figure 6: Variation of ϵ_u , ϵ_c and ϵ_{cc} with plate size b and (b) Variation of w_u , w_c and w_{cc} with plate size b (in bi-logarithmic scale).

plates ($b \geq 0.5\text{m}$) the correct value of final strain ε_c must be lower than ε_u , and rupture becomes instable. It is possible to obtain the true values of the critical strain by extrapolating the values for the large plates ($b \geq 0.5\text{m}$) using the data obtained for the smaller plates ($b < 0.5\text{m}$). The final strain that coincides with the critical strain, denoted ε_{cc} , was obtained fitting the ε_c curve in Figure 6(a) for lengths smaller than 0.5m, to a straight line. Taking b in mm, it follows that:

$$\log \varepsilon_{cc} = \log 0.144 - 0.966 \log b \quad (34)$$

Equation (34) allows the estimation of the *true* final strain for the larger plates ($b \geq 0.5\text{m}$). Table 4 presents the results obtained for all the plates, also shown in Figures 6(a) and (b) in terms of strain and displacement vs the plate size respectively.

Table 4: *True* final strain ε_{cc} and displacement w_{cc} vs plate size.

L	ε_{cc}	w_{cc}
[mm]	[mm/mm]	[mm]
50	3.24E-03	0.1619
75	2.30E-03	0.1725
100	1.64E-03	0.1640
150	1.16E-03	0.1743
200	8.51E-04	0.1703
250	6.94E-04	0.1734
500	3.56E-04	0.1779
750	2.40E-04	0.1803
1000	1.82E-04	0.1821
1500	1.23E-04	0.1847
3500	5.43E-05	0.1900

Using the corrected critical displacement w_{cc} and equation (31) it is found that $\varepsilon_c^* = 0.144$ [mm/mm^{0.034}], resulting a fractal coefficient $d_\varepsilon = 0.966$. Note that in the present case the fractal tensile strength σ_u^* is equal to the maximum stress σ_u because the fractal dimension coefficient d_σ was negligible and taken equal to zero.

Carpinteri [1–3] define w as:

$$w = w_T - w_{pre-peak} \quad (35)$$

where w_T is the total displacement and $w_{pre-peak}$ is the displacement due to elastic and anelastic deformations before the peak stress is attained in the test under examination. In the reported DEM simulations, size independence of the σ^* vs ε^* curve using this definition of w is not confirmed.

However, size independence of this curve is verified when in equation (35) $w_{pre-peak}$ is replaced by w_e , the displacement due *only to elastic deformations*. The notation is clarified in Figure 7 below.

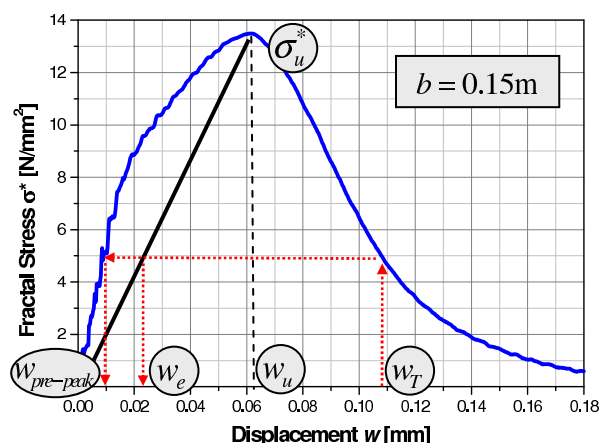


Figure 7: Stress-displacement curve for $b=0.15\text{m}$ showing various displacement definitions.

Figure 8(a) presents the results in terms of $\sigma^* = \sigma b^{d_\sigma}$ and the fractal strain ε^* , for $\varepsilon = \varepsilon_u$. The definition of the fractal strain is given by equation (36). In the fractal *dominium*, this relation is independent of size.

$$\varepsilon^* = (w_T - w_e) b^{-(1-d_\varepsilon)} \quad \text{or} \quad \varepsilon^* = \left(w_T - \frac{w_u}{\sigma_u^*} \sigma(w_T) \right) b^{-(1-d_\varepsilon)} \quad (36)$$

Similarly, equation (37) presents the fractal strain ε^* in terms of strains:

$$\varepsilon^* = \left(\varepsilon_T b - \frac{\varepsilon_u b}{\sigma_u^*} \sigma(\varepsilon_T b) \right) b^{-(1-d_\varepsilon)} \quad (37)$$

Using the fact illustrated in Figure 7, that the stress corresponding to w_T , $w_{pre-peak}$ and w_e is the same, ε_T may be computed as:

$$\varepsilon_T = \varepsilon^* b^{(1-d_\varepsilon)} + \frac{\varepsilon_u}{\sigma_u^*} \sigma(\varepsilon^*) \quad (38)$$

Figure 8(b) shows the stress-strain curves for the larger plates ($b = 0.5\text{m}$) with the softening branch computed with equation (38) considering the invariant fractal strain-stress curve σ^* vs ε^* presented in Figure 8(a). To measure *directly* the unstable post-peak part of the stress-strain curves, it would be necessary to apply non conventional boundary conditions. Experimental evidence presented by van Mier and van Vliet [13] lets support to the unstable branches of the corrected stress-strain curves shown in Fig.(8a).

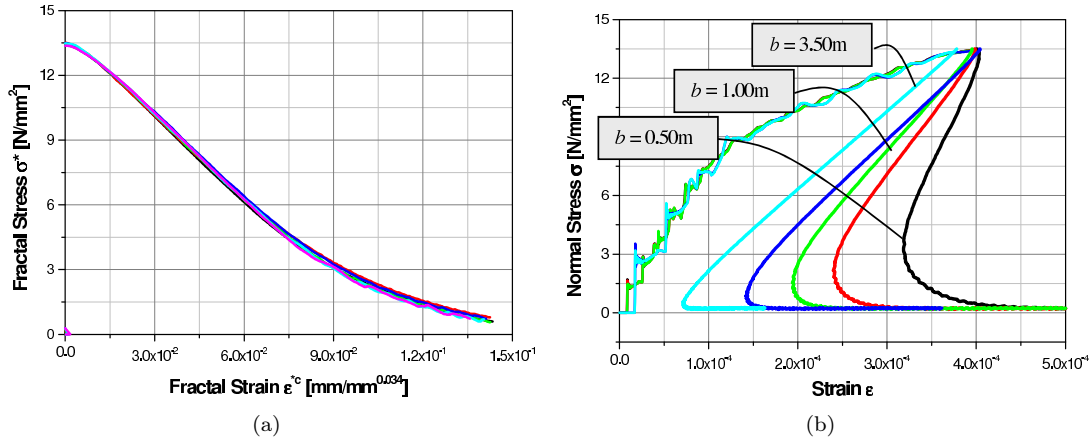


Figure 8: (a) Corrected fractal law diagrams and (b) corrected stress-strain curves for larger plates.

In summary, using the methods proposed by Kostaski *et al* [14], values of the fractal dimensions of the invasive area described by equation (29) were obtained by simulation, leading to values of d_G between 0.03 and 0.065. Thus, the values of the dimensional coefficients are compatible with the CML proposed by Carpinteri, that establishes that the sum of the three fractal exponents equals unity.

$$d_\sigma \approx 0, d_\epsilon \approx 0.966, d_G \approx [0.032, 0.065], d_G + d_\epsilon + d_\sigma \approx 1 \quad (39)$$

6 Conclusions

The numerical analysis of plates subjected to tensile fracture employing the truss-like Discrete Element Method (DEM) is initially described in the paper. Then a brief explanation of the Carpinteri's multi-fractal law (CMF) is also presented. The determination of fractal dimension over a set of simulated DEM rock plates subjected to uniaxial tension is described next. The calculus of the three exponents d_σ , d_ϵ and d_G is finally presented.

The results show that the DEM model captures the CML predictions and therefore it remains a valid alternative to simulate fracture processes in quasi fragile materials, and to explore different aspects of fracture in real solids.

It is important to note, in agreement with the CML theory, that the sum of the three coefficients is approximately 1. The fractal exponent d_G obtained in the DEM simulations reported herein was considerably smaller than the value expected in real materials, which according to Refs. [1-3] ranges from 0.2 to 0.3. The values of the exponents obtained in DEM simulations depend on the variability and type of random distribution adopted in the definition of G_f as a random field, and also on the unloading criteria adopted in the elementary constitutive law. The influences of these factors, as well as objectivity requirements, are presently under study.

Acknowledgements The authors acknowledge the support of CNPq and CAPES (Brazil).

References

- [1] Carpinteri, A., Scaling laws and renormalization groups for strength and toughness of disordered materials. *Int J, Solids Struct*, **31**, pp. 291–302, 1994.
- [2] Carpinteri, A., Chiapa, B. & Invernizzi, S., Three-dimensional fractal analysis of concrete fracture at the meso-level. *Theoretical and Applied Fracture Mechanics*, **31**, pp. 163–172, 1999.
- [3] Carpinteri, A., Chiaia, B. & Cornetti, P., A scale-invariant cohesive crack model for quasi-brittle materials. *Engineering Fracture Mechanics*, **69**, pp. 207–217, 2002.
- [4] Nayfeh, A. & Hefzy, M., Continuum modeling of three-dimensional truss-like space structures. *AIAA Journal*, **16(8)**, pp. 779–787, 1978.
- [5] Dalguer, L., Irikura, K., Riera, J. & Chiu, H., The importance of the dynamic source effects on strong ground motion during the 1999 Chi-Chi, Taiwan, earthquake: Brief interpretation of the damage distribution on buildings. *Bull Seismol Soc Am*, **91**, pp. 1112–1127, 2001.
- [6] Hayashi, Y., *Sobre uma representação discreta de meios contínuos em dinâmica não-linear*. Master's thesis, CPGEC, UFRGS, Porto Alegre, Brazil, 1982.
- [7] Rocha, M., Riera, J. & Krutzik, N., Extension of a model that aptly describes fracture of plain concrete to the impact analysis of reinforced concrete. *Int. Conf. and Structural Mechanics in Reactor Technology, SMiRT 11*, Trans. Vol. J.: Tokyo, Japan, 1991.
- [8] Hillerborg, A., A model for fracture analysis. Technical Report Cod LUTVDG/TV BM-3005/1-8, 1978.
- [9] Rocha, M., *Ruptura e Efeitos de Escala em Materiais não Homogêneos*. Master's thesis, CPGEC, Universidade Federal do Rio Grande do Sul, Porto Alegre, Brazil, 1989.
- [10] Riera, J. & Rocha, M., A note on velocity of crack propagation in tensile fracture. *Revista Brasileira de Ciências Mecânicas*, **XII(3)**, pp. 217–240, 1991.
- [11] Puglia, B., Iturrioz, I., Riera, J. & Kostaski, L., Random field generation of the material properties in the truss-like discrete element method. *Cilamce-Mecom, 2010, Buenos Aires. Mecánica Computacional*, Asociación Argentina de Mecánica Computacional: Santa Fe, Argentina, volume XXIX, pp. 6793–6807, 2010.
- [12] Mandelbrot, B., *The Fractal Geometry of Nature*. Freeman: San Francisco, 1982.
- [13] van Vliet, M. & van Mier, J., Experimental investigation of size effect in concrete and sandstone under uniaxial tension. *Engineering Fracture Mechanics*, **65**, pp. 165–188, 2000.
- [14] Kostaski, L., Riera, J. & Iturrioz, I., Consideration of size effects and stress localization in response determinations using the dem. *Cilamce-Mecom, 2010, Buenos Aires. Mecánica Computacional*, Asociación Argentina de Mecánica Computacional: Santa Fe, Argentina, volume XXIX, pp. 2785–2801, 2010.

Vertical response of a rigid circular foundation embedded on a transversely isotropic bi-material interface

Josué Labaki, Euclides Mesquita

*Dept. of Comp. Mechanics, School of Mechanical Engineering,
Unicamp. 200 Mendeleev St, Campinas, SP – Brazil*

Nimal Rajapakse

*Faculty of Applied Sciences, Simon Fraser University. 8888 University Drive,
Burnaby, BC – Canada*

Abstract

This paper examines the vertical response of a rigid circular foundation embedded in a viscoelastic, transversely isotropic bi-material interface. The Cauchy-Navier equations, which describe the behavior of the aforementioned media, are solved by using Hankel integral transforms. A boundary-value problem corresponding to the case of a distributed vertical ring load in the interface of the two materials is introduced. The model of embedded disc is formulated in terms of a discretized integral equation, which couples the rigid displacement of the disc with the tractions acting over its surface. The disc is discretized by a number of annular discs, and over each of these elements the traction is considered to be constant. The system of the resulting discretized integral equations is solved numerically, which gives the tractions over each elementary disc. The weighted summation of these results by the respective area of the elements gives the total force applied over the disc corresponding to a unitary rigid displacement. The dynamic compliance of the media-inclusion system is shown in this paper for different constructions. The present solutions contribute to the study of the dynamic response of deeply buried foundations and anchors in non-homogeneous interfaces.

Keywords: Green's functions, soil-foundation interaction, transverse isotropy, deeply buried foundations.

1 Introduction

The study of the interaction of rigid foundations with transversely isotropic materials is a branch of the theory of elasticity which has important practical applications in earthquake engineering and seismology. The case of a rigid foundation embedded in the interface of two different transversely isotropic materials is of particular interest to the study of foundations deeply buried in soil.

The present study is concerned with the steady-state vertical response of a rigid annular or solid

circular disc embedded in the interface of two bonded viscoelastic, transversely isotropic, three-dimensional half-spaces. Figure 1 illustrates the present problem.

The first section of the paper introduces the Cauchy-Navier equations, which describe the behavior of the aforementioned media. This system of equations is solved by using Hankel integral transforms. Hankel transforms are the most suitable transforms in the present case because cylindrical coordinates are used. The viscoelastic behavior of the medium is introduced by Christensen's elastic-viscoelastic correspondence principle. In the following section, a boundary-value problem corresponding to the case of a distributed vertical ring load in the interface of the two half-spaces is introduced. Next, the model of embedded disc is formulated in terms of an integral equation, the kernel of which corresponds to the influence function regarding those buried ring load. This integral equation couples the rigid displacement of the disc with the tractions acting over its surface. The disc is discretized by a number of concentric rigid annular discs. The traction over each of these elements is considered to be constant. Because the disc is rigid, the displacement of all these elements is the same. The system of the resulting discretized integral equations is solved numerically, which gives the tractions over each elementary disc. The weighted summation of these results by the respective area of the elements gives the total force applied over the disc corresponding to a unitary rigid displacement. Finally, some numerical results are presented in the form of dynamic compliance of the disc. The paper shows the convergence of the solution for increasing discretization levels, for different types of transversely isotropic materials, for varying inner radii of an annular disc with unitary outer radius, and for different combinations of two materials at the interface.

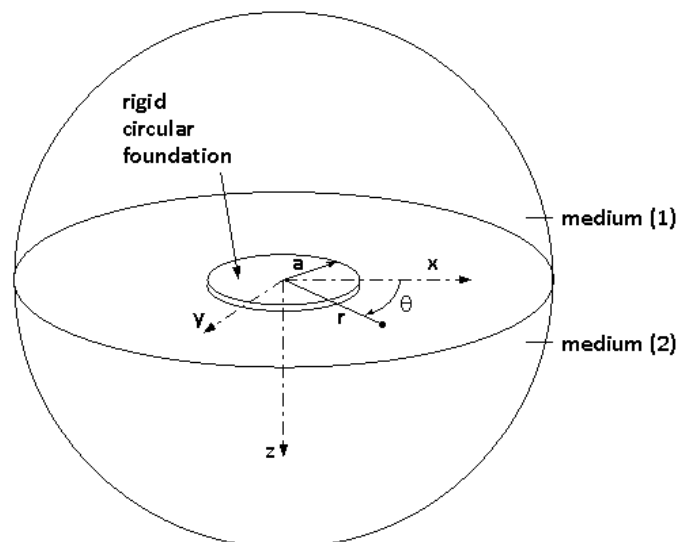


Figure 1: Interface between two infinite half-spaces containing a circular foundation.

2 Governing equations

Consider two transversely isotropic elastic half-spaces bonded together throughout an infinite plane. A cylindrical coordinate system $O(r, \theta, z)$ is adopted, the z -axis of which is perpendicular to the plane that interfaces the two media (see Fig. 1). The equations of motion in these media are expressed by:

$$c_{11} \left(\frac{\partial^2}{\partial r^2} u_r + \frac{1}{r} \frac{\partial}{\partial r} u_r - \frac{u_r}{r^2} \right) + \frac{c_{11} - c_{12}}{2} \frac{1}{r^2} \frac{\partial^2}{\partial \theta^2} u_r + c_{44} \frac{\partial^2}{\partial z^2} u_r + \frac{c_{11} + c_{12}}{2} \left(\frac{1}{r} \frac{\partial^2}{\partial r \partial \theta} u_\theta + \frac{1}{r^2} \frac{\partial}{\partial \theta} u_\theta \right) - 2c_{11} \frac{1}{r^2} \frac{\partial}{\partial \theta} u_\theta + (c_{13} + c_{44}) \frac{\partial^2}{\partial r \partial z} u_z = \rho \frac{\partial^2}{\partial t^2} u_r \quad (1)$$

$$\frac{c_{11} - c_{12}}{2} \left(\frac{\partial^2}{\partial r^2} u_\theta + \frac{1}{r} \frac{\partial}{\partial r} u_\theta - \frac{u_\theta}{r^2} \right) + c_{11} \frac{1}{r^2} \frac{\partial^2}{\partial \theta^2} u_\theta + c_{44} \frac{\partial^2}{\partial z^2} u_\theta + \frac{c_{11} + c_{12}}{2} \left(\frac{1}{r} \frac{\partial^2}{\partial r \partial \theta} u_r - \frac{1}{r^2} \frac{\partial}{\partial \theta} u_r \right) + 2c_{11} \frac{1}{r^2} \frac{\partial}{\partial \theta} u_r + (c_{13} + c_{44}) \frac{1}{r} \frac{\partial^2}{\partial \theta \partial z} u_z = \rho \frac{\partial^2}{\partial t^2} u_\theta \quad (2)$$

$$c_{44} \left(\frac{\partial^2}{\partial r^2} u_z + \frac{1}{r} \frac{\partial}{\partial r} u_z + \frac{1}{r^2} \frac{\partial^2}{\partial \theta^2} u_z \right) + c_{33} \frac{\partial^2}{\partial z^2} u_z + (c_{13} + c_{44}) \left(\frac{\partial^2}{\partial r \partial z} u_r + \frac{1}{r} \frac{\partial}{\partial z} u_r + \frac{1}{r} \frac{\partial^2}{\partial \theta \partial z} u_\theta \right) = \rho \frac{\partial^2}{\partial t^2} u_z \quad (3)$$

In Eqs. (1) to (3), ρ is the density of the medium and c_{ij} are material constants of the transversely isotropic material.

The solution of these coupled equations leads to the displacement field of the transversely isotropic media, expressed by:

$$u_r(r, \theta, z) = \int_0^\infty \left(g_1 A e^{-\delta \xi_1 z} + g_1 B e^{\delta \xi_1 z} + g_2 C e^{-\delta \xi_2 z} + g_2 D e^{\delta \xi_2 z} \right) \cdot J_0(\lambda r) \lambda d\lambda + \int_0^\infty \left(g_3 A e^{-\delta \xi_1 z} + g_3 B e^{\delta \xi_1 z} + g_4 C e^{-\delta \xi_2 z} + g_4 D e^{\delta \xi_2 z} + g_5 E e^{-\delta \xi_3 z} + g_5 F e^{\delta \xi_3 z} \right) \cdot J_1(\lambda r) \lambda d\lambda \quad (4)$$

$$u_\theta(r, \theta, z) = \int_0^\infty \left(g_6 A e^{-\delta \xi_1 z} + g_6 B e^{\delta \xi_1 z} + g_7 C e^{-\delta \xi_2 z} + g_7 D e^{\delta \xi_2 z} + g_8 E e^{-\delta \xi_3 z} + g_8 F e^{\delta \xi_3 z} \right) \cdot J_1(\lambda r) \lambda d\lambda + \int_0^\infty \left(g_9 E e^{-\delta \xi_3 z} + g_9 F e^{\delta \xi_3 z} \right) \cdot J_0(\lambda r) \lambda d\lambda \quad (5)$$

$$u_Z(r, \theta, z) = \int_0^\infty (-g_{10}Ae^{-\delta\xi_1z} + g_{10}Be^{\delta\xi_1z} - g_{11}Ce^{-\delta\xi_2z} + g_{11}De^{\delta\xi_2z}) \cdot J_1(\lambda r) \lambda d\lambda \quad (6)$$

In which,

$$g_{1,2} = \delta\zeta\vartheta_{1,2} \cos(\theta), \quad g_{3,4} = -\frac{1}{r}\vartheta_{1,2} \cos(\theta), \quad g_5 = \frac{1}{r} \cos(\theta) \quad (7)$$

$$g_{6,7} = -\frac{1}{r}\vartheta_{1,2} \sin(\theta), \quad g_8 = \frac{1}{r} \sin(\theta), \quad g_9 = -\delta\zeta \sin(\theta) \quad (8)$$

$$g_{10,11} = \delta\xi_{1,2} \cos(\theta) \quad (9)$$

$$\vartheta_{1,2} = \frac{\alpha\xi_{1,2}^2 - \zeta^2 + 1}{\kappa\zeta^2} \quad (10)$$

$$\zeta = \lambda/\delta \quad (11)$$

$$\xi_{1,2}(\zeta) = \frac{1}{\sqrt{2\alpha}} \left(\gamma\zeta^2 - 1 - \alpha \pm \sqrt{\Phi} \right)^{\frac{1}{2}} \quad (12)$$

$$\Phi(\zeta) = (\gamma\zeta^2 - 1 - \alpha)^2 - 4\alpha(\beta\zeta^4 - \beta\zeta^2 - \zeta^2 + 1) \quad (13)$$

$$\xi_3 = \pm\sqrt{\zeta\zeta^2 - 1} \quad (14)$$

$$\alpha = \frac{c_{33}}{c_{44}}, \quad \beta = \frac{c_{11}}{c_{44}}, \quad \kappa = \frac{c_{13} + c_{44}}{c_{44}}, \quad \varsigma = \frac{c_{11} - c_{12}}{2c_{44}}, \quad \delta = \frac{\rho a^2}{c_{44}} \omega^2 \quad \text{and} \quad \gamma = 1 + \alpha\beta - \kappa^2 \quad (15)$$

The stress field of the transversely isotropic media is derived from Eqs. (4) to (6):

$$\frac{\sigma_{ZZ}}{c_{44} \cos(\theta)} = \int_0^\infty (b_{21}Ae^{-\delta\xi_1z} + b_{21}Be^{\delta\xi_1z} + b_{22}Ce^{-\delta\xi_2z} + b_{22}De^{\delta\xi_2z}) J_1(\lambda r) \lambda d\lambda \quad (16)$$

$$\begin{aligned} \frac{\sigma_{\theta Z}}{c_{44} \sin(\theta)} &= \int_0^\infty (h_1Ae^{-\delta\xi_1z} - h_1Be^{\delta\xi_1z} + h_2Ce^{-\delta\xi_2z} - h_2De^{\delta\xi_2z} + h_3Ee^{-\delta\xi_3z} - h_3Fe^{\delta\xi_3z}) J_0(\lambda r) \lambda d\lambda \\ &+ \int_0^\infty (h_1Ae^{-\delta\xi_1z} - h_1Be^{\delta\xi_1z} + h_2Ce^{-\delta\xi_2z} - h_2De^{\delta\xi_2z} - h_3Ee^{-\delta\xi_3z} + h_3Fe^{\delta\xi_3z}) J_2(\lambda r) \lambda d\lambda \end{aligned} \quad (17)$$

$$\begin{aligned} \frac{\sigma_{\theta Z}}{c_{44} \sin(\theta)} &= \int_0^\infty (h_1Ae^{-\delta\xi_1z} - h_1Be^{\delta\xi_1z} + h_2Ce^{-\delta\xi_2z} - h_2De^{\delta\xi_2z} + h_3Ee^{-\delta\xi_3z} - h_3Fe^{\delta\xi_3z}) J_0(\lambda r) \lambda d\lambda \\ &+ \int_0^\infty (h_1Ae^{-\delta\xi_1z} - h_1Be^{\delta\xi_1z} + h_2Ce^{-\delta\xi_2z} - h_2De^{\delta\xi_2z} - h_3Ee^{-\delta\xi_3z} + h_3Fe^{\delta\xi_3z}) J_2(\lambda r) \lambda d\lambda \end{aligned} \quad (18)$$

$$\begin{aligned} \frac{\sigma_{RZ}}{c_{44} \cos(\theta)} = & - \int_0^\infty \left(h_1 A e^{-\delta \xi_1 z} - h_1 B e^{\delta \xi_1 z} + h_2 C e^{-\delta \xi_2 z} - h_2 D e^{\delta \xi_2 z} + h_3 E e^{-\delta \xi_3 z} - h_3 F e^{\delta \xi_3 z} \right) J_0(\lambda r) \lambda d\lambda \\ & - \int_0^\infty \left(-h_1 A e^{-\delta \xi_1 z} + h_1 B e^{\delta \xi_1 z} - h_2 C e^{-\delta \xi_2 z} + h_2 D e^{\delta \xi_2 z} + h_3 E e^{-\delta \xi_3 z} - h_3 F e^{\delta \xi_3 z} \right) J_2(\lambda r) \lambda d\lambda \end{aligned} \quad (19)$$

In which,

$$b_{2i} = \alpha \delta^2 \xi_i^2 - (\kappa - 1) \delta^2 \zeta^2 \vartheta_i \quad (20)$$

$$h_{1,2} = (1 + \vartheta_i) \delta \xi_i \frac{\delta \zeta}{2}, \quad h_3 = \delta \xi_3 \frac{\delta \zeta}{2}, \quad h_{4,5} = \vartheta_{1,2} \frac{\delta \zeta}{2} \quad \text{and} \quad h_6 = \frac{\delta \zeta}{2} \quad (21)$$

3 Influence functions

In this section, boundary-value problems regarding interior distributed annular loads are considered. The loads are applied at the interface between the media (1) and (2) (see Fig. 1). Figure 2 depicts a vertical load, uniformly distributed over the area of an annular disc of inner and outer radius s_1 and s_2 .

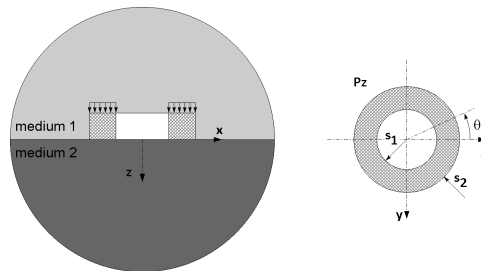


Figure 2: Distributed transversal load applied on an annular area.

The continuity conditions at the infinite bonded interface between media (1) and (2) are established as follows:

$$\frac{u_R^{(1)}(r, z=0)}{\cos(\theta)} - \frac{u_\theta^{(1)}(r, z=0)}{\sin(\theta)} = \frac{u_R^{(2)}(r, z=0)}{\cos(\theta)} - \frac{u_\theta^{(2)}(r, z=0)}{\sin(\theta)} \quad (22)$$

$$\frac{u_R^{(1)}(r, z=0)}{\cos(\theta)} + \frac{u_\theta^{(1)}(r, z=0)}{\sin(\theta)} = \frac{u_R^{(2)}(r, z=0)}{\cos(\theta)} + \frac{u_\theta^{(2)}(r, z=0)}{\sin(\theta)} \quad (23)$$

$$\frac{u_Z^{(1)}(r, z=0)}{\cos(\theta)} = \frac{u_Z^{(2)}(r, z=0)}{\cos(\theta)} \quad (24)$$

The upper indices (1) or (2) in Eqs. (22) to (24) indicate the medium which each component of displacement refers to. The arbitrary constants A, B, C, D, E and F in each case ($m = 1$ or $m = 2$) are selected so that the amplitude of the displacement vanishes with increasing depth in z . The material constants and other parameters also depend on the respective medium. For example, $g_6^{(1)}$ and $\xi_1^{(1)}$ are different than $g_6^{(2)}$ and $\xi_1^{(2)}$.

For the distributed vertical load depicted in Fig. 2, the stress boundary conditions are:

$$\sigma_{ZZ}^{(2)}(r, z = 0) - \sigma_{ZZ}^{(1)}(r, z = 0) = \cos(\theta) \int_0^\infty \{s_2 J_1(\lambda s_2) - s_1 J_1(\lambda s_1)\} J_0(\lambda r) d\lambda \quad (25)$$

$$\sigma_{RZ}^{(2)}(r, z = 0) = \sigma_{RZ}^{(1)}(r, z = 0) \quad (26)$$

$$\sigma_{\theta Z}^{(2)}(r, z = 0) = \sigma_{\theta Z}^{(1)}(r, z = 0) \quad (27)$$

The system of six equations comprising Eqs. (22) to (24) and Eqs. (25) to (27) can be solved to determine the arbitrary constants $A^{(2)}, B^{(1)}, C^{(2)}, D^{(1)}, E^{(2)}$ and $F^{(1)}$. Although this system can be solved analytically with the aid of some mathematical software, the solution for the constants is inconveniently long to be included in a program. In this present paper, this system of equations is solved numerically whenever necessary in the computer code.

4 Vertical vibrations of an embedded rigid disc

Consider the harmonic excitation of a rigid disc of radius a , with zero thickness and no mass, embedded in the interface of two infinite half-spaces as shown in Fig. 1. It is assumed that the disc experiences time-harmonic displacements due to the loads applied. The relationship between unknown tractions and the displacement of the disc can be expressed in terms of the following integral equation:

$$\int_0^a G_{ZZ}(r, \theta, z = 0, \omega) T_Z(r, \theta, z = 0, \omega) dr = U_Z(r, \theta, z = 0, \omega) \quad (28)$$

In Eq. (28), T_Z denotes a jump in tractions in the vertical direction; U_Z denotes the vertical displacements at a point of coordinates (r, θ) at the interface between the two materials ($z = 0$), and G_{ZZ} denote the vertical displacements due to vertical loads of unitary intensity $Pz = 1$ (see Fig. 2). The components G_{ZZ} are obtained from Eq. (??) when the boundary conditions in Eqs. (25) to (27) are considered.

In this work, the coupled equation system expressed by Eq. (28) is solved by discretizing the surface of the disc into M concentric annular disc of inner and outer radiuses s_{1k} and s_{2k} , $k = 1, M$. It is assumed that T_Z is constant within each of these elementary discs.

In the case in which a vertical load is applied uniformly over the surface of the rigid disc, the rigid vertical displacement of each elementary disc k ($k = 1, M$) is the same, Δ_0 . In this case, the discretized version of Eq. (28) becomes:

$$\sum_{k=1}^M G_{ZZ}(r_k, \theta = 0, z = 0, \omega) T_Z(r_k, \theta = 0, z = 0, \omega) dr = \Delta_0 \quad (29)$$

The tractions $T_Z(r_k)$ due to a unitary displacement are obtained from Eq. (29) by making $\Delta_0 = 1$. The total force acting on the surface of the disc corresponding to this case of unitary displacement is obtained by:

$$F(\omega) = \sum_{k=1}^M \pi (s_{2k}^2 - s_{1k}^2) T_Z(r_k, \omega) \quad (30)$$

The vertical dynamic compliance of the system comprising the two infinite half-spaces and the embedded rigid disc is obtained for each frequency as:

$$C_V(\omega) = \Delta_0 a E^{(m)} / F(\omega) \quad (31)$$

In Eq. (31), $E^{(m)}$ is the Young's modulus of one of the two materials ($m = 1, 2$).

5 Numerical results

Pak and Gobert [1] presented an analytical solution for the static vertical compliance (C'_V) of a rigid circular plate buried in an isotropic full-space. Their solution is given by $C'_V = (3 - 4\nu) / [32(1 - \nu)\mu a]$. Table 1 shows the error between their solutions and the ones obtained by the present program, as well as the convergence of the present solution with increasing discretization M . In these results, a homogeneous full-space with $\mu = 1$ and $\nu = 0.25$ is considered.

Table 1: Comparison of results with an analytical solution for the static problem.

M	$C_V(\omega = 0) / C'_V$
5	1.03493353664750
10	1.01678531868697
20	1.00834989295149
35	1.00404587193815
50	1.00227108618090

The next results are presented in terms of the normalized compliance $C_V^* = C_V / C_V(\omega = 0)$. The discretization of $M = 20$ disc is chosen, because it is enough to allow an error of less than 1% with the analytical solution (see Table 1).

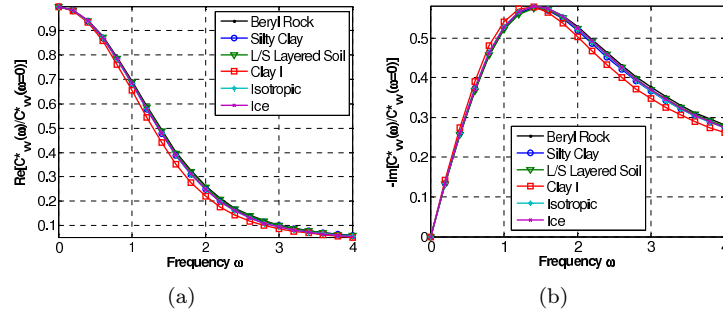


Figure 3: Vertical compliance of the system for different combinations of transversely isotropic bi-material interfaces.

Table 2: Material constants for some isotropic and transversely isotropic materials, with $c'_{ij} = c_{ij}/c_{44}$ [2].

Material	c'_{11}	c'_{12}	c'_{13}	c'_{33}	c_{44} (10^4 MN/m ²)
Beryl Rock	4.13	1.47	1.01	3.62	1.00
Silty Clay	2.11	0.43	0.47	2.58	2.70
Layered Soil	4.46	1.56	1.24	3.26	1.40
Clay	4.70	1.70	1.20	3.30	0.01
Ice (257K)	4.22	2.03	1.62	4.53	0.32
Isotropic ¹	3.00	1.00	1.00	3.00	0.99997

¹ Isotropic material considering $\mu = 1.0$ and $\nu = 0.25$.

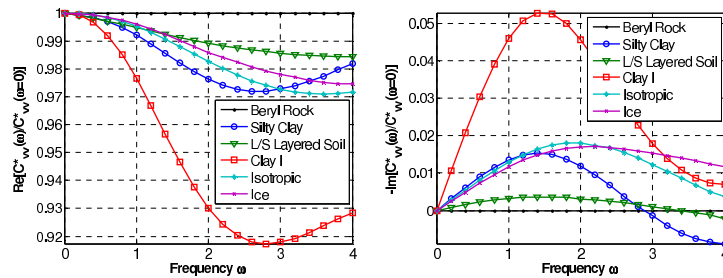


Figure 4: Normalized compliance of the system for different combinations of transversely isotropic bi-material interfaces for the case of vertical load.

Figure 3 shows the compliance of the system for some combinations of two transversely isotropic materials at the interface. In all six cases, the material of the bottom layer, medium (2), is Beryl Rock (see Table 2). The material of the upper layer, medium (1), is chosen from Table 2.

In order to show more clearly the difference between the combinations of materials, the normalized compliance C_V^* in Fig. 3 is also normalized by the homogeneous case, in which both media (1) and (2) are Beryl Rock.

6 Conclusion

A set of influence functions for displacements and stresses of two bonded transversely isotropic half-spaces subjected to time-harmonic circular loads has been introduced. These equations have been presented in terms of semi-infinite integrals which were solved using globally adaptive numerical quadratures. The problem of a circular rigid inclusion in the interface of the two half-spaces was formulated as coupled integral equations containing those influence functions and the displacements of the disc. A system of equations was obtained from these equations by considering the disc to be formed by a number of annular elementary discs. This system is solved for different frequencies, which yields the dynamic compliance function of the rigid circular inclusion under vertical loads. The solutions presented in this paper characterize the response of deeply buried foundations and anchors in bi-material interfaces.

Acknowledgements The research leading to this article has been funded by Capes, CNPq, Fapesp and Faepex/Unicamp. This is gratefully acknowledged.

References

- [1] Pak, R.Y.S. & Gobert, A.T., Forced vertical vibrations of rigid discs with arbitrary embedment. *Journal of Engineering Mechanics*, **117(11)**, pp. 2527–2548, 1991.
- [2] Wang, Y., *Fundamental Solutions for Multi-Layered Transversely Isotropic Elastic Media and Boundary Element Applications*. Ph.D. thesis, 1992.

Analysis and optimization of stepped conical shells with cracks

Jaan Lellep, Ella Puman

Institute of Mathematics, University of Tartu, 2 Liivi str., Tartu 50409 – Estonia

Abstract

Conical shells with stepped thickness loaded by a rigid central boss are studied. The optimization problem is posed in a general form involving several different problems as particular cases.

The necessary optimality conditions are derived by the use of the variational methods of the control theory. The problems regarding to the optimization of stepped conical shells in the case of the material obeying Hill's yield criterion and the associated gradientality law are studied in a greater detail.

Keywords: conical shell, optimization, anisotropic material, Hill's criterion.

1 Introduction

Due to their low weight amalgamated with necessary stiffness, strength and load carrying capacity thin-walled plates and shells are widely used in the mechanical and civil engineering. Conical shells have many applications in the machinery.

Optimization of elastic and inelastic beams, plates and shells have been studied by many researchers. Reviews of papers of this type can be found in the papers by Życzkowski [1], Lellep and Lepik [2] and others. Banichuk [3], Kirsch [4], also Życzkowski [1] concentrated on elastic structures.

Optimal designs of conical shells made of inelastic materials are established by Lellep and Puman [5, 6] whereas spherical caps made of von Mises material are studied by Lellep and Tungal [7].

It is well known that an especially high value of the strength-to-weight ratio is achieved by the use of composite materials which exhibit the orthotropic and anisotropic behaviour. Exploiting the upper bound theorem of limit analysis the anisotropic behaviour of structures was studied by Capsoni, Corradi, Vena [8]; Corradi, Luzzi, Vena [9]; Pan, Seshadri [10].

In the present paper stepped conical shells loaded by the rigid central boss are considered. An optimal design method is developed for conical shells made of non-linear inelastic materials which obey the Hill's yield criterion and the associated gradientality law.

2 Formulation of the problem and basic equations

Let us consider a thin-walled conical shell loaded by the central rigid boss with the loading P (Fig.1). Assume, that the shell is simply supported at the outer edge of radius R whereas the junction between the boss and the shell wall at $r = a$ can be considered as the clamped edge. In this paper shells of sandwich structure will be studied. Let the total thickness and the thickness of the face sheets be H and h , respectively.

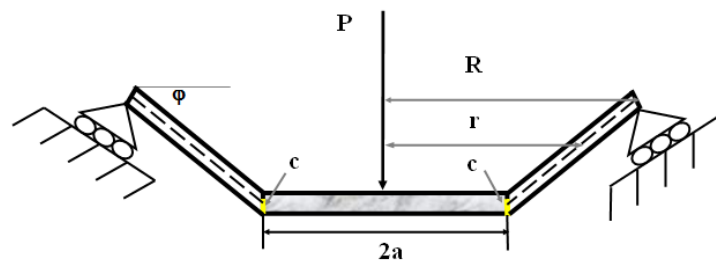


Figure 1: Shell geometry.

It is assumed that the face sheet thickness is piece wise constant, e.g.

$$h = h_j \quad (1)$$

for $r \in (a_j, a_{j+1})$ where $j = 0, \dots, n$. It is reasonable to denote $a_0 = a$, $a_{n+1} = R$. The parameters a_j ($j = 1, \dots, n$) and h_j ($j = 1, \dots, n$) will be treated as preliminarily unknown design parameters.

The aim of the paper is to determine the design parameters so that the given cost function attains its minimum value. In the particular case of minimization of the weight of the shell the cost function can be presented as

$$V = \frac{\pi}{\cos \varphi} \sum_{j=0}^n h_j (a_{j+1}^2 - a_j^2) \quad (2)$$

where φ stands for the angle of inclination of the middle surface. However, we shall consider herein a more general case of the optimization problem which involves a series of particular problems which can be solved from a unique point of view.

The cost function to be minimized will be presented as

$$J = G(a_1, \dots, a_n, h_0, \dots, h_n, W(r_*), U(r_*), M_1(r_*), N_1(r_*)) + \int_a^R F(W, U, N_1, M_1) dr \quad (3)$$

where F and G are given differentiable functions whereas W and U stand for displacements in the two orthogonal directions. Here and henceforth M_1 , M_2 stand for bending moments and N_1 , N_2 for membrane forces in the radial and tangential direction, respectively. The quantity r_* is assumed to be a given value of the current radius $r \in [a, R]$.

If, for instance, $G = W(r_*)$, $F = 0$, then the optimization problem consists in the minimization of the radial deflection at $r = r_*$. If, however, $F = 0$ and $G = V$, then one has the minimum weight problem for a stepped conical shell.

In particular cases the stress strain state of the shell can be constrained by certain constraints. In the present paper we are studying the case when additional constraints are given as isoparametric constraints

$$\int_a^R T_i(a_1, \dots, a_n, h_0, \dots, h_n, W, U, N_1, M_1) dr = A_i \quad (4)$$

where $i = 1, \dots, m$. In (4) T_i stand for given continuous and differentiable functions and A_i ($i = 1, \dots, m$) are fixed constants.

At the outer edge of the shell following boundary conditions must be satisfied

$$U(R) = 0, \quad W(R) = 0, \quad M_1(R) = 0, \quad N_1(R) = 0 \quad (5)$$

When minimizing the cost function (3) one has to take into account additional constraints (4) as well as the governing equations which consist of the equilibrium equations with geometrical and constitutive relations. The constitutive equations can be presented via strain components. In the case of a conical element the strain components have the form (see [5, 11, 12])

$$\begin{aligned} \varepsilon_1 &= \frac{dU}{dr} \cos \varphi, \\ \varepsilon_2 &= \frac{1}{r} (U \cos \varphi + W \sin \varphi), \\ \kappa_1 &= -\frac{d^2W}{dr^2} \cos^2 \varphi, \\ \kappa_2 &= -\frac{1}{r} \frac{dW}{dr} \cos^2 \varphi, \end{aligned} \quad (6)$$

where $\varepsilon_1, \varepsilon_2$ stand for linear extension ratios and κ_1, κ_2 are curvatures of the middle surface of the shell.

In what follows we will treat the shells made of different materials including elastic and inelastic materials. It is well known that in the case of an elastic material the Hooke's law holds good. The latter can be presented as (see Hodge [11], Ventsel and Krauthammer [13])

$$\begin{aligned}
N_1 &= D_{0j} (\varepsilon_1 + \nu\varepsilon_2), \\
N_2 &= D_{0j} (\varepsilon_2 + \nu\varepsilon_1), \\
M_1 &= D_j (\kappa_1 + \nu\kappa_2), \\
M_2 &= D_j (\kappa_2 + \nu\kappa_1)
\end{aligned} \tag{7}$$

for $r \in (a_j, a_{j+1})$, $j = 0, \dots, n$, where ν stands for the Poisson's modulus and

$$D_j = \frac{EH^2h_j}{2(1-\nu^2)}, \quad D_{0j} = \frac{2Eh_j}{1-\nu^2}. \tag{8}$$

Here E denotes the Young modulus.

Note that the relations (7) are obtained for a shell with sandwich cross section according to the formulas

$$\begin{aligned}
N_i &= (\sigma_i^+ + \sigma_i^-) h_j, \\
M_i &= (\sigma_i^+ - \sigma_i^-) h_j \frac{H}{2}
\end{aligned} \tag{9}$$

for each $i = 1, 2$. Here σ_i^+ and σ_i^- stand for the stress σ_i at the upper and lower sheet, respectively. It is assumed herein that the stress component σ_i is constant across the face sheet thickness.

Conical shells loaded beyond the elastic limit are investigated, as well. In this case it is assumed that the shell is fully plastic and the material obeys the Hill's yield criterion which can be presented as [8, 9]

$$\frac{1}{M_{0j}^2} (M_1^2 - \alpha M_1 M_2 + \beta M_2^2) + \frac{1}{N_{0j}^2} (N_1^2 - \alpha N_1 N_2 + \beta N_2^2) - Y_1^2 \leq 0 \tag{10}$$

for the section $r \in (a_j, a_{j+1})$. In (10) the quantities α , β and Y_1 are certain material parameters whereas N_{0j} and M_{0j} stand for the yield force and the yield moment for $r \in (a_j, a_{j+1})$. Evidently, in the case of a sandwich shell

$$M_{0j} = \sigma_0 H h_j, \quad N_{0j} = 2\sigma_0 h_j \tag{11}$$

where σ_0 is the yield stress of the material. It is known from the theory of plasticity that in a plastic region the associated flow law holds good. According to the associated flow law and the Hill's yield criterion (10) one has

$$\begin{aligned}
\dot{\epsilon}_1 &= \frac{\lambda_j}{N_{0j}^2} (2N_1 - \alpha N_2), \\
\dot{\epsilon}_2 &= \frac{\lambda_j}{N_{0j}^2} (2\beta N_2 - \alpha N_1), \\
\dot{\kappa}_1 &= \frac{\lambda_j}{M_{0j}^2} (2M_1 - \alpha M_2), \\
\dot{\kappa}_2 &= \frac{\lambda_j}{M_{0j}^2} (2\beta M_2 - \alpha M_1),
\end{aligned} \tag{12}$$

for $r \in (a_j, a_{j+1})$, $j = 0, \dots, n$. Here λ_j stands for a non-negative scalar multiplier and dots denote the differentiation with respect to time or a time like variable [12, 14]. In the present paper the deformation-type theory of plasticity will be applied. According to this concept the strain rate components in (12) are substituted with strain components themselves. Combining the obtained equations with (6) results in the system of equations

$$\begin{aligned}
\frac{dW}{dr} &= -\frac{\lambda_j r}{\cos^2 \varphi M_{0j}^2} (2\beta M_2 - M_1), \\
\frac{d^2W}{dr^2} &= -\frac{\lambda_j}{\cos^2 \varphi M_{0j}^2} (2M_1 - \alpha M_2), \\
\frac{dU}{dr} &= \frac{\lambda_j}{\cos \varphi N_{0j}^2} (2N_1 - \alpha N_2),
\end{aligned} \tag{13}$$

and

$$\frac{1}{r} (U \cos \varphi + W \sin \varphi) = \frac{\lambda_j}{N_{0j}^2} (2\beta N_2 - \alpha N_1) \tag{14}$$

The equilibrium of a shell element furnishes equations (see Hodge [11])

$$\begin{aligned}
\frac{d}{dr} N_1 &= \frac{1}{r} (N_2 - N_1), \\
\frac{d}{dr} M_1 &= \frac{1}{r} (M_2 - M_1) + \frac{1}{r \cos^2 \varphi} \left(r N_1 \sin \varphi - \frac{P}{2\pi} \right)
\end{aligned} \tag{15}$$

Note that (13) – (15) with the inequality (10) present the system of governing equations for a shell made of an ideal plastic material.

3 Necessary conditions for optimality

Since a lot of attention has been paid in the literature on optimization of elastic plates and shells let us concentrate on inelastic materials. In this case the problem consists in the minimization of the cost function (3) accounting for constraints (4), (13) – (15) and boundary conditions (5).

It is reasonable to rewrite the system (13) as

$$\begin{aligned}\frac{dW}{dr} &= Z, \\ \frac{dZ}{dr} &= \frac{Z(2M_1 - \alpha M_2)}{r(2\beta M_2 - \alpha M_1)}, \\ \frac{dU}{dr} &= -\frac{M_{0j}^2 \cdot Z(2N_1 - \alpha N_2)}{N_{0j}^2 \cdot r(2\beta M_2 - \alpha M_1)}\end{aligned}\quad (16)$$

where Z is an auxiliary variable and

$$\lambda_j = -\frac{\cos^2 \varphi \cdot M_{0j}^2 \cdot Z}{r(2\beta M_2 - \alpha M_1)} \quad (17)$$

Substituting (17) in (14) yields the equation

$$U \cos \varphi + W \sin \varphi + \frac{M_{0j}^2 \cos^2 \varphi}{N_{0j}^2} \cdot \frac{(2\beta N_2 - \alpha N_1) Z}{(2\beta M_2 - \alpha M_1)} = 0 \quad (18)$$

For derivation of necessary conditions of optimality the methods of the theory of optimal control will be used. Equations (15), (16) will be treated as state equations for $r \in (a_j, a_{j+1})$, $j = 0, \dots, n$ whereas variables W , Z , U , N_1 , M_1 are state variables and M_2 , N_2 – controls.

In order to minimize the cost function (3) under constraints (4), (15) – (18) let us introduce the extended (augmented) functional

$$\begin{aligned}
J_* = & G + \int_a^R \left(F + \sum_{i=1}^m \psi_{0i} T_i \right) dr + \sum_{j=0}^n \int_{a_i}^{a_{i+1}} \left\{ \psi_1 \left(\frac{dW}{dr} - Z \right) + \psi_2 \left(\frac{dZ}{dr} - \frac{Z(2M_1 - \alpha M_2)}{r(2\beta M_2 - \alpha M_1)} \right) + \right. \\
& + \psi_3 \left(\frac{dU}{dr} + \frac{M_{0j}^2(2N_1 - \alpha N_2)Z}{N_{0j}^2 r(2\beta M_2 - \alpha M_1)} \right) + \psi_4 \left(\frac{d}{dr} N_1 - \frac{N_2 - N_1}{r} \right) + \\
& + \psi_5 \left(\frac{d}{dr} M_1 - \frac{M_2 - M_1}{r} - \frac{1}{r \cos^2 \varphi} \left(r N_1 \sin \varphi - \frac{P}{2\pi} \right) \right) + \\
& + \nu_j \left(U \cos \varphi + W \sin \varphi + \frac{M_{0j}^2 \cos^2 \varphi Z(2\beta N_2 - \alpha N_1)}{N_{0j}^2(2\beta M_2 - \alpha M_1)} \right) + \\
& \left. + \varphi_j \left\{ \frac{1}{M_{0j}^2} (M_1^2 - \alpha M_1 M_2 + \beta M_2^2) + \frac{1}{N_{0j}^2} (N_1^2 - \alpha N_1 N_2 + \beta N_2^2) - Y_1^2 \right\} \right\} dr
\end{aligned} \tag{19}$$

In (19) ψ_1, \dots, ψ_5 stand for conjugate (adjoint) variables whereas $\nu_j, \lambda_j, (j = 0, \dots, n)$ and $\psi_{0i}, (i = 1, \dots, m)$ are Lagrangian multipliers. It is well known that $\psi_{0i} = \text{const}$ (see Bryson [15], Hull [16]) as multipliers corresponding to isoperimetric constraints must be constant.

When calculating the total variation of the extended functional (19) one has to take into account that

$$\Delta y(a_j \pm 0) = \delta y(a_j \pm 0) + \frac{dy}{dr}(a_j \pm 0) \Delta a_j \tag{20}$$

where Δy and δy stand for the total variation and the ordinary weak variation, respectively, of the variable y . In the case of a Lagrange functional one has (see Lellep, Puman [5, 6], Hull [16], Bryson [15])

$$\Delta \int_a^R F dr = \delta \int_a^R F dr + \sum_{j=1}^n (F(a_j - 0) - F(a_j + 0)) \Delta a_j \tag{21}$$

Calculating the total variation of (19) according to rules (20), (21) and applying the optimality condition $\Delta J_* = 0$ leads to a set of differential and algebraic equations with integral terms. First of all, one obtains the system of adjoint equations

$$\begin{aligned}
\frac{d\psi_1}{dr} &= \frac{\partial F}{\partial W} + \nu_j \sin \varphi + \sum_{i=1}^m \psi_{0i} \frac{\partial T_i}{\partial W}, \\
\frac{d\psi_2}{dr} &= -\frac{\psi_2}{r} \frac{2M_1 - \alpha M_2}{2\beta M_2 - \alpha M_1} + \frac{\psi_3}{r} \frac{M_{0j}^2}{N_{0j}^2} \frac{2N_1 - \alpha N_2}{2\beta M_2 - \alpha M_1} + \frac{\nu_j M_{0j}^2}{N_{0j}^2} \cos^2 \varphi \frac{2\beta N_2 - \alpha N_1}{2\beta M_2 - \alpha M_1}, \\
\frac{d\psi_3}{dr} &= \frac{\partial F}{\partial U} + \nu_j \cos \varphi + \sum_{i=1}^m \psi_{0i} \frac{\partial T_i}{\partial U}, \\
\frac{d\psi_4}{dr} &= \frac{\partial F}{\partial N_1} + \frac{\psi_3}{r} \frac{M_{0j}^2}{N_{0j}^2} \frac{2Z}{2\beta M_2 - \alpha M_1} + \frac{\psi_4}{r} - \frac{\psi_5 \sin \varphi}{\cos^2 \varphi} + \frac{\nu_j M_{0j}^2 \cos^2 \varphi (-\alpha Z)}{N_{0j}^2 (2\beta M_2 - \alpha M_1)} + \\
&\quad + \sum_{i=1}^m \psi_{0i} \frac{\partial T_i}{\partial N_1} + \frac{\varphi_j}{N_{0j}^2} (2N_1 - \alpha N_2), \\
\frac{d\psi_5}{dr} &= \frac{\partial F}{\partial M_1} - \frac{\psi_2}{r} \frac{Z (4\beta - \alpha^2) M_2}{(2\beta M_2 - \alpha M_1)^2} + \frac{\psi_3}{r} \frac{M_{0j}^2}{N_{0j}^2} \frac{Z\alpha (2N_1 - \alpha N_2)}{(2\beta M_2 - \alpha M_1)^2} + \frac{\psi_5}{r} + \\
&\quad + \frac{\nu_j M_{0j}^2 \cos^2 \varphi (2\beta N_2 - \alpha N_1) Z\alpha}{N_{0j}^2 (2\beta M_2 - \alpha M_1)^2} + \sum_{i=1}^m \psi_{0i} \frac{\partial T_i}{\partial M_1} + \frac{\varphi_j}{M_{0j}^2} (2M_1 - \alpha M_2).
\end{aligned} \tag{22}$$

Note that this system (22) holds good for $r \in (a_j, a_{j+1})$, where $j = 0, \dots, n$.

The arbitrariness of increments Δh_j ($j = 0, \dots, n$) in the equation $\Delta J_* = 0$ results in

$$\begin{aligned}
&\frac{\partial G}{\partial h_j} + \int_a^R \sum_{i=1}^m \psi_{0i} \frac{\partial T_i}{\partial h_j} dr + \\
&+ \int_{a_j}^{a_{j+1}} \left\{ -2\varphi_j M_{0j}^{-3} \delta_0 H (M_1^2 - \alpha M_1 M_2 + \beta M_2^2) - \frac{4\delta_0 \varphi_j}{N_{0j}^3} (N_1^2 - \alpha N_1 N_2 + \beta N_2^2) \right\} dr = 0
\end{aligned} \tag{23}$$

for $j = 0, \dots, n$.

For determination of controls M_2, N_2 one obtains the equations

$$\begin{aligned}
&\frac{\psi_2 Z (\alpha^2 - 4\beta) M_1}{r (2\beta M_2 - \alpha M_1)^2} - \frac{\psi_3}{r} \frac{M_{0j}^2}{N_{0j}^2} \frac{2Z\beta (2N_1 - \alpha N_2)}{(2\beta M_2 - \alpha M_1)^2} - \frac{\psi_5}{r} - \\
&- \frac{2\beta M_{0j}^2 \cos^2 \varphi (2\beta N_2 - \alpha N_1) Z}{N_{0j}^2 (2\beta M_2 - \alpha M_1)^2} + \frac{\varphi_j}{M_{0j}^2} (2\beta M_2 - \alpha M_1) = 0, \\
&- \frac{\psi_3}{r} \frac{M_{0j}^2}{N_{0j}^2} \frac{Z\alpha}{(2\beta M_2 - \alpha M_1)} - \frac{\psi_2}{r} + \frac{2\beta M_{0j}^2 \cos^2 \varphi Z \nu_j}{N_{0j}^2 (2\beta M_2 - \alpha M_1)} + \frac{\varphi_j}{N_{0j}^2} (2\beta N_2 - \alpha N_1) = 0.
\end{aligned} \tag{24}$$

Due to the arbitrariness on increments Δa_j ($j = 0, \dots, n$) in the equation $\Delta J_* = 0$ one has

$$\begin{aligned} & \frac{\partial G}{\partial a_j} + \sum_{j=0}^n \int_{a_j}^{a_{j+1}} \left(\frac{\partial F}{\partial a_j} + \sum_{i=1}^m \psi_{0i} \frac{\partial T_i}{\partial a_j} \right) dr - [\psi_1(a_j) Z(a_j)] - \\ & - \left[\frac{\psi_2 Z(a_j) (2M_1(a_j) - \alpha M_2(a_j))}{a_j (2\beta M_2(a_j) - \alpha M_1(a_j))} \right] + \left[\frac{M_{0j}^2 \psi_3(a_j) Z(a_j) (2N_1(a_j) - \alpha N_2(a_j))}{N_{0j}^2 a_j (2\beta M_2(a_j) - \alpha M_1(a_j))} \right] - \\ & - \left[\frac{\psi_4(a_j) N_2(a_j)}{a_j} \right] - \left[\frac{\psi_5(a_j) M_2(a_j)}{a_j} \right] = 0 \end{aligned} \tag{25}$$

for $j = 1, \dots, n$. Here the square brackets denote the finite jumps of corresponding variables at $r = a_j$. For instance, in the case of a variable $y = y(r)$ one has

$$[y(a_j)] = y(a_j + 0) - y(a_j - 0)$$

where $y(a_j + 0)$ and $y(a_j - 0)$ denote the right hand and left hand limits, respectively.

The independence of total variations of state variables $\Delta W(r_*)$, $\Delta U(r_*)$, $\Delta Z(r_*)$, $\Delta N_1(r_*)$, $\Delta M_1(r_*)$ results in the jump conditions of adjoint variables at $r = r_*$

$$\begin{aligned} [\psi_1(r_*)] &= \frac{\partial G}{\partial W(r_*)}, \\ [\psi_2(r_*)] &= 0, \\ [\psi_3(r_*)] &= \frac{\partial G}{\partial U(r_*)}, \\ [\psi_4(r_*)] &= \frac{\partial G}{\partial N_1(r_*)}, \\ [\psi_5(r_*)] &= \frac{\partial G}{\partial M_1(r_*)}. \end{aligned} \tag{26}$$

However, at $r = a_j$ ($j = 1, \dots, n$) one has

$$\psi_i(a_j + 0) = \psi_i(a_j - 0) \tag{27}$$

for $i = 1, \dots, 5$; $j = 1, \dots, n$.

Note that the continuity of adjoint variables (27) takes place, if $r_* \neq a_j$. In the alternative case one has to account for the jump conditions (26) applied at $r = a_j = r_*$.

Note that in the case of an elastic material optimality conditions can be derived in the similar manner with a modified extended functional. In this case the constraints (16) – (18) and (10) must be substituted by (7).

4 Results and discussion

The results of calculations are presented in Fig. 2 – 6 and Table 1. Calculations have been carried out for shells made of carbon steel. It was established by Corradi *et al.* [9] that for AISI-1018 carbon steel the Hill's criterion can be presented as

$$\alpha_{xy} (\sigma_x - \sigma_y)^2 + \alpha_{yz} (\sigma_y - \sigma_z)^2 + \alpha_{zx} (\sigma_z - \sigma_x)^2 + 6\eta_{xy}\tau_{xy}^2 + 6\eta_{yz}\tau_{yz}^2 + 6\eta_{zx}\tau_{zx}^2 \leq \sqrt{2}\sigma_0,$$

where

$$\alpha_{xy} = 1,104, \alpha_{yz} = 0,641, \alpha_{zx} = 1,254, \sigma_0 = 254,112MPa.$$

In Fig. 2 the results obtained for the current shell are compared with those corresponding to the shells made of a von Mises material for $k = 0,3$ in the cases

$h_0 = h_1 = h_*$ and $h_0 = 1,2h_*$, respectively. Note that in the case of a Mises material in (10) $\alpha = -1$, $\beta = Y_1 = 1$.

Here following notations are used

$$\gamma_{0,1} = \frac{h_{0,1}}{h_*}, \quad \alpha_{0,1} = \frac{a_{0,1}}{R}, \quad k = \frac{M_* \cos^2 \varphi}{RN_* \sin \varphi}, \quad p = \frac{PR}{N_* \sin \varphi}$$

where h_* is the thickness of carrying layers for the reference shell of constant thickness and $N_* = 2\delta_0 h_*$; $M_* = \delta_0 H h_*$. Note that in Fig. 2 – 6 p stands for the limit carrying capacity of the shell and $\alpha = a/R$. It is somewhat surprising that in Fig. 2 the curves are quite close to each other.

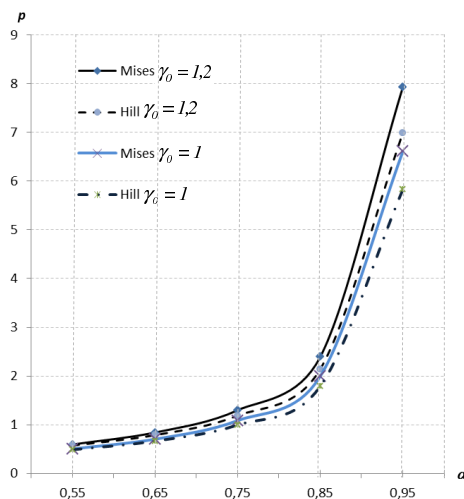


Figure 2: Load carrying capacity for Mises and Hill material.

Table 1: Limit loads for $k = 0,3$.

α_0	c	p_0	p	γ_0	γ_1	α_1	e	
0,55	0	0,4885	0,5107	1,05	0,4252	0,9717	1,0455	
			0,5752	1,2	0,4546	0,9016	1,1776	
			0,6156	1,3	0,4969	0,8599	1,2603	
	0,2	0,4118	0,4350	1,05	0,4252	0,9717	1,0564	
			0,50203	1,2	0,4546	0,9016	1,2191	
			0,54412	1,3	0,4969	0,8599	1,3213	
	0,4	0,3254	0,3508	1,05	0,4252	0,9717	1,0781	
			0,4224	1,2	0,4546	0,9016	1,2980	
			0,4668	1,3	0,4969	0,8599	1,4346	
	0,95	0	5,8268	6,1173	1,05	0,2819	0,9968	1,0498
				6,9869	1,2	0,3992	0,9878	1,1991
				7,5635	1,3	0,4734	0,9821	1,2980
0,2		4,6771	4,9679	1,05	0,2819	0,9968	1,0622	
			5,8387	1,2	0,3992	0,9878	1,2483	
			6,4170	1,3	0,4734	0,9821	1,3720	
0,4		3,5202	3,8114	1,05	0,2819	0,9968	1,0827	
			4,6838	1,2	0,3992	0,9878	1,3305	
			5,2637	1,3	0,4734	0,9821	1,4953	

Optimal values of parameters α_1 , γ_1 for given γ_0 and c are presented in Table 1. Here p_0 stands for the limit load for a shell of constant thickness whereas the coefficient of efficiency $e = p/p_0$. Here the problem of maximization of the limit load for given weight is studied.

In Fig. 3 the limit loads of stepped shells versus $\alpha = a/R$ are presented for different values of the ratio h_0/h_* . Calculations carried out showed that the load carrying capacity of the shell rapidly increases when a_0 tends to R . This result could be expected as the load carrying capacity of a narrow annulus can be very high.

In Fig.4 the limit load of a shell of constant thickness with a surface crack is depicted versus a/R for different values of the crack length c . The crack is a circular stable crack of a constant depth which is located at the position $r = a$.

Calculations implemented for various combinations of geometrical parameters showed that cracks with length $c < 0,1h_1$ have relatively small influence on the limit load. However, if $c > 0,9h_1$ then the load carrying capacity of the shell diminishes drastically.

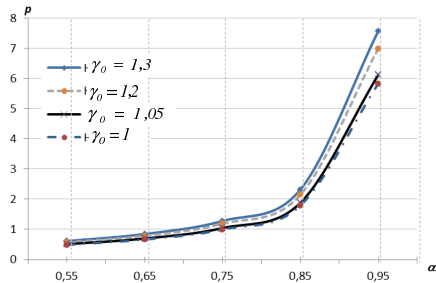


Figure 3: Load carrying capacity for stepped shell.

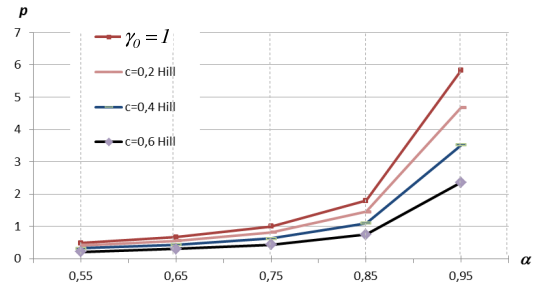


Figure 4: Limit load of a shell with crack.

Fig. 5 and Fig. 6 portray the dependencies of ratios h_1/h_* and a_1/R upon the non-dimensional radius a/R . It can be seen from Fig. 5, 6 that the optimized values of a_1/R are smaller for greater values of the thickness h_0 and h_1/h_* are smaller for greater values of the thickness.

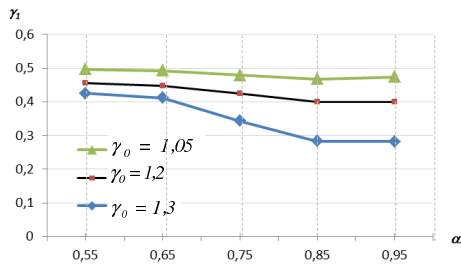


Figure 5: Optimal thickness vrs a/R .

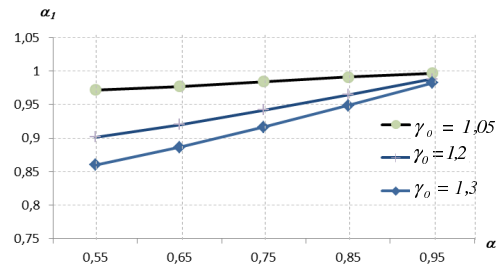


Figure 6: Optimal location of the step.

5 Conclusions

An optimization technique was established for circular conical shells loaded by a rigid central boss. The material of the shells assumed to be elastic or an inelastic one obeying the Hill's yield criterion and the associated gradientity law. Necessary optimality conditions are derived for conical shells with piece wise constant thickness. Calculations showed that the efficiency of the design can be essentially increased even in the case of a single step of the thickness. Making use of a shell with greater number of steps the eventual ascent of the efficiency of the design is more higher.

Acknowledgement The partial support from the Estonian Science Foundation Grant N° 7461 “Optimization of elastic and inelastic shells” and from the target financed project SF0180081s08 “Models of applied mathematics and mechanics” is gratefully acknowledged.

References

- [1] Życzkowski, M., Recent advances in optimal structural design of shells. *European Journal of Mechanics A Solids*, **11**, pp. 5–24, 1992.
- [2] Lellep, J. & Lepik, U., Analytical methods in plastic structural design. *Engineering Optimization*, **7(3)**, pp. 209–239, 1984.
- [3] Banichuk, N., *Introduction to Optimization of Structures*. Springer-Verlag: New York, p. 300, 1990.
- [4] Kirsch, U., *Structural Optimization: Fundamentals and Applications*. Springer: Berlin, 1993.
- [5] Lellep, J. & Puman, E., Optimization of plastic conical shells loaded by a rigid central boss. *International Journal of Solids and Structures*, **37**, pp. 2695–2708, 2000.
- [6] Lellep, J. & Puman, E., Optimization of inelastic conical shells with cracks. *Structural and Multidisciplinary Optimization*, **33**, pp. 189–197, 2007.
- [7] Lellep, J. & Tungal, E., Optimization of plastic spherical shells of mises material. *Structural and Multidisciplinary Optimization*, **30(5)**, pp. 381–387, 2005.
- [8] Capsoni, A., Corradi, L. & Vena, P., Limit analysis of orthotropic structures based on hill’s yield condition. *International Journal of Solids and Structures*, **38**, pp. 3945–3963, 2001.
- [9] Corradi, L., Luzzi, L. & Vena, P., Finite element analysis of anisotropic structures. *Computational Methods of Applied Mechanics and Engineering*, **195**, pp. 5422–5436, 2006.
- [10] Pan, L. & Seshadry, R., Limit analysis for anisotropic solids using variational principle and repeated finite element analysis. *Transactions of the Canadian Society for Mechanical Engineering*, **28(1)**, pp. 89–107, 2004.
- [11] Hodge, P., *Limit Analysis of Rotationally Symmetric Shells*. Prentice Hall: New Jersey, 1963.
- [12] Kaliszky, S., *Plasticity. Theory and Engineering Applications*. Elsevier: Amsterdam, 1989.
- [13] Ventsel, E. & Krauthammer, T., *Thin Plates and Shells. Theory, Analysis and Applications*. Marcel Dekker: New York, 2001.
- [14] Chakrabarty, J., *Theory of Plasticity*. Elsevier, 2006.
- [15] Bryson, A. & Ho, Y.C., *Applied Optimal Control*. Wiley: New York, 1975.
- [16] Hull, D., *Optimal Control Theory for Applications*. Springer: Berlin, 2003.

Simulating occupants injury in rollover crashes

Anderson de Lima

*General Motors of Brasil Ltda., Technological Center
Avenida Goiás, 2769, São Caetano do Sul, 09550-051, SP – Brazil*

Rogério José Marczak

*Mechanical Engineering Department, Federal University of Rio Grande do Sul
Rua Sarmiento Leite 425, Porto Alegre, 90050-170, RS – Brazil*

Abstract

During the last decades, a constant increase in the number of studies involving rollover crashes and injuries associated with it can be observed. The existing experimental standards and procedures to test rollover crashworthiness are still not suitable for direct computer simulation because of the huge computational effort required, and the need of faithful/overly complex representation of the aspects involved in actual crashes. Yet, numerical simulation play a key role in keeping the design cost low and in delivering reliable structural predictions. The objective of the present work is to show the application computational models adapted to simulate three different procedures commonly used to assess vehicle roof strength. The models are compared, and their advantages/disadvantages are discussed. It was found that one of the most used design procedures is not representative of realistic rollover phenomena. Finally, we include finite element models of dummies to simulate the occupants. These models allow retrieving important data concerning the severity of injuries caused during the rollover.

Keywords: crashworthiness, vehicle simulation, rollover crash, roof strength, car safety, occupant injury.

1 Introduction

Nowadays, the automotive engineers and the industry have been challenged to develop safer vehicles, and at the same time to reduce the design cycle time and cost. Physical crash tests are extremely expensive, and therefore computer simulations have been playing a key role in assisting and analyzing new vehicle designs.

Global numbers of manufactured cars are growing year by year; thereafter the number of occupants injured and deaths due to vehicular crashes are increasing proportionally. Vehicular accidents are among major causes of deaths in the country-region United States according to the PlaceNameplace-National PlaceTypeCenter for Health Statistics, 2005. Table 1 shows the rate of deaths per 100,000 standard population, where it can be verified that vehicular accidents have a significant participation.

Among all types of vehicle accidents, rollover crashes are the most complex and least understood. Rollover is defined as a maneuver in which the vehicle rotates 90 degrees or more around its longitudinal axis [1]. Major automotive manufacturers have achieved a high safety level of their vehicles concerning frontal, side, and rear crash situations. Rollovers, however, are still the most passenger threatening crash mode, with a fatality rate second only to frontal crashes [2]. Although 3.3% of all car accidents are characterized as rollover, they are responsible for more than 20% of the total passenger deaths.

Table 1: Causes of deaths per 100.000 U.S. standard population according to the US National Center for Disease Control and Prevention (2005).

Cause of death	2005	2004
Diseases of heart	210.3	217.0
Malignant neoplasms	183.8	185.8
Brain vascular diseases	46.6	50.0
Diabetes mellitus	24.5	24.5
Alzheimer's disease	22.9	21.8
<i>Vehicular accidents</i> [NHTSA, 2005]	<i>14.7</i>	<i>14.6</i>
Septicemia	11.2	11.2
Intentional self-harm (suicide)	10.6	10.9
Chronic liver disease and cirrhosis	8.9	9.0
Assault (homicide)	5.9	5.9

During the last decades a steady increase in studies of vehicular accidents and occupants injuries involving rollovers has been observed. There are several studies in the literature showing the effects of the vehicle's roof crushing on the occupants due to rollover. Initial works demonstrated that there were no correlation between roof crushing and the occupant injuries [3]. After reviewing some real cases of rollover crashes, researchers found out that the severity of injury was associated with the intrusion of the roof on the occupant survival space [4].

The roof strength clearly affects the likelihood of head and neck injuries in occupants during rollover incidents [5]. If significant roof crushing is observed in a severe vehicular accident the occupants have greater risk of injury. Even after several published studies on this field during the last two decades, the role of roof crushing and the associated injury caused in vehicle's occupant is still an area of intense research. It is also possible to identify various points of view regarding the mechanisms which cause the injuries and, accordingly, there has been considerable debate about the role of roof deformation in this context. One of the major difficulties in analyzing rollover crashes and designing countermeasures for it is the lack of a widely accepted standard measure of crash severity. The other is obviously the cost and complexity of a reliable numerical model able to capture all intrinsic phenomena associated

to vehicle crashes. Further discussion can be found in the partial reviews of Hoskins and El-Gindy [6], Goldman et al [7], and Herbst et al [8]. Mao et al [9] discuss the recent modifications proposed on FMVSS 216 standard to reflect more accurately the actual crash, as well as its main differences to the inverted drop test from the structural point of view. Bidez et al [10] is a good example of how a scientific work can be used to make more conspicuous bad practices by automotive industry, avoiding acceptance of standards based on subjective or disputable claims.

The objective of the present study is the development of computational models to simulate and compare different standards and procedures used to evaluate the roof resistance with respect to withstand the rollover loads. Weak roofs are responsible for most of the serious injuries in occupants who are not ejected during rollover accidents. The advantages/disadvantages of each approach are discussed. The results of numerical models for two types of vehicles are compared with experimental tests. In a second part, numerical models of dummies included in the FE analysis are used to predict possible injuries caused in the head, neck, thorax and cervical spine. Numerical models of passenger's vehicle and a sport utility vehicle (SUV) are simulated including anthropomorphic dummy to represent the driver. The injury risks and traumas are verified to the driver considering belted and unbelted dummies. The driver's risk of injury when driving a passenger car is also compared with the risks when driving a SUV. The computational methodology developed proved to be efficient for the evaluation of the vehicle's roof structure in rollover events. It is shown that numerical methods can be used to assess the structure of the vehicle and verify the occupants injury risk, reducing the amount of experimental tests to be performed.

2 Standards and procedures

2.1 Roof crush resistance – FMVSS 216 [11]

It is well known US National Highway Traffic Safety Administration standard requires a passenger car roof to withstand a load of 1.5 times its weight or 22.240 N (whichever is the smaller), applied on each side of vehicle's roof, and producing no more than 127 mm of crushing.

The load is applied by a rigid rectangular plate 762 mm by 1829 mm. The direction of the load is 5 degrees from the longitudinal axis, applied at the front header, and 25 degrees from lateral axis, applied at the side roof rails, as shown in Fig.1.

This standard has been criticized for being a static test which does not incorporate the dynamic events related to rollover events, i.e. it actually refers to a quasi-static test [12]. On the other hand, being devoid of highly transient effects imparts a more easily repetitive pattern in multiple tests carried under this standard. The widespread use of FMVSS 216 is, however, possibly more rooted its simplicity and low cost when compared to other tests than its statistical repeatability and simple implementation.

In 2005 the NHTSA proposed an update to FMVSS 216 [9] by extending the gross weight limit of vehicles to be subjected to it, by reducing the amount of roof intrusion allowed, and by increasing the applied force to 2.5 times the weight of the vehicle. This proposal is intrinsically related to the present work because, as it will be shown in section a3, a factor of 2.5 reflects more faithfully the loads

necessary to actually test the roof strength by producing significant roof intrusions. The update has been constantly delayed since then.

2.2 Inverted drop test [13]

The inverted drop test procedure was devised to minimize the occupant injury by assessing the structural integrity of roofs under dynamic loadings similar to those happening in actual rollovers. The most interesting features of this procedure when compared to FMVSS 216 are: (a) the lateral or slip velocity between the vehicle and pavement is taken into account during the testing; (b) the dynamics of the roof crushing and the geometry of the roof are more faithfully considered in the evaluation of occupant's injuries; and (c) it easily allows the realistic use of dummies to help to assess possible injuries in head, neck, backbone and other parts of the occupant's body.

According to this procedure the vehicle is hanged upside down in a 25° roll angle and 5° pitch angle attitude and then dropped (Fig.2). This orientation is the same as the FMVSS 216. The suggested drop heights are 304.8 mm and 457.2 mm.

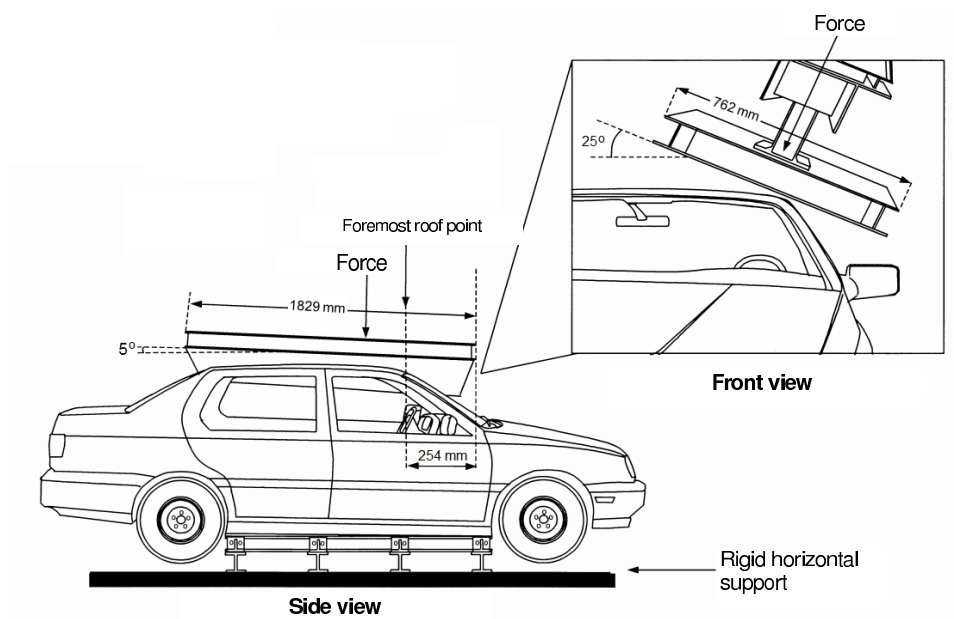


Figure 1: FMVSS 216 test illustration.

2.3 Dolly rollover test / FMVSS 216 [11, 14]

The SAE J2114 rollover test procedure was devised to emulate lateral rollover in laboratory conditions as closely as possible of the actual phenomenon. The test vehicle is placed on a device inclined by 23° to the horizontal plane, hold in position by a 102 mm high flange touching the tires (Fig.3). The distance of the inner corner of the flange and the concrete roll surface is 229 mm.

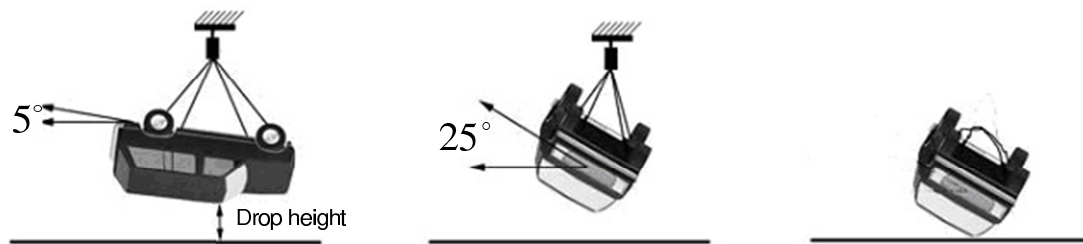


Figure 2: Inverted drop test setup.

The device is accelerated to a constant velocity of 48 km/h, and then halted to full stop within a distance of no more than 914 mm. The test vehicle must not show any significant transverse or rotational movement. The device deceleration cycle must reach at least 20 g during a minimum time of 40 ms.

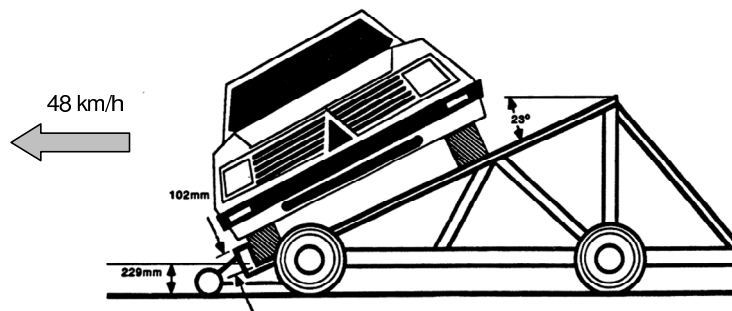


Figure 3: Dolly rollover test setup.

2.4 Some comments about the test procedures

Both the roof crush and the drop test procedures can be used primarily to validate the roof strength. Neither of them are particularly realistic to estimate the physical integrity of the vehicle occupants,

since the dynamics of the vehicle and the occupants as well are not considered during the rollover event. Any estimate of loads and accelerations over the passengers bodies obtained through these tests would be unreliable and, therefore, they cannot be used to analyze or quantify the probability of injuries caused during the rollover. This situation does not contribute to improve the design of new vehicles towards safer products.

Moreover, two opposing views exist in the published literature regarding whether roof crush causes serious injury or whether it is simply associated or correlated with serious injury [10], although NHTSA has already concluded that there is a relationship between roof intrusion and the risk of injury to belted occupants in rollover events [15]. One alternative to study the risk of injury would be the use of dummies in the tests, which curiously is not standardized.

Even though the SAE J2114 procedure does not require the use of dummies during the experimental test they could be included to retrieve further evaluations of the effects on the occupants. The use of dummies would allow the study and of several aspects which play key roles in the severity of the injuries caused to the vehicle occupants. Driver's neck forces produced during the roof crushing, size and position of the dummies, non fastened seat belts, effectiveness of different configurations for air bags, among other aspects, can be better understood if dummies are realistically included in the tests. This idea will be explored later in the present work.

Nonetheless, the SAE J2114 procedure is also extremely complex for numerical simulation and demand huge computational resources in both, the preparation of an accurate structural model and the solution of the nonlinear governing equations as well. In addition, the resulting data must be carefully retrieved from the analysis and interpreted.

These comments explain partially why the automotive industry in most cases has been relying on the roof crush resistance test alone. Not only it is a simple and less expensive test, but also requires far less computational efforts to be simulated when compared with the other two tests, if this is the case.

3 Numerical simulations

Any numerical model to be used in rollover analysis must incorporate two essential capabilities: to produce roof (and other structural parts) crushing and to deliver realistic dynamical behavior. Since the interest in the present work also includes studying injuries of the occupants, finite element models of the dummies belted to their seats will be necessary, too.

All three tests described in section 2 have been modeled in commercial finite element software for two actual vehicles, including the passenger dummies to take into account the inertial contribution of the occupants and verify possible contact between occupants and the vehicle structures. The simulations followed in detail the standards for each test, in order to reproduce as faithfully as possible the conditions of the testing [16], so they will be referred from now on as virtual tests.

3.1 Generalities about the FEA models used

The FEA models refer to two different vehicles. A small passenger car and a SUV. They will be referred as vehicle A and B from now on, but they share the same FE modeling techniques described herein. Besides the intricate details present in numerical models of this type, the computational cost of the analysis is an issue. Not only the CAD drawings were strictly followed, but also one must note that this is a nonlinear analysis, containing plastic behavior of the material as well as large displacements. In addition, the drop test and the dolly rollover test are fully transient dynamic cases.

Additionally, several important details must be considered. For instance, in the dolly rollover test it was observed in experimental tests that, when the dolly is stopped to trigger the take-off of the vehicle, the wheels hit the lower supporting tab of the dolly and break or deform permanently. This effect was included in the analysis by using special finite elements which simulate the breakage of these structural components at a given load magnitude. Features like this had to be modeled and tested at an earlier stage, without the need of the FE mesh of the whole vehicle body. Concentrated mass parameters were used instead. Figure 4 show the permanent deformation on the suspension during the initial moments of the dolly rollover virtual test.

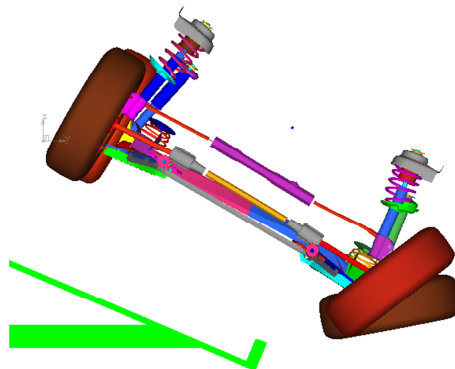


Figure 4: Permanent deformation on the suspension after the vehicle take-off.

None of the tests require the use of dummies. However the vehicles modeled in the present study included belted and unbelted dummies. Dolly rollover simulations, in particular, enable to obtain estimates for accelerations, deflections and loads on the human body. These values can be compared to head [17], neck [16] and thorax [18] injury mechanisms and criteria to further homologate the vehicles design. Table 2 summarizes the FE mesh used for the vehicle, while Fig.4 illustrates the FE model of one of the cars studied, including the dummy employed in the analysis [19]. The dummies were used in both configurations, belted and unbelted, and the windows of the vehicles were disregarded to simulate the vehicle riding with open windows.

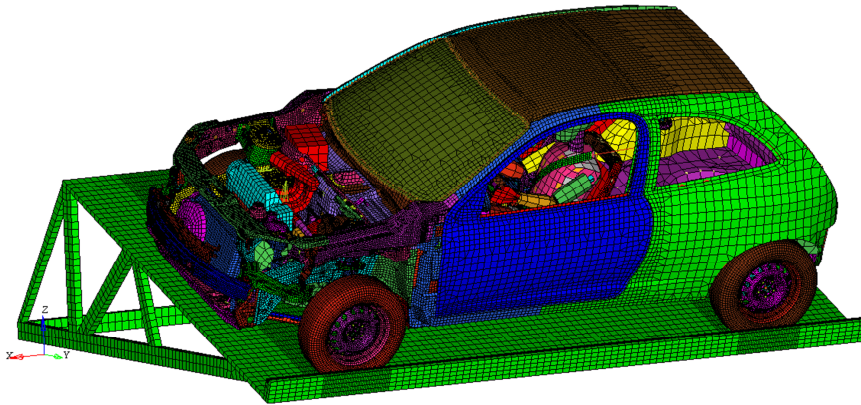


Figure 5: Renderized illustrations of the FE models of the vehicle and the dummy.

Table 2: Elements count in the numerical model of the passenger vehicle (not counting the dolly model).

Description	Number
Subregions	444
Nodes	235351
Mass elements	995
Rigid elements	4175
Discrete elements	415
Joints	32
Beam elements	149
3-noded shell elements	30412
4-noded shell elements	234861
Solid elements	6678

3.2 Numerical results for roof crush resistance test

The roof strength is extremely important to reduce the injury to vehicle occupants during the rollover phenomenon. FMVSS 216 states that the maximum allowed intrusion of the roof is 127 mm, under a load of 1.5 times the weight of the vehicle (the vehicle's mass considered in this work is 991 kg).

Figure 5 shows a displacement vs. normal force plot of roof intrusion of the vehicle. When the window is open, it is evident that the maximum roof displacement is much lower than the allowable value. It is worth to note that the suggested load of 1.5 times the weight of the vehicle seems to be too small for a realistic analysis.

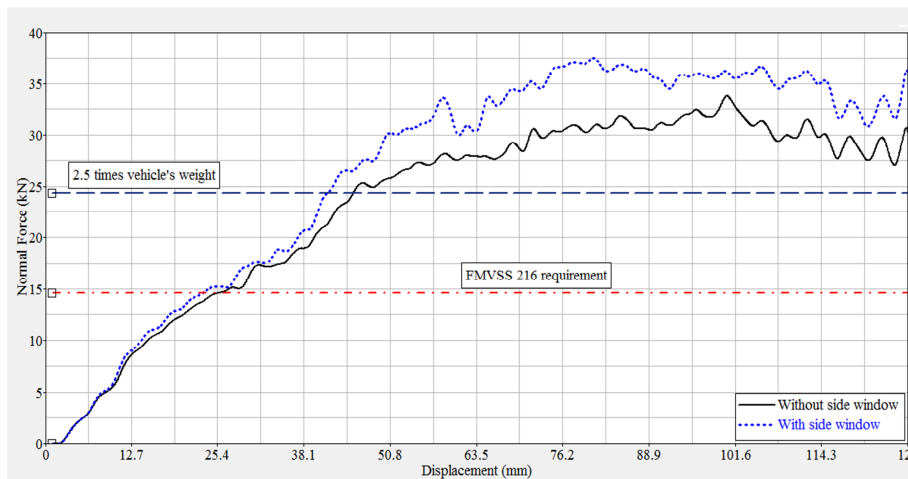


Figure 6: Results of normal force vs. roof displacement for the FMVSS 216 virtual test. The upper dashed line shows a more realistic strength requirement proposition.

According to the simulation results, the side windows are responsible by an increase of roughly 10% in the resistance of the roof [16], provided the windows do not fail. As it will be shown in section 3.3, the dynamic loads found in the drop test indicate a value of approximately 2,2 times the vehicle’s weight, much greater than the value proposed by the FMVSS 216 standard. Therefore, two reference loads are compared in Fig.5: 1.5 and 2.5 times the vehicle’s weight. The maximum allowed roof crush is not reached in none of them, though. Figure 6 shows the deformed configuration at the end of the virtual test.

3.3 Numerical results for the inverted drop test

Examples of numerical results for this test are shown in Figs.7 and 8. Figure 7 presents the force vs. time plots obtained in the simulations for both drop heights. The normal contact force peak between vehicle and the ground during the inverted drop test is 2.0 and 2.9 times the FMVSS 216 requirement, for 304.8 mm and 457.2 mm drop heights, respectively. As one can expect, this test is more severe than the FMVSS 216 test, and obviously take into account the dynamic effects more realistically, since the test vehicle actually falls on the ground.

Considering that the driver remain in the same relative position to the seat during the inverted

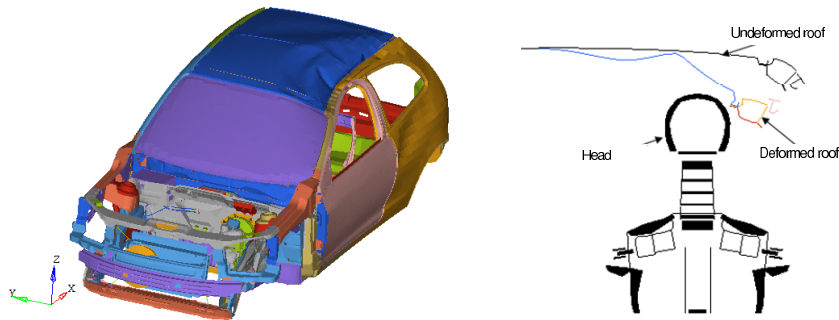


Figure 7: Deformed configuration after the 127 mm roof crushing.

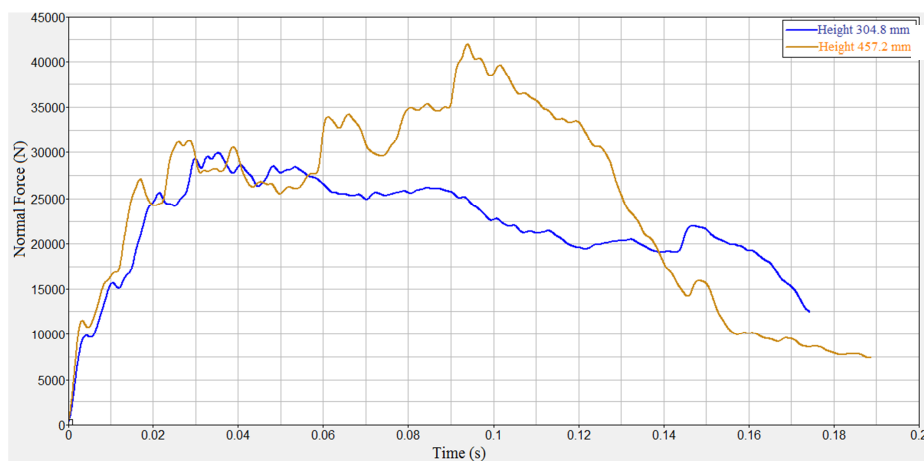


Figure 8: Numerical results of normal force vs. time for the SAE J996 test simulations.

drop test, the head would strike the roof 0.045s after the contact between roof and ground, for the 304.8 mm drop height. Figure 8 shows a detail view of the finite element mesh of the driver's head at about the contact vehicle-ground instant.

Because the dynamic effects, the region of the roof just above the driver's head (dummy) shows larger deformation in the inverted drop test (SAE J996) than in the roof crush test (FMVSS 216). This is expected, since besides the inertia effects, the latter does not allow rotation of the vehicle once it comes in contact to the ground, i.e., the orientation of the contact area in the roof crush test remains unchanged during the test.

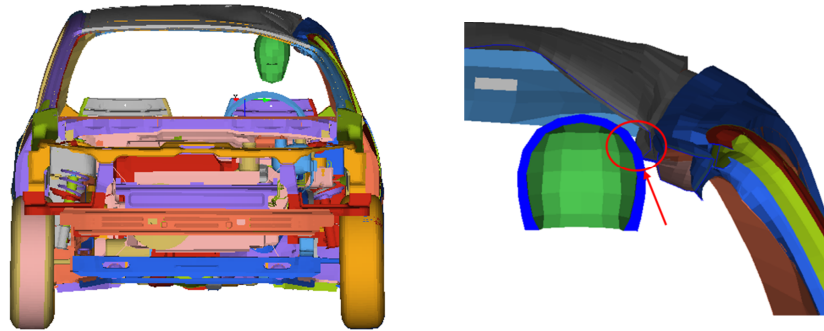


Figure 9: Detail view of the roof rail/dummy head contact during the inverted drop test (304.8 mm drop height) finite element simulation.

3.4 Numerical results for the dolly rollover test

The objective of this simulation was to reproduce numerically the rollover test. The finite element model used for one of the vehicles is shown in the Fig. 4. Obviously, the dolly rollover test simulation demanded much more computational effort and time than the previous ones. Besides the inherent greater complexity of the numerical model, it was found that it is required at least 1500 ms of simulation to capture all relevant events of the test, resulting in a huge computational cost.

An important aspect in simulations of this magnitude is the difficulty in calibrating/updating the FE models. Cost of sensitivity analysis in these cases is still prohibitively high, and experimental modal data are virtually useless here. However, if experimental data from actual tests are available, they can be used to minimally assess the confidence in the FE model. Two examples used in the present analysis is the time when the vehicle first touched the ground, and direct comparison with movie stills of the actual crash tests. Figure 9 shows the instant of tire-ground first contact, and they agree well with the laboratory data. Similar ideas can be used in other types of vehicle to verify FE models. It is very unlikely the specific data like this agree with experimental values when the numerical models are not faithful to the actual phenomenon. Figure 9 shows images of the first contact between the tire and the ground (375 ms) as well as the first contact between the roof and ground (530 ms). Although the number of complete rolls during the rollover event is an important parameter, in ninety percent of the cases the car do not exceed a complete turn [5]. During the present study it was found that one the tests which better estimate the number of complete turns of the vehicle is actually the J2114, as recommended by the Society of Automotive Engineers [14].

The graph in Fig.11 shows the contact force history obtained during the simulation. The peak contact force between the roof and the ground obtained is 22,000 N. This value is approximately 2.2 times the weight of the vehicle. This is an important aspect found during this work, since it differs

considerably from the 1.5 factor specified by FMVSS 216.

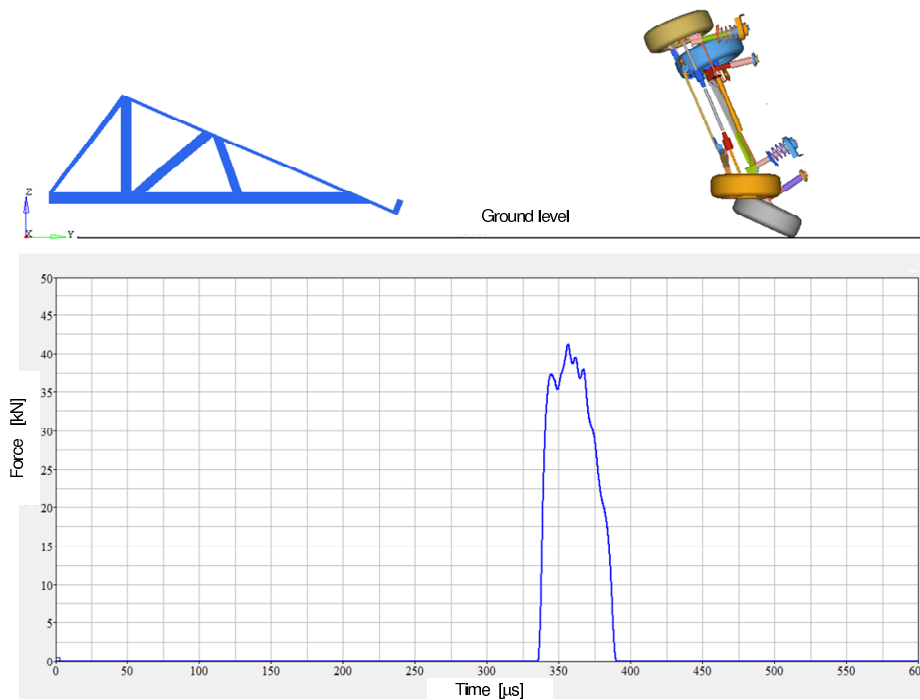


Figure 10: Retrieving the exact first contact time through force vs. time graphs.

Figure 12 shows the FE model used in the full rollover simulation of the SUV, while fig.13 compares the results of the virtual test with stills of movies made from actual vehicles tested experimentally. The agreement is surprisingly good, considering the complexity of both the FE model and analysis type.

Although highly expensive, the simulation of SAE J2114 procedure represents more faithfully the full size phenomenon, and incorporates more accurately the dynamic effects that occur during a rollover accident. Therefore, as one of the main conclusions of the present study, it is suggested that the FMVSS 216 standard cannot prevent or minimize the trauma and injuries in the vehicle occupants. Evidently conclusive claims will depend on of the actual conditions of the rollover, but the significant discrepancy found between the load factors of both methodologies, and the more faithful simulation of the SAE J2114 point out in favor of the SAE standard.

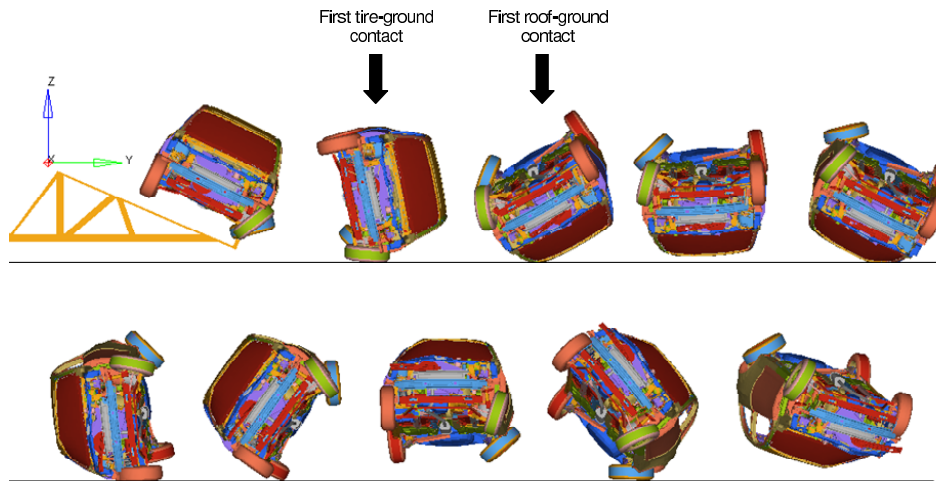


Figure 11: Images of the first contact between of the tire with the ground (375 ms) and the first contact of the roof with the ground (530 ms). SAE J2114 full vehicle simulation.

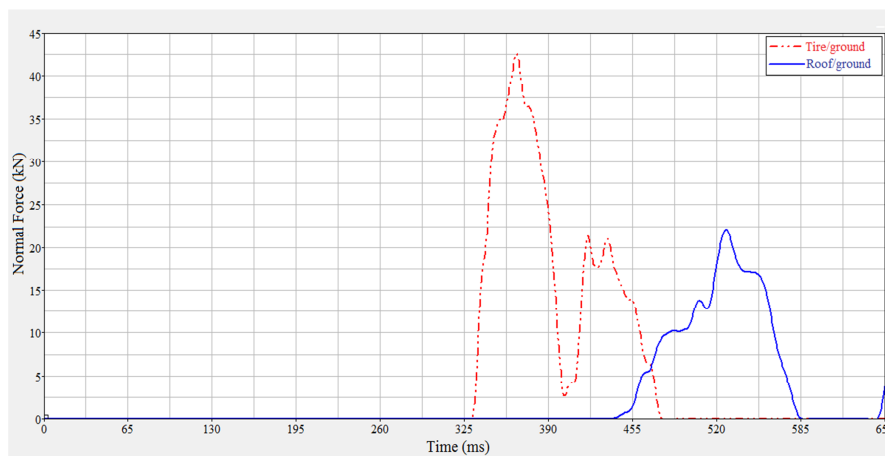


Figure 12: Normal contact force for tire/ground and roof/ground. SAE J2114 full vehicle simulation.

3.5 Estimating injuries using numerical models

Even though the SAE J2114 procedure also does not require the use of dummies, the present study advises to do so, at least in numerical simulations, since it provides an interesting way to verify directly integrity of the vehicle occupants. Furthermore, numerical models for dummies are available, and they

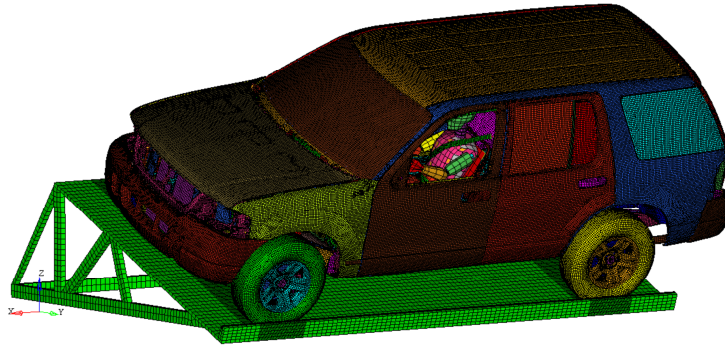


Figure 13: Finite element model of the SUV used in the SAE J2114 full vehicle simulation.

can be used to estimate the loads applied on occupants during the crash, helping to approve design changes.

Once the computational model was proved to be reliable, different accident situations can be simulated. While the first two tests can be used to assert the roof design strength, they are of little use to simulate the consequences of a rollover on the vehicle occupants. The present section will show some examples of data that can be retrieved to estimate the severity of the injuries caused during a rollover using the full vehicle simulation.

Hughes *et al.* showed that 85% of the rollover crashes involves only one roll or less. Due to the occupant dive toward the roof and the roof crush, as shown in Fig.14, the dummy's neck is submitted to a lateral moment. This occurs after the dummy's head strikes the roof and causes an increase in the neck load.

Table 3 shows the parameter values used to determine the injury criteria and to evaluate the probability of serious injury in drivers, using the results retrieved from the full vehicle simulation.

These values can change due to size, posture and position of the dummy. The significance of the initial cervical spine position at the time of axial impact loadings was studied by Hodgson and Thomas [21] in their cadaver impact tests for various neck and thorax positions and also for differing directions of loading. Of the varying positions of load application, axial loading at the vertex with the cervical spine neutral demonstrated the highest vertebral body strains, in comparison to more anterior force application positions.

According to the computational simulation results the belt occupant does not suffer injury, as shown in Table 4. However if the occupant does not use seat belt there is 21,8% probability that a serious injury on the neck will occur, consequently the occupant can have a injury in the cervical spine. If an occupant does not use seat belt during a rollover the probability a serious injury will occur is 3 times higher.

Moffatt [3] set forth the theory that occupant injury in rollovers was the result of diving into the roof rather than from the consequences of roof collapse or buckling. Subsequently other investigators have shown that these conclusions had been manipulated. Other crashworthiness experts state that

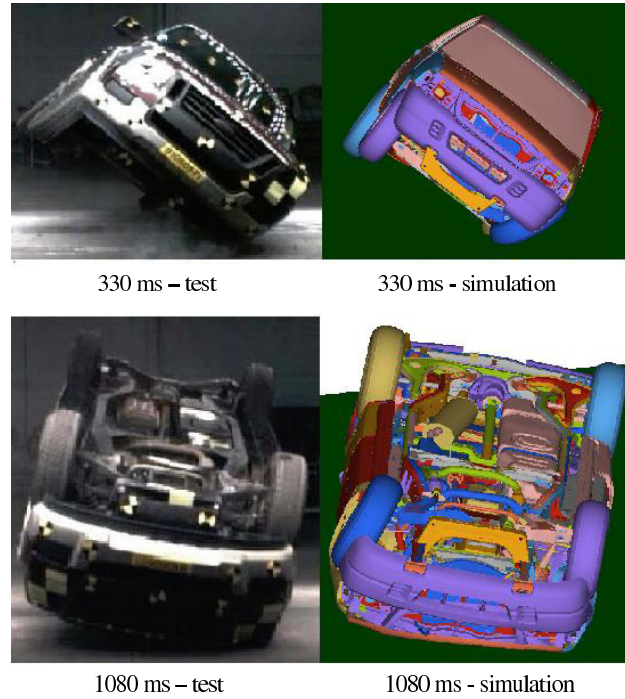


Figure 14: Comparison between experimental test movie stills [20] and the present computational model.

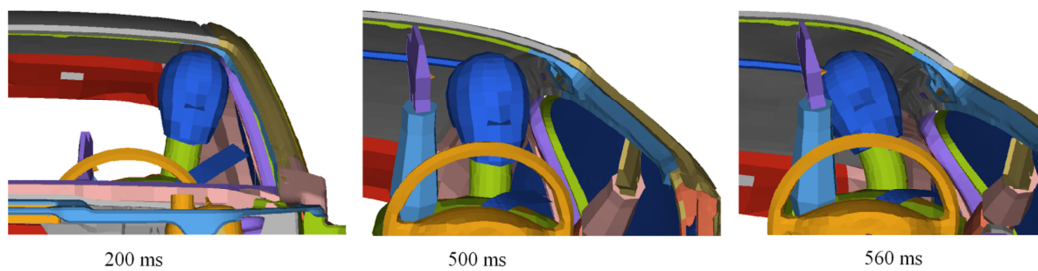


Figure 15: Head position up to first contact roof/ground.

roof crush is linked to fatal and serious head and neck injuries resulting from rollover crashes [4, 5].

Then, in order to investigate the influence or not of the roof crush in the increase of injuries and fractures of the neck, a passenger car with roof smaller resistance was simulated. Loads obtained

Table 3: Peak values considering belted and unbelted dummy.

	Peak values		Tolerable Values	Coefficient: Belted / Unbelted
	Dummy belted	Dummy unbelted		
Head Acceleration (g's)	45,6	62,6	80	1,373
HIC	33,9	75,8	700	2,236
Neck axial load (N)	-396,6	-1362,6	3300 ^(t) / 4000 ^(c)	3,436
Longitudinal moment (Nm)	88,8	238,9	57 ^(e) / 190 ^(f)	2,690
Lateral moment (Nm)	-111,2	-120,4	-	1,083
Neck shear load (N)	-223,8	939,9	3100	-4,200
Thorax acceleration (g's)	14,0	14,4	60	1,029
Thorax deflection (mm)	-5,2	-1,3	76	0,250

(^t): tension, (^c): compression, (^e): extension, (^f): flexion

Table 4: Injury AIS3 level probability for different body regions.

Region	Parameter	Probability of AIS3	
		Belted dummy	Unbelted dummy
Head	HIC	0,0082	0,249
Neck	N_{ij}	7,3	21,8
	A_{max}	9,4	9,6
Thorax	D_{max}	3,0	2,5
	CTI	0,2	0,1

through the neck of the dummy compared the results with the original model, without changing the structure of the roof, and found that the resistance of the roof, especially the side of the roof structure has great influence on the compression of the neck of the occupant. The comparison was between the original model of passenger car and a model with roof and side structure with reduced thickness as shown in Figure 15. Reducing the roof strength causes a high increase of the neck load, hence the conclusion is that the rigidity of the roof has a large influence on the probability of occurrence of injuries in the neck and consequently in the cervical spine.

Two examples of data retrieved from the virtual tests are the neck compression force and lateral neck bending. Figure 16 shows the compression force during the complete rollover. A peak force of 1913 N, being in accordance to the experimental limits of 958-1962 N [10].

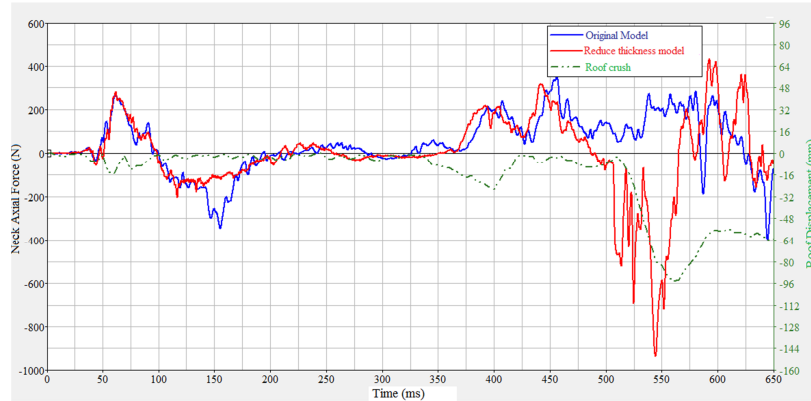


Figure 16: Influence of the roof resistance in the neck force.

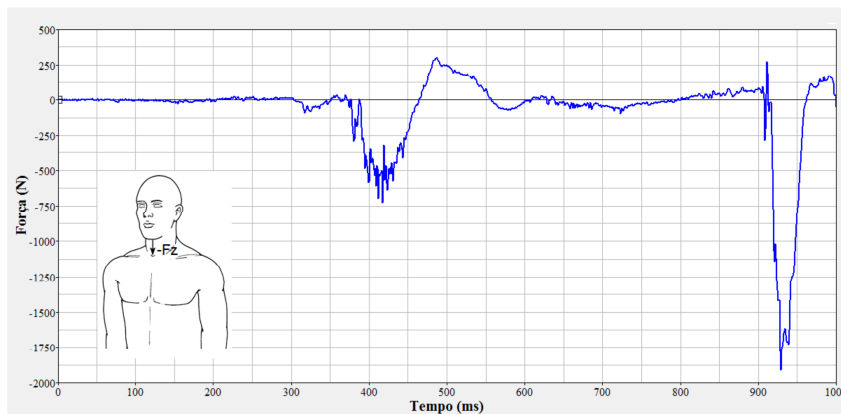


Figure 17: Dummy neck compression force during a complete rollover virtual test.

Bending forces are illustrated on Fig.17, showing a maximum value of 123,3 Nm. This value occurs when the wheel touches the ground and the dummy head is projected against the door window. Values registred by Bidez et al. [10] are in the 106-167 Nm range.

4 Conclusions

The main conclusions of the present study can be summarized as follows:

1. Regarding the FMVSS 216: This standard is not representative of the actual phenomenon. Besides the application of a quasi-static loading, it does not reproduce the real conditions of

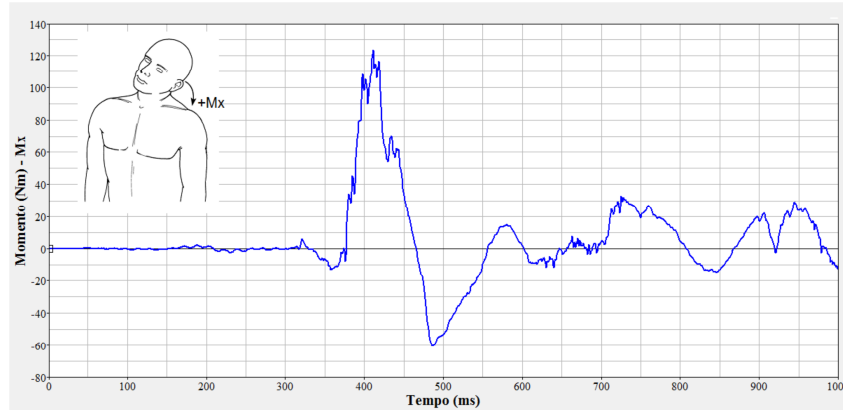


Figure 18: Dummy neck lateral bending moment during a complete rollover virtual test.

rollover. The 1.5 load factor was found to be much lower than the necessary for an accurate verification. In addition, the relative movement of the occupant is not taken into account. Even though a vehicle being approved in the FMVSS 216 requirement may not prevent occupant injuries.

2. Regarding the SAE J996: The inverted drop can be used to provide a better evaluation the roof strength. The computational simulations showed that the load factor in may vary between 2.0 or 2.9 times the vehicle's weight in order to preserve the survival space of the occupant. Although the dynamic effects of this test are present, it does not consider the lateral movement of a rollover. If used with the 457.2 mm drop height, it may be regarded as a conservative design procedure.
3. Regarding the SAE J2114: Among the three standards studied in this work, this is the one which more faithfully reproduces the actual conditions of a rollover. If dummies are included in the test, the SAE J2114 procedure allows the reproduction of secondary impacts (dummy movement) and therefore provides an attractive methodology determine the probability of occupant's injuries. According to the results of numerical simulations, the roof must withstand a minimum load of 2.2 times the vehicle's weight. Given the level of detail considered in these simulations, such load factor has the highest level of confidence among the standards tested here.

The SAE J2114 procedure proved to be extremely complex and demanding huge computational efforts. One should realize that the high costs are not only associated to the complexity of the vehicle structure, but mostly to the solution of nonlinear equations of the problem, which requires extremely high computational resources and well trained analysts.

As for the risk of injury, neither the roof crush resistance test nor the inverted drop test accurately reproduces the real dynamics of occupant and vehicle during rollover crashes. This work is yet another one suggesting that the load factor used in quasi-static tests such as FMVSS 216 must be increased. Although all the three standards studied can find use to estimate the roof strength, only the SAE J996

and the SAE J2114 should be used to estimate the probability and severity of occupant's injuries, although the search for a fully repeatable and accurate dynamic rollover test to be used for a new safety regulation is ongoing [6].

Our results showed, among other things, that roof crush combined with the dive of the dummy towards the roof cause neck axial load during the rollover test. This axial neck load can cause serious injuries. Current standards do not ensure occupants involved in a rollover will be safe because this kind of effect is not considered. The present study suggests the incorporation of dummies to the numerical models as an aid to predict the occupants' injury mechanisms and their severity. Results show that the belt occupant does not suffer injury, however if the occupant does not use seat belt there is a 21,8% probability of a serious injury on the neck will occur, consequently the occupant can have a injury in the cervical spine. During the first complete roll of the vehicle if a driver does not use seat belt the probability a serious injury will occur is 3 times higher than using seat belt. The roof crush has a great influence in the axial neck load.

Acknowledgements The authors would like to thank General Motors of Brazil for the support during this work.

References

- [1] Gillespie, T.D., Fundamentals of vehicle dynamics. Technical report, SAE, Warrendale, 1992.
- [2] Henty, M., El-Gindy, M. & Kulakowski, B., Physical and virtual rollover crash tests: Literature review, technical report. *Int Journal of Heavy Vehicle Systems*, **9(4)**, pp. 366–379, 2002.
- [3] Moffatt, E.A., Occupant motion in rollover collisions. *Proceedings of the 19th Conference of American Association for Automotive Medicine*, 1975.
- [4] Grzebieta, R., Young, D., Bambach, M. & McIntosh, A., Rollover crashes: Diving versus roof crush. *20th International Technical Conference on the Enhanced Safety of Vehicles (ESV)*, Lyon, France, 2007.
- [5] Friedman, D. & Nash, C.E., Advanced roof design for rollover protection. *17th International Technical Conference on the Enhance Safety of Vehicles*, Amsterdam, The Netherlands, 2001.
- [6] Hoskins, M.H. & El-Gindy, M., Virtual rollover tests. *Int J Heavy Veh Syst*, **13**, pp. 107–124, 2006.
- [7] Goldman, R., El-Gindy, M. & Kulakowski, B., Rollover dynamics of road vehicles: Literature survey, heavy vehicle systems. *Int J of Vehicle Design*, **8(2)**, pp. 103–141, 2001. (special series).
- [8] Herbst, B., Forrest, S., Orton, T., Meyer, S., Sances Jr., A. & Kumaresan, S., The effect of roof strength on reducing occupant injury in rollovers. *Biomedical Sciences Instrumentation*, **41**, pp. 97–103, 2005.
- [9] Mao, M., Chirwa, E. & Wang, W., Assessment of vehicle roof crush test protocols using FE models: Inverted drop tests versus updated FMVSS No.216. *Int J of Crashworthiness*, **1(1)**, pp. 49–63, 2006.
- [10] Bidez, M., Cochran Jr., J., King, D. & Burke III, D., Occupant dynamics in rollover crashes: Influence of roof deformation and seat belt performance on probable spinal column injury. *Annals of Biomedical Engineering*, **1(11)**, pp. 1973–1988, 2007.
- [11] NHTSA, Federal motor vehicle safety standards: Roof crush resistance. Technical Report FMVSS 571.216. Standard No. 216, National Highway Traffic Safety Administration, US Department of Transportation, Washington, DC, 2005.
- [12] Grzebieta, R., Young, D., McIntosh, A., Bambach, M., Fréchède, B., Tan, G. & Achilles, T., Rollover crashworthiness: the final frontier for vehicle passive safety. *Proc. Australasian Road Safety Research*

- Policing and Education Conference*, Melbourne, Australia, 2007.
- [13] SAE J996, Inverted vehicle drop test procedure. Technical report, Society of Automotive Engineers, 1967.
 - [14] SAE J2114, Dolly rollover recommended test procedure, surface vehicle recommended practice j2114. Technical report, Society of Automotive Engineers, 1999.
 - [15] Forrest, S., Pedder, D., Meyer, S. & Herbst, B., Inverted drop testing as a mechanism to evaluate rollover occupant injury potential. *Biomedical Sciences Instrumentation*, **43**, pp. 34–39, 2007.
 - [16] Lima, A., *Numerical Simulation of Vehicular Rollover – Comparison of Standards and Evaluation of Driver's Injury Risk*. Master's thesis, Mechanical Engineering Dept., Federal University of Rio Grande do Sul, Brazil, 2009. (in Portuguese).
 - [17] Lissner, H., Lebow, M. & Evans, F., Experimental studies on the relation between acceleration and intracranial pressure changes in man. *Surgery, Gynecology, and Obstetrics*, **III**, pp. 329–338, 1960.
 - [18] Neathery, R. et al., Prediction of thoracic injury from dummy responses. *Proceedings of the Nineteenth Stapp Car Crash Conference*, pp. 295 – 316, 1975. SAE Paper No. 751151.
 - [19] Livermore Software Technology Corp., <http://www.lstc.com/>.
 - [20] Chou, C., Hu, J., Yang, K. & King, A., A method for determining the vehicle-to-ground contact load during laboratory – based rollover tests. *2008 World Congress*, Society of Automotive Engineers: Detroit, Michigan, 2008.
 - [21] Hodgson, V.R. & Thomas, L.M., Mechanisms of cervical spine injury during impact to the protected head. Technical Report Paper # 801300, SAE, 1980.

Reliability-based design optimization strategies based on form: a review

Rafael H. Lopez

*Department of Physics, Universidade Tecnológica Federal do Paraná
80230-901 Curitiba, PR – Brazil*

André T. Beck

*Department of Structural Engineering, São Carlos School of Engineering,
University of São Paulo
13566-590 São Carlos, SP – Brazil*

Abstract

In deterministic optimization, the uncertainties of the structural system (i.e. dimension, model, material, loads, etc) are not explicitly taken into account. Hence, resulting optimal solutions may lead to reduced reliability levels. The objective of reliability based design optimization (RBDO) is to optimize structures guaranteeing that a minimum level of reliability, chosen *a priori* by the designer, is maintained. Since reliability analysis using the First Order Reliability Method (FORM) is an optimization procedure itself, RBDO (in its classical version) is a double-loop strategy: the reliability analysis (inner loop) and the structural optimization (outer loop). The coupling of these two loops leads to very high computational costs. To reduce the computational burden of RBDO based on FORM, several authors decoupled the structural optimization and the reliability analysis. These procedures may be divided in two groups: (i) serial single loop methods and, (ii) uni-level methods. The basic idea of serial single loop methods is to decouple the two loops and solve them sequentially, until some convergence criterion is achieved. On the other hand, uni-level methods employ different strategies to obtain a single loop of optimization to solve the RBDO problem. This paper presents a review of such RBDO strategies. A comparison of the performance (computational cost) of the main strategies is presented for a structure modeled using the finite element method.

Keywords: RBDO, structural reliability, structural optimization.

1 Introduction

In deterministic design optimization, the uncertainties of the structural system (i.e. dimensions, models, materials, loads, etc) are taken into account in a subjective and indirect way, by means of partial safety factors specified in design codes. As a consequence, deterministic optimal solutions may lead to reduced reliability levels [1]. Reliability Based Design Optimization (RBDO) has emerged as an

alternative to properly model the safety-under-uncertainty aspect of the optimization problem. With RBDO, one can ensure that a minimum (and measurable) level of safety, chosen *a priori* by the designer, is maintained by the optimum structure.

The RBDO problem may be stated as:

$$\begin{aligned} & \text{Minimize: } J(\mathbf{x}, \mathbf{B}) \\ & \text{subject to: } P_{f_i} = P(G_i(\mathbf{x}, \mathbf{B}) < 0) \leq P_{f_i}^{allowable} \quad i = 1 \dots n_c \end{aligned}$$

where $\mathbf{x} \in \mathcal{R}^n$ is the design vector (e.g. structural dimensions), $\mathbf{B} \in \mathcal{R}^m$ is comprised by all the random variables of the system under analysis (e.g. random loads, uncertain structural parameters), J is the objective function to be minimized (e.g. the structural weight, volume or manufacturing cost), P_{f_i} is the probability of failure of i^{th} constraint (G_i), and $P_{f_i}^{allowable}$ is the allowable (maximum) failure probability for the i^{th} constraint. Although the objective function is generally a random variable, it is usual to consider it a deterministic value by calculating it using only the mean values of the random variables \mathbf{B} . Hence, from now on, the objective function is written as $J(\mathbf{x})$. The reader is referred to Mínguez and Castillo [2] and references there in for problems dealing with probabilistic quantities in the objective function.

The failure probability P_{f_i} for each constraint may be obtained by evaluating the integral in Eq.(1), which is the fundamental expression of the structural reliability assessment:

$$P_{f_i} = \int_{G_i(\mathbf{x}, \mathbf{B}) < 0} f_B(\mathbf{B}) d\mathbf{B} \quad (1)$$

where $f_B(\mathbf{B})$ is the joint probability density function (PDF) of the random vector \mathbf{B} . In practice, it is impossible to obtain the joint PDF because of scarcity of joint observations for a high number of random variables. At best, what is known are the marginal probability distributions of each random variable and possibly correlations between pairs of random variables. Another difficulty in solving Eq. (1) is the fact that the limit state equation, G_i , is sometimes given in implicit form, as the response of finite element models, for example. Such difficulties have motivated the development of various approximate reliability methods.

Intensive research has been carried out to provide methods to approximate this integral. These methods may be divided into three major classes: (i) simulation methods; (ii) numerical integration and (iii) analytical methods [3]. For a detailed review on these methods, the reader is referred to Lee and Chen [4] and Melchers [5].

- i. Simulations methods using sampling and estimation are well known in the literature, the most widely used being the Direct Monte Carlo simulation (MCS) method [6]. The main drawback of MCS is that it requires a huge amount of calculations. Several derivations of the MCS have been developed to reduce the computational effort, such as the quasi-MCS [7], the directional simulation [8] and the importance sampling [9]. In practice, MCS is considered the *reference* response and is used to validate the results of other, approximate methods.

- ii. The multi-dimensional integral to determine the probabilistic characteristics of random output is evaluated numerically [10–12]. Numerical integration is limited, in practice, to dimension 5 or 6.
- iii. The main approaches of this class are the First and Second Order Reliability Methods (FORM and SORM, respectively). FORM and SORM are said to be transformation methods, because the integral in Eq. (1) is not solved in the original space (B), but is mapped to the Standard Gaussian space. In this space, the Most Probable Point of failure (MPP) is also the point, from all points in the failure domain, closest to the origin. The reliability index β [13], which is a measure of the reliability, can be evaluated as the distance between the MPP point and the origin, in the transformed Standard Gaussian space. The main advantage of FORM-based approaches is their computational cost, which is a fraction of the cost of Monte Carlo simulation, for instance.

Hence, FORM based approaches have been widely employed to evaluate Eq.(1) in RBDO problems. As will be detailed in Section 2, these approaches are optimization problems themselves and consequently, the RBDO using FORM is a double-loop strategy:

- the inner loop is the reliability analysis,
- the outer loop the structural optimization,

i.e. the two optimizations are coupled. Such coupling of optimization loops: structural optimization and reliability assessment – leads to very high computational costs. To reduce the computational burden of RBDO, several papers decoupled the structural optimization and the reliability analysis. Techniques for de-coupling the optimization loops may be divided in two groups: (i) serial single loop methods and, (ii) unilevel methods.

This paper presents a review of RBDO methods based on FORM. First, the two main FORM based approaches, Reliability Index Approach (RIA) and Performance Measure Approach (PMA), are described and compared. Then, a review on decoupling methodologies is presented, and two decoupling methodologies are described in detail. A comparison of the performance (computational cost) of the main strategies is presented for one practical problem.

It should be noted that the review presented herein does not intend to cover all the papers published on the subject, but to present the main techniques, in order to serve as a guide to those entering this exciting and challenging subject.

2 FORM based approaches

This section briefly details the approximation of Eq.(1) using RIA and PMA, then presents a review of the comparison between these two approaches. The interested reader is referred to Madsen et al. [14], Melchers [5] and Haldar and Mahadevan [15] for more details on the RIA, and to Tu et al. [16] for a full description of the PMA.

2.1 The iso-probabilistic transformation

In order to approximate the integral in Eq.(1), it is usual to introduce a vector of normalized and statistically independent random variables $\mathbf{U} \in \mathfrak{R}^m$ and a transformation T (Fig.1), so that $\mathbf{U} =$

$T(\mathbf{B})$. The most common transformations are the Rosenblatt and the Nataf ones [5, 17]. The mapping T transforms every realization \mathbf{b} of \mathbf{B} in the physical space into a realization \mathbf{u} in the normalized space. Note that it also holds for the constraints:

$$G_i(\mathbf{x}, \mathbf{B}) = G_i(\mathbf{x}, T^{-1}(\mathbf{x}, \mathbf{U})) = g_i(\mathbf{x}, \mathbf{U}), \quad (2)$$

where g_i is the i^{th} constraint in the normalized space.

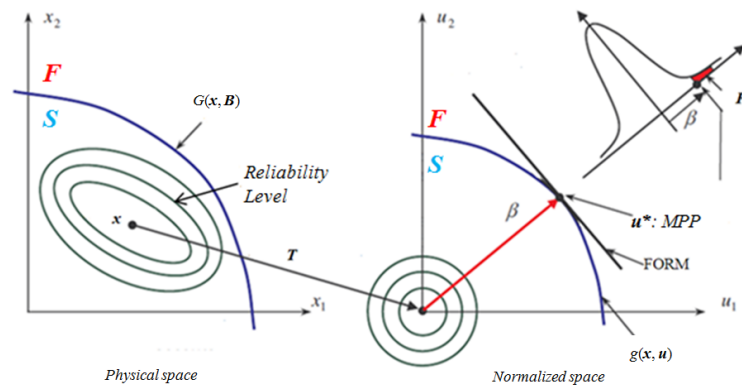


Figure 1: Transformation T and the FORM.

The main advantage in the use of this transformation is that the probability distribution on the resulting space depends only on its norm. This fact is illustrated in Fig.1 by the circular reliability levels of the normalized space. It must be highlighted that this transformation is the first approximation proposed to solve Eq.(1): it only is exact when \mathbf{B} is comprised by independent Gaussian random variables. However, even with this simplification, it is still not an easy task to evaluate Eq.(1). The FORM approximation is used to simplify this evaluation.

2.2 RIA and PMA

The main idea of the FORM is simple: it consists in replacing the limit state function G_i by a tangent hyper-plane at the most probable point of failure (MPP). Figures 1 and 2 illustrate the approximation made by this hyper-plane. The FORM approximates the probability of failure and the allowable failure probability for the i^{th} constraint by:

$$P_{f_i} \approx \Phi(-\beta_i) \quad \text{and} \quad P_{f_i}^{\text{allowable}} \approx \Phi(-\beta_i^{\text{target}}), \quad (3)$$

where Φ is the standard Gaussian cumulative distribution function (CDF) and β_i^{target} is the target reliability index of the i^{th} constraint. This is the second approximation proposed to solve Eq.(1) and it only provides an exact result when the constraint is linear.

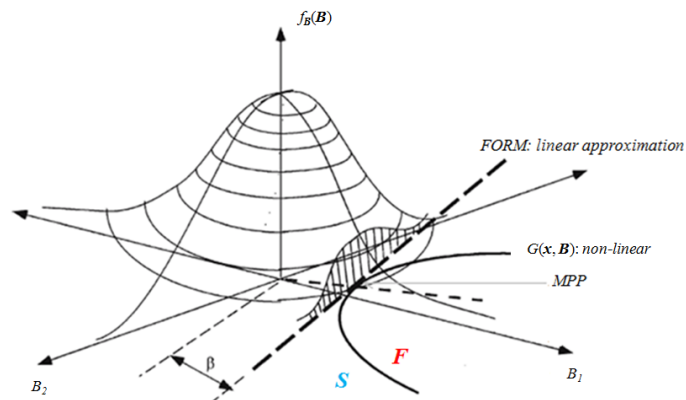


Figure 2: Illustration of the FORM approximation.

Now, recall that in order to evaluate β_i , one first needs to obtain the MPP: the point in the failure domain closest to the origin of the normalized space. The difference between the RIA and the PMA is the manner in which the MPP is calculated. The following optimization problems detail this difference:

RIA	PMA
for a given design \mathbf{x}	for a given design \mathbf{x}
find $\mathbf{u}_{RIA_i}^*$ which	find $\mathbf{u}_{PMA_i}^*$ which
minimizes: $\ \mathbf{u}\ = \beta_i$	minimizes: $g_i(\mathbf{x}, \mathbf{u})$
subject to: $g_i(\mathbf{x}, \mathbf{u}) = 0$	subject to: $\ \mathbf{u}\ = \beta_i^{\text{target}}$

The optimal solution $\mathbf{u}_{RIA_i}^*$ of the RIA yields the reliability index $\beta_i = \|\mathbf{u}_{RIA_i}^*\|$ of the i^{th} constraint on the current design \mathbf{x} . On the other hand, the optimal solution $\mathbf{u}_{PMA_i}^*$ of the PMA is the minimum performance target point (MPTP) on the target reliability sphere (defined by $\|\mathbf{u}\| = \beta_i^{\text{target}}$) and it provides the so-called performance measure $p_{m_i} = g_i(\mathbf{x}, \mathbf{u}_{PMA_i}^*)$ of the i^{th} constraint on the current design \mathbf{x} . The performance measure p_{m_i} is related to the reliability index β_i by the following relation:

$$p_{m_i} = F_{G_i}^{-1}(\Phi(-\beta_i)) \quad (4)$$

where F_{G_i} is CDF of the i^{th} constraint. It is important to note that $\mathbf{u}_{RIA_i}^*$ and $\mathbf{u}_{PMA_i}^*$ will be equal only when the reliability constraint is active, e.g., at the final design of a RBDO problem. At any other point, $\mathbf{u}_{PMA_i}^*$ only represents the point of minimal performance on the target reliability sphere.

2.3 RIA versus PMA

In the paper that introduced the PMA, Tu et al. [16] showed that PMA is inherently robust and yields a higher overall RBDO rate of convergence when compared to the RIA. Youn et al. [18], although reaching the same conclusions, showed that the PMA is far more effective when the probabilistic

constraint is either very feasible or very infeasible. In a different paper, Youn and Choi [19] concluded that the PMA is quite attractive when compared to other probabilistic approaches in RBDO, such as the RIA and the approximate moment approach [20].

The first main difference between the RIA and the PMA is the type of optimization problem which is solved in each case. It is easier to minimize a complicated function subject to a simple constraint (PMA) than to minimize a simple function subject to a complicated constraint (RIA). Different from the RIA, in the PMA only the direction vector needs to be determined by taking advantage of the spherical equality constraint $\|\mathbf{u}\| = \beta_i^{\text{target}}$ to find the MPP \mathbf{u}_{PMA}^* .

Still regarding the type of optimization problem, the conceptual iteration history during the search facilitates the PMA. Usually, the RIA search requires several iterations to reach the failure surface given by $g_i(\mathbf{x}, \mathbf{u}) = 0$, while the PMA search immediately lies on the $\|\mathbf{u}\| = \beta_i^{\text{target}}$ sphere; in other words, the number of iterations of RIA increases with the reliability index while the PMA search is independent of the target performance [20]. A second consequence is that, in the case of non-activated constraints, the PMA becomes even more effective.

Regarding non-linearities in the RBDO problem (i.e. use of non-normal random variables), Youn and Choi [21] showed that PMA is more stable, efficient and has a lower dependence on the distribution of the random variables, since it introduces small non-linearities in the space-transformations. PMA can thus handle a variety of distributions without significantly increasing the number of function evaluations. Furthermore, RIA diverged when uniform or Gumble random variables were employed. The former divergence was due to the fundamental nature of the uniform distribution and the latter was due to numerical difficulties when dealing either with a nonlinear failure surface or with a failure surface away from the design point.

3 Coupled method: the classical approach

As the reliability analysis is an optimisation procedure by itself, RBDO, in its classical version, is a double-loop strategy: the inner loop is the reliability analysis and the outer loop is the structural optimisation. Thus, the two optimisation loops are coupled:

for $k = 1, 2, \dots$

1) structural optimization

$$\begin{aligned} \text{minimize: } & J(\mathbf{x}^{(k)}) \\ \text{subject to: } & \beta_i(\mathbf{x}^{(k-1)}) + \left(\nabla_x \beta_i(\mathbf{x}^{(k-1)})\right)^T (\mathbf{x}^{(k)} - \mathbf{x}^{(k-1)}) \leq 0 \text{ (RIA),} \\ & p_{m_i}(\mathbf{x}^{(k-1)}) + \left(\nabla_x p_{m_i}(\mathbf{x}^{(k-1)})\right)^T (\mathbf{x}^{(k)} - \mathbf{x}^{(k-1)}) \leq 0 \text{ (PMA),} \\ & i = 1 \dots n_c, \\ & \mathbf{x}_l \leq \mathbf{x}^{(k)} \leq \mathbf{x}_u \end{aligned}$$

where, at each step k , the reliability analysis routine is called:

2) Reliability analysis: given current design $\mathbf{x}^{(k-1)}$

RIA	PMA
find $\mathbf{u}_{RIA_i}^{*(k-1)}$ which	find $\mathbf{u}_{PMA_i}^{*(k-1)}$ which
minimizes: $\ \mathbf{u}\ = \beta_i$	$g_i(\mathbf{x}^{(k-1)}, \mathbf{u})$
subject to: $g_i(\mathbf{x}^{(k-1)}, \mathbf{u}) = 0$	$\ \mathbf{u}\ = \beta_i^{target}$

and, at the end of each reliability analysis, a sensitivity analysis of the design variables with respect to the reliability index is pursued to obtain $\nabla_x \beta_i(\mathbf{x}^{(k-1)})$. This procedure is repeated until some convergence criterion is achieved and, of course, it leads to very high computational costs. A review of techniques developed to de-couple the RBDO problem, in order to reduce the computational burden, is presented in the next section.

4 Decoupling strategies

De-coupling the two optimization problems means not to have to call the reliability analysis routine at every step k of the structural optimization. In the sequel, the serial single loop and unilevel de-coupling methods are reviewed.

4.1 Serial single loop methods

The basic idea of the serial single loop methods is to decouple the structural optimization (outer loop) and the reliability optimization (inner loop). Each method of single-loop decoupling employs a specific strategy to decouple the loops and then solves them sequentially until some convergence criterion is achieved. Among these methods, the following may be cited: Traditional Approximation method [22], Single Loop Single Variable (SLSV) [23], Sequential Optimisation and Reliability Assessment (SORA) [24] and Safety Factor Approach (SFA) [25].

Yang and Gu [26] compared these four single-loop decoupling RBDO methods. Four different examples were solved including a vehicle side impact and a multidisciplinary optimization problem. According to their results, SLSV was the most effective method, converging nicely and requiring the fewest number of function evaluations. The other methods also showed promising results when compared to the classical approach. In a second paper [27], the authors investigated an engineering problem with a large number of constraints (144) and with many local minima. In addition to the four single-loop decoupling RBDO strategies, the Mean Value Method [28] was also studied. Results showed that the number of function evaluations depends on the RBDO method, optimization algorithm and implementation. Furthermore, algorithms with good active-constraint handling tended to perform better (e.g. SORA/SFA). Moreover, SORA/SFA and TAM have advantages over the other methods, as the target reliability is obtained at the end. Regarding the local minima, different methods and different starting points yielded different final results, since only local optimizers were used by the authors.

4.2 Unilevel methods

The central idea of unilevel methods is to replace the reliability analysis by some optimality criteria on the optimum (i.e. imposing it as a constraint in the outer loop). Thus, there is a concurrent convergence of the design optimization and reliability calculation or, in other words, they are sought simultaneously and independently.

Kuschel and Rackwitz [29] formulated a unilevel method based on replacing the inner loop of the classical approach (FORM analysis using RIA) by the first order Karush-Kuhn-Tucker (KKT) optimality conditions of the first-order reliability problem. In other words, the KKT optimality conditions of the RIA search are imposed as constraints in the outer loop of the RBDO. As already commented, the RIA may be ill-conditioned when the probability of failure given by a constraint is zero and it is not computationally efficient when the reliability index is large. With this in mind, Agarwal et al. [30] proposed a unilevel RBDO method which introduced the first order KKT necessary optimality conditions of PMA as constraints in the outer loop, eliminating the costly reliability analysis (inner loop) of RBDO.

Cheng et al. [31] proposed a unilevel strategy based on the sequential approximate programming (SAP) concept which was successfully applied in structural optimization. In the SAP approach, the original optimization problem is decomposed into a sequence of sub-optimization problems. Each sub-optimization problem consists of an approximate objective function subjected to a set of approximate constraint functions. A SAP strategy for RBDO using the PMA to approximate the reliability constraints was also developed [32, 33].

Studies comparing the different unilevel methods have not been found in the literature. Yi and Cheng [33] compared the SAP based on RIA and SAP based on PMA with SORA and SLSV methods. Several examples, including the 144 constraint problem, were solved. Based on the results, the authors concluded that SAP based on PMA achieved better results than the other methods. This result does not imply that SAP-PMA is the most effective method in all cases; but it is, at least, one of the most powerful algorithms in RBDO. As a general review of de-coupling approaches has been presented, one method of each approach is described in detail in the sequence in order to highlight the differences of each class of de-coupling schemes.

4.3 Sequential Optimization and Reliability Assessment (SORA)

The SORA [24] method is based on the strategy of serial single loops decoupling the structural optimization and the reliability analysis. At each iteration of the method, the reliability analysis is only conducted after the structural optimization. SORA makes use of three main artifices to increase the algorithm's performance:

- (i) reliability is evaluated only at the desired level: it means that SORA is based on the PMA having all the advantages when compared to RIA-based methods;
- (ii) Using an efficient and robust MPTP search algorithm [34];
- (iii) Employing sequential cycles of optimization and reliability.

The key concept of the method is to shift the boundaries of the violated equivalent deterministic constraints to the feasible direction based on the reliability information obtained in the previous cycle,

which makes the reliability constraints improve progressively and the cost of the search for the MPP be reduced.

Figure 3 shows an example of the SORA boundary shifting procedure. The equivalent deterministic constraint at iteration k and the probabilistic constraint that has to be fulfilled are represented in Figure 3. Based on the percentile information obtained through the reliability analysis, the shifting value s is found and the equivalent deterministic constraint is shifted towards the probabilistic constraint (dashed line). The reliability constraint is fulfilled when s is equal to zero, in other words, when the dashed line coincides with the probabilistic constraint.

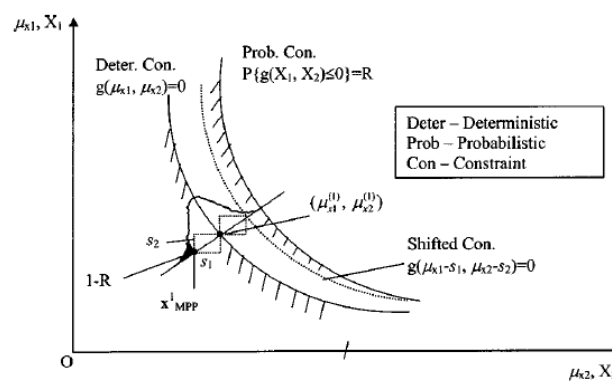


Figure 3: Shifting the boundaries of the violated deterministic constraints in SORA [24].

Thus, the RBDO-SORA works in the following manner:

for $k = 1, 2, \dots$

1) **Deterministic optimization:**

$$\begin{aligned} &\text{minimize: } J(\mathbf{x}^{(k)}) \\ &\text{subject to: } g_i(\mathbf{x}^{(k)}, \mathbf{u}_i - \mathbf{s}_i^{(k-1)}) = 0, \quad i = 1 \dots n_c \\ &\quad \mathbf{x}_1 \leq \mathbf{x}^{(k)} \leq \mathbf{x}_u \end{aligned}$$

where, at the end of each deterministic optimization k , the PMA routine is called:

2) **PMA:** given current optimal design $\mathbf{x}^{(k)*}$ find $\mathbf{u}_{PMA_i}^{*(k)}$ which

$$\begin{aligned} &\text{minimizes: } g_i(\mathbf{x}^{(k)*}, \mathbf{u}) \\ &\text{subject to: } \|\mathbf{u}\| = \beta_i^{target} \end{aligned}$$

and with the information provided by the MPTP, the shifting vector \mathbf{s} is updated. Notice that the optimization loops are no longer coupled, i.e., an entire deterministic optimization is performed and then, the reliability analysis routine is called. This procedure is repeated until some convergence criterion is achieved. Hence, the optimization problems are performed sequentially and by this reason the name of this class of de-coupling methods is *serial single loop methods*.

4.4 Sequential Approximate Programming (SAP)

Cheng et al. [31] proposed a strategy based on the sequential approximate programming (SAP) concept that was successfully applied in structural optimization. In the SAP approach, the original optimization problem is decomposed into a sequence of sub-optimization problems. Each sub-optimization problem consists of an approximate objective function subjected to a set of approximate constraint functions. Thus, the SAP method makes use of an approximation of the reliability constraint, where a linear Taylor approximation of the approximate reliability index is used instead of the accurate one, reducing the computational effort by eliminating the need for the reliability analysis. Such approximate reliability index and its sensitivity are determined from a recurrence formula that is derived from the optimality conditions of the PMA and end up being the iterative formula of the Advanced Mean Value (AMV) method [35]. The SAP-PMA problem is, then:

for $k = 1, 2, \dots$

$$\begin{aligned} & \text{minimize: } J(\mathbf{x}^{(k)}) \\ & \text{subject to: } \hat{p}_{m_i}(\mathbf{x}^{(k-1)*}) + \left(\nabla_{\mathbf{x}} \hat{p}_{m_i}(\mathbf{x}^{(k-1)*}) \right)^T (\mathbf{x}^{(k)} - \mathbf{x}^{(k-1)*}) \leq 0, \quad i = 1 \dots n_c \\ & \quad \mathbf{x}_l \leq \mathbf{x}_i^{(k)} \leq \mathbf{x} \leq \mathbf{x}_u^{(k)} \leq \mathbf{x}_u \end{aligned}$$

where k is the sub-optimization problem number, $\hat{p}_{m_i}(\mathbf{x}^{(k-1)*})$ is the approximate performance measure of the optimal design $\mathbf{x}^{(k-1)*}$ of the previous sub-optimization problem, $\mathbf{x}_l^{(k)}$ and $\mathbf{x}_u^{(k)}$ are the lower and upper bounds of $\mathbf{x}^{(k)}$, respectively. Notice that at the end of each sub-optimization problem k , the reliability analysis routine is **not** called. Instead, the approximate performance measure and the approximate MPTP of the i^{th} constraint are just updated by the following relations:

$$\begin{aligned} \mathbf{u}_i^{(k)} &= \frac{\nabla_{\mathbf{u}} g_i(\mathbf{x}^{(k)*}, \mathbf{u}_i^{(k-1)})}{\left\| \nabla_{\mathbf{u}} g_i(\mathbf{x}^{(k)*}, \mathbf{u}_i^{(k-1)}) \right\|} \\ \hat{p}_{m_i}(\mathbf{x}^{(k)*}) &= g_i(\mathbf{x}^{(k)*}, \mathbf{u}_i^{(k)}). \end{aligned} \quad (7)$$

It should be noted that, at the end of this process, the optimal solution of the original problem is found and that there is a concurrent convergence of the design optimization and reliability calculation; in other words, they are sought simultaneously and independently. It is this fact that gives name to this class of de-coupling methods: *unilevel methods*.

4.5 Further comments

Some aspects should be stressed based on papers cited in this section:

- (i) the observation that a given method's effectiveness depends on several factors suggests that different RBDO strategies may be better for different problems, and this, in turn, indicates that more benchmark studies need to be performed in order to identify which RBDO strategy is best for each type of problem (e.g., type of objective function and constraints);
- (ii) this dependence also indicates that more robust methods (e.g. those less sensible to variance of parameters) should be preferable;
- (iii) the presence of many local minima, which is normal in complex engineering problems, indicates the need of using global optimization algorithms in the solution of RBDO problems [36].

Recently, a benchmark study on several RBDO methods based on FORM was presented by Aoues and Chateaneuf [37], comparing the performance and robustness of these methods. In the next section, the classical approaches based on RIA and PMA, as well as the SORA and the SAP-PMA, are compared in the RBDO of a structure modeled using the finite element method.

5 Numerical analysis

The case of a 2D square plate with a quarter of circle retired from a corner (Figure 4), modelled using finite elements, is considered. The plate is made of steel with Young modulus $E = 200\text{GPa}$ and yield stress $\sigma_Y = 200\text{MPa}$. The plate is clamped at its lower boundary and loaded at its left boundary with a distributed load, with total magnitude of 800N. Uncertainties are considered on the plate thickness and on the radius, which are modelled as random variables: $H \sim \Gamma(h, s_h)$ and $R \sim \Gamma(r, s_r)$, respectively (where Γ and S_i are the probability distribution and the standard deviation of the random variable). These random variables are grouped into the random vector $\mathbf{B} = [H \ R]$.

Design variables of the optimization problem are the mean values h and r , which are grouped into the design vector $\mathbf{x} = [h \ r]$. The plate is optimized in order to minimize its volume under the constraint remaining in the elastic domain, hence the maximum stress must remain below the yield limit:

$$G(\mathbf{x}, \mathbf{B}) = 1 - \frac{\sigma_{MAX}(\mathbf{x}, \mathbf{B})}{\sigma_Y}, \quad (8)$$

where σ_{MAX} is the maximum stress on the structure. Thus, the RBDO problem may be stated as:

$$\begin{aligned} \text{Minimize: } & J(\mathbf{x}) = \left(l^2 - \frac{\pi \cdot r^2}{4} \right) \cdot h \\ \text{subject to: } & P_f = P \left(G(\mathbf{x}, \mathbf{B}) = 1 - \frac{\sigma_{MAX}}{\sigma_Y} < 0 \right) \leq P_f^{allowable} \\ & 1\text{mm} \leq h \\ & 20\text{mm} \leq r \leq 60\text{mm} \end{aligned}$$

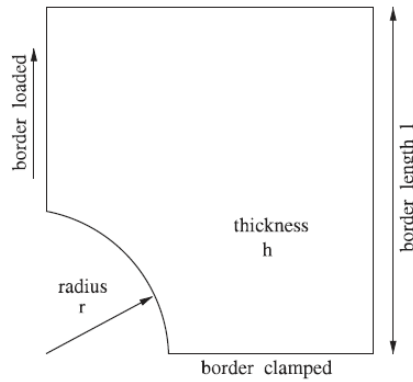


Figure 4: Square plate with a quarter of circle retired from a corner.

Notice that deterministic bounds were imposed on the design variables.

Two distributions are tested in this example: normal and lognormal. For both cases, the standard deviations are $s_h = 0.1\text{mm}$ and $s_r = 4.0\text{mm}$. The length of the plate's border is fixed to $l = 1\text{m}$. A convergence study lead to a mesh with 1352 elements and 1458 nodes. Stresses are evaluated on Gauss integration points. The normal stress in the s -direction is used for the evaluation of the limit state function G (Figure 5).

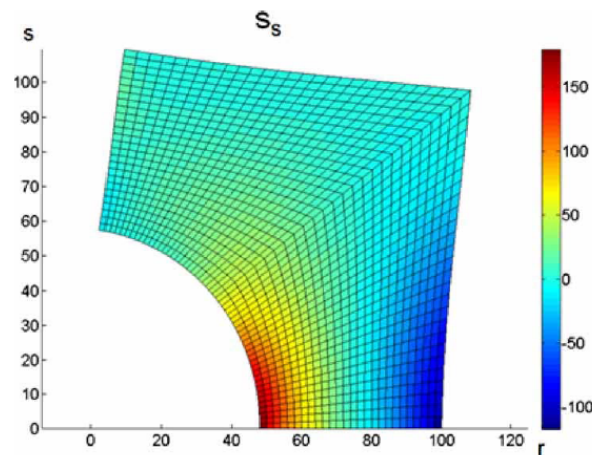


Figure 5: Stress distribution (MPa) in the s -direction.

The probabilistic constraint was approximated using FORM (recall Eq. 3):

$$P_f \approx \Phi(-\beta) \quad \text{and} \quad P_f^{\text{allowable}} \approx \Phi(-\beta^{\text{target}}),$$

and the optimization was performed for different values of β^{target} . All the final designs are presented in Table 1. The computational cost is evaluated in terms of the number of calls to the finite element code.

Table 1: Comparison of the computational cost (number of calls to the finite element code) of RBDO based methods.

Distribution Γ	β^{target}	RIA	PMA	SORA	SAP-PMA	\mathbf{x}^*
Normal	2	372	291	192	48	(1.00, 39.4)
	3	356	319	216	48	(1.00, 34.6)
	4	464	347	244	56	(1.00, 29.1)
LogNormal	2	500	311	196	64	(1.00, 39.5)
	3	624	398	229	72	(1.00, 34.9)
	4	816	455	290	96	(1.00, 29.9)

In comparison to the standard, most expensive approach (RIA), the methods PMA, SORA and SAP-PMA lead to average reductions of 67%, 56% and 88%, respectively, on the computational cost of the solution. The SAP-PMA approach significantly out-performed the other methods in solution of this particular RBDO problem.

The reduction in computational cost is very significant in this example due to use of finite element modeling for the mechanical problem. In the case of Lognormal random variables with $\beta^{\text{target}} = 4$, for example, the RIA method needed 816 finite element calls (about 3h20min) to obtain the optimal design, whereas the SAP-PMA method required only 96 finite element calls (about 27 minutes).

Surely, other benchmark comparisons are required in order to make any more definite conclusions. This will be the subject of future work.

6 Concluding remarks

The main goal of this paper was to review the main Reliability-based Design Optimization (RBDO) methods based on the First-Order Reliability Method (FORM). The two main FORM approaches were presented: the RIA and the PMA. A review and a comparison between them were presented. The coupled approach to solving the resulting RBDO problems was detailed and its high computational cost was highlighted. A general review of de-coupling techniques was also presented, and two of the main de-coupling methods were presented in detail (SORA and SAP-PMA). The review presented herein suggests that SORA and SAP-PMA should be the methods of better performance and robustness, in

comparison to the other methods described herein. Finally, this review presented the main techniques and references on the subject, and should serve as a guide to those entering this exciting and challenging subject.

References

- [1] Beck, A. & Gomes, W., A comparison of deterministic, reliability-based and risk-based design optimization. *MECSOL 2011*, 2011.
- [2] Míngues, R. & Castillo, E., Reliability-based optimization in engineering using decomposition techniques and FORMS. *Structural Safety*, **31(3)**, pp. 214–223, 2008.
- [3] Lopez, R., *Optimisation en présence d'incertitudes*. Ph.D. thesis, INSA de Rouen, France, 2010.
- [4] Lee, S. & Chen, W., A comparative study of uncertainty propagation methods for black-box-type problems. *Structural and Multidisciplinary Optimization*, 2009. DOI 10.1007/s00158-008-0234-7.
- [5] Melchers, R., *Structural Reliability Analysis and Prediction*. John Wiley & Sons: Chichester, 1999.
- [6] Rubinstein, R., *Simulation and the Monte Carlo method*. Wiley: New York, NY, 1981.
- [7] Niederreiter, H. & Spanier, J., *Monte Carlo and quasi-Monte Carlo methods*. Springer: Berlin, 2000.
- [8] Nie, J. & Ellingwood, B., Directional methods for structural reliability analysis. *Struct Safety*, **22**, pp. 233–49, 2000.
- [9] Englund, S. & Rackwitz, R., A benchmark study on importance sampling techniques in structural reliability. *Struct Safety*, **12**, pp. 255–76, 1993.
- [10] Seo, H. & Kwak, B., Efficient statistical tolerance analysis for general distributions using three-point information. *Int J Prod Res*, **40**, pp. 931–944, 2002.
- [11] Lee, S. & Kwak, B., Response surface augmented moment method for efficient reliability analysis. *Structural Safety*, **28**, pp. 261–272, 2006.
- [12] Rahman, S. & Xu, H., A univariate dimension-reduction method for multi-dimensional integration in stochastic mechanics. *Probabilistic Engineering Mechanics*, **19**, pp. 393–408, 2004.
- [13] Hasofer, A. & Lind, N., An exact and invariant first order reliability format. *Journal of the Engineering Mechanics Division*, **100(EM1)**, pp. 111–21, 1974.
- [14] Madsen, H., Krenk, S. & Lind, N., *Methods of structural safety*. Prentice Hall: Englewood Cliffs, 1986.
- [15] Haldar, A. & Mahadevan, S., *Reliability Assessment Using Stochastic Finite Element Analysis*. John Wiley & Sons: New York, 2000.
- [16] Tu, J., Choi, K. & Park, Y., A new study on reliability-based design optimization. *Journal of Mechanical Design*, **121(4)**, pp. 557–64, 1999.
- [17] Lemaire, M., Chateaneuf, A. & Mitteau, J., *Fiabilité des structures*. Lavoisier: Paris, 2005.
- [18] Youn, B., Choi, K. & Park, Y., Hybrid analysis method for reliability-based design optimization. *J Mech Des*, **125(2)**, pp. 221–32, 2003.
- [19] Youn, B. & Choi, K., Selecting probabilistic approaches for reliability based design optimization. *AIAA Journal*, **124**, pp. 131–42, 2004.
- [20] Lee, J., Yang, S. & Ruy, W., A comparative study on reliability index and target performance based probabilistic structural design optimization. *Computer & Structures*, **257**, pp. 269–80, 2002.
- [21] Youn, B. & Choi, K., An investigation of nonlinearity of reliability-based design optimization approaches. *J Mech Des*, **126**, pp. 403–11, 2004.
- [22] Torng, T. & Yang, R., An advanced reliability based optimization method for robust structural system design. *Proc. 34th AIAA/ASME/ASCE/AHS/ASC Structures, Structural Dynamics, and Material*

- Conference*, AIAA-93-1443-CP, 1993.
- [23] Chen, X., Hasselman, T. & Neill, D., Reliability based structural design optimization for practical applications. *Proc. 38th AIAA SDM Conf*, AIAA-97-1403: Kissimmee, 1997.
 - [24] Du, X. & Chen, W., Sequential optimization and reliability assessment method for efficient probabilistic design. *ASME J Mech Des*, **126**(2), pp. 225–233, 2004.
 - [25] Wu, Y., Shin, Y., Sues, R. & Cesare, M., Safety-factor based approach for probability-based design optimization. *Proceedings of the 42nd AIAA SDM Conference*, Seattle, 2001.
 - [26] Yang, R. & Gu, L., Experience with approximate reliability based optimization methods. *Struct Multidisc Optim*, **26**(1-2), pp. 152–159, 2004.
 - [27] Yang, R., Chuang, C., Gu, L. & Li, G., Experience with approximate reliability based optimization methods II: an exhaust system problem. *Structural Multidisciplinary Optimization*, **29**, pp. 488–497, 2005.
 - [28] Gu, L. & Yang, R., Recent applications on reliability-based optimization of automotive structures. *SAE World Congress and Exhibition, 2003-01-0152*, 2003.
 - [29] Kuschel, N. & Rackwitz, R., A new approach for structural optimization of series systems. *Applications of Statistics and Probability*, **2**(8), pp. 987–994, 2000.
 - [30] Agarwal, H., Mozumder, C., Renaud, J. & Watson, L., An inverse-measure-based unilevel architecture for reliability-based design. *Structural and Multidisciplinary Optimization*, **33**, pp. 217–227, 2007.
 - [31] Cheng, G., Xu, L. & Jiang, L., Sequential approximate programming strategy for reliability-based optimization. *Computers and Structures*, **84**(21), pp. 1353–67, 2006.
 - [32] Yi, P., Cheng, G. & Jiang, L., A sequential approximate programming strategy for performance measure based probabilistic structural design optimization. *Structural Safety*, **30**, pp. 91–109, 2008.
 - [33] Yi, P. & Cheng, G., Further study on efficiency of sequential approximate programming strategy for probabilistic structural design optimization. *Structural and Multidisciplinary Optimization*, **35**, pp. 509–522, 2008.
 - [34] Du, X., Sudjianto, A. & Chen, W., An integrated framework for optimization under uncertainty using inverse reliability strategy. *DETC2003/DAC-48706, 2003 ASME International Design Engineering Technical*, Chicago, Illinois, 2003.
 - [35] Wu, Y., Millwater, H. & Cruse, T., Advanced probabilistic structural analysis method for implicit performance functions. *AIAA Journal*, **28**, pp. 1663–1669, 1990.
 - [36] Lopez, R., Cursi, E. & Lemosse, D., Approximating the probability density function of the optimal point of optimization problems. *Engineering Optimization*, **43**(3), pp. 281–303, 2011.
 - [37] Aoues, Y. & Chateaufneuf, A., Benchmark study of numerical methods for reliability-based design optimization. *Structural and Multidisciplinary Optimization*, **41**, pp. 277–294, 2010.

Improvements on the numerical structural assessment of a half scale model of a nuclear spent fuel elements transportation package under 9m drop tests

Miguel Mattar Neto, Carlos Alexandre de Jesus Miranda,
Gerson Fainer

*Instituto de Pesquisas Energéticas e Nucleares,
IPEN – CNEN/SP, SP – Brazil*

Rogério Pimenta Mourão
*Centro de Desenvolvimento da Tecnologia Nuclear,
CDTN – CNEN/MG, MG – Brazil*

Abstract

The applied qualification requirements for the packages used in the transportation of nuclear spent fuel elements are very severe due the nature of the radioactive content. They include the so-called normal conditions of transport and the hypothetical accident conditions. The 9 m drop tests are the most critical hypothetical accident conditions. The package qualification under these conditions shall be conducted using full scale models (prototypes), small scale models, numerical simulations and/or a combination of physical tests and numerical simulations. The choice of the qualification approach depends on economical and safety aspects. To comply with the nuclear safety functions, as the containment of the internal products and biological shielding, the package itself has several components connected to each other in different ways (impact absorbers, welded parts, flanged connections, surface contacts, etc.). This paper presents a discussion on the combination approach with tests and numerical simulations for the structural assessment of a half scale model of a package for transportation of nuclear research reactor spent fuel elements under 9 m drop tests. The numerical simulations of the 9 m free drops over a rigid surface of half scale model of the transportation package under different orientations were conducted using a finite element explicit code considering several nonlinear aspects as the nonlinear materials models and properties, with emphasis on the impact absorbers behavior, the different package materials stiffness, and the different types of the contacts between the package components and between the package and the rigid surface, including the friction in the contacts. Also, several 9 m drop tests were conducted in a half scale model in different drop orientations. The numerical and experimental results are compared and comments and conclusions are addressed based on the comparison. Also, some recommendations are issued on the use of the numerical simulations for the full scale tests of the package.

Keywords: transportation package, drop test, impact, contact.

1 Introduction

The radioactive materials transportation is regulated by guides and standards like [1] and [2]. The main purpose of these regulations is to protect persons, property and the environment from the effects of radiation during the transport of radioactive material. This protection is achieved by requiring the containment of the radioactive contents, the control of external radiation levels, the prevention of criticality, and the prevention of damage caused by heat.

The packages for the transportation of nuclear research reactors spent fuel elements are classified as type B due the nature of the radioactive content. The applied qualification requirements are very severe including the so-called normal conditions of transport and the hypothetical accident conditions. These conditions are defined in the regulations [1,2] and it must be demonstrated that the package has to be sturdy enough to resist, among others:

- a drop onto a rigid target so as to suffer maximum damage, and the height of the drop measured from the lowest point of the package to the upper surface of the target shall be 9 m;
- a puncture resultant from drop so as to suffer maximum damage onto a bar rigidly mounted perpendicularly on a rigid target. The height of the drop measured from the intended point of impact of the package to the upper surface of the bar shall be 1 m. The bar shall be of solid mild steel of circular section, 15.0 ± 0.5 cm in diameter and 20 cm long unless a longer bar would cause greater damage, in which case a bar of sufficient length to cause maximum damage shall be used. The upper end of the bar shall be flat and horizontal with its edge rounded off to a radius of not more than 6 mm;
- a fire resulting in a temperature of 800 °C for 30 min;
- a submersion to a 200 m depth of water.

The use of shock absorbers is allowed to assure that the resultant deceleration levels in the radioactive content (spent fuel elements) are low enough and to keep the containment functional and structural integrity in the free drop conditions. The shock absorbers are sacrifice devices that must absorb the package kinetic energy in the impact after the drop by means of their deformation. Several materials may be used to fill the shock absorbers such as natural wood, wood composites, low density concretes, metallic foams, polymeric foams, and metallic honeycombs.

The 9 m drop tests are the most critical hypothetical accident conditions. The package qualification under these conditions shall be conducted using full scale models (prototypes), small scale models, numerical simulations and/or a combination of physical tests and numerical simulations. The choice of the qualification approach depends on economical and safety aspects.

To comply with the nuclear safety functions, as the containment of the internal products and biological shielding, the package itself has several components connected to each other in different ways (welded parts, flanged connections, surface contacts, etc.). So, the package structural evaluation under the drop test conditions should be conducted by finite element numerical simulations using explicit methods and considering several nonlinear aspects as the nonlinear materials models and properties, the different package materials stiffness, and the different types of the contacts between the package components and between the package and the rigid surface, including the friction in the contacts.

This paper presents a discussion on the combination approach with tests and numerical simulations for the structural assessment of a half scale model of a package for transportation of nuclear research reactor spent fuel elements under 9 m drop tests. The numerical simulations of the 9 m free drops over a rigid surface of half scale model of the transportation package under different orientations were conducted using a finite element explicit code considering several nonlinear aspects as the nonlinear materials models and properties, with emphasis on the impact absorbers behavior, the different package materials stiffness, and the different types of the contacts between the package components and between the package and the rigid surface, including the friction in the contacts. Also, several 9 m drop tests were conducted in a half scale model in different drop orientations. The numerical and experimental results are compared and comments and conclusions are addressed based on the comparison. Also, some recommendations are issued on the use of the numerical simulations for the full scale tests of the package.

2 Package description

The package was designed to meet the transportation criteria established by the IAEA (International Atomic Energy Agency) for Type B packages carrying fissile materials [1, 2]. Since no long term storage strategy has been defined in Brazil for this kind of spent fuel, the package is regarded also as a potential storage option. For that reason, some of its features were designed to attend long term storage requirements, such as long-term stability of its constitutive materials and compatibility between them and with the radioactive contents. Also the access to its internal cavity has to be granted for periodical checks through gas sampling.

The package consists of a cylindrical body with internal cavity to accommodate the basket that holds the spent fuel elements. The package body has a sandwich-like shielded wall consisting of stainless steel outer and inner surfaces and lead in-between. A double lid system guarantees the required containment and the internal lid – which is part of the pressure boundary – has a double sealing system. The package is provided with two access ports to the internal cavity, one for pressurization and sampling of the cavity filling gas, embedded in the internal lid, and the other for the cavity draining, located at the lower region of the package wall. Both ports are equally equipped with two concentric seals. All double seals are metallic, whereas external lid seal is elastomeric.

The structure of the basket is made of square tubes. For protection against mechanical and thermal loads, the package is provided with top and bottom external removable shock absorbers. These are structures made of external stainless steel skin and an energy-absorbing filling material. The filling material chosen was an wood composite named Oriented Strand Board (OSB), which is an engineered, mat-formed panel product made of strands, flakes or wafers sliced from small diameter, round wood logs and bonded with a binder under heat and pressure. A schematic view of the package is shown in Fig. 1. The main dimensions of the natural scale package are: main body, $\varnothing 1,000 \times 1,400$ mm; overall dimension with shock absorbers, $\varnothing 2,160 \times 2,010$ mm. There are also four cylindrical tie bars equally spaced connecting both shock absorbers. These bars are not shown in Fig. 1.

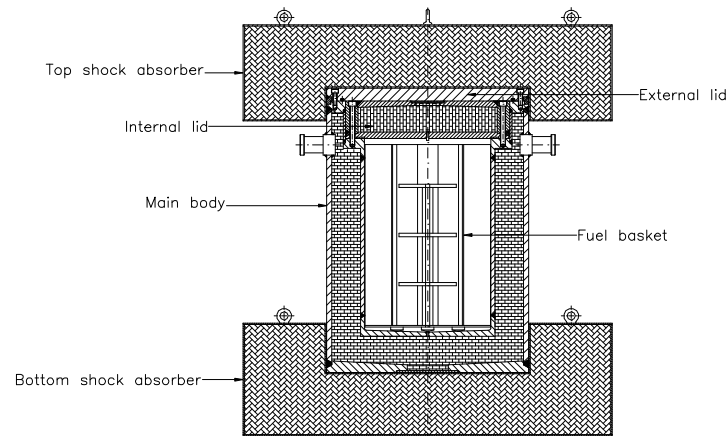


Figure 1: Transport package for research reactor spent fuel.

3 The half scale model of the package

Considering the scale 1:2, the model external cylinder has a diameter of $\approx 0.50\text{m}$ and it is $\approx 0.60\text{m}$ high. With the shock absorbers the package overall dimensions are: external diameter $\approx 0.90\text{m}$ and $\approx 1.00\text{m}$ high.

Regarding the half scale model, Fig. 2 to 5 show, respectively, the overall dimensions, a lateral view, an internal view, and the bottom shock absorber partially assembled.

The half scale package model materials are indicated in Tab. 1.

Table 1: Half scale package model materials.

Cask Part	Material
Lower shell	stainless steel
Bottom shock absorber	wood (OSB)
Inner shell	stainless steel
Shielding	lead
Outer shell	stainless steel
Top shock absorber	wood (OSB)
Upper shell	stainless steel
Tie bars	stainless steel

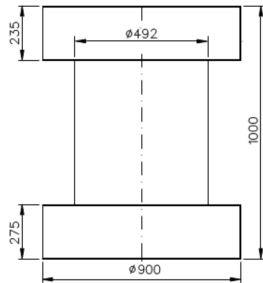


Figure 2: Overall dimensions of the half scale model of the package (in mm).



Figure 3: Lateral view of the package half scale model.

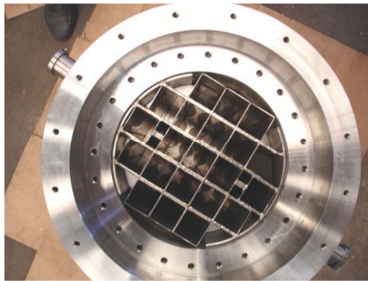


Figure 4: Internal view of the package half scale model.



Figure 5: Bottom shock absorber partial assembling.

4 Shock absorbers material characterization

As the properties of the OSB are not well known, especially its response to dynamic loads, a testing campaign was conducted to determine the parameters of interest for the intended use.

To study the effect of the lateral constraint in the dynamic response of the OSB, both encased and non encased specimens were submitted to impact tests [3]. The specimens, also made of glued layers of OSB, consisted of cylinders with 60 mm in diameter and 30 mm height. The direction normal to the glued surfaces was defined as the specimen perpendicular direction, whereas the glued surfaces define the specimen parallel directions. Besides the perpendicular and parallel directions, the specimens were also tested at 45° angle. The encased specimens were surrounded by a 0.5 mm thick metallic shell.

The averaged stress-strain curves obtained are shown in Fig. 6 (all curves were filtered at 500 Hz, low pass filter) [3]. As can be seen, from Fig. 6, the non encased specimens respond as an anisotropic material. On the other hand, the OSB behaves as a nearly isotropic material when tested under lateral constraint (encased) condition.

This behavior can also be seen clearly in Tab. 2, which shows the values for specific energy U absorbed at 0.45 of strain. The difference in U values in parallel and perpendicular directions for

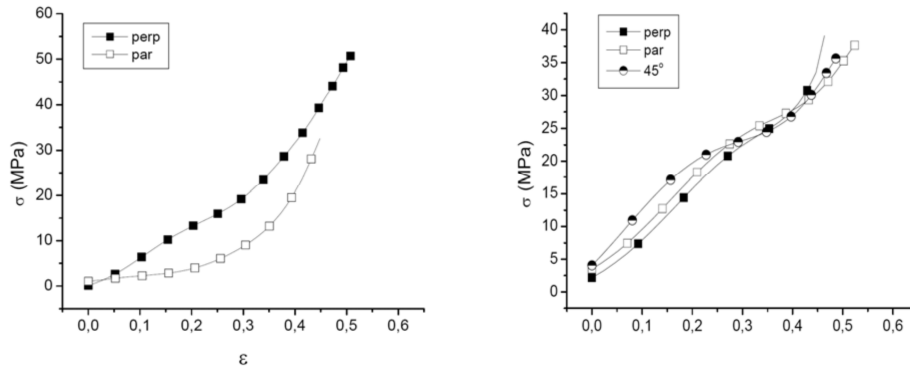


Figure 6: Shock absorbers material stress-strain curves for different directions.

the unconstrained situation is 47% (7.0 to 3.7 MJ/m³), while the average difference for the encased specimens between the three test directions is less than 10%.

Table 2: Specific energy absorbed (U) @ $\varepsilon = 0.45$.

		U (MJ/m ³)
Non-encased specimens	Perpendicular	7.0
	Parallel	3.7
Encased specimens	Perpendicular	7.5
	Parallel	8.2
	45°	8.4

For the encased specimens, the values of Young modulus determined in the three impact test directions are: $E_{perp} = 68$ MPa (perpendicular direction), $E_{par} = 65$ MPa (parallel direction) and $E_{45} = 81$ MPa (45° angle).

Although having the OSB mechanical properties characterization in two conditions obtained from tests with non encased and encased specimens, the choice for the use of the properties of the later may be justified by three reasons:

- The encased behavior of the OSB is not given only by the surrounding steel shell but also from the self lateral constraining without splintering.
- The deformed configurations of the non encased specimens after the impact tests show splintering in outer parts that are not expected to occur in the shock absorbers.

- According to [4], only a minor increase in the compression forces can be observed due to the influence of the steel casing with thicknesses of 0,5 mm in wood specimens of diameter of 100 mm, avoiding the specimens lateral splintering in the impact tests.

5 Numerical simulations of the package half scale model 9m drop tests

The half scale model of the package structural evaluation under the drop test condition was conducted by finite element numerical simulations considering several nonlinear aspects as the nonlinear materials models and properties, the different package materials stiffness, and the different types of the contacts between the package components and between the package and the rigid surface, including the friction in the contacts.

In this paper, the numerical simulations of the 9 m free drops over a rigid surface of half scale model of the described transportation package under different orientations were conducted using the finite element explicit code ANSYS LS-DYNA [5].

5.1 Contacts modeling

The following discussion is based on some recommendations from the LS-DYNA manual [5]. A contact is defined by identifying (via parts, part sets, segment sets, and/or node sets) what locations are to be checked for potential penetration of a slave node through a master segment. A search for penetrations, using any of a number of different algorithms, is made every time step. In the case of a penalty-based contact, when a penetration is found a force proportional to the penetration depth is applied to resist, and ultimately eliminate, the penetration. Unless otherwise stated, the contacts discussed here are penalty-based contacts as opposed to constraint-based contacts. Rigid bodies may be included in any penalty-based contact but in order that contact force is realistically distributed, it is recommended that the mesh defining any rigid body be as fine as that of a deformable body.

In high velocity impact analysis, the deformations can be very large and predetermination of where and how contact will take place may be difficult or impossible. For this reason, the automatic contact options are recommended as these contacts are non-oriented, meaning they can detect penetration coming from either side of an element.

Due to the impact condition and due to the geometric features of package and of the the half scale model of the package (see Fig. 1 to 5), it was used the so-called AUTOMATIC SURFACE TO SURFACE contact option of the ANSYS LS-DYNA code.

This type of contact is a two way contact allowing for compression loads to be transferred between the slave nodes and the master segments. Tangential loads are also transmitted if relative sliding occurs when contact friction is active. A Coulomb friction formulation is used with an exponential interpolation function to transition from static to dynamic friction. This transition requires that a decay coefficient be defined and that the static friction coefficient be larger than the dynamic friction coefficient. The constraint algorithm used in the LS-DYNA program is based on the algorithm developed in [6].

This involves a two-pass symmetric approach and allows for compression loads to be transferred

between the slave nodes and the master segments. The definition of the slave surface and master surface is arbitrary since the results will be the same.

Modeling the contact between the OSB material (soft) and other steel package parts (rigid) poses several challenges in impact conditions. This is due to its relatively low stiffness of the first when compared with other structural materials which has an indirect effect on its contact-impact interactions with other materials.

In ANSYS LS-DYNA the default procedure to compute the time-step and the contact stiffness is based on the maximum value of the Young's Modulus E , the maximum slope from the stress-strain curve (E_{curve}). This default approach is conservative to ensure that the computed time-step is stable for all compressive strains. The default value of the modulus from this approach could either be too small (if E is greater than E_{curve}) or too large (if the E_{curve} is greater than E). ANSYS LS-DYNA allows the overriding of this default logic. Suppose a case where the E_{curve} is 10 MPa and E is 50 MPa. Consequently, the E value of 50 MPa was used in the time-step and contact stiffness calculations which is roughly 0.025% of the modulus of steel (200,000 MPa). This huge disparity in stiffness values between the impacting bodies is naturally going to cause instabilities in contact. The alternative approach is to use a penalty contact using soft-constraint algorithm. However, ANSYS LS-DYNA always uses a penalty based approach based on material stiffness for contact between a rigid body and deformable bodies. Therefore, it is recommended to alter the modulus to a value at least 1% of the modulus of the impacting material (which, in this case, is steel).

An important point in contact modeling of the impact between materials with large differences in their stiffness is the procedure to avoid the collapse of the first row of soft materials, due to large compressive strains, that leads to an abnormal run ending with negative volumes issues. ANSYS LS-DYNA follows strictly the stress-strain curve to the last input stress-strain point. For strain magnitudes larger than the last input point in the curve, the code extrapolates using the last slope. This may yield small stress values and fails to model the bottoming out effect that occurs at large compressive strains. The fix to this is to manually provide an exponentially increasing curve to cover compressive strains to a minimum of 95-99%. It must be noticed that the manual curve must be smooth.

Some penetration between soft and rigid materials can be found during the maximum compressive strain. This may be attributed to the way the segment thickness is computed for solid elements. Much like shell elements, in which the mid-surface is offset in both directions of the segment normal, the solid segments maximum allowable thickness is also computed. The amount of maximum allowable thickness is based on a small percentage (5%) of the solid element diagonal which, based on the element geometry, could be very small making it vulnerable to nodal release. So, it is recommended to increase the offset thickness to a value adequate to ensure that no nodes are released from contact.

5.2 Materials modeling

The shock absorbers filling material (OSB) was modeled as crushable foam with its correspondent curve following an isotropic linear behavior until a strain of $\varepsilon = 0.45$, extended until $\varepsilon = 0.95$ to avoid numerical instabilities. The rigid surface was modeled with the ANSYS LS-DYNA RIGID option. The steel parts, including the round bars, as well as the lead ones were modeled as Bilinear Isotropic Material (BISO). The basket was modeled in a simplified way as a continuous mass with fictitious

values and a density value ‘calibrated’ to reproduce the mass predicted to fill the package. This was done to capture the package overall behavior. All adopted material properties, except OSB, can be seen in Tab. 3.

Table 3: Materials properties adopted in the analyses.

	Steel	Lead	Mass	Bar	Rigid Surface	units
E – Young’s modulus	200e9	14e9	2e9	200e9	200e9	N/m ²
ν – Poisson’s ratio	0.3	0.42	0.0	0.30	0.30	—
ρ – Density	7500	11500	600	7500	7500	Kg/mm ³
σ_{ys} – Yield stress	310e6	14e6	—	310e6	—	N/m ²
E' – Tangent modulus	7.6e8	1.0e7	—	7.6e8	—	N/m ²

5.3 Finite element model

A 180° finite element model, showed in Fig. 7, was developed using solid and shell elements and considering the symmetries in the structures. Parts as trunnions, bolts and threads were not modeled. This model can be rotated to cover all drop orientations that must be simulated (see Fig. 7).

5.4 Numerical simulations

The analysis starts as the model touches the rigid surface, so the applied initial velocity (13.3 m/s) corresponds to the 9 m free drop. Additionally the gravity acceleration was applied to the model.

Three analyses were performed simulating the vertical, the horizontal and the corner impact. In general, the results in terms of displacements along the time are smooth while in terms of accelerations a filter like Butterworth-type should be adopted due to the noise introduced by the successive integrations [7].

5.5 Deformed shapes

In Fig. 8, the contact modeling does not include the improvements discussed in section 5.1 above related to time-step and contact stiffness and increased solid element thickness in contact while in Fig. 9 all improvements were included in the contact modeling.

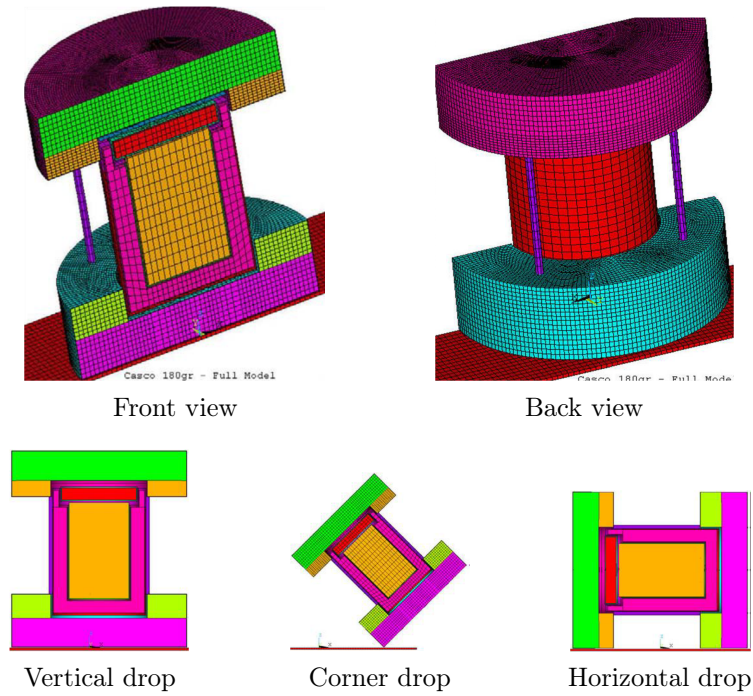


Figure 7: 180° finite element model and drop orientations.

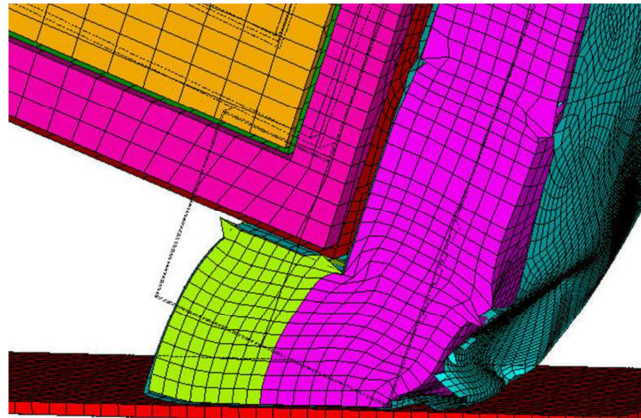


Figure 8: 180° finite element model deformed shape without improved contact modeling.

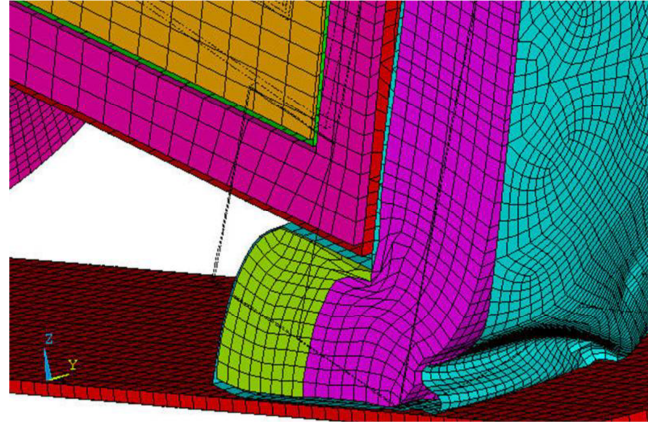


Figure 9: 180° finite element model deformed shape with improved contact modeling.

6 Half scale transportation package 9 m drop tests

The half scale transportation package 9 m drop tests were performed in the following sequence: corner drop, horizontal and vertical orientations. The shock absorbers were replaced from one test to other. Figure 10 shows the model prepared to 9 m drop in the three orientations. Before the drop itself the model, suspended by a crane, was carefully positioned to assure the desired position and angle. Some deformed shapes after tests are showed in Fig. 11.



Vertical drop



Corner drop



Horizontal drop

Figure 10: Tests drop orientations.

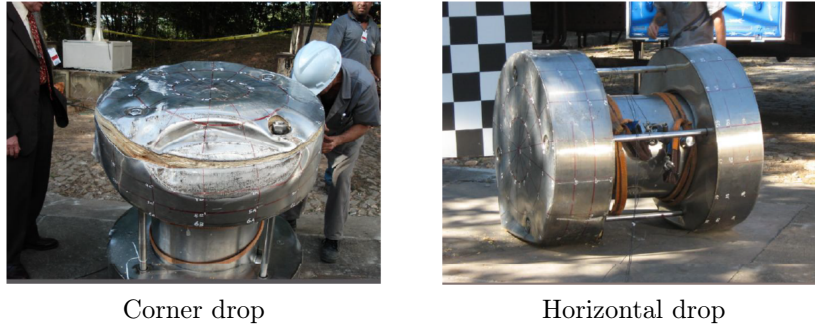


Figure 11: Final deformed shapes for two impact orientations from tests.

7 Results comparison

The main results of numerical simulations and tests are related to the displacements, velocities and accelerations of some chosen points, the maximum decelerations in the internal content of the package and the deformed shapes of the structures in the time of their maximum deformation.

As an example, Fig. 12 shows the typical curves of displacement versus time, velocity versus time and acceleration versus time of the finite element central node for the horizontal 9 m drop test.

The maximum deceleration can be observed in Fig. 12 (c). In this case, the value is $\approx 280g$ (g is the acceleration of the gravity) (as mentioned before, it should be applied a Butterworth-type low pass filter [7]).

Some important results for the package project are those related to maximum decelerations and deformations. Table 4 presents some of the obtained results in terms of the package maximum decelerations (after a filtering operation) and deformation in the shock absorbers from the numerical simulations and from the tests.

Table 4: Internal content maximum decelerations and shock absorbers maximum displacements from numerical simulations and tests.

	Numerical simulations		Tests		Error	
	Decel. (g)	Disp. (mm)	Decel. (g)	Disp. (mm)	Decel. (%)	Disp. (%)
Corner drop	138	46	116	51	+19	-10
Horizontal drop	237	28	280	23	-15	+22
Vertical drop	299	13	273	16	+10	-19

g – gravity acceleration

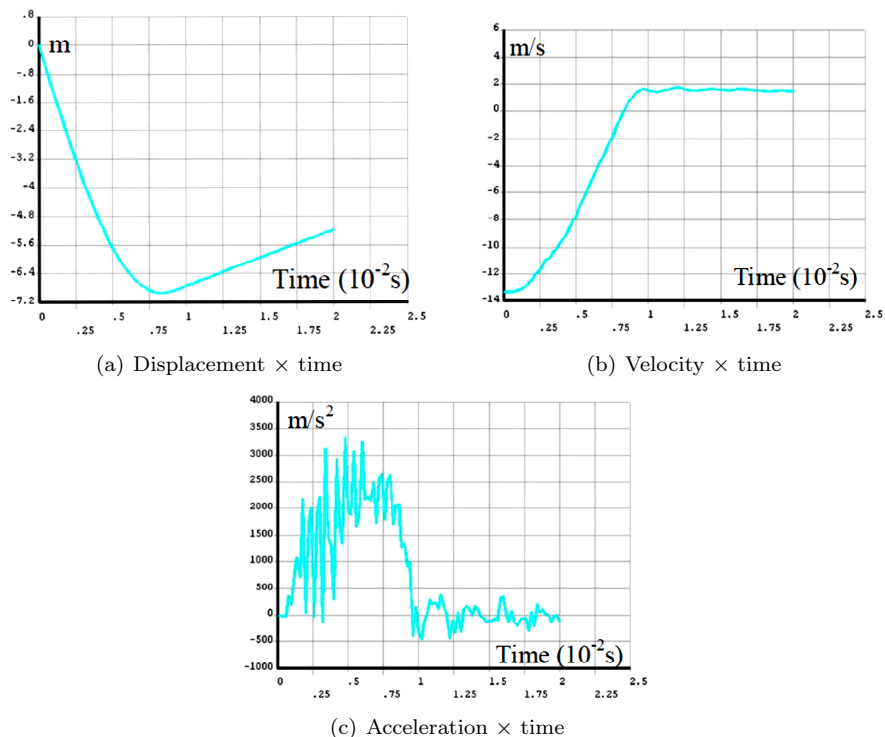


Figure 12: Movement curves of the 180° finite element model central node under 9 m drop test in the horizontal orientation.

8 Comments and conclusions

At a first glance, there is a reasonable agreement between the numerical and experimental results with errors [(numerical-experimental)/experimental] around $\pm 20\%$. Nevertheless, with a deeper look on the results, it is clear that the drop orientation has an important influence on the results comparison and this influence is related to the shock absorbers behavior.

Although the numerical and experimental maximum displacements values have differences, the final shock absorbers deformed shapes are quite similar.

For the corner and vertical drops, the observed maximum displacements in the tests were greater than that obtained from the numerical simulations. Also, the correspondent decelerations were smaller. On the other hand, for the horizontal drop the opposite situation occurred.

Also, during the tests, some rebound of the model was observed in an extension not reproduced in the numerical simulations, especially in the vertical orientation. This indicates that the energy absorption of the shock absorbers in the vertical orientation (impact load perpendicular to the OSB

fiber/grain) appeared to be less than expected. The OSB energy absorption characteristics appear to vary more with respect to wood fiber/grain orientation than it is considered in the material modeling used for the OSB.

As one of the main objectives of the comparison between the results from numerical simulations and from tests is to establish a qualified methodology to simulate the 9 m drop tests of a package prototype further assessments must be done in the future numerical simulations such as:

- Review of the shock absorbers material characterization.
- Review of the shock absorbers material model used in the numerical simulations.

Acknowledgements The work presented in this paper was supported by the International Atomic Energy Agency (IAEA) Latin American Projects RLA/4/020 and RLA/3/008 on Engineering of Casks for the Transport of Spent Fuel from Research Reactors.

Responsibility notice

The authors are the only responsible for the printed material included in this paper.

References

- [1] Regulations for the safe transport of radioactive material. Technical Report Safety Requirements No. TS-R-1, IAEA, Vienna, Austria, 2005.
- [2] Transporte de materiais radioativos. Technical Report CNEN NE- 5.01, CNEN, Comissão Nacional de Energia Nuclear, Rio de Janeiro, RJ, 1988. (in Portuguese).
- [3] Mourão, R.P., Characterization of shock absorbing materials for packages. *Proceeding of the 2007 International Nuclear Atlantic Conference – INAC 2007*, Santos, SP, Brazil, p. 7, 2007. CD-ROM, paper R13-1240.
- [4] Diersch, R., Weiss, M. & Dreier, G., Investigation of the impact behaviour of wooden shock absorbers. *Nuclear Engineering and Design*, **150**, pp. 341–348, 1994.
- [5] ANSYS, *ANSYS Mechanical and LS-DYNA 12.1 Release*. ANSYS Inc.: Canonsburg, PA, USA, 2011.
- [6] Taylor, L.M. & Flanagan, D.P., Pronto3d a three dimensional transient solid dynamics program. Technical Report Report SAND87-1912, SANDIA, NM, USA, 1989.
- [7] Advisory material for the iaea regulations for the safe transport of radioactive material – safety guide. Technical Report IAEA SAFETY STANDARDS SERIES No. TS-G-1.1 (Rev. 1), IAEA, Vienna, Austria, 2008.

Limit moment of local wall thinning in rigid pipeline repaired with composite material under bending

R. Mattedi

*Pós-Graduação em Engenharia Mecânica – PGMEC
Departamento de Engenharia Mecânica, TEM, Universidade Federal Fluminense,
UFF, RJ – Brazil*

L.C.S. Nunes

*Laboratório de Mecânica Teórica e Aplicada – LMTA
Rua Passo da Pátria, 156, Bloco E, Sala 216, CEP 24210-240,
Niterói, RJ – Brazil*

Abstract

Local wall thinning on pipelines or pressure vessels are common in industry and, usually, they occur because of the corrosion or mechanical damages. To study the impacts that these cracks do on pipelines, some analytical models and some failure criterion are mentioned. One of them is called Net-Section-Collapse Analysis (NSC), which predicts the maximum moment of a circumferentially cracked pipe with a variable-depth internal surface crack subject to loads like bending moment and, eventually, tension (pressure-induced). To preserve the structural integrity and stop the external corrosion on crack point, an important method has been developed. It is a composite overwrap pipeline repair system. In this method, a composite, usually a carbon fiber, is applied circumferentially around the defect on external face of pipeline. In this paper will be presented the study of limit moment of local wall thinning in rigid pipeline under bending and repaired by a composite around the crack. In this context the value of limit bending moment will be analyzed as a function of some discrete values of depth and angle of surface crack. In order to validate the method, the analytical results are compared with a commercially available finite element code.

Keywords: limit moment, local wall thinning, pipeline, repair system.

1 Introduction

In industry, especially of oil and gas, there is a wide application of rigid pipelines. According to Duell *et al.* [1] there are more than 1.7 million kilometers of oil and gas pipelines in operation. In North America, it is expended around two or three billion dollars with repairing or replacement of pipelines with failing, been by wear or abrasion, or even mechanical damage.

Nomenclature

θ	Half of local thinning angle
β	Half of neutral angle
R_o	External radius of pipe
R_i	Internal radius of pipe
R_m	Average radius of pipe
t_a	Thickness of pipe
t_c	Thickness of composite repair
d	Crack depth (radial direction)
η	$(t - d)/t$
L_d	Longitudinal thinning length
L	Pipe length
$N.A.$	Neutral axis
σ_{adm}	Allowable strength (Limit strength considered for each material)
σ_0	Strength for pipe without crack under limit bending moment
$a(\xi)$	Function of crack depth
M_0	Limit bending moment for pipe without crack
M	Limit bending moment for pipe with crack and repair applied

For example, on offshore/subsea segment the risers can be rigid pipelines. They are called Steel Catenary Riser (SCR) [2]. These pipes are usually submitted to external loads from their laying step to their operation step. In other engineering areas like energy and mining, they also have rigid pipelines in production plants. All of them are subjected to beginning of failing on their structures and in this case, it is important to know how to solve the problem.

Several works have been developed to have the knowledge of mechanical properties of material and the limit loads allowable for determinate application of pipeline. Rahman [3] offers a generalized method of *Net-Section-Collapse* (NSC), where the limit bending moment depends on the angle (2θ) and the radial depth of local thinning, which is a function of crack $a(\xi)$, where $0 \leq \xi \leq \theta$. Nevertheless, ASME Section XI [4] considers the same methodology NSC, but the depth of crack is a constant (d) and it is defined by the biggest value of $a(\xi)$.

The longitudinal thinning length has theoretically no effect on limit bending moment in analytical calculation, however Han *et al.* [5] have proved by finite elements method that there is an effect, which is associated to the constraint of remaining material surrounding local wall thinning. In work developed by Han *et al.* [5], the same methodology of ASME Section XI was used.

The Net-Section limit moments was also the subject of papers issued by Song *et al.* [6] and Moulim *et al.* [7]. However, both made an additional calculation for elbows. Moulim *et al.* have performed an

experimental to confirm the analytical methodology.

The purpose of this work is to investigate the limit moment of local wall thinning in rigid pipeline under bending. It is considered a failing the loss of material in a determinate section of a pipe. In the present analysis, this cracked pipeline is repaired using composite material. In this context the value of limit bending moment is analyzed as a function of some discrete values of depth and angle of surface crack. Finally, the analytical results are confronted to commercially available finite element code.

2 Case description

A pipe was considered with length L and external and internal radius, R_o and R_i , respectively. The local wall thinning, which has longitudinal length L_d , is in the centre of the pipe, see Figure 1. Then, a carbon fiber composite with length L_c and thickness t_c was applied around the damage. Normally, an epoxy resin is applied between the pipe and composite, in the failing region, but this was not considered in the present calculation.

The strength for a pipe without crack under bending moment (M_0) can be calculated as:

$$\sigma_0 = \frac{4M_0R_o}{\pi(R_o^4 - R_i^4)} \quad (1)$$

Then, considering a material that presents an allowable strength σ_{adm} , the limit bending moment will be:

$$M_0 = \frac{\sigma_{adm}\pi(R_o^4 - R_i^4)}{4R_o} \quad (2)$$

This paper will consider that the yield strength of material is equal to allowable strength σ_{adm} .

It is important to mention that the value of longitudinal thinning length L_d was considered constant and it follows the relation described on ref. [5]. That is to avoid divergence on results, and it is given by:

$$\left(\frac{L_d}{\sqrt{R_m t}} \right) \geq 1,5 \quad (3)$$

Other important assumptions were adopted about the composite to expedite the analyses. Although carbon fiber gives orthotropic properties its Young modulus, tangent modulus and Poisson coefficient were considered isotropic. Another simplification was to consider the equation 3 also for composite length (L_c) to avoid divergence on results.

The behavior of materials was assumed as elastic-plastic, or bilinear, during numerical analyses by finite elements analysis (FEA). The table 1 presents the mechanical properties of the materials of pipeline and its repair.

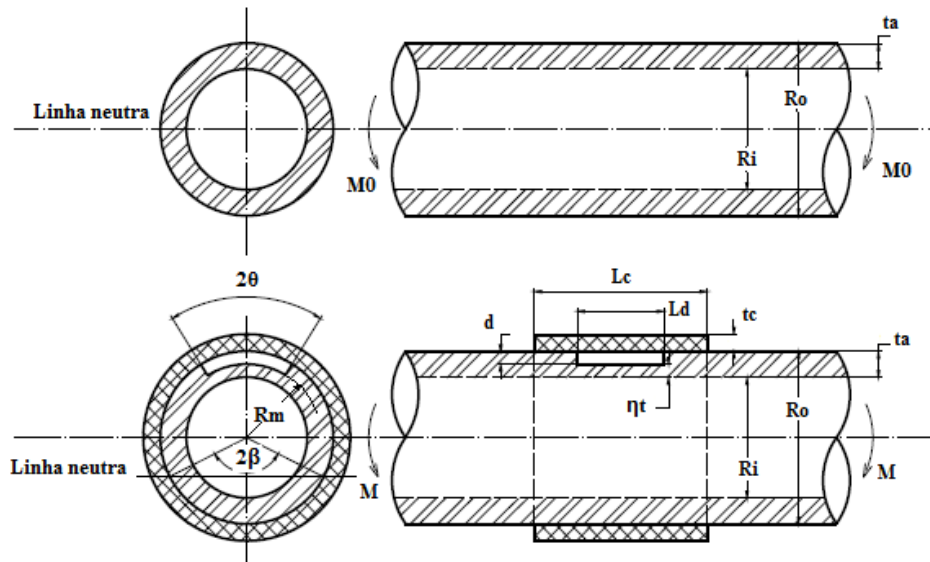


Figure 1: Geometry of pipeline, a) without crack, b) with crack and composite.

Table 1: Mechanical properties of materials.

Component	Material	Properties			
		σ_{adm} (Mpa)	E (GPa)	Poisson (ν)	Tangent Mod. (Mpa)
Pipe	ASTM A36	250	200	0.3	2535
Repair	Carbon fiber	355	23.4	0.196	7882

3 Analytical model for pipe with external local wall thinning repaired by composite

An analytical model was developed considering all data of the problem, to represent the relation of crack and repair geometries in a tube under bending. The Thin-walled tube method ($R_m \ll t$) was considered for the formulation.

According ref. [5], considering NSC simplified criterion, which its depth is a constant (d), the limit bending moment (M) can be performed by two cases, for now without repair:

1. **First case:** The crack exists only in one side of neutral axis so, $\theta \leq \pi - \beta$ (Figure 1). In this case the limit bending moment is represented by:

$$M \approx M_0 \left(\sin(\beta) - \frac{(1-\eta)}{2} \sin(\theta) \right) \quad (4)$$

Where β is,

$$\beta = \frac{\pi}{2} \left(1 - \frac{(1-\eta)\theta}{\pi} \right) \quad (5)$$

2. **Second case:** The crack geometry overpasses to the other side of neutral axis so, $\theta > \pi - \beta$. Then, the limit bending moment is:

$$M \approx M_0 \left(\eta \sin(\beta) + \frac{(1-\eta)}{2} \sin(\theta) \right) \quad (6)$$

Where β is,

$$\beta = \frac{\pi}{2\eta} \left(2\eta + \frac{(1-\eta)\theta}{\pi} - 1 \right) \quad (7)$$

Now considering the repair, the same relation can be performed. From the force equilibrium equation, on Figure 1:

$$M = \int dF_r = \int_0^\beta (\sigma_{adm} R_m t dy) R \cos(y) \quad (8)$$

Solving,

$$M = \sigma_{adm} R_m^2 t \int_0^\beta \cos(y) dy \quad (9)$$

$$M = \sigma_{adm} R_m^2 t \operatorname{sen}(\beta) \quad (10)$$

Considering both materials (steel and composite), the force equilibrium relation is:

$$\sum F = 2R \left[-(\sigma_{adm}^a t_a + \sigma_{adm}^c t_c) \int_0^\beta dy + (\sigma_{adm}^a t_a + \sigma_{adm}^c t_c) \int_\theta^{\pi-\beta} dy + (\sigma_{adm}^a (t_a - d) + \sigma_{adm}^c t_c) \int_0^\theta dy \right] = 0 \quad (11)$$

Assuming that,

$$\bar{\sigma}_{eq} = \sigma_{adm}^a t_a + \sigma_{adm}^c t_c \quad (12)$$

For the first case ($\theta \leq \pi - \beta$):

$$\beta = \frac{\bar{\sigma}_{eq} \pi - \sigma_{adm}^a d \theta}{2\bar{\sigma}_{eq}} \quad (13)$$

So, the bending moment equilibrium equation is:

$$M = 2R_m^2 \left[[\sigma_{adm}^a (t_a - d) + \sigma_{adm}^c t_c] \int_0^\theta \cos(y) dy + [\sigma_{adm}^a t_a + \sigma_{adm}^c t_c] \int_\theta^{\pi-\beta} \cos(y) dy + [\sigma_{adm}^a t_a + \sigma_{adm}^c t_c] \int_0^\beta \cos(y) dy \right] \quad (14)$$

Then, the limit bending moment relation for the first case is given by:

$$M = 2R_m^2 [2\bar{\sigma}_{eq} \sin(\beta) - \sigma_{adm}^a d \sin(\theta)] \quad (15)$$

$$M_0 = 4R_m^2 \sigma_f^a t_a \quad (16)$$

$$\frac{M}{M_0} = \frac{1}{2\sigma_{adm}^a t_a} [2\bar{\sigma}_{eq} \sin(\beta) - \sigma_{adm}^a d \sin(\theta)] \quad (17)$$

Analogously, in second case ($\theta > \pi - \beta$):

$$\beta = \frac{\sigma_{adm}^a d (2\pi - \theta) - \bar{\sigma}_{eq} \pi}{2(\sigma_{adm}^a d - \bar{\sigma}_{eq})} \quad (18)$$

$$M = 2R_m^2 [2(\bar{\sigma}_{eq} - \sigma_{adm}^a d) \sin(\beta) + \sigma_{adm}^a d \cdot \sin(\theta)] \quad (19)$$

$$\frac{M}{M_0} = \frac{1}{2\sigma_{adm}^a t_a} [2(\bar{\sigma}_{eq} - \sigma_{adm}^a d) \sin(\beta) + \sigma_{adm}^a d \sin(\theta)] \quad (20)$$

4 Numerical model – finite elements analysis (FEA)

A numerical model was performed to validate the analytical method presented in section 3. This model was developed in finite elements software. The pipeline was modeled with the local wall thinning and the repair and all the mechanical properties presented on table 1 were also inserted on analyses.

Two symmetry planes were applied in the geometry, one concerning the longitudinal plane and the other one concerning the transversal plane in the center of the pipe. Then, bending moment was applied only on pipe, not in the composite, in the end section of the pipe, only in one side, because of its symmetry.

The Shell method was used to streamline the processing of results, being possible the modeling of three membranes; the first layer represents the internal sheath of pipe (the layer without failing); the second layer represents the external sheath of pipe (the layer with failing); and the last one represents the composite sheath. The Figure 2 presents the geometry rendered by Shell method.

It is important to mention that this model was compared to a conventional model (considering solid elements) used in [5] and there were not significant differences on the results.

With the Shell model was possible to perform a refined mapped mesh that offers confinable results, as illustrated in Fig. 3. The mesh applied is the Shell Quadrilateral Linear type, which gives four nodes per element, with six degrees of liberty each, translation and rotation in direction x , y and z .

Due to the symmetry of the pipe, the bending moment was applied only in one side. It guarantees the major plane of stresses is in the middle of the length pipeline.

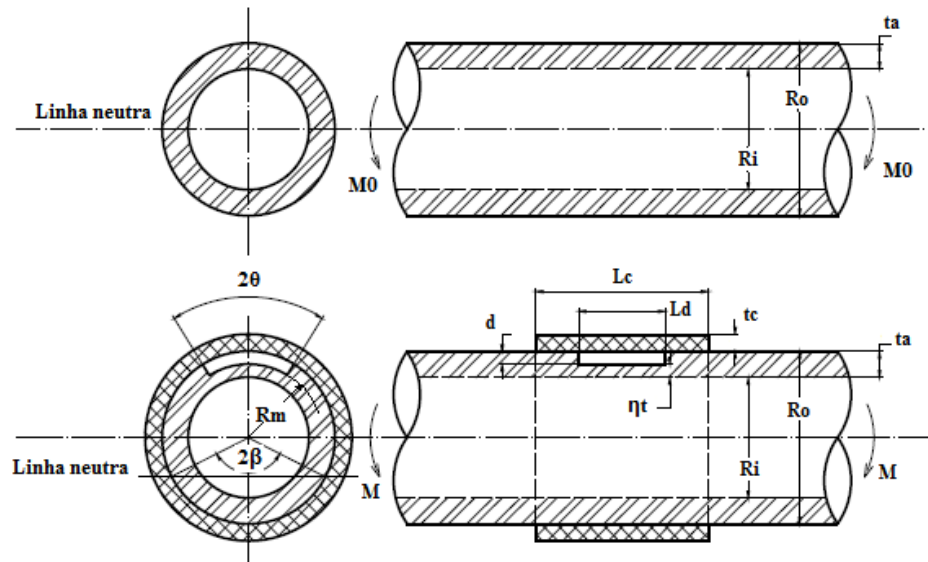


Figure 2: Shell model of pipeline with external local wall thinning repaired.

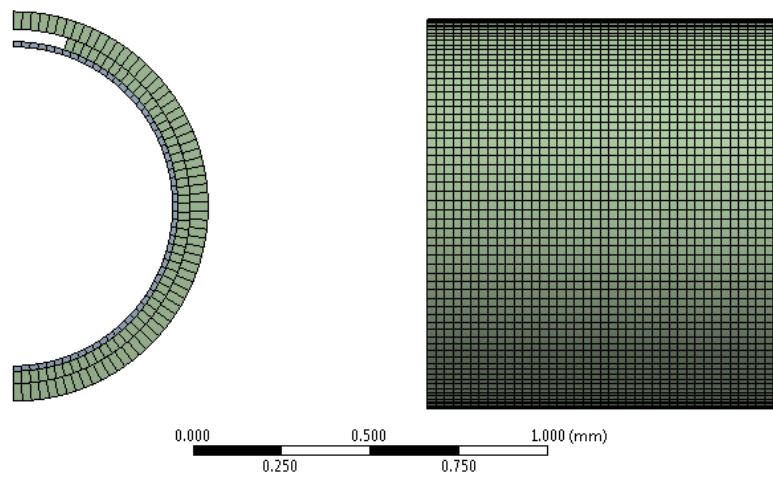


Figure 3: Mesh of model.

5 Results and discussion

By analytical model and numerical solution presented in previous sections, the results of the behavior of the pipeline considering different geometries of the crack and different mechanical properties of the composite was plotted and analyzed.

Figure 4 presents a decrease of limit bending moment considering a gradual growth of the angle and depth of local wall thinning for a pipeline without repair. This result is only for comparison. The others present the same relation, nevertheless, with the composite.

In order to investigate the mechanical behavior of cracked pipe with repair the thickness of composite is varied. In Figure 5, the thickness of composite (t_c) is taken equal to the thickness of the pipe (t_a). In Figure 6, t_c is equal to $1.5t_a$. Analyzing these results, it can be seen that the variation of t_c displaces all the curves proportionally to up or down. This occurs because of σ_{eq} from equations (17 e 20), which depends directly on t_c .

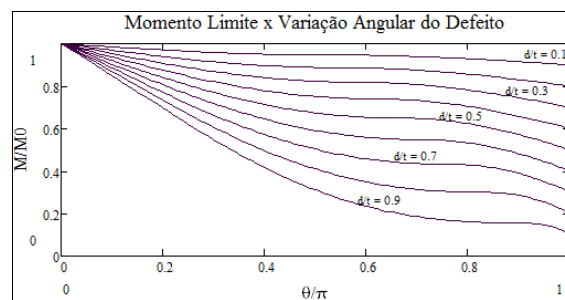


Figure 4: Limit bending moment considering the growth of angle and depth of crack for a pipeline without repair.

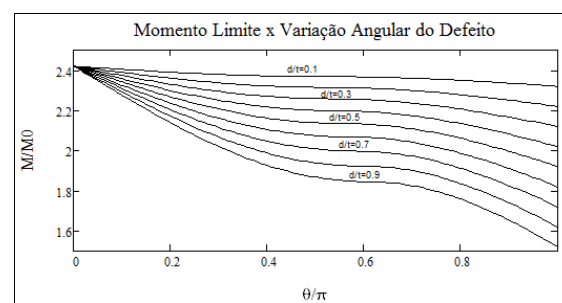


Figure 5: Limit bending moment considering the growth of angle and depth of crack for a pipeline with repair ($t_c = t_a$).

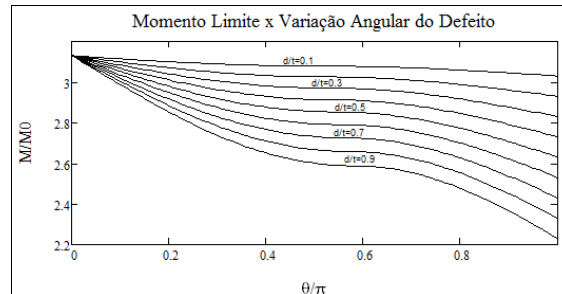


Figure 6: Limit bending moment considering the growth of angle and depth of crack for a pipeline with repair ($t_c = 1.5t_a$).

Another important variable from the equation of limit bending moment is σ_{adm}^c . In the present work, this value was adopted as 355 MPa in the beginning. Now, for evaluating the influence of this parameter, the Figure 7 presents the variation of limit bending moment with $\sigma_{adm}^c = 500$ MPa. This result proves that the limit bending moment also varies with mechanical properties of the composite.

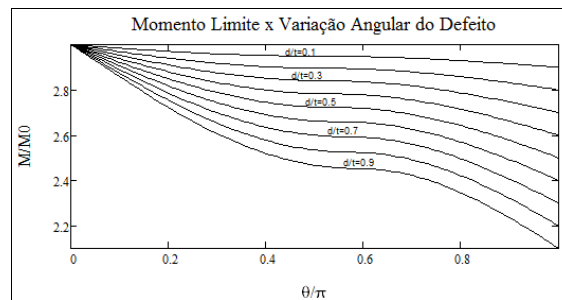


Figure 7: Limit bending moment considering the growth of angle and depth of crack for a pipeline with repair ($t_c = t_a$ and $\sigma_{adm}^c = 500$ MPa).

Figure 8 and Figure 9 show the compatibility of analytical and numerical results, and proves that the analytical model developed in this paper is valid. The discrete points on graph are the numerical results and gives trend lines close to analytical curves. The geometry and mechanical proprieties are the same previously presented in above analyses.

The major deviation founded between the analyses was 2.29%. Some of these results were added in the following tables, where is possible to compare the deviation for different cases.

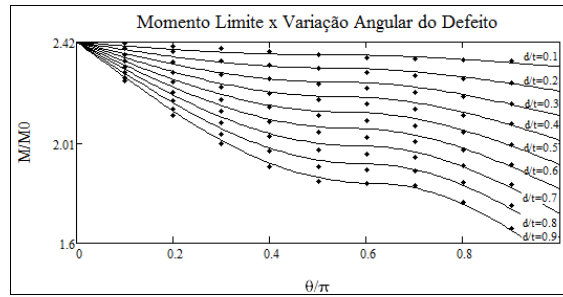


Figure 8: Limit bending moment: Analytical model x Numerical model ($t_c = t_a$).

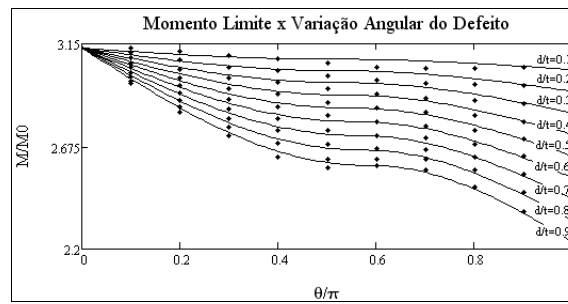


Figure 9: Limit bending moment: Analytical model x Numerical model ($t_c = 1.5t_a$).

Table 2: Analytical results x numerical results for $\theta/\pi = 0.1$.

d/t	t_c/t_a	σ_{adm}^c (MPa)	Deviation M/M_0 (%)
0,2	1	355	1.16
0,4	1	500	0.36
0,6	1.5	355	-0.64
0,8	1.5	500	-0.09

Table 3: Analytical results x numerical results for $\theta/\pi = 0.3$.

d/t	t_c/t_a	σ_{adm}^c (MPa)	Deviation
			M/M_0 (%)
0,2	1	355	-0.17
0,4	1	500	-0.81
0,6	1.5	355	-0.95
0,8	1.5	500	-0.92

Table 4: Analytical results x numerical results for $\theta/\pi = 0.5$.

d/t	t_c/t_a	σ_{adm}^c (MPa)	Deviation
			M/M_0 (%)
0,2	1	355	-0.15
0,4	1	500	-0.13
0,6	1.5	355	-1.59
0,8	1.5	500	-1.69

6 Conclusion

The utilization of composite around the failing influences considerably on limit bending moment of the pipeline. The NSC method used to develop the expression of limit bending moment for a pipeline repaired was validated and gives inexpressive deviations when compared to numerical results. The thickness of the composite and its admissible strength are directly proportional to the limit bending moment, in other words, higher are these values, as higher will be the pipeline resistance for bending moment.

The described analysis of limit bending moment for a pipeline with external local wall thinning repaired by composite presents consistent and reliable results for industry application. It is important to emphasize that using the simple expression, developed in this work, is possible to estimate the thickness of composite necessary to repair a damaged pipeline, in which the original mechanical behavior can be recovered.

References

- [1] Duell, J., Wilson, J. & Kessler, M., Analysis of a carbon composite overwrap pipeline repair system. *International Journal of Pressure Vessels and Piping*, **85**, pp. 782–788, 2008.
- [2] Submarine pipeline systems. Technical Report DNV-OS-F101, Det Norske Veritas, 2000.
- [3] Rahman, S. & Wilkowski, G., Net-section-collapse analysis of circumferentially cracked cylinders – part I: arbitrary-shaped cracks and generalized equations. *Engineering Fracture Mechanics*, **61**, pp. 191–211, 1998.
- [4] ASME Boiler & Pressure vessel Code Section XI, Rules for in-service inspection of nuclear power plant components. Technical Report IWB-3500 and IWB-3600, Division 1, 1997.
- [5] Han, L., He, S., Wang, Y. & Liu, C., Limit moment of local wall thinning in pipe under bending. *International Journal of Pressure Vessels and Piping*, **76**, pp. 539–542, 1999.
- [6] Song, T., Kim, Y., Oh, C., Jin, T. & Kim, J., Net-section limit moments and approximate J estimates for circumferential cracks at the interface between elbows and pipes. *International Journal of Pressure Vessels and Piping*, **86**, pp. 495–507, 2009.
- [7] Moulin, D., Touboul, F., Foucher, N., Lebey, J. & Acker, D., Experimental evaluation of j in cracked straight and curved pipes under bending. *Nuclear Engineering and Design*, **171**, pp. 33–43, 1997. CEA-CEN Saclay, Gif sur Yvette.

Evaluating velocity and mass correction when scaling structures subjected to impact loading

Leonardo M. Mazzariol, Roberto E. Oshiro, Miguel A.G. Calle,
Rafael T. Moura, Marcílio Alves
*Group of Solid Mechanics and Structural Impact, Department of Mechatronics
and Mechanical Systems Engineering,
University of São Paulo, 05505-900, São Paulo – Brazil*

Abstract

Velocity and mass factors can be troublesome to be set in some experimental impact tests, mainly for scaled structures that demands extreme conditions. Therefore, the present study introduces a method for scaling structures subjected to dynamic loads in which both velocity and mass can be changed in a rational manner. A set of factors different from the usual scaling laws is developed considering strain rate effects into the formulation. Two examples are used to infer the approach: an analytical study of a double plate subjected to a top impact load and a numerical analysis of a double bottom structure hit by a mass. The numerical analysis indicates that the velocity factor yields closer results to the real size structure when it is enclosed between 0.8 and 2.0, with the striker mass calculated via the equations here illustrated.

Keywords: scaling, similarity, ship collision, strain-rate sensitive.

1 Introduction

Scaling (or similarity) laws are employed by engineers to represent a structure response using scaled models. The inherent difficulty to experiment full-scaled structures lead authors to study reduced models [1, 2]. Despite the huge development on numerical methods, real tests are still needed in order to find and understand some phenomena [2]. It is well established in many investigations, such as Booth et al. [3], Jones [4], Oshiro and Alves [5], that the direct application of “traditional” similarity laws on dynamic-impact-driven events leads to unmatched results for strain rate sensitive materials. This fact is attributed to the non-scalability of strain rate effects, resulting in higher stresses in the scaled models, stiffening their response [6]. Oshiro and Alves [5, 7] overcame this issue by distorting the scaling laws, modifying the striker velocity to take strain rate effects into account. Later, Oshiro [8] proposed a procedure to change the impact mass, which was explored numerically and experimentally by Mazzariol et al [9]. This study detected that the velocity fine-tuning is critical and hard to set due

to many experimental details. The use of constant impact mass and a corrected impact velocity [5] adds even more complexity to the experiment setup.

The present investigation deals with scaled model behaviour where first the velocity is defined, and only later the impact mass is calculated, respecting the relations between mass and velocity factors. This flexibility would be a benefit when velocity must be reduced or increased as a result of the impact rig limitations.

The behaviour of two different scaled structures is investigated when both impact mass and velocity are modified. A velocity factor is defined while the impacted mass is analytically calculated. One structure is a double plate, axially impacted, and the second is a simplified ship double bottom, impacted in a cross intersection. In Section 2 details of both similarity procedures and material model are described. The results for the double plate model are presented in Section 3, while Section 4 analyses the simplified double bottom. Discussion and main findings are presented in Section 5, with Section 6 concluding the paper.

2 Similarity

The technique in which a structure scaled by a factor β (model) is used to infer the real size structure (prototype) behaviour is termed similarity or similitude. This method has been extensively studied [10, 11] and widely applied in many works [4, 12]. For impact phenomena, the main variables scaling factors are long known and summarized in Table 1.

In order to achieve perfect similarity, the Π theorem asserts that all predominant dimensionless numbers of the model must be equal to the corresponding prototype dimensionless numbers [13],

$$(\Pi_i)_m = (\Pi_i)_p \quad (1)$$

with m and p referring to model and prototype.

It is also known that structures under severe dynamic loads usually do not follow scaling laws due to effects such as material strain rate sensitivity, material failure, material thermal response and gravity. A distorted or imperfect similarity model is defined as a model that cannot be related to the corresponding prototype by a single geometric scaling factor [3, 7, 14, 15].

Oshiro and Alves [5] proposed a method that correct strain rate distortion effects. The initial impact velocity is changed, compensating the yield stress increase due to strain rate, according to

$$\beta_V = \beta^{q/(q-2)}, \quad (2)$$

with β being the prototype to model length ratio, q a material parameter and, $\beta_V = V_m/V_p$ a ratio between the velocities applied to the model and prototype.

Oshiro [8] proposed a modification in the impact mass, G , to correct strain rate effects, according to

$$\beta_G = \beta^{3-q}, \quad (3)$$

being,

Table 1: Factors relating the model variables to the prototype

Variable	Factor	Variable	Factor
length, L	β	time, t	β
displacement, δ	β	velocity, V	1
mass, G	β^3	strain rate, $\dot{\epsilon}$	$1/\beta$
strain, ϵ	1	acceleration, A	$1/\beta$
stress, σ	1	energy, E'	β^3
force, F	β^2		

$$\beta_G = \frac{G_m}{G_p}. \quad (4)$$

The material constant, q , is used in the Norton's law

$$\sigma_d = \sigma_0 \left(\frac{\dot{\epsilon}}{\dot{\epsilon}_0} \right)^q \quad (5)$$

to take the material strain rate sensitivity into account, being σ_0 and σ_d the quasi-static and dynamic flow stresses, evaluated at a reference strain rate $\dot{\epsilon}_0$.

In the present study, the impact mass and velocity are changed in the following manner. An impact mass velocity is defined considering only experimental aspects, such as maximum height of a free fall hammer or even the maximum pressure used to initially accelerate the impact mass in a free hammer with limited height. The following step consists in calculating the impact mass factor as function of β_V with the use of a proposed general equation.

The indirect similitude technique employed by Drazetic et al. [14] defined different dimensionless numbers. In this study, rather than mass-length-time, the basis comprises the initial velocity, V_0 , dynamic yielding stress, σ_d , and impact mass, G . The analysis of the main variables of the impact phenomena lead to the dimensionless numbers [7]

$$\Pi_1 = \left[\frac{A^3 G}{V_0^4 \sigma_d} \right], \quad \Pi_2 = \left[\frac{t^3 \sigma_d V_0}{G} \right], \quad \Pi_3 = \left[\frac{\delta^3 \sigma_d}{G V_0^2} \right], \quad \Pi_4 = \left[\frac{\dot{\epsilon} G^{1/3}}{(\sigma_d V_0)^{1/3}} \right] \quad \text{and} \quad \Pi_5 = \left[\frac{\sigma}{\sigma_d} \right] \quad (6)$$

Rearranging Π_3 , one can obtain

$$(\Pi_3)_m = (\Pi_3)_p \rightarrow \left[\frac{\delta_m^3 \sigma_{dm}}{G_m V_{0m}^2} \right] = \left[\frac{\delta_p^3 \sigma_{dp}}{G_p V_{0p}^2} \right] \rightarrow \left(\frac{\delta_m}{\delta_p} \right)^3 \cdot \left(\frac{\sigma_{dm}}{\sigma_{dp}} \right) \cdot \left(\frac{G_p}{G_m} \right) \cdot \left(\frac{V_p}{V_m} \right)^2 = 1 \quad (7)$$

and defining $\beta_\sigma = \sigma_{dm}/\sigma_{dp}$, Eq. (7) can be rewritten as

$$(\beta)^3 \cdot (\beta_\sigma) \cdot \left(\frac{1}{\beta_G}\right) \cdot \left(\frac{1}{\beta_V}\right)^2 = 1 \rightarrow \frac{\beta^3 \beta_\sigma}{\beta_G \beta_V^2} = 1 \rightarrow \beta_G = \frac{\beta^3 \beta_\sigma}{\beta_V^2} \quad (8)$$

following the same procedure, Π_4 can be also rearranged in such a way

$$\begin{aligned} (\Pi_4)_m = (\Pi_4)_p \rightarrow \left[\frac{\dot{\varepsilon}_m G_m^{1/3}}{(\sigma_{dm} V_{0m})^{1/3}} \right] &= \left[\frac{\dot{\varepsilon}_p G_p^{1/3}}{(\sigma_{dp} V_{0p})^{1/3}} \right] \rightarrow \\ \left(\frac{\dot{\varepsilon}_m}{\dot{\varepsilon}_p} \right) \cdot \left(\frac{G_m}{G_p} \right)^{1/3} \cdot \left(\frac{\sigma_{dp}}{\sigma_{dm}} \right)^{1/3} \cdot \left(\frac{V_{0p}}{V_{0m}} \right)^{1/3} &= 1 \end{aligned} \quad (9)$$

and using Eq. (4), from the definition of β_σ and defining $\beta_\varepsilon = \dot{\varepsilon}_m / \dot{\varepsilon}_p$, Eq. (9) can be rewritten as

$$(\beta_\varepsilon) \cdot (\beta_G)^{1/3} \cdot \left(\frac{1}{\beta_\sigma}\right)^{1/3} \cdot \left(\frac{1}{\beta_V}\right)^{1/3} = 1 \rightarrow \beta_\varepsilon \left(\frac{\beta_G}{\beta_\sigma \beta_V}\right)^{1/3} = 1 \rightarrow \beta_\varepsilon = \left(\frac{\beta_\sigma \beta_V}{\beta_G}\right)^{1/3} \quad (10)$$

If model and prototype are made of the same material, β_σ can be expressed as

$$\beta_\sigma = \frac{\sigma_{dm}}{\sigma_{dp}} = \frac{\sigma_{0m} \left(\frac{\dot{\varepsilon}_m}{\dot{\varepsilon}_{0m}}\right)^q}{\sigma_{0p} \left(\frac{\dot{\varepsilon}_p}{\dot{\varepsilon}_{0p}}\right)^q} = \left(\frac{\dot{\varepsilon}_m}{\dot{\varepsilon}_p}\right)^q = (\beta_\varepsilon)^q \quad (11)$$

Using Eq. (10) in Eq. (11) one can find

$$\beta_\sigma = (\beta_\varepsilon)^q \rightarrow \beta_\sigma = \left(\left(\frac{\beta_\sigma \beta_V}{\beta_G} \right)^{1/3} \right)^q \rightarrow \beta_\sigma = \left(\frac{\beta_V}{\beta_G} \right)^{\frac{q}{3-q}} \quad (12)$$

Substituting Eq. (12) in Eq. (8), it is possible to define the impact mass factor as function of scaling factor, β , velocity factor, β_V , and parameter q as

$$\beta_G = \frac{\beta^3}{\beta_V^2} \beta_\sigma \rightarrow \beta_G = \frac{\beta^3}{\beta_V^2} \left(\frac{\beta_V}{\beta_G} \right)^{\frac{q}{3-q}} \rightarrow \beta_G = \beta_V^{(q-2)} \beta^{(3-q)} \quad (13)$$

By noting from Eqs. (12,13) that the stress scaling factor can be written as $\beta_\sigma = (\beta_V/\beta)^q$, the dimensionless numbers in Eq. (6) can be rewritten as a function of q , β_V and β as

$$\Pi_1 = \frac{A^3 G}{V_0^4 \sigma_d} \rightarrow \frac{\beta_A^3 \beta_G}{\beta_V^4 \beta_\sigma} = 1 \rightarrow \beta_A = \frac{\beta_V^2}{\beta}, \quad (14)$$

$$\Pi_2 = \frac{t^3 \sigma_d V_0}{G} \rightarrow \frac{\beta_t^3 \beta_\sigma \beta_V}{\beta_G} = 1 \rightarrow \beta_t = \frac{\beta}{\beta_V}, \quad (15)$$

$$\Pi_4 = \frac{\dot{\epsilon} G^{1/3}}{(\sigma_d V_0)^{1/3}} \rightarrow \frac{\beta_\epsilon \beta_G^{1/3}}{(\beta_\sigma \beta_V)^{1/3}} = 1 \rightarrow \beta_\epsilon = \frac{\beta_V}{\beta} \quad \text{and} \quad (16)$$

$$\Pi_5 = \frac{\sigma}{\sigma_d} \rightarrow \beta_\sigma = (\beta_\epsilon)^q \rightarrow \beta_\sigma = \left(\frac{\beta_V}{\beta} \right)^q. \quad (17)$$

being β_A the acceleration scaling factor and β_t the time scaling factor.

As a result, after defining the geometric scaling factor, β , and the possible impact velocity (and consequently the velocity scaling factor), β_G is calculated via Eq. (13). From β_G and the prototype impact mass it is possible to calculate the model impact mass capable of correcting disparities due to strain rate effects.

In the following sections, the models based on traditional scaling laws, with a *Mass-Length-Time* basis, will be referred as MLT models. The models that applies factors defined by Eqs. (13-17) will be termed VSG, in reference to *Initial Velocity - Dynamic Yield Stress - Impact Mass G* basis.

3 Double plate model

The structural configuration in Fig. 1, also called Calladine model, was extensively explored by Calladine and English [16], Tam and Calladine [17] and Zhang and Yu [18]. It consists of two plates pre-bent to form three plastic hinges (θ_0) and bolted at top and bottom, struck by an impact mass G at velocity V_0 . This structure was chosen due to its high strain rate sensitivity [17]. The plates compression leads to two phases of motion described as a function of time [17]. Considering that θ remains small, strain rate is simplified to V_0/l and the first phase equation can be obtained from equilibrium forces acting on the lateral links,

$$V_0 - \frac{S \sigma_d t}{G} = 2 \left(\frac{12 \sigma_d S}{lm} \right)^{1/2} \frac{w_0^2}{l} \sinh \left[2 \left(\frac{12 \sigma_d S}{lm} \right)^{1/2} t \right] + \dot{c}, \quad (18)$$

being c the plate shortening, S the cross section of the plate, m the mass of the plates, l the total length ($2L$) and w_0 the initial horizontal displacement on midspan, that corresponds to initial rotation, i.e. $w_0 = L \sin \theta_0$. The first phase finishes when there is no more shortening, meaning $\dot{c} = 0$, but only the evolution of plastic hinges.

From Eq. (18) one obtains horizontal displacement, w_1 and velocity, \dot{w}_1 , used to obtain θ_1 and $\dot{\theta}_1$, which are initial conditions for the second phase of motion [18], described by

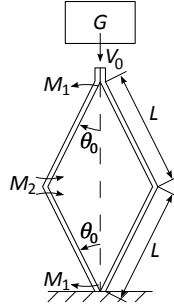


Figure 1: Calladine structure

$$\ddot{\theta}_1 + \frac{l^2(m+G)(\sin(\theta)\cos(\theta)\dot{\theta}^2 + (M_1 + M_2))}{l^2[m/3 + (m+G)\sin(\theta)^2]} = 0. \quad (19)$$

in which, M_1 and M_2 are bending moments (Fig. 1) given by Oshiro and Alves [5]

$$M_1 = \frac{M_0 K}{\sigma_0(q+2)2^{q-1}} \left(\frac{\dot{\theta}}{4}\right)^q \text{ and} \quad (20)$$

$$M_2 = \frac{M_0 K}{\sigma_0(q+2)2^{q-1}} \left(\frac{\dot{\theta}}{2}\right)^q, \quad (21)$$

being $M_0 = \sigma_0 b h^2 / 4$, $K = \sigma_0 / \varepsilon^q$; b , the plate width and h , the plate thickness.

3.1 Results

The numerical solutions of Eqs. (18,19) for $L = 50$ mm, $b = h = 5$ mm, $\theta_0 = 1.07^\circ$, $G = 4.08$ kg, $\beta = 0.1$, $V_0 = 7$ m/s, $q = 0.077$, $\sigma_0 = 2.35 \times 10^8$ Pa, $\varepsilon_0 = 1.0 \times 10^{-3}$ 1/s and $\rho = 7800$ kg/m³ [5], are depicted in Fig. 2(a), showing the corrected θ as function of dimensionless time. This correction is made for comparison purposes, and consists in multiplying time and displacement by factors from Table 1 for the MLT model and, for VSG models, multiplying the displacement by β (defined above) and the time by β_t , evaluated with Eq. (15) for nine different β_V . It is worthy to state that both prototype and velocity-only correction model (VSG-V) θ dimensionless time curves are coincident.

Fig. 2(b) describes discrepancy between the prototype and the corrected final rotation angle θ . For velocity factors between 0.3 and 2.0, the applied correction gives results with smaller error than the MLT model.

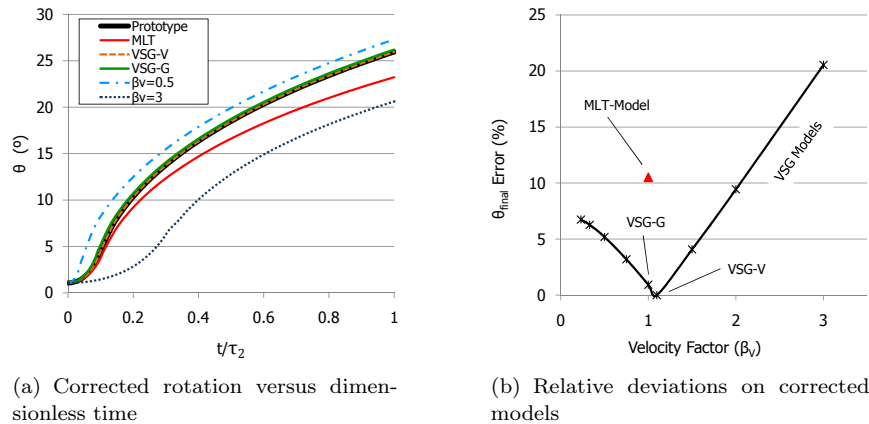


Figure 2: Calladine Model results

4 Double bottom

Ship collisions and ways to mitigate the consequences of these events have been studied and discussed by many authors [19–21]. Despite of the high cost involved, there were several large-scale tests providing important information for further analysis [22–25]. The inherent difficulty and costs lead studies to be ran in reduced models, many as quasi-static indentation [26, 27], some under dynamic load [28–30] and fewer using similarity to correlate model to prototype focusing on hydrodynamic effects [31] and internal mechanics on simplified structures [9]. Even though the list of publications in this area is quite extensive the correlation between a scaled model and prototype, both under dynamic load, is still a challenge.

This second example consists in a double bottom structure impacted transversely by a dropping mass, numerically, for a range of velocities. The calculated striker mass is capable of correcting the strain rate effects for each of many impact velocities. Concerning the prototype geometry, the simplified double bottom was designed with 30mm-thick sheets (sketch in Fig. 3(b)) and the striker designed as similar as possible to a simplified bulbous bow with 2000mm cylinder diameter and conical lower part with apex angle of 45° fit in a 600mm radius sphere nose. All finite element meshes were created using Altair Hypermesh 9.0.

The simulation was solved using LS-Dyna 971 R4.2.1 for velocity factors between 0.5 and 4.0 (described in details in Table 2) and respective calculated model impact mass (Fig. 3(a)) for the defined 800 ton prototype impact mass. For modelling the double bottom, it was used a 8-node Thick Shell Brick elements with 3 integration points through thickness and two elements through thickness in main cross area. The shell mesh refinement, required to well capture the buckling phenomena, resulted in an element size much smaller than the thickness, which was avoided. Between the two remaining element types, solid or thick shell, the later one was chosen based on the much smaller computational cost. Striker was modelled with solid elements.

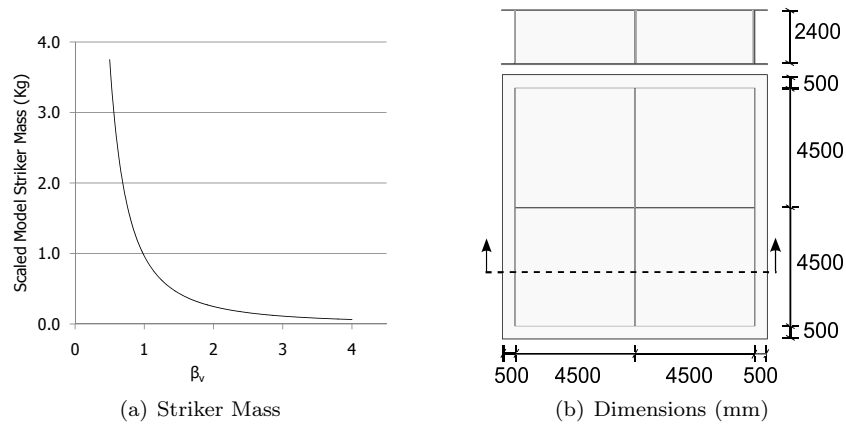


Figure 3: Double bottom general specification

Table 2: Summary of simulations for double bottom

Model	Scaling factor β	Impact Mass [g]	Initial Velocity [m/s]	Velocity Factor β_V	Energy $\times 10^6$ [kJ]
Prototype	1	8.00×10^8	5.00	-	1.0×10^6
MLT	0.01	8.00×10^2	5.00	1.0	1.000
VSG-V	0.01	8.00×10^2	5.50	1.10	1.209
VSG-G	0.01	9.64×10^2	5.00	1.0	1.205
$\beta_V = 0.5$	0.01	3.75×10^4	2.50	0.5	1.171
$\beta_V = 1.5$	0.01	4.36×10^2	7.50	1.5	1.225
$\beta_V = 2.0$	0.01	2.48×10^2	2.50	2.0	1.239
$\beta_V = 2.5$	0.01	1.60×10^2	12.5	2.5	1.250
$\beta_V = 3.0$	0.01	1.12×10^2	15.0	3.0	1.260
$\beta_V = 3.5$	0.01	8.76×10^1	17.5	3.5	1.268
$\beta_V = 4.0$	0.01	6.37×10^1	20.0	4.0	1.275

Concerning the representation of the material behaviour response, the impact mass was assumed to be rigid (MAT 020) and for the double bottom it was chosen a model that uses powerlaws to describe both hardening law and strain rate dependency, similar to Norton material model, Eq. (5). Among many material model options in LS-Dyna 971 R.4.2.1, the most suitable one is MAT 064, described as

$$\sigma = k\varepsilon^m \dot{\varepsilon}^q, \quad (22)$$

with the parameters listed in Table 3.

Table 3: Material properties for Finite Element Modelling

Material	ρ [ton/mm ³]	E [GPa]	ν [-]	k [MPa/s ^q]	m [-]	q [-]
1006 Steel	7.85×10^{-9}	6.63×10^2	0.3	680	0.206	0.0405

4.1 Results

Figure 5(a) shows the deformed mesh at the end of the simulation, defined by the striker reaching its maximum displacement. In order to compare the results from both scaling methods, the results must be multiplied by scaling factors following the same procedure used in Section 3. However, in this second example, the force is the main variable and, for VSG models, its scaling factor can be defined as the product of $\beta_G = \beta_V^{(q-2)} \beta^{(3-q)}$ and $\beta_A = \beta_V^2 / \beta$ (Eqs. 13 and 14 respectively), resulting in $\beta_{Force} = \beta_V^q \beta^{2-q}$. The application of this procedure for each case described in Table 2 is shown in Fig. 4. Moreover, Fig. 5(b) plots the model deviations in reference to prototype.

5 Discussion

The examples here presented that the proposed procedure provides excellent results, extending the results shown in [5] to a more general formulation that takes into account the real limitations of experimental testing, bringing the methodology to a more practical use. However, this methodology has some limitations.

The similarity technique does not distinguish variables with same dimensions. Hence, mass scaling factor is applied to both impact mass and structure mass, but the correction is applied only to the impact mass. For impact mass, G , much greater than the structure mass, m , the inherent errors are negligible. This fact can be verified in both examples by observing that high β_V values implies in low β_G values. Consequently, the impact and structure masses are similar, reducing drastically the inertia forces and increasing the results discrepancies. This is shown in Figs. 2(a) and 2(b), in which the errors increase monotonically for β_V within an optimal interval. For the Calladine example, this almost symmetric interval is centred on $\beta_V = 1.09$ (VSG-V, exact solution), although any β_V chosen

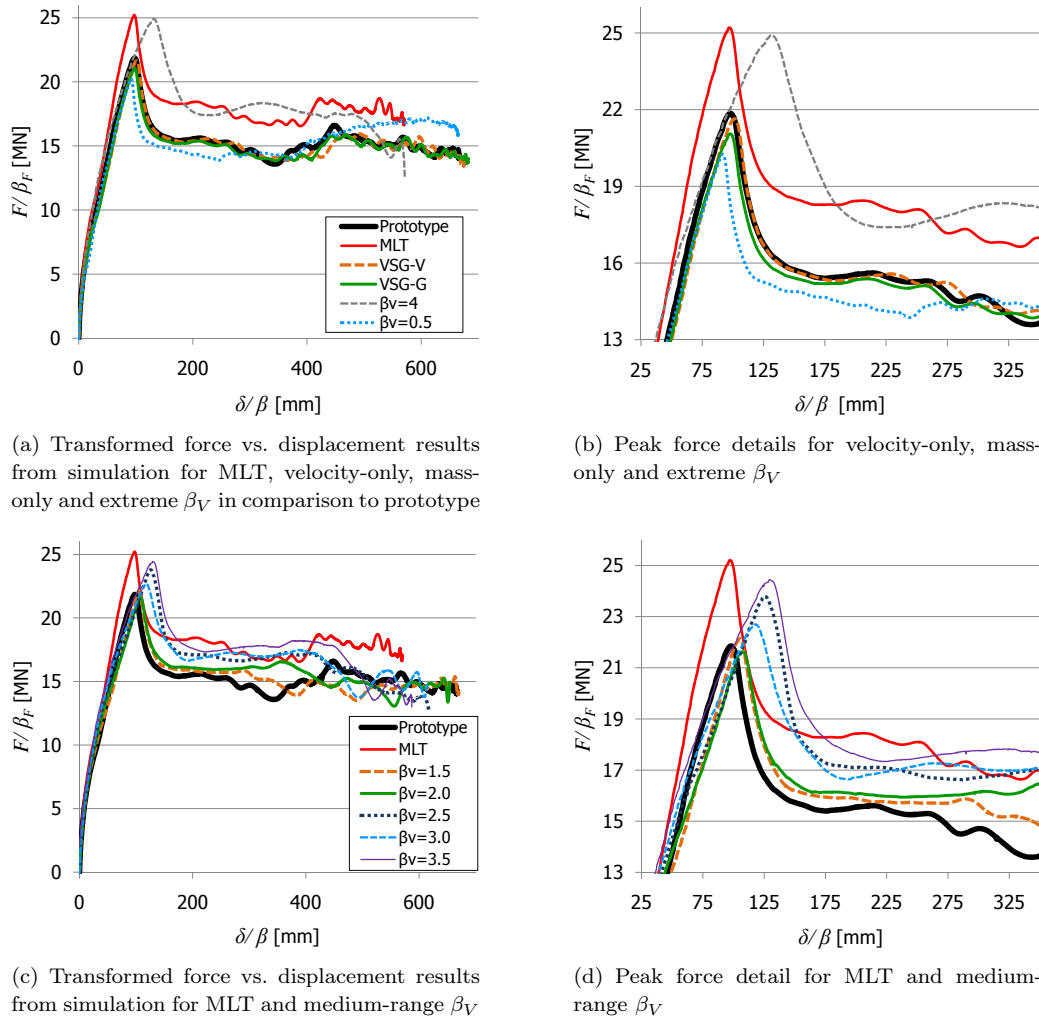


Figure 4: Simulation results for force acting on striker per displacement

between 0.3 and 2.0 provides better correlation results than MLT model. For the double bottom example, same stiffer behaviour is shown in Fig. 5(b).

A second limitation of the present study arises from the fact that there is no distinction between elastic and plastic stresses. This is why the results for the Calladine model, that uses analytic solution with a rigid-plastic material, are better (exact for VSG-V) than in the double bottom example, in which the material model considers also the elastic regime.

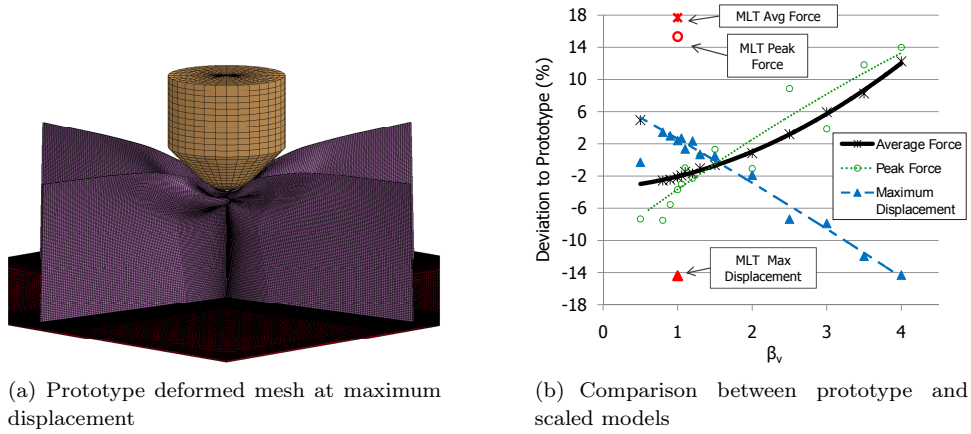


Figure 5: Prototype deformed mesh at maximum displacement

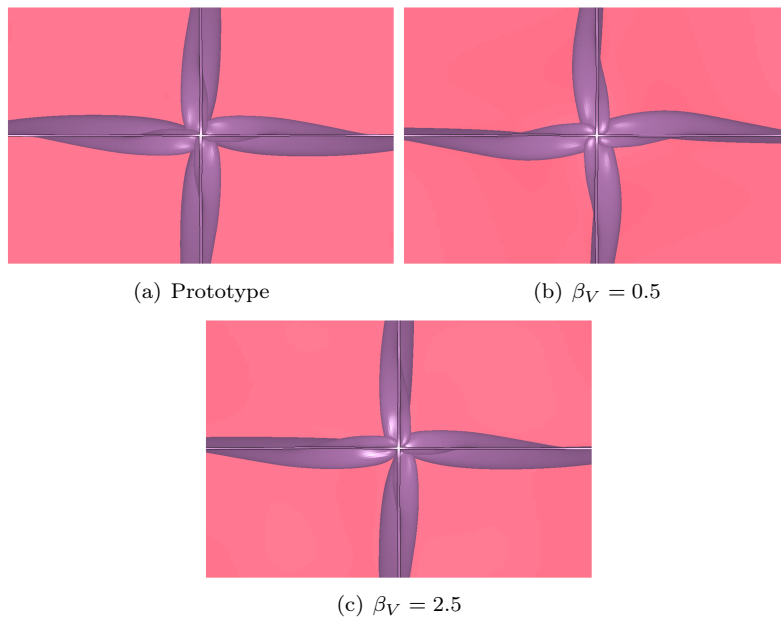


Figure 6: Different buckling modes for double bottom

When creating scaled models with factors as small as 0.01, tiny geometric imperfections can influence the results, since they would represent large deviations from the prototype. Moreover, model and prototype material will have different properties.

It is very important to assure that similar buckling modes are obtained. The buckling pattern for models $\beta_V = 0.5$ and $\beta_V = 2.5$ (Fig. 6) were not exactly similar to the reference, leading to different results. For example, $\beta_V = 2.5$ model had a higher maximum force than $\beta_V = 3.0$ and almost the same maximum displacement.

This study is also a further step on scaling models made of different materials. If β_G is function of material properties, then one is able to calculate the appropriate V_0 . For example, if the scaled model ($\beta = 0.01$) is made of aluminium, and $q = 0.04$ (same as steel, hypothetically), the velocity factor would be $\beta_V = (((2.7/7.85) * \beta^3)^{(3-q)} / \beta^{(3-q)})^{1/(q-2)} = 1.896$ and the errors of not correcting the model mass would not occur. One problem is that the parameter q is not the same for steel and aluminium. Hence, further development must be made in order to allow the scaling correction for even more general cases.

6 Conclusions

This paper presented a different approach for scaling of structures subjected to impact load. Via simulations of scaled models in addition to similarity laws, it was shown that the behaviour of a real-scale structure can be predicted while overcoming real experiment limitations. This is made by altering both the initial velocity and impact mass, without further information on the structure response. In order to calculate the correction of impacted mass one need: material parameter, q ; the scale factor, β , and the relation between desired velocity and real one, β_V .

Even though the present method does not contemplate the strain hardening and the material elastic portion, reasonable results could be achieved if velocity factors are not far from the unity, reducing the mass scaling factor disparities. It is important to remind that buckling modes of both prototype and scaled structure must be similar so to allow the use of similarity laws. This study also brought concepts for future development of scaling of structures made of different materials.

Acknowledgments The authors would like to thank the Brazilian research funding agency FINEP for the financial support.

References

- [1] Jones, N., Structural aspects of ship collisions. *Structural Crashworthiness*, eds. N. Jones & T. Wierzbicki, Butterworths: London, pp. 308–337, 1983.
- [2] Singer, J., Arbocz, J. & Weller, T., *Buckling Experiments: Experimental Methods in Buckling of Thin-Walled Structures*. John Wiley & Sons: England, 1st edition, p. 621, 1998.
- [3] Booth, E., Collier, D. & Miles, J., Impact scalability of plated steel structures. *Structural Crashworthiness*, eds. N. Jones & T. Wierzbicki, Butterworths: London, pp. 136–174, 1983.

- [4] Jones, N., Some comments on the scaling of inelastic structures loaded dynamically. *Impact, Waves and Fracture*, eds. R.C. Batra, A.K. Mal & G.P. Macsithigh, ASME, volume Vol.205, pp. 153–167, 1995.
- [5] Oshiro, R. & Alves, M., Scaling of structures subject to impact loads when using a power law constitutive equation. *International Journal of Solids and Structures*, **46(18-19)**, pp. 3412 – 3421, 2009.
- [6] Jones, N., *Structural Impact*. Cambridge University Press: New York, USA, 1st edition, p. 575, 1997.
- [7] Oshiro, R. & Alves, M., Scaling impacted structures. *Archive of Applied Mechanics*, **74**, pp. 130–145, 2004.
- [8] Oshiro, R.E., *Estudo da similaridade imperfeita em estruturas sujeitas a carregamentos de impacto*. Ph.D. thesis, EPUSP, Sao Paulo, 2010. In Portuguese.
- [9] Mazzariol, L.M., Oshiro, R.E., Calle, M.A.G. & Alves, M., Scaling of stiffened panels subjected to impact load. *MECOM-CILAMCE*, eds. E.N. Dvorkin & M.B. Goldschmidt, AMCA: Buenos Aires, pp. 1275–1289, 2010.
- [10] Baker, W.E., Westine, P.S. & Dodge, F.T., *Similarity Methods in Engineering Dynamics: Theory and Practice of Scale Modeling*. Elsevier Science Publishers: Amsterdam, 1st edition, p. 348, 1991.
- [11] Skoglund, V.J., *Similitude - Theory and Applications*. International Textbook Company, p. 320, 1967.
- [12] Neuberger, A., Peles, S. & Rittel, D., Scaling the response of circular plates subjected to large and close-range spherical explosions. part i: Air-blast loading. *International Journal of Impact Engineering*, **34(5)**, pp. 859 – 873, 2007.
- [13] Fox, R.W. & McDonald, A.T., *Introduction to Fluid Mechanics*. John Wiley & Sons: New York, 4th edition, pp. 192–206, 1998.
- [14] Drazetic, P., Ravalard, Y., Dacheux, F. & Marguet, B., Applying non-direct similitude technique to the dynamic bending collapse of rectangular section tubes. *International Journal of Impact Engineering*, **15(6)**, pp. 797 – 814, 1994.
- [15] Ferguson, G.L., Replica model scaling for high strain-rate events. *International Journal of Impact Engineering*, **16(4)**, pp. 571 – 583, 1995.
- [16] Calladine, C. & English, R., Strain-rate and inertia effects in the collapse of two types of energy-absorbing structure. *International Journal of Mechanical Sciences*, **26(11-12)**, pp. 689 – 701, 1984.
- [17] Tam, L. & Calladine, C., Inertia and strain-rate effects in a simple plate-structure under impact loading. *International Journal of Impact Engineering*, **11(3)**, pp. 349 – 377, 1991.
- [18] Zhang, T. & Yu, T., A note on a 'velocity sensitive' energy-absorbing structure. *International Journal of Impact Engineering*, **8(1)**, pp. 43 – 51, 1989.
- [19] Paik, J.K. et al., (eds.), *Committee V.3 Collision and Grounding*, International Ship and Offshore Structures Congress: San Diego, USA, 2003.
- [20] Wang, G. et al., (eds.), *Committee V.1 Collision and Grounding*, International Ship and Offshore Structures Congress: Southampton, UK, 2006.
- [21] Soares, C.G. et al., (eds.), *Committee V.1 Damage Assessment After Accidental Events*, International Ship and Offshore Structures Congress: Seoul, Korea, 2009.
- [22] Carlebur, A.F.C., Full-scale collision tests. *Safety Science*, **19(2-3)**, pp. 171 – 178, 1995. Safety of Transportation.
- [23] Ohtsubo, H., Kawamoto, Y. & Kuroiwa, T., Experimental and numerical research on ship collision and grounding of oil tankers. *Nuclear Engineering and Design*, **150(2-3)**, pp. 385 – 396, 1994.
- [24] Yamada, Y., Endo, H., Kawano, H. & Hirakata, M., Collapse mechanism of the buffer bow structure on axial crushing. *Proceeding of the Thirteenth International Offshore and Polar Engineering Conference*, eds. J.S. Chung & S. Prinsenberg, ISOPE: Honolulu, pp. 534–541, 2010.
- [25] Kitamura, O., Kuroiwa, T., Kawamoto, Y. & Kaneko, E., A study on the improved tanker structure

- against collision and grounding damage. *Practical design of ships and other floating structures*, eds. M.W.C. Oosterveld & S.G. Tan, Elsevier Science B V, pp. 173–179, 1998.
- [26] Wang, G., Arita, K. & Liu, D., Behavior of a double hull in a variety of stranding or collision scenarios. *Marine Structures*, **13(3)**, pp. 147 – 187, 2000.
- [27] Simonsen, B.C. & Ocakli, H., Experiments and theory on deck and girder crushing. *Thin-Walled Structures*, **34(3)**, pp. 195 – 216, 1999.
- [28] Amdahl, J., Kavlie, D. & Johansen, A., Tanker grounding resistance. *Practical design of ships and mobile units*, eds. H. Kim & J.W. Lee, SNAK, pp. 1072–1083, 1995.
- [29] Kitamura, O., Comparative study on collision resistance of side structure. *Marine Technology*, **34(4)**, pp. 292 – 308, 1997.
- [30] Lehmann, E. & Peschmann, J., Energy absorption by the steel structure of ships in the event of collisions. *Marine Structures*, **15(4-5)**, pp. 429 – 441, 2002.
- [31] Tabri, K., Maattanen, J. & Ranta, J., Model-scale experiments of symmetric ship collisions. *Journal of Marine Science and Technology*, **13**, pp. 71–84, 2008.

On the use of spherical, ellipsoidal and prismatic hulls to predict equivalent stress ranges in multiaxial fatigue

Marco Antonio Meggiolaro, Jaime Tupiassú Pinho de Castro
*Pontifical Catholic University of Rio de Janeiro,
Dept. of Mechanical Engineering, Rua Marquês de São Vicente 225,
Gávea 22453-900, Rio de Janeiro, RJ – Brazil*

Abstract

Non-proportional (NP) multiaxial fatigue life predictions require the calculation of equivalent stress or strain ranges associated with the history path. A traditional way to find such ranges is to use spherical, ellipsoidal or prismatic hull methods, which search for enclosures of the entire history path in stress or strain diagrams. In this work, all existing hull methods are presented and compared using results from more than 3,000,000 Monte Carlo simulations of random and especially chosen path topologies in stress or strain diagrams. New models are also proposed, based on Deperrois' idea of longest chords. It is found that the proposed models are very similar to the Maximum Prismatic Hull model, but with a much simpler and efficient algorithm to compute equivalent stresses. It is also shown that the Minimum Circumscribed Ellipsoid, Minimum Volume Ellipsoid, and Minimum Ball methods may result in very poor predictions of the stress or strain amplitudes. The only recommended method based on ellipsoids is the Minimum F-norm Ellipsoid which, together with the Maximum Prismatic Hull model and its variations, is efficient to predict equivalent amplitudes in NP histories.

Keywords: multiaxial fatigue, equivalent stress, convex hull.

1 Introduction

Multiaxial fatigue damage models are based on stress or strain ranges. It is not difficult to define these ranges for constant amplitude loadings, where only two stress or strain states need to be considered, one associated with the peak and the other with the valley. However, for multiaxial variable amplitude (VA) loadings, in special when the history is non-proportional (NP), it is not clear how these ranges should be defined and identified.

Consider that the periodic history is formed by repeatedly following a given loading path domain \mathbf{D} , where \mathbf{D} contains all points from the stress or strain variations along one period of the history. For a complex-shaped history, it is not easy to decide how to obtain the effective maximum strain range $\Delta\tau_{max}$ associated with \mathbf{D} . The so-called convex hull methods [1–5] try to find circles, ellipses or rectangles that contain the entire path (in the 2D case). In a nutshell, in the 2D case, the Minimum

Ball (MB) method [1] searches for the circle with minimum radius that contains D ; the minimum ellipse methods [2–4] search for an ellipse with semi-axes a and b that contains D with minimum area $\pi \cdot a \cdot b$ or minimum norm $(a^2 + b^2)^{1/2}$; and the maximum prismatic hull methods [3, 5] search among the smallest rectangles that contain D the one with maximum area or maximum diagonal (it's a max-min search problem). The value of $\Delta\tau_{max}$ in Fig. 1 would either be assumed as the value of the circle diameter, or twice the ellipse norm, or the rectangle diagonal. If the history path were represented in a shear strain $\gamma_B \times$ shear strain γ_{B2} diagram, these exact same methods would result in estimates for the effective maximum shear strain range $\Delta\gamma_{max}$.

The convex hull methods can also be applied to traction-torsion histories, if a $\sigma_x \times \tau_{xy}/\sqrt{3}$ diagram is considered. The effective range in this case is the Mises stress range $\Delta\sigma_{Mises}$. Similarly, for traction-torsion histories where plastic strains dominate, a strain diagram $\varepsilon_x \times \gamma_{xy}/\sqrt{3}$ can be used to predict an effective Mises strain range $\Delta\varepsilon_{Mises}$.

Such convex hull methods can be extended to histories involving more than two stress or strain components. E.g., if the history path is plotted in a 3D diagram representing 3 stress or strain components, the convex hull methods will search for spheres, ellipsoids or rectangular prisms. For higher dimension diagrams, the search is for hyperspheres, hyperellipsoids, and rectangular hyperprisms.

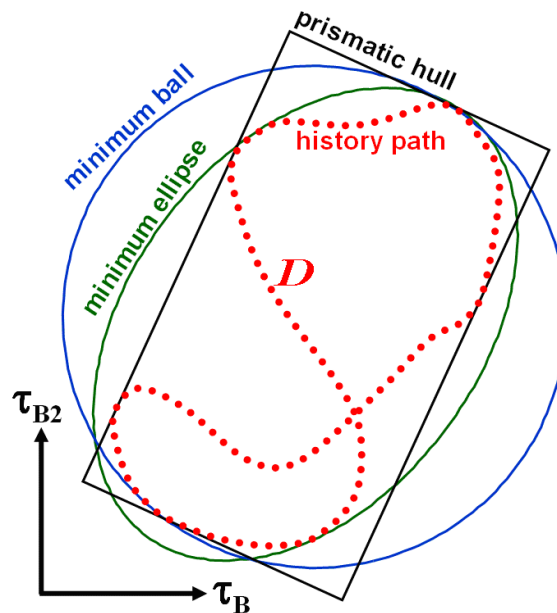


Figure 1: Stress history path D in a shear stress $\tau_B \times$ shear stress τ_{B2} diagram, enclosed in convex hulls based on circles (balls), ellipses and rectangular prisms.

The convex hull methods are described in detail in the following sections. Their framework is based on deviatoric stress (or strain) diagrams and Mises stress (or strain) parameters, which are discussed next.

2 Mises stress and strain parameters

The methods to obtain effective (or equivalent) stress and strain ranges usually make use of stress and strain parameters based on the Mises yield function. For linear elastic histories, both Mises effective stress σ_{Mises} and Mises (or octahedral) shear stress τ_{Mises} can be used as auxiliary parameters, where

$$\sigma_{Mises} = \frac{3}{\sqrt{2}}\tau_{Mises} = \frac{1}{\sqrt{2}}\sqrt{(\sigma_x - \sigma_y)^2 + (\sigma_y - \sigma_z)^2 + (\sigma_x - \sigma_z)^2 + 6(\tau_{xy}^2 + \tau_{yz}^2 + \tau_{xz}^2)} \quad (1)$$

Since the Mises stress σ_{Mises} (as well as the octahedral shear stress τ_{Mises}) equation is always positive, a Mises stress range $\Delta\sigma_{Mises}$ (also known as relative Mises stress σ_{RMises}) should be used to correctly evaluate the variation of σ_{Mises} due to a change $(\Delta\sigma_x, \Delta\sigma_y, \Delta\sigma_z, \Delta\tau_{xy}, \Delta\tau_{xz}, \Delta\tau_{yz})$ in the stress components along some loading path \mathbf{D} :

$$\Delta\sigma_{Mises} = \sigma_{RMises} = \frac{\sqrt{(\Delta\sigma_x - \Delta\sigma_y)^2 + (\Delta\sigma_x - \Delta\sigma_z)^2 + (\Delta\sigma_y - \Delta\sigma_z)^2 + 6(\Delta\tau_{xy}^2 + \Delta\tau_{xz}^2 + \Delta\tau_{yz}^2)}}{\sqrt{2}} \quad (2)$$

Note that the Mises stress range correlates with the octahedral shear range parameter $\Delta\tau_{Mises}$, used in both Sines and Crossland models, through $\Delta\sigma_{Mises} = \Delta\tau_{Mises} \cdot 3/\sqrt{2}$.

The Mises effective strain ε_{Mises} is another useful quantity in VA-NP histories, in special to deal with plastic strains. It uses the mean or effective Poisson coefficient $\bar{\nu} = (0.5\varepsilon_{pl} + \nu_{el}\varepsilon_{el})/(\varepsilon_{pl} + \varepsilon_{el})$ to include plastic effects, where ε_{el} and ε_{pl} are the elastic and plastic components of the strains, and ν_{el} and ν_{pl} are the elastic and plastic Poisson coefficients (where $\nu_{pl} = 0.5$). The Mises strain correlates with the octahedral (or Mises) shear strain γ_{Mises} , which is the combination of both shear strains that act in each of the octahedral planes, through

$$\varepsilon_{Mises} = \frac{3}{2\sqrt{2} \cdot (1 + \bar{\nu})} \gamma_{Mises} = \frac{\sqrt{(\varepsilon_x - \varepsilon_y)^2 + (\varepsilon_x - \varepsilon_z)^2 + (\varepsilon_y - \varepsilon_z)^2 + 1.5(\gamma_{xy}^2 + \gamma_{xz}^2 + \gamma_{yz}^2)}}{\sqrt{2} \cdot (1 + \bar{\nu})} \quad (3)$$

Since the ε_{Mises} (as well as the γ_{Mises}) equation is always positive, a Mises strain range $\Delta\varepsilon_{Mises}$ (also known as the relative Mises strain ε_{RMises}) should be used to evaluate its variation due to a change $(\Delta\varepsilon_x, \Delta\varepsilon_y, \Delta\varepsilon_z, \Delta\gamma_{xy}, \Delta\gamma_{xz}, \Delta\gamma_{yz})$ in the strain components along some loading path:

$$\Delta\varepsilon_{Mises} = \varepsilon_{RMises} = \frac{\sqrt{(\Delta\varepsilon_x - \Delta\varepsilon_y)^2 + (\Delta\varepsilon_x - \Delta\varepsilon_z)^2 + (\Delta\varepsilon_y - \Delta\varepsilon_z)^2 + 1.5(\Delta\gamma_{xy}^2 + \Delta\gamma_{xz}^2 + \Delta\gamma_{yz}^2)}}{\sqrt{2} \cdot (1 + \bar{\nu})} \quad (4)$$

An octahedral (or Mises) shear range parameter $\Delta\gamma_{Mises}$ can also be defined, related to the Mises strain range by

$$\Delta\varepsilon_{Mises} = \frac{3 \cdot \Delta\gamma_{Mises}}{2\sqrt{2}(1 + \bar{\nu})} \quad (5)$$

Note that the octahedral stress or strain shear ranges $\Delta\tau_{Mises}$ or $\Delta\gamma_{Mises}$ are measured on the octahedral planes, they are not equal to twice the shear amplitudes τ_a or γ_a acting on the considered plane. But those shear amplitudes could be easily obtained by

$$\tau_a = \frac{\sqrt{6}}{4} \Delta\tau_{Mises} = \frac{\sqrt{3}}{6} \Delta\sigma_{Mises} \quad \text{and} \quad \gamma_a = \frac{\sqrt{3}}{6} \Delta\gamma_{Mises} = \frac{1 + \bar{\nu}}{\sqrt{3}} \Delta\varepsilon_{Mises} \quad (6)$$

Finally, for the linear elastic case, all these relative Mises stresses and strains correlate with the Mises shear range parameters by

$$\Delta\sigma_{Mises} = E \cdot \Delta\varepsilon_{Mises} = \frac{3}{\sqrt{2}} \cdot \Delta\tau_{Mises} = \frac{3E}{2\sqrt{2} \cdot (1 + \bar{\nu})} \cdot \Delta\gamma_{Mises} \quad (7)$$

3 Reduced order stress and strain spaces

When dealing with incremental plasticity, it is convenient to represent the stresses or strains in a 9-dimensional (9D) space. In particular, when representing the deviatoric stress tensor in 9D, its norm $|\bar{S}|$ becomes directly proportional to the Mises stress and octahedral (or Mises) shear stress, namely $|\bar{S}| = \sigma_{Mises} \cdot \sqrt{6}/3 = \tau_{Mises} \cdot \sqrt{3}$. In addition, the Prandtl-Reuss flow rule results in slightly different (and probably better) equations when formulated in 9D space than the equations derived using a reduced 6-dimensional (6D) formulation.

But, to find effective ranges in VA-NP histories, it is a good idea to work in a space with reduced dimensions, saving computational effort without modifying the results. The reduction from 9D to 6D deviatoric stresses is simply a matter of eliminating the τ_{yx} , τ_{zx} and τ_{zy} components from the deviatoric stress tensor, which are redundant because $\tau_{yx} \equiv \tau_{xy}$, $\tau_{zx} \equiv \tau_{xz}$, and $\tau_{zy} \equiv \tau_{yz}$.

Since the deviatoric stresses S_x , S_y and S_z are linear-dependent, because $S_x + S_y + S_z = 0$, it is possible to further reduce the deviatoric stress dimension from 6D to 5D. There are infinite ways to do this, for example replacing the stresses S_x , S_y and S_z by new variables $S_1 \equiv a_{x1} \cdot S_x + a_{y1} \cdot S_y + a_{z1} \cdot S_z$ and $S_2 \equiv a_{x2} \cdot S_x + a_{y2} \cdot S_y + a_{z2} \cdot S_z$, where the user-defined coefficients a_{x1} , a_{y1} , a_{z1} , a_{x2} , a_{y2} and a_{z2} are any values that make the vectors $[a_{x1} \ a_{y1} \ a_{z1}]^T$, $[a_{x2} \ a_{y2} \ a_{z2}]^T$, and $[1 \ 1 \ 1]^T$ become linear independent. A notable example of such transformation is the one proposed by Papadopoulos et al. [6], who chose $[a_{x1} \ a_{y1} \ a_{z1}]^T = [\sqrt{3}/2 \ 0 \ 0]^T$ and $[a_{x2} \ a_{y2} \ a_{z2}]^T = [0 \ 0.5 \ -0.5]^T$, resulting in a reduced-order deviatoric stress tensor \bar{S}' represented in a 5D transformed Euclidean stress-space $E_{5\sigma}$, where

$$\left\{ \begin{array}{l} \bar{S}' \equiv [S_1 \ S_2 \ S_3 \ S_4 \ S_5]^T \\ S_1 \equiv \sigma_x - \frac{\sigma_y}{2} - \frac{\sigma_z}{2} = \frac{3}{2}S_x, \quad S_2 \equiv \frac{\sigma_y - \sigma_z}{2}\sqrt{3} = \frac{S_y - S_z}{2}\sqrt{3} \\ S_3 \equiv \tau_{xy}\sqrt{3}, \quad S_4 \equiv \tau_{xz}\sqrt{3}, \quad S_5 \equiv \tau_{yz}\sqrt{3} \end{array} \right. \quad (8)$$

The above defined 5D deviatoric stress \bar{S}' has three very interesting properties:

1. The norm of the 5D vector \bar{S}' from the $E_{5\sigma}$ transformed deviatoric stress-space is equal to the Mises equivalent stress σ_{Mises}
2. The Euclidean distance in the 5D $E_{5\sigma}$ stress-space between any 2 points $\bar{S}'_A = [S_{1A} \ S_{2A} \ S_{3A} \ S_{4A} \ S_{5A}]^T$ and $\bar{S}'_B = [S_{1B} \ S_{2B} \ S_{3B} \ S_{4B} \ S_{5B}]^T$, respectively associated with the 9D deviatoric stresses \bar{S}_A and \bar{S}_B , is equal to the Mises stress range $\Delta\sigma_{Mises}$ between these stress states
3. The locus of the points which have the same $\Delta\sigma_{Mises}$ with respect to a point \bar{S}' in the $E_{5\sigma}$ deviatoric stress-space is the surface of a hypersphere with center in \bar{S}' and radius $\Delta\sigma_{Mises}$. This is a simple corollary from the second property.

Note that, for unnotched specimens under histories combining uniaxial tension σ_x and torsion τ_{xy} , the 5D deviatoric stress \bar{S}' can be represented in the classical diagram $\sigma_x \times \tau_{xy}\sqrt{3}$ using the 2D projection $[S_1 \ S_3]^T$, since in this case $S_1 = \sigma_x$, $S_3 = \tau_{xy}\sqrt{3}$, and $S_2 = S_4 = S_5 = 0$.

After defining all involved stress and strain parameters, the convex hull methods are discussed. These methods are based on convex hulls enclosing the history path in the above defined stress or strain sub-spaces. There are 3 types of convex hulls: balls, ellipsoids and rectangular prisms. The Minimum Ball method is presented next.

4 Minimum Ball method

Dang Van [1] realized that the search for an effective stress range must take place on the deviatoric stress space. For periodic elastic histories, the mesoscopic stresses and strains in the critically oriented grain should stabilize by the process of elastic shakedown, generating a local residual stress $[\sigma_{ij}]_{res}$ at such critical grain. Dang Van assumed that the subsequent mesoscopic (μ) stress history at such grain, after the stabilization, is related to the macroscopic (M) history through

$$[\sigma_{ij}(t)]_\mu = [\sigma_{ij}(t)]_M + dev[\sigma_{ij}]_{res} \quad (9)$$

where $dev[\sigma_{ij}]_{res}$ is the deviatoric part of the residual stresses tensor stabilized in that grain.

The calculation of the mesoscopic stresses in Dang Van's model can be interpreted as a hardening problem, caused by elastic shakedown. When the periodic macroscopic history is represented in the deviatoric space, Dang Van assumes that the stabilized residual stress is the vector from the center of the minimum ball that circumscribes the history to the origin of the diagram. The word "ball" is used here to describe a circle, sphere or hypersphere, respectively for 2D, 3D or higher dimension histories. The same result holds if the reduced stress $E_{5\sigma}$ space is used, or a sub-space from it.

The values of the mesoscopic Tresca stress $\tau_\mu(t)$ and mesoscopic hydrostatic stress $\sigma_{\mu h}(t)$ (which is equal to the macroscopic hydrostatic stress) are calculated for each point in the mesoscopic history path \mathbf{D}_μ . Dang Van then predicts infinite life if and only if all points satisfy the inequality

$$\tau_\mu(t) + \alpha_{DV}\sigma_{\mu h}(t) \leq \beta_{DV} \quad (10)$$

In summary, Dang Van is a type of Minimum Ball (MB) method where each stress state along the history path is compared to a limiting stress level to predict infinite life. However, it is not useful to calculate finite fatigue lives, since it does not deal with stress (or strain) ranges, only with individual stress states.

But the same MB circumscribed to the macroscopic history can be used to estimate an effective Mises stress range $\Delta\sigma_{Mises}$ (or strain range $\Delta\varepsilon_{Mises}$). The diameter d of such MB in the transformed deviatoric stress-space $E_{5\sigma}$ or strain-space $E_{5\varepsilon}$ (or in a 2D, 3D or 4D sub-space of such spaces) is the magnitude of the variation $\Delta\bar{S}'$ (or the deviatoric strain variation $\Delta\bar{e}'$), which is equal to $\Delta\sigma_{Mises}$ (or $\Delta\varepsilon_{Mises}$). Therefore, the effective shear ranges $\Delta\tau_{max}$ (used in the Findley and McDiarmid models) and $\Delta\gamma_{max}$ (used in the Brown-Miller and Fatemi-Socie models), Mises ranges $\Delta\sigma_{Mises}$ and $\Delta\varepsilon_{Mises}$, and octahedral shear ranges $\Delta\tau_{Mises}$ (used in the Sines and Crossland models) and $\Delta\gamma_{Mises}$, can all be estimated from d using the MB method by

$$\begin{aligned} \Delta\sigma_{Mises} &= 3 \cdot \Delta\tau_{Mises}/\sqrt{2} = \Delta\tau_{max}\sqrt{3} = (2\tau_a) \cdot \sqrt{3} = |\Delta\bar{S}'| = d \equiv L \cdot \lambda_{MB} \quad \text{or} \\ \Delta\varepsilon_{Mises} &= 3 \cdot \frac{\Delta\gamma_{Mises}}{2\sqrt{2}(1+\bar{\nu})} = \frac{\Delta\gamma_{max}\sqrt{3}}{2(1+\bar{\nu})} = \frac{(2\gamma_a) \cdot \sqrt{3}}{2(1+\bar{\nu})} = |\Delta\bar{e}'| = d \equiv L \cdot \lambda_{MB} \end{aligned} \quad (11)$$

where L is the longest chord in the history (the maximum Euclidean distance in the transformed space between any two points along the history path, measured in either stress or strain units) and λ_{MB} is a dimensionless parameter defined as the ratio between the Mises stress or strain range and L .

In the 2D case, if any two points from the history define the diameter of a circle that contains the entire path, then their distance L is equal to the diameter d , therefore $\lambda_{MB} = 1.0$. A notable 2D case is for a path forming an equilateral triangle, where $\lambda_{MB} = 2/\sqrt{3} \cong 1.155$. For any other 2D path, it is found that $1.0 \leq \lambda_{MB} \leq 1.155$.

5 Minimum Ellipsoid methods

The Minimum Ball (MB) method is not efficient to represent the behavior of NP histories. For instance, it would predict the same Mises ranges for a NP 90° out-of-phase circular path and a proportional path defined by a diameter of this circle, both resulting in $\lambda_{MB} = 1.0$. But a higher value of λ_{MB} would certainly be expected for the NP history.

To solve this problem, Freitas et al. [2] proposed the Minimum Circumscribed Ellipsoid (MCE) method. It searches for an ellipse (or ellipsoid or hyperellipsoid, for higher dimensions) that circumscribes the entire history, with its longest semi-axis a_1 equal to the radius of the minimum ball, and with the smallest possible values for the remaining semi-axes a_i ($i > 1$). The Mises ranges are

$$\Delta\sigma_{Mises} \text{ or } \Delta\varepsilon_{Mises} = 2 \cdot \sqrt{\sum_{i=1}^{\dim} a_i^2} \equiv 2 \cdot F \quad (12)$$

where dim is the dimension of the history path, $2 \leq dim \leq 5$, and F is defined as the Frobenius norm of the ellipsoid, which is equal to the square root of the sum of the squares of the ellipsoid semi-axes. Here, the Frobenius norm is essentially an Euclidean distance (or Euclidean norm) between the origin and a point with coordinates $(a_1, a_2, \dots, a_{dim})$, since the axes of the reduced stress (or strain) space are orthonormal. In the case of tensors, the Euclidean norm is commonly called the Frobenius norm, usually abbreviated as F-norm.

The ratio λ_{MCE} between the Mises ranges calculated by the MCE method and the longest chord L reproduces experimental data better than λ_{MB} generated by the MB method. In the 2D case, a NP circular path would result in $\lambda_{MCE} = \sqrt{2}$ instead of the proportional value 1.0 , which is much more reasonable than the Minimum Ball prediction. It is also found that any 2D path results in $1.0 \leq \lambda_{MCE} \leq \sqrt{2}$, with the maximum value occurring e.g. for circular and square paths. In general, for any dimension dim , it is found that $1.0 \leq \lambda_{MCE} \leq \sqrt{dim}$, with the maximum value \sqrt{dim} occurring e.g. for paths that follow the edges of hypercubes or large portions of the surface of hyperspheres.

The downside of the MCE method is the requirement that the longest semi-axis must be equal to the radius of the Minimum Ball. For the rectangular path shown in Fig. 4, this requirement results in a circle as the minimum circumscribed ellipse, with $\lambda_{MCE} = \sqrt{2} \cong 1.414$. But this would be true even for very elongated rectangles with very low aspect ratios between their side lengths. The MCE would thus predict $\lambda_{MCE} = \sqrt{2}$ for an almost proportional rectangular path, instead of the expected value of 1.0 .

A possible alternative to the MCE method is to search for the Minimum Volume Ellipsoid (MVE), also known as the Löwner-John Ellipsoid. In the 2D case, it is basically the search for an enclosing ellipse with minimum area. Such MVE method solves the issue with rectangular paths, however it tends to find ellipses with lower aspect ratios than expected. In addition, the search for such ellipsoid or hyperellipsoid can be computationally intensive for 3D or higher dimension histories.

Another alternative to the MCE method is the search for the Minimum F-norm Ellipsoid (MFE) [3]. Instead of searching for the minimum volume (or area), the MFE looks for the ellipse, ellipsoid, or hyperellipsoid with minimum value of its F-norm F , defined in Eq. (12). Zouain et al. [4] present an efficient (although computationally intensive) method to numerically find such MFE. Other efficient algorithms can be found in [7].

The ratios between the Mises stress or strain ranges $2 \cdot F$, calculated from the MCE, MVE and MFE methods, and the longest chord L are defined, respectively, as λ_{MCE} , λ_{MVE} and λ_{MFE} . All these ratios must be greater than or equal to 1.0 . In the 2D case, a notable path is the one with the shape of an equilateral triangle with sides L (which are also its longest chords), where the resulting hull is a circle with diameter $d = 2L/\sqrt{3}$ and F-norm $F = d\sqrt{2}$, resulting in $\lambda_{MCE} = \lambda_{MVE} = \lambda_{MFE} = 2 \cdot F/L = 2\sqrt{2}/\sqrt{3} \cong 1.633$. For any other 2D path, it is found that $1.0 \leq \lambda_{MCE} \leq 1.633$ and $1.0 \leq \lambda_{MFE} \leq 1.633$, however λ_{MVE} can reach values beyond 2.0 when a very elongated enclosing ellipse is the solution with minimum area, an indication that the MVE method can be very conservative.

6 Maximum Prismatic Hull methods

Another class of convex hull methods tries to find a rectangular prism with sides $2a_1, \dots, 2a_{dim}$ that encloses a load history path, where dim is the dimension of the considered space. There are essentially 4 methods to fit rectangular prisms to the history path.

The first is the Maximum Prismatic Hull (MPH). This method searches for the smallest rectangular prism that encloses the history (the minimum prism), for each possible orientation of the prism. Among them, the one with highest F-norm is chosen. The F-norm and resulting Mises ranges are the same defined in Eq. (12), except that here a_i are the semi-lengths (half the length) of the sides of the rectangular prism. The MPH was originally proposed by Gonçalves et al. in [3] for sinusoidal time histories, and later extended by Mamiya et al. in [5] for a general NP loading.

Another prismatic hull method is the Maximum Volume Prismatic Hull (MVPH), which searches among the minimum prisms the one with maximum volume. Although the search is for a maximum volume, the F-norm is also used to compute the Mises range. In the 2D case, the MVPH method is essentially the search, among the minimum rectangles that enclose the entire path, of the one with maximum area (it's a max-min problem).

A third method is proposed here, called the Maximum Prismatic Hull with Longest Chords (MPHLC). It is basically an improvement of Deperrois' method [8]. In the Deperrois method, the longest chord L_5 between any two points of the path in the projected 5D deviatoric stress-space $E_{5\sigma}$ (or deviatoric strain-space $E_{5\epsilon}$, for strain histories) is determined. Then, the path is projected onto a 4D stress-subspace $E_{4\sigma}$ orthogonal to L_5 , and the new longest chord L_4 is computed in this subspace. The path is then projected onto a stress-subspace $E_{3\sigma}$ orthogonal to both L_5 and L_4 , and the new longest chord L_3 is computed in this subspace. Analogously, the longest chord L_2 is found in the stress-subspace $E_{2\sigma}$ orthogonal to L_5 , L_4 and L_3 . Finally, the longest chord L_1 is found in the stress-subspace $E_{1\sigma}$ orthogonal to L_5 , L_4 , L_3 and L_2 .

The Deperrois method provides satisfactory results [9]. However, Papadopoulos [6] criticizes it because, if any longest chord is non-unique, then different rectangular prisms and resulting shear amplitudes could be obtained for the same history. But this non-uniqueness could be easily solved by stating that, when the longest chords are non-unique, then the chosen prismatic hull would be the one with maximum F-norm among all possible results. The use of rectangular prisms with maximum F-norm has shown good results in the MPH method, therefore this could be the solution to Papadopoulos' criticisms.

The combination of the MPH and Deperrois' methods thus leads to the MPHLC method, performed in 4 steps:

1. define the longest side $2a_1$ of the rectangular prism in the direction of the longest chord L of the history;
2. project the history into the sub-space orthogonal to the directions of all sides of the prisms that have already been defined (for a history with dimension dim , if m sides have already been chosen, then such sub-space will have $dim - m$ dimensions);
3. define the next side $2a_i$ of the rectangular prism in the direction of the longest chord measured in the projected sub-space, and repeat step 2 until all sides are found;

4. if multiple solutions for the rectangular prism are found, the one with maximum F-norm is chosen – this step addresses Papadopoulos' criticisms [6].

The advantage of the MPHLC method over the MPH or MVPH is that it does not require a numerical search for the prismatic hull orientation. Its orientation is deterministically defined by the longest chords. In special for 3D or higher dimension histories, the MPHLC method can lead to a huge decrease in computational effort. For instance, the orientation of a 5D hyperprism is given by 10 angles, therefore the search for the orientation associated with maximum F-norm (or maximum volume) involves a search in a 10-dimensional space, which can be very costly. In addition, the next sections will show that the MPHLC predictions give almost the same results as the MPH and MVPH methods.

A variation of the MPHLC is also proposed, called the Maximum Prismatic Hull with Container Chords (MPHCC). It is similar to the MPHLC, but all chords that contain the orthogonal projection of the entire history onto them (called here “container chords”) are considered as candidate directions for the sides of the rectangular prism. Note that every longest chord LC is a “container chord” CC, but not every CC is a LC. From the probable multiple solutions for the resulting rectangular prisms, the one with maximum F-norm is chosen.

The ratios between the Mises stress or strain ranges $2.F$, calculated from the MPH, MVPH, MPHLC and MPHCC methods, and the longest chord L are defined, respectively, as λ_{MPH} , λ_{MVPH} , λ_{MPHLC} and λ_{MPHCC} . All these four ratios are, in average, very close to each other, therefore any of the four variations of the prismatic hull methods could be used interchangeably. For a history path with dimension dim , it is found that $1 \leq \lambda_{MPHLC} \leq \lambda_{MPHCC} \leq \lambda_{MPH} \leq \sqrt{dim}$, therefore the MPHCC results in Mises ratios slightly closer to the MPH predictions than the MPHLC. In addition, it is also found that $1 \leq \lambda_{MVPH} \leq \lambda_{MPH} \leq \sqrt{dim}$.

In the next section, all convex hull methods presented in this paper are evaluated and compared.

7 Comparison among the Convex Hull methods

To compare all convex hull methods, it is necessary to study all possible history path topologies in 2D, 3D, 4D and 5D deviatoric stress or strain spaces. placeMonte Carlo simulations are performed for $3 \cdot 10^6$ random 2D history paths, in addition to a few selected paths to try to cover all possible path topologies. All convex hull methods are applied to each of these simulated paths, to evaluate and compare the λ predictions.

Figure 2 compares the λ ratios estimated from the MPH and MPHCC methods, for the $3 \cdot 10^6$ Monte Carlo simulations. The point $(\lambda_{MPH}, \lambda_{MPHCC}) = (1, 1)$ in the graph denotes a proportional path, while the point $(\sqrt{2}, \sqrt{2})$ is obtained for rectangular or circular paths. The “belly” in the graph under the straight line $\lambda_{MPHCC} = \lambda_{MPH}$ shows that the MPHCC tends to underestimate λ when compared to the MPH, as expected. However, the points located in this “belly” are quite rare: for 2D paths, in average, λ_{MPHCC} is about 98% of λ_{MPH} , with a standard deviation of only 2%. And, even for the rare paths where the $(\lambda_{MPH}, \lambda_{MPHCC})$ points are located in such “belly,” λ_{MPHCC} never underestimates λ_{MPH} by more than 10%. In addition, the MPHLC and MPHCC usually give almost identical results, with λ_{MPHLC} being in average about 99.85% of λ_{MPHCC} , with a standard deviation

of only 0.9% for these $3 \cdot 10^6$ simulations.

The Monte Carlo simulations are now used to compare the other convex hull methods. Figure 3 shows that the MPH and MVPH have a very good agreement, except for low values of λ . In addition, $\lambda_{MVPH} \leq \lambda_{MPH}$ and, in average, λ_{MVPH} is about 98.6% of λ_{MPH} , with a standard deviation of only 1.8%. Similar conclusions are found for 3D, 4D and 5D histories.

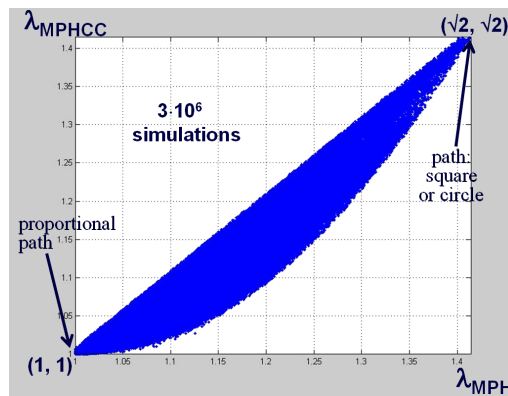


Figure 2: Comparison between the λ ratios predicted by the MPH and MPHCC methods for $3 \cdot 10^6$ Monte-Carlo simulations with random 2D history paths.

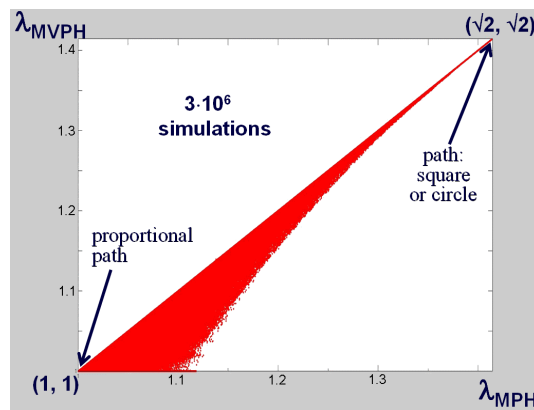


Figure 3: Comparison between the λ ratios predicted by the MPH and MVPH methods for $3 \cdot 10^6$ Monte-Carlo simulations with random 2D history paths.

Figure 4 compares the MPH and MFE methods in 2D. Even though these methods seem coherent in the graph, they can lead to very different λ predictions. It is found that $\lambda_{MFE} \geq \lambda_{MPH}$ and, in average, λ_{MPH} is about 92.9% of λ_{MFE} , with a standard deviation of 4.3%. Similar conclusions are found for 3D, 4D and 5D histories. Note that the point $(\lambda_{MPH}, \lambda_{MFE}) = (0.5 + \sqrt{3}/2 \cong 1.366, 2\sqrt{2}/\sqrt{3} \cong 1.633)$ in the graph denotes the (extreme) case of a path with the shape of an equilateral triangle. This significant difference between λ predictions suggests that a path shaped like an equilateral triangle would provide a very good discriminant experiment to compare the adequacy of the MPH and MFE methods for a certain material.

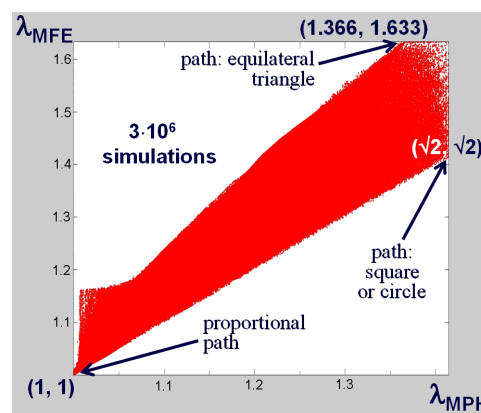


Figure 4: Comparison between the λ ratios predicted by the MPH and MFE methods for 3.10^6 Monte-Carlo simulations with random 2D history paths.

Figure 5 compares the MPH and MVE methods in 2D. It is easy to see from the graph that the MVE method can severely (and wrongfully) overestimate λ , in special for low values of λ_{MPH} , associated with almost proportional paths. As discussed before, almost proportional paths can lead to overly elongated ellipses in the MVE method, which can have a small area but an unrealistically large F-norm, leading to λ_{MVE} values larger than 2.0 in some extreme cases. Similar conclusions are found for 3D, 4D and 5D histories.

Figure 6 compares the MFE and MCE methods in 2D, suggesting that λ_{MCE} overestimates λ , in special for low values of λ_{MFE} , associated with almost proportional paths. For instance, for an almost proportional history defined by a rectangular path with very low aspect ratio, the expected λ would be close to 1.0 (which is the expected value of λ for proportional histories), however the MCE method would circumscribe a circle (instead of an elongated ellipse) to such elongated rectangular path, wrongfully predicting $\lambda_{MCE} = \sqrt{2}$. An almost proportional triangular path would also result in this same notable point $(\lambda_{MFE}, \lambda_{MCE}) = (1, \sqrt{2})$ in the graph, revealing the inadequacy of the MCE method. Similar conclusions are found for 3D, 4D and 5D histories.

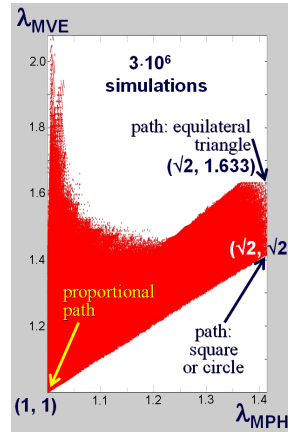


Figure 5: Comparison between the λ ratios predicted by the MPH and MVE methods for $3 \cdot 10^6$ Monte-Carlo simulations with random 2D history paths.

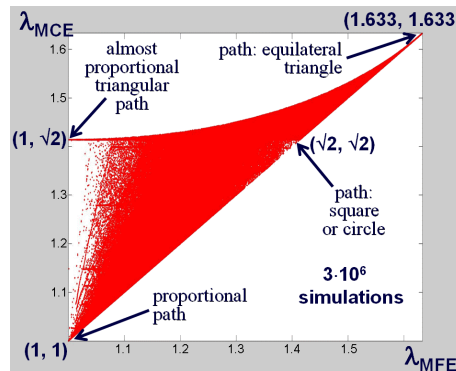


Figure 6: Comparison between the λ ratios predicted by the MFE and MCE methods for $3 \cdot 10^6$ Monte-Carlo simulations with random 2D history paths.

Figure 7 compares the MFE and MB methods in 2D. It is easy to see from the graph that the MB method can severely (and wrongfully) underestimate λ , except for almost proportional load histories (where $\lambda_{MB} \cong \lambda_{MFE} \cong 1.0$). Good discriminant experiments to confirm the inadequacy of the MB method could make use of a square or circular path, where $(\lambda_{MFE}, \lambda_{MB}) = (\sqrt{2}, 1)$, or a path shaped as an equilateral triangle, where $(\lambda_{MFE}, \lambda_{MB}) = (2\sqrt{2}/\sqrt{3} \cong 1.633, 2/\sqrt{3} \cong 1.155)$, see Fig. 7. Both cases would result in $\lambda_{MFE}/\lambda_{MB} = \sqrt{2}$, a 41% difference that could be easily verified experimentally. Similar conclusions are found for 3D, 4D and 5D histories.

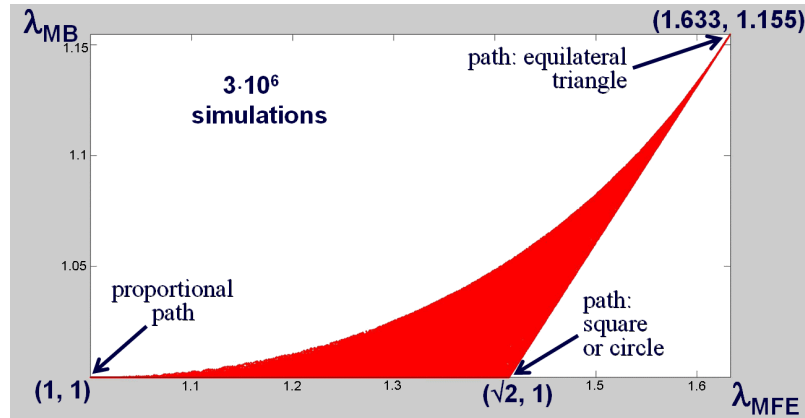


Figure 7: Comparison between the λ ratios predicted by the MFE and MB methods for 3.10^6 Monte-Carlo simulations with random 2D history paths.

8 Conclusions

In this work, all convex hull methods from the literature were reviewed and compared, and new methods were proposed. The conclusions from the comparisons are:

1. the prismatic hull methods MPHLC and MPHCC are very similar to the MPH and MVPH methods, but with a much simpler search algorithm for 3D to 5D histories;
2. the only recommended ellipsoid hull is the Minimum F-norm Ellipsoid (MFE), which results in similar (but not equal) λ predictions when compared to the prismatic hull methods; and
3. the Minimum Circumscribed Ellipsoid (MCE), Minimum Volume Ellipsoid (MVE), and Minimum Ball (MB) methods may result in very poor predictions of the stress or strain amplitudes.

In summary, the Minimum F-norm Ellipsoid and all four Maximum Prismatic Hull (MPH) models are efficient to predict equivalent amplitudes in NP histories.

References

- [1] Dang Van, K. & Papadopoulos, I., *High-Cycle Metal Fatigue*. Springer, 1999.
- [2] Freitas, M., Li, B. & Santos, J., Multiaxial fatigue and deformation: Testing and prediction. *ASTM STP 1387*, 2000.
- [3] Gonçalves, C., Araújo, J. & Mamiya, E., Multiaxial fatigue: a stress based criterion for hard metals. *International Journal of Fatigue*, **27**, pp. 177–187, 2005.
- [4] Zouain, N., Mamiya, E. & Comes, F., Using enclosing ellipsoids in multiaxial fatigue strength criteria. *European Journal of Mechanics – A, Solids*, **25**, pp. 51–71, 2006.
- [5] Mamiya, E., Araújo, J. & Castro, F., Prismatic hull: A new measure of shear stress amplitude in multiaxial high cycle fatigue. *International Journal of Fatigue*, **31**, pp. 1144–1153, 2009.

- [6] Papadopoulos, I., Davoli, P., Gorla, C., Filippini, M. & Bernasconi, A., A comparative study of multiaxial high-cycle fatigue criteria for metals. *Int Journal of Fatigue*, **19**, pp. 219–235, 1997.
- [7] Bernasconi, A., Efficient algorithms for calculation of shear stress amplitude and amplitude of the second invariant of the stress deviator in fatigue criteria applications. *International Journal of Fatigue*, **24(6)**, pp. 649–657, 2002.
- [8] Deperrois, A., *Sur le calcul des limites d'endurance des aciers*. Ph.D. thesis, Ecole Polytechnique, Paris, 1991.
- [9] Ballard, P., Dang Van, K., Deperrois, A. & Papadopoulos, I., High cycle fatigue and a finite element analysis. *Fatigue Fract Engng Mater Struct*, **18(3)**, pp. 397–411, 1995.

Modeling nonlinear viscoelastic behavior of high density polyethylene (HDPE): application of stress-time equivalence versus interpolation of rheological properties

Pablo A. Muñoz-Rojas, André Kühn

*Departamento de Engenharia Mecânica, Univ. do Estado de Santa Catarina,
Campus Universitário Avelino Marcante s/n, Bom Retiro, 89223-100,
Joinville, SC – Brazil*

Paulo T. R. de Mendonça

*Grante – Grupo de Análise de Tensões, Departamento de Engenharia Mecânica,
Univ. Federal de Santa Catarina, 88040-900, Florianópolis, SC – Brazil*

Isac J. Benvenutti

Vettore Engenharia Ltda., Costa e Silva, 89219-200, Joinville, SC – Brazil

Guillermo J. Creus

*CEMACOM – EE, Universidade Federal do Rio Grande do Sul, 90035-190,
Porto Alegre, RS – Brazil*

Abstract

In recent years, favored by good strength/stiffness ratio and to chemical inertness, high density polyethylene (HDPE) has gained sustained and increasing space in civil construction, particularly for use in pipe manufacturing. Pipelines made of this material are laid either submersed or buried for water and gas transportation. Owing to typical polymeric viscoelastic (time-dependent) material behavior, a proper design using these materials must account for long term effects. Linear viscoelasticity implies that creep deformation of the material for different load levels differ only by a scale factor. However, some polymers – as HDPE – present a nonlinear stress dependence even at very low stresses, which makes their modeling more involved. In this work, two modeling approaches to account for nonlinear viscoelasticity are compared: the stress-time equivalence and a new method based on the interpolation of Prony coefficients which are obtained experimentally in uniaxial creep tests for different stress levels. In both cases, the generalized Kelvin rheological model is adopted. The strategies are applied to HDPE samples taken from water distribution pipes. It is observed that the approach that interpolates the Prony coefficients is simpler and provides better results in all the considered cases. A slight modification with respect to the original formulation of the interpolation procedure is proposed in this work, which shows better agreement with experimental results.

Keywords: nonlinear viscoelasticity, high density polyethylene, stress-time equivalence.

1 Introduction

High Density Polyethylene (HDPE) is a semi-crystalline thermoplastic which, according to Lai [1], exhibits a unique combination of excellent properties such as abrasion and impact resistance, outstanding fatigue behavior and an optimum balance between stiffness, creep behavior and processability. Owing to these properties, the use of HDPE in structural engineering applications has gained sustained increase in last years. In particular, due to the additional feature of chemical inertness, a growing application is the manufacture of submersed or buried large-diameter pipes for water and oil distribution [2, 3]. Figure 1 shows the laying of a submersed water pipeline for distribution of fresh water in the coast of São Francisco do Sul, Santa Catarina, Brazil [4].



Figure 1: Use of HDPE for submersed water distribution pipes.

Polymers exhibit viscoelastic (and possibly viscoplastic) material behavior, and so, their constitutive relation is a function of time. Two time scales can be considered in this context: the first one refers to chronological time, which can be measured in a clock; and the second one is a material intrinsic time, which can be determined via a relaxation test and is influenced by different factors such as temperature, damage, stress and strain levels, etc [5].

Viscoelastic and viscoplastic behavior can be linear or nonlinear, and usually a given material will behave either linearly or nonlinearly depending on the stress level. Although not a unanimous opinion, HDPE is generally considered to exhibit a nonlinear viscoelastic behavior up to nearly vanishing stresses [6]. Some researchers even hold that for these materials there is no threshold under which the viscolastic behavior is linear. This statement has been questioned, for instance by Elleuch and Taktak [7], who found a linear viscoelastic behavior for HDPE in both tensile and compressive creep tests in the range of 3 to 10 MPa. In fact, a correlation between linear-nonlinear viscoelastic behavior and temperature is presented by Papanicolau et al. [8]. If experimental evidence leads to nonlinear viscoelastic behavior in the full stress range at a given temperature for HDPE, the Boltzmann superposition principle cannot be used to determine strains, and a different strategy must be sought for.

Many theories exist for this purpose, but all of them bring practical difficulties. Among the possibilities described in the literature, the Schapery model [9] is the most frequently employed. Nonetheless, two methods which seem to be simpler to use in practice are studied in this work. These methods are the stress-time equivalence [5, 6, 10–14] and a procedure based on interpolation of rheological properties proposed by Liu et al. [3]. It is noteworthy that the former is many times used in conjunction with the Schapery model, but in the present study a different approach will be discussed.

2 Linear and nonlinear viscoelasticity modeling

2.1 Linear viscoelasticity

In linear viscoelasticity, for given constant constitutive parameters, the material response depends only on time and the Boltzmann superposition principle can be applied. Linear viscoelastic models can be expressed either in differential or integral forms. While an integral representation of the time-dependent stress is given by

$$\sigma(t) = \int_0^t D(t - \tau) \dot{\varepsilon}(\tau) d\tau, \quad (1)$$

the analogous integral representation for time-dependent strain is given by

$$\varepsilon(t) = \int_0^t J(t - \tau) \dot{\sigma}(\tau) d\tau \quad (2)$$

where $D(t)$ is a stress-relaxation function and $J(t)$ is a creep-compliance function, both known in advance. Since linear viscoelastic material properties are ideally independent of experimental tests, Eqs. (1) and (2) completely define the material response.

Phenomenological modeling requires macroscopic evaluation of the stress-relaxation and creep-compliance functions. In the latter, stress is kept constant and strain is monitored in time. Hence, Eq. (2) becomes

$$\varepsilon(t) = \sigma_C J(t) \quad (3)$$

Material modeling aims to find the creep-compliance function $J(t)$ which best matches experimental tests. In order to represent the creep-compliance, different rheological models can be used. The present work adopts the generalized Kelvin model, which consists of a spring and a series of dashpots and springs in parallel, as displayed in Fig. 2. The inclusion of the spring sometimes is emphasized by naming the model as *generalized Voigt-Kelvin solid model* [15].

The material properties are the spring (E_0, E_i) and dashpot (η_i) coefficients in the Kelvin arrangement. From these, the relaxation time ($\tau_i = \eta_i/E_i$) can be defined. Each lower index i corresponds to a *rheological block*.

When subjected to a constant unit stress state during a finite time interval, linear viscoelastic materials show an instantaneous elastic strain, followed by a viscous strain which grows along time.

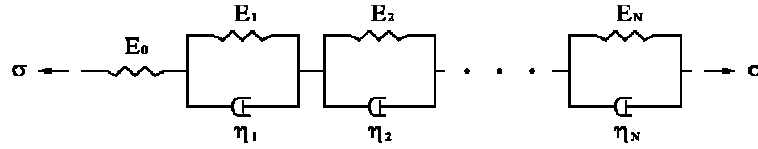


Figure 2: Generalized Kelvin viscoelastic model.

This behavior is represented by the Kelvin model in Fig. 2 and the corresponding exponential equation, in terms of a Prony series is given by

$$J(t) = J_e + J_v(t) = \frac{1}{E_0} + \sum_{i=1}^{nr b} \frac{1}{E_i} \left(1 - e^{-\frac{t}{\tau_i}}\right) \quad (4)$$

where J_e represents the instantaneous elastic component, $J_v(t)$ represents the time-dependent viscoelastic effects and $nr b$ stands for the number of rheological blocks adopted. No attempt is made here to evaluate and/or model the presence of permanent strain. The material constants are the elasticity E_0 , which defines the instantaneous response and the moduli E_i , which correspond to the relaxation time τ_i . When the compliance functions are independent of the stress level, the model given by Eq. (4) is linear [3].

2.2 Nonlinear viscoelasticity

Several polymeric materials, such as HDPE, exhibit simultaneous dependence on stress and time for a given temperature. In these cases, a single compliance curve does not suffice to describe the material behavior. In creep tests, for each stress level a different compliance curve is found and so, different material parameters must be identified (see Fig. 3).

Equation (4) can be adapted for the nonlinear case as

$$J(\sigma, t) = J_e(\sigma) + J_v(\sigma, t) = \frac{1}{E_0(\sigma)} + \sum_{i=1}^{nr b} \frac{1}{E_i(\sigma)} \left(1 - e^{-\frac{t}{\tau_i(\sigma)}}\right) \quad (5)$$

where $E_0(\sigma)$ and $E_i(\sigma)$ are stress dependent functions, which must be appropriately found for a successful modeling. Then, the nonlinear constitutive response is given by replacement of Eq. (5) in Eq. (2), yielding

$$\varepsilon(t) = \int_0^t \{J(\sigma, t - \tau)\} \dot{\sigma}(\tau) d\tau \quad (6)$$

2.2.1 Interpolation of rheological properties

Liu et al. [3] proposed a simple procedure to account for the nonlinear dependence of the creep-compliance on stress. The procedure can be summarized in the following steps:

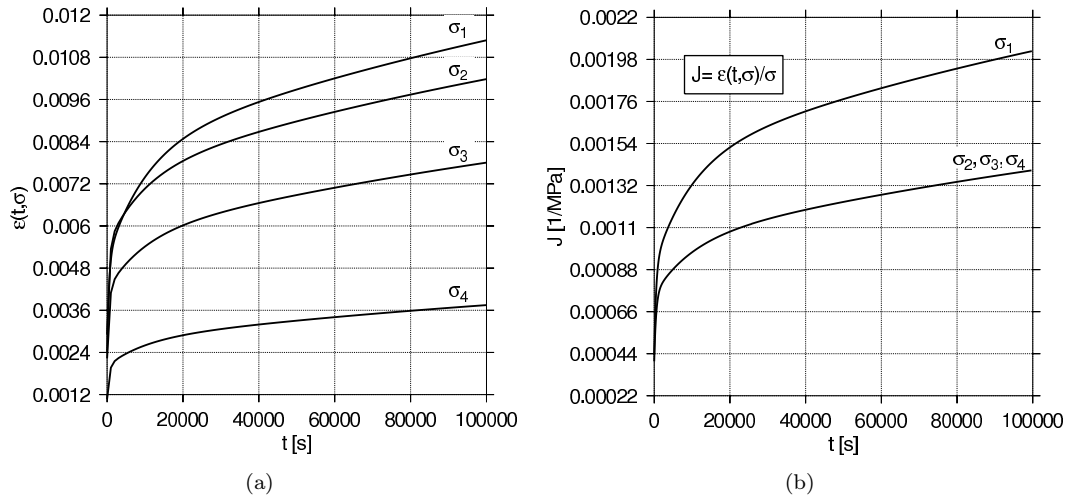


Figure 3: Linear and nonlinear viscoelasticity. (a) Strain and (b) creep-compliance curves for different stress levels: the behavior associated to σ_1 characterizes nonlinear viscoelasticity.

1. Step 1: Creep tests are conducted for different stress levels ($\sigma_1, \dots, \sigma_n$);
2. Step 2: For each stress level a set of material parameters ($E_0, E_i, \tau_i, i = 1, n_{nr}, b$) is obtained using Eq. (5) and least-squares fitting (the same number of parameters must be considered for each stress level);
3. Step 3: The compliance curve at any arbitrary stress state is obtained by Eq. (5) in which the material parameters are obtained via linear interpolation based on the values found in Step 2.

In step 2, a finite number of rheological blocks must be adopted. In his work, Liu considered three rheological blocks to be enough in order to obtain acceptable errors for engineering purposes. He proposed to evaluate the material parameters for intermediate stresses using the following linear interpolation

$$J_i(\sigma) = \frac{1}{E_i(\sigma)} = J_i(\sigma_m) + \frac{\sigma - \sigma_m}{\sigma_n - \sigma_m} [J_i(\sigma_n) - J_i(\sigma_m)] \quad (7)$$

where $J_i = 1/E_i$; σ_m and σ_n are the stresses corresponding to step 1, such that $\sigma_m < \sigma < \sigma_n$.

The use of a reciprocal variable simplifies the least-squares fitting in step 2, leading to a linear programming problem. The static stiffness (instantaneous response) $E_0(\sigma)$, is interpolated directly by

$$E_0(\sigma) = E_0(\sigma_m) + \frac{\sigma - \sigma_m}{\sigma_n - \sigma_m} [E_0(\sigma_n) - E_0(\sigma_m)] \quad (8)$$

Since linear interpolation of the reciprocals might lead to substantial error, as depicted in Fig. 4, this work introduces a slight modification to the interpolation in Eq. (7). The least-squares fitting is

performed in terms of compliance coefficients, but these are inverted before executing the interpolation. Hence, the following expression is proposed:

$$E_i(\sigma) = E_i(\sigma_m) + \frac{\sigma - \sigma_m}{\sigma_n - \sigma_m} [E_i(\sigma_n) - E_i(\sigma_m)] \quad (9)$$

Although the proposed procedure results in enhanced accuracy, it has the disadvantage that if the nonlinear fit leads to $J_i = 0$, the inverse is infinity and cannot be interpolated. Thus, this situation must be avoided.

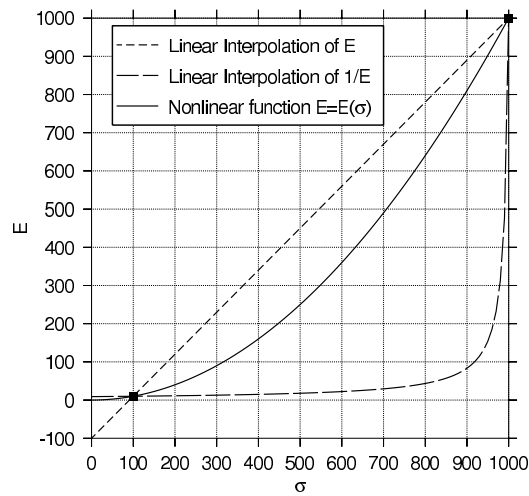


Figure 4: Interpolation of material properties.

2.2.2 Temperature-stress-time equivalence

The principle of stress – temperature – time equivalence is based on the theory of free volume. According to Riande et al. [16], the free volume is the space in a solid or liquid which is not occupied by the molecules (intermolecular space). Within this theory, the material viscosity, η , can be defined by the free volume fraction (f) through Doolittle's equation:

$$\eta = Ae^{B/f} \quad (10)$$

where A and B are material constants.

The dependence of the fraction of free volume on a temperature change is widely considered to be linear, and given by

$$f = f_0 + \alpha_T(T - T_0) \quad (11)$$

where α_T is the thermal expansion coefficient of the free volume's fraction and f_0 is the fraction of free volume at the reference temperature. A time-temperature shift factor can be defined by $\varphi_T = \tau/\tau_0 = \eta/\eta_0$, where η_0 and τ_0 are the viscosity of the material and the relaxation time at a reference temperature T_0 ; and η and τ are the viscosity of the material and the relaxation time in an arbitrary temperature T [5], so that

$$\log \varphi_T = \frac{B}{2.303} \left(\frac{1}{f} - \frac{1}{f_0} \right) \quad (12)$$

Replacing Eq. (11) in (12), results in the William-Landel-Ferry (WLF) equation [12, 16]

$$\log \varphi_T = -\frac{B}{2.303} \left(\frac{T - T_0}{f_0/\alpha_T + T - T_0} \right) = \frac{-C_1(T - T_0)}{C_2 + (T - T_0)} \quad (13)$$

where $C_1 = B/(2.303f_0)$ and $C_2 = f_0/\alpha_T$.

Based on a similar reasoning, Bernstein and Shokoh [11] proposed the concept of "stress-clock" or stress-time equivalence. In this theory, it is assumed that just as the relaxation time is affected by temperature, it is also affected by the applied stress level, which modifies the free volume fraction. Considering the influence of both, temperature and stress on the free volume fraction, Eq. (11) can be modified to [5]

$$f = f_0 + \alpha_T(T - T_0) + \alpha_\sigma(\sigma - \sigma_0) \quad (14)$$

where α_σ is the stress-induced expansion coefficient of the free volume fraction. Supposing that there exists a shift factor $\varphi_{T\sigma}$, which combines stress and temperature effects and satisfies

$$\eta(T, \sigma) = \eta(T_0, \sigma_0)\varphi_{T\sigma} \quad (15)$$

It comes from Eq. (10) and (14) that

$$\log \varphi_{T\sigma} = -C_1 \left[\frac{C_3(T - T_0) + C_2(\sigma - \sigma_0)}{C_2C_3 + C_3(T - T_0) + C_2(\sigma - \sigma_0)} \right] \quad (16)$$

where $C_3 = f_0/\alpha_\sigma$.

If there is no change in stress, Eq. (16) reduces to Eq. (13). A stress shift factor at constant temperature, and a temperature shift factor at constant stress are defined as φ_σ^T and φ_T^σ , respectively. These shift factors result from

$$\eta(T, \sigma) = \eta(T, \sigma_0)\varphi_\sigma^T = \eta(T_0, \sigma_0)\varphi_T^{\sigma_0}\varphi_\sigma^T = \eta(T_0, \sigma)\varphi_T^\sigma = \eta(T_0, \sigma_0)\varphi_\sigma^{T_0}\varphi_T^\sigma \quad (17)$$

so that

$$\log \varphi_{\sigma}^T = -C_1 \frac{C_2}{C_2 + (T - T_0)} \left[\frac{C_2(\sigma - \sigma_0)}{C_2 C_3 + C_3(T - T_0) + C_2(\sigma - \sigma_0)} \right] \quad (18)$$

$$\log \varphi_T^{\sigma} = -C_1 \frac{C_3}{C_3 + (\sigma - \sigma_0)} \left[\frac{C_3(T - T_0)}{C_2 C_3 + C_3(T - T_0) + C_2(\sigma - \sigma_0)} \right] \quad (19)$$

From Eq. (14) and (16), it follows that

$$\varphi_{T\sigma} = \varphi_T^{\sigma_0} \varphi_{\sigma}^T = \varphi_{\sigma}^{T_0} \varphi_T^{\sigma} \quad (20)$$

It must be emphasized that temperature and stress shifts are only allowed for thermorheologically and piezorheologically simple materials, respectively [17]. Provided these conditions are satisfied, it is shown from Eq.(20) that time-dependent mechanical properties of viscoelastic materials at different temperatures and stress levels can be shifted along the time scale to construct a master curve, valid in a wider time scale, at a given temperature T_0 and stress σ_0 . This shifting can be performed in one step by the application of the combined stress-temperature shift factor $\varphi_{T\sigma}$, or in two steps by the sequential application of the stress and the temperature shift factors φ_{σ}^T and φ_T^{σ} [5]. HDPE is a semi-crystalline polymer, and thus not thermorheologically simple, so time-temperature equivalence cannot be applied. However, successful application of the stress-time equivalence has been reported in some references [5, 6].

Defining φ_{σ} as the stress shift factor at reference temperature T_0 ,

$$\log \varphi_{\sigma} = -\frac{C_1(\sigma - \sigma_0)}{C_3 + (\sigma - \sigma_0)} \quad (21)$$

the *creep-compliance* curves at different stress levels can be related by the concept of reduced time ξ ($\xi = t/\varphi_{\sigma}$) as

$$J(t, \sigma) = b_{\sigma} J(t/\varphi_{\sigma}, \sigma_0) = \tilde{J}(\xi, \sigma_0) \quad (22)$$

where $\tilde{J}(\xi, \sigma_0)$ is the *creep-compliance master curve* at the reference stress σ_0 , and b_{σ} is the vertical shift factor which reflects the effects of microstructural changes due to the induced stress on the mechanical properties of the material and has the form below, similar to the horizontal stress shift factor

$$\log b_{\sigma} = -\frac{D_1(\sigma - \sigma_0)}{D_2 + (\sigma - \sigma_0)} \quad (23)$$

where D_1 and D_2 are material constants. In the present work b_{σ} has not been considered.

3 Parameters identification and models fitting

The nonlinear viscoelastic modeling approaches described in Section 2 were coded using Maple software, which gives access to numerical libraries, including optimization routines and enables the use of symbolic algebra for obtaining analytical gradients with ease. Two Maple worksheets were developed:

one for determining the material parameters at each stress level, as discussed in step 2 of Section 2.2.1 and the other for obtaining the master curve for the stress-time equivalence corresponding to Section 2.2.2.

4 Experimental set-up

Firstly, aiming at validation of the proposed procedure, experimental results were taken from the literature [3], and the stress-time equivalence theory was applied. In a second stage (after validation), actual experiments were conducted for HDPE pipes and the viscoelastic properties were modeled by both Liu's and Luo's methods. This Section discusses some aspects of the experimental settings in the studied cases.

Small deformation is assumed for the tensile creep tests. Engineering stress and strain are used in calculating the material responses.

4.1 Validation study: experimental results taken from literature [3]

The experiments conducted by Liu et al. were performed in a four-pole frame with a tensile rod-clipper device going vertically along the centre axis. A clip-on strain gauge was used to measure displacement in the sample between the gauge knife edges, which are 25.4 mm apart initially (gauge length). The measured displacement is recorded at 30 second intervals by a data acquisition system connected to the strain gauge (data stored in the computer's hard drive).

The tensile specimens have dimensions that conform to ASTM D638-02A (ASTM 2002), shown in Fig. 5. The specimen's thickness and width are measured at three locations along the length of the sample to account for the dimension variation along the specimen length. The measurement averages are taken in calculating the initial cross-sectional area for the specimen.

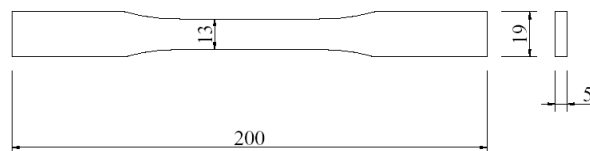


Figure 5: Specimen dimensions of the tests conducted by Liu [3]. Dimensions in [mm].

4.2 Experimental results conducted in the present work

Material samples were taken from HDPE – PE80 water pipes according to the NBR 96-22 Brazilian norm (similar to ISO 6259), as displayed in Fig. 6(a). The thickness of the specimen is 5 mm (thickness

of the pipe wall) and the other dimensions are shown in Fig. 6(b). The samples were cut out from the pipe using a mechanical press. This procedure is discussed in more detail, for instance in Dusunceli and Colak [18]. An important aspect is that after removing the specimens from the pipe, all of them bent in the axis direction due to residual stresses probably introduced in the manufacturing process, as shown in Fig. 7.

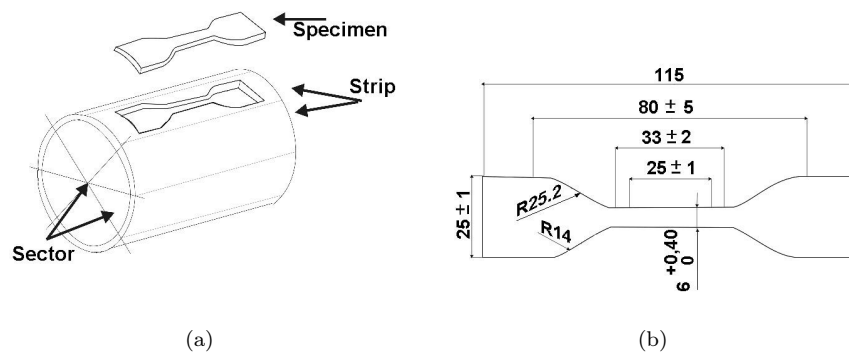


Figure 6: Material sample cut off from the pipe according to ISO 6259 norm. (a) orientation; (b) dimensions in [mm].



Figure 7: Detail of the specimen showing the curvature along the axial direction.

The material probes were separated into 2 groups: one group was tested at the Mechanical Engineering Department of the Federal University of Santa Catarina, and the other one at the Civil Engineering Department of the Federal University of Rio Grande do Sul, both in Brazil. In the tests, the temperature was kept constant at $T = 24(\pm 1) ^\circ C$.

4.2.1 Creep tests conducted at the Federal University of Santa Catarina

The tests were performed at GRANTE – Stress Analysis Group (Mechanical Engineering Department) under supervision of Prof. P. T. R. Mendonça. The ASTM D2990 norm was followed using 15 HPDE specimens subjected to 5 different stress levels (2, 4, 6, 8, 10 MPa).

The material samples were subjected to axial loading given by dead weight during 24 hours. The strains were measured by means of a clip-gage and the load was monitored using a load cell positioned in series with the sample axis. Load, time and strain were all measured using a data acquisition system in order to store the necessary information for further determination of the creep-compliance curves.

4.2.2 Creep tests conducted at the Federal University of Rio Grande do Sul

The tests were performed at the Viscoelasticity Laboratory (Civil Engineering Department) under supervision of Prof. G. J. Creus. In this case the creep tests were performed by applying axial traction induced by dead weights by means of a device designed for this task. Details of the sample fixture in the testing device are shown in Fig. 8. The stress levels of the creep tests were set as 2.3, 3.98, 11.34 MPa and were applied during 24 hours. A LVDT (*Linear Variable Differential Transformer*) was employed for displacement measurement and the information was stored using a data acquisition system for further determination of creep-compliance curves.



Figure 8: Detail of the experimental set-up.

5 Results and discussion

The results below show the comparison between the interpolation of rheological properties, studied by Liu, the stress-time equivalence presented by Luo and the modified interpolation of rheological properties proposed in this work.

5.1 Stress-time equivalence: evaluation of the creep behavior of HDPE samples studied by Liu et al. [3].

As a first study, the creep-compliance curves presented Liu et al. [3] for two different sample types (HDPE made of resin and HDPE extracted from a pipe, as shown in Fig. 6) were compared to Luo's stress-time equivalence method. The material modeling adopted by Liu corresponds to Eq. (4)

with three rheological blocks, whose material parameters are given in Tables 1 and 2 for the resin and for the pipe, respectively. The comparison of the creep-compliance curves for the HDPE resin is shown in Figure 9, indicating higher disagreement as the stress level increases. The creep-compliance master curve was obtained using nine rheological blocks and is shown in Figure 10 which includes the corresponding material parameters. Figures 11 and 12 display the master curve in linear coordinates and the associated horizontal stress shifts.

Table 1: Material (rheological) properties. HDPE resin [3].

Stress level	E_0	τ_1	τ_2	τ_3
		500	10000	200000
		E_1	E_2	E_3
2.68	2500	2848.6134	3650.6457	1053.8829
5.58	2300	2125.6411	1811.4240	696.3469
7.28	1700	1515.4295	1537.4866	603.9634
10.60	1200	1180.3846	1111.9421	405.5838
13.72	1100	999.9933	810.1940	145.0453

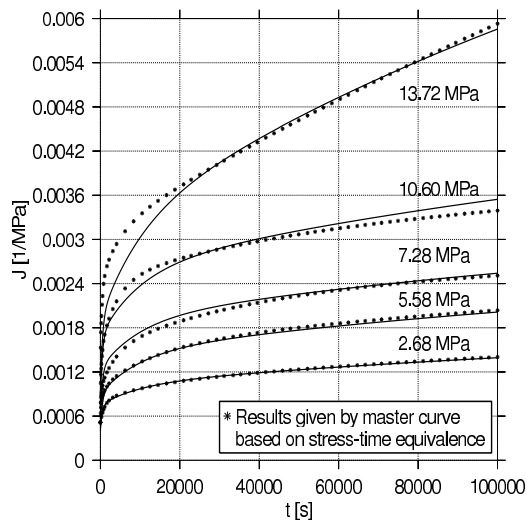


Figure 9: Comparison between the two methods for HDPE resin.

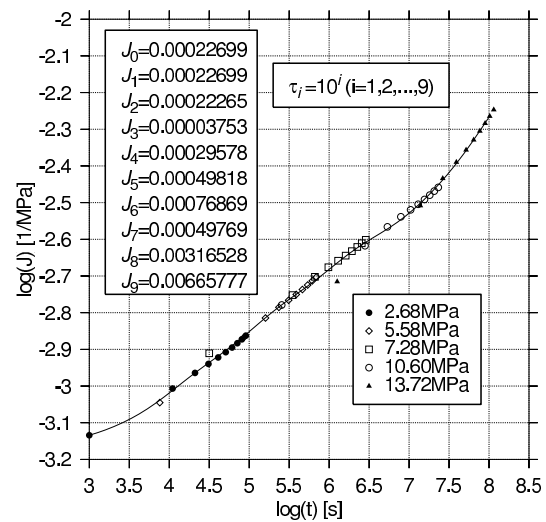


Figure 10: Master curve for HDPE resin in logarithmic coordinates.

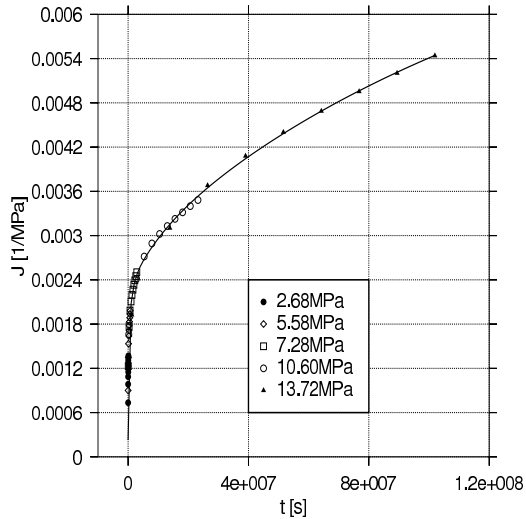


Figure 11: Master curve for HDPE resin in linear coordinates.

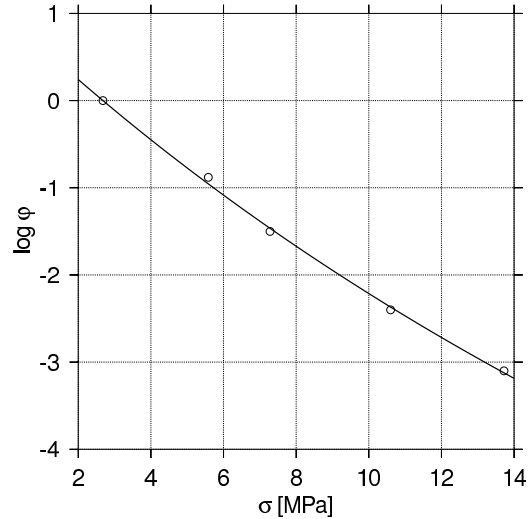


Figure 12: Horizontal shift for each stress level for HDPE resin.

Table 2: Material (rheological) properties. HDPE pipe [3].

Stress level	E_0	τ_1	τ_2	τ_3
		500	10000	200000
		E_1	E_2	E_3
2.97	650	797.3889	2320.3566	925.0882
5.97	580	913.5936	1212.2605	695.0461
7.71	520	1224.7911	1104.9922	385.8572
10.31	500	1034.2045	694.1084	226.4555
12.19	470	1128.4448	806.0972	140.6875

Figures 13-16 reproduce the analyses shown in Figs. 9-12, now for the HDPE samples extracted from the pipe. One possibility that could explain the large difference between the curves in Fig. 13 and the difficulty to match a master curve (Fig. 14) is the presence of initial strain in the specimen, as depicted in Fig.7. The master curve employed 7 rheological blocks and is shown in Fig. 14 together with its corresponding material parameters. The master curve in linear coordinates is displayed in Fig. 15 and the horizontal shifts are shown in Fig. 16.

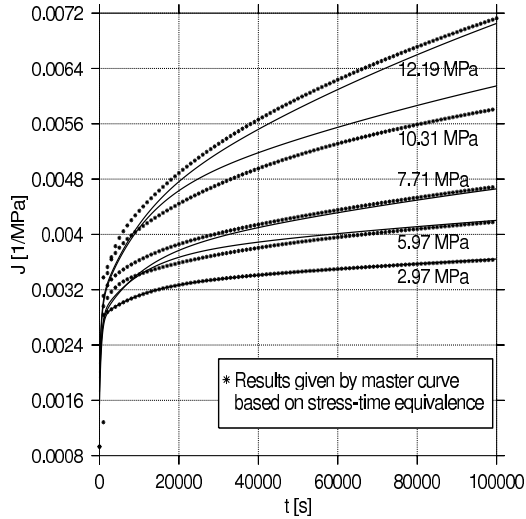


Figure 13: Comparison between the two methods for HDPE pipe.

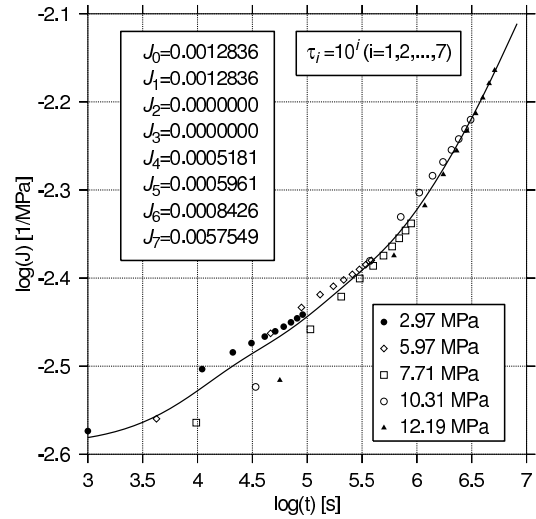


Figure 14: Master curve for HDPE pipe in logarithmic coordinates.

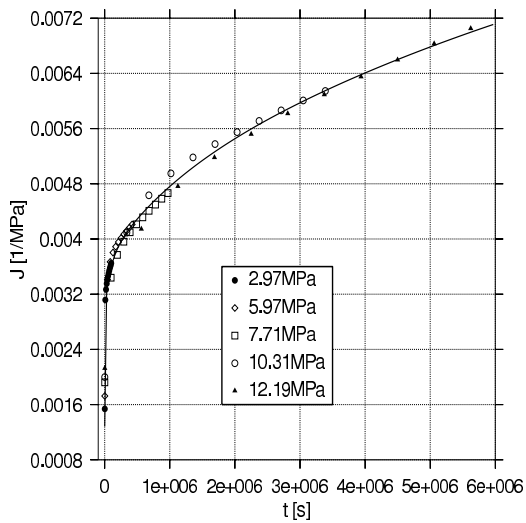


Figure 15: Master curve for HDPE pipe in linear coordinates.

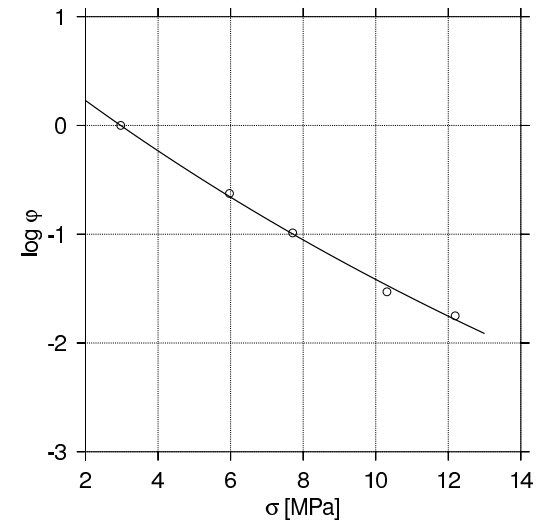


Figure 16: Horizontal shift for each stress level for HDPE pipe.

5.2 Stress-time equivalence versus interpolation of rheological properties: evaluation of the creep behavior of HDPE samples taken from water pipes in the present research.

The results below are based in creep experimental tests made in HDPE samples taken from water pipes during this research. Figure 17(a) presents the comparison between the creep-compliance curves obtained by experiments and by the stress-time equivalence at five different stress levels. Figure 17(b) shows the creep-compliance curves obtained by direct fitting of a Prony series using three rheological blocks at each stress level. The material parameters obtained are shown in Table 3. The creep-compliance master curve associated to Fig. 17(a) used 11 rheological blocks and is depicted in Figures 18(a) and (b). The corresponding horizontal stress shifts are presented in Fig. 19.

Table 3: Material (rheological) properties. HDPE pipe (this work).

Stress level	E_0	τ_1	τ_2	τ_3
		500	10000	200000
		E_1	E_2	E_3
2.00	515.3614	1623.7904	2555.0553	2350.5472
4.00	763.6466	503.0608	1047.8427	992.2184
6.00	815.0536	346.7152	1829.3498	378.7913
10.00	951.4141	294.6865	481.1448	152.2551
11.34	556.8556	262.0088	303.6087	107.3255

In the sequence, each of the methods was used to interpolate the creep behavior at stress levels within the range adopted for identification. Three intermediate stress values were considered: 6, 8 and 10 MPa. For 6 and 10 MPa, the experimental result was suppressed in the respective stress, interpolating the rheological properties between 4 and 10 MPa, and between 6 and 11.34MPa, respectively. Figures 20, 21 and 22 show the creep-compliance functions for 6, 8 and 10MPa respectively, comparing to the corresponding experimental result. It is noteworthy that the modified interpolation proposed in this work [Eq.(9)], provided a better matching with experimental results in all the cases.

5.3 Unloading of creep tests for 6 and 10 MPa. Comparison between the modified linear interpolation and Liu's method with the experimental results.

When the loading is removed, the stress in the sample becomes zero and there is an instantaneous strain recovery. The remaining deformation recovers gradually with time and if there is no permanent deformation, the strain becomes zero in long recovery times. Figures 23 and 24 illustrate the creep curves for loading/unloading at 6MPa and 10MPa respectively, evaluated by the modified and the original approaches for the interpolation of rheological properties [Eqs. (9) and (7), respectively]. The

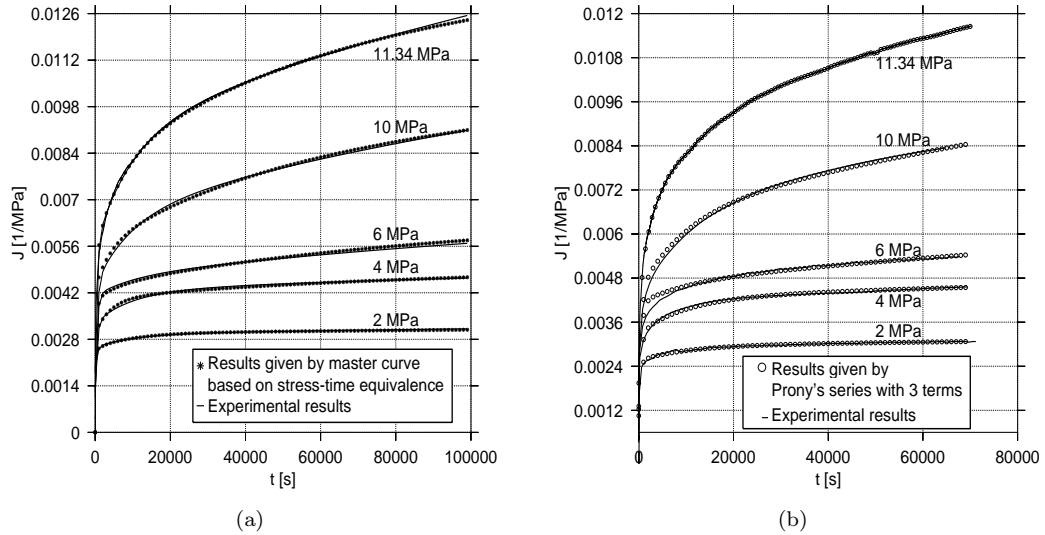


Figure 17: Creep-compliance at different stress levels obtained: (a) by using a master curve based on stress-time equivalence and (b) by curve fitting using Prony series at each stress level.

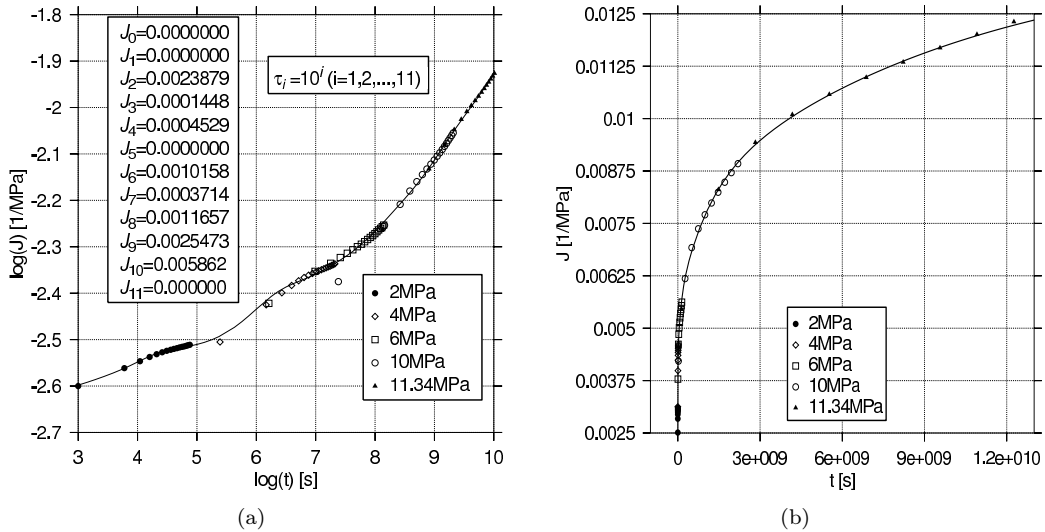


Figure 18: Master curve for creep-compliance based on stress-time equivalence compared to experimental results. (a) Logarithmic coordinates and (b) linear coordinates.

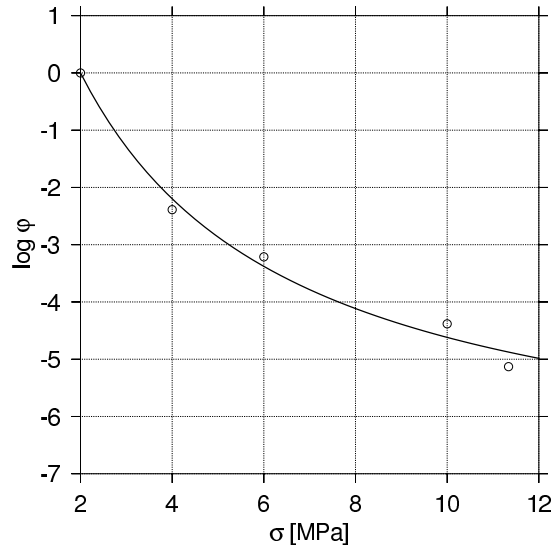


Figure 19: Horizontal stress shifts associated to the master curve in Fig. 18.

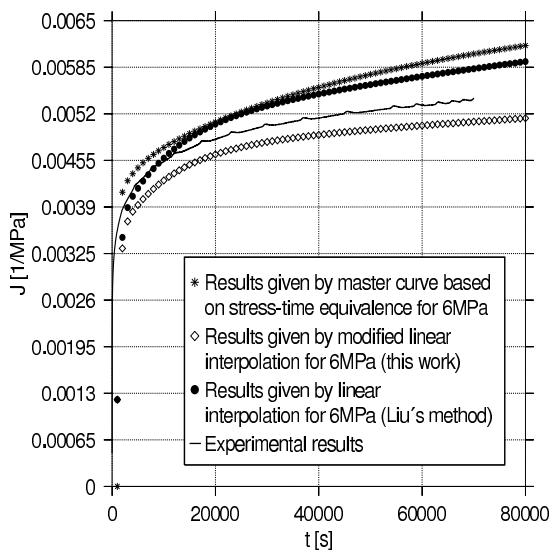


Figure 20: Interpolations for 6MPa.

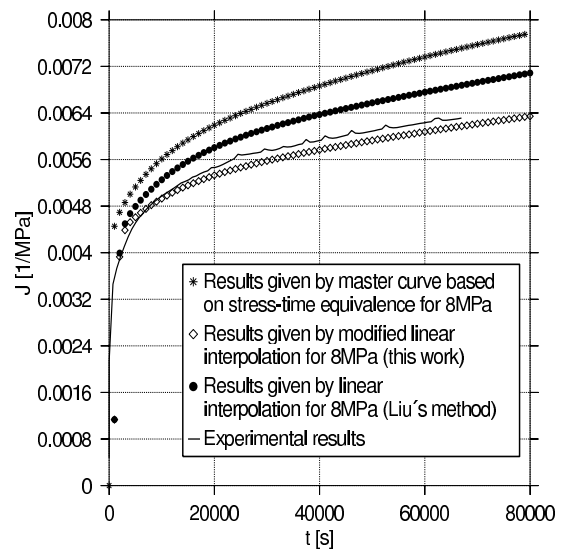


Figure 21: Interpolations for 8MPa.

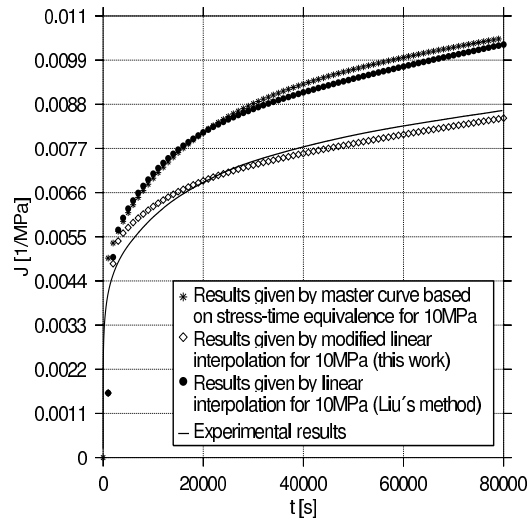


Figure 22: Interpolations for 10MPa.

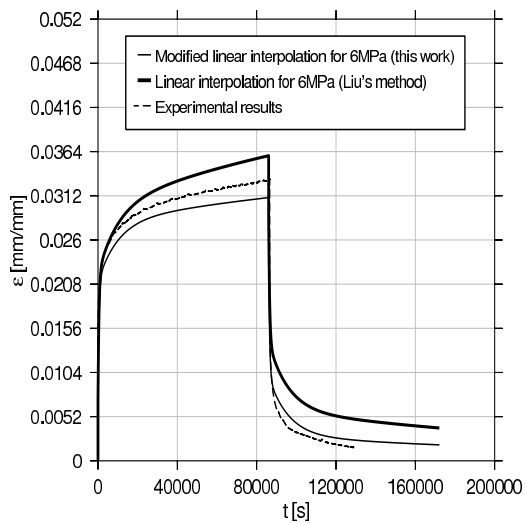


Figure 23: Loading/Unloading creep curve for 6MPa.

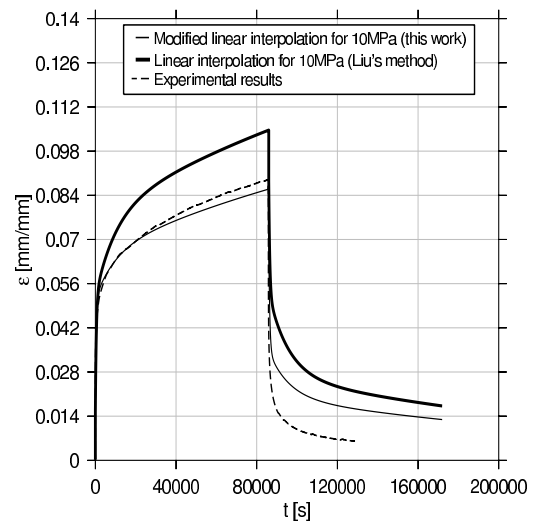


Figure 24: Loading/Unloading creep curve for 10MPa.

loading/unloading simulation was done in a homemade finite element code inspired in the incremental procedure described in Zienkiewicz et al. [19]. The Figures are merely illustrative, since further experiments and a more elaborate procedure, such as the one proposed by Dasappa et al. [20], are necessary in order to verify the presence of viscoplastic effects.

6 Conclusions

Aiming at a good and simple modeling of nonlinear viscoelasticity, particularly for HDPE pipes, a modified interpolation of rheological properties was proposed and compared with some methods described in the literature. The modified method was inspired in Liu et al. [3], and showed a slightly better agreement to experimental data. The results obtained were also compared to the stress-time equivalence [5] providing better matching. The original and modified interpolation approaches were also applied to loading/unloading cases, just for illustrative purpose, since additional research is needed in order to evaluate the presence of viscoplasticity.

References

- [1] Lai, J., *Non-linear time-dependent deformation behavior of high density polyethylene*. Ph.D. thesis, Delft University of Technology, 1995.
- [2] Janson, L., *Plastics Pipes for Water Supply and Sewage Disposal*. Borealis, Sven Axelsson AB/Affisch & Reklamtryck AB: Boras, 1996.
- [3] Liu, H., Polak, M. & Penlidis, A., A practical approach to modeling time-dependent nonlinear creep behavior of polyethylene for structural applications. *Polymer Engineering and Science*, **48(1)**, pp. 159–167, 2008.
- [4] Benvenuti, I., Internal report. Technical report, Vettore Engenharia Ltda., 2005.
- [5] Luo, W., Yang, T. & An, Q., Time-temperature-stress equivalence and its application to nonlinear viscoelastic materials. *Acta Mechanica Solida Sinica*, **14(3)**, pp. 195–199, 2001.
- [6] Lai, J. & Bakker, A., Analysis of the nonlinear creep of high-density polyethylene. *Polymer*, **36(1)**, pp. 93–99, 1995.
- [7] Elleuch, R. & Taktak, W., Viscoelastic behavior of hdpe polymer using tensile and compressive loading. *Journal of Materials Engineering and Performance*, **15(1)**, pp. 111–116, 2006.
- [8] Papanicolaou, G., Xepapadaki, A., Karagounaki, K. & Zaoutsos, S., Time and temperature effect on the linear-nonlinear viscoelastic transition threshold of a polymeric system. *Journal of Applied Polymer Science*, **108**, pp. 640–649, 2008.
- [9] Schapery, R., On the characterization of nonlinear viscoelastic materials. *Polymer Engineering and Science*, **9**, pp. 295–310, 1969.
- [10] Fillers, R. & Tschoegl, N., Effect of pressure on mechanical-properties of polymers. *Transactions of The Society of Rheology*, **21(1)**, pp. 51–100, 1977.
- [11] Bernstein, B. & Shokooh, A., The stress clock function in viscoelasticity. *Journal of Rheology*, **24**, pp. 189–198, 1980.
- [12] Ferry, J.D., *Viscoelastic properties of polymers*. John Wiley & Sons, Inc, 1970.
- [13] Moonan, W. & Tschoegl, N., Effect of pressure on the mechanical-properties of polymers. 2. Expansivity

- and compressibility measurements. *Macromolecules*, **16(1)**, pp. 55–59, 1983.
- [14] Brostow, W., Time-stress correspondence in viscoelastic materials: an equation for the stress and temperature shift factor. *Materials Research Innovations*, **3**, pp. 347–351, 2000.
- [15] Brinson, H. & Brinson, L., *Polymer, Engineering Science and Viscoelasticity: An Introduction*. Springer, 2008.
- [16] Riande, E., Díaz-Calleja, R., Prolongo, M.G., Masegosa, R.M. & Salom, C., *Polymer Viscoelasticity*. Marcel Dekker, 2000.
- [17] Tschoegl, N., Knauss, W. & Emri, I., The effect of temperature and pressure on the mechanical properties of thermo- and/or piezorheologically simple polymeric materials in thermodynamic equilibrium – a critical review. *Mechanics of Time-Dependent Materials*, **6(1)**, pp. 53–99, 2002.
- [18] Dusunceli, N. & Colak, O., High density polyethylene (HDPE): Experiments and modeling. *Mechanics of Time-Dependent Materials*, **10(4)**, pp. 331–345, 2006.
- [19] Zienkiewicz, O., Watson, M. & King, I., A numerical method of visco-elastic stress analysis. *International Journal of Mechanical Sciences*, **10(10)**, p. 807, 1968.
- [20] Dasappa, P., Lee-Sullivan, P. & Xiao, X., Development of viscoplastic strains during creep in continuous fibre GMT composites. *Composites: Part B*, **41**, pp. 48–57, 2010.

Topology design of Kirchhoff plates based on topological derivative and a level-set domain representation

A.A. Novotny and D.E. Campeão

*Laboratório Nacional de Computação Científica LNCC/MCT,
Coordenação de Matemática Aplicada e Computacional,
Av. Getúlio Vargas 333, 25651-075 Petrópolis, RJ – Brazil*

Abstract

In this work, we propose an optimization algorithm based on the topological derivative and a level-set domain representation for the compliance topology design of Kirchhoff plates, with volume constraint. We start by deriving the topological asymptotic expansion of the total potential energy associated to the Kirchhoff plate bending problem, considering as topological perturbation the nucleation of a circular inclusion. Next, we present a topology optimization algorithm based on the topological derivative together with a level-set domain representation method. Finally, some numerical examples are presented in the context of compliance topology optimization with volume constraint.

Keywords: topological derivative, level-set domain representation, topology optimization, Kirchhoff plates.

1 Introduction

The topological derivative measures the sensitivity of a given shape functional with respect to an infinitesimal singular domain perturbation, such as the insertion of holes, inclusions, source-terms or even cracks. The topological derivative was rigorously introduced by Sokołowski & Żochowski 1999 [1]. Since then, this concept has proved to be extremely useful in the treatment of a wide range of problems, namely, topology optimization [2–8], inverse analysis [9–13] and image processing [14–18], and has become a subject of intensive research. See, for instance, applications of the topological derivative in the multi-scale constitutive modeling context [19] and fracture mechanics sensitivity analysis [20]. Concerning the theoretical development of the topological asymptotic analysis, the reader may refer to [21–23], for instance.

In [7] the topological derivative was obtained, through the approach developed in [6], for the total potential energy associated to the Kirchhoff plate bending problem, considering as singular perturbation the nucleation of a circular hole. This result was used to devise a hard-kill like topology algorithm

and some numerical experiments were presented. More recently, in [24] the closed formulas associated to a large class of shape functionals were derived using the approach proposed in [21] and a full mathematical justification for the formula obtained in [7] was provided. In addition, the result derived in [7] was extended by considering as topological perturbation the nucleation of an infinitesimal circular inclusion instead of a hole. This last result allows to devise a topology design algorithm as proposed in [3].

Therefore, as a natural sequence of this research, in this work we propose an optimization algorithm based on the topological derivative and a level-set domain representation for the compliance topology design of Kirchhoff plates, with volume constraint. For the sake of completeness, we start by deriving the topological asymptotic expansion of the total potential energy associated to the Kirchhoff plate bending problem, considering as singular perturbation the nucleation of a circular inclusion. The topological derivative is obtained through the approach proposed in [6]. Next, we present an optimization algorithm based on the topological derivative together with a level-set domain representation method as proposed in [3]. Finally, some numerical examples are presented in the context of compliance topology optimization with volume constraint.

1.1 The topological derivative concept

Let us consider a bounded domain $\Omega \subset \mathbb{R}^2$, which is subject to a non-smooth perturbation confined in a small region $\omega_\varepsilon(\hat{x}) = \hat{x} + \varepsilon\omega$ of size ε , as shown in fig. 1. Here, \hat{x} is an arbitrary point of Ω and ω is a fixed domain of \mathbb{R}^2 . We introduce a characteristic function associated to the unperturbed domain, namely $\chi = \mathbf{1}_\Omega$. Then, we define a characteristic function associated to the topologically perturbed domain of the form χ_ε . In the present case, the perturbed domain is obtained when a circular hole $\omega_\varepsilon(\hat{x}) = B_\varepsilon(\hat{x})$ is introduced inside Ω , where $B_\varepsilon(\hat{x})$ is used to denote a ball of radius ε and center at $\hat{x} \in \Omega$. Next, this region is filled by an inclusion with different material property. In particular, we introduce a piecewise constant function γ_ε of the form

$$\gamma_\varepsilon = \gamma_\varepsilon(x) := \begin{cases} 1 & \text{if } x \in \Omega \setminus \overline{B_\varepsilon} \\ \gamma & \text{if } x \in B_\varepsilon \end{cases}, \quad (1)$$

where $\gamma \in \mathbb{R}^+$ is the contrast in the material property. Therefore the characteristic function will take the form $\chi_\varepsilon(\hat{x}) = \mathbf{1}_\Omega - (1-\gamma)\mathbf{1}_{\overline{B_\varepsilon(\hat{x})}}$. Note that in this case the topologies of the original and perturbed domains are preserved. However, we are introducing a non-smooth perturbation in the coefficients of the differential operator through the contrast γ_ε , by changing the material property of the background in a small region $B_\varepsilon \subset \Omega$. Therefore, the sensitivity of the shape functional with respect to the nucleation of an inclusion can also be studied through the topological asymptotic analysis concept, which is, in fact, the most appropriate approach for such a problem. Then, we assume that a given shape functional $\psi(\chi_\varepsilon(\hat{x}))$, associated to the topologically perturbed domain, admits the following topological asymptotic expansion

$$\psi(\chi_\varepsilon(\hat{x})) = \psi(\chi) + f(\varepsilon)\mathcal{T}_\Omega(\hat{x}) + o(f(\varepsilon)), \quad (2)$$

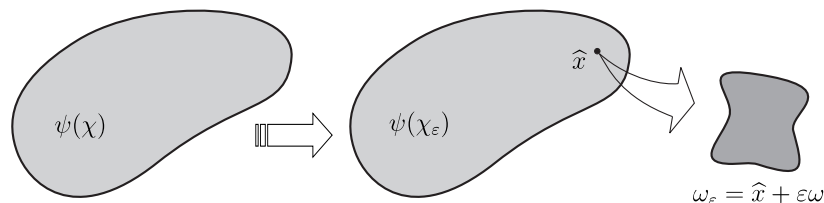


Figure 1: The topological derivative concept.

where $\psi(\chi)$ is the shape functional associated to the original (unperturbed) domain, $f(\varepsilon)$ is a positive function such that $f(\varepsilon) \rightarrow 0$, when $\varepsilon \rightarrow 0$. The function $\hat{x} \mapsto \mathcal{T}_\Omega(\hat{x})$ is called the topological derivative of ψ at \hat{x} . Therefore, this derivative can be seen as a first order correction of $\psi(\chi)$ to approximate $\psi(\chi_\varepsilon(\hat{x}))$.

1.2 Relation between shape and topological changes

The topological derivative can be considered as the singular limit of the shape derivative, so it is a generalization of the classical tool in shape optimization. Among the methods for calculation of the topological derivative currently available in literature (see, for instance, [25, 26]), here we shall adopt the methodology developed in [27], which is given by the following result:

Theorem 1. *Let $\psi(\chi_\varepsilon(\hat{x}))$ be the shape functional associated to the topologically perturbed domain, which admits, for ε small enough, the topological asymptotic expansion of the form*

$$\psi(\chi_\varepsilon(\hat{x})) = \psi(\chi) + f(\varepsilon)\mathcal{T}_\Omega(\hat{x}) + \mathcal{R}(f(\varepsilon)) , \tag{3}$$

where $\psi(\chi)$ is the shape functional associated to the original (unperturbed) domain, the positive function $f(\varepsilon)$ is such that $f(\varepsilon) \rightarrow 0$, with $\varepsilon \rightarrow 0$, and the function $\mathcal{T}_\Omega(\hat{x})$ is the topological derivative of the shape functional ψ . We assume that the remainder $\mathcal{R}(f(\varepsilon)) = o(f(\varepsilon))$ has the following additional property $\mathcal{R}'(f(\varepsilon)) \rightarrow 0$, when $\varepsilon \rightarrow 0$. Then, the topological derivative can be written as

$$\mathcal{T}_\Omega(\hat{x}) = \lim_{\varepsilon \rightarrow 0} \frac{1}{f'(\varepsilon)} \frac{d}{d\varepsilon} \psi(\chi_\varepsilon(\hat{x})) , \tag{4}$$

where $\frac{d}{d\varepsilon} \psi(\chi_\varepsilon(\hat{x}))$ is the derivative of $\psi(\chi_\varepsilon(\hat{x}))$ with respect to the small parameter ε .

Proof. See, for instance, [6]. □

The derivative of $\psi(\chi_\varepsilon(\hat{x}))$ with respect to ε can be seen as the sensitivity of $\psi(\chi_\varepsilon(\hat{x}))$, in the classical sense [28, 29], to the domain variation produced by an uniform expansion of the perturbation B_ε . Therefore, since we are dealing with topologically identical domains, we can use the concept of shape sensitivity analysis as an intermediate step in the topological derivative calculation. We will see later that this procedure enormously simplifies the analysis. In the case of a circular inclusion, we can

construct a shape change velocity field $\mathfrak{V} \in C^\infty(\Omega)$ that represents an uniform expansion of $B_\varepsilon(\hat{x})$. In fact, it is sufficient to define \mathfrak{V} on the boundaries $\partial\Omega$ and ∂B_ε in the following way

$$\begin{cases} \mathfrak{V} = 0 & \text{on } \partial\Omega \\ \mathfrak{V} = -n & \text{on } \partial B_\varepsilon \end{cases}, \quad (5)$$

where $n = -(x - \hat{x})/\varepsilon$, with $x \in \partial B_\varepsilon$, is the normal unit vector field pointing toward the center of the circular inclusion B_ε .

2 The topological derivative for the kirchhoff plate bending problem

In this section we evaluate the topological derivative for the total potential energy associated to the Kirchhoff plate bending problem, considering the nucleation of a small inclusion, represented by $B_\varepsilon \subset \Omega$, as the topological perturbation.

2.1 Problem formulation

The shape functional in the unperturbed domain which we are dealing with is defined as

$$\psi(\chi) := \mathcal{J}_\chi(u) = -\frac{1}{2} \int_\Omega M(u) \cdot \nabla \nabla u - \int_{\Gamma_{N_q}} \bar{q}u + \int_{\Gamma_{N_m}} \bar{m} \partial_n u + \sum_{i=1}^{ns} \bar{Q}_i u(x_i), \quad (6)$$

The scalar function u is the solution to the variational problem:

$$\begin{cases} \text{Find } u \in \mathcal{U}, \text{ such that} \\ - \int_\Omega M(u) \cdot \nabla \nabla \eta = \int_{\Gamma_{N_q}} \bar{q} \eta - \int_{\Gamma_{N_m}} \bar{m} \partial_n \eta - \sum_{i=1}^{ns} \bar{Q}_i \eta(x_i) \quad \forall \eta \in \mathcal{V}, \\ \text{with } M(u) = -\frac{h^3}{12} \mathbf{C} \nabla \nabla u. \end{cases} \quad (7)$$

In the above equation, \mathbf{C} is the constitutive tensor given by

$$\mathbf{C} = \frac{E}{1-\nu^2} ((1-\nu)\mathbf{I} + \nu I \otimes I), \quad (8)$$

where I and \mathbf{I} are the second and fourth order identity tensors, respectively, E is the Young modulus and ν the Poisson ratio, both considered constants everywhere. The set \mathcal{U} and the space \mathcal{V} are respectively defined as

$$\mathcal{U} := \{\varphi \in H^2(\Omega) : \varphi|_{\Gamma_{D_u}} = \bar{u}, \partial_n \varphi|_{\Gamma_{D_p}} = \bar{\rho}\}, \quad (9)$$

$$\mathcal{V} := \{\varphi \in H^2(\Omega) : \varphi|_{\Gamma_{D_u}} = 0, \partial_n \varphi|_{\Gamma_{D_p}} = 0\}. \quad (10)$$

In addition, h is the plate thickness assumed to be constant everywhere, \bar{q} is a shear load distributed on the boundary Γ_{N_q} , \bar{m} is a moment distributed on the boundary Γ_{N_m} and \bar{Q}_i is a concentrated shear

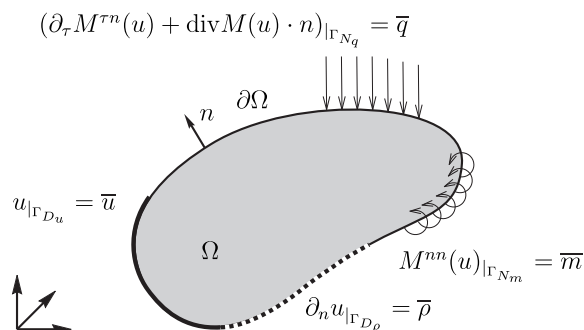


Figure 2: The Kirchhoff problem defined in the unperturbed domain.

load supported at the points x_i where there are some geometrical singularities, with $i = 1, \dots, ns$, and ns the number of such singularities. The displacement field u has to satisfy $u|_{\Gamma_{D_u}} = \bar{u}$ and $\partial_n u|_{\Gamma_{D_\rho}} = \bar{\rho}$, where \bar{u} and $\bar{\rho}$ are a displacement and a rotation respectively prescribed on the boundaries Γ_{D_u} and Γ_{D_ρ} . Furthermore, $\Gamma_D = \overline{\Gamma_{D_u} \cup \Gamma_{D_\rho}}$ and $\Gamma_N = \overline{\Gamma_{N_q} \cup \Gamma_{N_m}}$ are such that $\Gamma_{D_u} \cap \Gamma_{N_q} = \emptyset$ and $\Gamma_{D_\rho} \cap \Gamma_{N_m} = \emptyset$. See the details in fig. 2.

The strong formulation associated to the variational problem (7) reads:

$$\left\{ \begin{array}{ll} \text{Find } u, \text{ such that} & \\ \operatorname{div}(\operatorname{div}M(u)) & = 0 \quad \text{in } \Omega, \\ M(u) & = -\frac{h^3}{12} \mathbf{C} \nabla \nabla u \\ u & = \bar{u} \quad \text{on } \Gamma_{D_u}, \\ \partial_n u & = \bar{\rho} \quad \text{on } \Gamma_{D_\rho}, \\ M^{nn}(u) & = \bar{m} \quad \text{on } \Gamma_{N_m}, \\ \partial_\tau M^{\tau n}(u) + \operatorname{div}M(u) \cdot n & = \bar{q} \quad \text{on } \Gamma_{N_q}, \\ \llbracket M^{\tau n}(u(x_i)) \rrbracket & = \bar{Q}_i \quad \text{on } x_i \in \Gamma_{N_q}. \end{array} \right. \quad (11)$$

Now, let us state the same problem in the perturbed domain. In this case, the shape functional reads

$$\psi(\chi_\varepsilon) := \mathcal{J}_{\chi_\varepsilon}(u_\varepsilon) = -\frac{1}{2} \int_\Omega M_\varepsilon(u_\varepsilon) \cdot \nabla \nabla u_\varepsilon - \int_{\Gamma_{N_q}} \bar{q} u_\varepsilon + \int_{\Gamma_{N_m}} \bar{m} \partial_n u_\varepsilon + \sum_{i=1}^{ns} \bar{Q}_i u_\varepsilon(x_i), \quad (12)$$

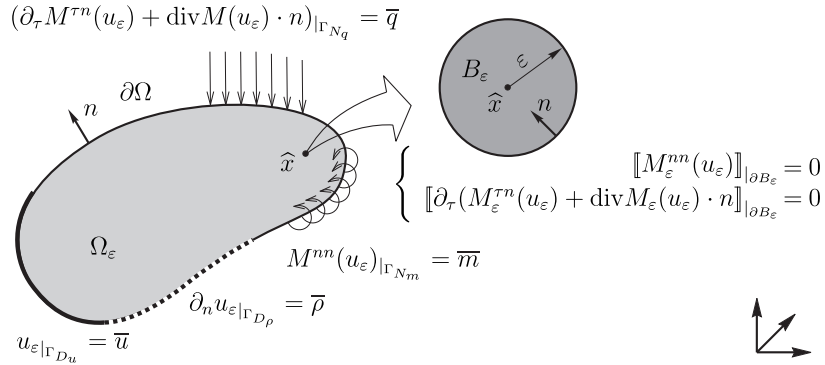


Figure 3: The Kirchhoff problem defined in the perturbed domain.

where the scalar function u_ε solves the variational problem:

$$\left\{ \begin{array}{l} \text{Find } u_\varepsilon \in \mathcal{U}_\varepsilon, \text{ such that} \\ - \int_{\Omega} M_\varepsilon(u_\varepsilon) \cdot \nabla \nabla \eta = \int_{\Gamma_{Nq}} \bar{q} \eta - \int_{\Gamma_{Nm}} \bar{m} \partial_n \eta - \sum_{i=1}^{ns} \bar{Q}_i \eta(x_i) \quad \forall \eta \in \mathcal{V}_\varepsilon, \\ \text{with } M_\varepsilon(u_\varepsilon) = -\frac{h^3}{12} \gamma_\varepsilon \mathbf{C} \nabla \nabla u_\varepsilon. \end{array} \right. \quad (13)$$

with γ_ε defined by (1). The set \mathcal{U}_ε and the space \mathcal{V}_ε are defined as

$$\mathcal{U}_\varepsilon := \{ \varphi \in \mathcal{U} : \llbracket \varphi \rrbracket = 0, \llbracket \partial_n \varphi \rrbracket = 0 \text{ on } \partial B_\varepsilon \}, \quad (14)$$

$$\mathcal{V}_\varepsilon := \{ \varphi \in \mathcal{V} : \llbracket \varphi \rrbracket = 0, \llbracket \partial_n \varphi \rrbracket = 0 \text{ on } \partial B_\varepsilon \}, \quad (15)$$

where the operator $\llbracket \varphi \rrbracket$ is used to denote the jump of function φ on the boundary of the inclusion ∂B_ε , namely $\llbracket \varphi \rrbracket := \varphi|_{\Omega \setminus \overline{B_\varepsilon}} - \varphi|_{B_\varepsilon}$ on ∂B_ε . See the details in fig. 3. The strong formulation associated

to the variational problem (13) reads:

$$\left\{ \begin{array}{l} \text{Find } u_\varepsilon, \text{ such that} \\ \begin{array}{ll} \operatorname{div}(\operatorname{div}M_\varepsilon(u_\varepsilon)) = 0 & \text{in } \Omega, \\ M_\varepsilon(u_\varepsilon) = -\frac{h^3}{12}\gamma_\varepsilon \mathbf{C}\nabla\nabla u_\varepsilon & \\ u_\varepsilon = \bar{u} & \text{on } \Gamma_{D_u}, \\ \partial_n u_\varepsilon = \bar{\rho} & \text{on } \Gamma_{D_\rho}, \\ M^{nn}(u_\varepsilon) = \bar{m} & \text{on } \Gamma_{N_m}, \\ \partial_\tau M^{\tau n}(u_\varepsilon) + \operatorname{div}M(u_\varepsilon) \cdot n = \bar{q} & \text{on } \Gamma_{N_q}, \\ \llbracket M^{\tau n}(u_\varepsilon(x_i)) \rrbracket = \bar{Q}_i & \text{on } x_i \in \Gamma_{N_q}, \\ \llbracket u_\varepsilon \rrbracket = 0 & \\ \llbracket \partial_n u_\varepsilon \rrbracket = 0 & \\ \llbracket M_\varepsilon^{nn}(u_\varepsilon) \rrbracket = 0 & \\ \llbracket \partial_\tau M_\varepsilon^{\tau n}(u_\varepsilon) \rrbracket + \llbracket \operatorname{div}M_\varepsilon(u_\varepsilon) \rrbracket \cdot n = 0 & \end{array} \end{array} \right. \quad \text{on } \partial B_\varepsilon. \tag{16}$$

2.2 Shape sensitivity analysis

The next step is to evaluate the shape derivative of functional $\mathcal{J}_{\chi_\varepsilon}(u_\varepsilon)$ with respect to an uniform expansion of the inclusion B_ε . Before starting, we note that after considering the constitutive relation $M_\varepsilon(u_\varepsilon) = -\frac{h^3}{12}\gamma_\varepsilon \mathbf{C}\nabla\nabla u_\varepsilon$ in (12), with the contrast γ_ε given by (1), the shape functional $\mathcal{J}_{\chi_\varepsilon}(u_\varepsilon)$ can be written as follows

$$\begin{aligned} \mathcal{J}_{\chi_\varepsilon}(u_\varepsilon) = & -\frac{1}{2} \left(\int_{\Omega \setminus \overline{B_\varepsilon}} M(u_\varepsilon) \cdot \nabla\nabla u_\varepsilon + \int_{B_\varepsilon} \gamma M(u_\varepsilon) \cdot \nabla\nabla u_\varepsilon \right) \\ & - \int_{\Gamma_{N_q}} \bar{q}u_\varepsilon + \int_{\Gamma_{N_m}} \bar{m}\partial_n u_\varepsilon + \sum_{i=1}^{ns} \bar{Q}_i u_\varepsilon(x_i). \end{aligned} \tag{17}$$

where $M(u_\varepsilon) = -\frac{h^3}{12}\mathbf{C}\nabla\nabla u_\varepsilon$. Thus, we have the explicit dependence with respect to parameter ε . Therefore, let us start by proving the following result:

Proposition 2. *Let $\mathcal{J}_{\chi_\varepsilon}(u_\varepsilon)$ be the shape functional defined by (12). Then, the derivative of this functional with respect to the small parameter ε is given by*

$$\dot{\mathcal{J}}_{\chi_\varepsilon}(u_\varepsilon) = - \int_{\partial B_\varepsilon} \llbracket \Sigma_\varepsilon \rrbracket n \cdot n - \int_{\partial B_\varepsilon} \llbracket M_\varepsilon(u_\varepsilon) \rrbracket n \cdot \nabla n^\top \nabla u_\varepsilon, \tag{18}$$

where Σ_ε is a generalization of the classical Eshelby energy-momentum tensor [30] given by

$$\Sigma_\varepsilon = -\frac{1}{2}(M_\varepsilon(u_\varepsilon) \cdot \nabla\nabla u_\varepsilon)I + (\nabla\nabla u_\varepsilon)M_\varepsilon(u_\varepsilon) - \nabla u_\varepsilon \otimes \operatorname{div}(M_\varepsilon(u_\varepsilon)). \tag{19}$$

Proof. By making use of the Reynolds' transport theorem and taking into account the velocity field (5), the shape derivative of the functional (12) results in

$$\begin{aligned} \dot{\mathcal{J}}_{\chi_\varepsilon}(u_\varepsilon) &= - \left(\frac{1}{2} \int_{\Omega} M_\varepsilon(u_\varepsilon) \cdot \nabla \nabla u_\varepsilon \right)' - \int_{\Gamma_{Nq}} \bar{q} \dot{u}_\varepsilon + \int_{\Gamma_{Nm}} \bar{m} \partial_n \dot{u}_\varepsilon + \sum_{i=1}^{ns} \bar{Q}_i \dot{u}_\varepsilon(x_i) \\ &= - \int_{\Omega} M_\varepsilon(u_\varepsilon) \cdot \nabla \nabla u'_\varepsilon + \frac{1}{2} \int_{\partial B_\varepsilon} \llbracket M_\varepsilon(u_\varepsilon) \cdot \nabla \nabla u_\varepsilon \rrbracket n \cdot n \\ &\quad - \int_{\Gamma_{Nq}} \bar{q} \dot{u}_\varepsilon + \int_{\Gamma_{Nm}} \bar{m} \partial_n \dot{u}_\varepsilon + \sum_{i=1}^{ns} \bar{Q}_i \dot{u}_\varepsilon(x_i). \end{aligned} \quad (20)$$

In addition, from the relation between shape and material derivatives [29], we have

$$\begin{aligned} \dot{\mathcal{J}}_{\chi_\varepsilon}(u_\varepsilon) &= \frac{1}{2} \int_{\partial B_\varepsilon} \llbracket M_\varepsilon(u_\varepsilon) \cdot \nabla \nabla u_\varepsilon \rrbracket n \cdot n + \int_{\Omega} M_\varepsilon(u_\varepsilon) \cdot \nabla \nabla (\nabla u_\varepsilon \cdot \mathfrak{V}) \\ &\quad - \int_{\Omega} M_\varepsilon(u_\varepsilon) \cdot \nabla \nabla \dot{u}_\varepsilon - \int_{\Gamma_{Nq}} \bar{q} \dot{u}_\varepsilon + \int_{\Gamma_{Nm}} \bar{m} \partial_n \dot{u}_\varepsilon + \sum_{i=1}^{ns} \bar{Q}_i \dot{u}_\varepsilon(x_i). \end{aligned} \quad (21)$$

Since \dot{u}_ε is a variation of u_ε in the direction of the velocity field \mathfrak{V} , then $\dot{u}_\varepsilon \in \mathcal{V}_\varepsilon$ [29]. Now, by taking into account that u_ε is the solution to the variational problem (13), we have that the last four terms of the above equation vanish. From integration by parts, we obtain

$$\begin{aligned} \dot{\mathcal{J}}_{\chi_\varepsilon}(u_\varepsilon) &= \frac{1}{2} \int_{\partial B_\varepsilon} \llbracket M_\varepsilon(u_\varepsilon) \cdot \nabla \nabla u_\varepsilon \rrbracket n \cdot n - \int_{\partial B_\varepsilon} \llbracket (\nabla \nabla u_\varepsilon) M_\varepsilon(u_\varepsilon) \rrbracket n \cdot n \\ &\quad + \int_{\partial B_\varepsilon} \llbracket \nabla u_\varepsilon \otimes \operatorname{div} M_\varepsilon(u_\varepsilon) \rrbracket n \cdot n - \int_{\partial B_\varepsilon} \llbracket M_\varepsilon(u_\varepsilon) \rrbracket n \cdot \nabla n^\top \nabla u_\varepsilon \\ &\quad + \int_{\Omega} \operatorname{div}(\operatorname{div}(M_\varepsilon(u_\varepsilon))) \nabla u_\varepsilon \cdot \mathfrak{V}. \end{aligned} \quad (22)$$

Finally, taking into account that u_ε is the solution to the state equation (16), $\operatorname{div}(\operatorname{div} M_\varepsilon(u_\varepsilon)) = 0$, we have that the last term in the above equation vanishes, which leads to the result \square

2.3 Asymptotic analysis of the solution

The shape derivative of functional $\mathcal{J}_{\chi_\varepsilon}(u_\varepsilon)$ is given in terms of an integral over the boundary of the inclusion ∂B_ε (18). Therefore, in order to apply the result of Theorem 1, we need to know the behavior of the function u_ε with respect to ε . In particular, once we know this behavior explicitly, we can identify function $f(\varepsilon)$ and perform the limit passage $\varepsilon \rightarrow 0$ in (4) to obtain the final formula for the topological derivative \mathcal{T}_Ω of the shape functional ψ . However, in general this is not an easy task. In fact, we need to perform an asymptotic analysis of u_ε with respect to ε . In this section we present the formal calculation of the expansion of the solution u_ε associated to the transmission condition on

the inclusion. For a rigorous justification of the asymptotic expansion of u_ε , the reader may refer to [31, 32], for instance. Let us start by proposing an expansion for u_ε of the form [33]

$$u_\varepsilon(x) = u(x) + w_\varepsilon(x) + \tilde{u}_\varepsilon(x) . \quad (23)$$

After applying the operator M_ε we have

$$\begin{aligned} M_\varepsilon(u_\varepsilon(x)) &= M_\varepsilon(u(x)) + M_\varepsilon(w_\varepsilon(x)) + M_\varepsilon(\tilde{u}_\varepsilon(x)) \\ &= M_\varepsilon(u(\hat{x})) + \nabla M_\varepsilon(u(\xi))(x - \hat{x}) \\ &\quad + M_\varepsilon(w_\varepsilon(x)) + M_\varepsilon(\tilde{u}_\varepsilon(x)) , \end{aligned} \quad (24)$$

where ξ is an intermediate point between x and \hat{x} . On the boundary of the inclusion ∂B_ε we have

$$\llbracket M_\varepsilon^{nn}(u_\varepsilon) \rrbracket n = 0 \quad \Rightarrow \quad (M^{nn}(u_\varepsilon)|_{\Omega \setminus \overline{B_\varepsilon}} - \gamma M^{nn}(u_\varepsilon)|_{B_\varepsilon})n = 0 , \quad (25)$$

and

$$\begin{aligned} \llbracket \partial_\tau M_\varepsilon^{\tau n}(u_\varepsilon) \rrbracket + \llbracket \operatorname{div} M_\varepsilon(u_\varepsilon) \rrbracket \cdot n &= 0 \\ \Rightarrow (\partial_\tau M^{\tau n}(u_\varepsilon)|_{\Omega \setminus \overline{B_\varepsilon}} - \gamma \partial_\tau M_\varepsilon^{\tau n}(u_\varepsilon)|_{B_\varepsilon}) + \\ &\quad (\operatorname{div}(M(u_\varepsilon)|_{\Omega \setminus \overline{B_\varepsilon}} - \gamma M^{nn}(u_\varepsilon)|_{B_\varepsilon})) \cdot n = 0 , \end{aligned} \quad (26)$$

with $M_\varepsilon(\varphi) = -\frac{h^3}{12}\gamma_\varepsilon \mathbf{C}\nabla\nabla\varphi$ and $M(\varphi) = -\frac{h^3}{12}\mathbf{C}\nabla\nabla\varphi$. The above expansion, evaluated on ∂B_ε , leads to

$$(1 - \gamma)M(u(\hat{x}))n \cdot n - \varepsilon(1 - \gamma)(\nabla M(u(\xi))n)n \cdot n + \llbracket M_\varepsilon^{nn}(w_\varepsilon(x)) \rrbracket + \llbracket M_\varepsilon^{nn}(\tilde{u}_\varepsilon(x)) \rrbracket = 0 \quad (27)$$

and

$$\begin{aligned} (1 - \gamma)(\partial_\tau M(u(\hat{x}))n \cdot \tau + \operatorname{div} M(u(\hat{x})) \cdot n) - \\ \varepsilon(1 - \gamma)(\partial_\tau(\nabla M(u(\xi))n)n \cdot \tau + \operatorname{div}(\nabla M(u(\xi))n) \cdot n) + \\ \llbracket \partial_\tau M_\varepsilon^{\tau n}(w_\varepsilon(x)) \rrbracket + \llbracket \operatorname{div} M_\varepsilon(w_\varepsilon(x)) \cdot n \rrbracket + \\ \llbracket \partial_\tau M_\varepsilon^{\tau n}(\tilde{u}_\varepsilon(x)) \rrbracket + \llbracket \operatorname{div} M_\varepsilon(\tilde{u}_\varepsilon(x)) \cdot n \rrbracket = 0 . \end{aligned} \quad (28)$$

Thus, we can choose $M_\varepsilon(w_\varepsilon)$ such that

$$\llbracket M_\varepsilon^{nn}(w_\varepsilon(x)) \rrbracket = -(1 - \gamma)M(u(\hat{x}))n \cdot n , \quad (29)$$

$$\llbracket \partial_\tau M_\varepsilon^{\tau n}(w_\varepsilon(x)) \rrbracket + \llbracket \operatorname{div} M_\varepsilon(w_\varepsilon(x)) \cdot n \rrbracket = -(1 - \gamma)(\partial_\tau M(u(\hat{x}))n \cdot \tau + \operatorname{div} M(u(\hat{x})) \cdot n) . \quad (30)$$

Now, the following exterior problem is considered, and formally obtained with $\varepsilon \rightarrow 0$:

$$\left\{ \begin{array}{l} \text{Find } M_\varepsilon(w_\varepsilon), \text{ such that} \\ \begin{array}{l} \operatorname{div}(\operatorname{div} M_\varepsilon(w_\varepsilon)) = 0 \quad \text{in } \mathbb{R}^2, \\ M_\varepsilon(w_\varepsilon) \rightarrow 0 \quad \text{at } \infty, \\ \llbracket M_\varepsilon^{nn}(w_\varepsilon) \rrbracket = \hat{u}_1 \\ \llbracket \partial_\tau M_\varepsilon^{\tau n}(w_\varepsilon) \rrbracket + \llbracket \operatorname{div} M_\varepsilon(w_\varepsilon) \rrbracket \cdot n = \hat{u}_2 \end{array} \end{array} \right\} \text{ on } \partial B_\varepsilon. \quad (31)$$

with

$$\hat{u}_1 = -(1 - \gamma)M(u(\hat{x}))n \cdot n, \quad (32)$$

$$\hat{u}_2 = -(1 - \gamma)(\partial_\tau M(u(\hat{x}))n \cdot \tau + \operatorname{div} M(u(\hat{x})) \cdot n). \quad (33)$$

The above boundary-value problem admits an explicit solution, which will be used later to construct the expansion for $M_\varepsilon(u_\varepsilon)$. Now we can construct $M_\varepsilon(\tilde{u}_\varepsilon)$ in such a way that it compensates the discrepancies introduced by the higher-order terms in ε as well as by the boundary-layer $M_\varepsilon(w_\varepsilon)$ on the exterior boundary $\partial\Omega$. It means that the remainder $M_\varepsilon(\tilde{u}_\varepsilon)$ must be the solution to the following boundary-value problem:

$$\left\{ \begin{array}{l} \text{Find } M_\varepsilon(\tilde{u}_\varepsilon), \text{ such that} \\ \begin{array}{l} \operatorname{div}(\operatorname{div} M_\varepsilon(\tilde{u}_\varepsilon)) = 0 \quad \text{in } \Omega, \\ M_\varepsilon(\tilde{u}_\varepsilon) = -M_\varepsilon(w_\varepsilon) \quad \text{on } \partial\Omega, \\ \llbracket M_\varepsilon^{nn}(\tilde{u}_\varepsilon) \rrbracket = \varepsilon g_1 \\ \llbracket \partial_\tau M_\varepsilon^{\tau n}(\tilde{u}_\varepsilon) \rrbracket + \llbracket \operatorname{div} M_\varepsilon(\tilde{u}_\varepsilon) \rrbracket \cdot n = \varepsilon g_2 \end{array} \end{array} \right\} \text{ on } \partial B_\varepsilon. \quad (34)$$

with

$$g_1 = (1 - \gamma)(\nabla M(u(\xi))n)n \cdot n, \quad (35)$$

$$g_2 = (1 - \gamma)(\partial_\tau(\nabla M(u(\xi))n)n \cdot \tau + \operatorname{div}(\nabla M(u(\xi))n) \cdot n). \quad (36)$$

Observe that $M_\varepsilon(\tilde{u}_\varepsilon)$ has the following estimate $M_\varepsilon(\tilde{u}_\varepsilon) = O(\varepsilon^2)$ [33]. Therefore, the expansion for $M_\varepsilon(u_\varepsilon)$ (see, for instance, the book by Little 1973 [34]) can be written in a polar coordinate system (r, θ) centered at the point \hat{x} (see fig. 4) as:

- For $r \geq \varepsilon$ (outside the inclusion)

$$M_\varepsilon^{rr}(u_\varepsilon(r, \theta)) = \varphi_1 \left(1 - \frac{1-\gamma}{1+\gamma\alpha} \frac{\varepsilon^2}{r^2} \right) + \varphi_2 \left(1 - \frac{1-\gamma}{1+\gamma\beta} \left(\frac{4\nu}{3+\nu} \frac{\varepsilon^2}{r^2} + 3\beta \frac{\varepsilon^4}{r^4} \right) \right) \cos 2\theta + O(\varepsilon^2), \quad (37)$$

$$M_\varepsilon^{\theta\theta}(u_\varepsilon(r, \theta)) = \varphi_1 \left(1 + \frac{1-\gamma}{1+\gamma\alpha} \frac{\varepsilon^2}{r^2} \right) - \varphi_2 \left(1 + \frac{1-\gamma}{1+\gamma\beta} \left(\frac{4}{3+\nu} \frac{\varepsilon^2}{r^2} - 3\beta \frac{\varepsilon^4}{r^4} \right) \right) \cos 2\theta + O(\varepsilon^2), \quad (38)$$

$$M_\varepsilon^{r\theta}(u_\varepsilon(r, \theta)) = -\varphi_2 \left(1 - \beta \frac{1-\gamma}{1+\gamma\beta} \left(2 \frac{\varepsilon^2}{r^2} - 3 \frac{\varepsilon^4}{r^4} \right) \right) \sin 2\theta + O(\varepsilon^2); \quad (39)$$

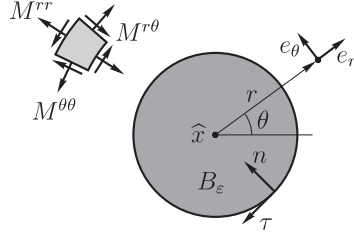


Figure 4: Polar coordinate system (r, θ) centered at the point $\hat{x} \in \Omega$.

- For $0 < r < \varepsilon$ (inside the inclusion)

$$M_\varepsilon^{rr}(u_\varepsilon(r, \theta)) = \varphi_1 \frac{2}{(1-\nu)(1+\gamma\alpha)} + \varphi_2 \frac{4}{(3+\nu)(1+\gamma\beta)} \cos 2\theta + O(\varepsilon^2), \tag{40}$$

$$M_\varepsilon^{\theta\theta}(u_\varepsilon(r, \theta)) = \varphi_1 \frac{2}{(1-\nu)(1+\gamma\alpha)} - \varphi_2 \frac{4}{(3+\nu)(1+\gamma\beta)} \cos 2\theta + O(\varepsilon^2), \tag{41}$$

$$M_\varepsilon^{r\theta}(u_\varepsilon(r, \theta)) = -\varphi_2 \frac{4}{(3+\nu)(1+\gamma\beta)} \sin 2\theta + O(\varepsilon^2). \tag{42}$$

Some terms in the above formulae require explanations. The coefficients φ_1 and φ_2 are given by

$$\varphi_1 = \frac{1}{2}(m_1(u(\hat{x})) + m_2(u(\hat{x}))), \quad \varphi_2 = \frac{1}{2}(m_1(u(\hat{x})) - m_2(u(\hat{x}))), \tag{43}$$

where $m_1(u(\hat{x}))$ and $m_2(u(\hat{x}))$ are the eigenvalues of tensor $M(u(\hat{x}))$, which can be expressed as

$$m_{1,2}(u(\hat{x})) = \frac{1}{2} \left(\text{tr}M(u(\hat{x})) \pm \sqrt{2M^D(u(\hat{x})) \cdot M^D(u(\hat{x}))} \right), \tag{44}$$

with $M^D(u(\hat{x}))$ standing by the deviatoric part of the momentum tensor $M(u(\hat{x}))$, namely

$$M^D(u(\hat{x})) = M(u(\hat{x})) - \frac{1}{2} \text{tr}M(u(\hat{x}))I. \tag{45}$$

In addition, the constants α and β are given by

$$\alpha = \frac{1 + \nu}{1 - \nu} \quad \text{and} \quad \beta = \frac{1 - \nu}{3 + \nu}. \tag{46}$$

Finally, $M_\varepsilon^{rr}(u_\varepsilon)$, $M_\varepsilon^{\theta\theta}(u_\varepsilon)$ and $M_\varepsilon^{r\theta}(u_\varepsilon)$ are the components of tensor $M_\varepsilon(u_\varepsilon)$ in the polar coordinate system, namely $M_\varepsilon^{rr}(u_\varepsilon) = e^r \cdot M_\varepsilon(u_\varepsilon)e^r$, $M_\varepsilon^{\theta\theta}(u_\varepsilon) = e^\theta \cdot M_\varepsilon(u_\varepsilon)e^\theta$ and $M_\varepsilon^{r\theta}(u_\varepsilon) = M_\varepsilon^{\theta r}(u_\varepsilon) = e^r \cdot M_\varepsilon(u_\varepsilon)e^\theta$, with e^r and e^θ used to denote the canonical basis associated to the polar coordinate system (r, θ) , such that, $\|e^r\| = \|e^\theta\| = 1$ and $e^r \cdot e^\theta = 0$. See fig. 4.

2.4 Topological derivative evaluation

Now, we can evaluate the integrals in formula (18) to collect the terms in power of ε and recognize function $f(\varepsilon)$. With these results, we can perform the limit passage $\varepsilon \rightarrow 0$. The integrals in (18) can be evaluated by using the expansions for $M_\varepsilon(u_\varepsilon)$ given by (37)-(42). The idea is to introduce a polar coordinate system (r, θ) with center at \hat{x} (see fig. 4). Then, we can write u_ε in this coordinate system to evaluate the integrals explicitly. In particular, the integrals in (18) lead to

$$-\int_{\partial B_\varepsilon} \llbracket \Sigma_\varepsilon \rrbracket n \cdot n - \int_{\partial B_\varepsilon} \llbracket M_\varepsilon(u_\varepsilon) \rrbracket n \cdot \nabla n^\top \nabla u_\varepsilon = 2\pi\varepsilon \mathbf{P}_\gamma M(u(\hat{x})) \cdot \nabla \nabla u(\hat{x}) + o(\varepsilon). \quad (47)$$

Finally, the topological derivative given by (4) can be obtained as follows

$$\mathcal{T}_\Omega(\hat{x}) = \lim_{\varepsilon \rightarrow 0} \frac{1}{f'(\varepsilon)} (2\pi\varepsilon \mathbf{P}_\gamma M(u(\hat{x})) \cdot \nabla \nabla u(\hat{x}) + o(\varepsilon)), \quad (48)$$

where the polarization tensor \mathbf{P}_γ is given by the following fourth order isotropic tensor

$$\mathbf{P}_\gamma = \frac{1}{2} \frac{1-\gamma}{1+\gamma\beta} \left(\frac{4\beta}{1-\nu} \mathbf{I} + \alpha\beta \frac{1+3\nu}{1-\nu^2} \frac{1-\gamma}{1+\gamma\alpha} I \otimes I \right). \quad (49)$$

with the parameters α and β given by (46). Now, in order to extract the main term of the above expansion, we choose

$$f(\varepsilon) = \pi\varepsilon^2, \quad (50)$$

which leads to the final formula for the topological derivative, namely (see also [24])

$$\mathcal{T}_\Omega(\hat{x}) = \mathbf{P}_\gamma M(u(\hat{x})) \cdot \nabla \nabla u(\hat{x}). \quad (51)$$

Remark 3. Formally, we can take the limit cases $\gamma \rightarrow 0$ and $\gamma \rightarrow \infty$. For $\gamma \rightarrow 0$, the inclusion leads to a void and the transmission condition on the boundary of the inclusion degenerates to homogeneous Neumann boundary condition. In fact, in this case the polarization tensor is given by

$$\mathbf{P}_0 = \frac{2}{3+\nu} \mathbf{I} + \frac{1+3\nu}{2(1-\nu)(3+\nu)} I \otimes I. \quad (52)$$

In addition, for $\gamma \rightarrow \infty$, the elastic inclusion leads to a rigid one and the polarization tensor is given by

$$\mathbf{P}_\infty = -\frac{2}{1-\nu} \mathbf{I} + \frac{1+3\nu}{2(1-\nu^2)} I \otimes I. \quad (53)$$

3 Numerical results

In this section, we present an optimization algorithm based on the topological derivative and a level-set domain representation for the compliance topology design of Kirchhoff plates, with volume constraint.

Finally, some numerical examples are presented in the context of compliance topology optimization with volume constraint. The sought topology of the structure is the solution of the general optimization problem stated as

$$\text{Minimize}_{\Omega \subset \mathbb{R}^2} \mathcal{F}_\Omega(u) = -\mathcal{J}_\chi(u) + \lambda |\Omega| , \tag{54}$$

where $|\Omega|$ is the Lebesgue measure of Ω and $\lambda > 0$ is a fixed multiplier which imposes a constraint on the volume of elastic material. It means that the shape functional to be minimized is the strain energy stored in the structure with a volume constraint. It should be stressed that the design variable in problem (54) is the topology of the domain Ω . Hence, the use of the *exact* topological sensitivity information provided by the topological derivative (51) emerges as a natural alternative in the development of a numerical optimization algorithm to tackle the problem.

For computational purposes, we consider strong and weak materials representing the elastic part and the voids, respectively. We decompose Ω into two disjoint parts Ω^s and Ω^w , representing the strong and weak materials domains respectively. The topological derivative of the volume constraint in (54) is trivial. According to (51) and remark 3, the topological derivatives of $\mathcal{F}_\Omega(u)$ are given by:

- For the strong material domain Ω^s

$$\mathcal{T}_\Omega^s = -\frac{2}{3+\nu} M(u) \cdot \nabla \nabla u - \frac{1+3\nu}{2(1-\nu)(3+\nu)} \text{tr} M(u) \text{tr}(\nabla \nabla u) - \lambda . \tag{55}$$

- For the weak material domain Ω^w

$$\mathcal{T}_\Omega^w = \frac{2}{1-\nu} M(u) \cdot \nabla \nabla u - \frac{1+3\nu}{2(1-\nu^2)} \text{tr} M(u) \text{tr}(\nabla \nabla u) + \lambda . \tag{56}$$

Having made the above considerations, the topological derivative-based optimization algorithm devised in [3] stands out as a particularly well-suited choice to solve problem (54). The procedure relies on a level-set domain representation [35] and the approximation of the topological optimality conditions by a fixed point iteration. In particular, the algorithm displays a marked ability to produce general topological domain changes uncommon to other methodologies based on a level-set representation and has been successfully applied in [3] to topology optimization in the context of two-dimensional elasticity and flow through porous media. For completeness, the algorithm is outlined in the following. For further details we refer to [3].

With the adoption of a level-set domain representation, the strong material is characterized by a function $\Psi \in L^2(\Omega)$ such that

$$\Omega^s = \{x \in \Omega, \Psi(x) < 0\} , \tag{57}$$

whereas the weak material domain is defined by

$$\Omega^w = \{x \in \Omega, \Psi(x) > 0\} . \tag{58}$$

Now, let us consider the topological derivative of the shape functional $\mathcal{F}_\Omega(u)$. According to [3], an obvious sufficient condition of local optimality of problem (54) for the class of perturbations consisting

of circular inclusions is

$$\mathcal{T}_\Omega(x) > 0 \quad \forall x \in \Omega. \quad (59)$$

To devise a level-set-based algorithm whose aim is to produce a topology that satisfies (59) it is convenient to define the function

$$g(x) = \begin{cases} -\mathcal{T}_\Omega^s(x) & \text{if } x \in \Omega^s \\ \mathcal{T}_\Omega^w(x) & \text{if } x \in \Omega^w \end{cases}. \quad (60)$$

With the above definition and (57,58) it can be easily established that the sufficient condition (59) is satisfied if the following equivalence relation between g and the level-set function Ψ holds

$$\exists \tau > 0 \quad \text{s.t.} \quad g = \tau \Psi, \quad (61)$$

or, equivalently,

$$\theta := \arccos \left[\frac{\langle g, \Psi \rangle_{L^2(\Omega)}}{\|g\|_{L^2(\Omega)} \|\Psi\|_{L^2(\Omega)}} \right] = 0, \quad (62)$$

where θ is the angle between the vectors g and Ψ in $L^2(\Omega)$.

Starting from a given level-set function $\Psi_0 \in L^2(\Omega)$ which defines the chosen initial guess for the optimum topology, the algorithm proposed in [3] produces a sequence $(\Psi_i)_{i \in \mathbf{N}}$ of level-set functions that provides successive approximations to the sufficient condition for optimality (61). The sequence satisfies

$$\begin{aligned} \Psi_0 &\in L^2(\Omega), \\ \Psi_{n+1} &\in \text{co}(\Psi_n, g_n) \quad \forall n \in \mathbf{N}, \end{aligned} \quad (63)$$

where $\text{co}(\Psi_n, g_n)$ is the convex hull of $\{\Psi_n, g_n\}$. In the actual algorithm the initial guess Ψ_0 is normalized. With \mathcal{S} denoting the unit sphere in $L^2(\Omega)$, the algorithm is explicitly given by

$$\begin{aligned} \Psi_0 &\in \mathcal{S}, \\ \Psi_{n+1} &= \frac{1}{\sin \theta_n} \left[\sin((1 - \kappa_n)\theta_n)\Psi_n + \sin(\kappa_n\theta_n) \frac{g_n}{\|g_n\|_{L^2(\Omega)}} \right] \quad \forall n \in \mathbf{N}, \end{aligned} \quad (64)$$

where $\kappa_n \in [0, 1]$ is a step size determined by a line-search in order to decrease the value of the cost functional $\mathcal{F}_\Omega(u)$ and, by construction of (64)₂, we have that $\Psi_{n+1} \in \mathcal{S} \forall n \in \mathbf{N}$. The iterative process is stopped when for some iteration the obtained decrease in $\mathcal{F}_\Omega(u)$ is smaller than a given numerical tolerance. If, at this stage, the optimality condition (61,62) is not satisfied to the desired degree of accuracy, i.e. if $\theta_{n+1} > \epsilon_\theta$, where ϵ_θ is a pre-specified convergence tolerance, then a uniform mesh refinement of the structure is carried out and the procedure is continued.

In order to explain briefly the significance of the topological derivative in topology optimization we present some numerical examples. The *Discrete Kirchhoff Triangle* three node finite element (DKT-9), which is fully detailed in [36], is adopted for the discretization of the variational problem (7). The topology is identified by the strong material distribution and the inclusions of weak material are used to mimic the holes. In the examples we consider as initial guess a unit square plate, with Poisson's

ratio $\nu = 0.3$ and the product $Eh^3 = 1$. The contrast is given by $\gamma = 0.001$. Furthermore, the thick lines that appear on the figures are used to denote clamped ($u = \partial u / \partial n = 0$) boundary conditions. We start with a uniform mesh containing 3200 elements. Then we perform 3 steps of uniform mesh refinement for the first three examples and 5 steps of uniform mesh refinement for the last example.

3.1 Example 1

In this first example we present a plate submitted to a pair of uniform bending moments, $\bar{m} = 1$ and $\bar{m} = -1$ applied on a region of length 0.5 of the middle of the opposite sides, as shown in fig. 5(a). We set $\lambda = 3.80$, corresponding to a volume constraint of 50% of hard material. The final topology is presented in fig. 5(b).

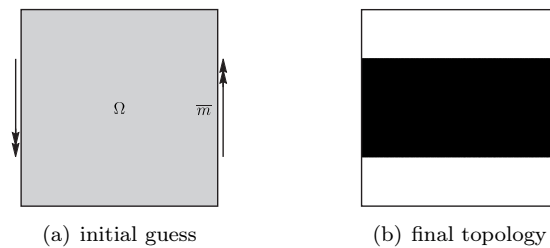


Figure 5: Example 1: plate submitted to a pair of uniform bending moments.

3.2 Example 2

In this example we present a plate submitted to three uniform bending moments, $\bar{m} = 1$ applied on a region of length 0.5 (middle) of the right edge and $\bar{m} = -1$ acting on two regions of length 0.25 (top and bottom) of the left edge, as shown in fig. 6(a). We set $\lambda = 3.88$, corresponding to a volume constraint of 50% of hard material. The final topology is presented in fig. 6(b).

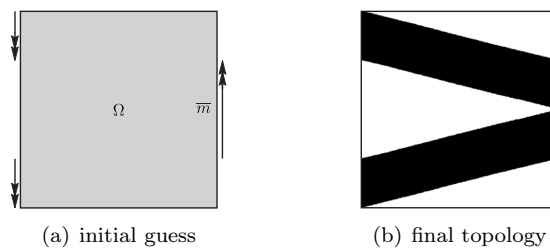


Figure 6: Example 2: plate submitted to three uniform bending moments.

3.3 Example 3

In this next example we present a plate submitted to two pairs of uniform bending moments $\bar{m} = 1$ and $\bar{m} = -1$, as shown in fig. 7(a). The first pair is applied on two regions of length 0.20 of the top and bottom edges. The second pair is acting on two regions of length 0.20 of the left and right edges. We set $\lambda = 4.40$, corresponding to a volume constraint of 50% of hard material. The final topology is presented in fig. 7(b).

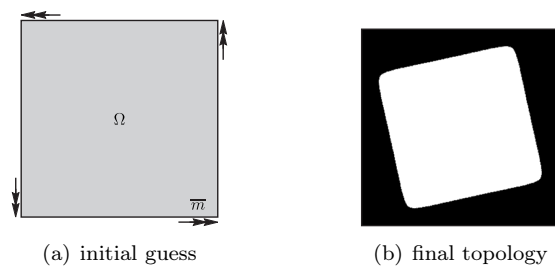


Figure 7: Example 3: plate submitted to two pairs of uniform bending moments.

3.4 Example 4

In this last example the plate is clamped in two adjacent sides and a concentrated load $\bar{Q}_i = 1$ is applied at the free corner, as illustrated in fig. 8(a). We set $\lambda = 4$. The topological derivative evaluated in the hold-all domain is shown in fig. 8(b). The obtained topology is presented in fig. 8(c). The convergence history for the shape functional and theta angle are presented in fig. 9.

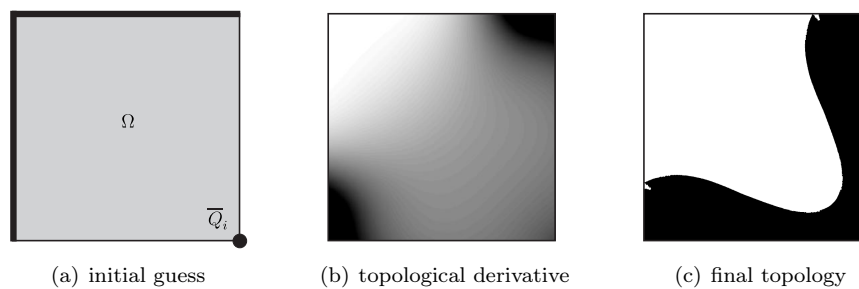


Figure 8: Example 4: clamped plate submitted to a concentrated load.

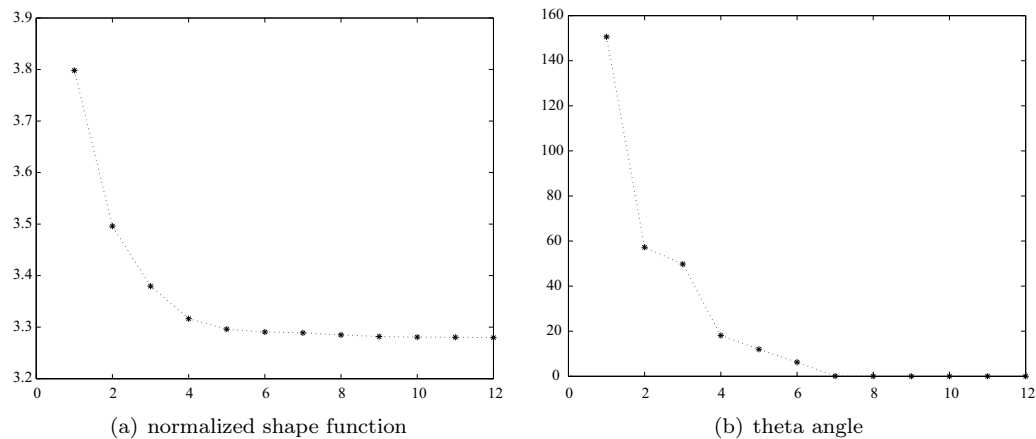


Figure 9: Example 4: convergence history.

4 Conclusions

The topological derivative of the total potential energy associated to the Kirchhoff plate bending problem, considering as singular perturbation the insertion of a small circular inclusion, has been calculated through the approach proposed in [6]. We have formally performed the limit passages when the contrast $\gamma \rightarrow 0$ and $\gamma \rightarrow \infty$. For $\gamma \rightarrow 0$, the inclusion leads to a void and the transmission condition on the boundary of the inclusion degenerates to homogeneous Neumann boundary condition. In addition, for $\gamma \rightarrow \infty$, the elastic inclusion leads to a rigid one. The closed forms of the polarization tensors are identified for both cases. Then, we have devised an optimization algorithm based on the topological derivatives and a level-set domain representation, as proposed in [3], for the compliance topology design of Kirchhoff plates, with volume constraint. The topology is identified by the strong material distribution and the inclusions of weak material are used to mimic the holes. Finally, in order to explain the significance of the topological derivative in topology optimization, we have presented some numerical examples in the context of compliance topology optimization with volume constraint, where the DKT-9 finite element was adopted for the problem discretization.

References

- [1] Sokółowski, J. & Żochowski, A., On the topological derivative in shape optimization. *SIAM Journal on Control and Optimization*, **37(4)**, pp. 1251–1272, 1999.
- [2] Allaire, G., de Gournay, F., Jouve, F. & Toader, A., Structural optimization using topological and shape sensitivity via a level set method. *Control and Cybernetics*, **34(1)**, pp. 59–80, 2005.
- [3] Amstutz, S. & Andrä, H., A new algorithm for topology optimization using a level-set method. *Journal of Computational Physics*, **216(2)**, pp. 573–588, 2006.

- [4] Amstutz, S. & Novotny, A., Topological optimization of structures subject to von Mises stress constraints. *Structural and Multidisciplinary Optimization*, **41(3)**, pp. 407–420, 2010.
- [5] Giusti, S., Novotny, A. & Sokolowski, J., Topological derivative for steady-state orthotropic heat diffusion problem. *Structural and Multidisciplinary Optimization*, **40(1)**, pp. 53–64, 2010.
- [6] Novotny, A., Feijóo, R., Padra, C. & Taroco, E., Topological sensitivity analysis. *Computer Methods in Applied Mechanics and Engineering*, **192(7-8)**, pp. 803–829, 2003.
- [7] Novotny, A., Feijóo, R., Padra, C. & Taroco, E., Topological derivative for linear elastic plate bending problems. *Control and Cybernetics*, **34(1)**, pp. 339–361, 2005.
- [8] Novotny, A., Feijóo, R., Taroco, E. & Padra, C., Topological sensitivity analysis for three-dimensional linear elasticity problem. *Computer Methods in Applied Mechanics and Engineering*, **196(41-44)**, pp. 4354–4364, 2007.
- [9] Amstutz, S., Horchani, I. & Masmoudi, M., Crack detection by the topological gradient method. *Control and Cybernetics*, **34(1)**, pp. 81–101, 2005.
- [10] Feijóo, G., A new method in inverse scattering based on the topological derivative. *Inverse Problems*, **20(6)**, pp. 1819–1840, 2004.
- [11] Guzina, B. & Bonnet, M., Small-inclusion asymptotic of misfit functionals for inverse problems in acoustics. *Inverse Problems*, **22(5)**, pp. 1761–1785, 2006.
- [12] Hintermüller, M. & Laurain, A., Electrical impedance tomography: from topology to shape. *Control and Cybernetics*, **37(4)**, pp. 913–933, 2008.
- [13] Masmoudi, M., Pommier, J. & Samet, B., The topological asymptotic expansion for the Maxwell equations and some applications. *Inverse Problems*, **21(2)**, pp. 547–564, 2005.
- [14] Auroux, D., Masmoudi, M. & Belaid, L., Image restoration and classification by topological asymptotic expansion. *Variational formulations in mechanics: theory and applications*, Barcelona, Spain, 2007.
- [15] Belaid, L., Jaoua, M., Masmoudi, M. & Siala, L., Application of the topological gradient to image restoration and edge detection. *Engineering Analysis with Boundary Element*, **32(11)**, pp. 891–899, 2008.
- [16] Hintermüller, M., Fast level set based algorithms using shape and topological sensitivity. *Control and Cybernetics*, **34(1)**, pp. 305–324, 2005.
- [17] Hintermüller, M. & Laurain, A., Multiphase image segmentation and modulation recovery based on shape and topological sensitivity. *Journal on Mathematical Imaging and Vision*, **35**, pp. 1–22, 2009.
- [18] Larrabide, I., Feijóo, R., Novotny, A. & Taroco, E., Topological derivative: a tool for image processing. *Computers & Structures*, **86(13-14)**, pp. 1386–1403, 2008.
- [19] Amstutz, S., Giusti, S., Novotny, A. & de Souza Neto, E., Topological derivative for multi-scale linear elasticity models applied to the synthesis of microstructures. *International Journal for Numerical Methods in Engineering*, **84**, pp. 733–756, 2010.
- [20] Goethem, N.V. & Novotny, A., Crack nucleation sensitivity analysis. *Mathematical Methods in the Applied Sciences*, **33(16)**, pp. 197–1994, 2010.
- [21] Amstutz, S., Sensitivity analysis with respect to a local perturbation of the material property. *Asymptotic Analysis*, **49(1-2)**, pp. 87–108, 2006.
- [22] de Faria, J.R. & Novotny, A., On the second order topological asymptotic expansion. *Structural and Multidisciplinary Optimization*, **39(6)**, pp. 547–555, 2009.
- [23] Nazarov, S. & Sokolowski, J., Asymptotic analysis of shape functionals. *Journal de Mathématiques Pures et Appliquées*, **82(2)**, pp. 125–196, 2003.
- [24] Amstutz, S. & Novotny, A., Topological asymptotic analysis of the Kirchhoff plate bending problem. *ESAIM: Control, Optimisation and Calculus of Variations*, **To appear**, 2010.
- [25] Amstutz, S., *Aspects théoriques et numériques en optimisation de forme topologique*. Phd thesis, Institut

- National des Sciences Appliquées, Toulouse, France, 2003.
- [26] Laurain, A., *Singularly perturbed domains in shape optimisation*. Phd thesis, University Henri Poincaré, Nancy, France, 2006.
 - [27] Novotny, A., *Análise de sensibilidade topológica*. Phd thesis, Laboratório Nacional de Computação Científica, Petrópolis, Brazil, 2003.
 - [28] Delfour, M. & Zolésio, J., *Shapes and Geometries. Advances in Design and Control*. SIAM: Philadelphia, 2001.
 - [29] Sokółowski, J. & Zolésio, J., *Introduction to shape optimization - shape sensitivity analysis*. Springer-Verlag: New York, 1992.
 - [30] Eshelby, J., The elastic energy-momentum tensor. *Journal of Elasticity*, **5(3-4)**, pp. 321–335, 1975.
 - [31] Ammari, H. & Kang, H., *Reconstruction of small inhomogeneities from boundary measurements*. Lectures Notes in Mathematics vol. 1846, Springer-Verlag: Berlin, 2004.
 - [32] Ammari, H. & Kang, H., *Polarization and moment tensors with applications to inverse problems and effective medium theory*. Applied Mathematical Sciences vol. 162, Springer-Verlag: New York, 2007.
 - [33] Kozlov, V., Maz'ya, W. & Movchan, A., *Asymptotic analysis of fields in multi-structures*. Clarendon Press: Oxford, 1999.
 - [34] Little, R., *Elasticity*. Prentice-Hall: New Jersey, 1973.
 - [35] Osher, S. & Sethian, J., Front propagating with curvature dependent speed: algorithms based on hamilton-jacobi formulations. *Journal of Computational Physics*, **78**, pp. 12–49, 1988.
 - [36] Batoz, J.L., An explicit formulation for an efficient triangular plate-bending element. *Advances in Applied Mechanics*, **18**, pp. 1077–1089, 1982.

Analysis of non-linear hyperelastic constitutive models under simple shear deformation

L.C.S. Nunes

*Laboratory of Opto-Mechanics (LOM/LMTA), Department of Mechanical Engineering, TEM/PGMEC, Universidade Federal Fluminense – UFF
Rua Passo da Pátria 156, 24210-240, Niterói, RJ – Brazil*

Abstract

The purpose of this paper is to analyze the hyperelastic behavior, which is characterized by large deformation, of a rubberlike material under simple shear deformation. In order to do this, some classical constitutive models available in the literature are used to reproduce the experimental data. The idea is to investigate the hyperelastic models widely used in finite elements code and to verify the agreement between the theoretical and experimental data, taking into account simple shear conditions. The experimental procedure is performed using digital image correlation (DIC) method, which is an optical-numerical approach to estimate full-field displacements.

Keywords: simple shear, hyperelasticity, full-field method, constitutive models.

1 Introduction

Hyperelastic behavior is commonly observed in some polymers, mainly the long chain polymers, like as elastomers (or rubbers) that are characterized by flexibility and stability. Polydimethylsiloxane (PDMS) is a silicone rubber, which has a wide range of applications in mechanical sensors [1, 2], electronic components [3, 4] and medical devices [5].

For determining mechanical behavior and properties of polymeric materials several mechanical tests have been developed [6–8]. There are a number of testing machines which give rise to shear stresses including lap shear, punch shear, torsion and four point loading. Guélon *et al.* [9] proposed a new characterization method for rubber, which consists of performing only one heterogeneous mechanical test. A test method for determining the shear modulus of elastomeric bearing was developed by Topkaya and Yura [10]. Nunes [11] proposes to analyze small deformations of the adhesive in the single lap joint specimen and to estimate the shear modulus of Polydimethylsiloxane (PDMS) using the DIC method.

The polymer PDMS can be classified as a hyperelastic material, in which the strains may be large

[12,13]. In order to describe this behavior, a function so-called strain-energy function is taken into consideration. There are many proposed strain-energy function expressions, some of them, which are well tried within the constitutive theory of finite elasticity and frequently employed in the literature [14]. The most widely cited strain-energy formulations are the Mooney-Rivlin and Ogden models [15–17]. Recently, new hyperelastic models have been proposed [18–21]. Treloar [22] presented a well-developed experimental work, in which the experimental data have been widely used in many articles. Mechanical characterization tests of hyperelastic rubber-like materials using optical methods can be found in recent literatures [23, 24].

The purpose of the present work is to investigate the mechanical behavior of the hyperelastic polymer under large shear deformations, comparing some constitutive models found in literature. The angular distortions are estimated by means of an experimental method known as Digital Image Correlation (DIC). In order to do this, an arrangement based on single lap joint is used to generate a simple shear deformation [11, 23]. The material parameters, taking into account Mooney-Rivlin, Yeoh, Nunes and Ogden models and experimental data, are estimated using Levenberg-Marquardt method [25–27].

2 Digital Image Correlation Method

Digital Image Correlation (DIC) is an optical-numerical full-field surface displacement measurement method [28–30]. It is based on a comparison between two images of a specimen coated by a random speckled pattern in the undeformed and in the deformed states. Its special merits encompass non-contact measurements, simple optic setups, no special preparation of specimens and no special illumination.

The basic principle of the DIC method is to search for the maximum correlation between small zones (subsets) of the specimen in the undeformed and deformed states, as illustrated in Fig. 1. From a given image-matching rule, the displacement field at different positions in the analysis region can be computed. The simplest image-matching procedure is the cross-correlation, which provides the in-plane displacement fields $u(x,y)$ and $v(x,y)$ by matching different zones of the two images.

A commonly used correlation coefficient is defined as follows

$$c(u, v) = \frac{\sum_{i=1}^m \sum_{j=1}^n [f(x_i, y_j) - \bar{f}] [g(x'_i, y'_j) - \bar{g}]}{\sqrt{\sum_{i=1}^m \sum_{j=1}^n [f(x_i, y_j) - \bar{f}]^2} \sqrt{\sum_{i=1}^m \sum_{j=1}^n [g(x'_i, y'_j) - \bar{g}]^2}} \quad (1)$$

$$\begin{aligned} x' &= x + u_0 + \frac{\partial u}{\partial x} dx + \frac{\partial u}{\partial y} dy \\ y' &= y + v_0 + \frac{\partial v}{\partial x} dx + \frac{\partial v}{\partial y} dy \end{aligned} \quad (2)$$

where $f(x, y)$ is the pixel gray level value (ranging from 0 to 255) at the coordinates (x, y) , for the undeformed or original image; $g(x', y')$, is the pixel gray level value at the coordinates (x', y') for the

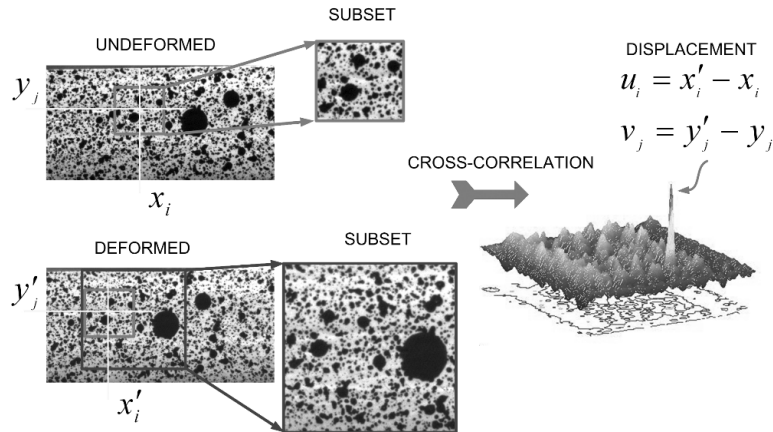


Figure 1: Schematic of the principle of digital image correlation method.

deformed or target image; \bar{f} and \bar{g} are the average gray values for images and, finally, u and v are, respectively, the displacement components for the subset centers in the x and y directions.

3 Constitutive model of rubber elasticity

A material element $d\mathbf{X}$ in the reference configuration can be transformed, into a material element $d\mathbf{x}$ in the current configuration, using the deformation gradient tensor \mathbf{F} . The relation between these elements is given by $d\mathbf{X} = \mathbf{F}d\mathbf{x}$ [14,16]. Let us consider the case of simple shear deformation, illustrated in Fig. 2, which the rectangular Cartesian coordinate of any point of deformed element can be written as

$$x_1 = X_1 + \gamma X_2; \quad x_2 = X_2; \quad x_3 = X_3 \quad (3)$$

where γ is the amount of shear. Using the Eqs. (3), the deformation gradient tensor for simple shear, \mathbf{F} , can be expressed as

$$\mathbf{F} = \begin{bmatrix} 1 & \gamma & 0 \\ 0 & 1 & 0 \\ 0 & 0 & 1 \end{bmatrix} \quad (4)$$

From Eq. (4), the right Cauchy-Green deformation tensor for simple shear, \mathbf{C} , can be written as

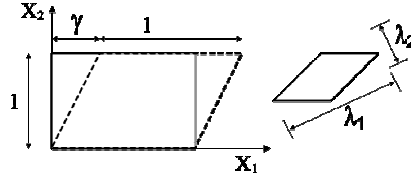


Figure 2: Simple shear deformation.

$$\mathbf{C} = \mathbf{F}^T \mathbf{F} = \begin{bmatrix} 1 & \gamma & 0 \\ \gamma & \gamma^2 + 1 & 0 \\ 0 & 0 & 1 \end{bmatrix} \quad (5)$$

The characteristic equation $\det(\mathbf{C} - \lambda^2 \mathbf{I}) = 0$, considering $\lambda_3 = 1$, reduces to $\lambda - \lambda^{-1} = \gamma$, since we may take $\lambda_2^{-1} \equiv \lambda_1 = \lambda \geq 1$ without loss of generality. Consequently, the principal stretches can be given by

$$\lambda_1 = \sqrt{1 + \frac{\gamma^2}{2} + \gamma \sqrt{1 + \frac{\gamma^2}{4}}} \quad \text{and} \quad \lambda_2 = \sqrt{1 + \frac{\gamma^2}{2} - \gamma \sqrt{1 + \frac{\gamma^2}{4}}} \quad (6)$$

There are many tensor invariants that can be written in terms of the metric tensor in the undeformed and deformed, as well as the relative stretches. The principal scalar invariants of the right Cauchy-Green deformation tensor can be determined as

$$I_1 = \text{tr} \mathbf{C} = \gamma^2 + 3$$

$$I_2 = \frac{1}{2} \left[(\text{tr} \mathbf{C})^2 - \text{tr} \mathbf{C}^2 \right] = \gamma^2 + 3 \quad (7)$$

$$I_3 = J = \det \mathbf{C} = 1 \quad (8)$$

A suitable strain-energy function for incompressible isotropic hyperelastic materials can be expressed as a set of independent strain invariant of the right Cauchy-Green tensor \mathbf{C} , given by

$$W = W [I_1(\mathbf{C}), I_2(\mathbf{C}), I_3(\mathbf{C})] \quad (9)$$

The second Piola-Kirchhoff stress tensor is defined by [14]

$$\mathbf{S} = 2 \frac{\partial W(\mathbf{C})}{\partial \mathbf{C}} = 2 \left[\left(\frac{\partial W}{\partial I_1} + I_1 \frac{\partial W}{\partial I_2} \right) \mathbf{I} - \frac{\partial W}{\partial I_2} \mathbf{C} + I_3 \frac{\partial W}{\partial I_3} \mathbf{C}^{-1} \right] \quad (10)$$

The Cauchy stress $\boldsymbol{\sigma}$ can be expressed in terms of the second Piola-Kirchhoff stress tensor \mathbf{S} by the Piola transformation and it is given by $\mathbf{s} = J^{-1} \mathbf{F} \mathbf{S} \mathbf{F}^T$.

Substituting Eqs. (5) and (3) into (10), the shear stress component can be given by

$$\sigma_{12} = 2 \left(\frac{\partial W}{\partial I_1} + \frac{\partial W}{\partial I_2} \right) \gamma \quad (11)$$

In order to investigate the hyperelastic behavior from experimental data four constitutive models are taken into consideration. Mooney and Rivlin [14, 16] observed that rubber response was linear under simple shear loading conditions. With this observation, they proposed a strain energy function based on the first two invariants and the first order model can be defined by

$$W(I_1, I_2) = c_{10}(I_1 - 3) + c_{01}(I_2 - 3) \quad (12)$$

where c_{10} and c_{01} are the material parameters. The shear modulus is defined by $\mu = 2(c_{01} + c_{10})$

Yeoh [14] proposes a model based on classical Mooney-Rivlin model, it can be expressed by

$$W(I_1) = c_1(I_1 - 3) + c_2(I_1 - 3)^2 + c_3(I_1 - 3)^3 \quad (13)$$

where c_1 , c_2 and c_3 are material constant. Moreover, in this case, the shear modulus is $\mu = 2c_1 + 4c_2(I_1 - 3) + 6c_3(I_1 - 3)^2$

A simple model developed to predict non-linear hyperelastic behavior of rubber-like material under simple shear deformation was proposed by Nunes [23]. The model is

$$W(I) = \frac{1}{2} \left[c_1(I - 3) + c_2(I - 3)^{3/4} \right] \quad (14)$$

with constant parameters given by c_1 and c_2 . The invariants are $I = I_1 = I_2$.

A very sophisticated development for simulating incompressible materials in the phenomenological context is due to Odgen [14, 16]. The strain-energy as a function of principal stretches is given by

$$W(\lambda_1, \lambda_2, \lambda_3) = \sum_{p=1}^N \frac{\mu_p}{\alpha_p} (\lambda_1^{\alpha_p} + \lambda_2^{\alpha_p} + \lambda_3^{\alpha_p} - 3) \quad (15a)$$

In the present case,

$$W(\lambda) = \sum_{p=1}^N \frac{\mu_p}{\alpha_p} (\lambda^{\alpha_p} + \lambda^{-\alpha_p} - 2) \quad (15b)$$

where the shear modulus is $\mu = \frac{1}{2} \sum_{p=1}^N \mu_p \alpha_p$ with $\mu_p \alpha_p > 0$.

Substituting Eqs. (12), (13), (14) and (15) into Eq. (11), yields the component of Cauchy stresses associated with Mooney-Rivlin, Yeoh, Nunes and Odgen, respectively, given by

$$\begin{aligned}
 \sigma_{12} &= \mu\gamma \\
 \sigma_{12} &= 2c_1\gamma + 4c_2\gamma^3 + 6c_3\gamma^5 \\
 \sigma_{12} &= 2c_1\gamma + \frac{3}{2}c_2\sqrt{\gamma} \\
 \sigma_{12} &= \frac{2}{1+\lambda^2} \sum_{p=1}^N \mu_p (\lambda^{\alpha_p-1} - \lambda^{-\alpha_p-1})
 \end{aligned} \tag{16}$$

4 Experimental tests

In this work, a single lap joint is used to transfer load from one adherend to another by a simple shearing mechanism [11, 23]. The stiffness of the adherends (steel A36) is much greater than the adhesives (Polydimethylsiloxane) as can be found in literatures [11, 23]. Therefore, it is suitable to assume the hypothesis of the adherends do not deform and the adhesives only deform in shear. The experimental setup and geometry are schematically illustrated in Fig. 3.

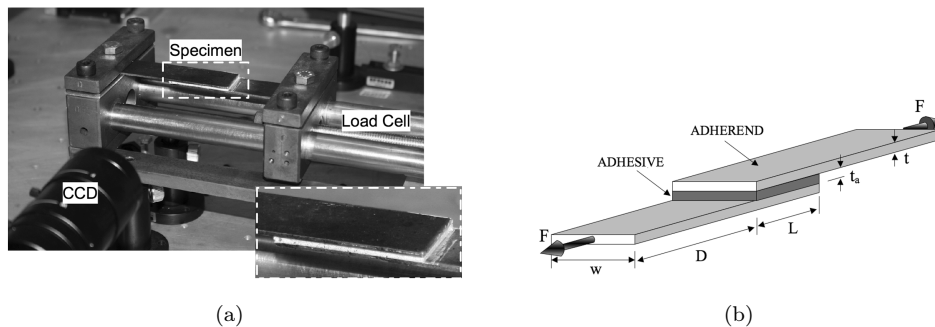


Figure 3: (a) Experimental arrangement and (b) simple lap joints.

The shear test was performed and the geometric shape for the single lap joint, schematically illustrated in Fig. 3(b), was considered with the following data: (a) different tensile forces, F ; (b) length of restraint against transversal motion of 25 mm; segment of length, $D = 50$ mm; joint lengths, L , equal to 51 mm; joint width, $w = 25.4$ mm; adherend and adhesive thickness, $t = 1.6$ mm and $t_a = 1.6$ mm, respectively. The upper and lower adherends have the same characteristics, i.e., Steel A36 and the material of adhesive was a Silicone rubber (Polydimethylsiloxane).

The tests were performed with an apparatus developed for applying load in a single lap joint, a CCD camera set perpendicularly to the specimen and a computer for capturing and processing the

images. The experimental arrangement is presented in Fig. 3(a). The single lap joint, fixed in the strain apparatus, was covered with painted speckles (random black and white pattern). The geometry is in agreement with the schematic view illustrated in Fig 2. The CCD camera (Sony XCD-SX910) used to record the images of the specimen has a resolution of 1376x1024 pixels. In this experimental configuration, one pixel of the CCD camera corresponds to an area approximately equal to $4.65 \times 4.65 \mu\text{m}^2$ on the specimen.

The basic idea of the experimental procedure was to take the images of specimen in the undeformed and deformed states. With these data, it was determined the full-field displacements by means of DIC program and consequently was estimated the angular distortion [11, 23]. The experiments were conducted at room temperature considering quasi-static processes.

5 Results and discussion

Figure 4(a) illustrates the stress-strain curve for simple shear test, moreover, Mooney-Rivlin, Yeoh and Nunes models are presented to describe the experimental behavior. Furthermore, stress and principal stretch relationship is shown in Fig. 4(b), in this case, the experimental results is confronted with Odgen model. Clearly, non-linear behavior may be observed. However, it is important to note that Mooney-Rivlin model is a linear model.

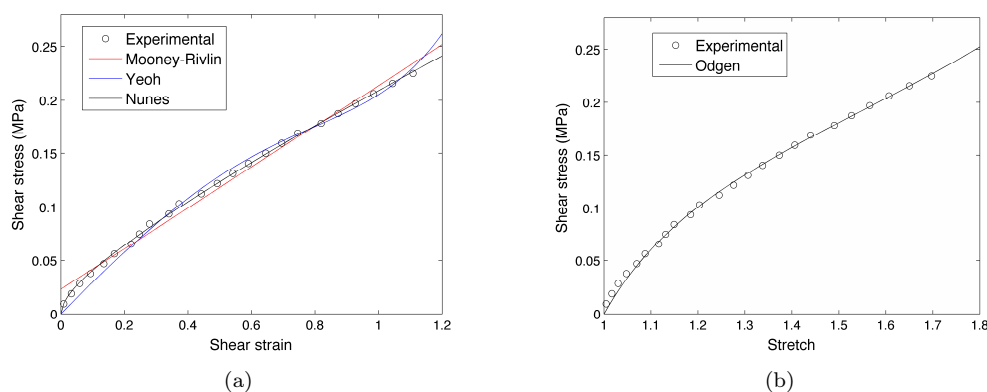


Figure 4: Simple shear deformation. Comparison between experimental data and model: Mooney-Rivlin, Yeoh, Nunes and Odgen.

Values for nine parameters associated with constitutive models, present in Eqs. (16), were estimated using Levenberg-Marquardt method, which is a well-known and powerful iterative method for solving nonlinear least squares problems of parameter estimation. Parameters of Mooney-Rivlin, Yeoh, Nunes and Odgen models, previously presented in section 3 are displayed in Table 1.

Table 1: Fitted parameters for different constitutive models.

Fitted parameters
<u>Mooney-Rivlin</u>
$\mu = 1.91 \times 10^5$
<u>Yeoh</u>
$c_1 = 1.48 \times 10^5$; $c_2 = -4.35 \times 10^4$; $c_3 = 1.39 \times 10^4$
<u>Nunes</u>
$c_1 = 5.89 \times 10^4$; $c_2 = 6.08 \times 10^4$
<u>Odgen</u>
$\mu_1 = 4.86 \times 10^6$; $\mu_2 = 4.86 \times 10^6$; $\mu_3 = 3.44 \times 10^4$
$\alpha_1 = 0.0202$; $\alpha_2 = 0.0206$; $\alpha_3 = 5.201$
$\mu = 1.89 \times 10^5$

6 Conclusion

The aim here was to compare some constitutive model to describe the simple shear behavior under large deformation. In order to do that, a simple shear test was performed and the full-field displacements were estimated by means of the Digital Image Correlation method. Based on these results, values of angular distortion (i.e. shear strain), which are associated with different applied loads, were determined. In order to find a best model to the experimental data, Mooney-Rivlin, Yeoh, Nunes and Odgen models were investigated. As could be observed, there was a significant difference between the experimental data and the classic Mooney-Rivlin model, whereas the Nunes model is much closer.

Acknowledgements The authors would like to express their gratitude to the Ministry of Science and Technology. The present paper received financial support from Brazilian agencies CNPq and FAPERJ.

References

- [1] Kim, J., Lau, K., Shepherd, R., Wu, Y., Wallace, G. & Diamond, D., Performance characteristics of a polypyrrole modified polydimethylsiloxane (PDMS) membrane based microfluidic pump. *Sens Actuators A*, **148**, pp. 239–244, 2008.
- [2] Lin, Y., Kang, S. & Wu, T., Fabrication of polydimethylsiloxane (PDMS) pulsating heat pipe. *Appl Therm Eng*, **29**, pp. 573–580, 2009.
- [3] Khosla, A. & Gray, B., Preparation, characterization and micromolding of multi-walled carbon nanotube polydimethylsiloxane conducting nanocomposite polymer. *Mater Lett*, **63**, pp. 1203–1206, 2009.

- [4] Lee, D., Mekar, H., Hiroshima, H., Matsumoto, S., Itoh, T., Takahashi, M. & Maeda, R., 3d replication using pdms mold for microcoil. *Microelectr Eng*, **86**, pp. 920–924, 2009.
- [5] Lawrence, B., Marchant, J., Pindrus, M., Omenetto, F. & Kaplan, D., Silk film biomaterials for cornea tissue engineering. *Biomater*, **30**, pp. 1299–1308, 2009.
- [6] Lee, G., Kang, S. & Kwon, D., Characterization of elastic modulus and work of adhesion in elastomeric polymers using microinstrumented indentation technique. *Mater Sci Eng A*, **496**, pp. 494–500, 2008.
- [7] Ward, I. & Sweeney, J., *An Introduction to the Mechanical Properties of Solid Polymers*. John Wiley & Sons Ltd, 2nd edition, 2004.
- [8] Brown, R., *Handbook of Polymer Testing*. Rapra Technology Limited: Shropshire, UK, 2002.
- [9] Guélon, T., Toussaint, E., Le Cam, J.B., Promma, N. & Grédiac, M., A new characterisation method for rubber. *Polym Test*, **28**, pp. 715–723, 2009.
- [10] Topkaya, C. & Yura, J., Test method for determining the shear modulus of elastomeric bearings. *J Struct Eng*, **128(6)**, pp. 797–805, 2002.
- [11] Nunes, L., Shear modulus estimation of the polymer polydimethylsiloxane (PDMS) using digital image correlation. *Mater Design*, **31**, pp. 583–588, 2010.
- [12] Yu, Y. & Zhao, Y., Deformation of pdms membrane and microcantilever by a water droplet: Comparison between Mooney-Rivlin and linear elastic constitutive models. *J Colloid Interface Sci*, **332**, pp. 467–476, 2009.
- [13] Beda, T., Modeling hyperelastic behavior of rubber: A novel invariant-based and a review of constitutive models. *J Polym Sci B: Polym Phys*, **45**, pp. 1713–1732, 2007.
- [14] Holzapfel, G., *Nonlinear Solid Mechanics: A continuum approach for engineering*. John Wiley & Sons Ltd, 2008.
- [15] Mooney, M., A theory of large elastic deformation. *J Appl Phys*, **11**, pp. 582–592, 1940.
- [16] Ogden, R., *Non-Linear Elastic Deformations*. Dover Publications: Mineola, NY, 1997.
- [17] Boyce, M. & Arruda, E., Constitutive models of rubber elasticity: a review. *Rubber Chem Technol*, **73**, pp. 504–523, 2000.
- [18] Lopez-Pamies, O., A new i_1 -based hyperelastic model for rubber elastic materials. *C R Mécanique*, **338**, pp. 3–11, 2010.
- [19] Farahani, K. & Bahai, H., Hyper-elastic constitutive equations of conjugate stresses and strain tensors for the Seth-Hill strain measures. *Int J Eng Sci*, **42**, pp. 29–41, 2004.
- [20] Attard, M. & Hunt, G., Hyperelastic constitutive modeling under finite strain. *Int J Solids Struct*, **41**, pp. 5327–5350, 2004.
- [21] Lahellec, N., Mazerolle, F. & Michel, J., Second-order estimate of the macroscopic behavior of periodic hyperelastic composites: theory and experimental validation. *J Mech Phys Solids*, **52**, pp. 27–49, 2004.
- [22] Treloar, L., Stress-strain data for vulcanised rubber under various types of deformation. *Trans Faraday Soc*, **40**, pp. 59–70, 1944.
- [23] Nunes, L., Mechanical characterization of hyperelastic polydimethylsiloxane by simple shear test. *Mat Scie Eng A*, **528**, pp. 1799–1804, 2011.
- [24] Meunier, L., Chagnon, G., Favier, D., Orgéas, L. & Vacher, P., Mechanical experimental characterisation and numerical modelling of an unfilled silicone rubber. *Polym Test*, **27**, pp. 765–777, 2008.
- [25] Levenberg, K., A method for the solution of certain problems in least squares. *Quart Appl Math*, **2**, pp. 164–168, 1944.
- [26] Marquardt, D., An algorithm for least-squares estimation of nonlinear parameters. *SIAM J Appl Math*, **11**, pp. 431–441, 1963.

- [27] Gill, P.R., Murray, W. & Wright, M.H., The levenberg-marquardt method. *Practical Optimization*, Academic Press: London, pp. 136–137, 1981. S. 4.7.3.
- [28] Dournaux, J., Bouvier, S., Aouafi, A. & Vacher, P., Full-field measurement technique and its application to the analysis of materials behaviour under plane strain mode. *Mater Sci Eng A*, **500**, pp. 47–62, 2009.
- [29] Dally, J. & Riley, W., *Experimental Stress Analysis*. McGraw Hill, 4th edition, 2005.
- [30] Sharpe Jr., W.N., (ed.) *Springer Handbook of Experimental Solid Mechanics*. Springer Science and Business Media, LLC: New York, 2008.

Peridynamic analysis for predicting damage initiation and growth in metallic and composite structures

Erkan Oterkus

National Institute of Aerospace, Hampton, VA 23666 – United States

Erdogan Madenci

*Department of Aerospace and Mechanical Engineering, The University of Arizona,
Tucson, AZ 85721-0119 – United States*

Abstract

A recently introduced nonlocal peridynamic theory removes the obstacles present in classical continuum mechanics that limit the prediction of crack initiation and growth in materials. Furthermore, damage growth in composites involves complex and progressive failure modes. Current computational tools are incapable of predicting failure in composite materials mainly due to their mathematical structure. However, the peridynamic theory removes these obstacles by taking into account non-local interactions between material points. This study presents an application of the peridynamic theory for predicting the propagation of a pre-existing crack in an isotropic plate subjected to velocity boundary conditions, and damage progression from a central crack in fiber reinforced composite plates subjected to uniaxial tension loading.

Keywords: progressive, failure, composites, nonlocal, peridynamic theory.

1 Introduction

Despite the development of many important concepts to predict material behavior and failure, the prediction of failure modes and residual strength of materials is a challenge within the framework of the finite element method (FEM). Furthermore, the previous methods cannot address the nucleation of damage in a continuous material. The field of fracture mechanics is primarily concerned with the evolution of pre-existing defects within a body, rather than the nucleation of new defects. Even when addressing crack growth, the FEM suffers from the inherent limitation that it requires remeshing after each incremental crack growth. In addition to the need to remesh, existing methods for fracture modeling also suffer from the requirement of an external crack growth criterion. This criterion prescribes how damage evolves a priori based on local conditions, and guides the analysis as to when and how damage initiates and propagates. Considering the difficulty in obtaining and generalizing experimental fracture data, providing such a criterion for damage growth, especially in composite structures,

clearly presents a major obstacle to fracture modeling using conventional methods. This prevents such methods from being applicable to problems in which multiple damage growth occurs and interacts in complex patterns.

The governing equations of the FEM are based on the partial differential equations (PDEs) of classical continuum mechanics and that the spatial derivatives required by the PDEs do not, by definition, exist at crack tips or along crack surfaces. Therefore, the basic mathematical structure of the formulation breaks down whenever a crack appears in a body. Various special techniques have been developed in fracture mechanics to deal with this limitation. Generally, these techniques involve redefining a body in such a way as to exclude the crack, then applying conditions at the crack surfaces as boundary conditions.

In order to overcome these problems, Silling [1] introduced a nonlocal theory that does not require spatial derivatives—the peridynamic (PD) theory. The main difference between the PD theory and classical continuum mechanics is that the former is formulated using integral equations as opposed to derivatives of the displacement components. This feature allows damage initiation and propagation at multiple sites, with arbitrary paths inside the material, without resorting to special crack growth criteria. In the PD theory, internal forces are expressed through nonlocal interactions between the material points within a continuous body, and damage is a part of the constitutive model. Interfaces between dissimilar materials have their own properties and damage can propagate when and where it is energetically favorable for it to do so.

This study presents an application of the PD theory to predict the propagation of a pre-existing crack in an isotropic plate subjected to velocity boundary conditions, and damage progression from a central crack in fiber reinforced composite plates subjected to uniaxial tension loading.

2 Peridynamic theory

The deformation response of solid structures subjected to external forces can be obtained by assuming the structure to be a continuous body or a continuum, without paying attention to its atomistic structure. Hence, it is possible to perform both static and dynamic analyses of large structures within a reasonable amount of time. The conventional approach that is used to analyze solid structures is known as “classical continuum mechanics” and has been successfully applied to numerous problems in the past. Within the classical continuum mechanics framework, it is assumed that the continuous body is composed of an infinite number of infinitesimal volumes, which are called material points. These material points interact with each other only if they are within the nearest neighborhood of each other. These interactions are expressed in terms of contact forces or tractions, \mathbf{T} , as shown in Figure 1.

Using the conservation of linear momentum and relating the traction vectors, \mathbf{T} , to the well-known stress tensor, $\boldsymbol{\sigma}$, results in the equation of motion of the material point, \mathbf{x} , in classical continuum mechanics

$$\rho(\mathbf{x}) \ddot{\mathbf{u}}(\mathbf{x}, t) = \nabla \cdot \boldsymbol{\sigma} + \mathbf{b}(\mathbf{x}, t), \quad (1)$$

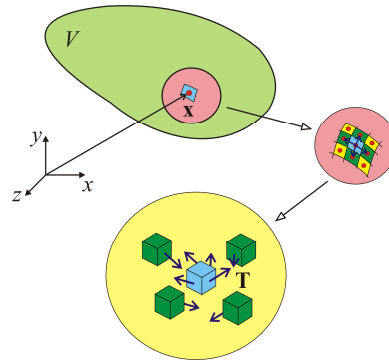


Figure 1: Interaction of material points in classical continuum mechanics.

where $\rho(\mathbf{x})$, $\mathbf{b}(\mathbf{x}, t)$, and $\ddot{\mathbf{u}}(\mathbf{x}, t)$ represent the mass density, body force density, and acceleration, respectively, of the material point located at \mathbf{x} . The spatial derivatives in the divergence operation associated with the stress tensor, $\boldsymbol{\sigma}$, do not exist on the discontinuity in the structure. Therefore, Equation (1) is not valid for problems including discontinuities, such as cracks. Silling [1] replaced the divergence term in Equation (1) with an integral term, which makes the new form of the equation of motion applicable whether or not a discontinuity exists in the structure:

$$\rho(\mathbf{x}) \ddot{\mathbf{u}}(\mathbf{x}, t) = \int_H \mathbf{f}(\mathbf{x}' - \mathbf{x}, \mathbf{u}' - \mathbf{u}) dH + \mathbf{b}(\mathbf{x}, t). \tag{2}$$

In Equation (2), the horizon, H , includes all the material points that the material point \mathbf{x} can interact with inside the body. The interaction force or peridynamic force between material points \mathbf{x} and \mathbf{x}' can be expressed as $\mathbf{f}(\mathbf{x}' - \mathbf{x}, \mathbf{u}' - \mathbf{u})$, and it is a function of the relative position vector, $\mathbf{x}' - \mathbf{x}$, and relative displacement vector, $\mathbf{u}' - \mathbf{u}$. The peridynamic force is along the same direction of the relative position of these material points in the deformed configuration, i.e., $\mathbf{y}' - \mathbf{y} = (\mathbf{x}' + \mathbf{u}') - (\mathbf{x} + \mathbf{u})$. For an elastic isotropic material, the peridynamic force takes the form

$$\mathbf{f} = c s \frac{\mathbf{y}' - \mathbf{y}}{|\mathbf{y}' - \mathbf{y}|}, \tag{3}$$

where c , and s represent the peridynamic material parameter and stretch between material points \mathbf{x} and \mathbf{x}' , respectively. The stretch, s is defined as

$$s = \frac{|\mathbf{y}' - \mathbf{y}| - |\mathbf{x}' - \mathbf{x}|}{|\mathbf{x}' - \mathbf{x}|} \tag{4}$$

The material parameter, c , can be related to the engineering material constants by equating the strain energy densities of the PD and classical continuum theories at a material point inside a body due to simple loading, such as uniform expansion. Silling and Askari [2] derived an explicit expression for parameter c in the form

$$c = \frac{18 \kappa}{\pi \delta^4}, \quad (5)$$

where κ is the bulk modulus of the material and δ represents the radius of a spherical horizon.

It can also be assumed that two material points, \mathbf{x} and \mathbf{x}' , cease to interact with each other if the mechanical stretch between these material points exceeds a critical stretch value, s_0 , as shown in Figure 2. This material model represents an elastic material behavior without allowing any permanent deformation.

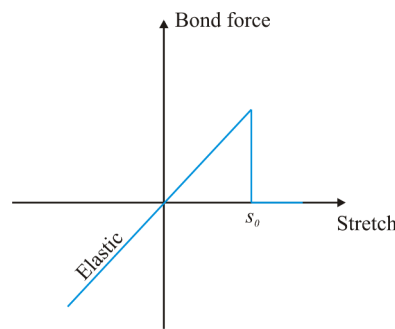


Figure 2: Constitutive relation between material points in an elastic material.

Termination of the interaction between material points can be associated with the failure of the material by modifying the peridynamic force relation given in Equation (3) by introducing the failure parameter $\mu(\mathbf{x}' - \mathbf{x}, t)$

$$\mathbf{f} = \mu(\mathbf{x}' - \mathbf{x}, t) c s \frac{\mathbf{y}' - \mathbf{y}}{|\mathbf{y}' - \mathbf{y}|}, \quad (6)$$

where the failure parameter can be defined as

$$\mu(\mathbf{x}' - \mathbf{x}, t) = \begin{cases} 1 & \text{if } s(\mathbf{x}' - \mathbf{x}, t') < s_0 \text{ for all } 0 < t' < t \\ 0 & \text{otherwise} \end{cases}. \quad (7)$$

The inexplicit nature of local damage at a material point, \mathbf{x} , arising from the introduction of failure in the constitutive model, is removed by defining the local damage as

$$\varphi(\mathbf{x}, t) = 1 - \frac{\int_H \mu(\mathbf{x}' - \mathbf{x}, t) dH}{\int_H dH}. \quad (8)$$

Thus, local damage is the weighted ratio of the number of the broken interactions to the total number of interactions within the horizon, H . The extent of damage is defined by a value between 0

and 1, where 0 indicates that a material point has no damage and 1 indicates complete damage at the material point. Also, a damage value of 0.5 and above indicates possible cracking.

In the case of isotropic materials, the critical stretch, s_0 , value can be related to the equivalent energy release rate as derived by Silling and Askari [2]

$$s_0 = \sqrt{\frac{5 G_0}{9 \kappa \delta}}, \quad (9)$$

where G_0 is the critical energy release rate of the material and can be related to the fracture toughness of the material.

In order to solve Equation (2), a collocation method is adopted and the numerical treatment involves the discretization of the domain of interest into subdomains. The domain can be discretized into square subdomains. With this discretization, the volume integration in Equation (2) is approximated, leading to

$$\rho(\mathbf{x}_{(i)}) \ddot{\mathbf{u}}(\mathbf{x}_{(i)}, t) = \sum_{j=1}^M \mathbf{f}(\mathbf{u}(\mathbf{x}_{(j)}, t) - \mathbf{u}(\mathbf{x}_{(i)}, t), \mathbf{x}_{(j)} - \mathbf{x}_{(i)}) V_{(j)} + \mathbf{b}(\mathbf{x}_{(i)}, t), \quad (10)$$

where $\mathbf{x}_{(i)}$ is the position vector located at the i^{th} collocation (material) point and M is the number of subdomains within the horizon of the i^{th} material point. The position vector $\mathbf{x}_{(j)}$ represents the location of the j^{th} collocation point. The volume of the j^{th} subdomain is $V_{(j)}$.

Since peridynamics is a nonlocal theory and its equations of motion utilize integro-differential equations as opposed to partial differential equations in the case of the classical continuum theory, the application of boundary conditions is different from that of the classical continuum theory. The tractions or point forces cannot be applied as boundary conditions since their volume integrations result in a zero value [3]. Therefore, the boundary conditions are applied over the volumes as body forces, displacements, and velocities. As explained by Macek and Silling [4], the thickness of the region over which the boundary conditions are applied should be comparable to the size of the horizon.

3 Peridynamic modeling of composite materials

The peridynamic formulation described in the previous section concerns an isotropic material where there is no directional dependence of the interactions between the material points. However, if anisotropic materials such as a fiber-reinforced composite structure are considered, the directional dependency must be included in the peridynamic analysis. Therefore, four different peridynamic material parameters are introduced, as shown in Figure 3, to model a fiber-reinforced composite laminate. Note that a material point of interest can only interact with a material point located either in the same ply or in the adjacent plies.

Associated with a ply, the material parameter concerning the interaction of material points in the fiber direction only is denoted with c_f . The interaction of material points in all other directions within a ply is governed by the material parameter, c_m . The interaction between material points in adjacent

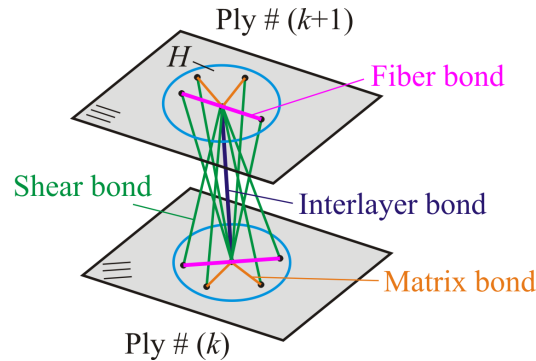


Figure 3: Peridynamic bonds for a fiber-reinforced composite laminate.

plies is described by the material parameter c_{in} and c_{is} accounting for transverse normal and shear deformations between the neighboring plies.

As in the case of isotropic materials, the peridynamic material parameters, c_f , c_m , c_{in} and c_{is} can be expressed analytically in terms of the engineering material constants, E_1 , E_2 , E_3 , G_{12} , and ν_{12} , as

$$c_f = \frac{2 E_1 (E_1 - E_2)}{(E_1 - \frac{1}{9} E_2) \left(\sum_{q=1}^N \xi_{qi} V_q \right)} \quad \text{and} \quad (11a)$$

$$c_m = \frac{8 E_1 E_2}{(E_1 - \frac{1}{9} E_2) \pi t \delta^3} \quad (11b)$$

and

$$c_{in} = \frac{E_m}{t \bar{V}} \quad \text{and} \quad (11c)$$

$$c_{is} = \frac{2 G_m}{\pi t} \frac{1}{\left(\delta^2 + t^2 \ln \left(\frac{t^2}{\delta^2 + t^2} \right) \right)}, \quad (11d)$$

where E_m and G_m are the elastic modulus and shear modulus of the matrix material, respectively, and \bar{V} is the volume of a material point. The initial length of the bond in the fiber direction and its stretch after deformation between material points q and i are denoted by ξ_{qi} and s_{qi} , respectively. The volume of the material point, q that interacts with material point, i is denoted by V_q which can be approximated as

$$V_q = \frac{\pi t \delta^2}{N}, \quad (12)$$

in which N is the number of material points within its horizon, δ and t is the thickness of the lamina. The detailed derivations of these expressions are given by Oterkus [3].

Because of the pair-wise interaction of the material points, four independent material constants of a lamina reduce to two independent constants.

along with constraints on material constants, G_{12} and ν_{12} as

$$G_{12} = \frac{\nu_{12} E_2}{1 - \nu_{21} \nu_{12}} = \frac{E_1 E_2}{3 \left(E_1 - \frac{1}{3} E_2 \right)} \quad \text{and} \quad (13a)$$

$$\nu_{12} = \frac{1}{3} \quad (13b)$$

The constitutive or the force-stretch relations for the in-plane interactions of two material points, referred to as fiber and matrix bonds, are shown in Figure 4.

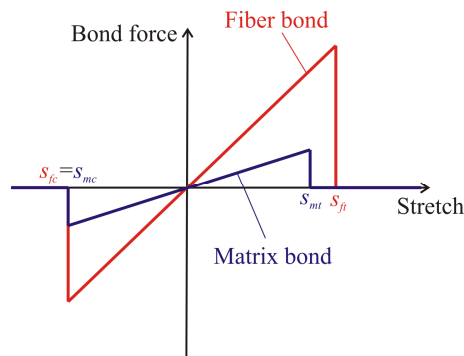


Figure 4: Force-stretch relation for fiber and matrix bonds.

The critical parameters that define the failure of these bonds under tension and compression are (s_{ft}, s_{mt}) and (s_{fc}, s_{mc}) , respectively, and can be determined based on the experimental measurements. Interlayer damage represents the breakage of (interlayer) bonds between a layer and its adjacent layers above and below. Hence, it provides the extent of delamination between the adjacent layers. Therefore, the interlayer bonds are assumed to fail only in tension. The critical stretch value for the interlayer bonds, s_{it} , can be obtained analytically by equating the energy consumed by an advancing Mode-I crack to the work required to break all interlayer bonds as

$$s_{it} = \sqrt{\frac{2 G_{Ic}}{t E_m}} \quad (14)$$

where G_{Ic} and E_3 correspond to the Mode-I critical energy release rate and elastic modulus of the matrix material, respectively, and t is the ply thickness.

The transverse shear bonds can fail if the shear angle of the bonds exceeds the critical shear angle value, φ_c . This value can also be obtained analytically by equating the energy consumed by an advancing Mode-II crack to the work required to break all shear bonds as

$$\varphi_c = \sqrt{\frac{G_{IIC}}{t G_m}} \quad (15)$$

where G_{IIC} and G_m correspond to the Mode-II critical energy release rate and the transverse shear modulus of the matrix material, respectively. The derivations of the relationships between the critical stretch value for the interlayer bonds, s_{it} and the Mode-I critical energy release rate and between the critical shear angle value, φ_c and the Mode-II critical energy release rate, respectively, are given by Oterkus [3].

4 Numerical results

The present approach is demonstrated by considering the propagation of a pre-existing crack in a plate subjected to velocity boundary conditions, and damage initiation and growth patterns from a pre-existing crack in two distinct laminate constructions under tension loading.

Plate with a pre-existing crack under velocity boundary conditions. A square plate with a pre-existing central crack is shown in Figure 5. It has an edge length of $L = W = 0.05$ m and a thickness of $h = L/500$ m. The plate is made of steel with an elastic modulus of $E = 192$ GPa and a Poisson's ratio of $\nu = 1/3$. A velocity boundary condition of $V_0(t) = 20$ m/s is applied in the vertical direction along both of the horizontal edges through a boundary region with a thickness of $b = 3\Delta x$. The grid size in the PD model is $\Delta x = h$ and the horizon is specified as $\delta = 3.015\Delta x$. This particular value of the grid size was determined based on a convergence study. The pre-existing central crack with an initial length of $2a = W/5$ is included in the PD model by allowing no interaction between the material points that are defining the crack surfaces. Based on the unconditional convergence requirement as explained by Silling and Askari [2], the time step is specified as $\Delta t = 1.3367 \times 10^{-8}$ s.

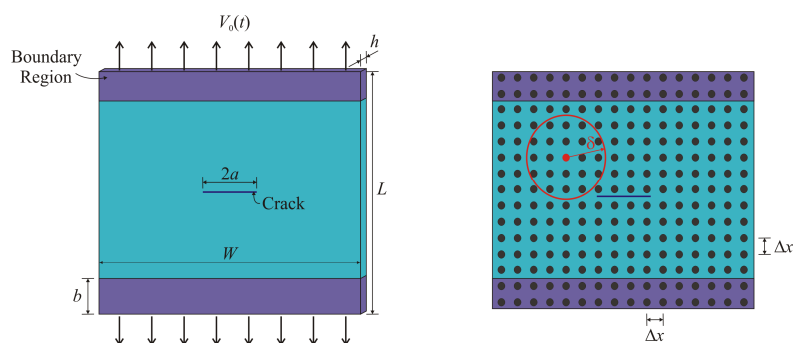


Figure 5: Square plate with a pre-existing central crack under velocity boundary conditions.

If the interaction between the material points never ceases, i.e., no bond failure is allowed, the crack opening displacement is computed as shown in Figure 6. Unlike the elliptical crack opening displacement of classical continuum mechanics, the PD analysis predicts a cusp-like crack opening displacement near the crack tip. As explained by Silling [1], the elliptical crack opening displacement is a mathematical requirement of the unbounded stresses near the crack tips, which are physically unacceptable. The PD theory successfully captures a more physically meaningful crack opening shape.

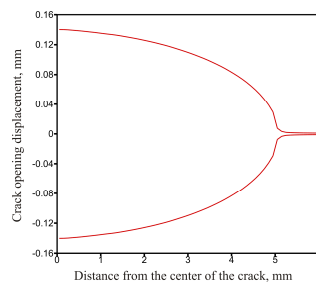


Figure 6: Crack opening displacement near the crack tip at the end of 1250 time steps when no failure is allowed.

When failure of the PD bonds is allowed by using a critical stretch value of $s_0 = 0.04472$, a self-similar crack growth is observed at the end of 1250 time steps as shown in Figure 7. This growth is typical for a mode-I type of loading. The position of the crack tip or crack growth is determined based on the local damage value of any material point that exceeds $\varphi = 0.5$ along the x -axis. The growth of a crack as a function of time is shown in Figure 8, and the crack growth speed can be evaluated as 1650 m/s. This crack speed is less than the Rayleigh wave speed of 2800 m/s, which is considered to be the upper limit of the crack growth speed for a mode-I type of loading [2].

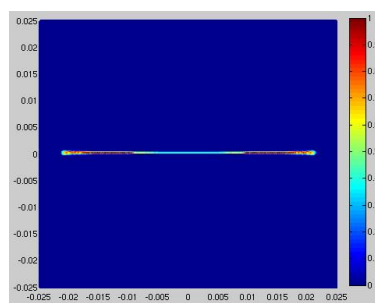


Figure 7: Damage indicating self-similar crack growth at the end of 1250 time steps under the velocity boundary condition of $V_0(t) = 20$ m/s.

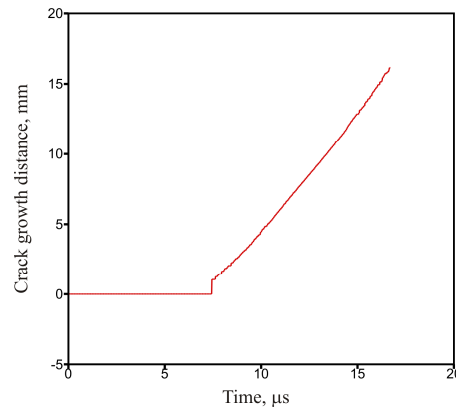


Figure 8: Crack growth as a function of time.

If the applied velocity boundary condition is increased from $V_0(t) = 20 \text{ m/s}$ to $V_0(t) = 70 \text{ m/s}$, the crack growth characteristics change from self-similar to branching, as shown in Figure 9. It is worth noting that the only parameter that was different between the two PD analyses while obtaining Figures 7 and 9 is due to the applied velocity boundary condition. All other parameters remain the same. The PD theory captures a very complex phenomenon of crack branching without resorting to any external criteria that triggers branching.

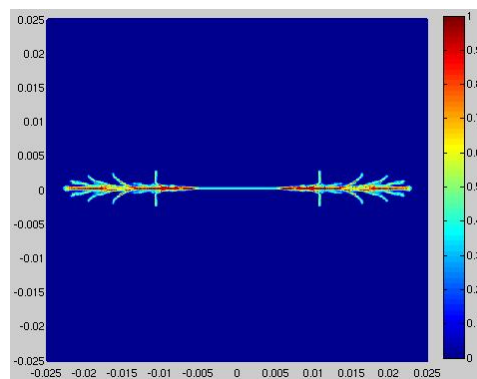


Figure 9: Damage indicating crack branching at the end of 1000 time steps under a velocity boundary condition of $V_0(t) = 70 \text{ m/s}$.

Laminates with a pre-existing central crack under tension. The failure prediction capability of the PD theory is demonstrated by introducing a central crack in the two laminate layups of $[0^\circ/90^\circ/0^\circ]$

and $[0^\circ/45^\circ/0^\circ]$. Its elastic moduli in the fiber and transverse directions are $E_1 = 159.96$ GPa and $E_2 = 8.96$ GPa, respectively. The length and width of the lamina are specified as $L = 15.24$ mm and $W = 7.62$ mm, respectively. Ply thickness is specified as $t = 0.1651$ mm. As shown in Figure 10, the crack is aligned with the y -axis and has a length of $2a = 0.01778$ m. The laminates are subjected to a velocity boundary condition of $v_0 = 2.02 \times 10^{-7}$ m/s along the edges of the lamina through a volumetric region with a depth of $b = 2.54 \times 10^{-3}$ m. The PD model is generated by using a single layer of material points with a grid size of $\Delta x = 6.35 \times 10^{-4}$ m. The horizon radius is specified as $\delta = 3.015 \Delta x$. Using Equation (11), the fiber and matrix bond constants are computed as $c_f = 5.72 \times 10^{23}$ N/m⁶ and $c_m = 1.86 \times 10^{22}$ N/m⁶. The critical stretch parameters specified for the fiber and matrix bonds are $s_{ft} = 0.027$ and $s_{mt} = 0.0135$, respectively. The critical stretch and angle values for interlayer and shear bonds can be specified as equal to the critical stretch of the matrix bond, i.e., $s_{in} = \varphi_c = 0.0135$. The quasi-static solution is obtained by using the adaptive dynamic relaxation technique by using a time increment of 1 and stable mass density value of 7.005×10^{18} kg/m³ [5].

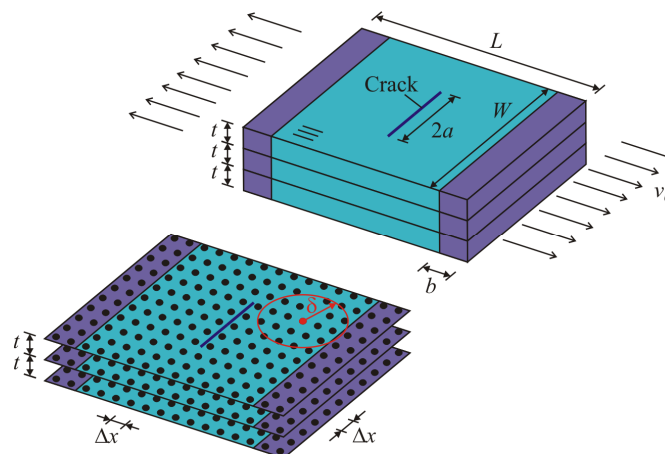


Figure 10: Loading and geometry of a laminate with a crack under tension loading.

For the $[0^\circ/90^\circ/0^\circ]$ laminate, an “H”-type splitting failure mode is observed for all plies, as shown in Figure 11. In this case, 0° plies are dominant in the loading direction; therefore, 0° plies determine the failure behavior of the laminate. However, in the $[0^\circ/45^\circ/0^\circ]$ laminate, a “Z”-type failure mode is obtained in all plies due to the presence of a 45° ply, as shown in Figure 12. The delamination failure mode between the plies due to the breakage of shear bonds around crack tip regions, shown in Figures 13 and 14. These damage patterns are consistent with those observed in a study by Bogert et al. [6].

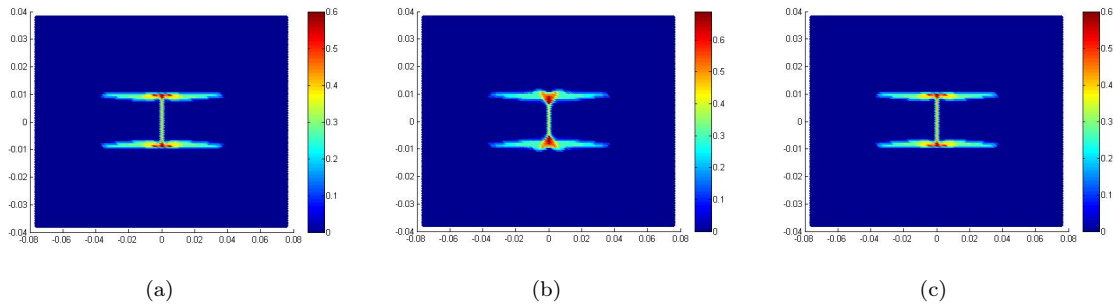


Figure 11: Matrix bond damage plots for a laminate of $[0^\circ/90^\circ/0^\circ]$ with a pre-existing crack for $s_{mt} = s_{in} = \varphi_c$: (a) bottom ply, 0° ; (b) center ply, 90° , and (c) top ply, 0° .

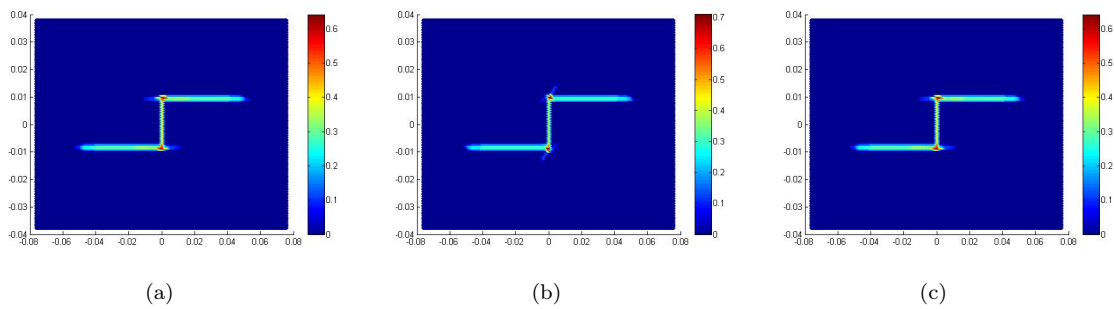


Figure 12: Matrix bond damage plots for a laminate of $[0^\circ/45^\circ/0^\circ]$ with a pre-existing crack for $s_{mt} = s_{in} = \varphi_c$: (a) bottom ply, 0° ; (b) center ply, 90° , and (c) top ply, 0° .

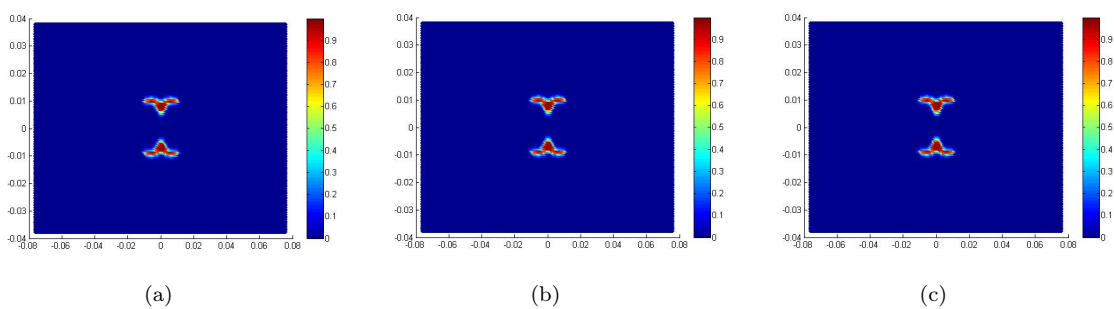


Figure 13: Shear bond damage plots for a laminate of $[0^\circ/90^\circ/0^\circ]$ with a pre-existing crack for $s_{mt} = s_{in} = \varphi_c$: (a) bottom ply, 0° ; (b) center ply, 90° , and (c) top ply, 0° .

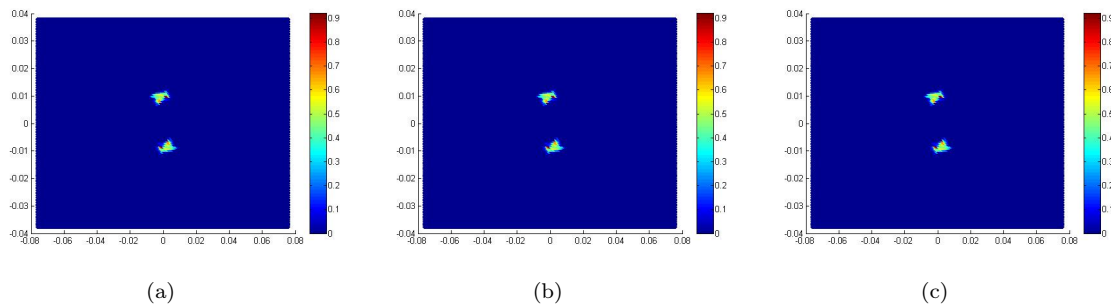


Figure 14: Shear bond damage plots for a laminate of $[0^\circ/45^\circ/0^\circ]$ with a pre-existing crack for $s_{mt} = s_{in} = \varphi_c$: (a) bottom ply, 0° ; (b) center ply, 90° , and (c) top ply, 0° .

5 Conclusions

Based on the numerical results, the PD approach successfully predicts the damage growth patterns in fiber-reinforced laminates with a pre-existing crack while considering the distinct properties of the fiber and matrix, as well as of the interlayer material between the plies. The predictions capture the correct failure mechanisms of matrix cracking, fiber breakage, and delamination without resorting to any special treatments, and agree with the experimental observations published in the literature. The simulations also capture failure modes among each ply, which are usually distinct; they heavily depend on fiber direction, which is realistically exhibited in the current results. It can be concluded that the peridynamic theory is a powerful method that can be employed for failure analysis of composite materials.

References

- [1] Silling, S., Reformulation of elasticity theory for discontinuities and long-range forces. *J Mech Phys Solids*, **48**, pp. 175–209, 2000.
- [2] Silling, S.A. & Askari, E., A meshfree method based on the peridynamic model of solid mechanics. *Comput Struct*, **83**, pp. 1526–1535, 2005.
- [3] Oterkus, E., *Peridynamic theory for modeling three-dimensional damage growth in metallic and composite structures*. Ph.D. thesis, University of Arizona, 2010.
- [4] Macek, R.W. & Silling, S.A., Peridynamics via finite element analysis. *Finite Elem Anal Des*, **43**, pp. 1169–1178, 2007.
- [5] Kilic, B., *Peridynamic theory for progressive failure prediction in homogeneous and heterogeneous materials*. Ph.D. thesis, University of Arizona, 2008.
- [6] Bogert, P.B., Satyanarayana, A. & Chuncu, P.B., Comparison of damage path predictions for composite laminates by explicit and standard finite element analysis tools. *7th AIAA/ASME/ASCE/AHS/ASC Structures, Structural Dynamics, and Materials Conference*, AIAA 2006-1750: Newport, Rhode Island,

2006.

Hybrid and mixed variational principles for the fully nonlinear analysis of shells of Reissner-Mindlin type

Paulo M. Pimenta

*Polytechnic School at the University of São Paulo,
PO Box 61548, 05424-970, São Paulo – Brazil*

Abstract

This paper addresses the development of some alternative hybrid and mixed variational formulations for the geometrically-exact three-dimensional first-order-shear shell boundary value problem. In the framework of the complementary-energy-based formulations, a Legendre transformation is used to introduce the complementary energy density in the variational statements as a function of the cross-sectional resultants only. The corresponding variational principles are shown to feature stationarity within the framework of the boundary-value problem. The main features of the principles are highlighted, giving special attention to their relationships from both theoretical and numerical point of view.

Keywords: nonlinear analysis of shells, mixed-hybrid variational principles, geometrically exact shells.

1 Introduction

Variational principles constitute the core of the development of numerical methods in Solid Mechanics. The utility of such principles is two-fold: first, they provide a very convenient method for the derivation of the governing equations and natural boundary conditions of the boundary value problem and, second, they provide the mathematical foundation required to produce consistent numerical approximations. In this second role, the variational methods have been most useful in Computational Solid Mechanics.

Many different variational principles can be constructed depending on the equations enforced in the weak form. Perhaps the most remarkable variational principle is the *Principle of Stationary Total Potential Energy*, which states that, among all kinematically admissible displacement fields, those that satisfy the equilibrium conditions in the domain and at the boundary, lead to a stationary value of the total potential energy functional.

Throughout the text, italic Latin or Greek lowercase letters ($a, b, \dots, \alpha, \beta, \dots$) denote scalar quantities, bold italic Latin or Greek lowercase letters ($\mathbf{a}, \mathbf{b}, \dots, \boldsymbol{\alpha}, \boldsymbol{\beta}, \dots$) denote vectors, while bold italic

Latin or Greek capital letters (\mathbf{A} , \mathbf{B} , ...) denote second-order tensors. Summation convention over repeated indices is adopted, with Greek indices ranging from 1 to 2 and Latin indices from 1 to 3.

2 The geometrically-exact first-order-shear shell model

In this work, we recall the geometrically-exact six-parameter shell formulation presented in Campello *et al* [1] (which is one of the existing shell models undergoing large strains and finite rotations, see [1] for further references).

Although it may be not necessary, our approach defines energetically conjugated cross-sectional stresses and strains, based on the concept of shell director with a standard Reissner-Mindlin kinematical assumption. Due to the use of cross-sectional quantities, the derivation of equilibrium equations in strong and weak forms is considerably simpler, and the linearization of the latter leads naturally to a symmetric bilinear form for hyperelastic materials and conservative loadings (even far from equilibrium states). The resulting expressions are much similar to those obtained for geometrically-exact spatial rods, rendering a very convenient pattern for the simultaneous coding of rod and shell finite elements. Finite rotations may be treated here by the Euler-Rodrigues formula in a total or updated Lagrangian way. Two different parameterizations may be considered: (i) the usual Euler rotation vector and (ii) the Rodrigues vector-like parameters [1]. The first is singularity-free for any rotation increment while the latter delivers computationally more efficient expressions.

It is assumed that the middle surface of the shell is plane at the initial reference configuration. Initially curved shells can be regarded as a stress-free deformed state from the plane initial position, as shown in [2]. Let $\{e_1^r, e_2^r, e_3^r\}$ be an orthogonal system, with the vectors e_α^r placed on the shell reference mid-plane and e_3^r normal to this plane, as shown in Fig. 1. The position of any shell material point in the reference configuration can be described by

$$\boldsymbol{\xi} = \boldsymbol{\zeta} + \mathbf{a}^r, \quad (1)$$

where the vector $\boldsymbol{\zeta} = \xi_\alpha \mathbf{e}_\alpha^r$ defines a point on the reference mid-surface and \mathbf{a}^r is the shell director at this point, given by $\mathbf{a}^r = \zeta \mathbf{e}_3^r$. Here $\zeta \in H = [-h^b, h^t]$ is the thickness coordinate, with $h = h^b + h^t$ being the shell thickness in the reference configuration (observe that $\{\xi_\alpha, \zeta\}$ sets a three-dimensional Cartesian frame).

In the current configuration the position \mathbf{x} of any material point can be expressed by the vector field

$$\mathbf{x} = \mathbf{z} + \mathbf{a}, \quad (2)$$

where $\mathbf{z} = \hat{\mathbf{z}}(\zeta_\alpha)$ describes the current position of a point in the middle surface and \mathbf{a} is the current director at this point, obtained as $\mathbf{a} = \mathbf{Q}\mathbf{a}^r$, with \mathbf{Q} as the rotation tensor. Notice that no thickness change is assumed during the motion and that first order shear deformations are accounted for since \mathbf{a} is not necessarily normal to the current mid-surface. Let now $\{\mathbf{e}_1, \mathbf{e}_2, \mathbf{e}_3\}$ be a local orthogonal system on the current configuration, with $\mathbf{e}_i = \mathbf{Q}\mathbf{e}_i^r$, as depicted in Fig. 1.

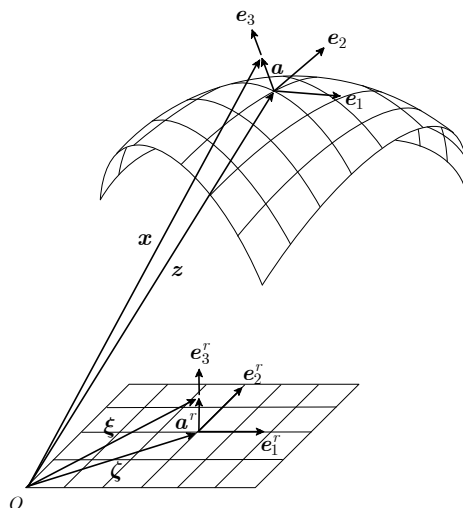


Figure 1: Shell description and basic kinematical quantities.

The rotation tensor $\mathbf{Q} = \hat{\mathbf{Q}}(\boldsymbol{\theta})$ may be expressed in terms of the Euler rotation vector $\boldsymbol{\theta}$, by means of the well-known Euler-Rodrigues formula

$$\mathbf{Q} = \mathbf{I} + \frac{\sin \theta}{\theta} \boldsymbol{\Theta} + \frac{1}{2} \left(\frac{\sin \theta/2}{\theta/2} \right)^2 \boldsymbol{\Theta}^2, \quad (3)$$

in which θ is the rotation angle given by $\theta = \|\boldsymbol{\theta}\|$. Still in (3) $\boldsymbol{\Theta} = \text{Skew}(\boldsymbol{\theta})$ is the skew-symmetric tensor whose axial vector is $\boldsymbol{\theta}$. Here, we will keep the presentation in terms of $\boldsymbol{\theta}$ and for simplicity we will adopt the total Lagrangian description for the rotation.

Having defined \mathbf{z} and $\boldsymbol{\zeta}$, the displacements of any point of the reference middle plane can be computed by

$$\mathbf{u} = \mathbf{z} - \boldsymbol{\zeta}. \quad (4)$$

The components of \mathbf{u} and $\boldsymbol{\theta}$ on a global Cartesian system constitute the 6 degrees-of-freedom of this shell model.

Two skew-symmetric tensors that describe the specific rotations of the director can be defined as $\mathbf{K}_\alpha = \mathbf{Q}_{,\alpha} \mathbf{Q}^T$. One can show that the corresponding axial vectors are $\boldsymbol{\kappa}_\alpha = \text{axial}(\mathbf{K}_\alpha) = \boldsymbol{\Gamma} \boldsymbol{\theta}_{,\alpha}$, with the tensor $\boldsymbol{\Gamma}$ given in [1].

From differentiation of (2) with respect to $\boldsymbol{\xi}$ one can evaluate the deformation gradient \mathbf{F} . This leads to the definition of the following material cross-sectional strain vectors

$$\boldsymbol{\eta}_\alpha^r = \mathbf{Q}^T \mathbf{z}_{,\alpha} - \mathbf{e}_\alpha^r \quad \text{and} \quad \boldsymbol{\kappa}_\alpha^r = \boldsymbol{\Gamma}^T \boldsymbol{\theta}_{,\alpha}. \quad (5)$$

These two vectors may be regarded as cross-sectional generalized strains, with $\mathbf{z}_{,\alpha} = \mathbf{e}_\alpha^r + \mathbf{u}_{,\alpha}$, where we have introduced the notation $(\bullet)_{,\alpha} = \partial(\bullet)/\partial\xi_\alpha$ for derivatives. One may understand that the components $\boldsymbol{\eta}_\alpha^r \cdot \mathbf{e}_\beta^r$ of $\boldsymbol{\eta}_\alpha^r$ operate as membrane strains, while $\boldsymbol{\eta}_\alpha^r \cdot \mathbf{e}_3^r$ as transversal shear strains. Expressions (5) are the back-rotated counterparts of $\boldsymbol{\eta}_\alpha = \mathbf{z}_{,\alpha} - \mathbf{e}_\alpha$ and $\boldsymbol{\kappa}_\alpha$, respectively.

Let the first Piola-Kirchhoff stress tensor be written as $\mathbf{P} = \boldsymbol{\tau}_i \otimes \mathbf{e}_i^r$. The quantities $\boldsymbol{\tau}_i$ are nominal stress vectors, and act on cross-sectional planes whose normal vectors on the reference configuration are \mathbf{e}_i^r . Integration of two first vectors stress vectors along the shell thickness allows the definition of generalized cross-sectional stresses, i.e.

$$\mathbf{n}_\alpha = \int_H \boldsymbol{\tau}_\alpha d\zeta \quad \text{and} \quad \mathbf{m}_\alpha = \int_H \mathbf{a} \times \boldsymbol{\tau}_\alpha d\zeta. \quad (6)$$

The third vector is assumed to perform no work in this shell model (see a discussion on the plane stress issue in [1]).

On the other hand, let $\tilde{\mathbf{n}}$ and $\tilde{\mathbf{m}}$ be the applied external forces and moments respectively, both per unit area of the middle surface in the reference configuration. The shell local equilibrium can be stated by Statics in a standard way. The result in the shell domain $\Omega \subset \mathbb{R}^2$ is

$$\begin{aligned} \mathbf{n}_{\alpha,\alpha} + \tilde{\mathbf{n}} &= \mathbf{o} \quad \text{and} \\ \mathbf{m}_{\alpha,\alpha} + \mathbf{z}_{,\alpha} \times \mathbf{n}_\alpha + \tilde{\mathbf{m}} &= \mathbf{o}. \end{aligned} \quad (7)$$

On the other hand, the back-rotated cross-sectional resultants are defined by

$$\mathbf{n}_\alpha^r = \mathbf{Q}^T \mathbf{n}_\alpha \quad \text{and} \quad \mathbf{m}_\alpha^r = \mathbf{Q}^T \mathbf{m}_\alpha. \quad (8)$$

The boundary of the domain Ω is denoted by $\Gamma = \Gamma_D \cup \Gamma_N$, subdivided, as usual, in Dirichlet and Neumann parts according to the following boundary conditions

$$\begin{aligned} \mathbf{u} = \bar{\mathbf{u}} \quad \text{and} \quad \boldsymbol{\theta} = \bar{\boldsymbol{\theta}} \quad \text{on } \Gamma_D \\ \nu_\alpha^r \mathbf{n}_\alpha = \bar{\mathbf{n}} \quad \text{and} \quad \nu_\alpha^r \mathbf{m}_\alpha = \bar{\mathbf{m}} \quad \text{on } \Gamma_N, \end{aligned} \quad (9)$$

respectively, where $\nu_\alpha^r = \boldsymbol{\nu}^r \cdot \mathbf{e}_\alpha^r$ are the components of the unitary normal to the boundary. In (9), $\bar{\mathbf{u}}$ and $\bar{\boldsymbol{\theta}}$ are respectively the prescribed displacements and rotations on Γ_D , as well as, $\bar{\mathbf{n}}$ and $\bar{\mathbf{m}}$ are respectively the applied external forces and moments per unit reference length on Γ_N .

For the sake of convenience, let us define the following assembled vectors

$$\boldsymbol{\sigma}_\alpha^r = \begin{bmatrix} \mathbf{n}_\alpha^r \\ \mathbf{m}_\alpha^r \end{bmatrix}, \quad \boldsymbol{\varepsilon}_\alpha^r = \begin{bmatrix} \boldsymbol{\eta}_\alpha^r \\ \boldsymbol{\kappa}_\alpha^r \end{bmatrix}, \quad \tilde{\mathbf{q}} = \begin{bmatrix} \tilde{\mathbf{n}} \\ \tilde{\boldsymbol{\mu}} \end{bmatrix}, \quad \bar{\mathbf{q}} = \begin{bmatrix} \bar{\mathbf{n}} \\ \bar{\boldsymbol{\mu}} \end{bmatrix} \quad \text{and} \quad \mathbf{d} = \begin{bmatrix} \mathbf{u} \\ \boldsymbol{\theta} \end{bmatrix}, \quad (10)$$

where the pseudo-moments $\tilde{\boldsymbol{\mu}} = \boldsymbol{\Gamma}^T \tilde{\mathbf{m}}$ and $\bar{\boldsymbol{\mu}} = \boldsymbol{\Gamma}^T \bar{\mathbf{m}}$ have been introduced (see the remark in [1] on this matter). Note that (5) can be recast as

$$\boldsymbol{\varepsilon}_\alpha^r = \hat{\boldsymbol{\varepsilon}}_\alpha^r(\mathbf{d}). \quad (11)$$

Let us also introduce the following operators

$$\mathbf{\Lambda} = \begin{bmatrix} \mathbf{Q} & \mathbf{O} \\ \mathbf{O} & \mathbf{Q} \end{bmatrix} \quad \text{and} \quad \mathbf{H}_\alpha = \begin{bmatrix} \mathbf{Q} & \mathbf{O} \\ \mathbf{O} & \mathbf{\Gamma} \end{bmatrix}. \quad (12)$$

Making use of this generalized vectors and operators, the equilibrium boundary-value problem, described by (7) and (9), is reduced to the following synthetic form

$$\begin{aligned} \mathcal{T}_\alpha^e(\mathbf{d})\boldsymbol{\sigma}_\alpha^r + \tilde{\mathbf{q}} &= \mathbf{o} & \text{in } \Omega \\ \nu_\alpha^r \mathbf{H}\boldsymbol{\sigma}_\alpha^r - \bar{\mathbf{q}} &= \mathbf{o} & \text{on } \Gamma_N \end{aligned}, \quad (13)$$

where (with $\mathbf{Z}_{,\alpha} = \text{Skew}(\mathbf{z}_{,\alpha})$)

$$\begin{aligned} \mathcal{T}_\alpha^e(\mathbf{d}) &= \boldsymbol{\psi}_\alpha^e \boldsymbol{\Delta}_\alpha^e \mathbf{\Lambda} \quad (\text{no sum}), \quad \text{with} \\ \boldsymbol{\psi}_\alpha^e &= \begin{bmatrix} \mathbf{I} & \mathbf{O} & \mathbf{O} \\ \mathbf{O} & \mathbf{\Gamma}^T \mathbf{Z}_{,\alpha} & \mathbf{\Gamma}^T \end{bmatrix} \quad \text{and} \quad \boldsymbol{\Delta}_\alpha^e = \begin{bmatrix} \mathbf{I} \frac{\partial}{\partial \xi_\alpha} & \mathbf{O} \\ \mathbf{I} & \mathbf{O} \\ \mathbf{O} & \mathbf{I} \frac{\partial}{\partial \xi_\alpha} \end{bmatrix}. \end{aligned} \quad (14)$$

Let us introduce the trial displacement space given by

$$\mathcal{D} = \{ \mathbf{d} \in \mathcal{H}^1(\Omega) \mid \mathbf{d} = \bar{\mathbf{d}} \text{ on } \Gamma_D \}, \quad (15)$$

where \mathcal{H}^1 is the Sobolev space of first order. \mathcal{D} contains functions that satisfy the Dirichlet boundary conditions. Let us also introduce the corresponding the test function linear space given by

$$\delta\mathcal{D} = \{ \delta\mathbf{d} \in \mathcal{H}^1(\Omega) \mid \delta\mathbf{d} = \mathbf{o} \text{ on } \Gamma_D \}. \quad (16)$$

The weak form of the equilibrium boundary-value problem (13) is

$$\int_\Omega [\mathcal{T}_\alpha^e(\mathbf{d})\boldsymbol{\sigma}_\alpha^r + \tilde{\mathbf{q}}] \cdot \delta\mathbf{d} d\Omega + \int_{\Gamma_N} [\bar{\mathbf{q}} - \nu_\alpha^r \mathbf{H}\boldsymbol{\sigma}_\alpha^r] \cdot \delta\mathbf{d} d\Gamma = 0, \quad \forall \delta\mathbf{d} \in \delta\mathcal{D}, \quad (17)$$

which, after the application of the divergence theorem, delivers

$$\int_\Omega [-\boldsymbol{\sigma}_\alpha^r \cdot \mathcal{T}_\alpha^c(\mathbf{d})\delta\mathbf{d} + \tilde{\mathbf{q}} \cdot \delta\mathbf{d}] d\Omega + \int_{\Gamma_N} \bar{\mathbf{q}} \cdot \delta\mathbf{d} d\Gamma = 0, \quad \forall \delta\mathbf{d} \in \delta\mathcal{D}, \quad (18)$$

where

$$\begin{aligned} \mathcal{T}_\alpha^c(\mathbf{d}) &= \mathbf{\Lambda}^T \boldsymbol{\Psi}_\alpha^c \boldsymbol{\Delta}_\alpha^c \quad (\text{no sum}), \quad \text{with} \\ \boldsymbol{\Psi}_\alpha^c &= \begin{bmatrix} \mathbf{I} & \mathbf{O} & \mathbf{Z}_{,\alpha}\mathbf{\Gamma} \\ \mathbf{O} & \mathbf{\Gamma} & \mathbf{\Gamma}_{,\alpha} \end{bmatrix} \quad \text{and} \quad \boldsymbol{\Delta}_\alpha^c = \begin{bmatrix} \mathbf{I} \frac{\partial}{\partial \xi_\alpha} & \mathbf{O} \\ \mathbf{O} & \mathbf{I} \frac{\partial}{\partial \xi_\alpha} \\ \mathbf{O} & \mathbf{I} \end{bmatrix}. \end{aligned} \quad (19)$$

(18) is a necessary and sufficient condition for (13). The expression of $\mathbf{\Gamma}_{,\alpha}$ can be found in [1].

For hyperelastic material behavior, a *strain energy density per unit reference area* $\psi = \hat{\psi}(\varepsilon_1^r, \varepsilon_2^r)$ can be defined such that

$$\boldsymbol{\sigma}_\alpha^r = \partial_\alpha \psi = \frac{\partial \psi}{\partial \varepsilon_\alpha^r}. \quad (20)$$

Let us assume that ψ is a differentiable and convex function with respect to its arguments. On the basis of these assumptions, equation (20) establishes a one-to-one correspondence between the stress-resultant vectors $\boldsymbol{\sigma}_\alpha^r$ and the generalized cross-sectional strains ε_β^r . Legendre has shown that this type of equation can be transformed into a conjugate form by introducing a new function $\hat{\psi}^*(\boldsymbol{\sigma}_1^r, \boldsymbol{\sigma}_2^r)$ defined by

$$\hat{\psi}^*(\boldsymbol{\sigma}_1^r, \boldsymbol{\sigma}_2^r) = \boldsymbol{\sigma}_\alpha^r \cdot \varepsilon_\alpha^r - \hat{\psi}(\varepsilon_1^r, \varepsilon_2^r), \quad (21)$$

which is called *complementary strain energy density*. Differentiation of this function leads to

$$\varepsilon_\alpha^r = \partial_\alpha \psi^* = \frac{\partial \psi^*}{\partial \boldsymbol{\sigma}_\alpha^r}. \quad (22)$$

The strong form of the boundary value problem governing the response of our shell model with hyperelastic material behavior consists of the following three sets of differential equations to be solved in Ω

$$\begin{aligned} \mathcal{T}_\alpha^e(\mathbf{d}) \boldsymbol{\sigma}_\alpha^r + \tilde{\mathbf{q}} &= \mathbf{o} & \text{in } \Omega \\ \boldsymbol{\sigma}_\alpha^r - \partial_\alpha \psi &= \mathbf{o} & \text{in } \Omega \\ \varepsilon_\alpha^r - \hat{\varepsilon}_\alpha^r(\mathbf{d}) &= \mathbf{o} & \text{in } \Omega \end{aligned} \quad (23)$$

representing equilibrium, constitutive and compatibility conditions in the domain, respectively, and, additionally, a set of prescribed boundary conditions on the boundary $\Gamma = \Gamma_D \cup \Gamma_N$, divided into Dirichlet (kinematical) and Neumann (statical) conditions, respectively, as follows

$$\begin{aligned} \mathbf{d} - \bar{\mathbf{d}} &= \mathbf{o} & \text{on } \Gamma_D \\ \nu_\alpha^r \mathbf{H} \boldsymbol{\sigma}_\alpha^r - \bar{\mathbf{q}} &= \mathbf{o} & \text{on } \Gamma_N \end{aligned} \quad (24)$$

3 Some multi-field variational principles

We present now some multi-field variational principles that correspond to problem (23) with boundary conditions (24) (see also [3]).

3.1 Principle of total potential energy

We start with the well-known Principle of Stationary Total Potential Energy for didactic purposes. The Total Potential Energy is defined by the one-field functional $U : \mathcal{D} \rightarrow \mathbb{R}$ given by

$$U(\mathbf{d}) = \int_{\Omega} \psi \circ \hat{\varepsilon}_{\alpha}^r(\mathbf{d}) d\Omega - \int_{\Omega} \tilde{\mathbf{q}} \cdot \mathbf{d} d\Omega - \int_{\Gamma_N} \bar{\mathbf{q}} \cdot \mathbf{d} d\Gamma. \quad (25)$$

In order to (25) be stationary, one gets the necessary condition $\delta U = 0, \forall \delta \mathbf{d} \in \delta \mathcal{D}$, where

$$\delta U = \int_{\Omega} [-\partial_{\alpha} \psi \cdot \mathcal{T}_{\alpha}^c(\mathbf{d}) \delta \mathbf{d} + \tilde{\mathbf{q}} \cdot \delta \mathbf{d}] d\Omega + \int_{\Gamma_N} \bar{\mathbf{q}} \cdot \delta \mathbf{d} d\Gamma. \quad (26)$$

is the Gâteaux derivative of (25). Introducing the constitutive equation (23)₂ in (26), one arrives at (18), which, after the application of the divergence theorem, delivers (17).

Hence, it can be concluded that a geometrically exact first-order-shear shell model is in equilibrium if and only if its total potential energy has a stationary value at the solution. This result is known as the *Principle of Stationary Total Potential Energy*.

3.2 Three-field principle of Veubeke-Hu-Washizu type

The Principle of Stationary Total Potential Energy can be generalized through the well-known method of Lagrange multipliers, which allows to introduce the compatibility equation (23)₃ and the kinematical boundary condition (24)₁, assumed now as subsidiary conditions, into the framework of the variational expression (25). The result is the three-field functional of Veubeke-Hu-Washizu Type, $\Pi_{VHW} : \mathcal{H}^1(\Omega) \times \mathcal{H}^0(\Omega) \times \mathcal{H}^0(\Omega) \rightarrow \mathbb{R}$, given by

$$\begin{aligned} \Pi_{VHW}(\mathbf{d}, \boldsymbol{\sigma}_{\alpha}^r, \varepsilon_{\alpha}^r) &= \int_{\Omega} [-\psi + \boldsymbol{\sigma}_{\alpha}^r \cdot (\varepsilon_{\alpha}^r - \hat{\varepsilon}_{\alpha}^r(\mathbf{d})) + \tilde{\mathbf{q}} \cdot \mathbf{d}] d\Omega + \\ &+ \int_{\Gamma_N} \bar{\mathbf{q}} \cdot \mathbf{d} d\Gamma + \int_{\Gamma_D} \nu_{\alpha}^r \mathbf{H} \boldsymbol{\sigma}_{\alpha}^r \cdot (\mathbf{d} - \bar{\mathbf{d}}) d\Gamma. \end{aligned} \quad (27)$$

Equations (23) and both boundary conditions (24) render this functional stationary. The major advantage of (27) is the fact that it avoids the inversion of the constitutive equation (23)₂. On the other hand it is a mixed functional, with the well-known stability problems in the approximation of saddle-points.

3.3 Two-field principle of Hellinger-Reissner type

It is interesting to note that, the two-field Principle of Hellinger-Reissner owes its origin to the idea that, in geometrically non-linear problems, the difficulties with the Complementary Potential Energy could be circumvented by considering stresses and displacements as primal variables.

The two-field Principle of Hellinger-Reissner Type in our framework can be obtained from (27), considering the inverse of the constitutive equation given by (21). The result is a two-field functional $\Pi_{HR} : \mathcal{H}^1(\Omega) \times \mathcal{H}^0(\Omega) \rightarrow \mathbb{R}$ given by

$$\begin{aligned} \Pi_{HR}^*(\mathbf{d}, \boldsymbol{\sigma}^r) &= \int_{\Omega} [\psi^* - \boldsymbol{\sigma}_{\alpha}^r \cdot \hat{\varepsilon}_{\alpha}^r(\mathbf{d}) + \tilde{\mathbf{q}} \cdot \mathbf{d}] d\Omega + \\ &+ \int_{\Gamma_N} \bar{\mathbf{q}} \cdot \mathbf{d} d\Gamma + \int_{\Gamma_D} \nu_{\alpha}^r \mathbf{H} \boldsymbol{\sigma}_{\alpha}^r \cdot (\mathbf{d} - \bar{\mathbf{d}}) d\Gamma. \end{aligned} \quad (28)$$

The corresponding Euler-Lagrange equations are

$$\begin{aligned} \mathcal{T}_{\alpha}^e(\mathbf{d}) \boldsymbol{\sigma}_{\alpha}^r + \tilde{\mathbf{q}} &= \mathbf{o} \quad \text{in } \Omega \\ \partial_{\alpha} \psi^* - \hat{\varepsilon}_{\alpha}^r(\mathbf{d}) &= \mathbf{o} \quad \text{in } \Omega \end{aligned} \quad (29)$$

and the boundary conditions (24). It is a mixed functional, with the known stability problems in the approximation of saddle-points.

3.4 Two-field principle of total complementary potential energy

Although in the framework of the two-field Principle of Hellinger-Reissner Type, the equilibrium equations (29)₁ have been obtained as Euler-Lagrange equations, they can be instead considered as subsidiary conditions to be satisfied *a priori*. Accordingly, assuming that equilibrium holds, when subjecting (28) to the equilibrium equations by means of appropriate Lagrange multipliers, the following augmented Lagrangian is obtained

$$L^*(\mathbf{d}, \boldsymbol{\sigma}_{\alpha}^r) = \Pi_{HR}^*(\mathbf{d}, \boldsymbol{\sigma}_{\alpha}^r) - \int_{\Omega} [\mathcal{T}_{\alpha}^e(\mathbf{d}) \boldsymbol{\sigma}_{\alpha}^r + \tilde{\mathbf{q}}] \cdot \mathbf{d} d\Omega + \int_{\Gamma_N} (\nu_{\alpha}^r \mathbf{H} \boldsymbol{\sigma}_{\alpha}^r - \bar{\mathbf{q}}) \cdot \mathbf{d} d\Gamma. \quad (30)$$

which, after the use of the divergence theorem, delivers the following functional

$$U^*(\mathbf{d}, \boldsymbol{\sigma}_{\alpha}^r) = \int_{\Omega} [\psi^* + \boldsymbol{\sigma}_{\alpha}^r \cdot (\mathcal{T}_{\alpha}^e(\mathbf{d}) \mathbf{d} - \hat{\varepsilon}_{\alpha}^r(\mathbf{d}))] d\Omega - \int_{\Gamma_D} \nu_{\alpha}^r \mathbf{H} \boldsymbol{\sigma}_{\alpha}^r \cdot \bar{\mathbf{d}} d\Gamma. \quad (31)$$

Now we introduce the function space

$$\varepsilon \mathbf{d} = \left\{ \boldsymbol{\sigma}_{\alpha}^r \in \mathcal{H}^1(\Omega) \left| \begin{array}{l} \mathcal{T}_{\alpha}^e(\mathbf{d}) \boldsymbol{\sigma}_{\alpha}^r + \tilde{\mathbf{q}} = \mathbf{o} \text{ in } \Omega \text{ and} \\ \nu_{\alpha}^r \mathbf{H} \boldsymbol{\sigma}_{\alpha}^r = \bar{\mathbf{q}} \text{ on } \Gamma_N \end{array} \right. \right\}$$

and the linear space

$$\delta \varepsilon(\mathbf{d}) = \left\{ \delta \boldsymbol{\sigma}_{\alpha}^r \in \mathcal{H}^1(\Omega) \left| \begin{array}{l} \mathcal{T}_{\alpha}^e(\mathbf{d}) \delta \boldsymbol{\sigma}_{\alpha}^r = \mathbf{o} \text{ in } \Omega \text{ and} \\ \nu_{\alpha}^r \mathbf{H} \delta \boldsymbol{\sigma}_{\alpha}^r = \mathbf{o} \text{ on } \Gamma_N \end{array} \right. \right\},$$

in order to write $U^* : \mathcal{H}^1(\Omega) \times \mathcal{E}(\Omega) \rightarrow \mathbb{R}$ and to get the Gâteaux derivative of (31), which is

$$\delta U^* = \int_{\Omega} [\partial_{\alpha} \psi^* - \hat{\varepsilon}_{\alpha}^r(\mathbf{d})] \cdot \delta \boldsymbol{\sigma}_{\alpha}^r d\Omega + \int_{\Gamma_D} (\mathbf{d} - \bar{\mathbf{d}}) \cdot \nu_{\alpha}^r \mathbf{H} \delta \boldsymbol{\sigma}_{\alpha}^r d\Gamma. \quad (32)$$

Hence, the corresponding Euler-Lagrange equations emanating from $\delta U^* = 0$, $\forall \delta \mathbf{d} \in \mathcal{H}^1(\Omega)$, $\forall \delta \boldsymbol{\sigma}^r \in \delta \mathcal{E}(\Omega)$, are

$$\begin{aligned} \partial_{\alpha} \psi^* - \hat{\varepsilon}_{\alpha}^r(\mathbf{d}) &= \mathbf{o} \quad \text{in } \Omega \\ \mathbf{d} - \bar{\mathbf{d}} &= \mathbf{o} \quad \text{on } \Gamma_D \end{aligned} \quad (33)$$

which are clearly the compatibility equations in the domain and at the boundary.

3.5 Hybrid principle of Hellinger-Reissner type

Relaxing the continuity requirements of the displacements along the interelement boundaries (here indicated by Γ_{IE}) by means of a Lagrange multiplier \mathbf{q}^{Γ} , a generalized hybrid form of the functional (28) can be built. It is a (2+2)-field hybrid-mixed functional of Hellinger-Reissner type indicated by $\Pi_{HR}^2: \mathcal{H}^1(\Omega) \times \mathcal{H}^0(\Omega) \times \mathcal{H}^0(\Gamma_{IE}) \times \mathcal{H}^0(\Gamma_{IE}) \rightarrow \mathbb{R}$ and defined as

$$\Pi_{HR}^2(\mathbf{d}, \boldsymbol{\sigma}^r, \mathbf{d}^{\Gamma}, \mathbf{q}^{\Gamma}) = \Pi_{HR}(\mathbf{d}, \boldsymbol{\sigma}^r) + \int_{\Gamma_D} \mathbf{q}^{\Gamma} \cdot (\mathbf{d}^{\Gamma} - \bar{\mathbf{d}}) d\Gamma + \int_{\Gamma_{IE}} \mathbf{q}^{\Gamma} \cdot (\mathbf{d} - \mathbf{d}^{\Gamma}) d\Gamma. \quad (34)$$

For this functional, the Euler-Lagrange equations are (29) and

$$\begin{aligned} \bar{\mathbf{q}} - \mathbf{q}^{\Gamma} &= \mathbf{o} \quad \text{on } \Gamma_N \\ \mathbf{d}^{\Gamma} - \bar{\mathbf{d}} &= \mathbf{o} \quad \text{on } \Gamma_D \\ \mathbf{q}^{\Gamma} - \nu_{\alpha}^r \mathbf{H} \boldsymbol{\sigma}_{\alpha}^r &= \mathbf{o} \quad \text{on } \Gamma_{IE} \\ \mathbf{d} - \mathbf{d}^{\Gamma} &= \mathbf{o} \quad \text{on } \Gamma_{IE} \end{aligned} \quad (35)$$

A hybrid form of the Two-field Principle of Total Complementary Potential Energy (31) is also possible. Due to the lack of space, it will not be presented. This functional will be used in the derivation of equilibrated co-rotational finite elements. This is our next goal.

References

- [1] Campello, E., Pimenta, P. & Wriggers, P., A triangular finite shell element based on a fully nonlinear shell formulation. *Comput Mech*, **31**, pp. 505–518, 2003.
- [2] Pimenta, P. & Campello, E., Shell curvature as an initial deformation: geometrically exact finite element approach. *Int J Num Meth Eng*, **78**, pp. 1094–1112, 2009.
- [3] Santos, H., Pimenta, P. & Almeida, J., Hybrid and multi-field variational principles for geometrically exact three-dimensional beams. *Int J Nonlinear Mech*, **45**, pp. 809–820, 2010.

Dynamical analysis of a van der Pol oscillators system used for human gait simulation

Armando Carlos de Pina Filho

*Universidade Federal do Rio de Janeiro, Urban Engineering Program, POLI,
Technology Center, Rio de Janeiro, RJ – Brazil*

Max Suell Dutra

*Universidade Federal do Rio de Janeiro, Mechanical Engineering Program,
COPPE,
Technology Center, Rio de Janeiro, RJ – Brazil*

Abstract

Human gait is controlled, in part, by central pattern generator (CPG), responsible for the production of rhythmic movements. This CPG can be modeled by means of a oscillators system, which generates patterns similar to human CPG, becoming possible the human gait simulation. In order to create this system, a set of coupled van der Pol oscillators was used, simulating the behavior of the hip and knees angles of a two-dimensional locomotor model. The objective of the work presented here is to analyze the dynamics of this oscillators system by means of bifurcation diagrams and Poincaré maps. From the analysis and graphs generated in MATLAB, it was possible to evaluate characteristics of the system, such as: sensitivity to the initial conditions, presence of strange attractors and other phenomena of chaos. In the course of tests, we verify that diagrams did not clearly present bifurcation as simple curves, but as a cloud of points. Considering the complexity of the system, this fact can be explained by two points of view: one is related to the coupling terms and their relationship, and other one is related to the quasi-periodic response of the system. Both of them will be presented and analyzed in this work. Based on the results of the study, we conclude that although the use of oscillators represents an excellent way for generating pattern signals of locomotion, its application in the control of a bipedal locomotor will only be possible with the correct choice of parameters, which must be done from the data provided by the dynamical analysis.

Keywords: locomotion, CPG, oscillators, chaos.

1 Introduction

Year after year, from technological advances, based on theoretical and experimental researches, the man tries to copy or to imitate some systems of the human body. It is the case, for example, of the central pattern generator (CPG), responsible for the production of rhythmic movements [1], [2], and

[3]. Figure 1 presents a scheme of the control system of the human locomotion, controlled by the central nervous system, which the central pattern generator supplies a series of pattern curves for each part of the locomotor. This information is passed to the muscles by means of a network of motoneurons, and the conjoined muscular activity performs the locomotion. Sensorial information about the conditions of the environment or some disturbance are supplied as feedback of the system, providing a fast action proceeding from the central pattern generator, which adapts the gait to the new situation.

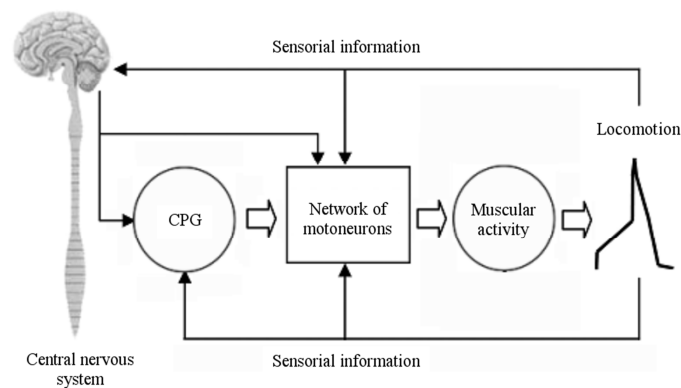


Figure 1: Control system of the human locomotion.

Modelling of a CPG can be made by means of coupled oscillators, and this system generates patterns similar to human CPG, becoming possible the human gait simulation. There are some significant works about the locomotion of vertebrates controlled by central pattern generators: [4], and [5].

From a model of two-dimensional locomotor, oscillators with integer relation of frequency can be used for simulating the behaviour of the hip angle and of the knees angles. Each oscillator has its own parameters and the link to the other oscillators is made through coupling terms. We intend to evaluate a system with coupled van der Pol oscillators. Some previous works about CPGs using nonlinear oscillators, applied in the human gait simulation, can be seen in [6–10].

From the oscillators system, we achieve the dynamical analysis by means of bifurcation diagrams and Poincaré maps. With graphs generated in MATLAB, it was possible to evaluate some characteristics of the system, such as: sensitivity to the initial conditions, presence of strange attractors and other phenomena of the chaos.

2 Human gait

Despite the people not walk in completely identical way, some characteristics in the gait can be considered universal, and these similar points serve as base for description of patterns of the kinematics, dynamics and muscular activity in the locomotion.

In this work, our interest is related to the patterns of the hip and knee angles, more specifically, in sagittal plane. According [11], Fig. 2 presents the graphs of angular displacement and phase space of the hip, while Fig. 3 presents the graphs of angular displacement and phase space of the knee.

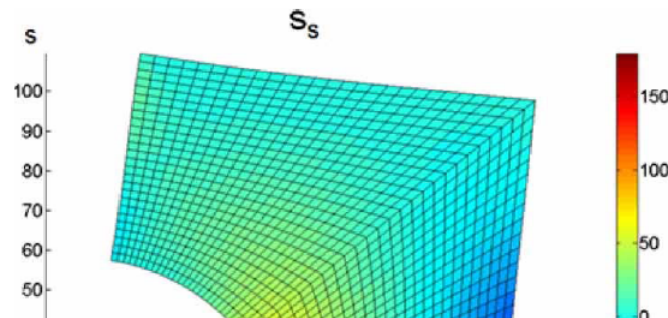


Figure 2: Angular displacement and phase space of the hip (mean \pm deviation).

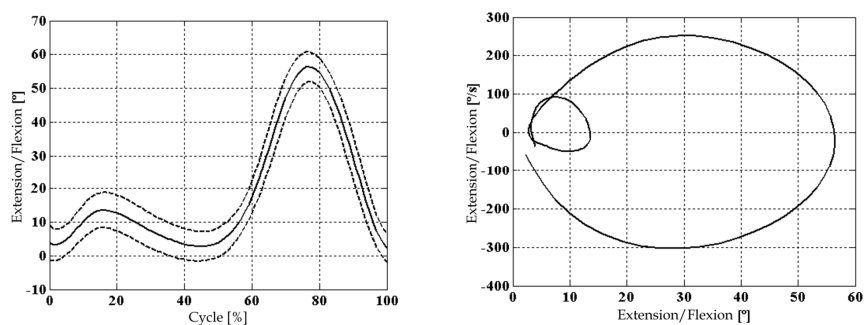


Figure 3: Angular displacement and phase space of the knee (mean \pm deviation).

From the knowledge of these patterns of behaviour, we intend to create a CPG using the system of coupled oscillators. This system will be applied in a biped locomotor model to simulate the human gait.

In order to specify this model, we consider some particularities of the human locomotion, such as the determinants of gait [12], and [13]. The model presented here characterises the three most important determinants of gait: the compass gait that is performed with stiff legs like an inverted pendulum (the pathway of the centre of gravity is a series of arcs); the knee flexion of the stance leg, which combined with pelvic rotation and pelvic tilt achieve minimal vertical displacement of the centre of gravity; and

the plantar flexion of the stance ankle, where the effects of the arcs of foot and knee rotation smooth out the abrupt inflexions at the intersection of the arcs of translation of the centre of gravity.

Figure 4 presents the biped model with its angles and lengths, where: l_s is the length of foot responsible for the support (toes), l_p is the length of foot that raises up the ground (sole), l_t is the length of tibia, and l_f is the length of femur. The angle of the hip θ_4 and the angles of the knees θ_3 and θ_5 will be determined by the CPG system, while the other angles are calculated by the kinematical analysis of the mechanism. In this work we will not present details of this analysis, which can be seen in [8].

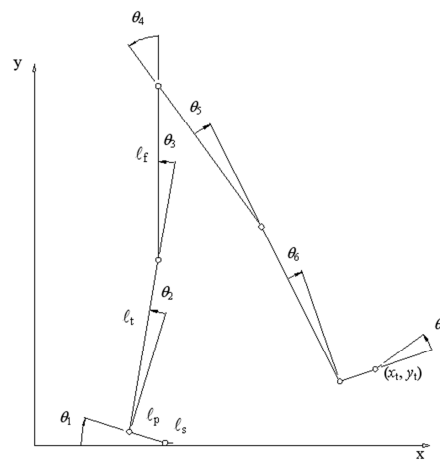


Figure 4: Biped model with the determinants of gait, angles and lengths.

3 CPG system

Coupled oscillators systems have been extensively used in studies of physiological and biochemical modelling. Since the years of 1960, many researchers have studied the case of coupling between two oscillators, because this study is the basis to understand the phenomenon in a great number of coupled oscillators. One of the types of oscillators that can be used in coupled systems is the auto-excited ones, which have a stable limit cycle without external forces. The van der Pol oscillator is an example of this type of oscillator, and it will be used in this work. Then, considering a system of n coupled van der Pol oscillators, from van der Pol equation:

$$\ddot{x} - \varepsilon \left(1 - p(x - x_0)^2\right) \dot{x} + \Omega^2 (x - x_0) = 0 \quad \varepsilon, p \geq 0 \quad (1)$$

where ϵ , p and Ω correspond to the parameters of the oscillator, and adding coupling terms that relate the oscillators velocities, we have:

$$\ddot{\theta}_i - \epsilon_i \left[1 - p_i (\theta_i - \theta_{io})^2 \right] \dot{\theta}_i + \Omega_i^2 (\theta_i - \theta_{io}) - \sum_{j=1}^n c_{i,j} (\dot{\theta}_i - \dot{\theta}_j) = 0 \quad i = 1, 2, \dots, n \quad (2)$$

which represents coupling between oscillators with the same frequency, where θ corresponds to the system degrees of freedom. In the case of coupling between oscillators with integer relation of frequency, the equation would be:

$$\ddot{\theta}_h - \epsilon_h \left[1 - p_h (\theta_h - \theta_{ho})^2 \right] \dot{\theta}_h + \Omega_h^2 (\theta_h - \theta_{ho}) - \sum_{i=1}^m c_{h,i} \left[\dot{\theta}_i (\theta_i - \theta_{io}) \right] - \sum_{k=1}^n c_{h,k} (\dot{\theta}_h - \dot{\theta}_k) = 0 \quad (3)$$

where $c_{h,i} [\dot{\theta}_i (\theta_i - \theta_{io})]$ is responsible for the coupling between oscillators with different frequencies, while $c_{h,k} (\dot{\theta}_h - \dot{\theta}_k)$, also seen in Eq. (2), effects the coupling between oscillators with the same frequency [14].

To generate the angles θ_3 , θ_4 and θ_5 as a periodic attractor of a nonlinear net, three coupled van der Pol oscillators were used. These oscillators are mutually coupled by terms that determine the influence of one oscillator on the others (Fig. 5).

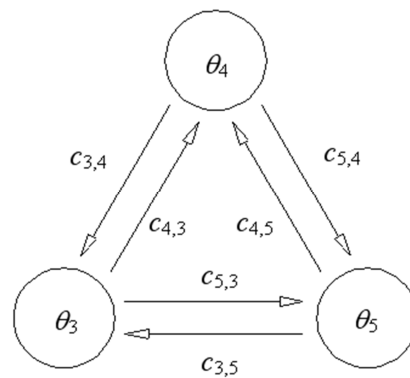


Figure 5: Structure of coupling oscillators.

Applying Eq. (2) and (3) to the proposed problem, knowing that the frequency of θ_3 and θ_5 (knee angles) is double of θ_4 (hip angle), we have the following equations:

$$\ddot{\theta}_3 - \varepsilon_3[1 - p_3(\theta_3 - \theta_{3o})^2] \dot{\theta}_3 + \Omega_3^2(\theta_3 - \theta_{3o}) - c_{3,4}[\dot{\theta}_4(\theta_4 - \theta_{4o})] - c_{3,5}(\dot{\theta}_3 - \dot{\theta}_5) = 0 \quad (4)$$

$$\ddot{\theta}_4 - \varepsilon_4[1 - p_4(\theta_4 - \theta_{4o})^2] \dot{\theta}_4 + \Omega_4^2(\theta_4 - \theta_{4o}) - c_{4,3}[\dot{\theta}_3(\theta_3 - \theta_{3o})] - c_{4,5}[\dot{\theta}_5(\theta_5 - \theta_{5o})] = 0 \quad (5)$$

$$\ddot{\theta}_5 - \varepsilon_5[1 - p_5(\theta_5 - \theta_{5o})^2] \dot{\theta}_5 + \Omega_5^2(\theta_5 - \theta_{5o}) - c_{5,4}[\dot{\theta}_4(\theta_4 - \theta_{4o})] - c_{5,3}(\dot{\theta}_5 - \dot{\theta}_3) = 0 \quad (6)$$

From Eq. (4)-(6), using the parameters shown in Table 1 together with values supplied by [8], the graphs were generated in MATLAB as shown in Fig. 6, which present, respectively, the behaviour of θ_3 , θ_4 and θ_5 as a function of time and stable limit cycles of oscillators.

Table 1: Parameters of van der Pol oscillators.

$c_{3,4}$	$c_{4,3}$	$c_{3,5}$	$c_{5,3}$	$c_{4,5}$	$c_{5,4}$	ε_3	ε_4	ε_5
0.001	0.001	0.1	0.1	0.001	0.001	0.01	0.1	0.01

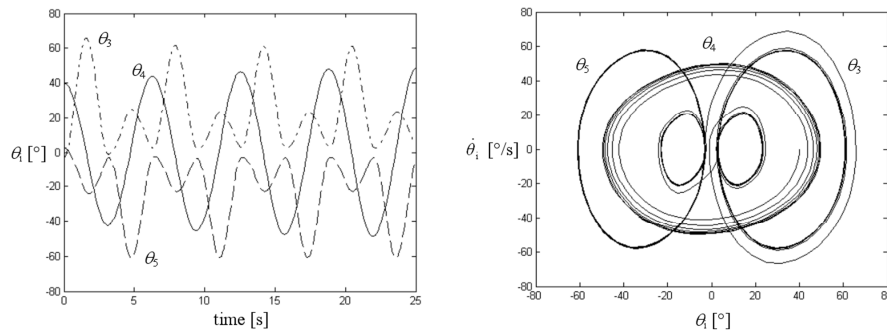


Figure 6: Angles as a function of time, and trajectories in the phase space.

Comparing Fig. 6 with the experimental results presented in Fig. 2 and 3, it is verified that the coupling system supplies similar results, what confirms the possibility of use of mutually coupled van der Pol oscillators in the modelling of the CPG.

Figure 7 shows, with a stick figure, the gait with a step length of 0.63 m. Dimensions used in the model can be seen in Table 2.

Table 2: Model dimensions.

Thumb	Foot	Leg (below the knee)	Thigh
0.03 m	0.11 m	0.37 m	0.37 m

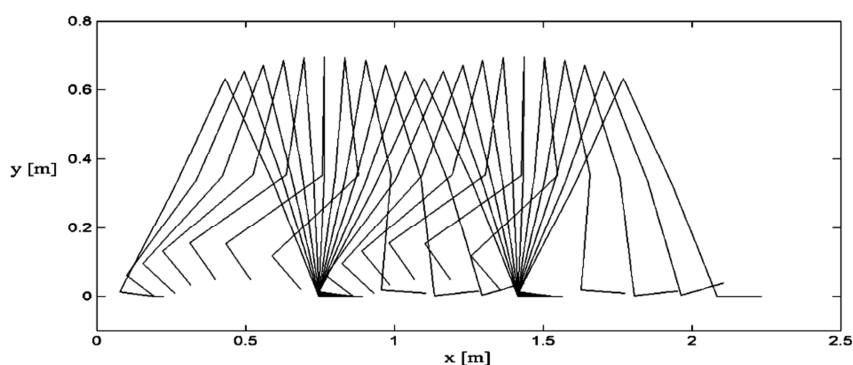


Figure 7: Stick figure showing the gait with a step length of 0.63 m.

4 Dynamical analysis

The nonlinear dynamical analysis of the system presented here requires the definition of some usual concepts. Usually, for some values of parameters, the system behaviour is periodic, and for other values the behaviour is chaotic. A periodic system returns to its state after a finite time t . The trajectory in the phase space is represented by a closed curve. The chaotic system presents trajectories of non-closed orbits that are generated by the solution of a deterministic set of ordinary differential equations.

Two conditions must be satisfied to make possible that a system presents chaotic behaviour: the equations of motion must include a nonlinear term; and the system must have at least three independent dynamic variables. The main consequence associated with the chaos is the sensitivity to the initial conditions. In chaotic systems, a small change in the initial conditions results in a drastic change in the system behaviour.

Also, in chaotic systems, we observe the bifurcation phenomenon, which represent the stroboscopic distribution of the system response from slow variation of a parameter. This method was applied here, which implies to simulate different parameter values that we want to analyze, evaluating the response in bifurcation diagrams and Poincaré maps.

More details about the Chaos theory and its characteristics can be found in [15–17].

Then, considering different values for the parameters ϵ_3 , ϵ_4 and ϵ_5 , the tests have been performed using MATLAB to generate the bifurcation diagrams and Poincaré maps. In principle, keeping values of $\epsilon_4 = 0.1$ and $\epsilon_5 = 0.01$, the value of ϵ_3 was varied from 0 to 2. Other values of the system have

been kept. Figure 8 presents the bifurcation diagram showing the behaviour of knee oscillator θ_3 with variation of parameter ϵ_3 , which represents the damping term related with this oscillator. Also, we have the strange attractor generated in the analysis of knee oscillator θ_3 , observed in a Poincaré map.

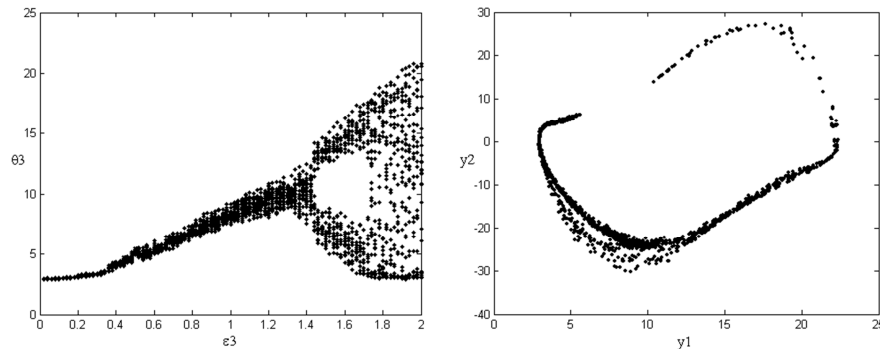


Figure 8: Bifurcation diagram for θ_3 with variation of ϵ_3 , and strange attractor for θ_3 .

This diagram does not represent the bifurcation as simple curves, which normally happens in dynamical analysis of a system, but with a cloud of points. Considering the complexity of coupled oscillators system, this fact can be explained by relation between coupling terms or by quasiperiodic response of the system.

A great variation between coupling terms, with one of them approaching to zero, makes the system presents practically a unidirectional coupling, and consequently the response in bifurcation diagram is represented by a cloud of points, characterizing not only the presence of periodic and chaotic orbits, but also pseudo-trajectories [18], and [19].

In relation to system behaviour, with small values of damping term, below 0.1, the system presents a periodic response. With the increase of damping term, the system starts to present a quasiperiodic response (Fig. 9) and later chaotic response (Fig. 10), when $\epsilon_3 = 2$.

More details about transition between quasiperiodic and chaotic response are presented in [20–22].

Sensitivity to the initial conditions can be verified considering two simulations with different conditions, for example, with $\epsilon_3 = 3$ (chaotic regime), choosing initial values for the angles: $\theta_3 = 3^\circ$, $\theta_4 = 50^\circ$, $\theta_5 = -3^\circ$, and changing $\theta_3 = 3.001^\circ$, we observed the influence of initial conditions in the system response (Fig. 11).

Considering the coupling oscillators, the degree of influence between them is defined by the coupling term. Then, a change of oscillator parameters must influence the behaviour of other oscillators. In the case of the hip angle, the influence of knee oscillator θ_3 on the hip is small, therefore the behaviour of θ_4 does not show many alterations. This occurs due to small value adopted for the coupling term between the oscillators ($c_{34} = c_{43} = 0.001$). In relation to the knees, the coupling term is greater ($c_{35} = c_{53} = 0.1$), configuring a more significant influence.

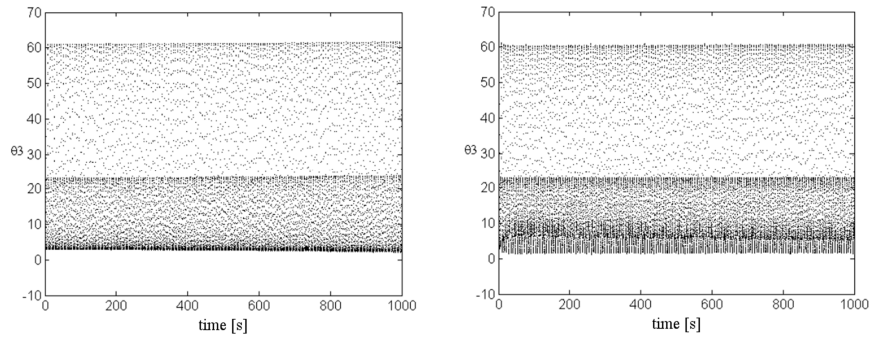


Figure 9: Periodic response: $\epsilon_3 = 0.01$, and Quasiperiodic response: $\epsilon_3 = 1$.

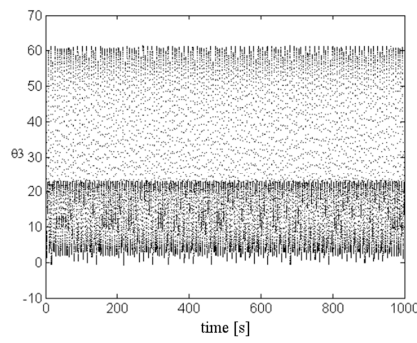


Figure 10: Chaotic response: $\epsilon_3 = 2$.

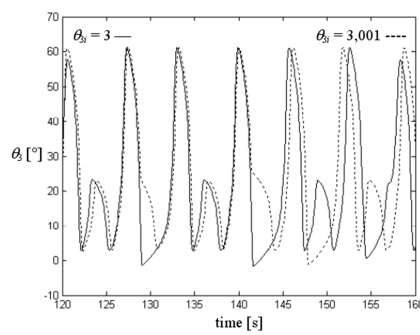


Figure 11: Sensitivity to the initial conditions in chaotic response.

Similarly to analysis of ϵ_3 , the system response can be analyzed by varying the values of ϵ_4 (from 0 to 2) and keeping the other values fixed. Figure 12 presents the bifurcation diagram showing the behaviour of hip oscillator θ_4 with variation of parameter ϵ_4 , which represents the damping term related with this oscillator. Also, we have the strange attractor generated in the analysis of this oscillator.

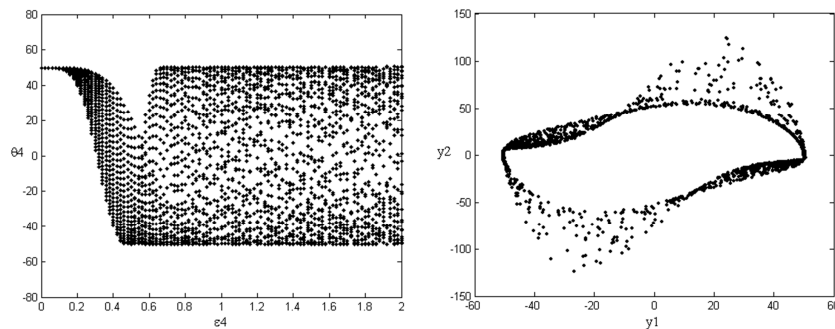


Figure 12: Bifurcation diagram for θ_4 with variation of ϵ_4 , and strange attractor for θ_4 .

As seen previously in the analysis of ϵ_3 , the influence of hip on the knees is small, then a variation of ϵ_4 does not cause great changes in θ_3 and θ_5 .

Finally, the system response can be analyzed by varying the values of ϵ_5 (from 0 to 2) and keeping the other system values fixed. Figure 13 presents the bifurcation diagram showing the behaviour of knee oscillator θ_5 with variation of the parameter ϵ_5 , which represents the damping term related with this oscillator. Also, we have the strange attractor generated in the analysis of this oscillator.

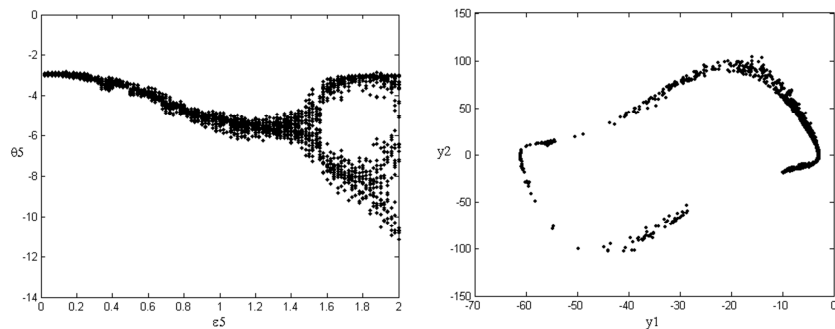


Figure 13: Bifurcation diagram for θ_5 with variation of ϵ_5 , and strange attractor for θ_5 .

5 Conclusion

In this work, we present the study of a biped locomotor with a CPG formed by a system of coupled van der Pol oscillators. A biped locomotor model with three of the six most important determinants of human gait was used in the analyses. After the modelling of the oscillators system, a dynamical analysis was performed to verify the performance of the system, in particular, aspects related to the chaos. From presented results and discussion, we come to the following conclusions: the use of mutually coupled nonlinear oscillators of van der Pol can represent an excellent way to generate locomotion pattern signals, allowing its application for the control of a biped by the synchronization and coordination of the legs, once the choice of parameters is correct, which must be made from the data supplied by the analysis of bifurcation and chaos. Through the dynamical analysis it was possible to evidence a weak point of coupling systems. The influence of the knee oscillators on the hip, and vice versa, is very small, what can harm the functionality of the system. The solution for this problem seems immediate: to increase the value of the coupling term between the hip and knees. However, this can make the system unstable. Then, it is necessary a more refined study of the problem, which will be made in future works, as well as a study of the behaviour of the ankles, and simulation of the hip and knees in the other anatomical planes, increasing the network of coupled oscillators, and consequently simulating with more details the human locomotion CPG. This study has great application in the project of autonomous robots and in the rehabilitation technology, not only in the project of prosthesis and orthosis, but also in the searching of procedures that help to recuperate motor functions of human beings.

References

- [1] Calancie, B., Needham-Shropshire, B., Jacobs, P., Willer, K., Zych, G. & Green, B., Involuntary stepping after chronic spinal cord injury. evidence for a central rhythm generator for locomotion in man. *Brain*, **117**, pp. 1143–1159, 1994. (Pt 5).
- [2] Dimitrijevic, M., Gerasimenko, Y. & Pinter, M., Evidence for a spinal central pattern generator in humans. *Annals of the New York Academy of Sciences*, **860**, pp. 360–376, 1998.
- [3] Mackay-Lyons, M., Central pattern generation of locomotion: A review of the evidence. *Physical Therapy*, **82(1)**, 2002.
- [4] Grillner, S., Neurobiological bases of rhythmic motor acts in vertebrates. *Science*, **228**, pp. 143–149, 1985.
- [5] Pearson, K., Common principles of motor control in vertebrates and invertebrates. *Annu Rev Neurosci*, **16**, pp. 265–297, 1993.
- [6] Bay, J. & Hemami, H., Modelling of a neural pattern generator with coupled nonlinear oscillators. *IEEE Trans Biomed Eng*, **34**, pp. 297–306, 1987.
- [7] Dutra, M., de Pina Filho, A. & Romano, V., Modelling of a bipedal locomotor using coupled nonlinear oscillators of van der pol. *Biological Cybernetics*, **88(4)**, pp. 286–292, 2003.
- [8] de Pina Filho, A., *Study of Mutually Coupled Nonlinear Oscillators Applied in the Locomotion of a Bipedal Robot*. Ph.D. thesis, PEM/COPPE/UFRJ, Brazil, 2005.
- [9] de Pina Filho, A. & Dutra, M., Application of hybrid van der pol-rayleigh oscillators for modeling of a bipedal robot. *Mechanics of Solids in Brazil 2009*, eds. H. da Costa Mattos & M. Alves, Brazilian Society

- of Mechanical Sciences and Engineering: Brazil, pp. 209–221, 2009.
- [10] Zielinska, T., Coupled oscillators utilised as gait rhythm generators of a two-legged walking machine. *Biological Cybernetics*, **74**, pp. 263–273, 1996.
 - [11] de Pina Filho, A., Dutra, M. & Raptopoulos, L., Modelling of bipedal robots using coupled nonlinear oscillators. *Mobile Robots, Toward New Applications*, ed. A. Lazinica, Pro Literatur Verlag: Germany/ARS, Austria, pp. 57–78, 2006.
 - [12] McMahon, T., *Muscles, Reflexes and Locomotion*. Princeton University Press, 1984.
 - [13] Saunders, J., Inman, V. & Eberhart, H., The major determinants in normal and pathological gait. *J Bone Jt Surgery*, **35A**, 1953.
 - [14] Dutra, M., *Bewegungskoordination und Steuerung einer zweibeinigen Gehmaschine*. Shaker Verlag: Germany, 1995.
 - [15] Baker, L. & Gollub, J., *Chaotic Dynamics, an Introduction*. Cambridge University Press, 2nd edition, 1996.
 - [16] Strogatz, S., *Nonlinear Dynamics and Chaos*. Addison-Wesley, 1994.
 - [17] Thompson, J. & Stewart, H., *Nonlinear Dynamics and Chaos*. John Wiley and Sons: Chichester, 1986.
 - [18] Grebogi, C., Poon, L., Sauer, T., Yorke, J. & Auerbach, D., *Handbook of Dynamical Systems*, volume 2. Elsevier: Amsterdam, 2002.
 - [19] dos Santos, A., Lopes, S. & Viana, R., Rhythm synchronization and chaotic modulation of coupled van der pol oscillators in a model for the heartbeat. *Physica A*, **338**, pp. 335–355, 2004.
 - [20] Pazó, D., Sánchez, E. & Matías, M., Transition to high-dimensional chaos through quasiperiodic motion. *International Journal of Bifurcation and Chaos*, **11(10)**, pp. 2683–2688, 2001.
 - [21] Yang, J., Quasiperiodicity and transition to chaos. *Physical Review E*, **61**, pp. 6521–6526, 2000.
 - [22] Yoshinaga, T. & Kawakami, H., Bifurcations of quasi-periodic responses in coupled van der pol oscillators with external force. *IEICE Transactions on Fundamentals of Electronics, Communications and Computer Sciences*, **E77-A(11)**, pp. 1783–1787, 1994.

Teaching and assessing threshold concepts in solid mechanics using adaptive tutorials

B. Gangadhara Prusty

*School of Mechanical & Manufacturing Engineering,
University of New South Wales (UNSW), Sydney NSW 2052 – Australia*

Abstract

In large and diverse groups of students, it is often difficult to identify and help the students who are struggling with the basic concepts they need to progress in the study of solid mechanics. Adaptive Tutorials (ATs) use an online ‘intelligent’ tutoring system that provides a way of dealing with common sticking points, or ‘threshold concepts’. These can sometimes be addressed by skilled one-to-one coaching but are usually missed by traditional ‘book and board’ teaching in large classes. The ATs use online interactive virtual laboratory activities (simulations), and (a) track each student’s interaction with the simulation to provide tailored feedback; (b) generate data that teachers can use to identify common conceptual sticking points in large classes; and (c) provide information for adjusting the simulation, feedback and other learning activities in a course to help students through threshold concepts. ATs developed in stages since 2005, used in blended online and face-to-face teaching in mechanics, have been evaluated and are shown to improve both engagement in learning mechanics concepts and performance in assessments, particularly among lower performing students.

Keywords: adaptive tutorial, threshold concepts, online teaching, mechanics.

1 Challenges in engineering education

With the demand for new graduates in industry, and an increasing interest in engineering studies, students enter engineering through more flexible pathways into very large classes where it can be very difficult for the teacher to pick up on these students’ misconceptions and help them. Individualised feedback is almost impossible in situations like this.

Mechanics fundamentals provide a solid foundation for most engineering disciplines. Conventionally, at most engineering schools, the study of mechanics comprises up to 25% and 40% of 1st and 2nd Year levels respectively. Failure rates of up to 20% to 50% are common in introductory mechanics courses in engineering. This has been an issue of continuing concern. Poor understanding of basic engineering mechanics threshold concepts such as Free Body Diagrams, Equation of Equilibriums, Reaction Forces, Shear Force & Bending Moment calculations could lead to the production of new

generation of engineers with less conceptual understanding. Several studies [1–4] summarise the causes of failure and the degree of success achieved due to the strategies implemented by academics in various engineering universities for addressing this problem. In general, students are keen to correlate the subject matter with engineering reality and they want opportunities to visualize and explore the subject matter through experiments or similar exercises which demand a clear understanding of different components of their engineering program.

If 21st century students need more explanation and understanding of concepts than traditional teaching in large classes can provide, they could therefore benefit from opportunities to visualise and interact with abstract concepts from real life examples such as:

1. a bridge for explaining the fundamentals on free-body-diagrams
2. use of equation of equilibrium concepts through an example of a towing truck
3. the shear force and bending moment calculations due to various loading situations on a beam.

Many of these concepts have the characteristics of ‘threshold concepts’ in that they transform students’ thinking irreversibly [5]. It can therefore be hard for discipline experts to identify student sticking points without intensive one-to-one coaching, which does not lend itself to systematic recording and analysis.

2 Adaptive tutorials and the adaptive eLearning platform

Students can learn the basic skills with the development of a coherent approach to computer-assisted learning and assessment [6]. Participating in hands-on or interactive activities can improve the students’ motivational levels in learning [7–9]. Moreover, research suggests that students benefit from an interactive learning environment in which they can have some control of their learning experiences [10]. Computer-based games that have been developed for the students in Statics and Mechanics of Materials courses [11] were successful in both improving student performances and dramatically increasing engagement and motivation levels.

Although there are a number of initiatives by Universities around the world to use online educational tools, the ability to provide instant, intelligent (relevant and appropriate) feedback that is adapted to the learner’s knowledge level, is reserved to high end systems that utilize artificial intelligence, and which have had limited uptake [12].

On-line tutorial activities can be set up as a virtual laboratory where students can explore the interaction between variables in a safe and accessible environment. Getting students to experiment with real world cases is much too costly and dangerous. In contrast, an online tutorial can be re-used and customised for specific contexts with minimal cost and effort. Also, patterns of many student interactions with the virtual laboratory can be recorded systematically in detail.

Adaptive Tutorials (ATs) provide a way of dealing with common sticking points, or ‘threshold concepts’ that prevent students progressing in the study of mechanics. These can sometimes be addressed by skilled one-to-one coaching but are usually missed by traditional ‘book and board’ teaching in large classes. The ATs (Figure 1) use online interactive virtual laboratory activities (simulations), to: (a) track each student’s interaction with the simulation, and provide tailored feedback; (b) generate data that teachers can use to identify common conceptual sticking points in large classes; and (c) provide

information for adjusting the simulation, feedback and other learning activities in a course to help students through threshold concepts.

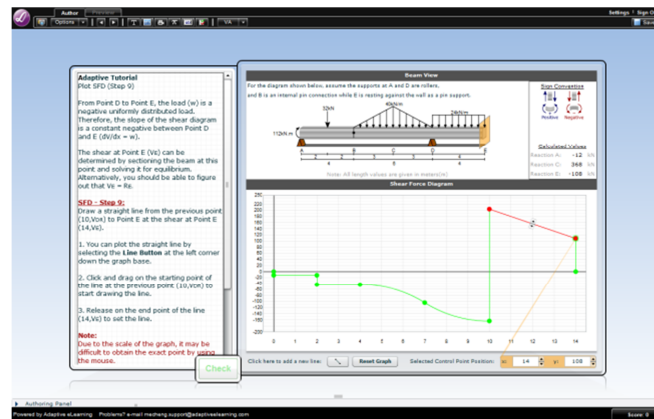


Figure 1: Adaptive tutorials on shear force and bending moment.

From a pedagogical point of view, ATs are similar to teaching laboratory activities and are analogous to the concept of Tutorial Simulations as described by [13]. They can be described as a hybrid between instructivist and constructivist educational theories, trying to strike a balance between guided and discovery learning – along the lines of the pragmatic approach to constructivism advocated by Perkins [14]. ATs are typically guided, featuring a detailed explanation that leads students through the interaction, while offering adaptive, remedial feedback in response to learners' misconceptions. ATs are also interactive, enabling students to investigate a phenomenon, or a relationship between parameters of a problem in a hands-on manner, thereby encouraging discovery learning.

3 Analysis tools that support teaching research

Adaptive Tutorials are not “launch and forget” projects. Once ATs are developed, teachers' use the AT-Analyser, which creates a visual trace of student performance (Figure 2) to scrutinise their students' interactions during the ATs, and to adapt the AT content as needed based on their students' demonstrated misconceptions. Tutorials can then be easily updated to address any misconceptions.

The ATs, equipped with a rich, highly visual set of interactive tools, as shown in Figure 3, provide intelligent remediation and instant feedback thereby promoting guided user exploration and discovery. With the implementation of AeLP tools, the academic is also able to monitor the progress of students using an analyser tool (Figure 2) available within the AeLP platform.

This creates a powerful educational experimentation environment where hypotheses about students' learning can be evaluated, adapted and then shared and published. Teachers thus become ‘action

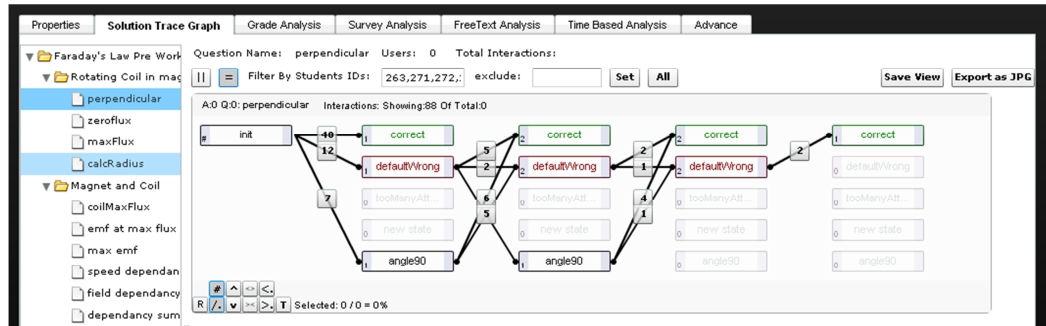


Figure 2: The adaptive tutorial analyser uses a solution trace graph to visually analyse students' solution-traces through the problem state-space.

researchers', confirming or disproving their hypotheses about the best way to help their students learn [15, 16].

4 Implementation and assessment

The aim of using the Adaptive Tutorials was to engage students in learning activities that help them attain the particular objectives set for the course, which are assessed through a number of methods. The delivery methods and teaching strategies for assessment and feedback were adapted to suit the level of courses and the learning styles of the students.

Teaching the foundation undergraduate courses across all disciplines within the School of Mechanical and Manufacturing Engineering at the University of New South Wales (UNSW) required the implementation of innovative teaching strategies into those courses in a staged manner, based on a pragmatic constructivist approach [14]. The assessments are made for the large classes in 1st and 2nd year courses at UNSW: Engineering Mechanics 1 (>275 students) and Solid Mechanics 1 (>300 students) courses. Because many of the students in 1st and 2nd year undergraduate students struggle with basic concepts in mechanics courses, the author has developed, used and evaluated ways of using online Adaptive Tutorials (Figure 3) to help students in Engineering Mechanics and Mechanics of Solids courses [17].

The ATs are intended to supplement and clarify the fundamental concepts in each course. Through the staged implementation of such tutorials, it can be demonstrated that such tools can help students learn, improve performance in assessments and they add to overall student satisfaction with the courses. The concept map (Figure 4) demonstrates the feasibility of adopting such ATs where the basic concepts feed into higher level concepts in solid mechanics courses.

To examine the usefulness of the tool in improved learning in Mechanics of Solids, two types of evidence were gathered:

1. survey data from students to gauge their engagement in learning with the ATs

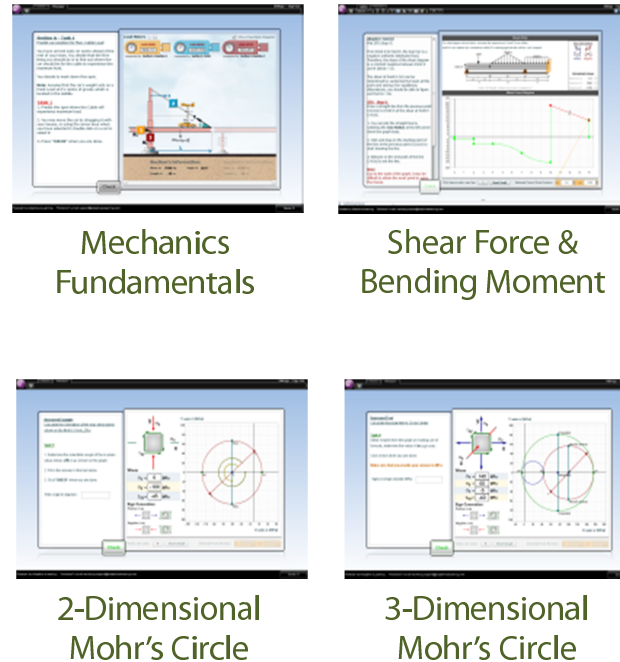


Figure 3: Snapshots of adaptive tutorials implemented at UNSW based on the targeted threshold concepts.

2. assessment results compared longitudinally through the years when the ATs were introduced, across 1st year engineering mechanics and later mechanics of solids classes.

This enables a comparison of guided vs. discovery based learning tasks, and also of performance across different cohorts of students with and without access to the Adaptive Tutorials.

5 Student feedback and response

A snapshot of the student evaluation questionnaire adopted within the ATs [17] clearly demonstrates that the students' like to see many more of such Adaptive Tutorials in a course (Figure 5):

Student feedback was collected via a questionnaire that featured within each AT as well as through a formal institutional evaluation. The survey indicated that students were generally very happy with the ATs and with the quality and challenge they provide. It was also indicated that the assessment methods were appropriate given the course aims. Students' comments include:

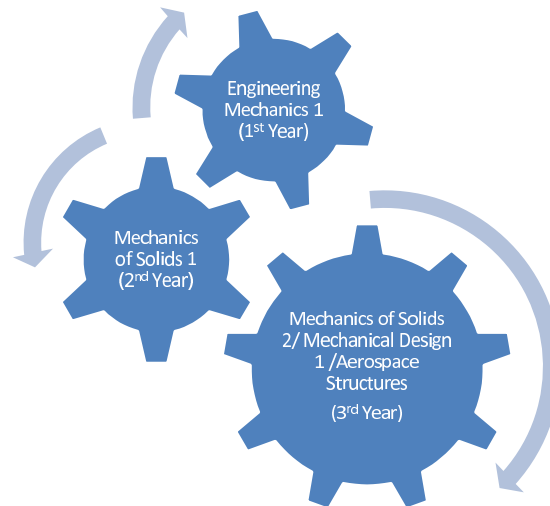


Figure 4: Concept map of the courses where AT activities can be beneficial.

1. *“Allow more of this kind of interactive lessons to better understand all our lesson. Hope to have more of this kind of online interactive lessons”*
2. *“Excellent tutorial. The tutorial has really furthered my knowledge of this topic. I would really like to see more of these tutorials. This tutorial has taught me the basic concepts and ideas I will need to undertake questions of a similar nature in the text book. Very helpful”*
3. *“awesome i understand the sign conventions regarding the angles now. thanks.”*
4. *“This tutorial was clear and helped me understand the concepts of Mohr’s circle to a much better degree than before. I highly recommend it.”*
5. *“Very good representation. Very helpful for my studies and understanding of Mohr Circles”*
6. *“It would have been better had i listen to you and completed this before my block test “*
7. *“Good for continued learning and to help with understanding – ie. getting more feedback then possible with general hand in assignments “*
8. *“This tutorial is great, I wish to see more course use something like this or at least put this kind of method in almost every chapter “*

Student feedbacks such as;

“Fantastic program I was really struggling with the force analysis, however this program has instilled confidence for understanding real-life application of engineering and mechanics”

“I highly recommend this tutorial. It has a very appealing practical approach yet at the same time helps me in improving my conceptual understanding of the topic at hand especially regarding the shear force and bending moment. The free body diagram on the side is also very helpful. Two thumbs up!”

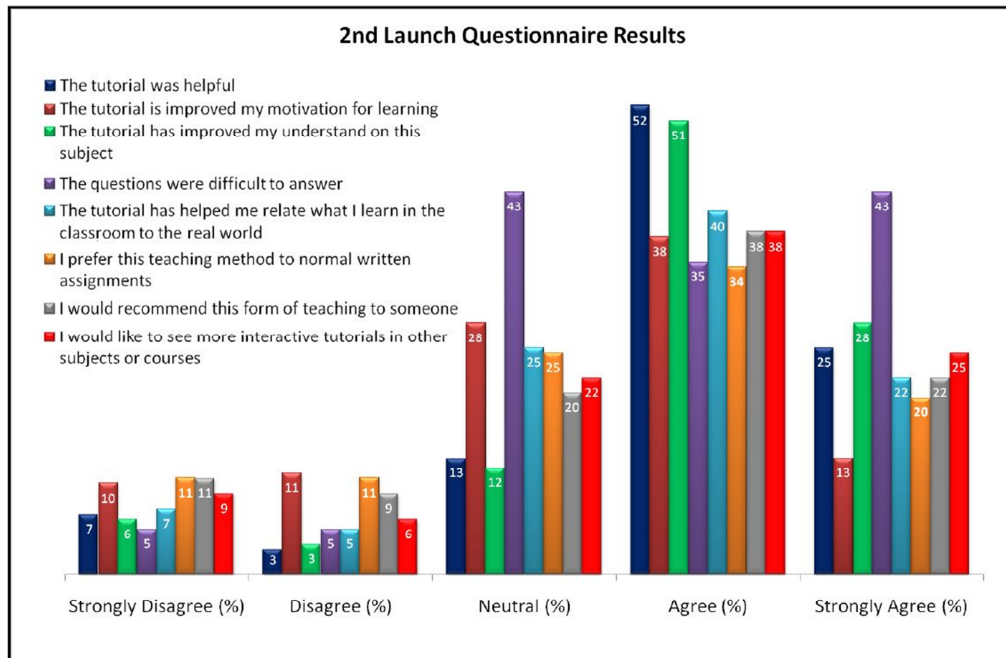


Figure 5: Questionnaire responses collected from the pilot study shows students engagement and interest in having more Adaptive Tutorials.

bears testimony to the success of this approach. The implementation of such ATs resulted a smooth and enjoyable learning process which goes beyond the book and board which engaged and stimulated the students to learn and achieve.

6 Effectiveness in teaching and performance

Results support the benefits of ATs for learning as well as for giving teachers control of the learning process. The improved performance of the students in Engineering Mechanics 1 and Mechanics of Solids 1 courses in 1st and 2nd year Mechanical Engineering is presented in Figure 6 (a & b).

These data indicate that the adopted teaching strategies are most effective in assisting at-risk students (as top students are already knowledgeable of the topic), which is demonstrated by the reduction in failure rates.

Since the first iteration of the revised mechanics of solids 1 course in 2007, student numbers have almost doubled, student satisfaction rate has increased (Figure 7) and student performance has improved (Figure 6 b). This is due to the effective staged implementation of aforementioned teaching strategies.

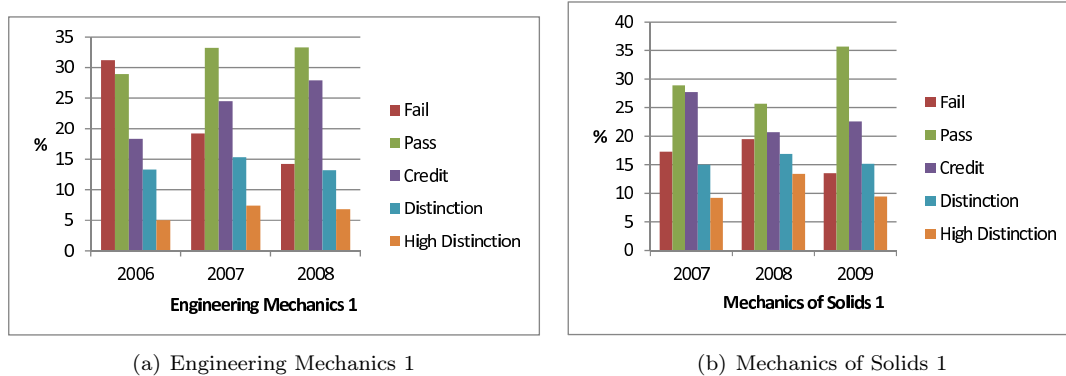


Figure 6: Improved pass percentage in mechanics courses.

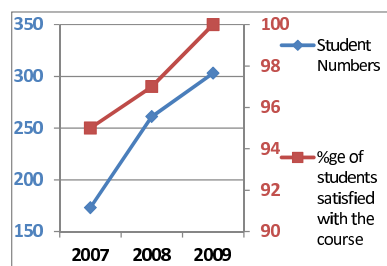


Figure 7: Increase in student numbers and improved student satisfaction in Mechanics of Solids 1.

Further evidence of the adopted teaching methodology in the foundation courses includes the very satisfying improvement in student performances in all the 3rd year undergraduate engineering courses that have Mechanics of Solids 1 as a pre-requisite (Figure 8).

Results support the benefits of Adaptive Tutorials for learning as well as for giving teachers control of the learning process. Significant reduction in failure rates (Figures 6 a & b), improved student satisfaction with the courses (Figure 7) and further improved performance in all the 3rd year undergraduate engineering courses (Figure 8) that have Engineering Mechanics and Mechanics of Solids 1 as a pre-requisite are the good evidences of the teaching effectiveness.

Through the staged implementation of ATs within the courses, the gathered evidence using student evaluation questionnaire [17] within the ATs that such tools help students learn, improve performance in assessments and add to students' satisfaction with courses. Students have found it as *“Excellent ... has really furthered my knowledge of this topic. I would really like to see more of these tutorials. This tutorial has taught me the basic concepts and ideas I will need to undertake questions of a similar nature in the text book. “Very helpful”*.

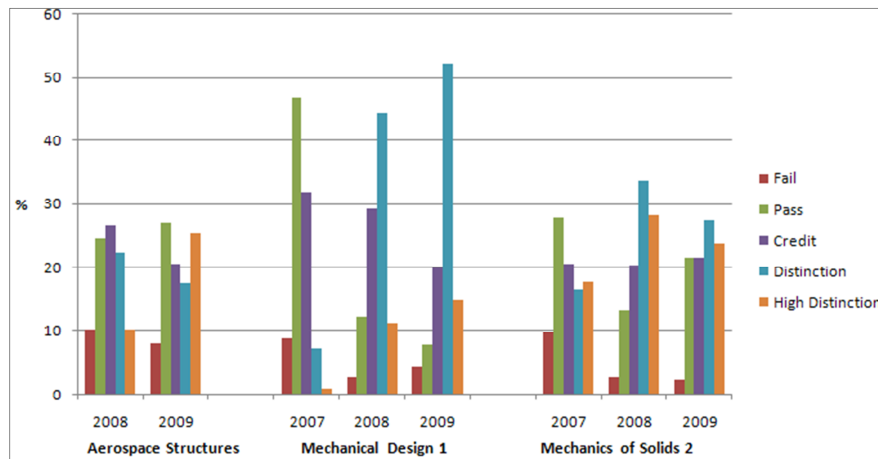


Figure 8: Improved student performances in 3rd year UG courses that have Mechanics of Solids 1 as the pre-requisite.

7 Impact and conclusion

This study has shown that Adaptive Tutorials are an effective tool in helping students with threshold concepts in Engineering Mechanics, and that the ATs improve their performance in later Solid Mechanics studies. The study also shows how the technology can support the identification of key threshold concepts that can cause problems if not addressed, especially in large classes.

Staged implementation of innovative teaching strategies using ATs in blended online and face-to-face teaching have had *sustained impacts* over the last 5 years. The continual improvement of courses in response to the targeted evaluation and feedback using the novel tools (explained above) are evidenced through the improved student engagement, greater student satisfaction, improved pass rate and further performance improvement in the courses that have mechanics courses as prerequisite.

Acknowledgements Currently the initiative is being financially supported by the Australian Learning and Teaching Council (grant ALTC CG 10-1586), an initiative of the Australian Government Department of Education, Employment and Workplace Relations.

References

- [1] Goldfinch, T., Carew, A.L., Gardner, A., Henderson, A., McCarthy, T. & Thomas, G., Cross-institutional comparison of mechanics examination: A guide for the curious. *Proc. 19th AaaE Annual Conf.*, Yeppoon, Australia, 2008.
- [2] Goldfinch, T., Carew, A.L. & McCarthy, T.J., Improving learning in engineering mechanics: The significance of understanding. *Proc. 19th AaaE Annual Conf.*, Yeppoon, Australia, 2008.

- [3] Goldfinch, T., Carew, A.L. & Thomas, G., Students views on engineering mechanics education and the implications for educators. *Proceedings of the 2009 AaeE conference*, Adelaide, 2009.
- [4] Dwight, R. & Carew, A., Investigating the causes of poor student performance in basic mechanics. *Proc. 17th AaeE Annual Conf.*, Auckland, New Zealand, 2006.
- [5] Meyer, J.H.F. & Land, R., Threshold concepts and troublesome knowledge (2): Epistemological considerations and a conceptual framework for teaching and learning. *Higher Education: The International Journal of Higher Education and Educational Planning*, **49(3)**, pp. 373–388, 2005.
- [6] Hadgraft, R., It's time for a coordinated approach to computer-aided learning and assessment. *Proceedings of the 2007 AaeE conference*, Melbourne, 2007.
- [7] Packard, B., Paris, S. & Yambor, K., Hands-on biology: A museum-school-university partnership for enhancing students' interest and learning in science. *The Elementary School Journal*, **98(3)**, 1998.
- [8] Jorgenson, O., What k-8 principals should know about hands-on science. *Principal*, **85(2)**, pp. 49–52, 2005.
- [9] Kessissoglou, N. & Prusty, B.G., Blended and innovative teaching strategies for a first year mechanics course. *Proceedings of the 2009 AaeE conference*, Adelaide, 2009.
- [10] Chandler, P. & Mayer, R., When learning is just a click away: Does simple user interaction foster deeper understanding of multimedia messages? *Journal of Educational Psychology*, **93**, pp. 390–397, 2001.
- [11] Philpot, T.A. et al., Games as teaching tools in engineering mechanics courses. *Proceedings of the 2003 American Society for Engineering education Annual Conference & Exposition, ASEE 2003*, 2003.
- [12] Ben-Naim, D., *A software architecture that promotes pedagogical ownership in intelligent tutoring systems*. Ph.D. thesis, School of Computer Science and Engineering, UNSW, Sydney, 2010.
- [13] Laurillard, D., Rethinking university teaching: A conversational framework for the effective use of learning technologies. *Routledge*, **268**, 2002.
- [14] Perkins, D., The many faces of constructivism. *Educational Leadership*, **57(3)**, 1999.
- [15] Ben Naim, D., Marcus, N. & Bain, M., Visualization and analysis of student interaction in an adaptive exploratory learning environment. *Proceedings of the 1st Int. Workshop in Intelligent Support for Exploratory Environments in the European Conference on Technology Enhanced Learning (EC-TEL'08)*, 2008.
- [16] Ben Naim, D., Marcus, N. & Bain, M., A user-driven and data-driven approach for supporting teachers in reflection and adaptation of adaptive tutorials. *Proceedings of Educational Data Mining 2009: 2nd International Conference on Educational Data Mining*, eds. T. Barnes, M. Desmarais, C. Romero & S. Ventura, Cordoba, Spain, pp. 21–30, 2009.
- [17] Prusty, B.G., Ho, O. & Ho, S., Adaptive tutorials using elearning platform for solid mechanics course in engineering. *Proceedings of the 2009 AaeE conference*, Adelaide, 2009.

An experimental investigation on the static structural behavior of helical bars

Marcos A. Rabelo, Celso P. Pesce, André L. C. Fajarra
*LMO – Offshore Mechanics Laboratory, Escola Politécnica
University of São Paulo, SP – Brazil*

Abstract

Motivated by understanding the structural behavior of flexible pipes under compressive loads, this paper presents results of an elementary experimental investigation on the static structural behavior of helical bars supported on rigid cylindrical surfaces. An experimental apparatus was specially designed and built for that purpose. Such a device allows one to apply a compressive load in the tangent direction of the helix, driven by a controlled step-motor actuator. Load cells, strain-gages and a high speed camera were used to investigate a possible instability behavior. Some preliminary considerations are given, based on comparisons with an analytical model by Stump and Van der Heijden.

Keywords: structural behavior, helical bars, experimental investigation.

1 Introduction

Flexible pipes used in offshore oil production are complex structures composed by a number of concentric layers made of distinct structural elements and materials. One of the most important layers, which provides axial structural strength to the tube, is formed by two helical armors, wound around the core of the pipe and made by a large number of helical high strength steel wires. Such kind of structure has been widely and thoroughly studied under a variety of loading conditions; Witz and Tan [1, 2]. An example of a still non comprehended behavior is the one related to ‘bird-caging’ formation, due to a combination of compressive axial loads and internal pressurization; see, e.g., Custódio [3]. Figure 1 shows a typical flexible pipe and an example of a bird-caging failure. A comprehensive picture and modeling of this type of failure, even of its triggering mechanism, depends on the understanding of the structural behavior of the helical wires, starting with elementary aspects.

An experimental apparatus was specially designed and built for that purpose. Such a device allows one to apply a compressive load in the tangent direction of the helix, driven by a controlled step-motor actuator. The apparatus is formed by a set of metallic rings, superimposed one over the other, such as generate a very rigid cylindrical support. Each ring is equipped with an adjustable system of

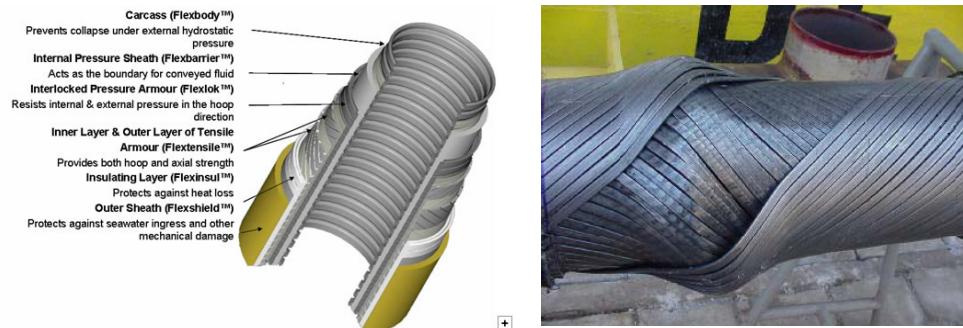


Figure 1: Typical flexible pipe (Source: Google Images – http://www.flexirisertest.com/images/l_home_f_2.jpg - 01/19/2009) and after instability failure (bird-caging). Source: Custódio [3].

rollers which provide constraints to the pre-conformed helical bar in the radial direction (normal to the helix) or in the transversal direction (bi-normal to the helix) and impose boundary conditions to their extremities. Load cells, strain-gages and a high speed camera (Figure 6) were used to investigate a possible instability behavior.

The experimental set up was first applied to straight bars, for verification purposes. A set of wires with circular and rectangular cross-sections were investigated. The classical Euler buckling was recovered.

Then, experiments with helical bars were carried out. Pitch angle and free-span length were taken as parameters. A set of ten samples for each pitch angle and type of bar was taken. The phenomenon of instability in helical bars is rather complex. In flexible pipes ‘radial instability’ is defined when the bar moves normally to the helix (in the cylinder radius direction), whereas ‘lateral instability’ when the bar moves in the helix bi-normal direction (tangentially to the cylinder surface). However, for helical bars, the phenomenon of instability could not be induced, in any test condition.

The influence of friction as well as the influences of the initial imperfection was accompanied during the tests and their importance in the final results are observed. The experimental results were analyzed and some preliminary considerations are given, based on an analytical model by Stump and Van der Heijden [4].

The paper is organized as follows. Section 2 introduces the experimental apparatus and methodology. Section 3 shows some studied cases, section 4 brings comparisons with analytical model results and section 5 draws some conclusions.

2 The apparatus and experimental methodology

To design and build the experimental apparatus the technical literature was examined. Timoshenko and Gere [5], Atanackovic [6], Love [7] are some classical references consulted. The compendiums of Singer, Arbocz and Weller [8, 9] are important references concerning experimental works.

The apparatus is formed by a set of metallic rings, superimposed one over the other, such as to generate a very rigid cylindrical support. Each ring, with 140 mm as external diameter, is equipped with an adjustable system of rollers which provide constraints to the straight bar and to the pre-conformed helical bar in the radial direction or in the lateral direction and to impose fixed boundary conditions to their extremities. The other components are: a steel structure to support the rings, an adjustable load cell device, a slider head assembled in guides, a ball screw system driven by a controlled step-motor actuator to apply the load, a template ring with three distinct laying angles. Figure 2 shows the experimental apparatus. The adjustable rollers allow to create the boundary conditions for each situation and to define the degree of freedom of the bars. Load cells, LVDTs, strain-gages, a linear measurement laser device and a high speed camera (Figure 6) were used. The main geometrical characteristics and material properties are given in Table 1.

Table 1: Main parameters and materials (BC: Boundary Condition).

Samples	Straight		Helical	
	Diameter = 5	9 × 3	Diameter = 5	9 × 3
Cross-section dimension [mm]	Diameter = 5	9 × 3	Diameter = 5	9 × 3
Material (steel)	SAE 1070	SAE 1070	SAE 1070	SAE 1070
Pitch angle [degree]	0	0	30	30
			35	35
			40	40
Internal radius [mm]			70	70
Length [mm]	free-span		Vertical distance between BC	
1	1355	1355	1365	1365
2	1230	1230	1050	1050
3	975	975	720	720
4	810	810	380	380
5	555	555		

The bars were fixed at both extremities. The free-span length is adjustable by a series of rollers positioned at both extremities; Figure 3, Figure 4 and Table 1. Straight bars were tested for five distinct free-span lengths values. Those with circular cross sections had their azimuthal positions changed, by rotating them in four steps of 90°. Those with rectangular cross-section were tested at two distinct positions, flipping the widest face that is tangent to the cylindrical support. Helical bars were tested for four distinct free lengths.



Figure 2: Experimental apparatus.



Figure 3: Rollers and free length.



Figure 4: Rollers adjustment in experiments with the straight bars. Left: free to move radially; right: free to move laterally. The rollers to the extremities were adjusted to restrain both radial and lateral displacements.

For the straight bars, the rollers close to the extremities were adjusted such as to restrain both radial and lateral displacements. The inner distance between these two sets of rollers thus defines the free length of the bar. Between those sets, the bar is allowed to move either in the radial or in the lateral direction by adjusting the rollers accordingly. Figure 4 shows the setups corresponding to both situations.

The procedure is similar in the case of helical bars. The experiments were carried out under radial or lateral freedom, with the rollers aligned helically. Figure 5 shows the rollers assemblies for each situation described.

The constant vertical velocity at the slider head used during the experiments was chosen following the maximum velocity offered by the controlled step-motor (0.00143 m/s with step-motor at 1500 rpm). This allowed imposing a quasi constant load at the upper extremity. The load variation was measured by a load cell (Figure 3 – right) at the bottom of the bar and the displacement of the slider head by a LVDT rigidly connected to it and to the external structure; see, e.g., Figure 7. Some helical bars were also instrumented with strain gages. A linear measurement laser device followed the radial displacement of the helical bar.

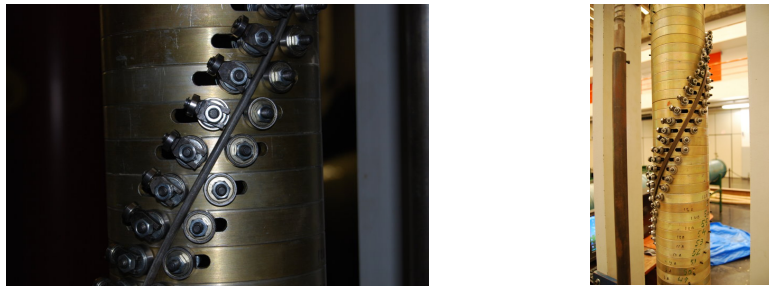


Figure 5: Rollers adjustment in the experiments with helical bars. Left: free to move radially; right: free to move laterally.

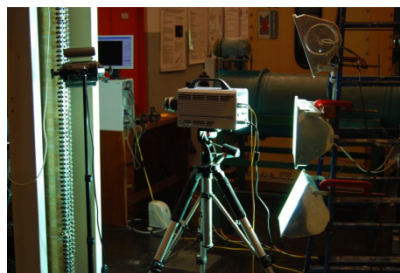


Figure 6: High speed camera.

All experiments were carried out respecting the linear regime. The experimental procedure is itemized in Table 2. The experimental methodology included first trials, during which the set up was adjusted and calibrated. The acquisition system was calibrated at the beginning of each test.

Table 2: Experimental procedure.

Experimental procedure	
Step	
1	adjust the bar
2	adjust the rollers
3	install the load cell
4	connect the accessories to the acquisition system
5	turn on the acquisition system
6	turn on the step motor
7	measurements

3 Case studies

3.1 Straight bars

The set of experiments with straight bars, free to move radially or laterally, aimed at obtaining additional information on the apparatus behavior, including the influence of friction and assembly imperfections. Euler instability loads were experimentally determined and the influence of real boundary conditions was addressed. An amount of 4060 experiments were carried out, providing a huge database.

The Euler load, achieved for a free-span length of 1355mm, is illustrated in Figure 7. In this example, the critical load calculated using classic Euler theory is 138,53N. This particular test gave 138,60N. In other cases, the influence of initial imperfections and friction provided Euler critical loads smaller than the calculated ones. Pre-existent curvature is an example of such an initial imperfection observed.

An experimental-theoretical comparative procedure (reference [10], chapter 2) was implemented, aiming at assessing the actual boundary conditions with respect to an idealized clamping. For the circular bars, a deviation less than 3.5% from an ideal clamping was obtained for slenderness (L/D) values above 200. For the rectangular cross section bars, buckling around the minimum moment of inertia, the same figure (4%) corresponds to slenderness (L/t) values larger than 250.

In Figure 7a it is possible to observe a residual load at the end of the experiment due to friction effects. In Figure 7b, the sharp peak corresponds to compressive load at the instant of instability.

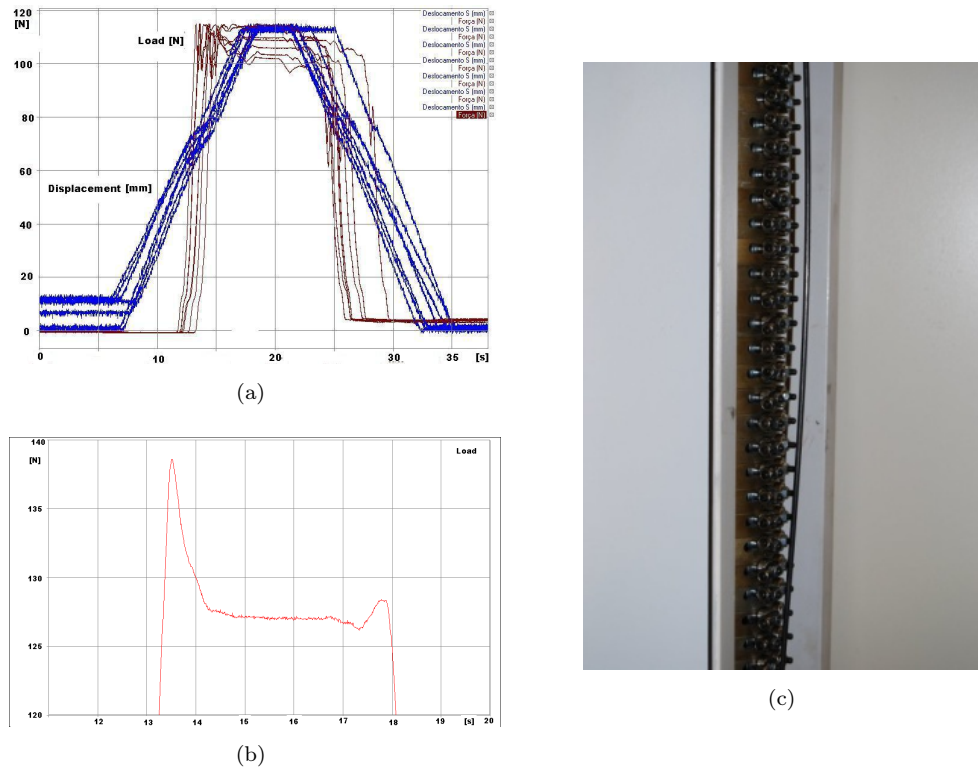


Figure 7: Straight bar with circular cross section; free length = 1355mm – (a) - time signals [s] of compressive load [N] (in brown color) and vertical displacement at the slider head [mm] (in blue). (b) - signal showing the critical load. (c) - bar after buckling.

3.2 Helical bars

The tests with helical conformed bars lying on rigid cylindrical surfaces were carried out with the compressive load applied tangent to the helix.

Bars with circular and rectangular cross-sections were tested. Two distinct values of laying angle, typical of flexible pipes, were adopted: 30° and 35° . The laying angle is measured with respect to the axis of the rigid cylindrical support. Four values of free span were taken, measured along the cylindrical support axis, as shown in Table 2. The experiments aim at observing the specimens behavior free to buckle radially or laterally. Friction effects were also assessed. Figure 8 shows an example of the loading process. Region A shows the influence of friction during loading. Beyond this region, the bar starts moving towards the instability.

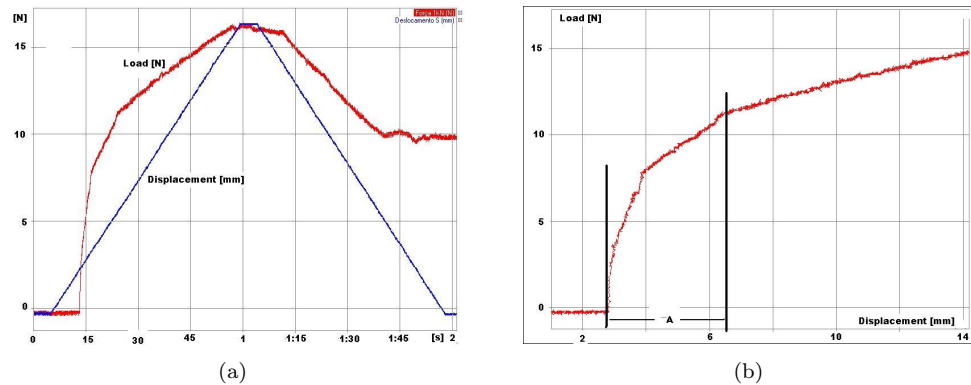


Figure 8: Helical bar with rectangular cross section free to move radially– laying angle 30° – $H = 1365\text{mm}$. H is the free vertical length, measured along the cylindrical support axis. (a) - time signals [s] of compressive load [N] (in red color) and vertical displacement at the slider head [mm] (in blue); (b) load [N] vs. vertical displacement measured at the slider head.

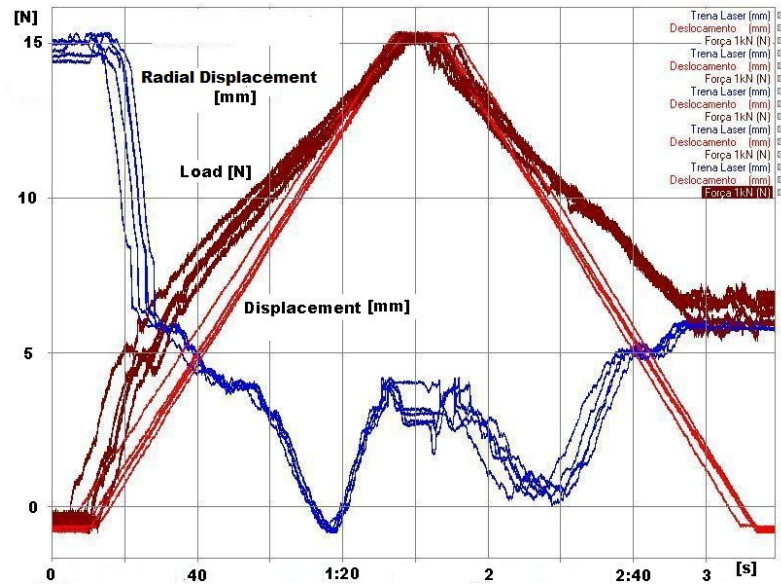
Geometrical limitations of the apparatus precluded the instability phenomenon to appear. The main limitation was the free distance available for the slider head.

The graphic in Figure 9, illustrates the structural behavior of a rectangular cross-section bar with two different free-span lengths. It is possible to observe friction effects occurring from 0N to 5N. To be remarked is the large residual load.

Another interesting behavior was observed during the tests with rectangular cross-sections bar, combining bending and torsion. This may be seen in Figure 9a by observing the radial displacement given in blue color, measured by the laser device (see Figure 9b). This curve actually gives the distance measured from a specific point of the bar (at mid free span) to the laser bead. Notice that the minimum distance corresponds to the maximum radial displacement of the bar. Observing Figure 10d, the slope of the radial displacement has a clear change at circa 5N, followed by an inflection at 10N, where a pronounced twist of the bar could be visually observed, reaching a sharp ‘peak’ around 13N. Beyond this point torsion inverts and the bar returns radially, up to the point the actuator stops. During the unloading process an inverse behavior may be observed. Figure 10 a, b and c complements the described behavior. Such a combined flexural-torsional behavior was not observed in the case of circular cross-section, due to symmetry.

4 Some comparisons with analytical model results

Figure 11a shows Stump and Van der Heijden [4] analytical results for a circular cross wire of wound cable. P is the compressive load applied along the tangent of the wire. L is the free-span length, measured along the wire. The slenderness is $L/a = 10$, where a is the helix radius. The normalized



(a)



(b)

Figure 9: (a) Helical bar with rectangular cross section free to move radially– laying angle 30° – $H = 735\text{mm}$. Nine distinct tests. Signals of compressive load [N] (in brown color), and vertical displacement (red) at the slider head [mm] and distance of a point of the bar at mid span measured from the laser bead (blue)[mm]. (b) the laser device position.

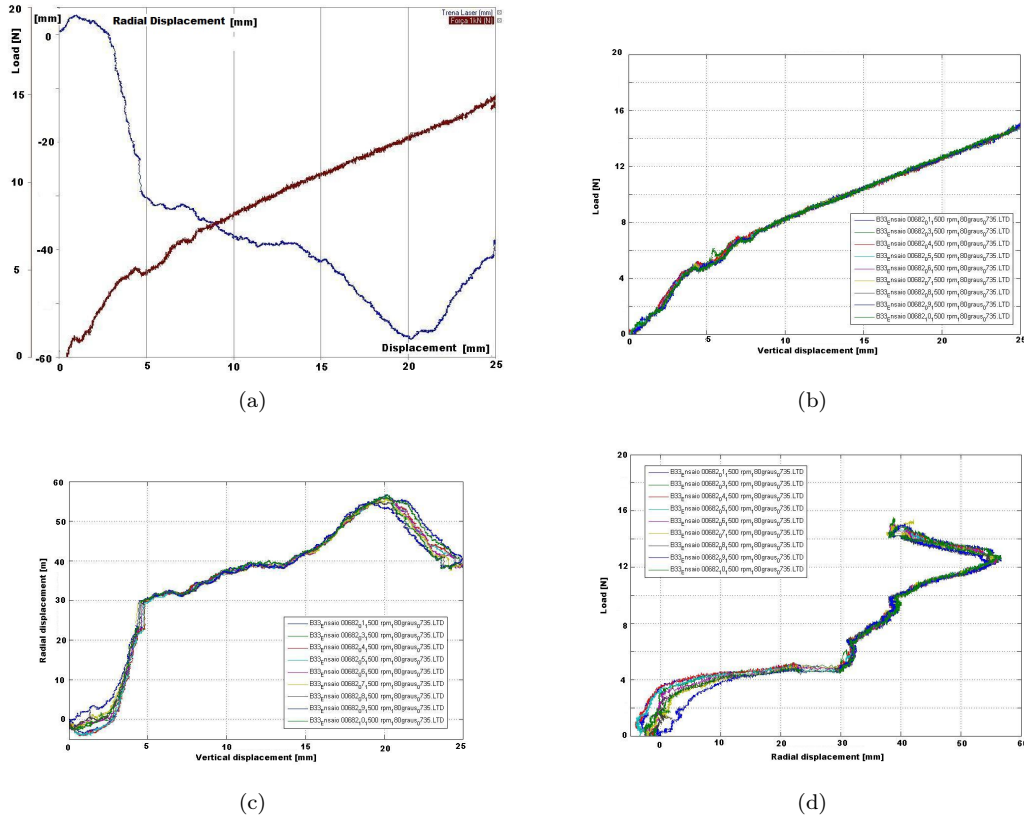
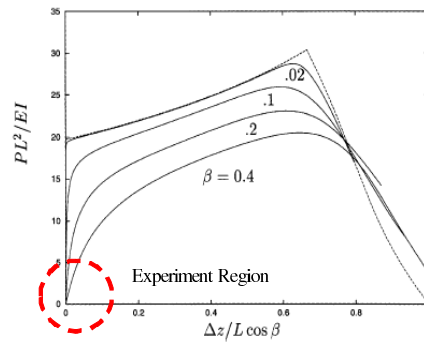
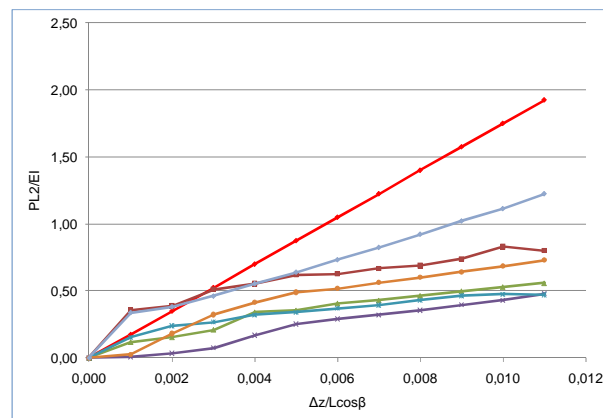


Figure 10: Same experiment showed in Fig. 9. For a single test: (a) - compressive load [N] vs. vertical displacement (brown) and radial distance of bar from laser bead [mm]. For nine distinct tests: (b) -load vs. vertical displacement; (c) radial distance from the laser bead vs. vertical displacement; (d) - load vs radial distance from the laser bead.

compressive load is plotted as a function of the displacement measured along the helix axis, for five distinct values of the laying angle b , including the asymptotic post-critical curve for a straight bar. Bifurcation becomes less evident the larger is the laying angle. As matter of fact for laying angles of order 0.1rad (5.7°) or larger, the sudden change in the slope, typical of pitchfork bifurcations, is not observed anymore. A first comparison of the experimental results is presented in Figure 11b. The experimental data are in the beginning of the Stump and Van der Heijden analysis range. The red straight line shows Stump and Van der Heijden [4] results for $b = 23^\circ$. The experimental results correspond to six tests with a circular cross section bar with $L/a = 11.3$ and a distinct value of a large laying angle, $b = 30^\circ$. A qualitatively correct trend may be seen. Moreover, no typical pitchfork behavior is observed, as expected.



(a)



(b)

Figure 11: (a) Stump and Van der Heijden analytical results at very small displacements [4] $\beta = 0.4$ (23°) (red line); (b) experimental data $\beta = 0.5$ (30°).

5 Conclusions

Motivated by understanding the behavior of helical structural components of flexible pipes, an elementary experimental investigation was carried out. An experimental apparatus was specially designed and built for testing helical bars supported on rigid cylindrical surfaces. Such a device allows one to apply a compressive load in the tangent direction of the helix, driven by a controlled step-motor actuator. Load cells, strain-gages and a high speed camera were also used to investigate possible instability behaviors.

A detailed description of the experimental setup and instrumentation was given. Standard experiments with straight bars of circular and rectangular cross sections were ascertained the suitability of the apparatus. Helical bars of circular and rectangular cross sections with laying angles typical of tensile armor layers of flexible pipes were then tested. For circular cross section helical bars, a classic large displacements behavior was observed. For rectangular cross section bars an interesting flexural-torsional behavior, at large displacements, was depicted.

Some preliminary comparisons of the circular cross section bars experiments with an analytical model by Stump and Van der Heijden [4], showed a compatible trend. Moreover, as could be expected, for the large laying angle values of the tested helical bars, no typical bifurcation pattern was observed.

Acknowledgement This study was carried out within a comprehensive research project on flexible pipes supported by Petrobras. The first author also acknowledges an ANP scholarship, within the PRH-19 program. The second author acknowledges a CNPq research grant. The authors especially thank Dr. Anderson B. Custódio, from Petrobras, as well as Professor Clovis de Arruda Martins, Eng. Alfredo Gay Neto and Eng. Rodrigo Provasi, from USP, for interesting discussions.

References

- [1] Witz, J. & Tan, Z., On the axial-torsional structural behavior of flexible pipes, umbilicals and marine cables. *Marine Structures*, **5**, pp. 205–227, 1992.
- [2] Witz, J. & Tan, Z., On the flexural structural behavior of flexible pipes, umbilicals and marine cables. *Marine Structures*, **5**, pp. 229–249, 1992.
- [3] Custódio, A. et al., Recent research on the instability of flexible pipe's armours. *Proceedings of ISOPE*, 2007.
- [4] Stump, D. & Van der Heijden, G., Birdcaging and the collapse of rods and cables in fixed-grip compression. *International journal of solids and structures*.
- [5] Timoshenko, S. & Gere, J., *Theory of elastic stability*. McGraw-Hill, Inc, 1961.
- [6] Atanackovic, T., *Stability theory of elastic rods*. World Scientific publishing: Singapore, 1997.
- [7] Love, A., *A treatise on the mathematical theory of elasticity*. Dover Publications: New York, 1944.
- [8] Ramos Jr, R. & Pesce, C., A stability analysis of risers subjected to dynamic compression coupled with twisting. *Journal of Offshore Mechanics and Arctic Engineering*, **125(2)**, pp. 183–189, 2003.
- [9] Singer, J., Arbocz, J. & Weller, T., *Buckling experiments: experimental methods in buckling of thin-walled structures – basic concepts, columns, beams and plates*, volume 1. John Willey & Sons, Inc, 1998.
- [10] Brush, D. & Almroth, B., *Buckling of bars, plates and shells*. McGraw-Hill, Inc, 1975.

Time domain analysis of concrete gravity dams using a generalized single degree of freedom approach

Paulo Marcelo Vieira Ribeiro

Universidade Federal de Pernambuco – UFPE, PE – Brazil

Lineu José Pedroso

Universidade de Brasília – UnB, DF – Brazil

Abstract

In a previous paper a simplified procedure for analysis of dam-reservoir interaction was presented, considering only the fundamental mode of vibration, followed by solution of a frequency equation and subsequent construction of a numerical equivalent model, using mass elements along the monolith's upstream face. This work extends this research line, exploring the highlights of the proposed method, such as: variation in the seismic excitation source, influence of the hydrodynamic pressure model and stress evaluation at an arbitrary time instant. Finally, an application example will be present along with the major advantages and limitations of the proposed procedure.

Keywords: dams, reservoir, fluid-structure interaction, semi-analytical, time domain.

1 Introduction

Dynamic analysis of dams subjected to reservoir interaction effects is a matter of great interest in seismically active regions. Great effort has been devoted to this problem, with contributions generally classified in three distinct categories: (i) Closed analytical formulations, (ii) Simplified analytical procedures and (iii) Numerical procedures such as the finite element and boundary element methods. A classic work by Lee and Tsai [1] describes an exact time domain solution for constant section prismatic beams using a linear combination of in-vacuum mode shapes. A recent paper by Koohkan *et al.* [2] extends this study to prismatic beams with variable cross sections using differential quadratures coupled with a finite difference scheme. This contrast illustrates that closed form solutions are limited to specific cases and lack the generality of complex dam geometries. Numerical solutions involving both domains (fluid and structure) are generally expensive with respect to computer processing time. Additionally, they are limited to specific softwares designed for analysis of coupled problems. Realistic approaches include tridimensional geometries. However, this problem can be greatly simplified

for gravity dams, using bidimensional models. Nevertheless, there are numerous possibilities for the designed monolith's dimensions, making a fully analytical approach virtually impossible, or applied only to a few specific cases. An alternative emerges with the use of intermediate solutions (semi-analytical), using the accuracy of analytical solutions combined with the broad scope of numerical methods.

A previous study [3] presents a simplified alternative for solution of this problem (Figure 1), with the aid of an analytical model (A) combined with an in-vacuum finite element modal analysis of the dam's geometry (B). Similar procedure has been recently described by Miquel and Bouaanani [4]. In the former case, generalized parameters of the fundamental vibration mode are identified (B) and latter applied on the solution of a frequency equation (C), providing the fundamental period of vibration including reservoir interaction effects.

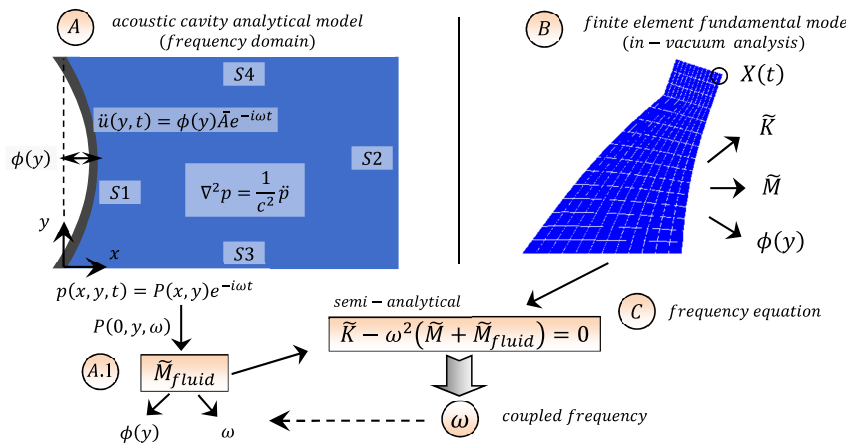


Figure 1: Semi-analytical procedure solution scheme (frequency equation).

The major output of the proposed procedure is the fundamental coupled frequency (ω), which is dependent of the adopted analytical model, with $S1 - S4$ related to boundary regions, $\ddot{u}(y, t)$ defining boundary $S1$ acceleration, and $\phi(y)$ standing for the normalized mode shape at a given coordinate. Generalized fluid mass (A.1) is defined by Equation (1).

$$\tilde{M}_{fluid} = \int_0^H \frac{P(0, y, \omega)}{\bar{A}} \phi(y) dy \tag{1}$$

where \bar{A} and H are related, respectively, to: an arbitrary amplitude with respect to the provided generalized coordinate $X(t)$ and the reservoir depth (or acoustic cavity vertical dimension). Equation (1) is added to the in-vacuum generalized mass term (inertial coupling), providing both undamped (Eq. 2) and damped (Eq. 3) equations of motion.

$$\left(\tilde{M} + \tilde{M}_{fluid}\right) \ddot{X}(t) + \tilde{K}X(t) = \tilde{F}(t) \quad (2)$$

$$\left(\tilde{M} + \tilde{M}_{fluid}\right) \ddot{X}(t) + \tilde{C}\dot{X}(t) + \tilde{K}X(t) = \tilde{F}(t) \quad (3)$$

Previous expressions are valid for a generalized coordinate $X(t)$ and consider in-vacuum parameters unaltered by interaction effects (mode shape and generalized rigidity are assumed identical to in-vacuum values, for example).

This procedure reveals an effective strategy, replacing the reservoir by equivalent effects on the fluid-structure interface. Thus, the problem can be simplified to the solution of a single dynamic equilibrium equation. Clearly, the proposed solution is valid only for the fundamental mode of the dam-reservoir system, with all parameters consistent with the in-vacuum structural mode shape. This presents a major drawback and will be explored in the next items.

2 Hydrodynamic pressure models

Equation (1) indicates a direct relationship between generalized added mass and dynamic fluid pressures. Therefore, boundary conditions shown on Figure 1 (Step A) as well as the cavity governing equation are responsible for the amount of additional mass of the equivalent system.

Boundary conditions for a cavity with undisturbed boundary at the limits of an infinite reservoir, reflective bottom and surface wave effects neglected are given, respectively, by:

$$S2 \rightarrow \lim_{x \rightarrow \infty} p(x, y, t) = 0 \quad (4)$$

$$S3 \rightarrow \left. \frac{\partial p(x, y, t)}{\partial y} \right|_{y=0} = 0 \quad (5)$$

$$S4 \rightarrow p(x, H, t) = 0 \quad (6)$$

Additional parameters involve the consideration of fluid compressibility and the characteristics of the vibrating boundary, which can be taken as rigid or flexible. Therefore, four hydrodynamic pressure models are possible, which are summarized on Figure 2 [5].

In Figure 2 case abbreviations are related to: (I) incompressible, (C) compressible, (R) rigid and (F) flexible. The general case is given by (CF), whose solution is provided by Equation (7). Remaining cases are achieved by reduction of the latter equation to incompressible fluid ($c \rightarrow \infty$), rigid boundary ($\phi = 1$), or both.

$$P(x, y, \omega) = \frac{2\rho_f \bar{A}}{H} \sum_{n=1}^{\infty} \frac{1}{\sqrt{\alpha_n}} \int_0^H \phi(y) \cos(\kappa_n y) dy \left[e^{-\sqrt{\alpha_n} x} \right] \cos(\kappa_n y) \quad (7)$$

where:

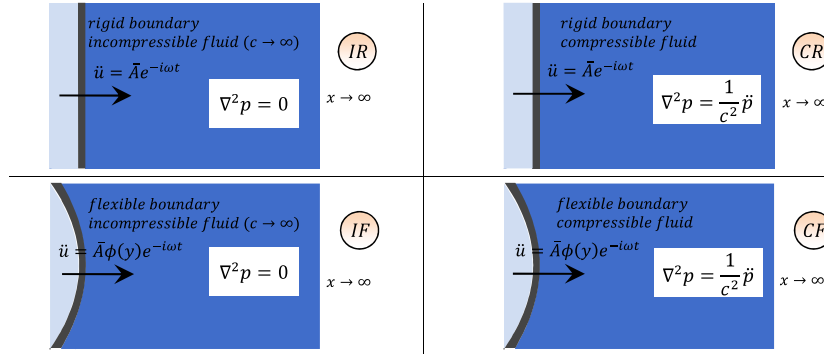


Figure 2: Hydrodynamic pressure models [5].

$$\hat{\alpha}_n = (\kappa_n)^2 - \frac{\omega^2}{c^2} \tag{8}$$

$$\kappa_n = \frac{(2n - 1) \pi}{2L_y} \tag{9}$$

and ρ_f indicates fluid density.

It is important to notice that cases (IF) and (IR) are independent of ω and Equation (1) is evaluated directly, disregarding step C (Figure 1). This leads to an incompressible fluid model with flexible or rigid vibrating boundaries.

3 Equivalent actions in a fluid-structure system subjected to ground motion

When studying a ground motion response it is convenient to analyze the problem in terms of ground (u_g) and relative (u_r) components, which together represent the total dynamic response of the structure. These concepts are clarified by Figure 3, which illustrates an undamped Single Degree of Freedom system (SDF).

The dynamic equilibrium equation is achieved directly. Therefore:

$$m\ddot{u}_t(t) + K u_r(t) = 0 \tag{10}$$

From Figure 3a results a total acceleration defined by: $\ddot{u}_t(t) = \ddot{u}_g(t) + \ddot{u}_r(t)$. Thus, substituting this latter expression on (10):

$$m\ddot{u}_r(t) + K u_r(t) = -m\ddot{u}_g(t) = p_{ef}(t) \tag{11}$$

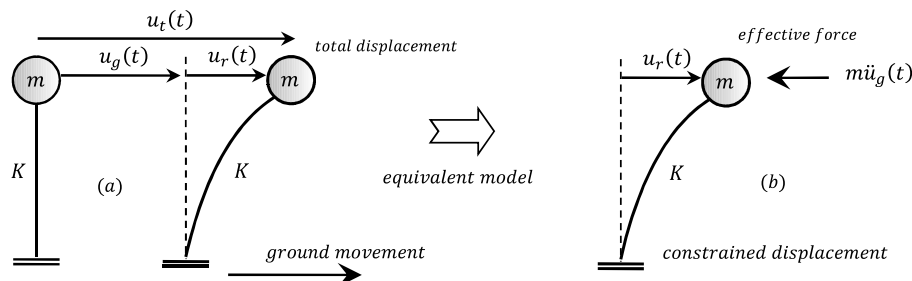


Figure 3: Seismic excitation of a SDF uncoupled system (a) and equivalent model (b).

where the right side of (11) stands for the effective force (p_{ef}) related to the ground motion (Figure 3b). Therefore, relative displacements (u_r) resulting from ground motion are equivalent to a fixed based system subjected to an external force given by $p_{ef} = -m\ddot{u}_g(t)$.

For systems with distributed parameters equivalent forces are achieved in a similar way with application of the Virtual Work Principle. Thus:

$$\tilde{F}(t) = -\ddot{u}_g(t) \int_0^H \mu(y) \phi(y) dy = -\ddot{u}_g(t) \tilde{L} \tag{12}$$

where \tilde{L} stands for the seismic excitation factor, which indicates the mode shape $\phi(y)$ contribution for a given ground motion. Therefore, the dynamic equation for an undamped distributed parameter system is given by:

$$\tilde{M}\ddot{X}(t) + \tilde{K}X(t) = -\ddot{u}_g(t) \tilde{L} \tag{13}$$

Previous expressions are valid for an uncoupled structure. When the problem involves both domains (fluid and structure) special considerations must be made, because the translational and relative motions induce different dynamic pressure fields (illustrated on Figure 2, for example). Thus, it is common to find in literature the division in rigid body motion and mode shape conformal pressure [6]. A simple interpretation of this phenomenon may be established by setting two different inertial forces: $\mathbf{f}_r\ddot{u}_r(t)$ and $\mathbf{f}_g\ddot{u}_g(t)$, proportional, respectively, to relative (\ddot{u}_r) and ground (\ddot{u}_g) accelerations. Therefore, the dynamic equation for an undamped SDF is defined by:

$$m\ddot{u}_t(t) + Ku_r(t) = -\mathbf{f}_r\ddot{u}_r(t) - \mathbf{f}_g\ddot{u}_g(t) \tag{14}$$

Substituting $\ddot{u}_t(t) = \ddot{u}_g(t) + \ddot{u}_r(t)$ in this latter expression results in:

$$[m + \mathbf{f}_r] \ddot{u}_r(t) + Ku_r(t) = -\ddot{u}_g(t) [m + \mathbf{f}_g] \tag{15}$$

The analysis of (15) reveals the presence of fluid inertial forces on both sides of the equation. It is important to notice that the left side mass (\mathbf{f}_r) is different from the right side term (\mathbf{f}_g), since the

former is related to the relative motion of the system, while the second is associated with translational motion. Additionally, it is observed that fluid inertial effects are still present when the ground acceleration is set to zero (in the case of a fixed base coupled system vibration, for example). Figure 4 clarifies these concepts with a force schema of the equivalent coupled model.

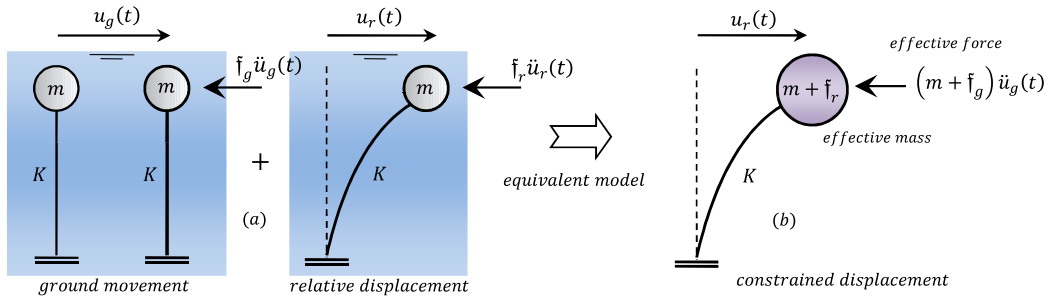


Figure 4: Seismic excitation of a SDF coupled system (a) and equivalent model (b).

The same reasoning can be employed in a system with distributed parameters. The identification of inertial terms is easily achieved with the scheme shown on Figure 4. In this case, the equation of undamped motion in terms of a generalized coordinate $X(t)$ is given by:

$$(\tilde{M} + \tilde{M}_{fluid}) \ddot{X}(t) + \tilde{K}X(t) = -\ddot{u}_g(t) [\tilde{L} + \tilde{N}] \tag{16}$$

The latter expression reveals the reservoir influence in both the system’s mass, defined by (1) and illustrated on Figure 5b, as well as the seismic excitation factor, which now includes an additional term, \tilde{N} . In the latter case the problem resembles the movement of a dam-reservoir-foundation block, with intensity given by the magnitude of ground acceleration (Figure 5a). Thus, the term \tilde{N} indicates inertial effects of the reservoir in contact with a uniformly accelerated rigid wall, which can be adequately represented by case (IR), shown on Figure 2. Therefore, by analogy with (12):

$$\tilde{N} = \int_0^H \mathbf{f}_g(y) \phi(y) dy \tag{17}$$

where:

$$\mathbf{f}_g(y) = \frac{P(0,y)}{A} = \frac{2\rho_f}{H} \sum_{n=1}^{\infty} \frac{(-1)^{n+1}}{\kappa_n^2} \cos(\kappa_n y) \rightarrow IR \tag{18}$$

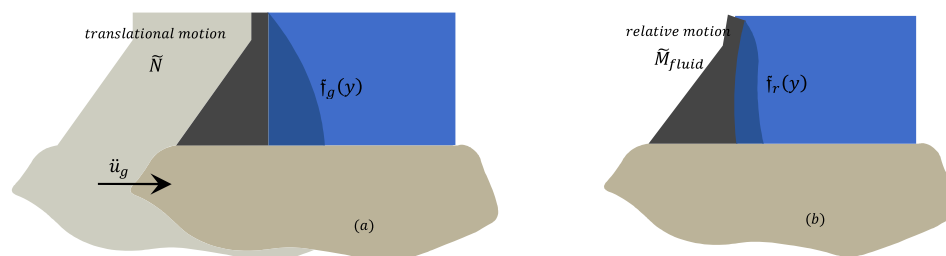


Figure 5: Fluid interaction translational (a) and relative (b) inertial components.

4 Dynamic response evaluation and equivalent static analysis

Dynamic response evaluation of (13) or (16) for an arbitrary ground motion is performed using a numerical integration routine (although for simple functions an analytical evaluation is possible). In this work a fourth order Runge-Kutta procedure developed in Fortran 90 language was applied. Immediate results of relative displacements are obtained and then employed in a stress analysis of the corresponding monolith.

It is important to introduce the concept of equivalent lateral forces (q), whose effects produce deformations similar to those induced by the ground motion [7, 8]. From classical theory of structural dynamics results expression (19), related to an analysis without the influence of the reservoir. Thus:

$$q_e(y, t) = m_s(y) \phi(y) \left[\omega^2 \frac{\tilde{L}}{\tilde{M}} \mathcal{D}(t) \right] \quad (19)$$

where $m_s(y)$ defines the mass distribution along the dam's height and $\mathcal{D}(t)$ indicates the relative displacement of a SDF with in-vacuum frequency ω . The term in brackets is defined as pseudo-acceleration, since it corresponds to the acceleration that effectively produces deformations in the structure, being distinct from the total acceleration on damped systems (and identical in the case of undamped models). The latter expression allows an equivalent static analysis (using beam theory or by applying static loads on a numerical model, for example) of the dam geometry subjected to the maximum absolute value of \mathcal{D} (\mathcal{D}_{mx} , obtained using a spectral analysis).

For analysis with hydrodynamic effects included results the following expression [9]:

$$q_r(y, t) = \{m_s(y) \phi(y) + m_f(y)\} \left[\omega^2 \frac{\tilde{L}_r}{\tilde{M}_r} \mathcal{D}(t) \right] \quad (20)$$

where $\tilde{L}_r = \tilde{L} + \tilde{N}$ and $\tilde{M}_r = \tilde{M} + \tilde{M}_{fluid}$ indicate, respectively, the earthquake participation factor and generalized mass including reservoir interaction effects. And $\mathcal{D}(t)$ stands for the relative displacement of a SDF with coupled frequency ω . An additional term is given by $m_f(y)$, which is related to the inertial fluid effect load distributed along the dam's height, defined by:

$$m_f(y) = \frac{P(0,y)}{A} \quad (21)$$

Expressions (19) and (20) are defined by terms established on previous sections and can be applied on the construction of equivalent lateral forces and subsequent solution of a static problem.

5 Application example

A typical dam geometry illustrated in Figure 6a was evaluated using the proposed procedure. Analyses involve both the dynamic displacement response as well as stress field at an arbitrary time instant. Three seismic records with distinct characteristics were used and results compared to those obtained from a coupled numerical model shown on Figure 6b. Structural parameters include transverse elastic modulus $E = 25 \cdot 10^9 \text{ Pa}$ and mass density $\rho_s = 2400 \text{ kg/m}^3$. For the acoustic fluid model a mass density $\rho_f = 1000 \text{ kg/m}^3$ and fluid sonic velocity $c = 1500 \text{ m/s}$ were considered in the analyses.

Numerical model was built using ANSYS v. 11 with a structural mesh of 4 nodes plane strain elements. Foundation is neglected in the analyses and base nodes are constrained in both directions. Four nodes plane acoustic elements were used in fluid mesh. Reservoir geometry is built using a $L/H = 3$ ratio, with null pressure conditions at reservoir limit $x = L$ and fluid surface $y = H$.

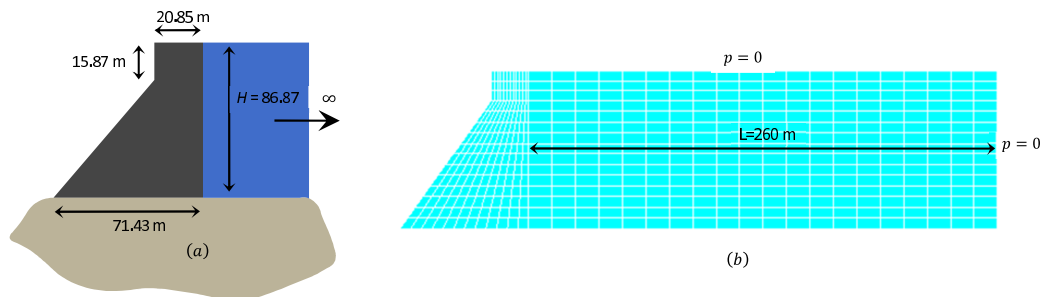


Figure 6: Analytical (a) and finite element (b) models.

Major analysis steps and results are presented in the next items.

5.1 Finite element auxiliar fundamental mode analysis

According to Figure 1 schema three structural parameters related to the fundamental mode are obtained, shown in Table 1. In this case fundamental frequency is given by $\omega = 26.846 \text{ rad/s}$.

An interpolation function is established for horizontal displacement on the upstream nodes of the dam geometry, resulting in the following expression:

Table 1: Generalized parameters – fundamental mode uncoupled analysis.

Generalized Mass $\left(\frac{Ns^2}{m}\right)$ \tilde{M}	Generalized Stiffness $\left(\frac{N}{m}\right)$ \tilde{K}	Earthquake Participation Factor $\left(\frac{Ns^2}{m}\right)$ \tilde{L}
$1.0638 \cdot 10^6$	$7.6669 \cdot 10^8$	$2.1049 \cdot 10^6$

$$\phi(y) = -0.7663\left(\frac{y}{H}\right)^4 + 1.5247\left(\frac{y}{H}\right)^3 - 0.1043\left(\frac{y}{H}\right)^2 + 0.3482\left(\frac{y}{H}\right) - 0.0003 \quad (22)$$

5.2 Frequency equation solution

The general form of frequency equation is given by expression (23), which is solved using fundamental mode auxiliary parameters given by Table 1.

$$\tilde{K} - \omega^2 \left[\tilde{M} + \int_0^H \frac{P(0, y, \omega)}{A} \phi(y) dy \right] = 0 \quad (23)$$

The term $P(0, y, \omega)$ depends on considerations taken on the adopted fluid model, with schema shown on Figure 2. Table 2 illustrates results of the latter expression for CF and IF cases.

Table 2: Frequency equation results (fundamental coupled frequency).

Compressible and Flexible (CF)		Incompressible and Flexible (IF)	
Number of terms in summation (n)	ω (rad/s)	Number of terms in summation (n)	ω (rad/s)
3	22.108	3	23.222
5	22.008	5	23.083
10	21.966	10	23.025

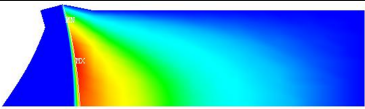
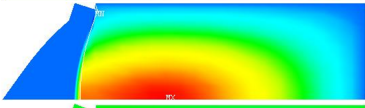

Generalized fluid mass (\tilde{M}_{fluid}) is readily obtained with rearrangement of (23). Thus, for the CF case with $n = 10$ results:

$$\omega^2 = \frac{\tilde{K}}{\tilde{M} + \tilde{M}_{fluid}} \quad \therefore \quad \tilde{M}_{fluid} \cong 0.5203 \cdot 10^6 N s^2 / m \quad (24)$$

5.3 Modal analysis reference results for the coupled model

Modal analysis results of the numerical model shown in Figure 6b are presented on Table 3, including vibration modes and corresponding frequencies. Fundamental mode frequency achieved by means of the frequency equation (previous item, case CF) is in agreement with the value indicated on this table, with a relative error of about 1%.

Table 3: Coupled numerical model analysis results.

mode number	ω (rad/s)	mode shape
1	22.274	
2	30.014	
3	38.734	

5.4 Semi-analytical dynamic equilibrium equation

Generalized parameters of Table 1 and expressions (1) and (17) are substituted on (16), resulting in the semi-analytical dynamic equilibrium equation for the coupled structure. Thus:

$$1.58 \cdot 10^6 \ddot{X}(t) + 7.67 \cdot 10^8 X(t) = -\ddot{u}_g(t) 3.17 \cdot 10^6 \rightarrow \text{coupled} \quad (25)$$

where $X(t)$ stands for the upstream displacement of a position at the dam's crest.

This latter expression enables relative displacement and equivalent lateral load evaluation for a given ground motion $\ddot{u}_g(t)$.

5.5 Dynamic response for distinct seismic sources

Three distinct seismic records and their frequency spectra are shown on Figures 7, 8 and 9. The corresponding data is associated to real events, such as Imperial Valley (1940, El Centro station, north-south component), Hollister (1974, City Hall station) and Loma Prieta (1989, Emeryville station) earthquakes.

Figures 7b, 8b and 9b reveal a similar aspect: dominant amplitudes at lower frequencies. This characteristic justifies greater participation of initial modes at the system's dynamic response. Comparative curves between numerical displacements of the coupled model and evaluation of expression (25) in a

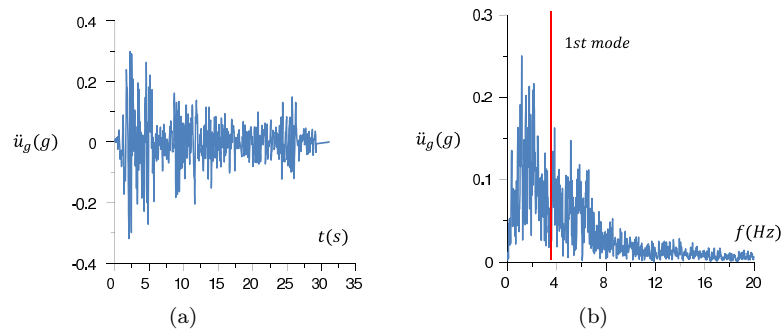


Figure 7: Imperial Valley ground motion (a) and frequency spectrum (b).

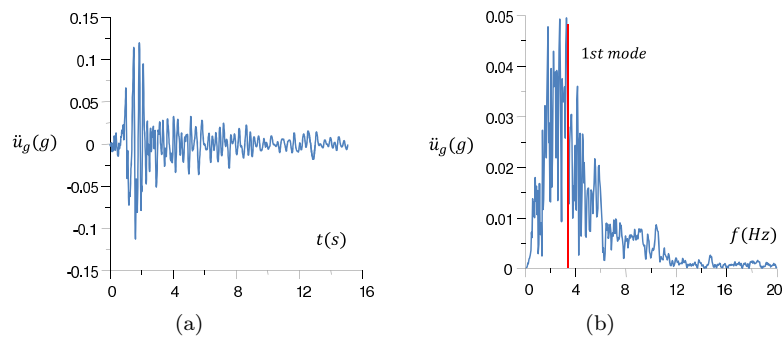


Figure 8: Hollister ground motion (a) and frequency spectrum (b).

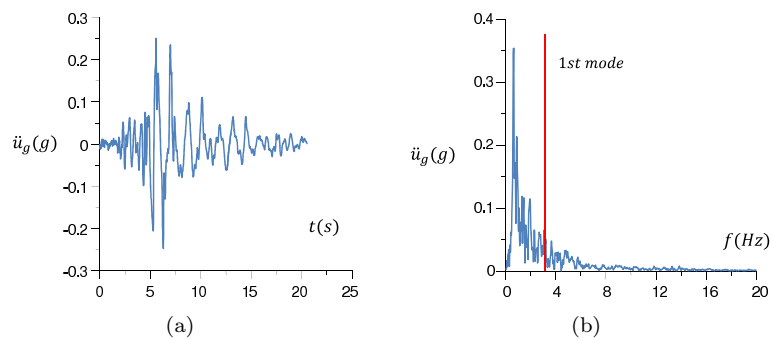


Figure 9: Loma Prieta ground motion (a) and frequency spectrum (b)

numerical integration routine are shown in Figure 10, for the Imperial Valley earthquake. Excellent results are observed for initial time instants, with cumulative errors occurring under time window increments (as shown on Figure 10b).

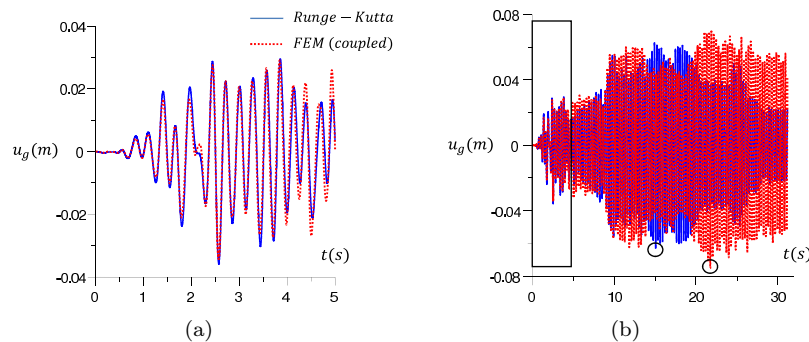


Figure 10: Imperial Valley event relative displacement response. Time window (a). Complete record (b).

Figure 10b also indicates maximum absolute displacement results on both solutions. For the proposed procedure a maximum value of $u_g = 0.063$ m occurs at $t = 15.07$ s. For the coupled model a maximum $u_g = 0.075$ m is provided at $t = 21.74$ s. The proposed solution provides approximately 84% of the corresponding maximum displacement on the coupled solution. These differences are due to cumulative errors produced during the event time window, related to differences between semi-analytical and numerical frequencies, and are important on evaluation of equivalent loads.

Relative displacement results for Hollister and Loma Prieta events are shown, respectively, on Figures 11 and 12. As in the previous event, results are excellent for initial time instants, with cumulative errors at greater time windows. Short duration events are related to best results, such as the 15 seconds Hollister earthquake, for example.

5.6 Evaluation of maximum relative displacement response and stress analysis

Maximum relative displacement and stress results of the coupled model are achieved immediately using ANSYS. In the case of the proposed procedure a time domain analysis becomes unnecessary, since the use of displacement spectra emerges as an alternative, illustrated on Figure 13 for the three distinct seismic events. These plots were achieved using SeismoSignal v. 3.3.0 software for an undamped SDF system. Values of interest are signed on this illustration for the coupled fundamental period of vibration $T = 0.286$ s (22 rad/s).

As mentioned earlier, equivalent displacements are obtained using Equation (20) along the upstream face of the dam. Thus, the dynamic analysis of a coupled problem is reduced to an equivalent static analysis of the structural geometry. Table 4 presents stress results using the proposed procedure and the finite element coupled model.

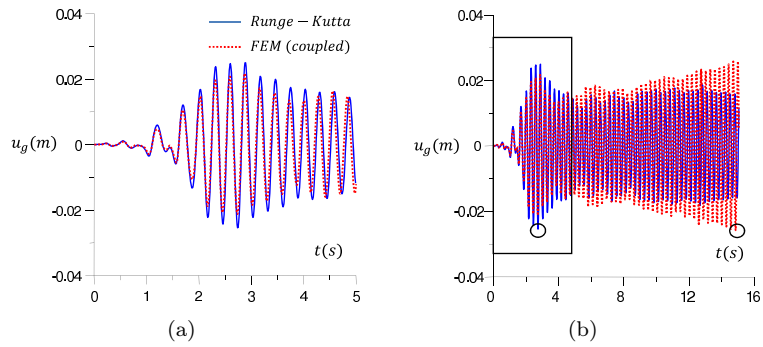


Figure 11: Hollister event relative displacement response. Time window (a). Complete record (b).

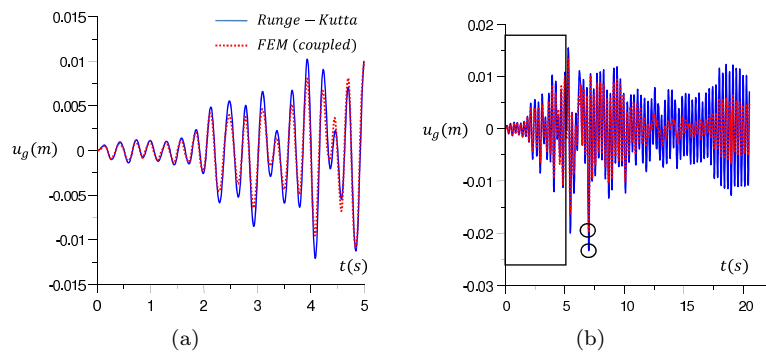


Figure 12: Loma Prieta event relative displacement response. Time window (a). Complete record (b).

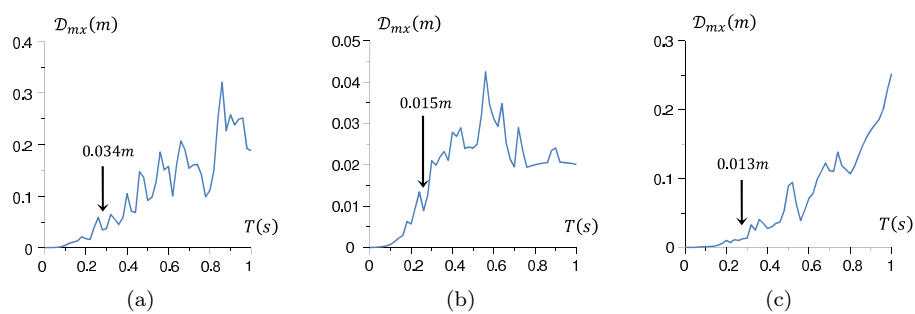
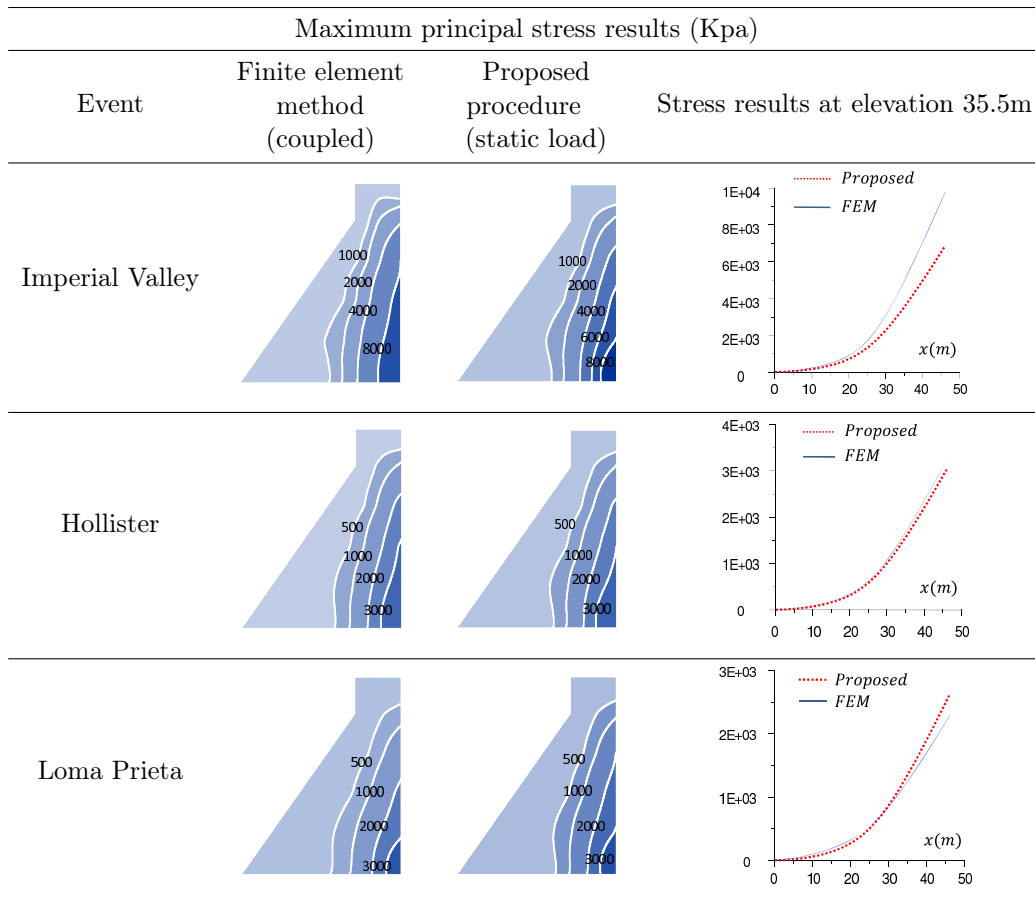


Figure 13: Imperial Valley (a), Hollister (b) and Loma Prieta (c) events displacement spectrums.

Table 4: Principal stress results (finite element method and proposed procedure).



6 Concluding remarks

A semi-analytical procedure was presented for concrete gravity dams response evaluation under earthquake actions. The process basis is simple and begins with an in-vacuum modal analysis of the dam's geometry in a conventional finite element software. Latter, a dynamic equilibrium equation of the fundamental mode is constructed using a generalized coordinate approach and evaluated using a numerical integration routine. Plots shown on Figures 10a, 11a and 12a reveal an excellent approximation at initial time instants when compared to a fully coupled solution. On the other hand, cumulative errors lead to significant differences between responses for greater time windows. In general, absolute amplitudes are similar in both methods. Therefore, the use of response spectra is proven as valuable tool

for stress field evaluation, as shown in Figure 13. An equivalent lateral load is built according to the displacement spectra and then applied to a static finite element analysis of the dam's geometry. Comparison results between the proposed procedure and a fully coupled solution are shown on Table 4, with great resemblance in both cases. Clearly, result quality is a direct function of the relative differences between displacements of the coupled model and those obtained with the proposed method. In Hollister and Loma Prieta events, for example, the semi-analytical approach results were excellent. However, in the Imperial Valley earthquake results were only satisfactory.

Two points deserve special emphasis in the proposed procedure. The first one is evaluation of stress distribution in finite element codes involving only one domain: the structure. In this case, the study of a relatively complex problem is possible on softwares without fluid-structure capabilities. This technique provides a universal method of dam-reservoir interaction analysis in project offices where a basic finite element package is available. The second one is construction of reference semi-analytical equations that provide a validation resource for solutions obtained from a fully coupled analysis. Although the approximation occurs only at initial instants, frequency corrections can be applied by modifying generalized parameters towards a better approximation between semi-analytical and numerical frequencies. Thus, a tool is developed to assist convergence and validation tests in numerical coupled models. The main limitation arises due to contribution of fundamental mode only. However, previous results shown that the approximation is satisfactory, enabling preliminary analysis of this type of structure.

References

- [1] Lee, G. & Tsai, C., Time domain analysis of dam-reservoir system. I: Exact solution. *Journal of Engineering Mechanics*, **117**, pp. 1990–2006, 1991.
- [2] Koohkan, M.R., R., A. & Nasserli, M., Time domain analysis of dam-reservoir interaction using coupled differential quadrature and finite difference methods. *Engineering Computations*, **27(2)**, pp. 280–294, 2010.
- [3] Ribeiro, P.M.V., Melo, C.A.E. & Pedroso, L.J., Analytical solution of dam-reservoir interaction in the fundamental mode shape. *Solid Mechanics in Brazil – 2009*, eds. M. Alves & H.S. da Costa Mattos, ABCM – Associação Brasileira de Engenharia e Ciências Mecânicas: São Paulo, pp. 445–473, 2009.
- [4] Miquel, B. & Bouaanani, N., Simplified evaluation of the vibration period and seismic response of gravity dam-water systems. *Engineering Structures*, **32**, pp. 2488–2502, 2010.
- [5] Silva, S.F., *Interação Dinâmica Barragem-Reservatório: Modelos Analíticos e Numéricos*. Ph.D. thesis, Departamento de Engenharia Civil e Ambiental, Universidade de Brasília, Brasília, DF, 2007. Publicação E.TD-05A/07.
- [6] FERC (Federal Energy Regulatory Commission), Chapter iii gravity dams. *Engineering guidelines for evaluation of hydropower projects*, Federal Energy Regulatory Commission, Office of Hydropower Licensing: Washington, 2002.
- [7] Clough, R.W. & Penzien, J., *Dynamics of Structures*. McGraw-Hill, Inc.: New York, 2nd edition, 1993.
- [8] Chopra, A.K., *Dynamics of Structures: Theory and Applications to Earthquake Engineering*. Prentice Hall: New Jersey, 2nd edition, 2001.
- [9] Chopra, A.K., Earthquake resistant design of concrete gravity dams. *Journal of the Structural Division, ASCE*, **104(ST6)**, pp. 953–971, 1978.

Reliability assessment of composite plates against normally struck conical-nosed projectiles

Nadeem A. Siddiqui

*Department of Civil Engineering, King Saud University,
Riyadh 11421 – Saudi Arabia*

Abstract

In this contribution, a procedure has been presented for the reliability assessment of composite plates against conical-nosed projectiles penetration. For this purpose, using formulations available in the literature, expressions for ballistic-limit of composite targets were derived and then employing Monte Carlo Simulation (MCS) technique 100,000 possible values of ballistic-limit was simulated using the statistical properties of its dependent variables and parameters. Statistical analysis of simulated ballistic-limit velocities was then carried out and an appropriate probability distribution for ballistic-limit was established. With the correlated probabilistic information of ballistic-limit and striking velocity, reliability analysis was carried out using First Order Reliability Method (FORM) to obtain that thickness of selected composite plates which can provide reliable ballistic protection against given shape and velocity-range of projectiles. Effect of striking velocity on the reliability of given thickness of laminated composite targets was also studied.

Keywords: laminated composites, FRP, projectiles, Monte Carlo simulation, FORM.

1 Introduction

One of the popular applications of composite laminates, such as Fiber Reinforced Plastic (FRP) plates, is to provide ballistic protection against striking missiles and projectiles. The reliability assessment of such laminates is concerned with the estimation of its probability of survival against given projectiles impact. In the present study, a composite laminate is assumed as failed if projectile of given velocity completely penetrates (i.e. perforates) its thickness. This is due to the fact that, in many real life applications, when laminates are used for ballistic protection they serve their purpose if they are not perforated by the striking missile or projectile. In technical terms, composite laminates can effectively provide ballistic protection if ballistic-limit of the laminate is above the striking velocity of the projectile. The ballistic-limit of composite laminates primarily depends on the laminate and striking-projectile's geometric and material properties. However, these properties have some inherent uncertainties which make the estimation of ballistic-limit of composite laminates uncertain and thus

require its reliability analysis against possible projectiles attack.

In the last decade substantial work has been carried out to identify the deformation mechanisms which occur during dynamic penetration and perforation of FRP laminates by striking projectiles [1–7]. Wen [1] predicted the penetration and perforation of monolithic fibre-reinforced plastic (FRP) laminates struck normally by projectiles with different nose shapes over a wide range of impact velocity. The approach was based on the assumption that the deformation is localized and that the mean pressure offered by the laminate targets to resist the projectiles can be decomposed into two parts. One part is a cohesive quasi-static resistive pressure due to the elastic-plastic deformation of the laminate materials. The other is a dynamic resistive pressure arising from velocity effects. He obtained the expressions for predicting the depth of penetration (DOP) in the FRP laminate targets and the ballistic limits in the case of perforation. It was shown that the model predictions are in good correlation with available experimental data. Tarim et al. [2] experimentally studied the ballistic performance of some polymer-based composites. They carried out ballistic testing using a variety of commonly available firearms and resulting properties were obtained using mechanical and ultrasonic methods. The results were compared with previous studies. The potential benefit for using such materials on an armored saloon car was also highlighted. Naik and Shirao [3] investigated the ballistic impact behavior of two-dimensional woven fabric composites. Ballistic impact behavior of plain weave E-glass/epoxy and twill weave T300 carbon/epoxy composites was compared. Different damage and energy absorbing mechanisms during ballistic impact were identified. Analytical formulation was presented for each energy absorbing mechanism. Babu et al. [4] experimentally studied the behavior of unidirectional glass epoxy laminated composites as a function of fiber orientation angle, lamination configuration and projectile nose geometry. The energy absorbed by each type of target and the corresponding ballistic limit were determined. A theoretical model was also developed to theoretically predict the ballistic limit. He et al. [5] theoretically studied the penetration and perforation of fiber-reinforced plastic (FRP) laminates struck normally by conical-nosed projectiles over a wide range of velocities. The formulations were based on the assumption that the deformation is localized and that the pressure offered by the laminate targets to resist the projectiles is velocity dependent. They assumed that this pressure can be divided into two parts: a quasi-static part due to the elastic-plastic deformation of the laminate materials and a dynamic part due to penetration velocity. Equations were obtained for the depth of penetration, residual velocity, and ballistic limit. Transient response was solved numerically in terms of time-histories of displacement/penetration, velocity and deceleration. They observed that their theoretical predictions are in good agreement with available experimental results. Naik and Doshi [6] studied ballistic impact behavior of typical woven fabric E-glass/epoxy thick composites. Specifically they determined energy absorbed by different mechanisms, ballistic limit velocity and contact duration. The studies were carried out using the analytical method presented for the prediction of ballistic impact behavior of thick composites in their earlier published research. The analytical method was based on wave theory and energy balance between the projectile and the target. The inputs required for the analytical method were: diameter, mass and velocity of the projectile; thickness and material properties of the target. Analytical predictions were compared with typical experimental results. A good match between analytical predictions and experimental results was observed. Effect of incident ballistic impact velocity on contact duration and residual velocity; effect of projectile diameter

and mass on ballistic limit velocity; and effect of target thickness on ballistic limit velocity and contact duration were also studied. It was observed that shear plugging was the major energy absorbing mechanism. Gower et al. [7] investigated the ballistic response of laminated composite panels through direct impacts of two non-deforming projectiles (7.5 mm diameter hardened steel 1200 cylindrical-conical and 9 mm hemispherical nosed) selected to enhance different failure mechanisms including penetration and delamination. They also carried out experimental and numerical studies to determine the ballistic response of laminated Kevlar 29 and 129 composite panels, commonly used in protective body armors. These panels were impacted at velocities between 130 and 250 m/s, which were below the penetration limit of the panels. Their numerical simulations of the impact tests accurately predicted the back face signature (BFS; described as the maximum dynamic displacement of the armor during impact), one of the important performance indicators for assessing personal protection, and dynamic response for the conical projectile impacts. The BFS for the hemispherical projectiles was slightly low. The numerical analysis, however, accurately predicted the initial velocity of the panel back face for the hemispherical projectiles and the time to reach maximum BFS for the conical projectiles.

A detailed review of literature shows that although considerable work is available on mechanics of projectile penetration into laminated composite targets, but the studies on reliability assessment of such laminated targets against projectile impacts is very limited. Further, the available reliability studies e.g. [8–11] are on such targets which are made up of conventional materials such as concrete, steel, aluminum etc. Keeping this scope in view, in the present study, a procedure has been presented for the reliability assessment of composite laminates against conical-nosed projectiles penetration. Using the presented procedure reliability analysis was carried out to obtain that thickness of selected composite plates which can provide reliable ballistic protection against given shape and velocity-range of projectiles. Effect of striking velocity on the reliability of given thickness of laminated composite targets was also studied.

2 Failure surface and reliability

Reliability of laminated composite target is nothing but its chances to survive under a possible projectile impact. In deterministic sense, if ballistic limit of a composite target is small compared to projectile striking velocity the target may be considered as safe or reliable. However, this safety is not an absolute safety but a “probable safety” as all material and geometric properties have some inherent variability, which makes determination of absolute safety almost impossible. The efforts are generally made to design a target with a desired reliability (β_D) against a given range of projectile impact. In the past, Choudhary *et al.* [8], Siddiqui *et al.* [9, 10] and Siddiqui [11] carried out reliability assessment of different types of targets under missiles, projectiles or jet aircraft impacts. In the present study, the failure surface $G(x)$ is defined as the difference between the composite plate’s ballistic limit V_b and the projectile striking velocity V_s i.e.

$$G(x) = V_b - V_s \quad (1)$$

Where $G(x) > 0$ indicates the safe condition, $G(x) < 0$ the failure condition and $G(x) = 0$ the limit state.

3 Statistics of striking velocity

For the purposes of the current investigation striking velocity in terms of nominal value was directly selected for the reliability analysis. The nominal striking velocity is assumed to be 250 m/s with bias factor 1.1 and COV equal to 20%. The randomness of the striking velocity is described using Extreme Type I distribution. The probability distribution function (PDF) and the cumulative distribution function (CDF) for Extreme Type I distributed random variables are given by:

$$\text{PDF : } f(x) = \alpha \exp \left\{ -e^{-\alpha(x-u)} \right\} \exp \{-\alpha(x-u)\} \quad (2)$$

$$\text{CDF : } F(x) = \exp \left\{ -e^{-\alpha(x-u)} \right\} \quad \text{for } -\infty \leq x \leq \infty \quad (3)$$

where u and α are distribution parameters. If the mean and standard deviation are known, values of the distribution parameters can be estimated using (Nowak and Collins [12])

$$\alpha \approx \frac{1.282}{\sigma_x} \quad (4)$$

$$u \approx \mu_x - 0.45\sigma_x \quad (5)$$

where μ_x and σ_x represent mean and standard deviation respectively.

4 Simulation of ballistic-limit velocity

In the present study the ballistic limit of three different composite targets has been simulated using the equations proposed by He et al. [5]. He et al. [5] derived equations for ballistic limit with the assumption that when a projectile penetrates laminated composite material it experience a normal pressure (σ_n), which can be decomposed into two parts, one part is the cohesive quasi-static resistive pressure (σ_s) and the other is the dynamic resistive pressure (σ_d) arising from velocity effects, viz. $\sigma_n = \sigma_s + \sigma_d$. Under the above idealizations, when a conical projectile with cone angle θ , nose length L_n and mass m impacts normally an FRP laminate of thickness T (Figure 1) with an initial striking velocity V_s , yields following implicit expression for ballistic limit V_b [5]

$$V_b = A/B \cdot \ln(1 + B/A \cdot V_b) + \frac{\pi B T L_n^2 \tan(\theta/2) [(\mu + \tan(\theta/2))]}{m} \quad (6)$$

Where, μ is the coefficient of friction, and $A = \sigma_e$; $B = \beta_1 \sqrt{\rho_t \sigma_e} \sin(\theta/2)$. Here σ_e is the quasi-static linear elastic limit in through-thickness compression, ρ_t is density of FRP laminate, and β_1 is an empirical constant.

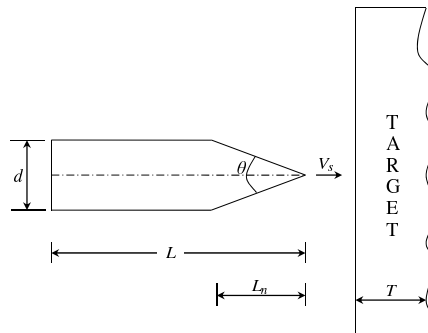


Figure 1: Problem formulation.

5 Reliability estimation and desired reliability index

In the present study, First Order Reliability Method (FORM) was used for the reliability calculations. In this approach, the reliability is measured in terms of a reliability index, β , which is defined as the shortest distance to the failure surface from the origin in reduced-coordinate system, and it is related to the probability of failure or probability of limit state violation for any limit state as

$$\beta = -\Phi^{-1}(P_f), \quad (7)$$

Where P_f is the failure probability and Φ^{-1} is the inverse of standard normal distribution function. The above value of reliability index β is compared with desired reliability index β_D to make sure that targets are as reliable as desired. The optimum value of desired reliability index β_D depends on many factors such as the expected cost of failure, consequences of failure, cost of manufacturing, cost of upgrading (cost of increasing safety) etc. In the present study $\beta_D = 3.0$ was considered. This is a typical desired value generally selected for a number of Engineering Structures (Choudhary *et al.* [8], Siddiqui *et al.* [9, 10] and Siddiqui [11]).

6 Numerical study and discussion of results

In the present study, three targets identified as Target 1, 2 and 3 were impacted by the same projectile. The statistical properties of the projectile and these three targets are given in Table 1. Using Eqn. (6) and the statistical properties of its dependent variables, considered random due to their uncertainty, and employing Monte Carlo simulation technique, 100,000 values of ballistic limit of three different targets were simulated. The randomness involved in the simulated ballistic limits of three targets is shown in Figure 2.

Notice that nominal values of coefficient of friction and laminate thickness were assumed. All other nominal values were taken from the reference of He *et al.* [5]. A constant value of laminate thickness was

Table 1: Statistical data used for the simulation of ballistic limit and subsequent reliability analysis.

Target/Projectile	Random variables	Distribution	Nominal value	Bias factor	COV
Target 1: Carbon/epoxy (Target size: 101.6 mm × 101.6 mm)	Density of FRP laminate, ρ_t	Normal	1550 kg/m ³	1.02	0.10
	Elastic limit of FRP laminate, σ_e	Lognormal	211 MPa	1.05	0.15
	Laminate thickness, T	Lognormal	15 mm	1.05	0.05
Target 2: E-glass/polyester (Target size: 200 mm × 200 mm)	Density of FRP laminate, ρ_t	Normal	1650 kg/m ³	1.02	0.10
	Elastic limit of FRP laminate, σ_e	Lognormal	225 MPa	1.05	0.15
	Laminate thickness, T	Lognormal	15 mm	1.05	0.05
Target 3: Kevlar 29/polyester (Target size: Circular disks of 40 mm diameter)	Density of FRP laminate, ρ_t	Normal	1231 kg/m ³	1.02	0.10
	Elastic limit of FRP laminate, σ_e	Lognormal	145 MPa	1.05	0.15
	Laminate thickness, T	Lognormal	15 mm	1.05	0.05
Projectile: Conical shaped 25.1 mm in length	Coefficient of friction, μ	Lognormal	0.001	1.03	0.15
	Projectile cone angle, θ	Normal	900	1.02	0.05
	Projectile mass, m	Lognormal	3.21 g	1.06	0.05
	Projectile shank diameter, d	Normal	4.76 mm	1.05	0.05
	Striking velocity, V_s	Extreme type 1	350 m/s	1.00	0.10

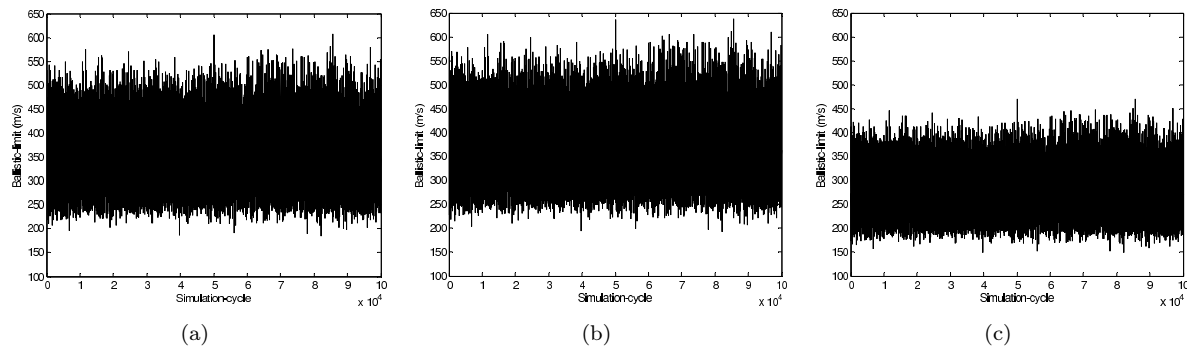


Figure 2: Simulated ballistic-limit velocity for (a) carbon/epoxy (b) E-glass/ polyester and (c) Kevlar 29/polyester targets impacted by a 90° cone angle, 3.21 g mass and 4.76 mm shank diameter conical projectile (Min. = 195.9 m/s, Max. = 654.7 m/s Mean = 349.4 m/s).

assumed in order to compare the reliability of different types of targets in protecting the projectiles of selected range of impact velocity. In order to establish the probability distribution of simulated ballistic-limit velocity, the bar charts were plotted also plotted and shown in Figure 3. These Charts infer that it is reasonable to assume the distribution of ballistic limit velocity as normal. In order to further develop the confidence on probability distribution of ballistic limit velocity, the simulated values of ballistic limit and their corresponding probability are plotted on probability paper in Figure 4. It is worth mentioning that in Figure 3, the scale of the y-axis is not uniform. The y-axis values are probabilities and, as such, go from zero to one. The distance between the tick marks on the y-axis matches the distance between the quantiles of a normal distribution. The quantiles are close together

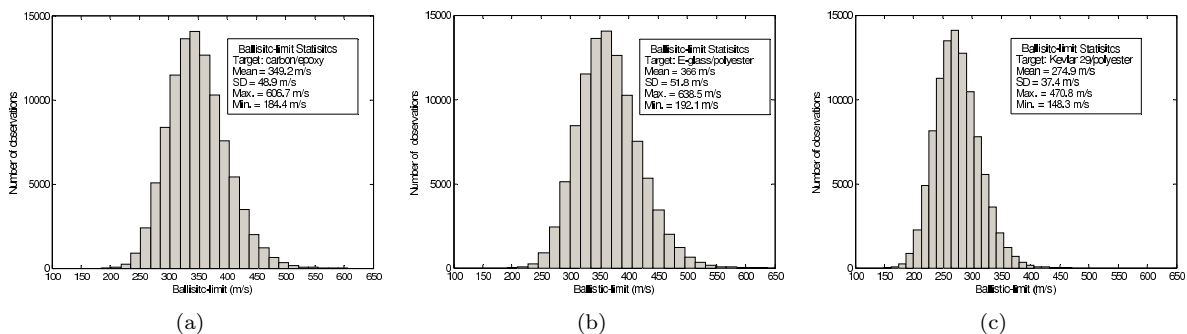


Figure 3: Histogram of simulated ballistic-limit velocity for (a) carbon/epoxy (b) E-glass/ polyester and (c) Kevlar 29/polyester targets impacted by a 900 cone angle, 3.21 g mass and 4.76 mm shank diameter conical projectile.

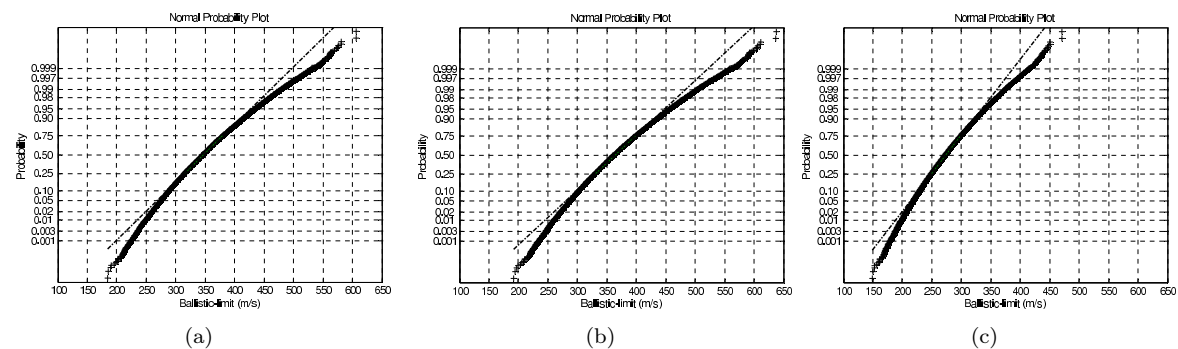


Figure 4: Normal probability plots for simulated ballistic-limit velocity for (a) carbon/epoxy (b) E-glass/ polyester and (c) Kevlar 29/polyester targets impacted by a 900 cone angle, 3.21 g mass and 4.76 mm shank diameter conical projectile

near the median (probability = 0.5) and stretch out symmetrically moving away from the median. As all the points fall near the line, it is reasonable to assume the distribution of simulated ballistic-limit velocity as normal. The empirical cumulative distribution function (CDF) was also drawn for simulated ballistic limits of each target and shown in Figure 5. The shape of the CDF also supports the above outcome that ballistic limit follows a normal distribution.

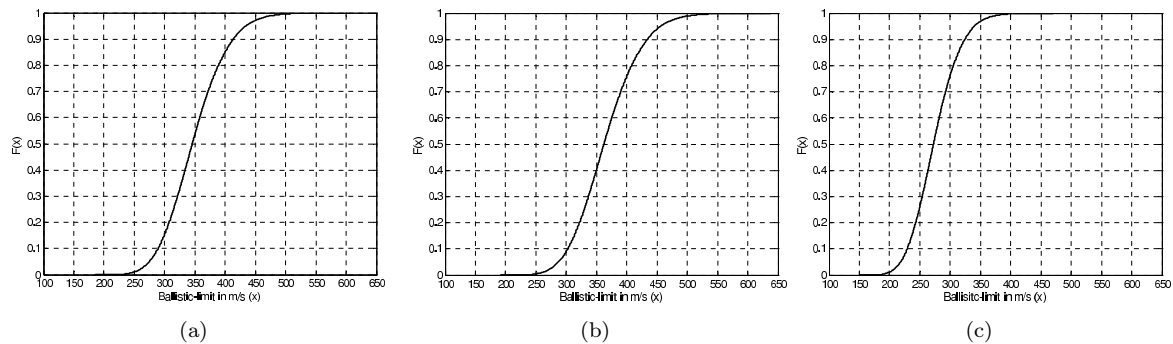


Figure 5: Empirical CDF drawn for simulated ballistic-limit of carbon/epoxy target.

Table 2 presents the results of reliability analysis. It is worth mentioning that the desirable range shown in the last column of Table 2 was chosen to cover a range which is generally desired to insure safety of engineering structures of importance (Siddiqui *et al.* [10], Siddiqui [11], Khan *et al.* [13]). However, in practice these values for any structure are decided on the basis of extensive calibration studies; the consideration of cost issues and the consequences of failure etc. The results show that for target thickness of 15 mm, none of the selected composite targets are able to provide ballistic protection with a desired level of reliability if these targets were hit by a nominal striking velocity of 250 m/s. Although reliability indices of targets 1 and 2 are closer to the desired reliability index, but Kevlar 29/polyester is far less than (about 72%) the desired reliability value. But, considering economy and other manufacturing benefits of Kevlar it is necessary to estimate the required thickness of Kevlar29 target to achieve the desired reliability. Figure 6 is plotted to obtain that thickness of

Table 2: Results of the analysis

Estimated Parameters	Target 1 Carbon/epoxy	Target 2 E-glass/polyester	Target 3 Kevlar29/polyester	Desirable range
Probability of failure, P_f	1.0×10^{-2}	0.51×10^{-2}	20.0×10^{-2}	$10^{-3}-10^{-5}$
Reliability index, β	2.31	2.57	0.84	3-4
% Difference (from $\beta_D = 3.0$)	23%	14.3%	72%	–

composite targets which can provide ballistic protection with the desired magnitude of reliability. This curve clearly illustrates that in order to obtain ballistic protection with desired reliability index of the magnitude 3.0, Carbon and E-glass thicknesses must be around 17.5 mm, however, for Kevlar 29 the required thickness is 25 mm. Figure 7 shows that if the target thickness is only 15 mm then targets made up of carbon and E-glass can provide reliable ballistic protection up to the striking velocity of 225 m/s. However, Kevlar 29 can provide reliable ballistic protection only up to 175 m/s.

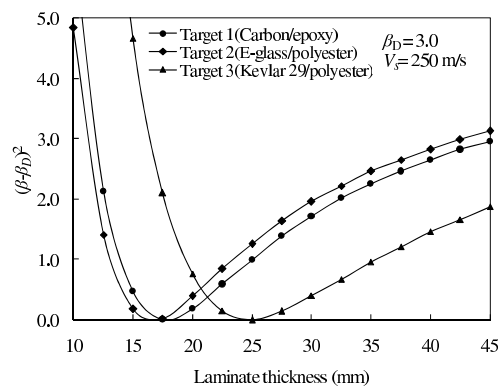


Figure 6: Effect of laminate thickness on ballistic reliability of target.

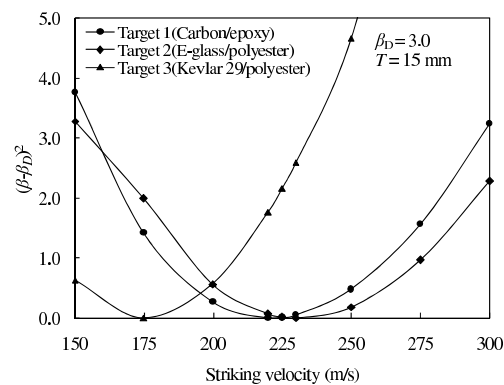


Figure 7: Effect of striking velocity on ballistic reliability of target.

7 Conclusion

In the present study, a procedure has been presented for the reliability assessment of composite plates against conical-nosed projectiles penetration. Using the proposed procedure, reliability of three targets made up of three different composites viz. Carbon/epoxy; E-glass/polyester; and Kevlar29/polyester was studied against a normal impact of conical-nosed projectiles. The results show that for target thickness of 15 mm, above composite targets are not able to provide reliable ballistic protection against impact of a conical-nosed projectile having nominal striking velocity of 250 m/s. For a reliable ballistic protection, Carbon and E-glass target thicknesses must be around 17.5 mm, however, for Kevlar 29 the required thickness is 25 mm. It was also found that if the target thickness is only 15 mm the targets made up of carbon and E-glass can provide reliable ballistic protection up to the striking velocity of 225 m/s. The Kevlar29 target, however, can provide reliable ballistic protection up to 175 m/s only.

Acknowledgement The work presented in this paper was supported by the Deanship of Scientific Research, Research Centre, College of Engineering, King Saud University, Riyadh, Saudi Arabia.

References

- [1] Wen, H., Predicting the penetration and perforation of frp laminates struck normally by projectiles with different nose shapes. *Composite Structures*, **49**, pp. 321–329, 2000.
- [2] Tarim, N., Findik, F. & Uzun, H., Ballistic impact performance of composite structures. *Composite Structures*, **56**, pp. 13–20, 2002.
- [3] Naik, N. & Shiraro, P., Composite structures under ballistic impact. *Composite Structures*, **66**, pp. 579–590, 2004.
- [4] Babu, M.G., Velmurugan, R. & Gupta, N., Heavy mass projectile impact on thin and moderately thick unidirectional fiber/epoxy laminates. *Latin American Journal of Solids and Structures*, **4**, pp. 247–265, 2007.
- [5] He, T., Wen, H. & Qin, Y., Penetration and perforation of frp laminates struck transversely by conical-nosed projectiles. *Composite Structures*, **81**, pp. 243–252, 2007.
- [6] Naik, N. & Doshi, A., Ballistic impact behaviour of thick composites: Parametric studies. *Composite Structures*, **82**, pp. 447–464, 2008.
- [7] Gower, H., Cronin, D. & Plumtree, A., Ballistic impact response of laminated composite panels. *International Journal of Impact Engineering*, **35**, pp. 1000–1008, 2008.
- [8] Choudhury, M., Siddiqui, N. & Abbas, H., Reliability analysis of a buried concrete target under missile impact. *International Journal of Impact Engineering*, **27**, pp. 791–806, 2002.
- [9] Siddiqui, N., Choudhury, M. & Abbas, H., Reliability analysis of projectile penetration into geological targets. *Reliability Engineering and System Safety*, **78**, pp. 13–19, 2002.
- [10] Siddiqui, N., Iqbal, M., Abbas, H. & Paul, D., Reliability analysis of nuclear containment without metallic liners against jet aircraft crash. *Nuclear Engineering and Design*, **224**, pp. 11–21, 2003.
- [11] Siddiqui, N., Reliability analysis of concrete barriers under normal missile impact. *Proceedings of National Conference on Advances in Civil Engineering: Perspectives of Developing Countries (ACEDEC 2003)*, HBTI: Kanpur, India, volume 1, pp. 20–29, 2003.

- [12] Nowak, A. & Collins, K., *Reliability of Structures*. Mc Graw Hill: Singapore, 2000.
- [13] Khan, R., Siddiqui, N.A., Naqvi, S. & Ahmad, S., Reliability analysis of tlp tethers under impulsive loading. *Reliability Engineering and System Safety*, **91(1)**, pp. 73–83, 2006.

Elastic collapse of corroded pipe repaired with composite material under uniform external pressure

T.C. Silva, L.C.S. Nunes

*Graduate Program of Mechanical Engineering, PGMEC – Universidade Federal Fluminense, UFF
Rua Passo da Pátria 156, 24210-240, Niterói, RJ – Brazil*

Abstract

The principal objective of this work is to study the collapse effect of pipes with internal corrosion defect, which is repaired with composite materials, under uniform external pressure. In this analysis, a pipe with large longitudinal defect, compared with the diameter, is considered. In this way, the boundary effects can be neglected. The goal is to estimate the required composite repair thickness for the pipe with internal defect recovers the original mechanical behavior. In order to do this, it is investigated the dependence of critical pressure on the defect geometry, i.e., depth and angular defects. Moreover, the normalized elastic buckling pressure is analytically estimated and this is compared with results obtained by means of finite elements.

Keywords: collapse, defect, pipe, repair.

1 Introduction

Recently, there has been growing interest in structural integrity of pipe. A large number of the pipes are made of metals, like carbon steel, and they are used extensively in the petrochemical, refinery, and pipeline industries [1]. The reason for this is simply economic. It is widely available, inexpensive, and maintainable. However, this type of material is susceptible to flaws such as cracks, pitting, local wall thinning, which can be generate by corrosion, erosion, and environmental exposure to various substances [2–4].

The marine environment is very aggressive to any type of material, in addition, the flow over the years contributes against pipe integrity. The transport of oil by pipes, despite being one of the safest modes, accidents have been caused by leaks or ruptures, and in some cases impact the environment for a long period.

Every day more is required to protect the environment. The environmental agencies, prosecutors and the Agência Nacional de Petróleo are stricter in fines and program for adjustment of conduct, to maintain this activity within an acceptable standard of safety worldwide.

Recently, pipeline integrity is frequently target of many studies [2, 5–8]. Some of them are based on analysing collapse behavior of pipelines with defects [9–11]. The use of composite materials, mostly carbon fiber, in order to repair structural defects in pipelines has also been widely studied in recent years [12–16].

The aim of this study is to analyze the pipelines collapse behavior with internal defect repaired with composite material, which is subjected to external pressure uniformly distributed. In this context, it intends to estimate the thickness of an ideal for duct repair faulty repaired has a behavior similar to a product without defect.

2 Description

Consider a pipeline with internal defect repaired with composite material, as illustrated in “Fig. 1”. Initially it is assumed that the length of the defect on the axial direction of the pipe is large compared with the diameter, thus the edge effects are neglected. Moreover, the region with defect has circumferential symmetry.

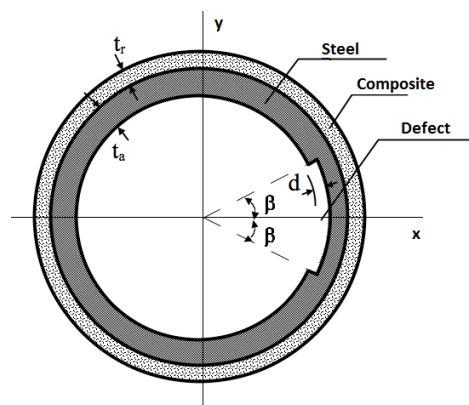


Figure 1: Schematic of a pipe with internal defect repaired with composite material.

In this case, the pipe with defect repaired has the following characteristics: thickness of pipe without defect, ie. (steel thickness), t_a , thickness of composite material (repair), t_r , defect depth, d , the defect angle 2β . Moreover, the structure will be subjected to a uniformly distributed external pressure, p , after that, it will be analyzed the influence of the repair thickness over the critical collapse pressure.

3 Analytical model for internal defect pipeline repaired

The differential equation governing radial deflection curve of a thin bar w , described by Timoshenko and Gere [17], is defined as

$$\frac{\partial^2 w}{\partial \theta^2} + w = -\frac{MR^2}{EI} \quad (1)$$

where M is the bending moment and R the average radius of curvature.

As the present analysis involves two different materials, namely steel and composite material, for simplicity, it is considered the equivalent stiffness, which can be given by

$$EI_{eq} = E_a I_a + E_c I_c \quad (2)$$

where $E_a I_a$ and $E_c I_c$ are the equivalent stiffness of steel and composite, respectively.

In the region with defect, i.e., $-\beta < \theta < \beta$:

$$E_{eq1} = \frac{E_a}{(1-\nu_a^2)} \frac{(t_a-d)^3}{12} + \frac{E_c}{(1-\nu_c^2)} \frac{t_c^3}{12} \quad (3)$$

In the region free from defect, i.e., $\beta < \theta < 2\pi - \beta$

$$E_{eq2} = \frac{E_a}{(1-\nu_a^2)} \frac{t_a^3}{12} + \frac{E_c}{(1-\nu_c^2)} \frac{t_c^3}{12} \quad (4)$$

where ν_a and ν_c are the Poisson coefficients of steel and composite material (repair).

According to Hoo Fat and Xue [9], the bending moment can be expressed by

$$M = pRw \quad (5)$$

Substituting Eq. (5) and (1), considering Eq. (3) and (4), then:

$$\begin{cases} \frac{\partial^2 w}{\partial \theta^2} + k_1^2 = 0, \text{ para } -\beta \leq \theta \leq \beta \\ \frac{\partial^2 w}{\partial \theta^2} + k_2^2 = 0, \text{ para } \beta \leq \theta \leq 2\pi - \beta \end{cases} \quad (6)$$

where the collapse parameters are given by

$$k_1^2 = 1 + 3\eta \frac{C_a t_a^3}{C_a (t_a - d)^3 + C_c t_c^3} \quad (7)$$

$$k_2^2 = 1 + 3\eta \frac{C_a t_a^3}{C_a t_a^3 + C_c t_c^3} \quad (8)$$

with $C_a = \frac{E_a}{12(1-\nu_a^2)}$ e $C_c = \frac{E_c}{12(1-\nu_c^2)}$

The analysis will be done using the normalized pressure given by $\eta = \frac{p}{p_e}$, where the elastic collapse pressure for a uniform tube is given by

$$p_e = \frac{E_a t_a^3}{4R^3 (1 - \nu_a^2)} \quad (9)$$

The parameters used in the equations above are: thickness $t_{a,c}$, Young modulus, $E_{a,c}$, Poisson's ratio, $\nu_{a,c}$, pipe radius R . The indices are related to steel and composite material respectively.

Solving Eq. (6), the following general solution is found

$$w = \begin{cases} A \sin k_1 \theta + B \cos k_1 \theta, & \text{para } -\beta \leq \theta \leq \beta \\ C \sin k_1 \theta + D \cos k_1 \theta, & \text{para } \beta \leq \theta \leq 2\pi - \beta \end{cases} \quad (10)$$

To determine the constants presented in Eq. (10), let us consider the case where the collapse solution presents symmetry as per Hoo Fat and Xue [9], taking the following boundary conditions,

$$\frac{dw}{d\theta} = 0, \text{ at } \theta = 0, \pi, \quad w|_{\theta=\beta^+} = w|_{\theta=\beta^-} \quad \text{and} \quad \left. \frac{dw}{d\theta} \right|_{\theta=\beta^+} = \left. \frac{dw}{d\theta} \right|_{\theta=\beta^-} \quad (11)$$

Using the boundary conditions presented in Eq. (11), it is possible find the next equation,

$$-k_1 \tan k_1 \beta = k_2 \tan k_2 (\pi - \beta) \quad (12)$$

4 Results and discussion

The purpose of this section is to analyze the permissible external pressure in a pipe with internal defect repaired with composite material, varying the defect geometry and repair thickness. The purpose is to observe what should be the thickness required to repair the pipe with defect back to the original collapse properties, i.e., on a pipe without defect this parameter is the elastic collapse pressure. For this analysis, the geometrical and material properties described in Tab. 1 were used.

Table 1: Material properties and geometric parameters.

Parameters	ASTM A106 steel	Resin epoxy with carbon fiber
Young modulus (GPa)	$E_a = 210$	$E_a = 49^*$
Poisson ratio	$\nu_a = 0.3$	$\nu_c = 0.43^*$
Thickness (mm)	$t_a = 18.29$	Variable
Nominal diameter (mm)	$R = 228.6$	Variable

* It was considered just the circumferential properties [13]

Solving Eq. (12), considering the values presented in Tab. 1, it was obtained the following results illustrated in Figs. 2 and 3. In this case, for each depth of normalized defect (d/t_a ranging from 0.1

to 0.9) is verified the variation of normalized pressure (i.e., pressure over elastic collapse pressure) according to defect angle ($\beta = 20, 30, 45$ e 60°) and the normalized repair thickness (tc/ta ranging from 0 to 1).

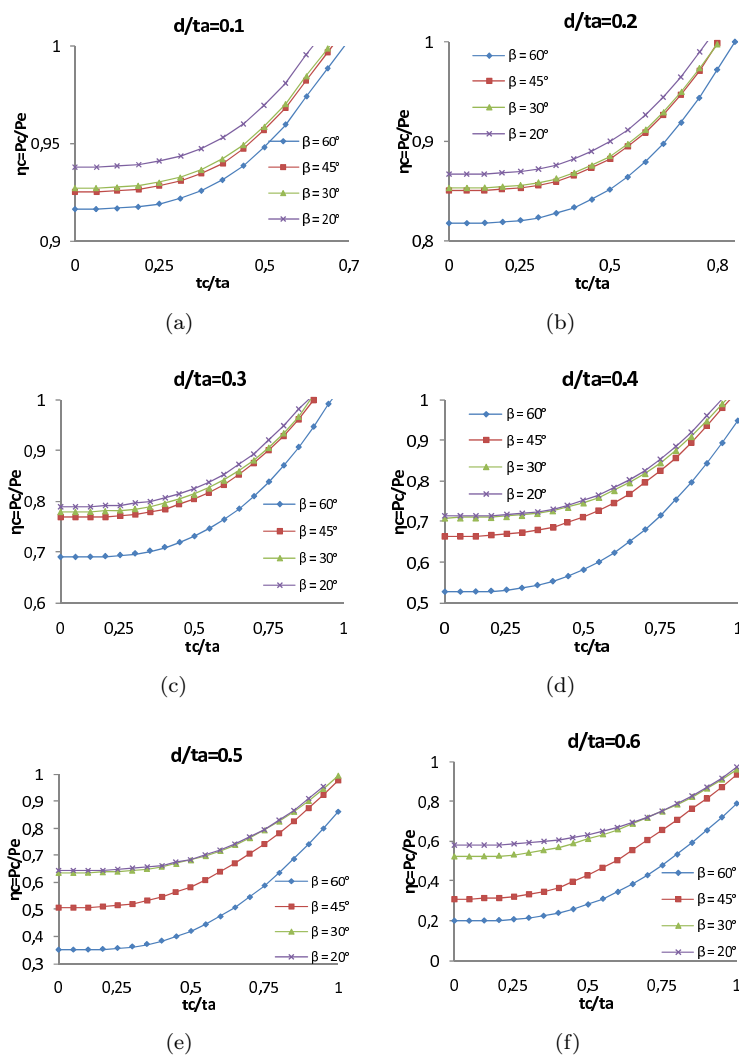


Figure 2: Normalized collapse pressure in function of defect geometry (angle and depth) and repair thickness.

In Figure 2, it is possible to see that in the case where the thickness of the defect is equal to or less than 60% of pipe thickness, the normalized pressure varies slowly to the value of the repair thickness equal to 50% of pipe thickness. Starting from this point, normalized pressure presents a considerable increase.

Considering the result shown in Fig. 2 (a) for a defect depth equal to 10% of pipe thickness, it is known that the thickness needed to repair the pipe with defect back to its collapse original features is 70% of pipe thickness. Another important observation is that there are not large variations associated to defect angle.

As defect depth is increased, it can be observed that the effect of the angle of the defect begin to be highlighted. Also, repair thickness needed is increased.

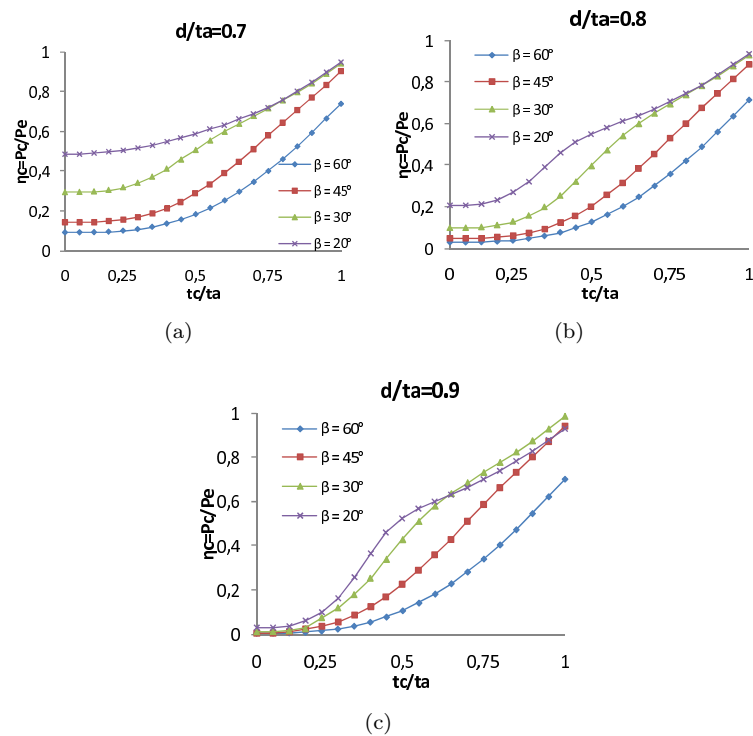


Figure 3: Normalized collapse pressure in function of defect geometry (angle and depth) and repair thickness.

The results illustrated in Fig. 3 present new interesting effects. With depth values equal and over 70% of repair thickness, it can be observed a large dependence on defect angle and repair thickness.

In Figures 4, 5, 6 and 7, it will be showed the FEA results comparing with the analytical results. It was assessed by a commercially available finite element code using the same properties of the Tab. 1. Of course it had its differences (analytical x FEA) because of non-linear analysis was used as mesh and contact as well. The purpose was approach as close as possible both models (analytical x FEA).

To FEA model, Fig. 1 should be adopted on its half, the side with defect was permitted just displacements on x -axis while on non-defect side was applied fixed support. The repair thickness was applied as contact to the half tube profile, which was the target. Pressure was applied on outer surface and the results were assessed by Linear Buckling connected after Structural block.

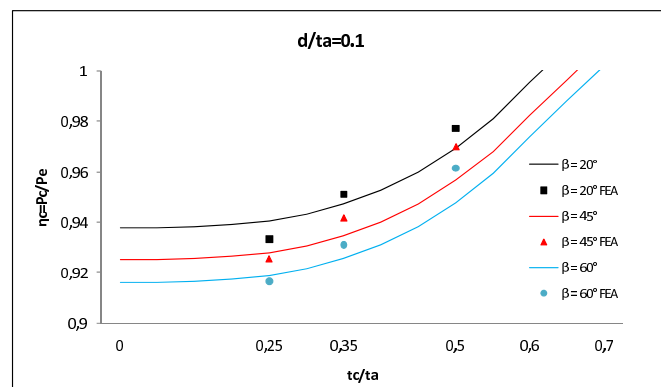


Figure 4: Comparison between FEA x Analytical results for $d/t_a=0.1$.

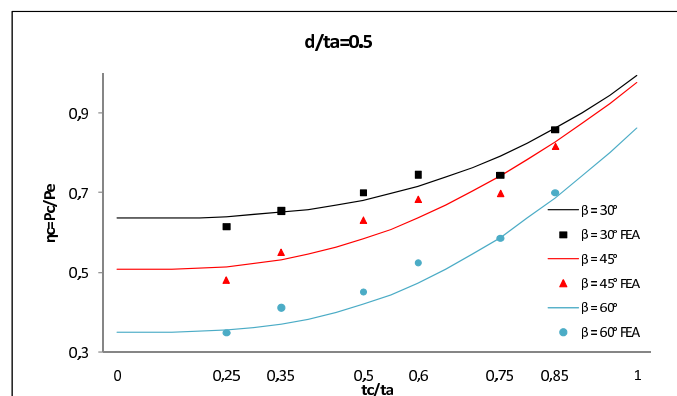


Figure 5: Comparison between FEA x Analytical results for $d/t_a=0.5$.

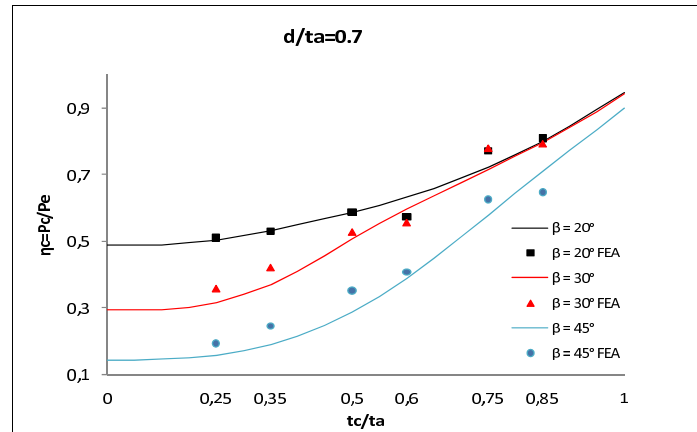


Figure 6: Comparison between FEA x Analytical results for $d/ta=0.7$.

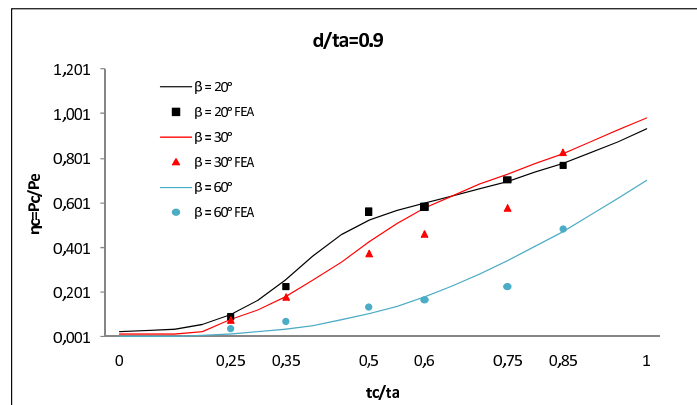


Figure 7: Comparison between FEA x Analytical results for $d/ta=0.9$.

In Figure 4 as the range varies only between 0 and 1 it turns harder to assess a good approach between results.

As illustrated in Figs. 5, 6 and 7, it should be noted that the analytical and numerical results is closer than the presented in Fig. 4. This is due a bigger range of normalized pressure.

5 Conclusions

The purpose of the present work was investigate the repair thickness behavior from a pipe with internal defect when subjected to uniform external pressure. It was assessed the critical pressure, which is compared with the elastic collapse pressure in pipelines without any defect. In addition, it was verified the geometry dependence of the defect, i.e., thickness and angle defect. Taking into account the approximations, it can be considered a very good agreement between the analytical predictions and numerical results using finite element method. With this analysis it is possible to estimate the repair thickness necessary to repair a pipe with defect to have the same behavior as a tube without defect, avoiding oversizing, and consequently, excessive waste of material.

Acknowledgements The authors would like to express their gratitude to Universidade Federal Fluminense and to the Ministry of Science and Technology. The present paper received financial support from Brazilian agencies CNPq and FAPERJ.

Responsibility notice The authors are the only responsible for the printed material included in this paper.

References

- [1] Escoe, A., *Piping and pipeline assessment guide*. Elsevier Inc., 2006.
- [2] Kim, Y., Kim, J., Ahn, J., Hong, S. & Park, C., Effects of local wall thinning on plastic limit loads of elbows using geometrically linear fe limit analyses. *Engineering Fracture Mechanics*, **75**, pp. 2225–2245, 2008.
- [3] Kim, Y. & Son, B., Finite element based stress concentration factors for pipes with local wall thinning. *International Journal of Pressure Vessels and Piping*, **81**, pp. 897–906, 2004.
- [4] Staat, M., Local and global collapse pressure of longitudinally flawed pipes and cylindrical vessels. *International Journal of Pressure Vessels and Piping*, **82**, pp. 217–225, 2005.
- [5] Netto, T., Ferraz, U. & Botto, A., On the effect of corrosion defects on the collapse pressure of pipelines. *International Journal of Solids and Structures*, **44**, pp. 7597–7614, 2007.
- [6] Takahashi, K., ando, K., Hisatsune, M. & Hasegawa, K., Failure behavior of carbon steel pipe with local wall thinning near orifice. *Nuclear Engineering and Design*, **237**, pp. 335–341, 2007.
- [7] Miyazaki, K., Kanno, S., M., I., Hasegawa, K., Ahn, S. & ando, K., Fracture and general yield for carbon steel pipes with local wall thinning. *Nuclear Engineering and Design*, **211**, pp. 61–68, 2002.
- [8] Karamanos, S.A. & Eleftheriadis, C., Collapse of pressurized elastoplastic tubular members under lateral loads. *International Journal of Mechanical Sciences*, **46**, pp. 35–56, 2004.
- [9] Hoo Fatt, M. & Xue, J., Buckling of a non-uniform, long cylindrical shell subjected to external hydrostatic pressure. *Engineering structures*, **24**, pp. 1027–1034, 2002.
- [10] Sakakibara, N., Kyriakides, S. & Corona, E., Collapse of partially corroded or worn pipe under external pressure. *International Journal of Mechanical Sciences*, **50**, pp. 1586–1597, 2008.
- [11] Hoo Fatt, M., Elastic-plastic collapse of non-uniform cylindrical shells subjected to uniform external pressure. *Thin-walled structures*, **35**, pp. 117–137, 1999.

- [12] Chapetti, M., Otegui, J., Manfredi, C. & Martins, C., Full scale experimental analysis of stress states in sleeve repairs of gas pipelines. *International Journal of Pressure Vessels and Piping*, **78**, pp. 379–387, 2001.
- [13] Duell, J., Wilson, J. & Kessler, M., Analysis of a carbon composite overwrap pipeline repair system. *International Journal of Pressure Vessels and Piping*, **85**, pp. 782–788, 2008.
- [14] Oteguia, J., Urquiza, S., Rivasa, A. & Trunzob, A., Local collapse of gas pipelines under sleeve repairs. *International Journal of Pressure Vessels and Piping*, **77**, pp. 555–566, 2000.
- [15] Toutanji, H. & Dempsey, S., Stress modeling of pipelines strengthened with advanced composites materials. *Thin-Walled Structures*, **39**, pp. 153–165, 2001.
- [16] Alexander, C. & Ochoa, O., Extending onshore pipeline repair to offshore steel risers with carbon-fiber reinforced composites. *Composite Structures*, **92**, pp. 499–507, 2010.
- [17] Timoshenko, S. & Gere, J., *Theory of elastic stability*. New York, 1961.

Simultaneous structural and control design for piezoelectric actuated structures using topology optimization

Otávio A. A. da Silveira, Jun S. O. Fonseca
*Grupo de Mecânica Aplicada, Universidade Federal do Rio Grande do Sul,
Rua Sarmento Leite 425, 90050-170, Porto Alegre, RS – Brazil*

Abstract

This research proposes a methodology for the optimal design of actively controlled structures, aiming to suppress vibrations induced by external disturbances. Design is conducted simultaneously for the structural topology and actuator locations. A topology optimization problem is formulated for three material phases (two solid materials and void) with two design variables groups. A non-piezoelectric elastic isotropic material forms the structural only part of the design, while a piezoelectric material composes the active part. To avoid the difficulties of treating structural and control design variables in the same optimization framework, this work proposes a nested solution approach, where the actuator locations and controller syntheses are considered as separately. The main optimization loop designs the structural variables, i.e., it is decided where there should be solid material and where there should be voids. The actuators are placed by an inner design loop within the structural problem, by a control law optimization that defines where the material should have piezoelectric properties. Numerical examples show that the approach used in this paper can produce a clear structural topology with effective actuators placement.

Keywords: simultaneous design, structural optimization, vibration control, piezoelectricity.

1 Introduction

The increasing demand for lightweight and adaptable structures to important applications spotlights the need of advanced structural optimization and control design methods. Smart structures, by the distribution of integrated sensors and actuators, have a great capacity for self-monitoring and self-control via a control system. Thereby, the system can detect induced vibration modes and generate control forces to reduce structural vibration. One can mention many applications for such smart structures, especially in the aerospace industry, but also in flexible robotic manipulators and light weight surface vehicles.

The development of efficient methods for design of smart structures is still a very promising field of

research, despite great achievements during the past two decades. The wide application field supports these researches and developments.

As part of structural design, the topology optimization method contributes effectively in the design of lighter structures, reducing transportation costs. Furthermore, the reduction of raw materials also becomes important for environmental sustainability issues.

These structures, however, are usually light in weight and presents low internal damping [1]. These characteristics favor the appearance of large amplitude vibrations, which are especially undesirable in the operation of precision machinery. Therefore, the use of an active vibration control system by automatic modification of its structural response is important. This control system requires actuators that generate control forces, such as, piezoelectric ceramic actuators.

The piezoelectric phenomenon is a form of electro-mechanical coupling in which some crystals and polymers generate an electrical charge when pressed (mechanical strain), and *vice versa*. The use of piezoelectric ceramics as mechanical force generator in control systems and in mechanical actuators is already well known. In general, these applications use pieces of specific size and standard shape; pre-set placement of piezoelectric ceramics in topology optimization is another problem. An alternative to these design constraints is using a methodology that optimally distributes the piezoelectric material to maximize the performance of the ceramics.

The fields of structural optimization and optimal control had significant progress during the last decades. Each discipline has developed several theoretical and computational methods for their own goals. Overall, the structural design precedes the control design, i.e., structural engineers define a layout in order to withstand the static and dynamic loads, and after that, the control engineers specify the control system using the pre-defined structure. In the field of structural design, topology optimization has emerged as an effective tool, where the goal usually is to minimize the costs under some requirements of resistance and/or dynamic or maximizing the global structure stiffness, both by the optimal distribution of material. In relation to the control project, several theories have been proposed to reduce vibration in structures, among which the optimum control theory.

Since the early 1990s, contrary to common practice, several theoretical works point that simultaneous design of structural optimization and control can reduce costs and increase performance, relative to the project in sequence.

Canfield and Meirovitch [2] dealt with the design of a structure and its control system as a problem of multi-objective optimization. Pareto optimal designs generated for a simple beam demonstrated the benefits of solving the problem of integrated structural optimization and control. A composite objective function consisting of structural and control parts was developed by Ou and Kikuchi [3], which is optimized by the method of topology optimization for steady state response. An independent modal space control algorithm (IMSC) is performed on the structure in order to reduce the transient response magnitude and, finally, the ideal placement for actuators is discussed. Wang et al. [1] treated the structural design variables and the matrix of feedback gains as independent design variables. Liu and Begg [4, 5] discussed the optimal control, sensitivity analysis and optimization of an integrated intelligent truss structure. Five algorithms for simultaneous design have been presented and applied to a multidisciplinary optimization in which both the structural layout and the control parameters are involved. Zhu et al. [6] investigated the simultaneous optimization for structural topology, piezoelectric

actuator locations and control parameters of a plate actively controlled by a H_2 control law. Using a nested solution approach, they could treat the structural and control variables separately. Finally, the control variables were projected on a sub-optimization solving the Ricatti equations. An integrated optimization for smart trusses using genetic algorithms is carried out by Xu et al. [7]. In this work, several constraints were considered: stresses, displacements, natural frequencies and voltage on piezoelectric actuators. Finally, Raja and Narayanan [8] considered the optimization of a multidisciplinary *tensegrity* structure using genetic algorithms. A nested strategy was also used, in which the robust control norms H_2 and H_∞ were considered as objective function of the control system.

A number of works concern about the placement of actuators and sensors. In general, some use a control performance index as objective function, while others use concepts of observability and controllability. Recently, Kumar and Narayanan [9] considered the optimal location of sensor-actuator pairs placed on piezoelectric flexible beam using a controller based on a linear quadratic regulator (LQR). The LQR performance index was used as the objective function of the optimization problem, which was solved using genetic algorithms. In a unique work, Carbonari et al. [10] studied the design, by topology optimization method, of piezoelectric actuators consisting of a flexible structure actuated by piezoelectric ceramics. In this kind of project formulation, the position of piezoelectric ceramic is usually held fixed in the design domain and only the flexible structure is designed by distributing some non-piezoelectric material. However, this work presents a formulation that allowed the simultaneous distribution of non-piezoelectric and piezoelectric material in the design domain in order to obtain some specific actuation movements, achieving excellent results.

In view of what was presented, this paper aims to develop a new methodology for simultaneous design of structural topology and control for reduction of vibration using piezoelectric actuators. It proposes a procedure that uses the topology optimization method, and finds the optimal actuators placement according to the optimal distribution of piezoelectric material, and automatically derives the optimal control. Moreover, unlike Carbonari et al. [10], considers the three-dimensional structure, what enables the practical application of electrical potential difference across the piezoelectric material. This paper considers the topology optimization of thin three-dimensional structures in the simultaneous project. The piezoelectric ceramic actuators are activated on the normal faces of the thinner dimension, which is the direction of polarization of piezoelectric ceramics.

2 Simultaneous design of structural topology and control

Several authors [11, 12] argue that the structural optimization and control combined can get better results than traditional sequential method. It is common to different works that the first paper investigating the integrated design for a structure and control system was conducted by Hale et al. [13], in which an optimization problem is developed to handle spatial structures where both structural parameters and active control forces are determined in order to minimize a specific cost function. Miller and Shim [14] worked with objective functions in order to reduce structural mass and strain, kinematics and control energy. Salama et al. [11] established a precedent followed by many others. They eliminated the variables of structural control considering permanent gains (constants) and selecting specific weight matrices (identity) for the quadratic performance index. Milman et al. [12] introduced the con-

cept of combined objective function, and provided the necessary conditions for the optimal design of Pareto. Some recent works on simultaneous design has been cited in the introduction.

2.1 Objective function and constraints

Generally, the simultaneous design of structural optimization and control can be put as a nonlinear programming problem in which certain cost function, often multi-objective, is minimized with respect to structural (ρ_e) and control (ρ_c) parameters in the form

$$\min_{\rho_e, \rho_c} f(\rho_e, \rho_c). \quad (1)$$

The original integrated optimization can be replaced by a nested structural optimization with the control optimization as a sub-process [6]. Thus, one can write:

$$\min_{\rho_e} f_1(\rho_e), \quad (2)$$

where

$$f_1(\rho_e) = \min_{\rho_c} f_2(\rho_e, \rho_c), \quad (3)$$

refers to the control optimization using a certain control law. As shown in the above equations, the first optimization, Eq. (2), is the structural optimization for structural design variables, while the sub-optimization, Eq. (3), is the optimization of control over the control variables. Therefore, when the structural variables are changed, the sub-process is called and new control variables are calculated.

Since the structural and control optimization are treated separately in this nested approach, the various techniques for structural and control design can be combined and implemented without difficulties [6]. But it is important to note that the original optimization represented by Eq. (1), and the new optimization represented by Eq. (2) and (3), may converge to different optimal solutions; this happens because obtaining identical solutions depends strongly on the details of the strategies of searching, initial values of design variables, characteristics of the objective function, etc.

In this work the structural optimization can be defined as the minimization of the compliance, depending of structural design variables that define where, on the structure, should be put solid material (elastic isotropic or piezoelectric material) and where should be put voids. The control optimization will be based on minimizing the performance index of an LQR optimal control, depending of design variables that define the control regions where should have elastic isotropic material and where should be taken piezoelectric material (actuators). Furthermore, the control optimization is able to define the gain matrix \mathbf{G} of LQR optimal control system. In order to solve the optimization problems this work uses the sequential linear programming (SLP).

2.2 Material model for simultaneous design with optimum placement of piezoelectric material

The material model for topology optimization proposed in this paper includes two solid, elastic isotropic material and piezoelectric material, and void. Therefore, the material model that defines the elastic properties, piezoelectric coupling properties and density is given by:

$$\begin{aligned} \mathbf{E} &= \rho_1^{p1} \left((1 - \rho_2^{p2}) \mathbf{E}_1 + \rho_2^{p2} \mathbf{E}_2 \right), \\ \gamma &= \rho_1^{p1} \left((1 - \rho_2^{p2}) \gamma_1 + \rho_2^{p2} \gamma_2 \right), \\ \mathbf{d} &= \rho_1^{p1} \rho_2^{p3} \mathbf{d}_2, \end{aligned} \quad (4)$$

where \mathbf{E} , γ and \mathbf{d} define the effective properties of the interpolated material. \mathbf{E}_1 and \mathbf{E}_2 are the elastic properties of non-piezoelectric and piezoelectric material respectively, as well as, γ refers to densities; \mathbf{d}_2 defines the properties of electro-mechanical coupling for the piezoelectric material, being null for non-piezoelectric material. ρ_1 and ρ_2 are the pseudo-density defined in each finite element and will be directly related to the design variables of structural and control respectively. It is observed by examining Eq. (4) that: common elastic isotropic material is obtained when $\rho_1 = 1$ and $\rho_2 = 0$, piezoelectric material is obtained when $\rho_1 = 1$ and $\rho_2 = 1$, and void is obtained when $\rho_1 = \rho_2 = 0$. $p1$, $p2$ and $p3$ are the penalty coefficients that try to recover the presence or absence of material, piezoelectric or non-piezoelectric material and finally, the coupling properties, respectively.

This material model distributes elastic isotropic material and piezoelectric material optimally. As consequence, automatically sets the placement of piezoelectric actuators contributing to the optimization of the control system. A material model similar to that, have already been presented in Bendsoe and Sigmund [15] and also in Carbonari et al. [10], but was not used in designing control system.

3 Structural design

As previously mentioned, the structural objective function that it is used in this work is the minimization of mechanical compliance (maximizing the global stiffness), which can be written as

$$f_1(\rho_1, \rho_2) = J_e = \mathbf{f}^T \mathbf{u}, \quad (5)$$

where \mathbf{f}^T is a vector of static loads and \mathbf{u} is the vector of global displacements of the structure generated by this loading. Although the compliance function depends on the design variable ρ_2 which defines where should have piezoelectric material, the design of structural optimization provides only the minimization of compliance on the variable ρ_1 , which defines the presence or absence of solid material (piezoelectric or non-piezoelectric.) Thus, one can write

$$\begin{aligned} &\min_{\rho_1} J_e(\rho_1, \rho_2) \\ &\text{subject to } \begin{cases} 0 < \rho_{1i} \leq 1 & (i = 1, 2, 3, \dots, n_1) \\ V_1 = \frac{\int_{\Omega} \rho_{1i} d\Omega}{\int_{\Omega} d\Omega} \leq V_1^{\max} \end{cases} \end{aligned} \quad (6)$$

where ρ_1 is a vector of structural design variables, ρ_{1i} is the i^{th} element component and n_1 is the number of structural design variables (equal to the number of finite elements.) The second restriction limits the total volume of material (piezoelectric or common) to a volume fraction V_1^{\max} pre-established.

4 System control design

The objective function for the control system used in this work is the minimizing of the performance index of an LQR optimal control [9], given by:

$$f_2(\rho_1, \rho_2) = J_c = \frac{1}{2} \int_0^\infty (\mathbf{x}^T \mathbf{Q} \mathbf{x} + \mathbf{j}^T \mathbf{R} \mathbf{j}) dt, \quad (7)$$

where \mathbf{x} is a vector of state variables, the vector of modal coordinates in this case, \mathbf{j} is a vector of control forces, \mathbf{Q} is a semi-positive definite matrix of weights for the state variables and \mathbf{R} is a positive definite matrix of weights for the control forces. Therefore, the optimization of control can be written as:

$$\begin{aligned} & \min_{\rho_2} J_c(\rho_1, \rho_2) \\ & \text{subject to } \begin{cases} 0 < \rho_{2i} \leq 1 & (i = 1, 2, 3, \dots, n_2) \\ V_2 = \frac{\int_{\Omega} \rho_{2i} d\Omega}{\int_{\Omega} d\Omega} \leq V_2^{\max} \end{cases} \end{aligned} \quad (8)$$

where ρ_2 is the vector of design variables of control, ρ_{2i} is the i^{th} component of the vector referring to the element i , and n_2 is the number of design variables for control (equal to the number of finite elements). The second restriction limits the total volume of piezoelectric material to a volume fraction V_2^{\max} pre-established.

5 Sensitivity analysis

First order optimization algorithms, such as the sequential linear programming, require sensitivities (derivatives) of objective and constraints with respect to design variables. In this case it was possible to derive analytical sensitivities.

5.1 Sensitivity of the material model

The sensitivities of the material model, described in the section 2.2, in relation to the design variables ρ_1 and ρ_2 are easily calculated, as follows:

$$\frac{\partial \mathbf{E}}{\partial \rho_1} = p_1 \rho_1^{p_1-1} \left((1 - \rho_2^{p_2}) \mathbf{E}_1 + \rho_2^{p_2} \mathbf{E}_2 \right), \quad \frac{\partial \mathbf{E}}{\partial \rho_2} = p_2 \rho_1^{p_1} \rho_2^{p_2-1} (\mathbf{E}_2 - \mathbf{E}_1), \quad (9)$$

$$\frac{\partial \gamma}{\partial \rho_1} = p_1 \rho_1^{p_1-1} \left((1 - \rho_2^{p_2}) \gamma_1 + \rho_2^{p_2} \gamma_2 \right), \quad \frac{\partial \gamma}{\partial \rho_2} = p_2 \rho_1^{p_1} \rho_2^{p_2-1} (\gamma_2 - \gamma_1), \quad (10)$$

$$\frac{\partial \mathbf{d}}{\partial \rho_1} = p_1 \rho_1^{p_1-1} \rho_2^{p_3} \mathbf{d}_2, \quad \frac{\partial \mathbf{d}}{\partial \rho_2} = p_3 \rho_1^{p_1} \rho_2^{p_3-1} \mathbf{d}_2. \quad (11)$$

5.2 Sensitivity of compliance

Compliance is defined as the work done by the external forces, given by Eq. (5). For simplicity sake derivation is show for a generic density ρ . By the adjoint method can be concluded that the compliance sensitivity in relation to a pseudo-density ρ can be written as:

$$\frac{\partial W}{\partial \rho} = -\tilde{\mathbf{u}}^T \frac{\partial \mathbf{K}}{\partial \rho} \mathbf{u}, \quad (12)$$

where $\tilde{\mathbf{u}} \in \mathfrak{R}^n$ is any arbitrary constant real vector, \mathbf{K} is the stiffness matrix and \mathbf{u} is the displacement vector. This equation is in the form of an equilibrium equation and for flexibility one can get directly $\tilde{\mathbf{u}} = \mathbf{u}$. Remembering that the stiffness matrix of a piezoelectric material can be written as

$$\mathbf{K} = \begin{bmatrix} \mathbf{K}_{uu}(\mathbf{c}) & \mathbf{K}_{uj}(\mathbf{e}) \\ \mathbf{K}_{ju}(\mathbf{e}) & -\mathbf{K}_{jj}(\kappa) \end{bmatrix}, \quad (13)$$

and that the compliance is related only to mechanical degrees of freedom, Eq. (12) can be rewritten as

$$\frac{\partial W}{\partial \rho} = -\mathbf{u}^T \frac{\partial \mathbf{K}_{uu}(\mathbf{c})}{\partial \rho} \mathbf{u}. \quad (14)$$

Therefore, the compliance derivatives are easily calculated. It is important to note that these derivatives are “localized”, i.e., only requires information at the element level, however, there is a hidden global effect because the displacement vector depends on the pseudo-densities of all elements [15].

Finally, observing Eq. (9) when applied to Eq. (14), one can note the sensitivity of compliance with respect to design variables ρ_1 will always be negative, i.e., the addition of material, piezoelectric or not, decreases the compliance (increases stiffness). Moreover, the sign of sensitivity to design variables ρ_2 depends on the difference between the values of the matrices of elastic properties of both materials (isotropic elastic and piezoelectric).

5.3 Sensitivity of performance index of the control system

Since the behavior of the control system depends heavily on the structural design variables and the feedback logic, a systematic sensitivity analysis is essential for the development of a well-behaved algorithm for solving a problem of this complexity. The sensitivities of the first order, for the control optimization part are given below.

According to Liu and Beeg [5], the first order sensitivity of the quadratic performance index J with respect to a design variable ρ is given by

$$\frac{\partial J}{\partial \rho} = \frac{\partial J}{\partial \mathbf{A}} \otimes \frac{\partial \mathbf{A}}{\partial \rho} + \frac{\partial J}{\partial \mathbf{B}} \otimes \frac{\partial \mathbf{B}}{\partial \rho} + \frac{\partial J}{\partial \mathbf{S}} \otimes \frac{\partial \mathbf{S}}{\partial \rho}, \quad (15)$$

where “ \otimes ” means the sum of all products of two entries for each matrix and

$$\frac{\partial J}{\partial \mathbf{A}} = \mathbf{P}\mathbf{L}, \quad (16)$$

$$\frac{\partial J}{\partial \mathbf{B}} = -\mathbf{P}\mathbf{L}\mathbf{S}^T\mathbf{G}^T, \quad (17)$$

$$\frac{\partial J}{\partial \mathbf{S}} = -\mathbf{G}^T\mathbf{B}^T\mathbf{P}\mathbf{L} + \mathbf{G}^T\mathbf{R}\mathbf{G}\mathbf{S}\mathbf{L}. \quad (18)$$

The sensitivities in relation to design variables can be obtained after by the Leibnitz’s chain rule. Thus, one can obtain:

$$\frac{\partial \mathbf{A}}{\partial \rho} = \begin{bmatrix} 0 & 0 \\ -\text{diag} \left[\frac{\partial \omega_i^2}{\partial \rho} \right] & -2\text{diag} \left[\xi_i \frac{\partial \omega_i}{\partial \rho} \right] \end{bmatrix}, \quad (19)$$

$$\frac{\partial \mathbf{B}}{\partial \rho} = \begin{bmatrix} 0 \\ \mathbf{\Phi}^T \mathbf{B}_0 + \mathbf{\Phi}^T \frac{\partial \mathbf{B}_0}{\partial \rho} \end{bmatrix}. \quad (20)$$

as \mathbf{S} was defined as a unitary matrix, it can be written

$$\frac{\partial \mathbf{S}}{\partial \rho} = 0, \quad (21)$$

And so the third term in Eq. (15) can be neglected. Finally, since the matrix \mathbf{B}_0 is directly related to region of the electro-mechanical (\mathbf{K}_{ju}) in the stiffness matrix, the sensitivity of \mathbf{B}_0 can be written as:

$$\frac{\partial \mathbf{K}_{uj}(\mathbf{d})}{\partial \rho} = \int_{\Omega_e} \mathbf{B}_u^T \frac{\partial \mathbf{d}}{\partial \rho} \mathbf{B}_j d\Omega_e, \quad (22)$$

where $\partial \mathbf{d} / \partial \rho$ is given by Eq. (11).

6 Summary of the proposed methodology

For clarity sake, the methodology proposed in this paper can be summarized in 11 steps:

1. Data entry (optimization and FEM);
2. Assemble elements neighborhood table for the sensitivity filters;
3. Start SLP loop;
4. Solve a static problem for the external loads;
5. Calculate the sensitivities of the structural problem and apply the filter to this data;

6. Solve the compliance minimization problem for the structural pseudo-density;
7. Solve a modal problem for the desired number of modes;
8. Calculate the sensitivities of the control problem and apply the filter to this data;
9. Solve the problem of minimizing LQR control system index;
10. Check the convergence:
 - If converged, go to step 11;
 - Else, recalculates the move limits and return to step 3 with the new pseudo-densities;
11. Exit and plot.

7 Results

In order to verify the performance of the proposed simultaneous design presented in this paper, this section shows some results. The material properties of the elastic isotropic material (aluminum) and piezoelectric material (PZT5A) are presented in Table 1. A cantilever beam is analyzed (Figure 1). Besides clamping one end of the beam, it is considered that the degrees of freedom in z -direction are restricted, allowing movements only in the xy plane. There is no topology change in z -direction since the structure presents just one layer of finite elements [16]. The beam measures $800 \times 100 \times 10$ [mm³] and is discretized by 3200 eight node brick finite element ($160 \times 20 \times 1$).

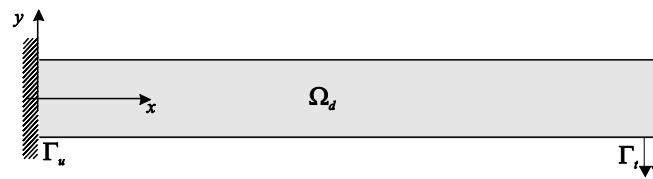


Figure 1: Cantilever beam.

The parameters used in design optimization are the same for all simulation cases analyzed. Volume constraints are 50% and 5% for total volume fraction and piezoelectric volume fraction, respectively; the initial values of the pseudo-densities ρ_1 and ρ_2 are uniform for all elements and equal to 0.40 and 0.04, respectively, in this way, the optimization problem starts just below the feasible limit.

The value of the static vertical load on the tip of the beam is set equal to 1000 [N], which is applied in four nodes. The weighting matrix of the quadratic performance index of the control system \mathbf{Q} and \mathbf{R} are respectively set equal to $1e+12$ and $1e+0$.

This model is used in three design cases, to verify the influence of the number of vibration modes considered in the control system. In the first one, the control system is set to control the first two vibration modes. In the second, it is considered four modes and in the last one, it is considered the first six vibration modes. The results are shown below.

The results considering the first two vibration modes for the control system can be seen in Figure 2. The final topologies for the distribution of solid material (elastic isotropic or piezoelectric), distribution

Table 1: Material properties.

PZT5A		Aluminum	
elastic constants	(10^{10} N.m $^{-2}$)	Young's modulus	71×10^9 N.m $^{-2}$
c_{11}^E	12.1	Density	2700 kg.m $^{-3}$
c_{12}^E	7.54	Poisson's ratio	0.33
c_{13}^E	7.52		
c_{33}^E	11.1		
c_{44}^E	2.11		
c_{66}^E	2.26		
piezoelectric constants	(C.m $^{-2}$)		
e_{31}	-5.4		
e_{33}	15.8		
e_{51}	12.3		
dielectric constants			
$\epsilon_{11}^S/\epsilon_0$	916		
$\epsilon_{33}^S/\epsilon_0$	830		
Density	7750 kg.m $^{-3}$		

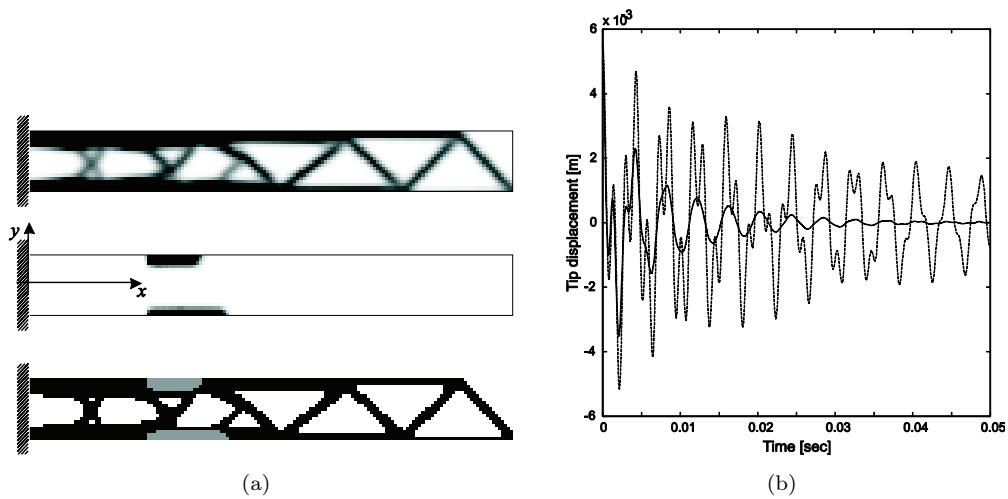


Figure 2: a) Optimal topologies and b) Tip displacement considering two vibration modes.

of piezoelectric material (actuators) and the post-processed image can be seen in Figure 2a. To check the structural response time, it was considered an initial modal displacement equal to ($\eta_1 = \eta_2 = 1e-3$ [m]). The beam tip displacement is plotted in Figure 2b; the solid and dashed lines show the response with and without control respectively.

In Figures 3a and 3b one can see the results considering four modes in the vibration control system. The optimal topologies for the distribution of solid material, piezoelectric material and the post-processed image, for this second case, can be seen in Figure 3a. The tip displacement response considering an initial modal displacement ($\eta_1 = \eta_2 = \eta_3 = \eta_4 = 1e-3$ [m]) can be seen in Figure 3b.

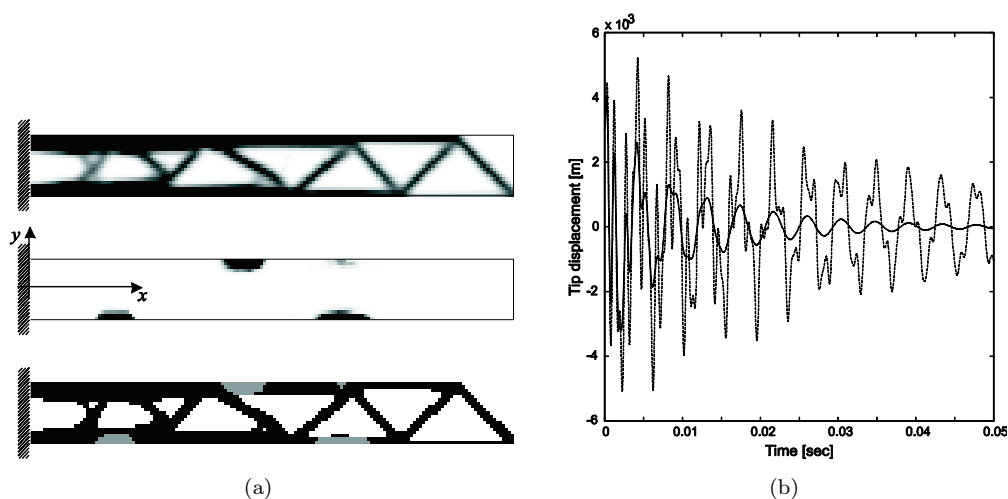


Figure 3: a) Optimal topologies and b) Tip displacement considering four vibration modes.

The results for optimal topology and temporal response to a control system considering six vibration modes can be seen in Figures 4a and 4b. Figure 4a shows the optimal topologies for the distribution of solid material, piezoelectric material and the post-processed image considering six vibration modes. Figure 4b displays the respective tip displacement time response considering an initial modal displacement ($\eta_1 = \eta_2 = \eta_3 = \eta_4 = \eta_5 = \eta_6 = 1e-3$ [m]).

It can be seen there are some differences among the topology results presented in Figures 2, 3 and 4. From these results, it can be concluded that the number of vibration modes used in the control system considerably changes the distribution of piezoelectric material (actuator location). In a subsequent study would be interesting to consider different weights for each eigenfunction since it is well known that the first modes are more influential. From the temporary responses can be noted that the control system can eliminate possible vibrations very efficiently.

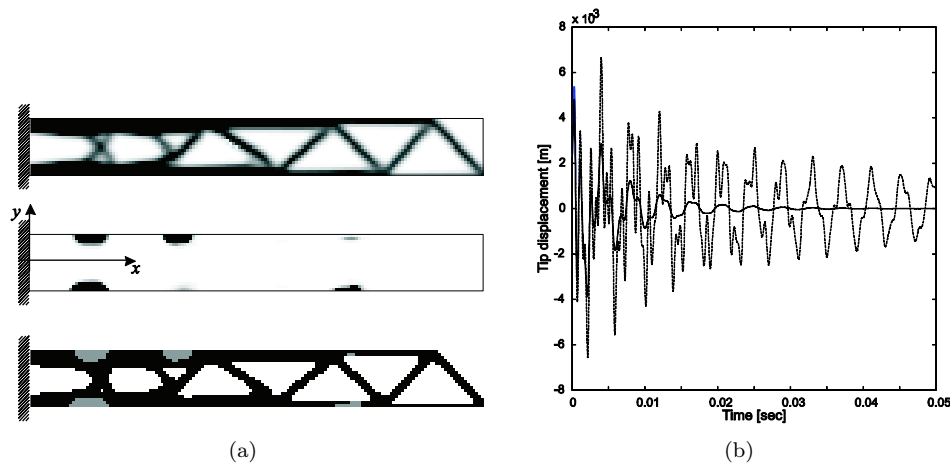


Figure 4: a) Optimal topologies and b) Tip displacement considering six vibration modes.

8 Conclusion

This work presents a new methodology of simultaneous structural and control design. The optimization is based in a nested approach that separates the two design procedures inside a SLP loop. Preliminary results for plane deformations and variable number of vibration modes are presented. Using this methodology, the structural topology, actuators placement and the control system are designed. This approach has great potential for application in the design of smart structures.

References

- [1] Wang, Z., Chen, S. & Han, W., Integrated structural and control optimization of intelligent structures. *Engineering Structures*, **21**, pp. 183–191, 1999.
- [2] Canfield, R. & Meirovitch, L., Integrated structural design and vibration suppression using independent modal space control. *AIAA Journal*, **32(10)**, pp. 2053–2060, 1994.
- [3] Ou, J. & Kikuch, N., Integrated optimal structural and vibration control design. *Structural and Multi-disciplinary Optimization*, **12**, pp. 209–216, 1996.
- [4] Liu, X. & Beeg, D., On simultaneous optimisation of smart structures – Part I: Theory. *Computer Methods in Applied Mechanics and Engineering*, **184**, pp. 15–24, 2000.
- [5] Liu, X. & Beeg, D., Sensitivity analysis of smart structures. *Computer Methods in Applied Mechanics and Engineering*, **163**, pp. 311–322, 1998.
- [6] Zhu, Y., Qiu, J., Du, H. & Tani, J., Simultaneous optimal design of structural topology, actuator locations and control parameters for a plate structure. *Computational Mechanics*, **29**, pp. 89–97, 2002.
- [7] Xu, B., Jiang, J. & Ou, J., Integrated optimization of structural topology and control for piezoelectric smart trusses using genetic algorithm. *Journal of Sound and Vibration*, **307**, pp. 393–427, 2007.

- [8] Raja, M. & Narayanan, S., Simultaneous optimization of structure and control of smart tensegrity structures. *Journal of Intelligent Material Systems and Structures*, **20(1)**, pp. 109–117, 2009.
- [9] Kumar, R. & Narayanan, S., Active vibration control of beams with optimal placement of piezoelectric sensor/actuator pairs. *Smart Materials and Structures*, **17**, pp. 01–15, 2008.
- [10] Carbonari, R., Silva, E. & Nishiwaki, S., Optimum placement of piezoelectric material in piezoactuator design. *Smart Materials and Structures*, **16**, pp. 207–220, 2007.
- [11] Salama, M., Garba, J., Demsetz, L. & Udewadia, F., Simultaneous optimization of controlled structures. *Computational Mechanics*, **3**, pp. 275–282, 1988.
- [12] Milman, M., Salaman, M., Scheid, R., Bruno, R. & Gibson, J., Combined control-structural optimization. *Computational Mechanics*, **8**, pp. 01–18, 1991.
- [13] Hale, A., Lisowski, R. & Dahl, W., Optimal simultaneous structural and control design of maneuvering flexible spacecraft. *Journal of Guidance, Control and Dynamics*, **8(1)**, pp. 86–93, 1985.
- [14] Miller, D. & Shim, J., Gradient-based combined structural and control optimization. *Journal of Guidance, Control, and Dynamics*, **10(3)**, pp. 291–298, 1987.
- [15] Bendsøe, M. & Sigmund, O., *Topology Optimization – Theory, Methods and Applications*. Springer, 2003.
- [16] da Silveira, O. & Fonseca, J., Simultaneous design of structural topology and control for vibration reduction using piezoelectric material. *CILAMCE 2010 - XXXI Iberian-Latin-American Congress on Computational Methods in Engineering, Mecánica Computacional*, volume XXIX, pp. 8375–8389, 2010.

Mechanical behavior of fiber-reinforcement beams with fiber orientation

Leandro Vanalli

*Universidade Estadual de Maringá – Departamento de Tecnologia
PR – Brazil*

Nilson Tadeu Mascia

*Universidade Estadual de Campinas - Faculdade de Engenharia Civil
Depto. de Estruturas, SP – Brazil*

Mário Rogério Scoaris

*Universidade Estadual de Maringá – Departamento de Tecnologia
PR – Brazil*

Rodrigo Ribeiro Paccola

*Universidade de São Paulo – Escola de Engenharia de São Carlos
Depto. de Estruturas, SP – Brazil*

Abstract

The study of mechanical behavior and of the constitutive relations is very important in scope of Structural Engineering. Many materials used as structural components, in diverse areas of engineering, are not isotropic, for example, the fiber-reinforced polymer materials. Searching a contribution for application of these materials, this paper deals with a theoretical study on anisotropy and on its influence in the stress distribution and displacements in plane laminate beams. Fiber-reinforcement beams are body with a mechanical behavior that is dependent on the direction of its fibers. Due to simplifications in analysis, fiber-reinforcement beams are generally treated as linear orthotropic, with the material directions ideally coincident with the longitudinal and transverse directions of a coordinate system associated with a structural member. When such coincidence does not occur in the practical cases, the effects the mechanical properties require a transformation of coordinates of the elastic coefficients to adjust them to the adopted model for structural analysis. Thus, additional terms appear in the constitutive relationship transforming fiber-reinforcement beams as an anisotropic body. By introducing these coefficients on the elastic model, a study of the stresses in beams was developed by applying an analytical method and a commercial program of finite elements. Numerical examples confirm that the fiber orientation, even for small angles, has a large influence on the mechanical behavior of fiber-reinforcement beams. The obtained results reveal that there is a non-symmetrical normal stress distribution in these beams.

Keywords: fiber-reinforcement beams, fiber orientation, Airy's function, elastic coefficients, coefficients of mutual influence.

1 Introduction

As structural elements, anisotropic solids are applied in some areas of modern technology. In general, an anisotropic material presents no elastic symmetry and its mechanical properties are different in arbitrary directions. Thus, the study of these solids become more complex than the study of other solids that possess other types of elastic symmetry, as for example, isotropic solids. Some works that evidence this complexity can be cited, as for example, Green and Zerna [1], Nair and Reissner [2], Kilic et al. [3], Mascia and Vanalli [4] and Mascia et al. [5].

In fact, the study of the anisotropy implies in the knowledge of the constitutive law that consequently governs the elastic behavior of the material and in determining the components of the constituent tensor S_{ijkl} . In an elastic model, completely anisotropic, this constitutive tensor possesses 81 unknown constants. Using convenient simplifications, this number can be reduced for 9 constants, which is called orthotropic model, or for 3 constants, called isotropic model.

Treating particularly about anisotropic beams, it appears other deformations besides the ones presented in isotropic beams, as for example, in steel beams. These deformations are associated to the certain constants of elasticity called of the mutual influence coefficients that quantify the participation of normal stresses in shear strains or shear stresses in normal strains.

During many years the studies in this area have been focused on the analysis of the behavior of the stresses and strains of anisotropic beams. As for example the application of the polynomial forms of the stress function of Airy, where Lekhnitskii et al. [6] studied the displacements and the stresses in some examples of anisotropic beams subjected to the different conditions of loadings and restrains. When particularized for isotropic beams, these solutions become similar those of Timoshenko and Goodier [7]. Hashin [8], also using of the stress function of Airy, developed a systematic way of develop polynomial solutions for anisotropic plane beams.

Murakami et al. [9], investigated the effect of the constitutive coupling, and the effect caused for the participation of the coefficients of mutual influence on stresses and strains of a cantilever anisotropic beam. In this way, the authors also studied the influence of the relation between the height of the cross section (h) and the span of the beam (l) on the behavior of anisotropic beams considering the theory of beam of Euler-Bernoulli and the theory of Timoshenko too.

In this context, considering the anisotropic formalism of Lekhnitskii [10], the goal of this paper is to analyze the influence of the anisotropy in the mechanical behavior of laminate beams, considered anisotropic and homogeneous. In order to carry out this, it is used the equations developed for Lekhnitskii et al., as well as, the method developed for Hashin. The obtained solutions are compared, by means of diagrams, with solutions for isotropic beams considering the theories of beam of Bernoulli-Euler, and also, with numerical solutions for orthotropic beams.

2 Description of problem

According to Lekhnitskii [10], all materials can be divided in homogeneous and not homogeneous, and on the other hand, in isotropic and anisotropic. Most of structural materials show some degrees of anisotropy. Materials, as laminate composites, are anisotropic due to the manufacture process.

Lekhnitskii [10] classifies as isotropic the solid whose properties of elasticity are constant for any directions established from one determined point, or either, the transformations of coordinates are invariant for all. An anisotropic solid, in general, shows different properties of elasticity for different directions associates to a given point. The directions in which the elasticity properties are constant are called elastically equivalent directions or principal directions of elasticity.

Apart from this if the structure of an anisotropic body presents some type of symmetry, its properties of elasticity also show it. The elastic symmetry expresses the fact that in each point of the solid exists equivalent symmetrical directions with respect the elastic properties. If the symmetry of the elastic properties of an anisotropic body exists, the equations of Hooke's Law can be simplified, also occurring many simplifications in the constituent tensors S_{ijkl} or in reduced form S_{ij} .

Dealing particularly with laminate beams, constituted by laminae of materials strengthened for fibers, the stress and strain analyses become more or less complex whether considering the coincidence or not between the geometric axis of the beam and the principal axes of elasticity of the laminae, that compose the structure. Thus, the constitutive tensor for the plane case, in case of having this coincidence, is simplified, as an orthotropic material with four independent terms.

$$S_{ij} = \begin{bmatrix} S_{11} & S_{12} & 0 \\ S_{12} & S_{22} & 0 \\ 0 & 0 & S_{66} \end{bmatrix} \quad (1)$$

However, the simplifications presented in the orthotropic tensor disappear when the coincidence between the geometric axis of the beam and the principal axes of the laminae are not considered, especially related to the directions of strengthened fibers, appearing then, other elements in the constitutive tensor, which becomes anisotropic. In a general point of view, the angles that relate reinforcement fibers of the laminae and the geometric axes of the analyzed structure establish the anisotropic behavior of the laminate beams (Figure 1).

Thus, considering the angle θ among the fibers of reinforcement of the laminae and the geometric axes of the beam, the constitutive tensor can be written by:

$$\begin{bmatrix} \bar{S}_{11} & \bar{S}_{12} & \bar{S}_{16} \\ \bar{S}_{12} & \bar{S}_{22} & \bar{S}_{26} \\ \bar{S}_{16} & \bar{S}_{26} & \bar{S}_{66} \end{bmatrix} = [T]^T \cdot \begin{bmatrix} S_{11} & S_{12} & 0 \\ S_{12} & S_{22} & 0 \\ 0 & 0 & S_{66} \end{bmatrix} \cdot [T] \quad (2)$$

where the constants \bar{S}_{16} and \bar{S}_{26} are present in anisotropic materials and are dependent of the coefficients of mutual influence and T is the matrix of transformation.

The anisotropic constitutive relations, or stress (σ or τ) and strain (ϵ or γ) relationship, that are involved in the analysis of a laminate beam, where it does not have coincidence between the local axes of the laminae and the geometric axis of the beam, for a plane case, are present in Equation 3 as:

$$\epsilon_x = \bar{S}_{11} \sigma_x + \bar{S}_{12} \sigma_y + \bar{S}_{16} \tau_{xy}; \quad \epsilon_y = \bar{S}_{12} \sigma_x + \bar{S}_{22} \sigma_y + \bar{S}_{26} \tau_{xy}; \quad \gamma_{xy} = \bar{S}_{16} \sigma_x + \bar{S}_{26} \sigma_y + \bar{S}_{66} \tau_{xy} \quad (3)$$

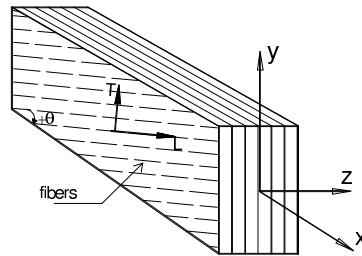


Figure 1: Laminate beam related to the geometric and local (of the fibers) systems.

Thus, it is evident that beams constituted by orthotropic materials can become anisotropic from these considerations, and that with the use of the transformation matrices, Equation 3, it is possible to obtain all the constants that are necessary for the development of the anisotropic constitutive relations, including the coefficients of mutual influence ($\eta_{xy,x}$ and $\eta_{xy,y}$), which are of difficult experimental determination.

To illustrate the transformations of the mentioned elastic properties, it is prepared, as follows, diagrams that show the variations of the values of the elastic constants, in function of the angle of inclination of reinforcement fibers, of the laminae considered orthotropic. For this analysis, it is considered that the laminae are strengthened with carbon fibers and possess the following elastic properties: $E_x = 140,00$ GPa; $E_y = 14,00$ GPa; $G_{xy} = 5,00$ GPa and $\nu_{xy} = 0,2$. Thus, using Equation 2 and considering that: $\bar{S}_{26} = \frac{\eta_{xy,y}}{E_y}$; $\bar{S}_{16} = \frac{\eta_{xy,x}}{E_x}$; $\bar{S}_{11} = \frac{1}{E_x}$; $\bar{S}_{22} = \frac{1}{E_y}$ and $\bar{S}_{12} = -\frac{\nu_{xy}}{E_x}$, the following diagrams with the values for the variations of the elastic constants in relation to the angles of carbon fibers can be obtained:

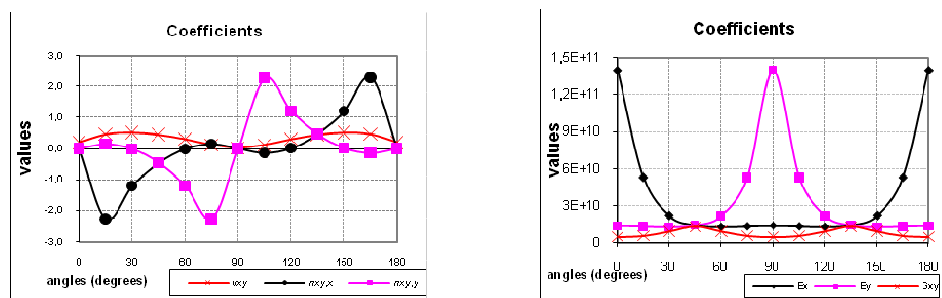


Figure 2: Values of the coefficients of mutual influence, Poisson's ratio, the longitudinal elastic moduli of and the shear modulus.

3 Elastic verification of Homogenization Method for anisotropic plates

It is well known from standard text books [11] that a usual way to calculate composite material structures is the use of homogenization process. This process is based on the determination of the anisotropic or orthotropic properties of reinforced materials considering matrix and reinforcement working together. In this article, a simple finite element code [12] that allows the insertion the several fibers in the bi-dimensional media considered homogeneous is applied. In this example a specimen of fiber reinforced plate (see Figure 3) is analyzed using the code. The space between bars and the cross section diameter of bars is also highlighted in Figure 3. The indicated constant displacements are applied separately. Applying the displacement in x direction one calculates the average stress (reaction) in x direction and the average displacement in the y direction, and it is possible to calculate E_x and ν_{xy} . Analogously for y direction one calculates E_y and ν_{yx} . Table 1 presents these material properties.

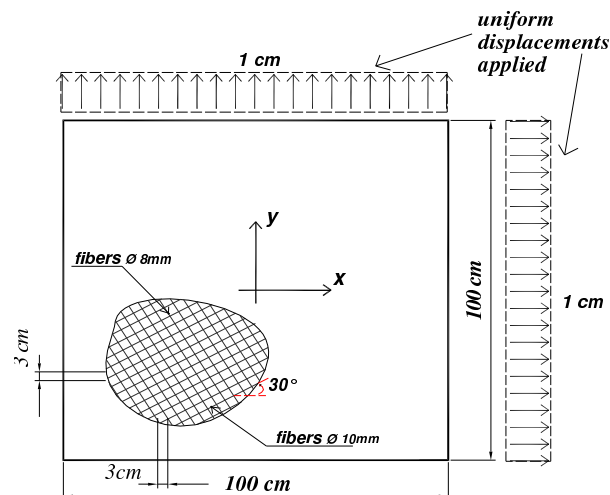


Figure 3: Two-directions off-axis elastic reinforced plates in the global axes of structure.

Thus, with the use of the bi-dimensional code is possible to calculate elastic properties of tensile plates with general anisotropy. When applied displacements in the global directions of plates of Figure 3, with the materials considering isolated have the properties showed in Table 1, is possible to obtain the anisotropic properties showed in tables 2 and 3:

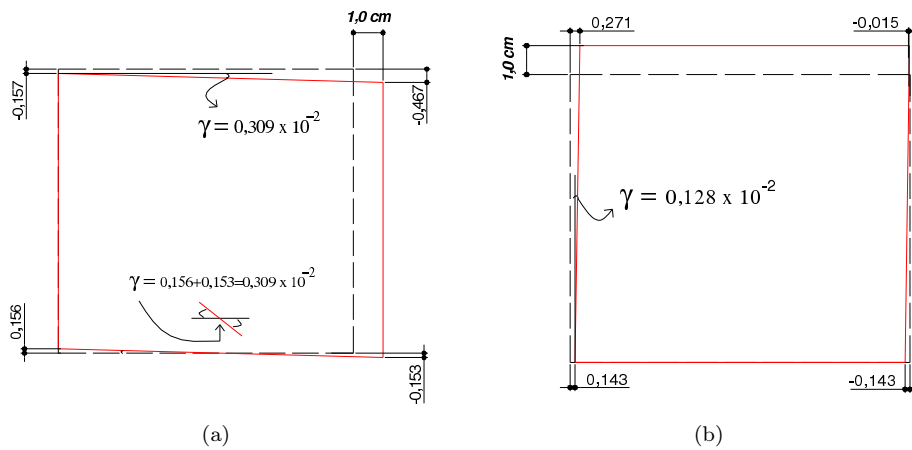
For the analytical determination the coefficients of mutual influence ($\eta_{xy,x}$ and $\eta_{xy,y}$), which are of difficult experimental determination is necessary to measure the distortions in the tensile plate after the application of the displacements, Figure 4.

Table 1: Elastic properties of fibers and matrix.

Material	Elastic Properties (Local directions of material)			
	E_1 (MPa)	E_2 (MPa)	ν	G_{12} (MPa)
Fiber of 10mm	210.000,0	210.000,0	0,3	80.000,0
Fiber of 8mm	150.000,0	150.000,0	0,3	62.500,0
Cementitious Matrix	20.000,0	20.000,0	0,2	8.333,0

Table 2: Elastic properties obtained from the anisotropic plates of Figure 3.

Material	Elastic Properties (Global directions)		
	E_x (MPa)	E_y (MPa)	G_{xy} (MPa)
Composite plate	24.855,65	22.648,91	9.465,21

Figure 4: Displacements applied in x direction (a) and Displacements applied in y direction (b).

Where,

$$\eta_{xy,x} = \frac{\gamma_{xy}}{\varepsilon_x} = \frac{0,309 \times 10^{-2}}{1,0 \times 10^{-2}} = 0,309 \Rightarrow -0,309 \quad \text{and} \quad \eta_{xy,y} = \frac{\gamma_{xy}}{\varepsilon_y} = \frac{0,128 \times 10^{-2}}{1,0 \times 10^{-2}} = 0,128 \Rightarrow -0,128$$

Table 3: Elastic coefficients obtained from anisotropic plate of Figure 3.

Material	Elastic Coefficients (global directions)			
	$\eta_{xy,x}$	$\eta_{xy,y}$	ν_{xy}	ν_{yx}
<i>Composite plate</i>	-0,309	-0,128	0,313	0,285

4 Displacements and stresses in anisotropic beams

It is analyzed in the these sections the displacements and the stresses in anisotropic laminate beams, subjected to uniformly distributed load, by means of the equations developed for Lekhnitskii et al. [6] and also using of the method developed for Hashin [8].

5 Displacements in anisotropic cantilever beams in accordance with Lekhnitskii et al. [6]

The displacements of laminate cantilever beams are analyzed, considered homogeneous (method of the homogeneity) and anisotropic, through the solutions obtained for Lekhnitskii et al. [6] for the analysis of anisotropic beams, as Figure 4:

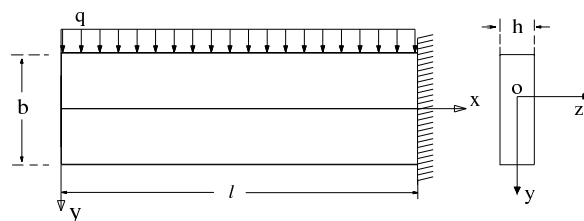


Figure 5: Cantilever beam subjected to uniformly distributed load.

This analysis is performed by means of comparative diagrams between the solutions of displacements for an anisotropic beam, according to Equation 4, and solutions obtained for isotropic beams, submitted and not submitted the influence of the shear, and also, with numerical solutions for deriving orthotropic beams of one commercial program of finite elements with linear approximation. According to Lekhnitskii et al. [6], the displacements (y – direction) for cantilever anisotropic beams, Figure 5, can be given by Equation 4:

$$v = \frac{q}{24E_x I} (x^4 - 6l^2 x^2 + 5l^4) + \frac{qh^2}{80I} \left(-3 \frac{\nu_{xy}}{E_x} + 4 \cdot \frac{1}{G_{xy}} - \frac{32}{3} \cdot \frac{\eta_{xy,x}^2}{E_x} \right) (l^2 - x^2) \quad (4)$$

In Equation 4, E_x is the longitudinal elastic modulus, G_{xy} is the shear modulus, ν_{xy} is Poisson's ratio and $\eta_{xy,x}$ is the coefficient of mutual influence of 1st kind that quantifies the influence of shear stresses in normal deformations. For the isotropic beams, when it is considered influence of the shear, the same equations of displacements of the anisotropic beams are used, however, omitting the terms where the coefficients of mutual influence of 1st kind ($\eta_{xy,x}$) are present. In case of not considering the influence of the shear, the first term of Equation 4 is used only.

Taking into account the presented elastic constants a strengthened polymeric lamina with carbon fibers into account, it is necessary to adopt a value for the angle of inclination of fibers, and thus, to determine the values of these constants for the geometric system of reference of the beam. Hence, an angle of inclination (θ) of $+15^\circ$ was adopted and considering Equation 2. The results of elastic constants are $E_x = 53,00$ GPa, $E_y = 13,40$ GPa, $G_{xy} = 5,92$ GPa, $\nu_{xy} = 0,47$ and $\eta_{xy,x} = -2,28$.

In this way, having the presented data, it is possible to prepare the comparative diagrams of displacements (y - direction) of the laminate beams (LEK) with the isotropic ones, considering the influence of the shear (Timoshenko's theory - ISO1) or not (Euler-Bernoulli's theory - ISO2) and with the orthotropic ones whose solutions are numerical (ANSYS [13] - COM). For the laminate beam whose relation $h/l = 1/10$ and $h/l = 1/5$, it has the following diagrams:

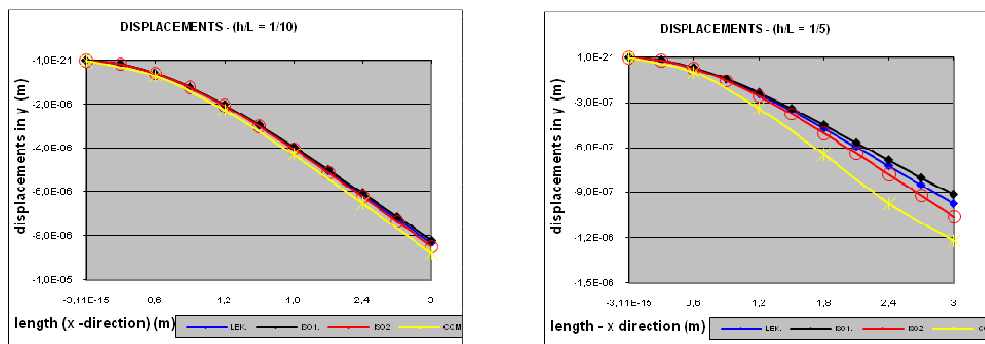


Figure 6: Displacement of a laminate cantilever beam, relations: ($h/l = 1/10$) and ($h/l = 1/5$), of two isotropic ones, considering the shear (ISO1) and not considering (ISO2), and of an orthotropic one.

After presenting the comparative diagrams of the displacements, it can be observed that, proportional to the increase of the relation (h/l), it exists an increase in the differences among the displacements of the cantilever beams analyzed here. Taking the influence of the shear into account, the isotropic beams present the lesser displacements. The laminate beams considered anisotropic (evidencing the presence of the coefficient of mutual influence $\eta_{xy,x}$) also possess lesser displacements than the isotropic beams (theory of Bernoulli-Euler) or the orthotropic ones.

Pointing out still that in the numerical response function of the orthotropic beam it was reckoned the influence of the modulus of elasticity E_y (lesser than the E_x) in the solution, what does not occur with the analytical expressions of displacements, for the plane case of the isotropic elasticity.

5.1 Stresses in anisotropic cantilever beams – Analytical Method of Hashin [8]

Here, the distributions of normal and shear stresses in laminate cantilever beams by means of an analytical method are analyzed, based on the stress function of Airy (ϕ), considered for Hashin [8] for the analysis of plane anisotropic beams, as Figure 7:

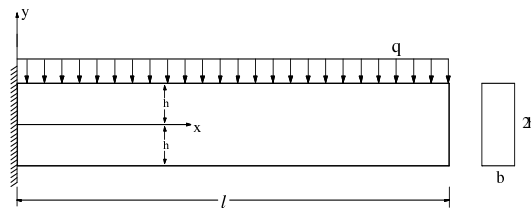


Figure 7: Cantilever beam, subjected to the uniformly distributed loads.

Thus, it is necessary to consider the formulation of anisotropic plane problem. According to Hashin [8], it can be written by:

$$S_{22}\phi_{,1111} - 2S_{26}\phi_{,1112} + (2S_{12} + S_{66})\phi_{,1122} - 2S_{16}\phi_{,1222} + S_{11}\phi_{,2222} = 0 \quad (5)$$

that models the anisotropic plane problem. As an application of it, as an example, the study of stresses in laminate beams, where are considered anisotropic and homogeneous. It is important to notice that the solution of Equation 5 can be given by the stress function of Airy (ϕ). In this way, Hashin presented an analytical method that allows the construction of a stress function polynomial that satisfies Equation 6:

$$\phi(x, y) = \sum_{m=0}^{m=M} \sum_{n=0}^{n=N} C_{mn} x^m y^n \quad (6)$$

where C_{mn} are constants to be determined by the resolution of a linear system of equations.

Introducing Equation 6 in Equation 5 and equating the coefficients $x^m y^n$ of equal powers, Hashin develops relations, among the C_{mn} coefficients, that are used for assembling of the system of equations:

$$\begin{aligned} & S_{2222}(m+2)(m+1)m(m-1)C_{m+2,n-2} - 4S_{2212}(m+1)m(m-1)(n-1)C_{m+1,n-1} \\ & + 2(S_{1122} + 2S_{1212})m(m-1)n(n-1)C_{mn} - 4S_{1112}(m-1)(n+1)n(n-1)C_{m-1,n+1} \\ & + S_{1111}(n+2)(n+1)n(n-1)C_{m-2,n+2} = 0 \end{aligned} \quad (7)$$

where $m \geq 2$ and $n \geq 2$. If in any problem, the biggest power of variable x in Equation 6 is M , then the biggest power of the variable y is given by $N = M + 3$.

The number of necessary equations for each specific problem, from the relations of Equation 7 and of the boundary conditions, can be obtained through the arithmetical series: $S = 1/2(M+1)(M+8)$.

From this, it is possible to find the coefficients C_{mn} and determined, then, the stress function that is the solution of the problem of stresses. Following this methodology of Hashin's method it is applied for the study of stresses in laminate beams. The obtained results of stresses are compared with solutions for isotropic beams too, considering the influence of the shear, and later, without this consideration, and also with numerical solutions for orthotropic beams. Indeed, for the cantilever beam of Figure 7 it has the following boundary conditions: $\phi(x, -h) = 0$; $\phi(x, h) = \frac{q}{2}(l-x)^2$; $\phi(x, -h)_{,2} = 0$ and $\phi(x, h)_{,2} = 0$.

The biggest power of x in the boundary conditions is $M = 2$. Thus, $N = M + 3 = 5$, and the stress function becomes:

$$\begin{aligned}\phi(x, y) &= \sum_{m=0}^{m=2} \sum_{n=0}^{n=5} C_{mn} x^m y^n = \\ &= C_{00} + C_{01}y + C_{02}y^2 + C_{03}y^3 + C_{04}y^4 + C_{05}y^5 + C_{10}x + C_{11}xy + C_{12}xy^2 + C_{13}xy^3 + C_{14}xy^4 + \\ &+ C_{20}x^2 + C_{21}x^2y + C_{22}x^2y^2 + C_{23}x^2y^3\end{aligned}\quad (8)$$

The number of necessary equations for the determination of the C_{mn} coefficients is given by $S = 15$.

Inserting the stress function in the boundary conditions and equating the coefficients x of equal powers it has 12 equations. The three remaining equations come from the relations of Equation 7, respecting thus the inequality $m + n \leq 5$. From the 15 equations it is possible to solve a system to find the 15 unknown coefficients C_{mn} . Substituting the coefficients, the stress function becomes:

$$\phi(x, y) = \frac{-q(h+y)^2 \left(\begin{aligned} &10\alpha_{04}^2(2h-y)(l-x)^2 - 2\alpha_{13}^2(h-y)^2y + \alpha_{04}(h-y)^2 \cdot \\ &\cdot (5\alpha_{13}(l-2x) + 2\alpha_{22}y) \end{aligned} \right)}{80 \cdot \alpha_{04}^2 \cdot h^3} \quad (9)$$

where the constants α_{ij} are substituted by the usual constants of engineering:

$$\alpha_{04} = S_{1111} = S_{11} = \frac{1}{E_x}; \quad \alpha_{22} = S_{1122} + 2 \cdot S_{1212} = \frac{-\nu_{xy}}{E_x} + \frac{1}{2 \cdot G_{xy}}; \quad \alpha_{13} = 4 \cdot S_{1112} = \frac{\eta_{xy,x}}{2 \cdot E_x}$$

By using Airy's function, it has the following stresses:

$$\begin{aligned}\sigma_x = \frac{\partial^2 \phi(x, y)}{\partial y^2} &= \frac{q \left[\left(3E_x y + 4G_{xy} \left(\begin{aligned} &-12y \cdot \eta_{xy,x}^2 + 5l \cdot \eta_{xy,x} - 10x \cdot \eta_{xy,x} \end{aligned} \right) \right) h^2 \right]}{40h^3 G_{xy}} + \\ &+ \frac{q \left[5y \left(2G_{xy} \left(\begin{aligned} &3l^2 - 6xl - 6 \cdot \eta_{xy,x} \cdot yl + 3x^2 + 8 \cdot \eta_{xy,x}^2 \cdot y^2 + \\ &+ 2 \cdot \nu_{xy} \cdot y^2 + 12 \cdot \eta_{xy,x} \cdot x \cdot y \end{aligned} \right) - E_x y^2 \right) \right]}{40h^3 G_{xy}}\end{aligned}\quad (10)$$

$$\tau_{xy} = \frac{\partial^2 \phi(x, y)}{\partial y \partial x} = \frac{q(3l - 3x - 4 \cdot \eta_{xy,x} \cdot y)(y^2 - h^2)}{4h^3} \tag{11}$$

In the comparative diagrams, presented as follows, it is considered the same type of composite laminae. With a load of 10 kN/m applied in the beams. For the beams whose relation $h/l = 1/10$, it has the following diagrams of normal and shear stresses in the cross section:

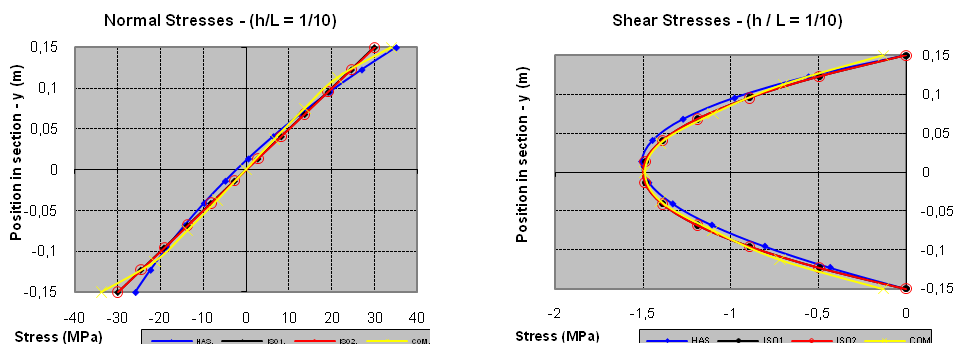


Figure 8: Normal and shear stresses in the laminate cantilever beam, relation ($h/l = 1/10$), in two isotropic ones, considering the shear (ISO1) and not considering (ISO2), and in an orthotropic one.

For the beams whose relation $h/l = 1/5$, it has the diagrams:

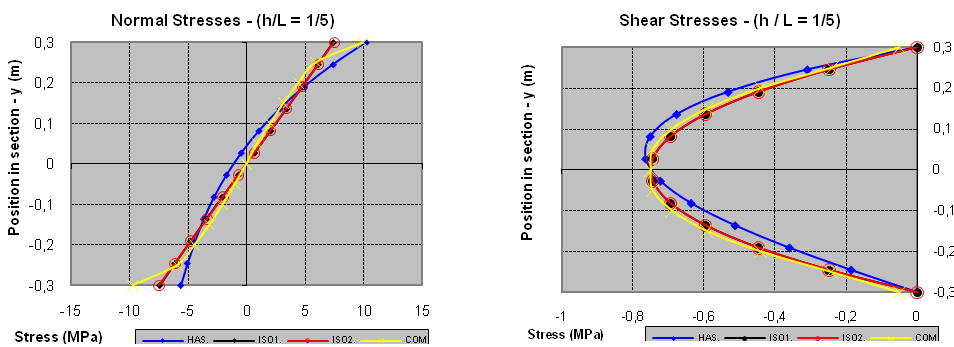


Figure 9: Normal and shear stresses in the laminate cantilever beam, relation ($h/l = 1/5$), in two isotropic ones, considering the shear (ISO1) and not considering (ISO2), and in an orthotropic one.

It is observed that an increase of the relation (h/l) results an increase in the differences between the isotropic and orthotropic elastic behavior of the beams. It also notices that the behavior of the stresses in the laminate beams is not symmetrical.

6 Conclusions

This paper presented both some general concepts on anisotropy and an analysis of the influence of the anisotropy on distributions of stresses and displacements in fiber-reinforcement laminate beams.

In the analysis of the displacements it was verified that the laminate beams presented greater difference of behavior in relation to the isotropic beams, especially when it is not taken the shear effect into consideration, for the two relations (h/l). With respect to the displacements of the isotropic beams, it is noticed that the consideration of the shear effect in these beams (Timoshenko's theory) leads to the different results of the presented for the isotropic beams where this consideration is not made (Euler-Bernoulli's theory), mainly for the beams of lesser span. Therefore, depending on the orientation of fibers in the laminae of the analyzed beam, the determination of the displacements of the beam, admitting the theory of Euler-Bernoulli, can originate results very different of whom that will really occur.

Considering the participation of the cross section height – beam span relation (h/l) in the behavior of the distributions of displacements and of stresses, it is observed that an increase in this relation produces greater differences in relation to the isotropic beams considered in this work. This is due to the fact that beams with lesser spans, the contribution of the shear in the displacements is bigger, bringing up then as consequence, a bigger participation of the anisotropy, associated with the mutual influence coefficients that relate shear with normal deformation.

In general, the stress functions have shown efficient to solve of problems of the mechanics of solids considering the analytical development only. However, it is necessary to point out, that the methods of solutions based on the stress functions are approached due to the polynomial form of the stress function cannot be admitted as an accurate solution.

Acknowledgement The authors gratefully acknowledge FAPESP, CNPq and CAPES, Brazilian Foundations for the financial supporting of this research.

References

- [1] Green, A. & Zerna, W., *Theoretical Elasticity*. Clarendon Press: Glasgow, p. 442, 1954.
- [2] Nair, S. & Reissner, E., On the determination of stresses and deflections for anisotropic homogeneous cantilever beams. *ASME Journal of Applied Mechanics*, **43**, pp. 75–80, 1976.
- [3] Kilic, O., Alaattin, A. & Dirikolu, M.H., An investigation of the effects of shear on the deflection of an orthotropic cantilever beam by the use of anisotropic elasticity theory. *Composite Science and technology*, **61**, pp. 2055–2061, 2001.
- [4] Mascia, N. & Vanalli, L., Analysis of stress and strain in wood beams. *Fifth International Conference on Space Structures*, University of Surrey: England, 2002.

- [5] Mascia, N.T., Vanalli, L., Paccola, R.R. & Scoarish, M., Mechanical behaviour of wood beams with grain orientation. *Mecom 2010-Cilamce 2010*, Asociacion Argentina de Mecanica Computacional: Buenos Aires, volume 1, pp. 1–16, 2010.
- [6] Lekhnitskii, S., Tsai, S. & Cheront, T., *Anisotropic plates*. Gordon and Breach Science Publishers: New York, 1st edition, p. 534, 1968.
- [7] Timoshenko, S.P. & Goodier, J.N., *Theory of Elasticity*. 3rd edition, p. 567, 1970.
- [8] Hashin, Z., Plane anisotropic beams. *Journal Applied Mechanics, Trans of Asme*, pp. 257–262, 1967.
- [9] Murakami, H., Reissner, E. & Yamakawa, J., Anisotropic beam theories with shear deformation. *ASME Journal of Applied Mechanics*, **63**, pp. 660–668, 1996.
- [10] Lekhnitskii, S., *Theory of Elasticity of an Anisotropic Body*. Mir: Moscou, 1st edition, p. 430, 1981.
- [11] Hyer, M.W., *Stress Analysis of fiber-reinforced Composite Materials*. McGraw-Hill Publ.: New York, p. 627, 1997.
- [12] Vanalli, L., *BEM and FEM applied to viscoplastic problem for anysotropic and composite media*. Ph.D. thesis, University of São Paulo, Brazil, 2004.
- [13] Ansys Inc., Houston, *ANSYS User's manual*, 1995. Revision 5.2.

Identification of material parameters for elastoplastic model using a Digital Image Correlation method

J.M. Vassoler, A.C.B. Guimarães Neto, L.F.C. Botega, E.A. Fancello
*Departamento de Engenharia Mecânica, Universidade Federal de Santa Catarina,
Campus Universitário, Trindade, 88040-970, Florianópolis, SC – Brazil*

Abstract

Accurate numerical simulations depend on appropriated constitutive models to represent the mechanical behavior of nonlinear materials. The material parameters of these models are usually obtained by means of parametric identification procedures using data acquired from experimental tests. In case of localized heterogeneous displacement fields, commonly found in specimens submitted to finite strains, contact measurement techniques are no longer appropriate. This limitation leads to the use of non-contact measurements, like the Digital Image Correlation (DIC) method. This method has shown a good performance in material characterization procedures due its capability to measure the entire displacement field over the specimen. In the present study, a procedure for material parameter identification of an elastoplastic model is tested. The experimental data was obtained from axial loading tests on a thermoplastic specimen. In the identification process, an initial guess of the material parameters is used as input data in a couple of numerical simulations of the experimental tests. The numerical solution of the reaction force and the displacement of points previously defined over the specimen surface compose the output data used in the cost function of the minimization problem. The displacements measured by the DIC method of the same points used in the numerical simulations are included in the cost function, which is calculated as the sum of squared differences between the experimental and numerical data of force and displacements. Loading and unloading cycles as well as monotonic loading with necking formation are performed at room temperature in order to obtain the beginning of the plastic region and the plastic evolution.

Keywords: Digital Image Correlation, parameter identification, material properties.

1 Introduction

The numerical simulation of structural components needs suitable constitutive models and appropriated material parameters to describe its mechanical behavior. In order to determine the material parameters, experimental tests are performed in specimens and the experimental conditions are numerically reproduced in a simulation.

The mixed numerical-experimental procedure has been used in inverse modeling in several areas and it is widely applied in parameter identification procedures. Several experimental procedures can be set up to analyze the material mechanical behavior. Tensile tests are commonly used due to its simplicity. In Mahnken [1] a material characterization is presented for an axisymmetric tensile bar of ferritic steel. A sensitivity analysis is performed and the gradient-based descent methods are used for the minimization of a least-square function. Other example of a possible approach for the inverse problem is found in Gavrus et al. [2] to characterize a thermal-viscoplastic model for Aluminum by means of a torsion test.

The presence of finite and localized strain in nonlinear materials, like metals, rubbers and plastics, turns the identification of material parameters a non trivial task. Experimental uniaxial tests provides non-useful or insufficient information about the mechanical behavior of the material, especially for nonlinear polymeric materials. In Frank and Brockman [3], the authors notice the formation of a traveling neck in glassy polymers materials under tension, differently of the metallic materials that have a localized necking phenomenon. Second the author, this particular behavior of the necking can mask the mechanical behavior of the real stress-strain curve.

The identification of the elastic limit, to determine the transition between elastic and plastic regions of the material, can be made by successive loading/unloading operations in the specimen, like shown in Fig. 1. The elastic limit is achieved when a permanent deformation is observed [4]. In Yoshida [5] the author performed four types of experimental tests and proposed a viscoplastic constitutive model for metallic materials.

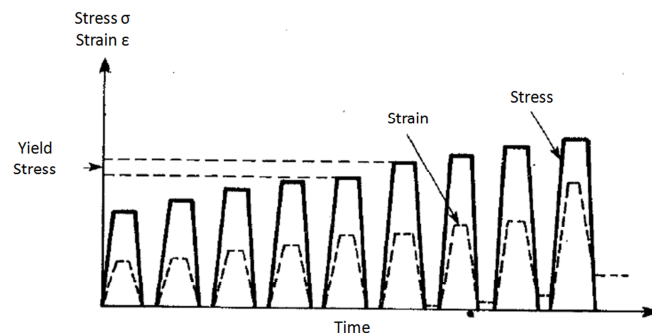


Figure 1: Elastic limit determination [4]

Nonhomogeneous deformation fields, as in the necking region, are capable to add extra information regarding of material behavior, as presented in Oomens et al. [6]. In this case, to correctly identify the constitutive parameters is useful to know the displacement field in a region within a triaxial stress states. Measurement techniques such as clip-gauges or extensometers have some limitations since they need physical contact, which complicate their use in the presence of finite and localized strains. Furthermore, non-contact techniques, like optical methods, can provide the needed displacement field

over a region of interest (ROI).

The optical method of digital image correlation (DIC) was extensively studied by Sutton et al. [7], Lu and Cary [8] and Pan et al. [9], showing a great acceptability in academic and industrial fields. This optical technique is capable to track predefined points on the specimen surface in a digital image sequence, obtained using video cameras in experimental tests. The DIC method has been applied into different engineering problems. In Roux et al. [10] the DIC method is presented as an alternative to capture the crack progressing in a cyclic tensile test. Parameters identification procedures using the DIC method have been performed to characterize different constitutive models involving elasticity, plasticity and viscosity. Avril et al. [11] uses the DIC method in a tensile test for notched steel bars in order to identify the material parameters of an elasto-visco-plastic constitutive model. In Kajberg and Lindkvist [12] the plastic behavior of thin sheets of two types of hot-rolled steel are analyzed using two models: piecewise linear plasticity model and a parabolic hardening model. The material parameters are adjusted to achieve a minimum in a objective function by means of a inverse modelling including finite element analysis. The inverse problem including the optical measurement method also demonstrated good results in different experimental tests, as observed in Sutton et al. [13] and Milani et al. [14]. In these works the authors performed a parameters identification of a Johnson-Cook model, respectively, for tensile and compressive tests. In Wang and Cuitiño [15] and Jin et al. [16], the authors use the DIC method to capture localized and heterogeneous strain fields in order to characterize polymeric foams in compressive tests.

In Meuwissen et al. [17] the author proposes the use of non-standard aluminum specimens, where the force obtained from the testing machine and the displacements measured optically at the clamps region are used as boundary conditions of its numerical simulation. Then, the objective function is constructed only with the displacements measured numerically and experimentally at the necking region. This study shown the flexibility provided by the use of measurement optical methods associated to numerical simulation of non-standard geometries of specimens. The DIC method is important to the identification of the material parameters, considering that it can provide essential information about the three-dimensional displacement field over the specimen surface [18], i.e., it can capture the formation and propagation of the necking during the tensile test.

Recently, the material characterization with optical methods has demonstrated interest in the medical community, especially in characterization of biological tissues. It is due to the fact that the optical method allows to test different geometries in experimental tests *in vivo*. Gambarotta et al. [19] studied the mechanical characterization *in vivo* of human skin to simulate a reconstructive surgery with the finite element method. In Gundiah et al. [20] is used a neo-Hookean isotropic model to characterize elastin networks of porcine arteries. The experimental data was captured from biaxial test in order to analyze the structural integrity of blood vessels in cycles simulating a pulsatile motion.

In view of the advantages of including a measurement optical method to a parameter identification procedure, the main objective of the present work is to study a methodology to characterize polymeric materials under finite strains using a optical method and modified standard specimens. The optical method provides extra information concerning the material mechanical behavior during test, mainly in the necking region where the nonhomogeneous fields are noticed.

2 Experimental procedure

2.1 Specimen definition

The identification of the mechanical behavior of nonlinear materials under finite strain can be a complicate task since they usually present a high level of localized strains. The polymers are known by their complex mechanical behavior under finite strains, which provides high levels of heterogeneous strain characterized by increasing stiffness due to internal molecular orientation.

The specimens used in this work were manufactured with the glassy polymer Polyvinyl Chloride (PVC). This material presents a complex mechanical behavior and its stress-strain curve have been subject of discussion in [3]. Many studies on the mechanical behavior of glassy polymers were published showing an apparent stress drop in the real stress-strain curve right after yield. In [21] the author show experimental curves for some glassy polymers exhibiting yielding followed by intrinsic strain softening and subsequent orientation hardening. This mechanical behavior is presented in Fig. 2. Unlike the widely accepted softening behavior (stress drop), [3] attribute this behavior to the formation of a traveling neck that masks the actual stress response, claiming that the true stress for most polymers in the glassy regime does not actually decrease after yield.

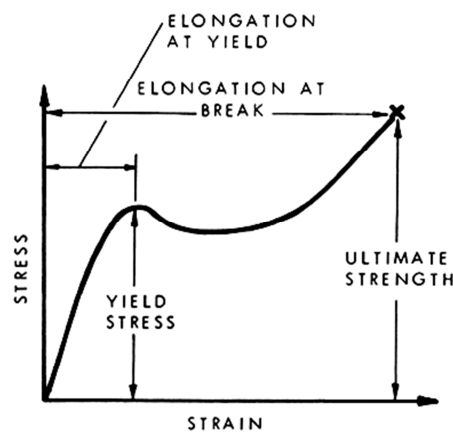


Figure 2: Generalized tensile stress-strain curve for polymeric materials [22]

The geometry of the specimen used in the present study is presented in Fig. 3, in which it was insert a notch at the central region in order to initiate the necking phenomenon in the ROI. This region is focused by the cameras and a clip-gauge is used to obtain its longitudinal displacement.

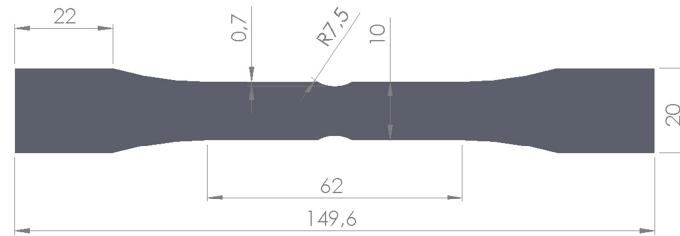


Figure 3: Test sample

2.2 DIC method

The DIC method tracks predefined points on the specimen surface in a sequence of digital images obtained by video cameras during an experimental test [7]. The method essentially finds the position of points, called markers, in a sequence of images, correlating the gray values of the neighbor pixels. The correlation is made within small squared areas of $(2M + 1) \times (2M + 1)$ pixels around the marker, called subsets, where the geometric center of each subset is a marker. A wide set of correlating coefficients may be found in the literature [9]. In this study is used the Zero-Normalized Sum Square Differences (ZNSSD) correlation criterion [23]:

$$C_{ZNSSD} = \sum_{i=-M}^M \sum_{i=-M}^M \left[\frac{f(x, y) - f_m}{\sqrt{\sum_{i=-M}^M \sum_{i=-M}^M (f(x, y) - f_m)^2}} - \frac{g(x', y') - g_m}{\sqrt{\sum_{i=-M}^M \sum_{i=-M}^M (g(x', y') - g_m)^2}} \right]^2 \quad (1)$$

where

$$\begin{aligned} x' &= x + \bar{u} = x + u + u_x \Delta x + u_y \Delta y + u_{xy} \Delta x \Delta y + u_{xx} \Delta x^2 + u_{yy} \Delta y^2, \\ y' &= y + \bar{v} = y + v + v_x \Delta x + v_y \Delta y + v_{xy} \Delta x \Delta y + v_{xx} \Delta x^2 + v_{yy} \Delta y^2, \end{aligned} \quad (2)$$

$f(x, y)$ is the gray value of the reference image at the pixel position (x, y) , $g(x, y)$ is the gray value of the target image at the pixel position (x', y') , f_m and g_m are respectively the means gray value of the reference and deformed subset, u and v are respectively the x - and y -directional displacement components of the reference subset center, u_x, u_y, v_x, v_y are the first-order displacement gradients and $u_{xx}, u_{xy}, u_{yy}, v_{xx}, v_{xy}, v_{yy}$ are the second-order displacement gradients. Equation 2, by means of the displacement gradients, allows to find the center of a deformed subset. Figure 4 shows the reference image with a reference subset of the marker $P(x_0, y_0)$ and its respective target subset (deformed) around the marker $P'(x'_0, y'_0)$ in the deformed image.

Two modifications proposed in Pan et al. [23] to deal with deficiencies of this method was implemented: a scanning strategy guided by the correlation coefficients of computed points to ensure the

convergence of consecutive points and the use of binary masks to modify the valid subset area in order to allow the computation of the markers displacement located near or at the boundaries of specimen. The mask is used in the subsets that may contain unwanted or foreign pixels from background image or other regions.

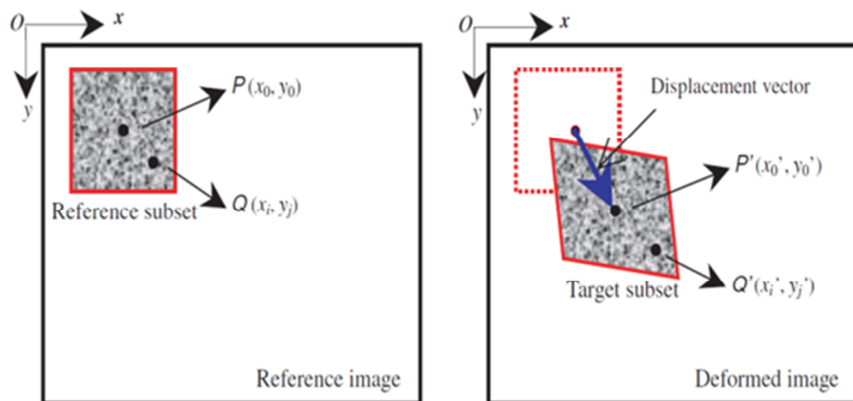


Figure 4: Reference subset and deformed/target subset [9].

To properly apply the method, a random speckle pattern is painted with an airbrush on the surface of the specimen, alternating black and white paint. The characteristics and randomness of this pattern has important influence on the accuracy of the correlation. According to Chu et al. [24], it should supply the information needed to correlate the subsets through the test.

2.3 Experimental tests

Two types of tensile tests were performed at room temperature, both in an universal testing machine equipped with a load cell and a clip-gauge that provide, respectively, the reaction force and longitudinal displacement along time. A monotonic loading test was conducted with a constant displacement rate of 2 mm/min , the same as the cyclic loading/unloading test. The cyclic test was included in this work in order to identify the transition between the elastic and plastic regions. The *Displacement x Time*, *Load x Time* and *Load x Displacement* curves recorded during both tests are shown in Fig. 5.

The optical information coming from DIC consists on the displacement field of a chosen ROI of the specimen surface along time. Figure 6 shows the image acquisition system in front of the specimen during the monotonic test, while Fig. 7 shows the three components X , Y and Z of the displacement at a deformed instant of time of the same test.

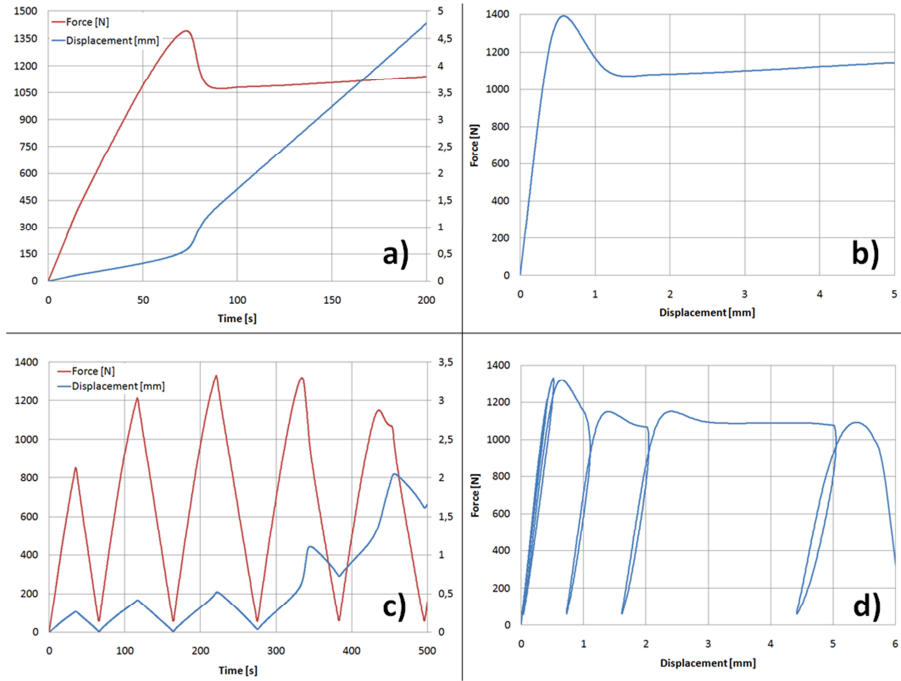


Figure 5: Uniaxial testing machine curves: a) and b) Monotonic test; c) and d) Cyclic test



Figure 6: Cameras arrangement during the test

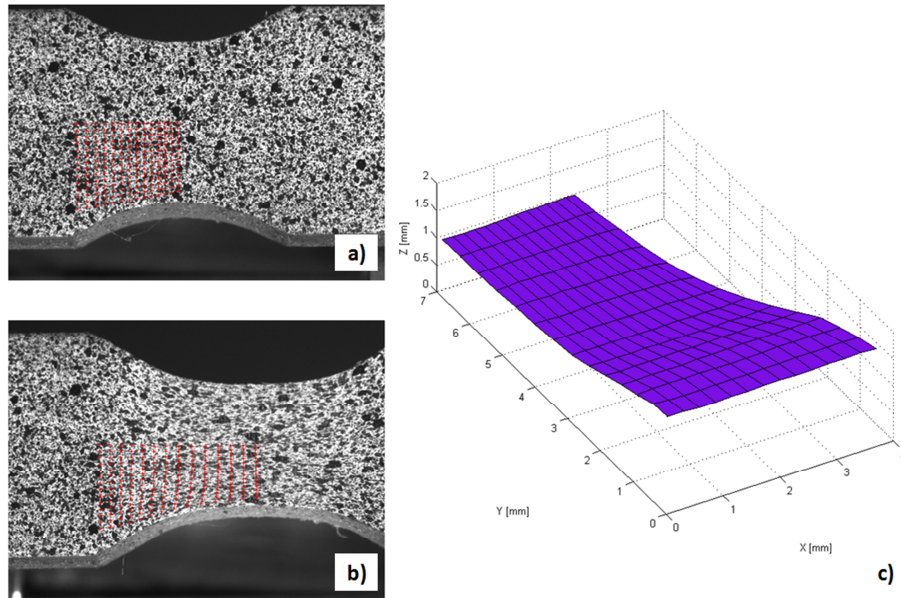


Figure 7: Displacement field: a) markers arrangement over the undeformed specimen; b) markers arrangement over the deformed specimen; c) total displacement of the deformed specimen

3 Numerical procedure

3.1 Geometry

A different 3D model of the specimen was generated for each performed test in order to have a perfect representation of the instrumented ROI of the specimen. The geometric models were generated from pictures captured by the cameras and measurements of the specimen. It was made in order to reduce the difference between the physical models and the mathematical representations, caused by the imprecisions on manufacturing process of the specimens. Only the region inside the clip gauge was used in the modeling and a symmetry condition in XZ plane was created in both cases, using only a half of the model. Additionally, vertices were added to the specimen surface with the same coordinates of the markers from DIC. Figure 8 shows the geometric models.

3.2 Finite Element model

The discretization in finite elements was made using the package ANSYS Workbench 12.1 [25]. The mesh generated for the monotonic and cyclic tests are shown in Fig. 9. For each test, the longitudinal displacement experimentally obtained from the clip-gauge is applied at one of the extremes of the

discretized specimen, while the longitudinal displacements at the other extreme are fixed.

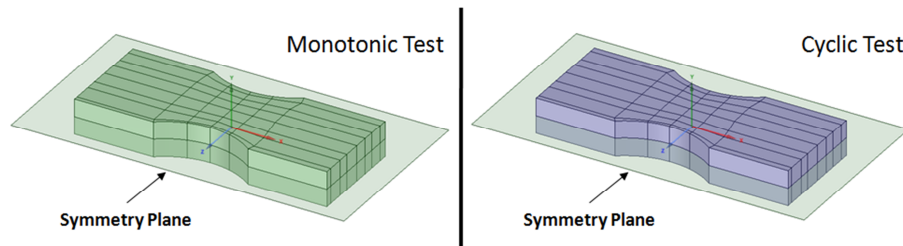


Figure 8: CAD model of the test specimens used for the monotonic and cyclic tests

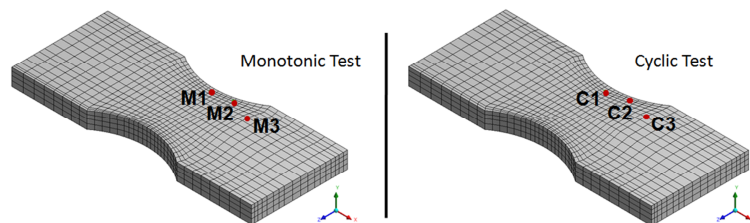


Figure 9: Finite element models for the monotonic and for the cyclic tests

In order to simulate the mechanical behavior of the material, the multi-linear elastoplastic model presented in Fig. 10 was chosen. This constitutive model was used due to its simplicity and capability to reproduce nonlinear elastoplastic behaviors, despite of its limitation to reproduce only stress-strain curves with positive tangent slopes. The material model has 2 parameters for the elastic part: elastic modulus E , Poisson ratio ν ; and 6 parameters for the multi-linear plastic part: the yield stress (σ_y), a stress increment (Δ), three tangent modulus (ϕ , H and I , where the last represent the orientation hardening of the molecules) and the hardening plastic strain (ε_p). The results of the numerical analysis provide the *Reaction force x Time* curve and *Displacement x Time* curves of X , Y and Z directions for each marker.

Since the true stress-strain curve of the PVC shows negative tangent slopes with a significant softening region (Fig. 2), this material model may not be able to reproduce the real mechanical behavior of the specimen. On other hand, if the true stress-strain curve of the PVC actually is in accordance to the assumption of [3], it is expected that the model will be able to achieve reasonable good solutions.

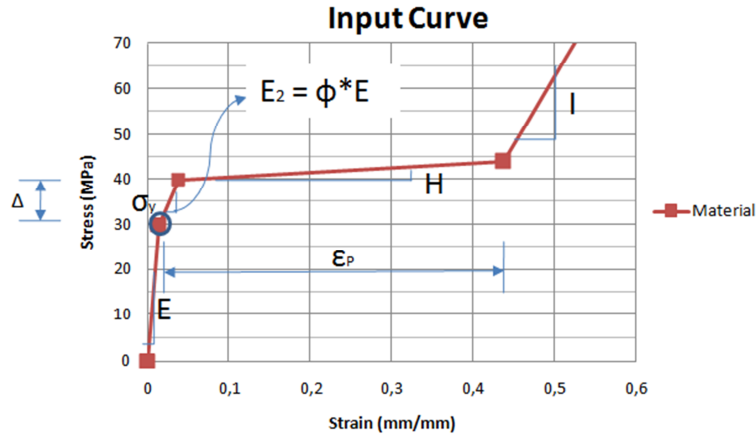


Figure 10: Constitutive model

4 Optimization process

The optimization procedure is used to seek a set of parameters that minimizes a cost function Ω . These parameters represent the best approximation between the experimental and numerical mechanical behavior. This cost function is defined based on the weighted least squares of the difference between experimental and numerical data, including monotonic and cyclic results in both:

$$\Omega = \sum_{i=1}^N [w^{F,m} (F^{num,m}(\mathbf{p})_{(i)} - F^{exp,m}_{(i)})^2 + w^{F,c} (F^{num,c}(\mathbf{p})_{(i)} - F^{exp,c}_{(i)})^2] + \sum_{i=1}^N \sum_{j=1}^M [w^{UX(j)} (UX^{num}(\mathbf{p})_{(i)}^{(j)} - UX^{exp(j)}_{(i)})^2] \quad (3)$$

where N is number of data used in the test, M is the number of markers analyzed, $w^{F,m}$ is the weight of the force for the monotonic case, $w^{F,c}$ is the weight of the force for the cyclic case, $w^{UX(j)}$ is the weight of the displacement of the j -th marker, $UX^{num(j)}$ is the i -th component of the numerical displacement of the j -th marker, $UX^{exp(j)}$ is the i -th component of the experimental displacement of the j -th marker, $F^{num,m}_{(i)}$, $F^{exp,m}_{(i)}$, $F^{num,c}_{(i)}$ and $F^{exp,c}_{(i)}$ are, respectively, the i -th component of the numerical force for the monotonic case, the i -th component of the experimental force for the monotonic case, the i -th component of the numerical force for the cyclic case and the i -th component of the experimental force for the cyclic case and \mathbf{p} represent the vector with the material parameters:

$$\mathbf{p} = \left[E \quad \nu \quad \sigma_y \quad \Delta \quad \phi \quad H \quad I \quad \varepsilon_p \right]. \quad (4)$$

The schematic representation of the parameter identification is shown in Fig. 11. The input data is the initial guess of the material parameters \mathbf{p} to approximate the experimental and numerical data. In the numerical analysis is computed the reaction force and the displacements of the markers. Then, the cost function Ω is computed in the optimization procedure and the material parameters are update. This procedure is repeated until the minimization of the cost function. In this study only the x -displacement of three markers (M1, M2 and M3) from the monotonic test (see Fig. 9) were used.

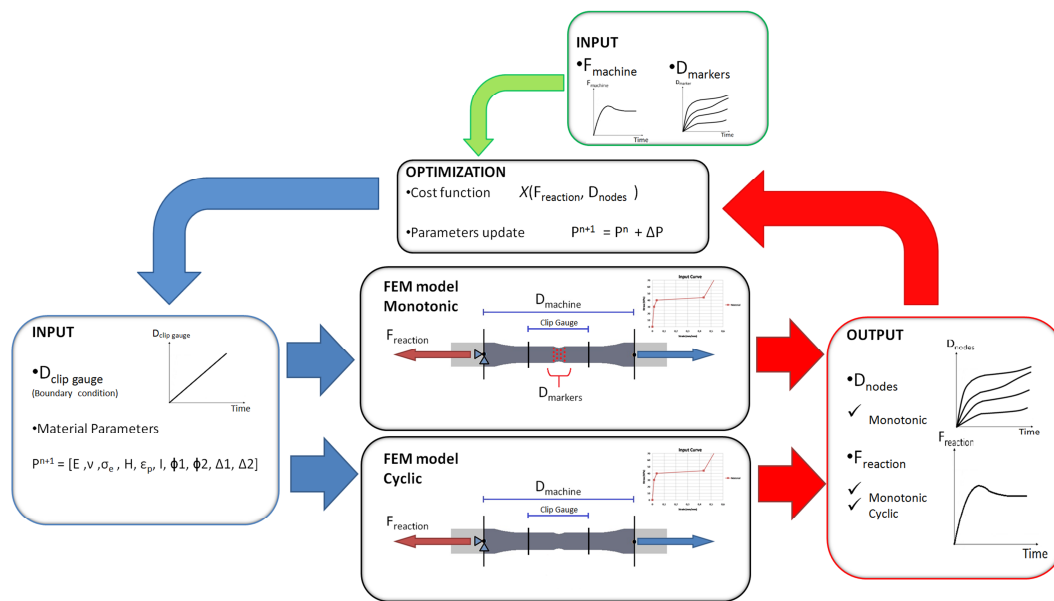


Figure 11: Optimization routine

The optimization process was performed in the commercial software modeFRONTIER [26]. Since the minimization involves 8 unknown parameters, a genetic optimization was used to obtain the global minimum candidates, and then, these candidates were used as initial guess of a gradient-based minimization. This strategy was used to avoid local minima.

5 Results

Different tests were carried out varying the weight of the force for the monotonic case $w^{F,m}$, for the cyclic case $w^{F,c}$ and of the displacements w^{UX} in the Eq. 3 in order to obtain an adequate fitting of the curves. Should be noted that $w^{F,m}$, $w^{F,c}$ and w^{UX} are used due to the magnitude of F, m and F, c being considerably higher than UX . When weights are set as $w^{F,m}$ and $w^{F,c} \gg w^{UX}$ good results were achieved for the force but the displacement over the surface shown considerable errors. Conversely,

when $w^{F,m}$ and $w^{F,c} \ll w^{UX}$ good results were achieved only for the displacement over the surface of the specimen. The material parameters obtained in the parameters identification procedure are shown in Table 1 and the numerical and experimental curves are shown in Fig. 12.

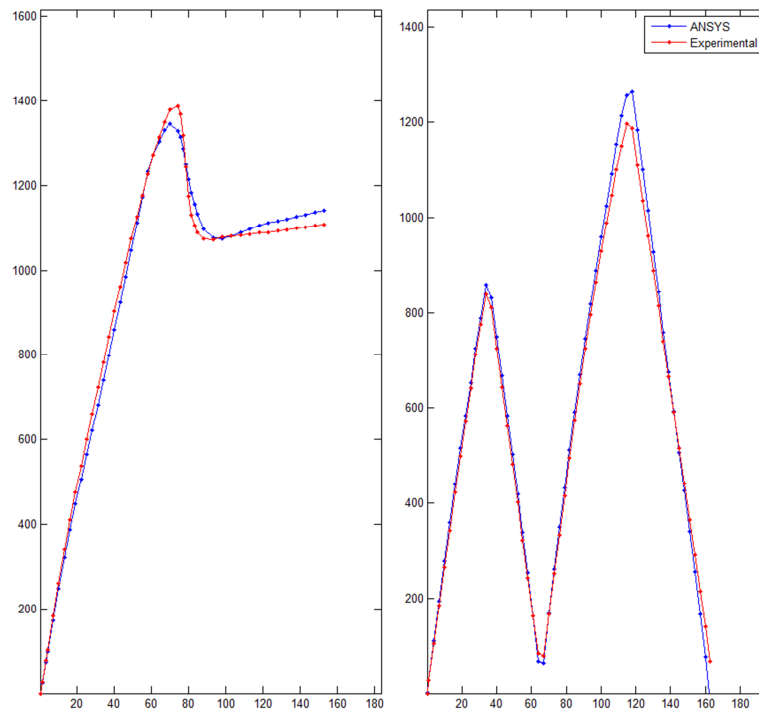


Figure 12: Numerical and experimental curves for the monotonic and cyclic cases

6 Conclusion

In this study, the parametric identification using data acquired from different types of mechanical tests using an optical measuring system was investigated. Even with the highly heterogeneous strain fields behavior of the PVC material, the implemented DIC method could obtain useful information regarding the mechanical behavior of the material, principally during the traveling neck, at the surface of the necking region where the control points were analyzed.

The multi-linear elastoplastic model was chosen to represent the mechanical behavior of the PVC. As expected, the experimental and numerical results show relative differences, mainly at the elastic-

PARAMETER	VALUE
E	2680 MPa
ν	0.43
σ_y	46.30 MPa
ϕ	0.198
Δ	6.05 MPa
H	0 MPa
ε_p	0.397
I	141.29 MPa

Table 1: Material parameters results

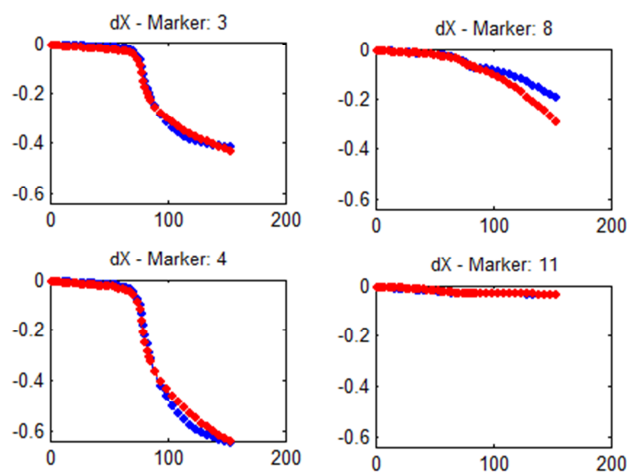


Figure 13: Numerical and experimental curves of four chosen markers

plastic transition (also observed by Meuwissen et al. [17]). It can be attributed to the elastic linear characteristic of the model or a possible tensile drop of the real stress-strain curve of the material (softening).

A cost function that has a multi-objective characteristic was used to deal with different magnitudes of the data present in the objective function (displacements and forces). From the results of the sensitivity analysis, only the experimental force is not enough to find the material parameters

since that different combinations of the parameters can result in exact match between the numerical and experimental reaction force, but quite different with regard to the experimental and numerical transverse displacement in the necking region.

Only three markers of the monotonic test were effectively used within the cost function and they seem to provide significative information of the traveling neck. In addition, only the data provided by the monotonic test is not enough to find the correct elastic limit. The data provided by the cyclic test was used to determine the range where the elastic limit occurs. It was necessary because the material doesn't have a clearly transition between the elastic and plastic region.

Despite of the simplifications, like the use of a simple material model and only three tracking points, it can be concluded that the use of DIC provided useful information to the inverse problem of material parameters characterization. In this context, the objective proposed with this study was successfully achieved and opens a promising field of further improvements with the use of nonlinear elastic-plastic or visco-elastoplastic models.

References

- [1] Mahnken, R., Aspects on the finite-element implementation of the gurson model including parameter identification. *International Journal of Plasticity*, **15(11)**, pp. 1111–1137, 1999.
- [2] Gavrus, A., Massoni, E. & Chenot, J.L., An inverse analysis using a finite element model for identification of rheological parameters. *Journal of Materials Processing Technology*, **60(1-4)**, pp. 447 – 454, 1996. Proceedings of the 6th International Conference on Metal Forming.
- [3] Frank, G.J. & Brockman, R.A., A viscoelastic-viscoplastic constitutive model for glassy polymers. *International Journal of Solids and Structures*, **38(30-31)**, pp. 5149–5164, 2001.
- [4] de Souza, S.A., *Ensaio Mecânicos de Materiais Metálicos. Fundamentos teóricos e práticos*. Edgard Bucher Ltda, 1982.
- [5] Yoshida, F., A constitutive model of cyclic plasticity. *International Journal of Plasticity*, **16(3-4)**, pp. 359 – 380, 2000.
- [6] Oomens, C., Ratering, M., Janssen, J., Kok, J. & Hendriks, M., A numerical-experimental method for a mechanical characterization of biological materials. *Journal of Biomechanics*, **26(4-5)**, pp. 617 – 621, 1993.
- [7] Sutton, M., McNeill, S., Helm, J. & Chao, Y., Advances in two-dimensional and three-dimensional computer vision. *Photomechanics*, pp. 323–372, 2000.
- [8] Lu, H. & Cary, P., Deformation measurements by digital image correlation: Implementation of a second-order displacement gradient. *Experimental Mechanics*, **40(4)**, pp. 393–400, 2000.
- [9] Pan, B., Qian, K., Xie, H. & Asundi, A., Two-dimensional digital image correlation for in-plane displacement and strain measurement: a review. *Measurement Science and Technology*, **20(6)**, pp. 062001–, 2009.
- [10] Roux, S., Réthoré, J. & Hild, F., Recent progress in digital image correlation: From measurement to mechanical identification. *Journal of Physics: Conference Series*, **135(1)**, p. 012002, 2008.
- [11] Avril, S., Pierron, F., Sutton, M.A. & Yan, J., Identification of elasto-visco-plastic parameters and characterization of Lüders behavior using digital image correlation and the virtual fields method. *Mechanics of Materials*, **40(9)**, pp. 729 – 742, 2008.
- [12] Kajberg, J. & Lindkvist, G., Characterisation of materials subjected to large strains by inverse modelling

- based on in-plane displacement fields. *International Journal of Solids and Structures*, **41(13)**, pp. 3439 – 3459, 2004.
- [13] Sutton, M., Yan, J., Avril, S., Pierron, F. & Adee, S., Identification of heterogeneous constitutive parameters in a welded specimen: Uniform stress and virtual fields methods for material property estimation. *Experimental Mechanics*, **48(4)**, pp. 451–464, 2008.
- [14] Milani, A., Dabboussi, W., Nemes, J. & Abeyaratne, R., An improved multi-objective identification of johnson-cook material parameters. *International Journal of Impact Engineering*, **36(2)**, pp. 294 – 302, 2009.
- [15] Wang, Y. & no, A.M.C., Full-field measurements of heterogeneous deformation patterns on polymeric foams using digital image correlation. *International Journal of Solids and Structures*, **39(13-14)**, pp. 3777 – 3796, 2002.
- [16] Jin, H., Lu, W.Y., Scheffel, S., Hinnerichs, T.D. & Neilsen, M.K., Full-field characterization of mechanical behavior of polyurethane foams. *International Journal of Solids and Structures*, **44(21)**, pp. 6930 – 6944, 2007.
- [17] Meuwissen, M.H.H., Oomens, C.W.J., Baaijens, F.P.T., Petterson, R. & Janssen, J.D., Determination of the elasto-plastic properties of aluminium using a mixed numerical-experimental method. *Journal of Materials Processing Technology*, **75(1-3)**, pp. 204 – 211, 1998.
- [18] Parker, J.W., *Development And Implementation Of A Low Cost Image Correlation System To Obtain Full-field In-plane Displacement And Strain Data*. Master of science in mechanical engineering, Montana State University, Bozeman, Montana, 2009.
- [19] Gambarotta, L., Massabò, R., Morbiducci, R., Raposio, E. & Santi, P., In vivo experimental testing and model identification of human scalp skin. *Journal of Biomechanics*, **38(11)**, pp. 2237–2247, 2005.
- [20] Gundiah, N., Ratcliffe, M.B. & Pruitt, L.A., The biomechanics of arterial elastin. *Journal of the Mechanical Behavior of Biomedical Materials*, **2(3)**, pp. 288–296, 2009.
- [21] Duan, Y., Saigal, A., Greif, R. & Zimmerman, M.A., A uniform phenomenological constitutive model for glassy and semicrystalline polymers. *Polym Eng Sci*, **41(8)**, pp. 1322–1328, 2001.
- [22] Blaga, A., Properties and behaviour of plastics. Report 157, NRC Institute for Research in Construction; National Research Council Canada, 1973.
- [23] Pan, B., Wang, Z. & Lu, Z., Genuine full-field deformation measurement of an object with complex shape using reliability-guided digital image correlation. *Opt Express*, **18(2)**, pp. 1011–1023, 2010.
- [24] Chu, T., Ranson, W. & Sutton, M., Applications of digital-image-correlation techniques to experimental mechanics. *Experimental Mechanics*, **25**, pp. 232–244, 1985.
- [25] ANSYS, Inc., *User guide for revision 12.1*. ANSYS, Inc., Pittsburgh, 2010. <http://www.ansys.com>.
- [26] modeFRONTIER, *The Multi-Objective Optimization and Design Environment. Manual do Usuário*. Esteco srl. Trieste, Itália., 2010. <http://www.modefrontier.com>.

Author Index

- Ávila, A.F., 25
Aguiar, A.R., 1
Alberti, A. R., 13
Alves, M., 353
Alves, M.K., 131
Beck, A.T., 41, 311
Benvenuti, I.J., 381
Bittencourt, M.L., 63
Botega, L.F.C., 555
Brilla, I., 77
Calle, M.A.G., 353
Campeão, D.E., 401
Campos Filho, A., 215
Cardoso, E.L., 175
Cavallante, I., 89
Coelho, J.L.V., 103
Creus, G.J., 381
da Costa Mattos, H.S., 113
da Costa-Mattos, H.S., 103
da Silveira, O.A.A., 527
de Almeida, S.F.M., 89, 197
de Castro, J.T.P., 367
de Deus, H.P.A., 131
de Faria, A.R., 89, 159
de Jesus Miranda, C.A., 327
de Lima, A., 291
de Mendonça, P.T.R., 381
de Pina Filho, A.C., 455
Donadon, M.V., 89, 159
Dumont, N.A., 143
Dutra, M.S., 455
Eduardo, A.C., 25
Fainer, G., 327
Fancello, E.A., 555
Farias, J.M.C., 175
Ferreira, A.P.C.S., 197
Figueiredo, M.P., 215
Fonseca, J.S.O., 527
Fujarra, A.L.C., 477
Furlan, F.A.C., 63
Gomes, W.J.S., 41
Guimarães Neto, A.C.B., 555
Iturrioz, I., 249
Kühl, A., 381
Karagiozova, D., 231
Kosteski, L.E., 249
Labaki, J., 267
Lellep, J., 277
Lopez, R.H., 311
Madenci, E., 431
Maghous, S., 215
Marczak, R.J., 291
Mascia, N.T., 541
Mattar Neto, M., 327
Mattedi, R., 341
Mazzariol, L.M., 353
Meggiolaro, M.A., 367
Mesquita, E., 267
Mourão, R.P., 327
Moura, R.T., 353
Muñoz-Rojas, P.A., 175, 381
Nicolazzi, L. C., 13

Novotny, A.A., 401
Nunes, L.C.S., 341, 421, 517
Oshiro, R.E., 353
Oterkus, E., 431
Pérez-Fernández, L.D., 1
Paccola, R.R., 541
Paim, L.M., 113
Pedroso, L.J., 489
Pereira, J. C. de C., 13
Pesce, C.P., 477
Pimenta, P.M., 445
Prusty, P.G., 467
Puman, E., 277
Rabelo, M.A., 477
Rajapakse, N., 267
Reis, J.M.L., 103, 113
Ribeiro, P.M.V., 489
Riera, J.D., 249
Rizzi, P., 89
Scoaris, M.R., 541
Siddiqui, N.A., 505
Silva Neto, A., 25
Silva, T.C., 517
Vanalli, L., 541
Vargas, E.Y.M., 143
Vassoler, J.M., 555